Hydro Place. 500 Columbus Drive.
P.O. Box 12400. St. John's. NL
Canada A1B 4K7
t. 709.737.1400 f. 709.737.1800
www.nlh.nl.ca

May 31, 2021

Board of Commissioners of Public Utilities
Prince Charles Building
120 Torbay Road, P.O. Box 21040
St. John's, NL A1A 5B2

Attention: Ms. Cheryl Blundon
Director of Corporate Services & Board Secretary

Dear Ms. Blundon:

Re: *Reliability and Resource Adequacy Study Review* – Labrador-Island Link Failure Investigation Reports

As committed in Newfoundland and Labrador Hydro's correspondence of April 12, 2021,[1] please find attached the following investigation reports provided by Nalcor Energy ("Nalcor") related to two separate Labrador-Island Link failure events earlier in 2021:

1. Failure Investigation Report – L3501/2 Tower and Conductor Damage, Icing Event January 2021 in Labrador; and

2. Failure Investigation Report – L3501/2 Pole Assembly Turnbuckle Failure, Failure Event February 2021 in Labrador.

As part of its investigation, Nalcor engaged Maskwa High Voltage Ltd. to complete a third-party engineering review of its root cause analysis related to the L3501/2 tower and conductor damage resulting from the January 2021 icing event. The review completed by Maskwa High Voltage Ltd. is also enclosed.

Should you have any questions, please contact the undersigned.

Yours truly,

NEWFOUNDLAND AND LABRADOR HYDRO

SWalsh

Shirley A. Walsh
Senior Legal Counsel, Regulatory
SAW/kd

Encl.

[1] Newfoundland and Labrador Hydro, "*Reliability and Resource Adequacy Study Review* – Labrador-Island Link Reliability Assessment – Board Questions – Hydro's Response," letter, April 12, 2021.

ecc: **Board of Commissioners of Public Utilities**
Jacqui Glynn
Maureen P. Greene, Q.C.
PUB Official Email

Newfoundland Power
Kelly C. Hopkins
Dominic J. Foley
Regulatory Email

Consumer Advocate
Dennis M. Browne, Q.C., Browne Fitzgerald Morgan & Avis
Stephen F. Fitzgerald, Browne Fitzgerald Morgan & Avis
Sarah G. Fitzgerald, Browne Fitzgerald Morgan & Avis
Bernice Bailey, Browne Fitzgerald Morgan & Avis

Industrial Customer Group
Paul L. Coxworthy, Stewart McKelvey
Denis J. Fleming, Cox & Palmer
Dean A. Porter, Poole Althouse

Labrador Interconnected Group
Senwung Luk, Olthuis Kleer Townshend LLP
Julia Brown, Olthuis Kleer Townshend LLP

Failure Investigation Report – L3501/2 Tower and Conductor Damage

Icing Event January 2021 in Labrador

May 28, 2021

REGISTERED PROFESSIONAL ENGINEER
PEG
MARIA VEITCH
SIGNATURE
28-May-2021
DATE
NEWFOUNDLAND & LABRADOR

Nalcor Reference No.: ILK-EG-ED-6200-TL-RP-0001-01 Rev.01

Prepared by:

Maria Veitch

Verified by:

Cheryl Sehn

Approved by:

John Walsh

REVISION LIST

Revision						Remarks
No	By	Rev.	Appr.	Appr.	Date	
1	MV	01	CS	JW	28-May-2021	
2						
3						

Table of Contents

Appendices

Table of Figures

1 Abbreviations and Acronyms

HVdc – High voltage direct current
TL – Transmission Line
L3501/2 – Line number assigned to the 350 kV HVdc line
OPGW – Optical Ground Wire
OTN – Optical Transport Network
EL – Electrode Line
LITL – Labrador-Island Transmission Link
Str. – Structure/Tower (used interchangeably)
CRREL – Cold Regions Research and Engineering Laboratory
ADSS – All-dielectric Self Supporting cable
CSA 60826-10 – CSA – C22.3 No. 60826-10: Design Criteria of Overhead Transmission Lines
WRF – Weather Research and Forecasting
KvT - Kjeller Vindteknik

2 Background

The Labrador-Island Transmission Link (LITL) is an important transmission line for the provincial energy grid due to its power carrying capacity that will be used to deliver a large portion of the winter peak energy and demand to the Island Interconnected System. Line L3501/2 is an overland transmission line that is a specific component of the LITL. It is an HVdc line between Muskrat Falls and Soldiers Pond that is to be operated at +/- 350 kV DC bi-pole, capable of transferring 900 MW. The overhead transmission line is a bipole line, with a single conductor per pole, and galvanized lattice steel towers. This line is constructed in harsh terrain subjected to heavy wind and ice loads, has been built since 2017, and has experienced multiple winter seasons and weather events.

During the first week of January 2021, a freezing rain storm event occurred within central southeastern Labrador with a larger than forecasted precipitation quantities. This storm caused damage to a specific region of L3501/2, within the central southeastern portion of Labrador where the line runs from Muskrat Falls to Forteau, Labrador. There are three specific sections of the L3501/2 sustained damage; towers from structure 335 to 352, 361 to 369, as well as towers 505 to 527. The specific damage is contained solely to the electrode cross arms and conductors, which are carried on the same towers as the pole conductors. The damage ranges from minor to severe conductor damage, severe electrode line cross arm damage, and electrode conductor breaks.

3 Purpose

Considering the importance of L3501/2 to the provincial energy grid and the need to understand the line's performance in severe weather conditions, a detailed failure investigation was completed in order to take necessary precautions and develop procedures to prevent further damage to the line.

The investigation will be described in detail within this report and includes the following components:

1. Location of the Damaged Towers;
2. Weather Loadings;
3. Storm Information/Modeling;
4. Construction Quality Review;
5. Material Testing; and
6. Failure Analysis.

Upon completion of these investigations, the root cause of the failures and recommendations for prevention of further of damage will be presented.

4 Location of Failures

4.1 Tower Types

There are 11 different tower types on L3501/2, consisting of both guyed and self-support structures. See Table 1 – Tower Types for more details.

Table 1 – Tower Types

Tower Type	Structure Type	Insulator Assembly Type	Deflection Angle Limit (degree)
A1, A2, A3, A4	Guyed	Suspension	0-1
B1	Guyed	Suspension	0-3
B2	Self-Support	Suspension	0-3
C1, C2	Self-Support	Dead End	0-30
D1, D2	Self-Support	Dead End	0-45
E1	Self-Support	Dead End	45-90

Ninety percent of all towers on the L3501/2 are suspension towers, types A1, A2, A3, A4, B1, and B2 respectfully. Figure 1 – Distribution of Tower Type on L3501/2 breaks down the tower distribution on the L3501/2.

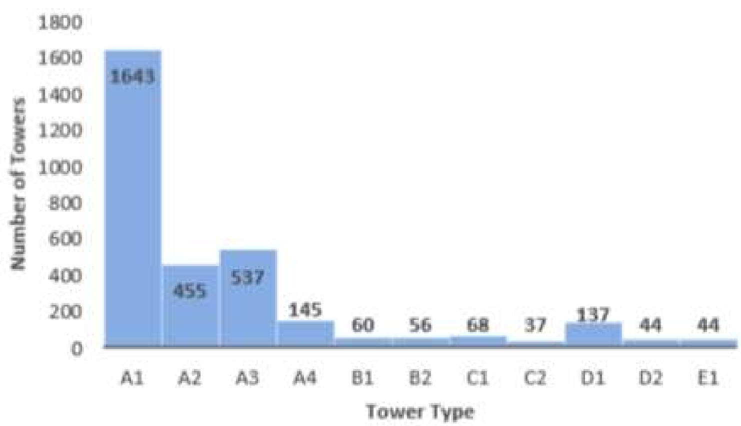

Figure 1 – Distribution of Tower Type on L3501/2

4.2 Damaged Structure Locations

The whole HVdc line is broken into 5 segments, Segments 1 and 2 located in Labrador and Segments 3–5 located on the island.

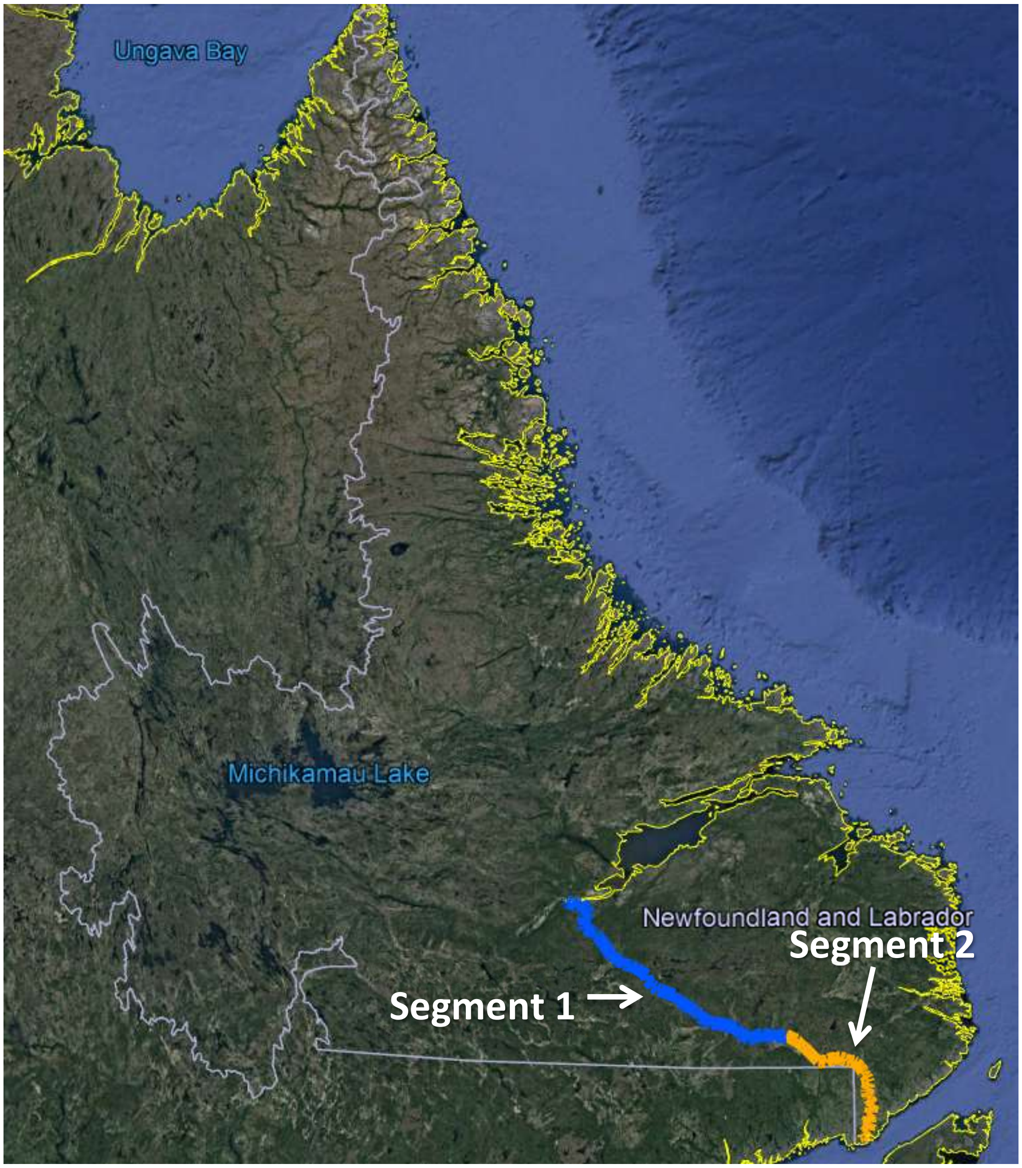

Figure 2 – Segments 1 and 2 of the L3501/2

The failures described within this report all occurred within Segment 1 of the L3501/2. Within Segment 1 there are 750 towers. Of these 750 towers, 36 were reported to have sustained damage after the ice storm of January 2021.

Damages on the L3501/2 are listed in Table 2 – L3501/2 Damages from 2021 Ice Storm.

Table 2 – L3501/2 Damages from 2021 Ice Storm

Structure Number	Cross arm EL1	Cross Arm EL2	Conductor EL1	Conductor EL2	Insulator EL1	Insulator EL2	Dampers	Cluster
335	x		x					1
336			x					1
338			x					1
339			x					1
340	x		x					1
342				x				1
343		x	x	x				1
344			x					1
351			x					1
352			x					1
361			x					2
362	x		x					2
363	x		x					2
364	x							2
365			x					2
366	x							2
367			x					2
368	x		x					2
369			x		x			2
505							x	3
506							x	3
507			x				x	3
513			x	x				3
514					x			3
515				x				3
516			x					3
517				x				3
518				x				3
519				x				3
520				x				3
521				x				3
522				x				3
523				x				3
525				x				3
526	x	x	x	x		x		3
527	x		x			x		3

The damages were contained on the electrode cross arms and conductors. The cross arm failure will be described in detail in Section 9.1, but typical cross arm and conductor failures are shown below.

Photo 1 – Str. 364 Broken EL1 Cross arm

Photo 2 – Str. 365 Severe E1 Conductor Damage

For the purpose of this report, the damages can be broken down into three separate clusters (as labeled in Table 2 – L3501/2 Damages from 2021 Ice Storm).

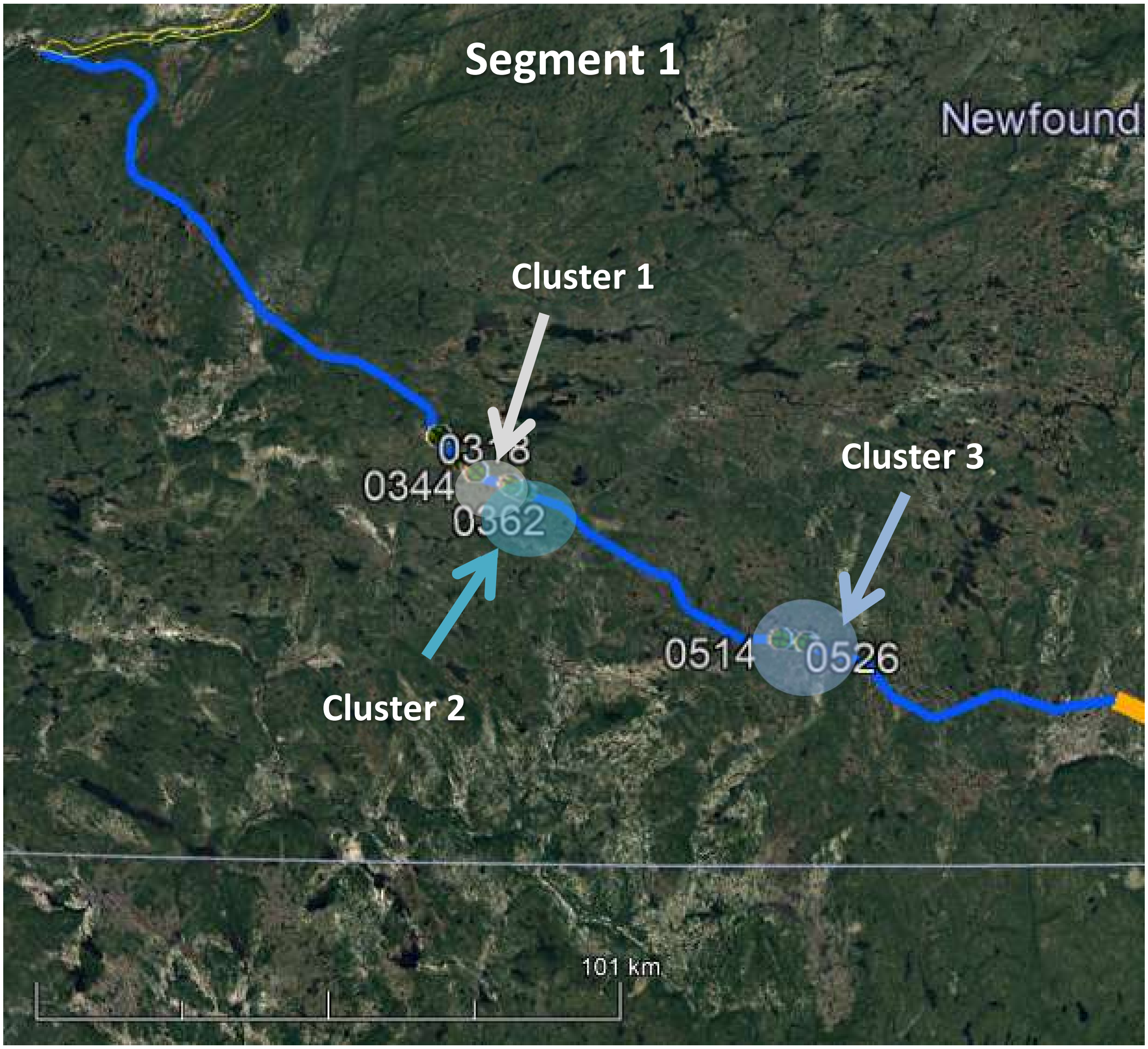

Figure 3 – Segment 1 Showing All Damages (Note: Scale of 101 km)

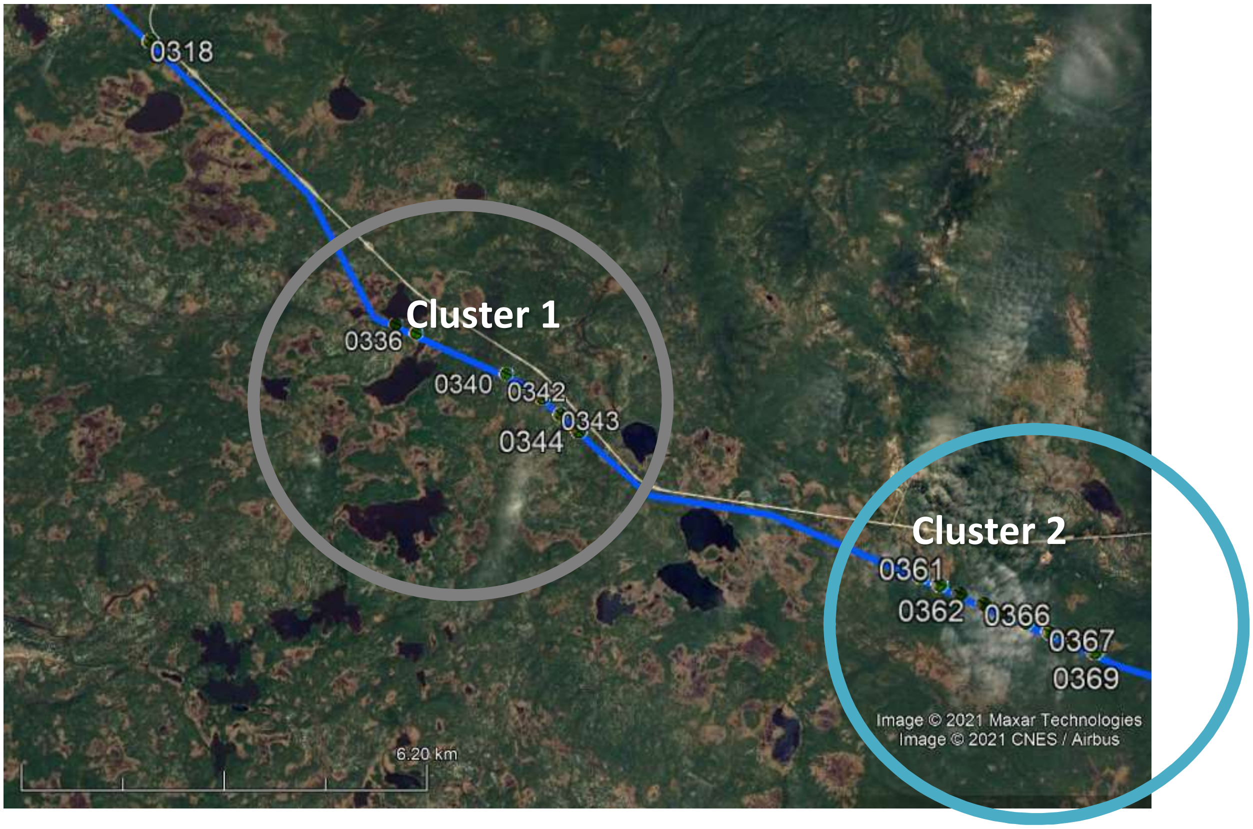

Figure 4 – Clusters 1 and 2 (Note: Scale of 6.2 km)

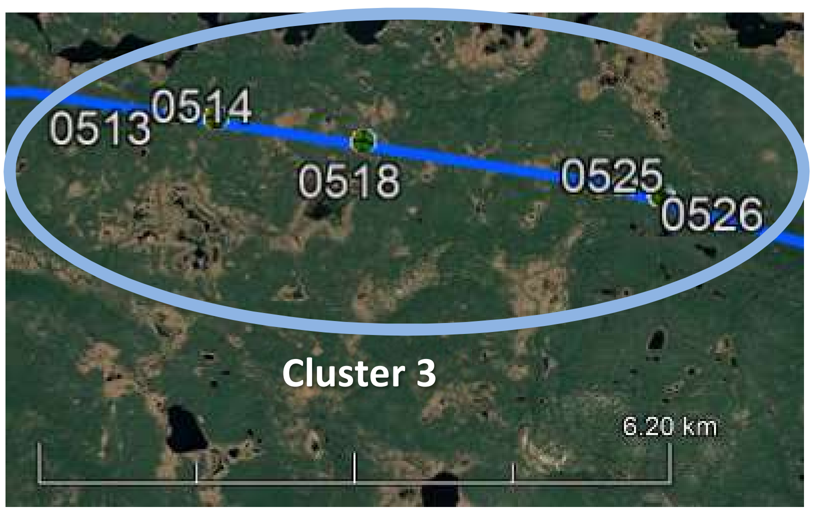

Figure 5 – Cluster 3 (Note: Scale of 6.2 km)

To better understand the positioning of the tower locations that sustained damage within each cluster, the clusters have been plotted with their tower elevations and span length. The span length is the horizontal distance in meters (m) between the centreline of two adjacent towers. Tower locations with damaged cross arms are shown in red, while lines shown in orange represent damaged conductors.

All the failures and damage identified followed a similar pattern throughout the clusters. The failure to the conductor consisted of longitudinal (along the line direction) slippage of the conductor within the suspension clamps and longitudinal bending of the electrode cross arms. The below charts also indicate a similarity with failure locations with respect to longer span locations and spans with large elevation differences.

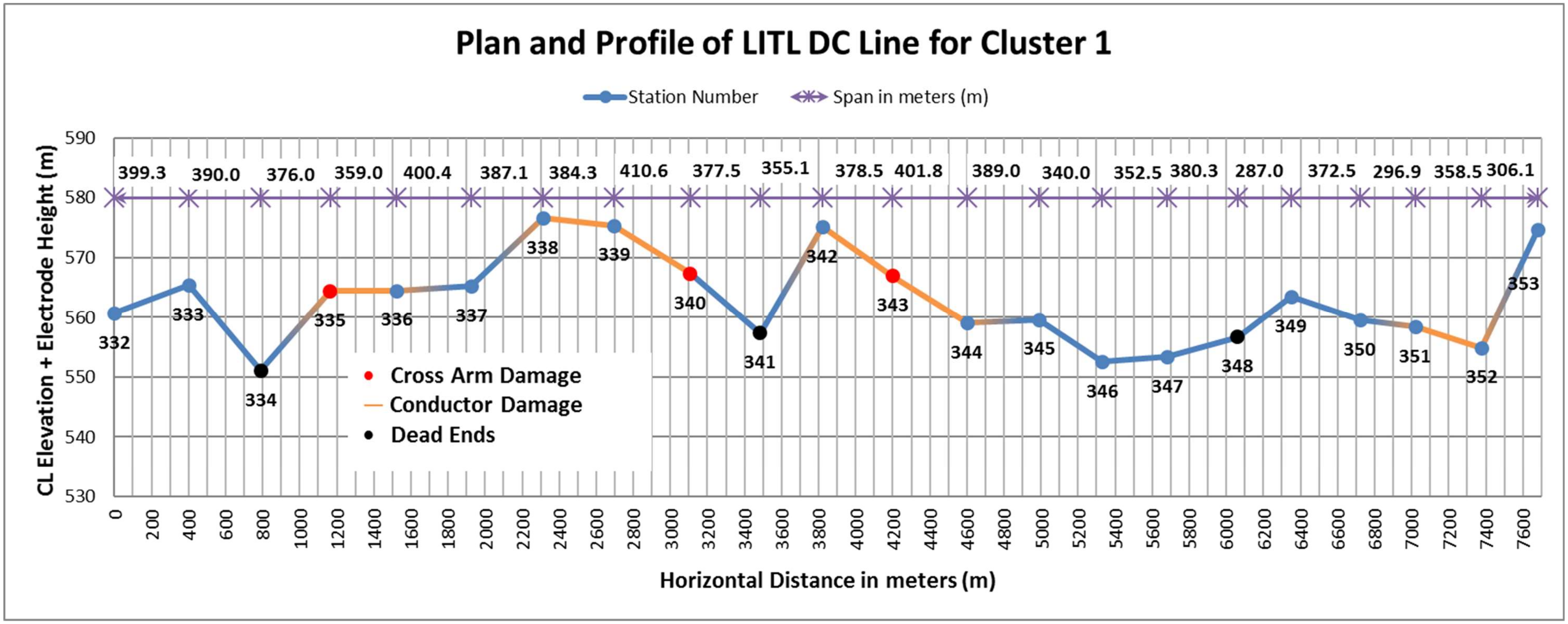

Figure 6 – Station 332 to 347 (Cluster 1)

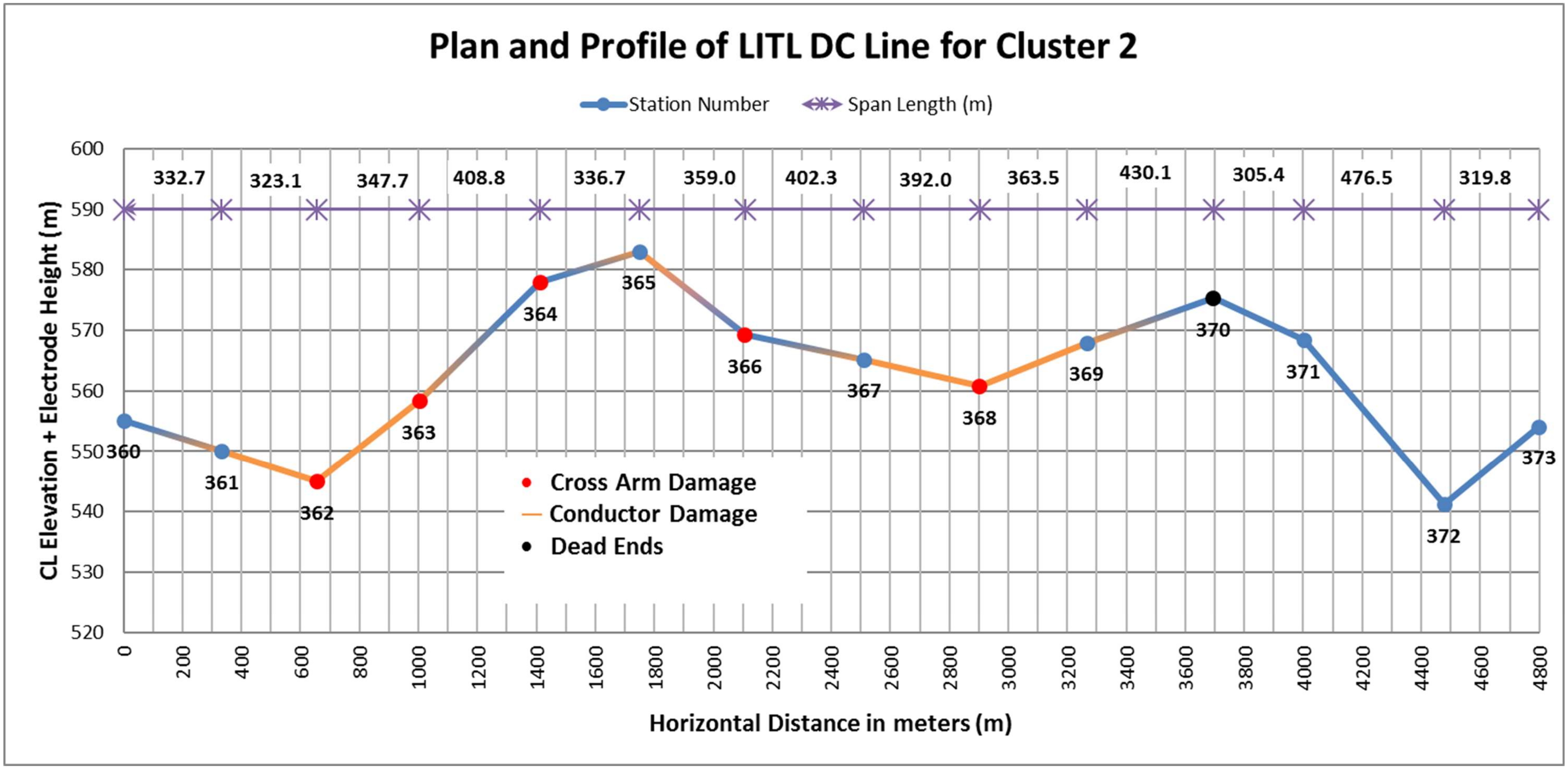

Figure 7 – Station 360 to 373 (Cluster 2)

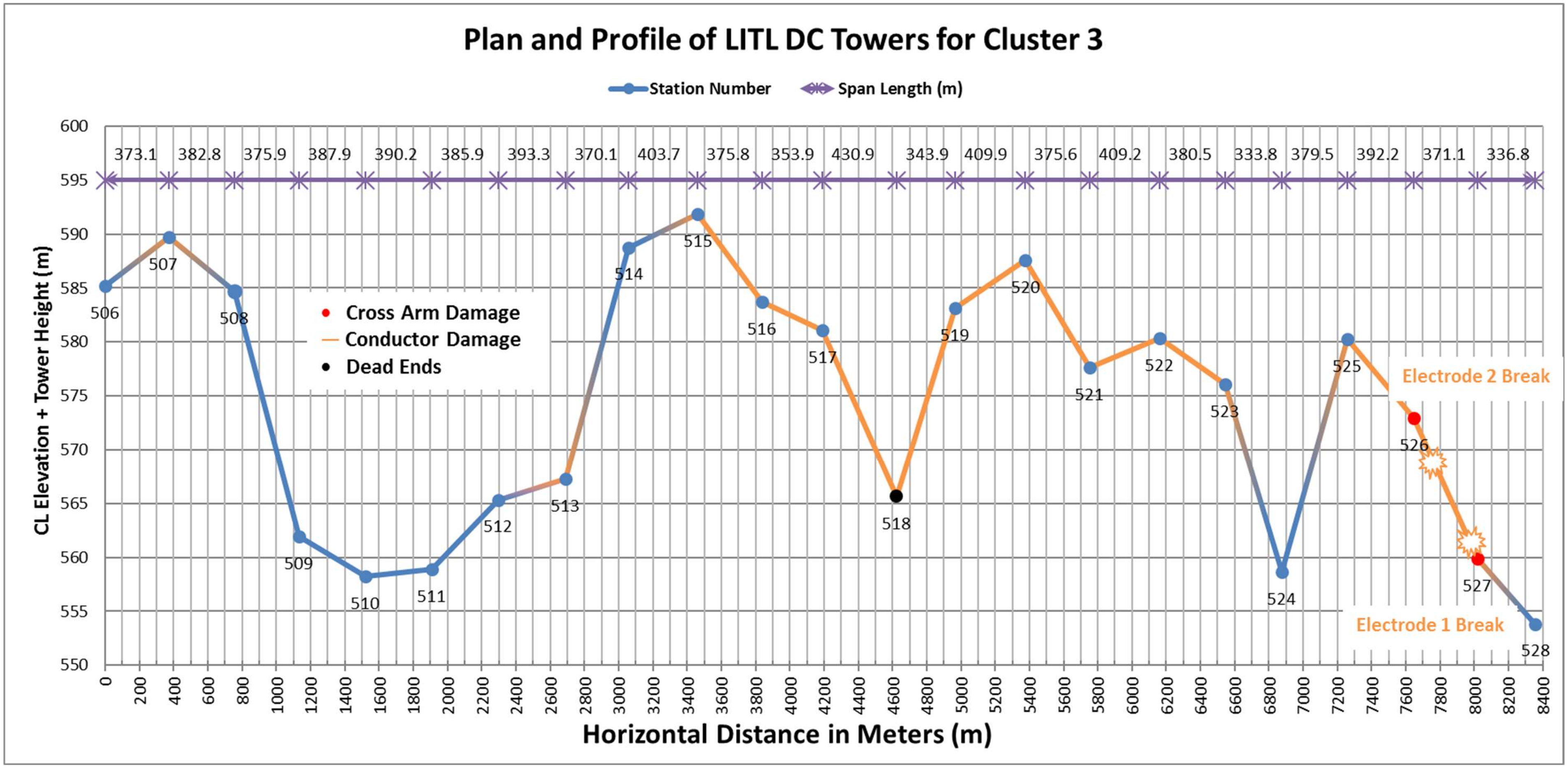

Figure 8 – Station 517 to 531 (Cluster 3)

5 Description of Line in Damaged Section

5.1 Zone 1 Description

L3501/2 is divided in to 11 different zones for climatic loading. The multiple loading zones are necessary due to the long line length and the variability in terrain including alpine, inland, and coastal regions. All damage that occurred during this icing event is in zone 1 of the line.

Zone 1 is the section of line from Str. 1 to 750, starting at Muskrat Falls and ending approximately 273 km along the line. L3501/2 in this zone is design for a maximum ice load of 50 mm of radial glaze ice, a maximum wind load of 105 km/h of wind, and a combined wind and ice load of 25 mm of radial glaze ice and 60 km/h of wind. See Table 3 for more details on the weather cases used for design.

Table 3 – Weather Cases Used for Design

Weather cases	Wire / Conductor Temp (℃)	Ambient Temp (℃)	Radial Ice (mm)	Ice Density (kg/m³)	10 min. Average Wind Speed at 10 m Height Above Ground (km/h)	Cable Wind Pressure (Pa)
Heavy – CSA C22.3 No. 1-10	-20	-20	12.5	900	-	400
EDT	0	0	0	0	-	0
Max wind	-20	-20	0	0	105	980[4]
Wind and Ice	-5	-5	25	900	60	305[4]
Max ice	-5	-5	50	900	-	0
Hot (Pole)	85[3]	30	0	0	-	0
Hot (Grackle)	72[3]	30	0	0	-	0
45 Pa	-30	-30	0	0	30[5]	45
Cold	-38	-38	0	0	-	0
Reduced Swing Wind (30%)	-20	-20	0	0	57	295[4]
Max Swing Wind (80%)	-20	-20	0	0	94	785[4]
Galloping Swing	0	0	12.7	900	45[5]	95.8
Galloping Sag	0	0	12.7	900	0	0
Catenary Limit 1900 m	-20	-20	0	0	0	0
10% Winter Design Temperature	-30	-30	0	0	0	0

Zone 1 is designed utilizing A1, B1, B2, C1, D1, and E1 towers.

5.2 Design Loading Selection

L3501/2 has three general categorized loading zones throughout its length from Muskrat Falls to Soldier's Pond:

- Average Loading Zone;
- Eastern Loading Zone; and
- Alpine Loading Zone.

Zone 1 of L3501/2, the subject of this investigation, would be classified as an Average Loading Zone with a "50 year Reliability Level Return Period of Loads, with respect to Nalcor Energy operating experience and LCP specific modelling and test programs" as specified in "Basis of Design – LCP-PT-ED-0000-EN-RP-0001-01" and "Overhead Transmission – Meteorological Loading for the Labrador-Island Link ILK-PT-ED-6200-TL-DC-0001-01".

Zone 1, 8b and 10 (see Attachment B.1)

The following load case is to be applied in the location shown in attachment B.1. Please note that this loading is valid for the northern corridor alternative only.

Maximum Ice	50 mm radial glaze, 0.9 g/cm^3 density
Maximum Wind	105 km/h (10 minute average wind speed at 10 m height above ground)
Combined Ice and Wind	25 mm radial glaze, 0.9 g/cm^3 density 60 km/h (10 minute average wind speed at 10 m height above ground)

LCP-PT-MD-0000-IM-PR-0001-01 Rev. B1 5

Overhead Transmission – Meteorological Loading For the Labrador – Island Transmission Link Doc. #: ILK-PT-ED-6200-TL-DC-0001-01 Rev. B1

Maximum wind and combined wind values assume Terrain Type C as per CSA C22.3 NO 60826-10. Any deviation for this terrain type for select locations along the corridor must be included in the HVdc tower design criteria.

Figure 9 – Zone 1 Description

5.3 Benchmarking Considerations in Design Load Selection

Zone 1 is located in central Labrador which has been historically characterized as a location that experiences less ice accumulation and freezing rain events in comparison to other zones throughout the province, where temperatures in the winter seasons are general well below freezing rain temperature. Existing transmission experience within similar regions (735 kV lines from Churchill Falls to Quebec and L1301 from Happy Valley-Goose Bay to Churchill Falls) have a maximum ice design of 12.7 mm – 25 mm with limited experience of freezing rain outages throughout their history. It is important to note that these lines are located in central Labrador but not in parallel corridors to L3501/2.

Furthermore, for Zone 1 a value of 11 mm maximum was predicted as a 1:50 year maximum freezing rain value in “Evaluation of extreme ice loads from freezing” conducted by Kathleen Jones of the Terrestrial and Cryosphere Science Branch of the Cold Regions Research and Engineering Laboratory (CRREL)” in January of 2010.

The CSA 60826-10 recommended reference loading for the region ranges from 25–30 mm for a 1:50 year return period. This reference load must be multiplied by a spatial factor of 1.3 and a height factor of 1.15 for a comparison to the 50 mm design load. Therefore the equivalent CSA ice thickness for the section for a 50-, 150- and 500-year return period would be 37, 45, and 53 mm respectively.

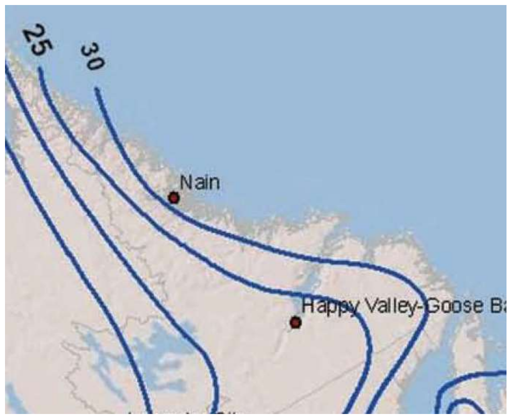

Figure 10 – CSA Recommended Ice Loading Map

6 Storm Information

6.1 Field Information

Early in the investigation, photos could only be captured from helicopters as the towers inaccessible by road. Earliest pictures were received on January 11, 2021. Exact Structure numbers were not known from this inspection.

6.1.1 Tower and Line Icing Photos

The following photos were taken from a helicopter during the early stages of the failure investigation. Dates range from January 10–15, 2021. Exact structure numbers at that time were not recorded. Note the ice accumulation on the towers. It is assumed that when ice is not present on the lines, but is present on the towers, that ice shedding had occurred (causing ice to fall off the lines themselves prior to the photo being taken).

Photo 3 – DSCN6388 (2021.01.11)

Photo 4 – DSCN6391 (2021.01.11)

Photo 5 – DSCN6392 (2021.01.11)

Photo 6 – IMG_2595 (2021.01.15)

There are two types of ice considered for the transmission line design: glaze ice, and rime ice. Glaze ice is clear, dense ice that occurs as a result of freezing rain. The density of glaze ice is approximately 900 kg/m^3. Rime ice is an opaque, less dense ice that occurs as a result of in-cloud icing or freezing fog. The density of rime ice is approximately 500 kg/m^3. It can be noted here the varying types of ice on the towers and lines. The following photos were taken of the towers in the 500 range (Cluster 3).

Photo 7 – IMG_2643 (2021.01.15) – Glaze Ice

Photo 8 – Pole Insulator Glaze Icing – IMG_2652 (2021.01.15)

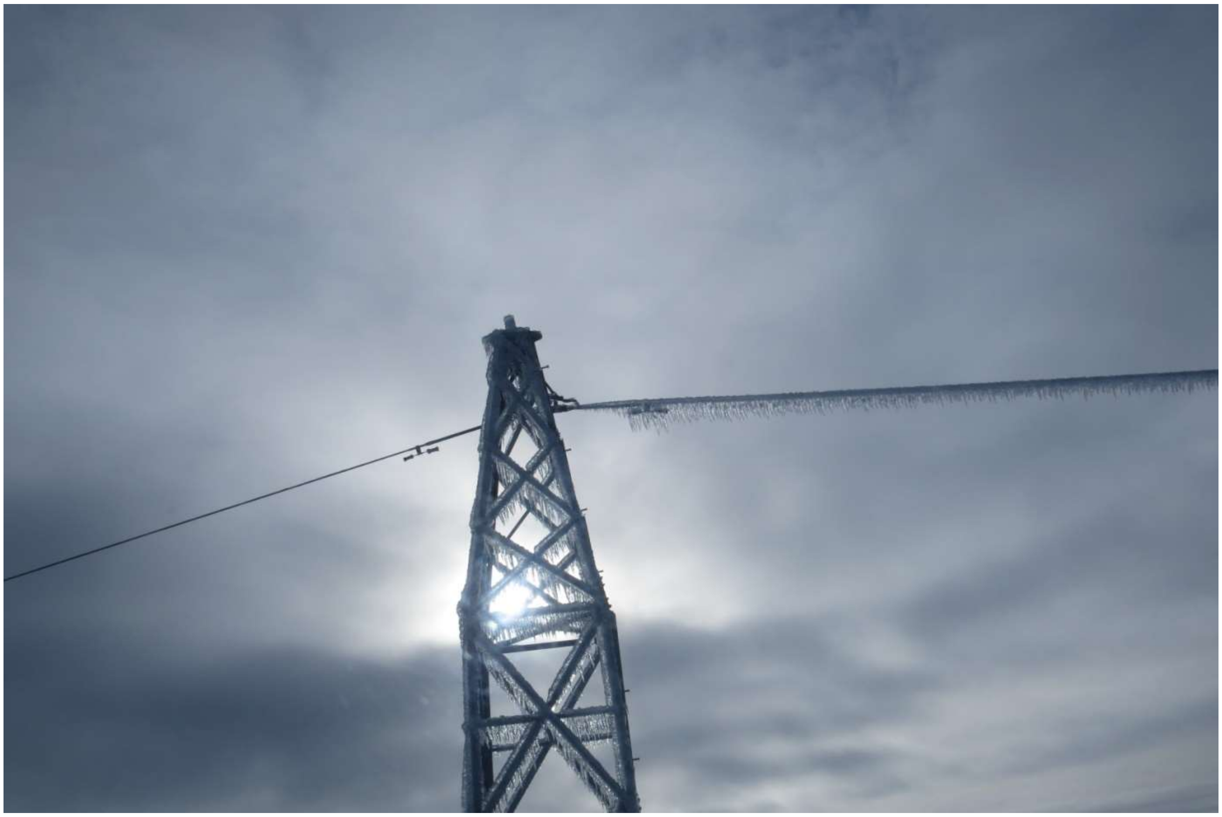

Photo 9 – Evidence Uneven Ice Shedding on OPGW – IMG_2663 (2021.01.15)

Photo 10 – IMG_2657 (2021.01.15)

6.1.2 **Ice Accumulation on Trees**

It should be noted that majority of trees are standing straight suggesting that excessive or consistent wind in a dominant direction is not typical. However, trees with disproportionate ice accumulation are all leaning in the same direction suggesting a consistent wind from the north/north west during the icing event.

Photo 11 – IMG_2583 (2021.01.15)

Photo 12 – Ice Accumulation on Tree – IMG_0145 (2021.01.19)

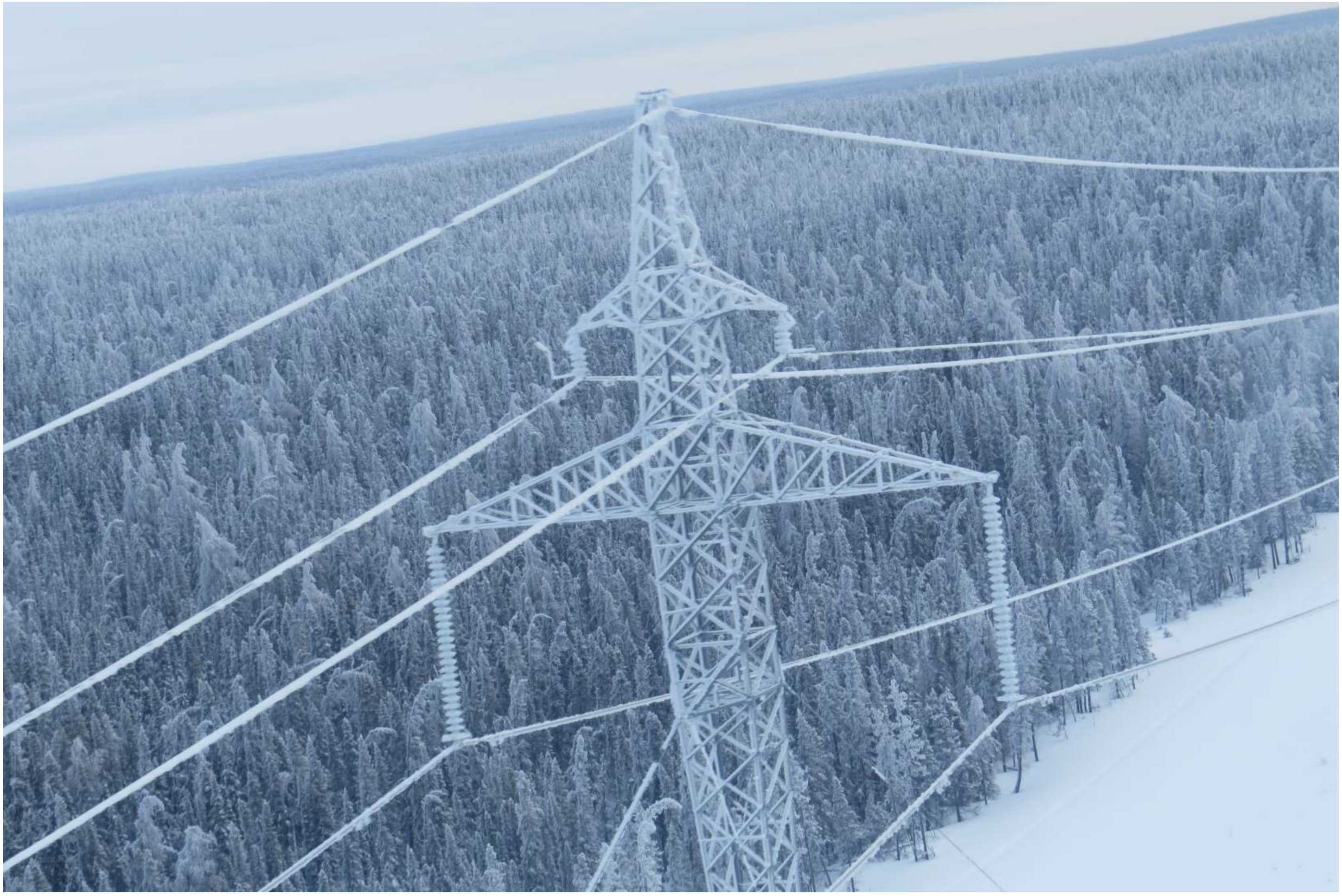

Photo 13 – Significantly Iced and Leaning Trees IMG_2587 (2021.01.15)

6.1.3 **Ice Sample Photos**

Photo 14 – Irregular Ice Accumulation – DSCN6473 (2021.01.14)

Photo 15 – Irregular Ice Accumulation – DSCN6477 (2021.01.14)

In the following photo, the lower (larger) conductor is the pole conductor and the conductor measuring 34mm is the electrode line conductor.

Figure 11 – Ice Thickness Estimation on Str. 340 (DSCN6402 2021.01.11)

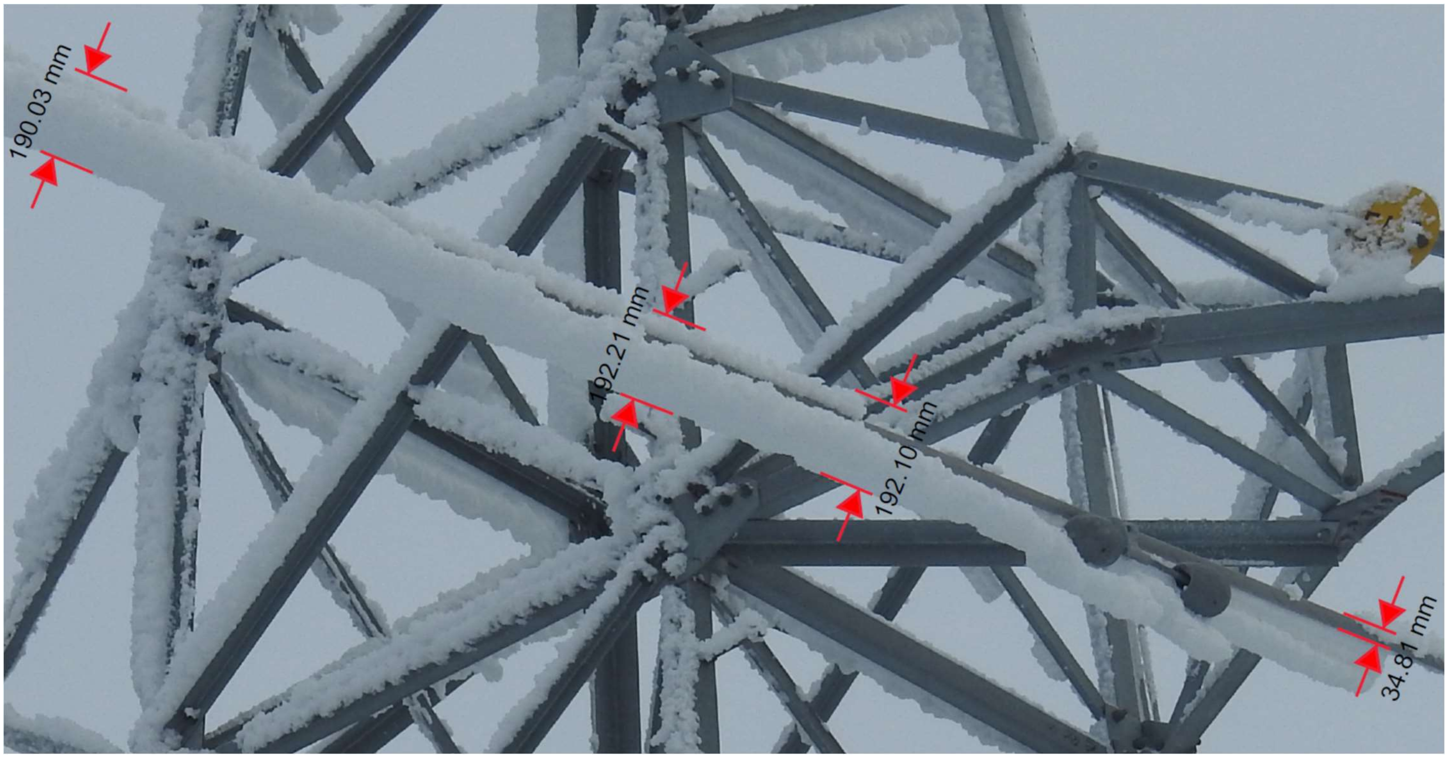

Figure 12 – Electrode Line Ice Measurements on Str. 527 (DSCN6494 2021.01.15)

The relation between the measured ice thickness in the above photos and the correlating radial ice thickness is summarized in the table below. Note that these number represent the actual radial thickness of ice (from the surface of the conductor) measured from the pictures. When comparing these number to design ice thicknesses, it is important to consider the icing type (glaze or rime) which is based on the density of the ice.

Table 4 – Ice Measurements from Pictures

Source Picture	Tower #	Conductor	Conductor Diameter (mm)	Total Diameter (mm)	Radial Ice (mm)
DSCN6402	340	Electrode	33.9	146.45	56.3
DSCN6402	340	Pole	57	207.28	75.1
525 OPGW	525	OPGW	14.5	142	63.8
DSCN6489	526	Pole	57	186.48	64.7
DSCN6494	527	Electrode	33.9	194.27	80.2
DSCN6501	528	OPGW	14.5	119	52.3
DSCN6506	529	OPGW	14.5	161.72	73.6
DSCN6511	530	OPGW	14.5	126.11	55.8
DSCN6515	531	OPGW	14.5	132.74	59.1
DSCN6515	531	OPGW	14.5	223.54	104.5

Note that the ice measurements vary from span to span and wire to wire.

Photo 16 – Fallen Ice from Conductor, Str. 340 (2021.01.18)

Photo 17 – Fallen Ice from Conductor, Str. 340 (2021.01.18)

Photo 18 – Fallen Ice from Conductor, Str. 340 (2021.01.18)

The following ice sample was collected from the Structures in the 340's structure location (Cluster 1). The sample weighs 1,651 grams and measures approximately 320 mm long (in direction of line) and 160 mm wide.

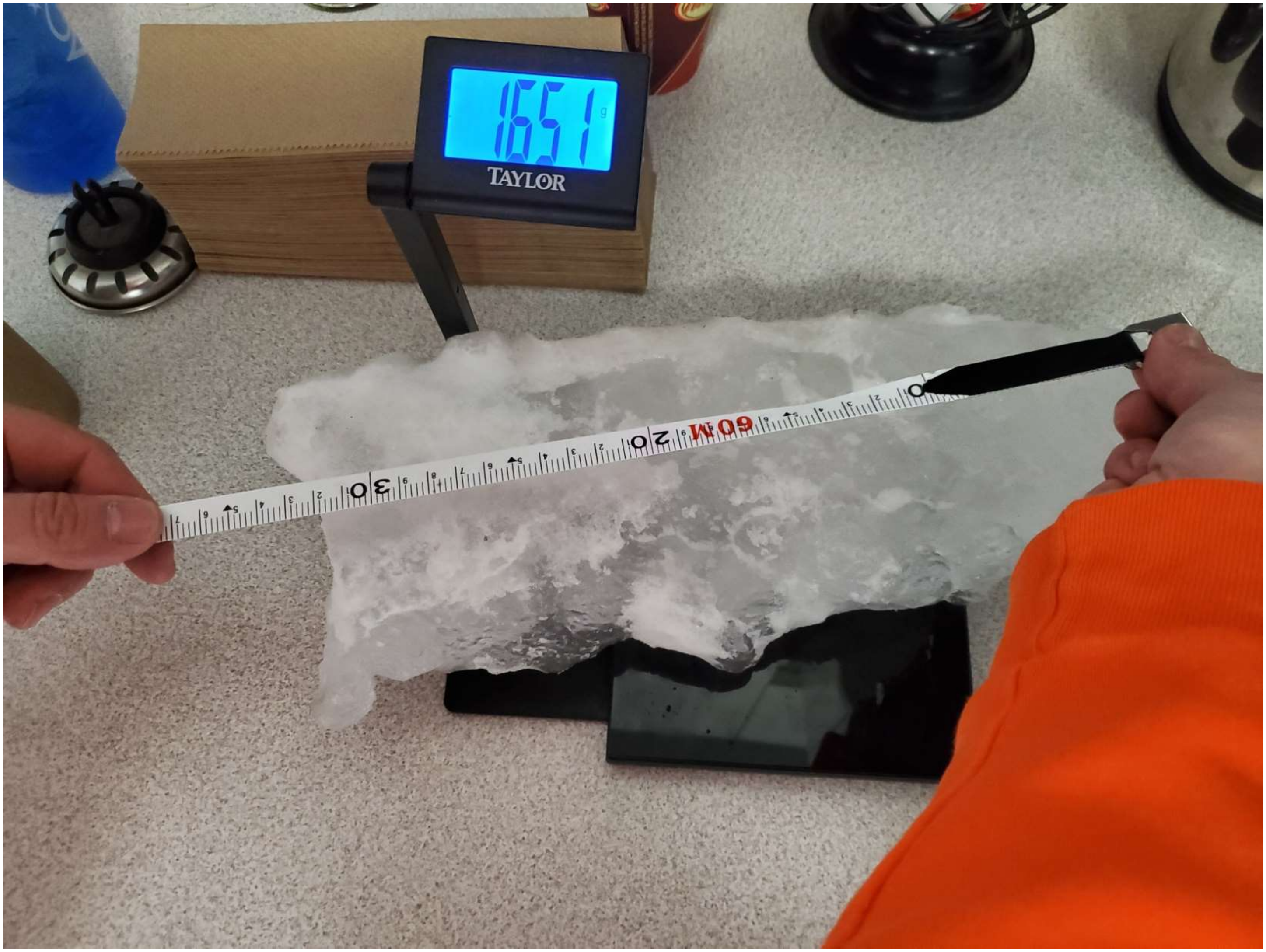

Photo 19 – Ice Sample Weight and Length Measurement from 340's

Photo 20 – Ice Sample Weight and Width Measurement from 340's

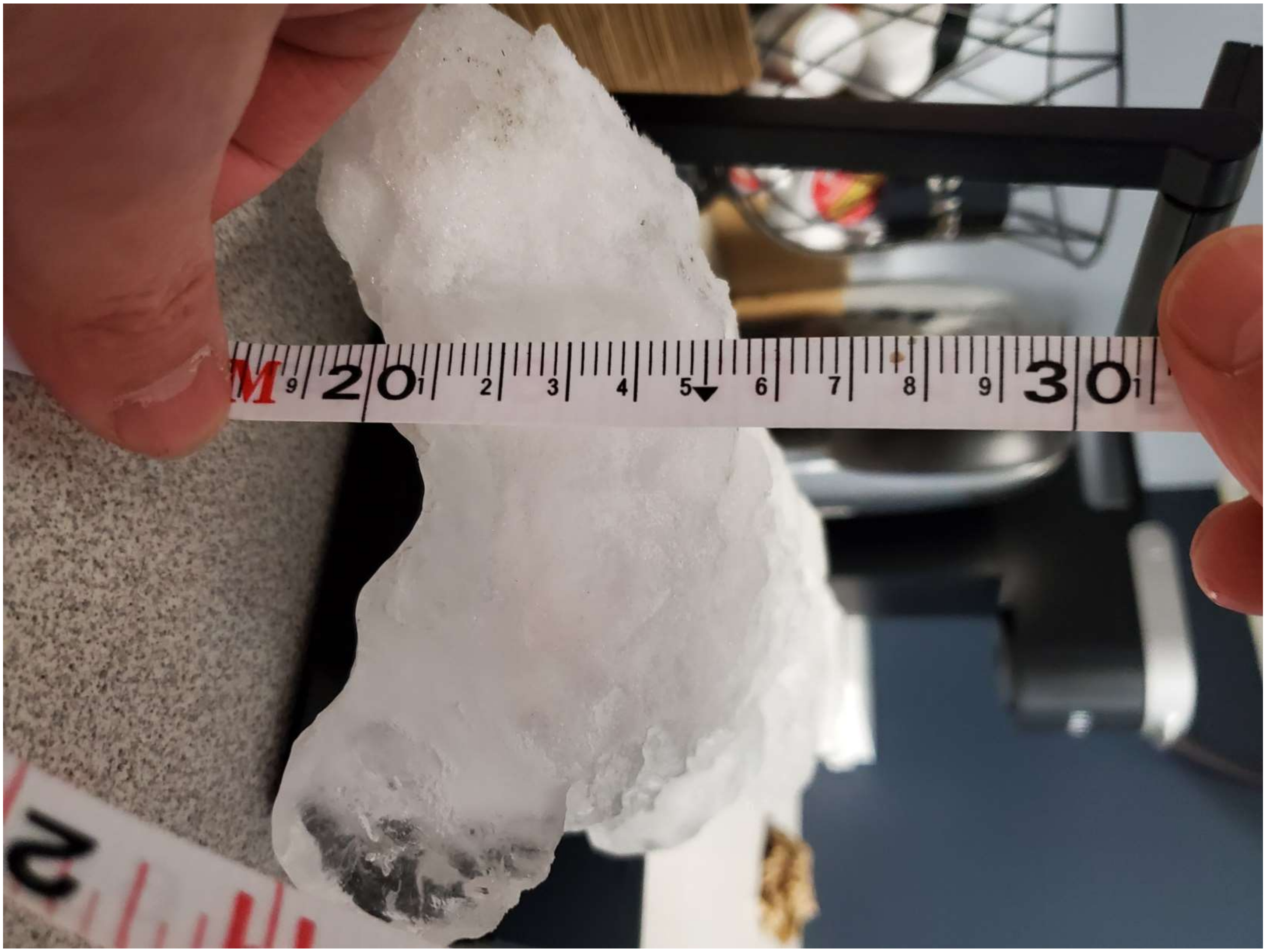

Photo 21 – Ice Sample Measurement from Edge of Conductor from the 340's

The ice samples that were measured and weighed were calculated to have a unit weights ranging from 5.1 to 10.6 kg/m. Note that the ice samples do not represent the total cross section of ice that was present on the line. The 10.6 kg/m sample, for example was estimate to represent approximately 80% of the total cross section. The total estimate unit weight of ice on the line based on this sample is therefore 13.3 kg/m.

The densities calculated from the samples range from 600 to 880 kg/m^3. These densities suggest a mix of rime and glaze ice.

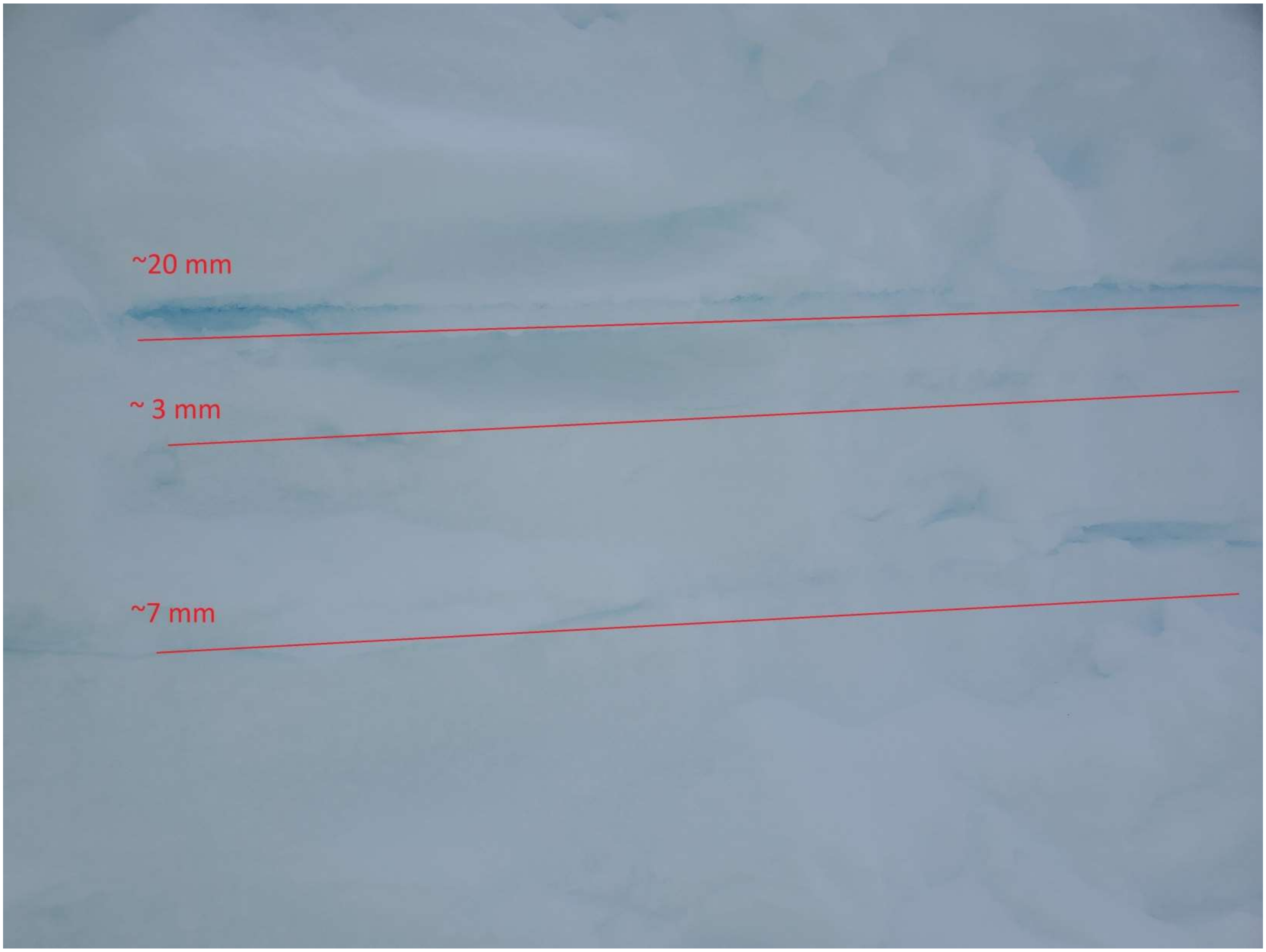

Figure 13 – Evidence of 3 Ice Events (2021.01.27)

Figure 13 shows a cross section of the ground snow located in the area of the damage. Three separate icing events were clearly identified within this cross section, indicating that in addition to the original ice storm, several smaller icing events occurred following adding to the overall accumulation on the line in certain segments.

In general, ice samples taken and recorded within the failure zones varied in both thickness, size and composition with a noted significant base of glaze ice covered in both rime ice and wet snow in locations as shown in Table 4. The thickness and size of samples were greater in the Cluster 3 (Str. 500's) locations. Furthermore, the ice itself formed as large ellipsoid shaped, predominately hanging from the bottom of the conductors as shown in the pictures above. Observations throughout the repair noted that the ice remained on the lines for more than four weeks and accumulated more ice/snow throughout time with is not typical for freezing rain events.

6.2 Weather Data from Nearby Weather Stations

6.2.1 Icing Event January 6–8, 2021 – Environment Canada Data

The data below supports the observations from site that a significant freezing event occurred throughout the region of identified damage. Furthermore, records from Environment Canada support that this past January has been the warmest on record for the region with an absence of the extreme cold weather that normally persists throughout the winter months. Temperatures ranged between -20°C to +2°C throughout the month. Cause frequent thaw and refreezing to ice in the region.

From January 6–8, 2021 there was an icing event in Labrador. The total precipitation in the area of L3501/2 ranged from 25 to 75 mm. See Figure 14 showing map of precipitation.

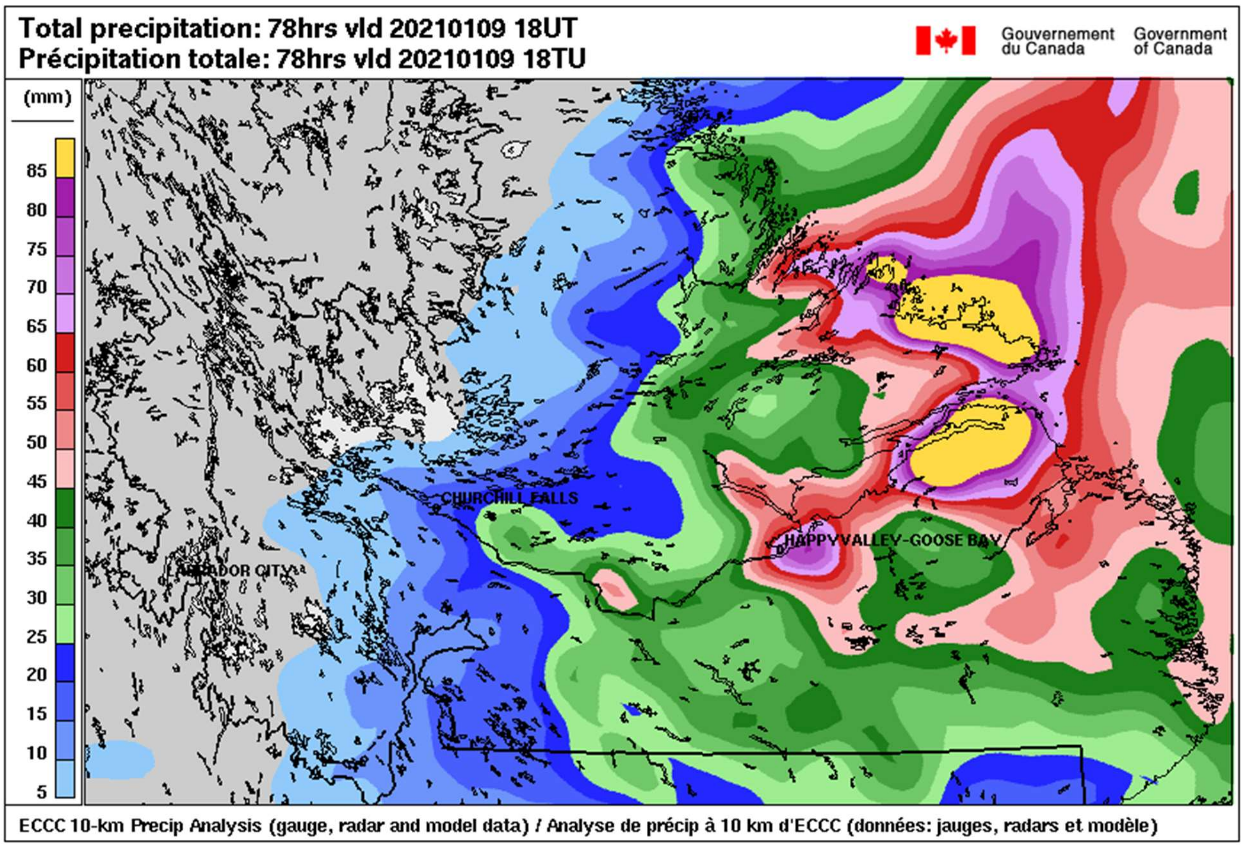

Figure 14 – Precipitation Map for January 6–8, 2021

There was significant freezing rain noted in Cartwright as reported in the CBC article on January 12, 2021 (https://www.cbc.ca/news/canada/newfoundland-labrador/cartwright-freezing-rain-1.5870286). Locals in the community noted this amount and duration of freezing rain was unusual for the area.

Figure 15 – Cartwright Freezing Rain (from CBC.ca)

The weather stations in the vicinity of L3501/2 are located at Happy Valley-Goose Bay, Cartwright, Mary's Harbour, and Blanc-Sablon. The precipitation types recorded at these four location during this event include rain, freezing rain, fog, freezing fog, snow, and ice pellets. See Figure 16 for precipitation types by time and location.

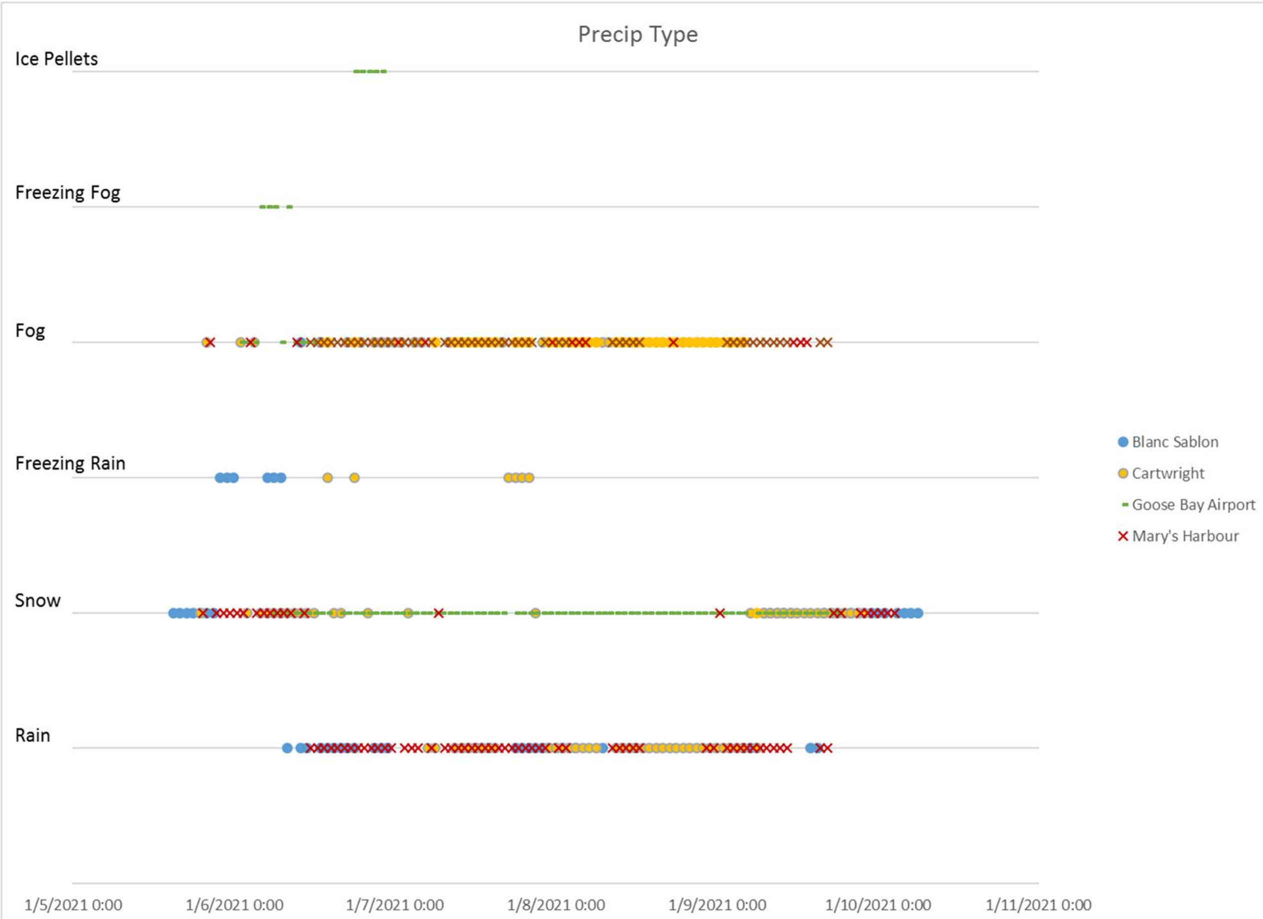

Figure 16 – Types of Precipitation by Time and Location (January)

Note that while freezing rain and freezing fog are only noted for short duration at these weather stations the precipitation types at the location along L3501/2 could vary as the stations are a significant distance from the line locations with large difference in exposure and elevation. It should also be noted that while rain and fog are noted for a longer time period at multiple weather stations the temperature as these stations are close to 0°C for the specified time frame. See Figure 17 for temperatures.

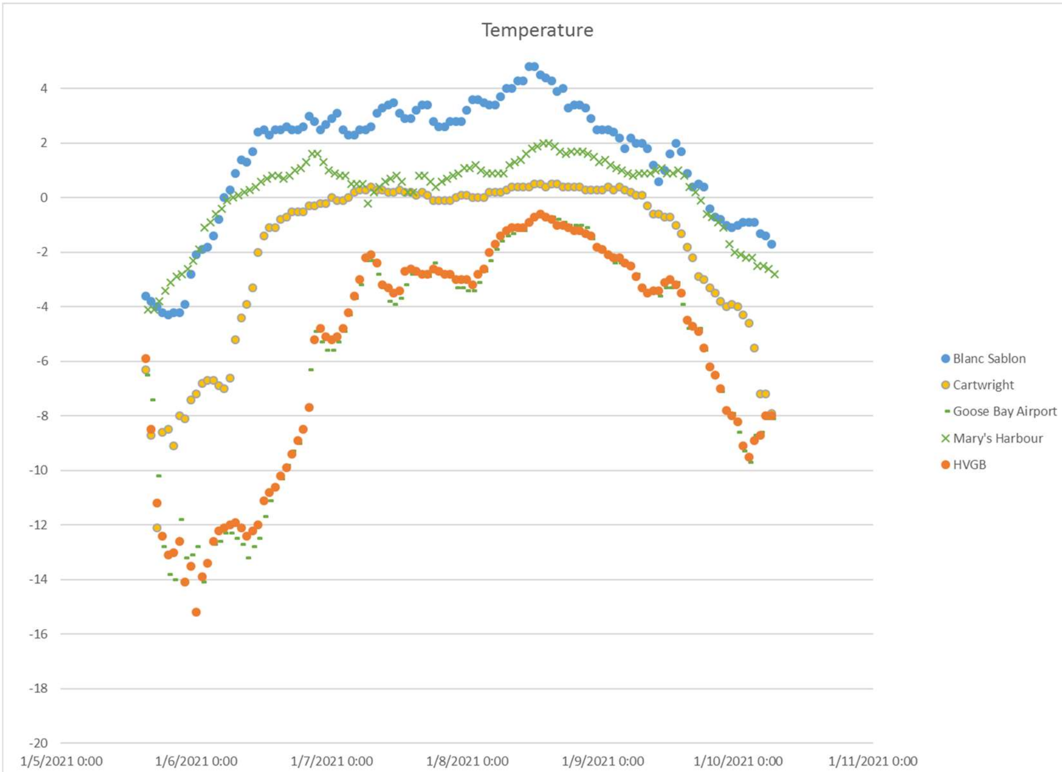

Figure 17 – Temperature at Various Locations during Event (January)

As shown in Figure 18, wind speeds at the time of the event were relatively low near the beginning of the line near Goose Bay ranging from approximately 0–30 km/h, with similar speed at the end of the line near Mary's Harbour. The winds at the time of the event were higher at Cartwright with speeds up to 40 km/h, and Blanc-Sablon (near the end of the line) with speeds up to 60 km/h. It is worth noting that Cartwright is on the coast of Labrador, north of Goose Bay and is the furthest away from the line of the stations included here.

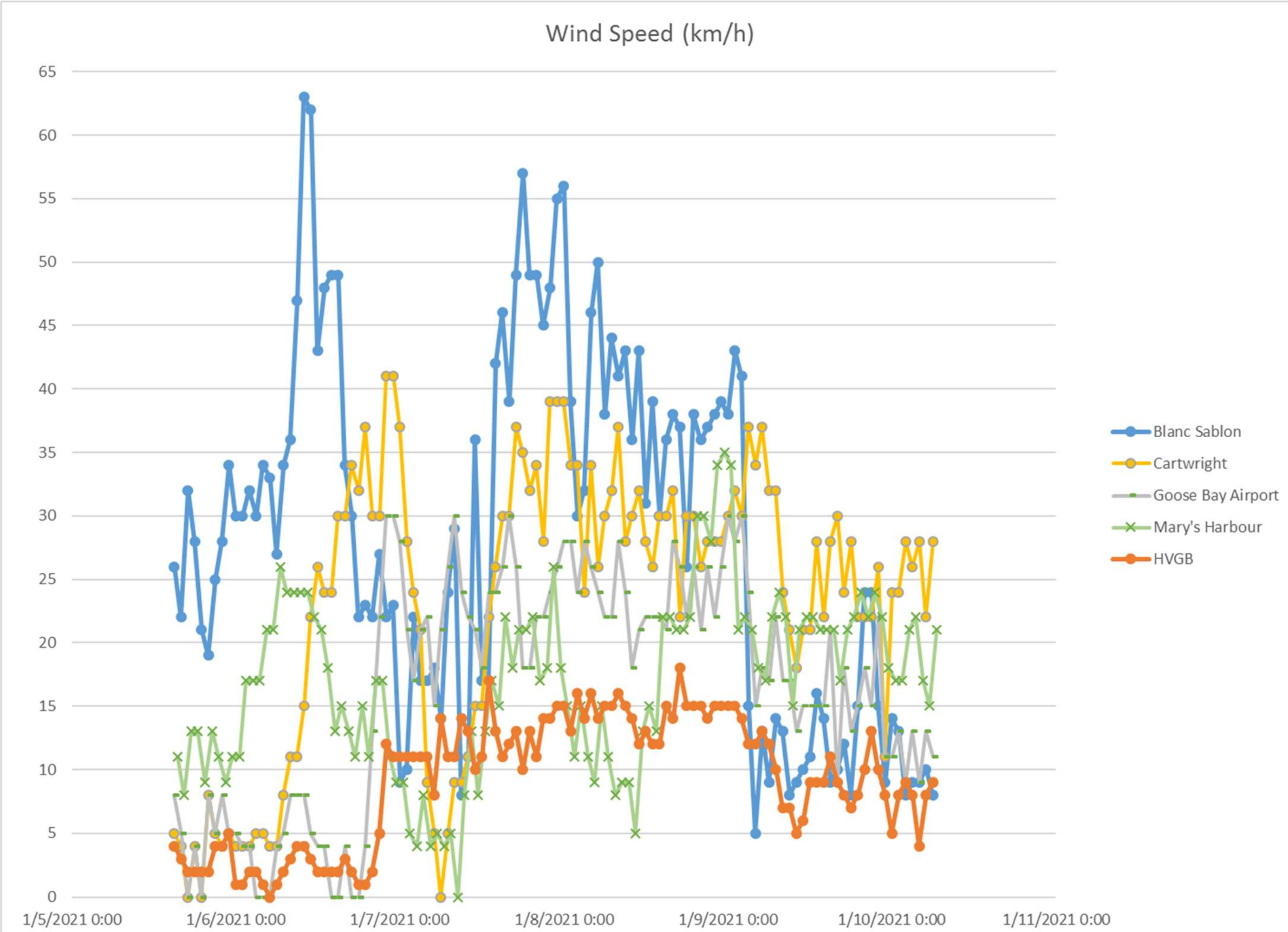

Figure 18 – Wind Speeds at Various Locations during Event (January)

6.2.2 Icing Event February 4–6, 2021

As mentioned in Section 5, there were reports from the site that during repairs ice was continuing to accumulate on L3501/2. In particular there was an icing event noted from February 4–6, 2021. Similar to the original event, weather station in the area recorded a variety of precipitation types, while the temperatures ranged from -2°C to 2°C which are ideal temperatures for ice accretion. See Figures 19 to 21.

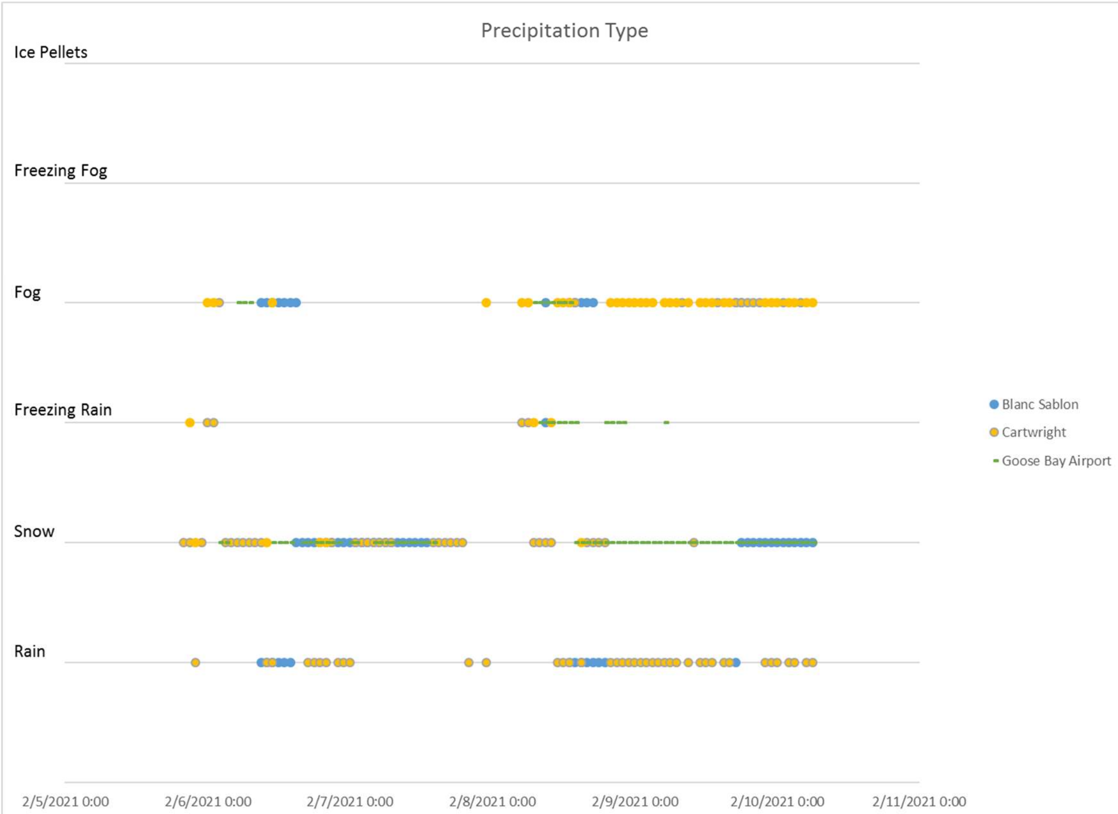

Figure 19 – Types of Precipitation by Time and Location (February)

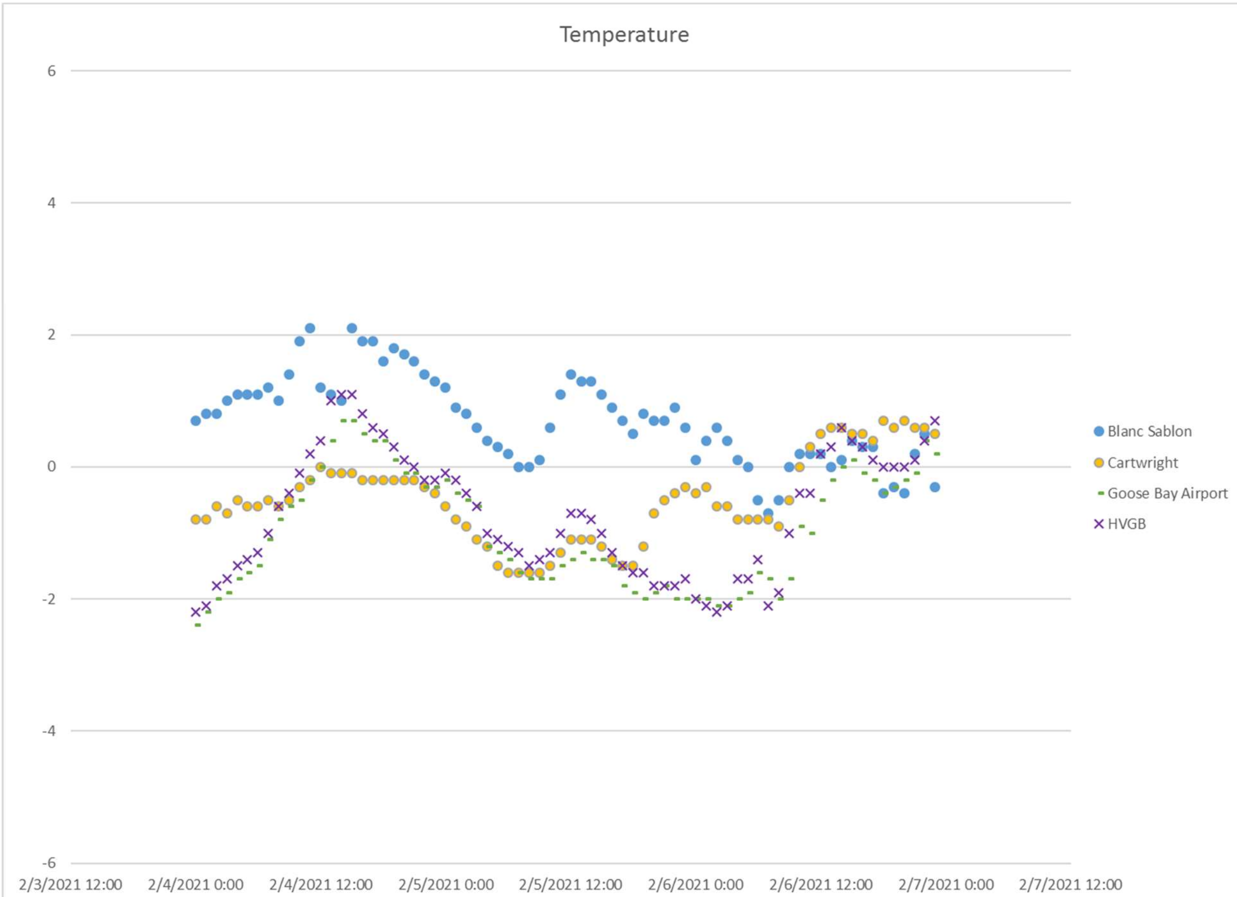

Figure 20 – Temperature at Various Locations during Event (February)

As shown in Figure 21, wind speeds at the time of the event ranged from approximately 0–55 km/h, with the highest wind speeds at the end of the line near Blanc-Sablon.

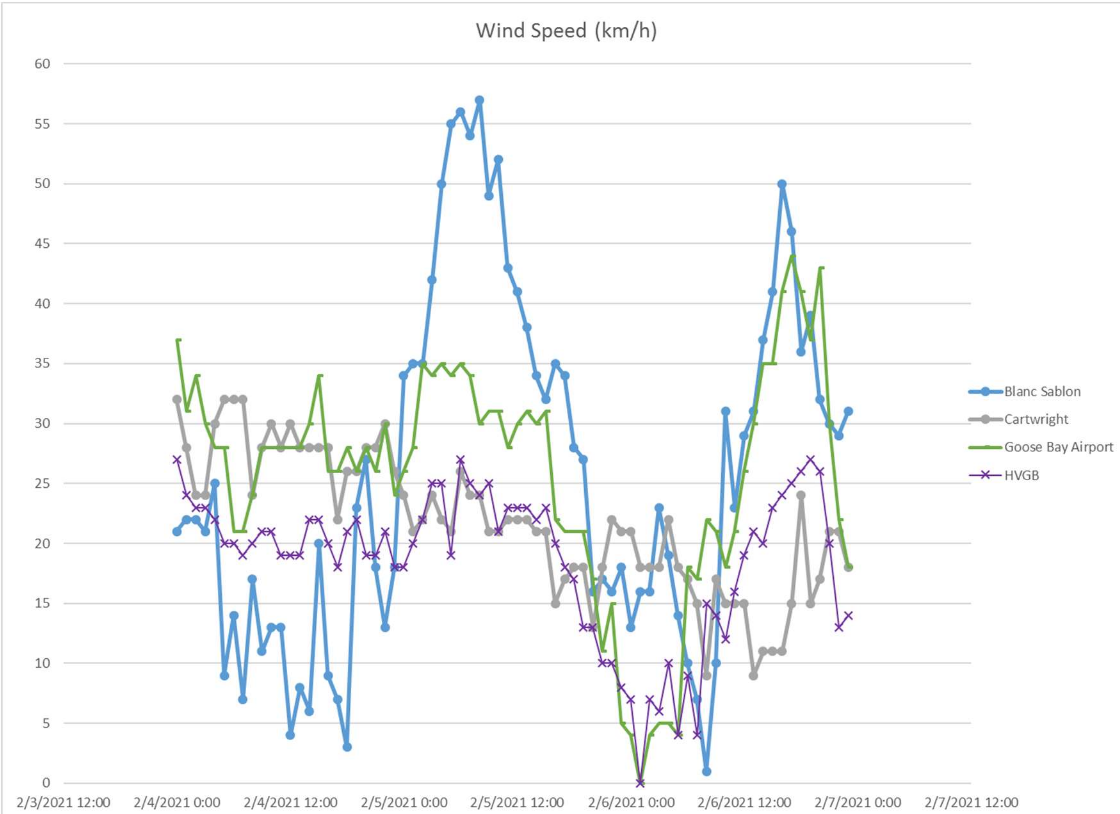

Figure 21 – Wind Speed at Various Locations during Event (February)

6.3 OPGW Alarm Indications

The Optical Transport Network (OTN) is designed to provide alarms when there is a degradation of the light level as measured by the Performance Monitor inherent in the OTN equipment at all sites. Baseline light levels were measured and set at the time of the OTN commissioning and if the light level changes beyond a predefined threshold limit an alarm is generated.

On January 5, 2021 the minor alarms began being received at the Three Rocks Repeater station at 5:00 PM and continued until January 6, 2021 at 8:00 PM, at which point the minor alarms ceased. On January 18, 2021 the minor alarms were being received at the Three Rocks Repeater station at 12:15 am and continued until 4:30 am that same day. No further minor alarms have been noted since January 18, 2021.

A Nalcor system integration and telecom specialist speculated the alerts to be an indication of an issue with the Mid-Line Amplifier at the Three Rocks repeater site, an issue on the OPGW between Forteau Point Transition Compound and the Three Rocks repeater site, or an issue with the ADSS Tail Circuits at either end.

6.4 Weather Modeling

Modern technology and modelling computing capacity has greatly improved recently and increased the ability to model large areas and freezing events in the last few years. EFLA Consulting Engineers (EFLA) were consulted to produce an icing model combined with the Weather Research and Forecasting (WRF) hindcast simulation to evaluate the January icing storm experienced on L3501/2.

EFLA performed this analysis with assistance from Kjeller Vindteknik (KvT). KvT provided the input data into the icing model by performing a hindcast simulation of the weather condition in January 2021 and by long-term simulation of the weather in 1979–2020. The icing model used was developed and used by EFLA. Three icing models are used in the study: (i) Chainé model, (ii) Simple model by K. Jones at CRREL. (iii) M1 icing model made by EFLA.

The Chainé model is widely used in Canada for modeling freezing rain and is used in the CSA standard. The Simple model was developed by Kathy Jones at CRREL. It generally predicts lower icing than the Chainé model. The M1 model was developed by EFLA for modeling rime ice, wet snow, and glaze ice.

Figure 22 shows the 50-year return load based on the 40 years of data modeled, compared to the design load, and CSA 50-, 150-, and 500-year return loads. The figure shows that the 50-year return load is always less than the design load. The 50-year return load varies depending on model type and structure number. In some case the 50-year return load is greater than the CSA 50-year return load, and even the CSA 150-year return load. It should be noted that the only field data available to calibrate the icing model for this area of Labrador was the event that is the subject of this report.

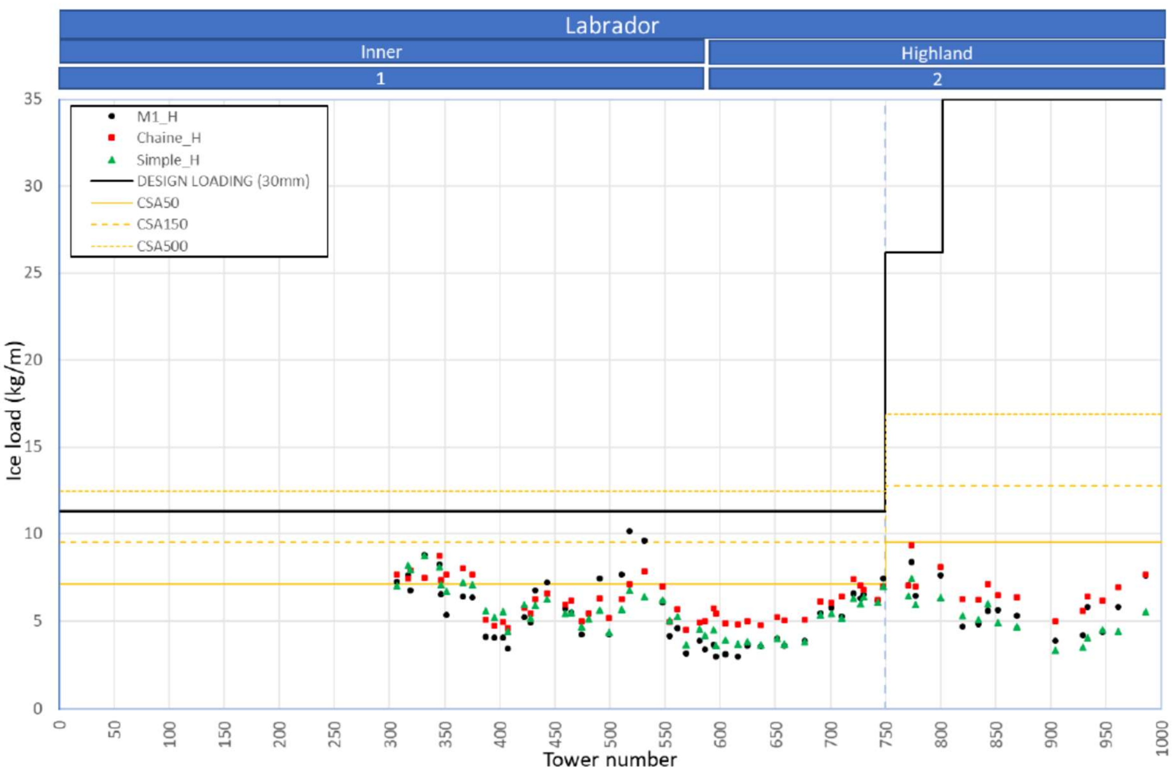

Figure 22 – Ice Load of 50-Year Return by Structure Location

It was noted that the largest icing events in the last 40 years have durations spanning multiple days. At structure 345 the duration of the icing events ranged from 1 to 156 days. See Figure 23.

Time from	Time to	Max Value (kg/m)	Length (days)	Weighted. acc.time
2001-11-06	2001-11-20	8.3	13.8	2001-11-10
1987-02-17	1987-03-31	6.9	42.7	1987-03-14
1981-11-07	1981-11-08	6.3	1.3	1981-11-07
1990-11-09	1990-12-06	5.6	27.4	1990-11-20
2013-02-20	2013-03-13	5.6	21.3	2013-03-02
2016-10-22	2016-10-23	5.2	0.9	2016-10-23
1996-04-03	1996-04-15	3.7	11.7	1996-04-05
2009-11-16	2009-11-28	3.7	12.8	2009-11-26
2018-11-25	2018-12-22	3.6	26.7	2018-12-08
2006-01-15	2006-03-09	3.3	52.8	2006-01-23
1979-11-28	1980-01-14	3.2	46.9	1979-12-26
2015-04-27	2015-10-01	3.0	156.2	2015-04-28
2005-04-12	2005-04-16	3.0	4.5	2005-04-13

Figure 23 – Largest Icing Events at Tower 345

Figure 24 shows the total ice load from the January icing event compared to the design load, and CSA return period loads. In some cases the ice load from the storm was more than the design load.

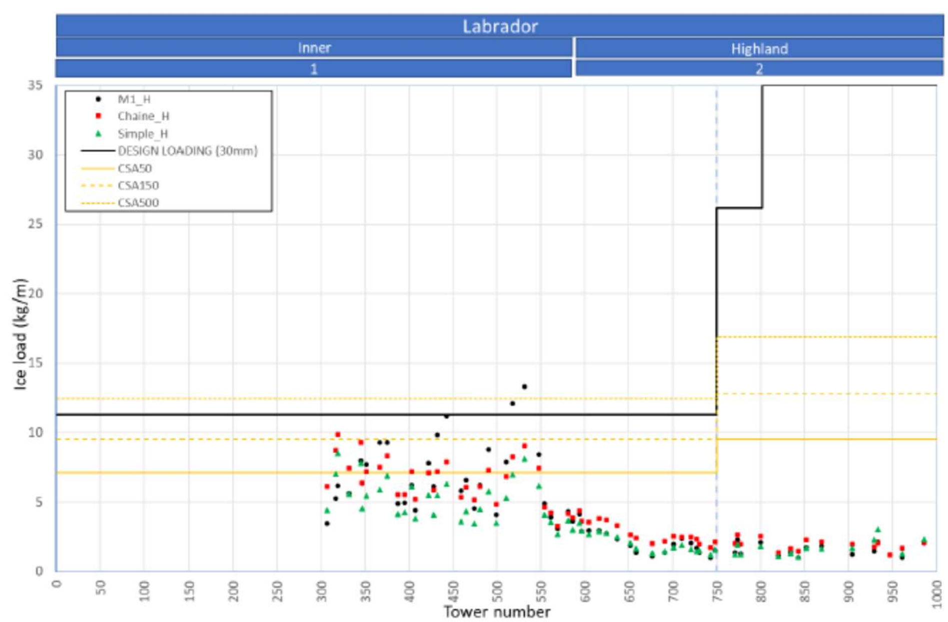

Figure 24 – Ice Load of Storm by Structure Location

The main conclusions of the analysis are the following:

- The icing model using WRF simulation as input data does capture the icing accumulation in the January ice storm quite well.
- Damage to structures shows that towers from 318 to 344, 361 to 369 and 507 to 527 were most exposed to icing. The icing models show that the area between towers 318 and 550 had the highest predicted ice load. Thus, the icing model captures the icing area quite well.
- The M1_H icing model predicts the highest ice load at tower 531 as 13.3 kg/m (on 30 mm conductor at 20 m), equal to 56 mm radial ice. The ice samples measured and weighed had unit weights ranging from 5.1 to 10.6 kg/m. Some of the ice samples did not represent the total ice cross-section. The whole ice cross-section weight of sample 10.6 kg/m is believed to be 13.3 kg/m at tower 340. It is not known if the sample is from the pole conductor, electrode, or the OPGW. Overall the ice weight of the M1_H model is found to be convincing compared to available icing data.
- The 50-year return period was estimated using 40 years of hindcast simulation. The ice load in the January ice storm exceeded the 50-year loading at most tower locations between 350 and 600.
- The icing type in the January ice storm was mostly glaze ice, but partly combined with rime icing. The glaze icing was due to supercooled rain in some areas, but the supercooled rain was mixed with snow and graupel in other areas.

From a failure investigation perspective the WRF modelling aligns with the observations that a significant icing event in excess of the design loading were seen in Segment 1 during January. Furthermore, this newer modelling technology suggests that this loading may be more frequent that a 50-year loading event. See Appendix A for complete report “Icing Storm in Labrador in January 2021 – Assessment of Icing in LITL”.

7 Construction Quality Review

7.1 Documentation Review

7.1.1 Cross Arms

During construction a “Lattice Tower Assembly Check” Quality Control (QC) form was filled out for all structures. Among various checks QC form requires inspection of steel for damage, and a torque check for 30% of the bolts on a guy tower. All torqued bolt heads were marked with red, and all verified torque bolt heads are marked with black. The form was completed by the construction contractor QC crew, and reviewed by the construction contractor Quality Assurance (QA) representative and the Nalcor QA Inspector. All forms for structures with reported cross arm damage were reviewed. All were complete with no noted issues.

In addition, there is also a “Lattice Tower Inspection” QC form. This is an additional check that can be performed by climbing, visual, or helicopter. This form requires checks of missing or damaged members, as well as a climbing inspection of all cross arm connections with a torque check of bolts. The form was completed by the construction contractor QC crew, and reviewed by the construction contractor QA representative and the Nalcor QA Inspector. All forms for structures with reported cross arm damage were reviewed. All were complete with no noted issues. See Appendix B for sample QC sheets.

7.1.2 **Suspension Clamps**

As all the conductor damage was located near the suspension clamp, the issue is suspected to be related to the clamps. The clamps are required to be torqued to 47.5 +/- 6.7 Nm, the reusable torque is 67.8 Nm, and the failure torque is 94.9 Nm as per the part drawing. There is no item on any of the QC check sheets to verify the torque of the bolts.

7.2 Site Inspections

Visual inspections on the cross arms did not indicate any over-torqueing of the bolts and it was noted that most cross arms that were removed had the QA/QC markings on the bolts to indicate proper torqueing was completed during construction.

Visual inspections of the suspension clamps did show differential torques were applied to the four bolts that were used to hold the suspension clamp in place on the conductor. However, it was not clear if some of the bolts were loosened during the repairs that took place in January and February 2021.

It should be noted that these clamps, if improperly or unevenly torqued, can lose a significant amount of their slippage strength capacity. It has been noted that the use of lockwashers is not considered an affective means of preventing bolts from backing off and are no longer used by many utilities for this reason. See Appendix C “Conductor Failures – LITL”.

Figures 25 – Suspension Clamp and Failed Conductor Location

Figures 26 – Suspension Clamp and Failed Conductor Location (2)

8 Material Testing

8.1 Materials for Testing

Once the damage on the L3501/2 was discovered, it was immediately decided that the damaged components were to be tested to help establish the cause of failure. Kinectrics Inc. from Toronto, Ontario was engaged to test the failed components on the L3501/2 and a meeting was held to determine how to conduct the testing as to provide insight on the failures as quickly as possible. It was proposed that testing the failed cross arm assemblies had the greatest possibility of identifying the cause of failure. Sections of damaged EL conductor were marked and stored to be tested as well.

8.1.1 Cross Arm Samples

Upon review of photos and description of the failures, Kinectrics stated that the failures appeared to be similar enough that only a sample of damaged assemblies was necessary for their investigation. Two of the first three damaged cross arm assemblies that were replaced on the line were packaged and shipped to Kinectrics as well as a new cross arm assembly. The first cross arm replaced (from Structure 340) was removed from the tower in a way that compromised the testing samples and therefore not sent for testing. The entire cross arms were then removed as whole units to ease testing requirements.

Testing of the cross arm included visual examination, fracture surface examination with a scanning electron microscope, chemical analysis, and charpy testing.

Sample photos of these assemblies are shown below in Figures 27 to 31.

Figure 27 – Str. 340 Damaged Members from Cross Arm

Figure 28 – Str. 340 Damaged Members from Cross Arm

Figure 29 – Str. 340 Damaged Members from Cross Arm

Figure 30 – Damaged Cross Arm from Str. 364

Figure 31 – Damaged Cross Arm from Str. 526

8.1.2 **Conductor Testing**

Site analysis of the broken conductors (as discussed below in Section 9.1) have led to the immediate requirement for conductor testing. Two separate companies have been contacted to conduct failure analysis on the conductor. Conductor testing will include visual examination, examination of the failure surface with a scanning electron microscope, chemical analysis, tension and elongation testing of aluminum strands. The purpose of this testing is to verify the conductor meets the specification, and determine the mechanism of failure.

8.1.3 **Suspension Clamp Testing**

All conductor failures occurred near the suspension clamp. It was observed that the conductor slipped in the clamps at the location of the failures. Testing of suspension clamps is required to determine if the slip strength is as per design, and if the bolts will become loose during vibration. Testing will include dimensional tolerance check, chemical analysis, hardness test, clamp pressure verification, and the effect of temperature and vibration on the loosening of the bolts.

8.2 Material Test Results

The material testing has been completed at this time for all critical components to help confirm the root cause of the failure. The suspension clamp and additional conductor analysis will further refine engineering knowledge but are not required at this time to finalize the root cause.

8.2.1 Cross Arm Testing Results

Test results from Kinectrics on the cross arm indicate there were no issues with the material specification. Hardness, charpy impact, and chemical analysis results are all acceptable. The failure analysis concluded that the failure occurred at the location of the bolt holes, and was a ductile failure indicating an overloading event. There were no signs of fatigue or other insidious failure mechanisms.

See attached report "Metallurgical Failure Analysis of Suspension Tower Cross Arm" in Appendix D.

8.2.2 Conductor Testing Results

Testing completed by Acuren determined that the conductor met the required specification and CSA standard. It also determined that the failure was due to overloading of the conductor. This was determined by the necking of the strands at the facture and dimpling on the surface of the strands. See complete report "Failure Analysis of a Conductor" attached in Appendix E.

9 Failure Analysis

9.1 Failed Members

Upon reviewing the failures, the following members within the Electrode Line cross arms failed during the 2021 icing event:

1. The cleat that the insulator string attaches to (consists of two angles, EA 186 and EA 187);
2. The two members that are located on the lower portion of the cross arm (EA 182/183); and
3. The two members on the upper portion of the electrode cross arm (EA 188/189).

Figure 32 – Str. 340

Figure 33 – Str. 340 Close up of Failed Bolt Hole Patterns

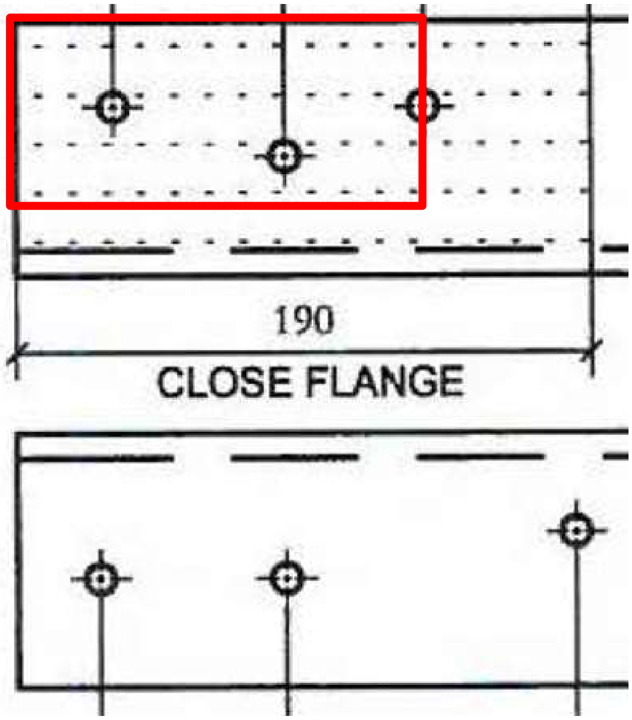

Figure 34 – Member 182 Failure Path on Str. 340

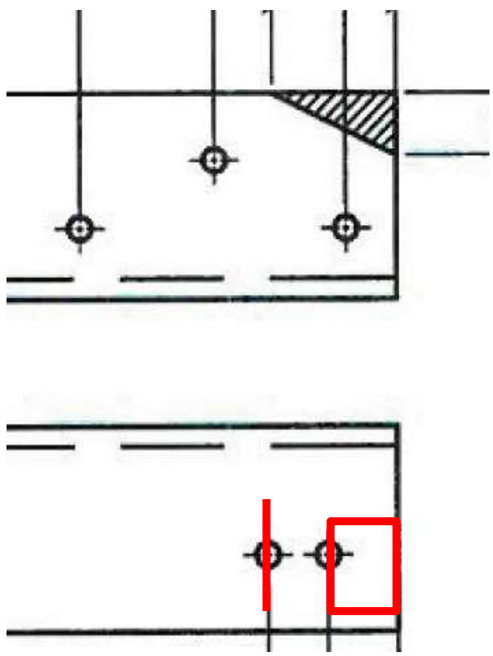

Figure 35 – Member 188 Failure Path on Str. 340

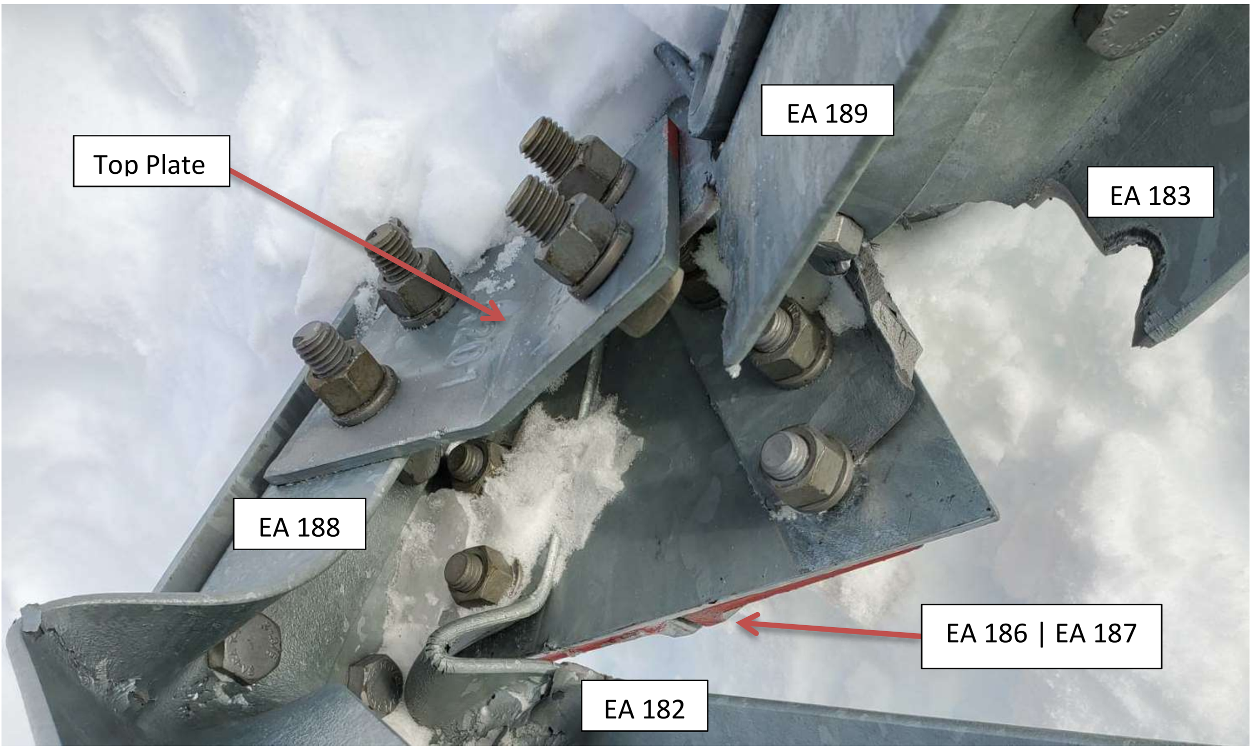

Figure 36 – Str. 343

The failure path of the bolt holes, although not identical, it is quite similar and is caused by similar loadings.

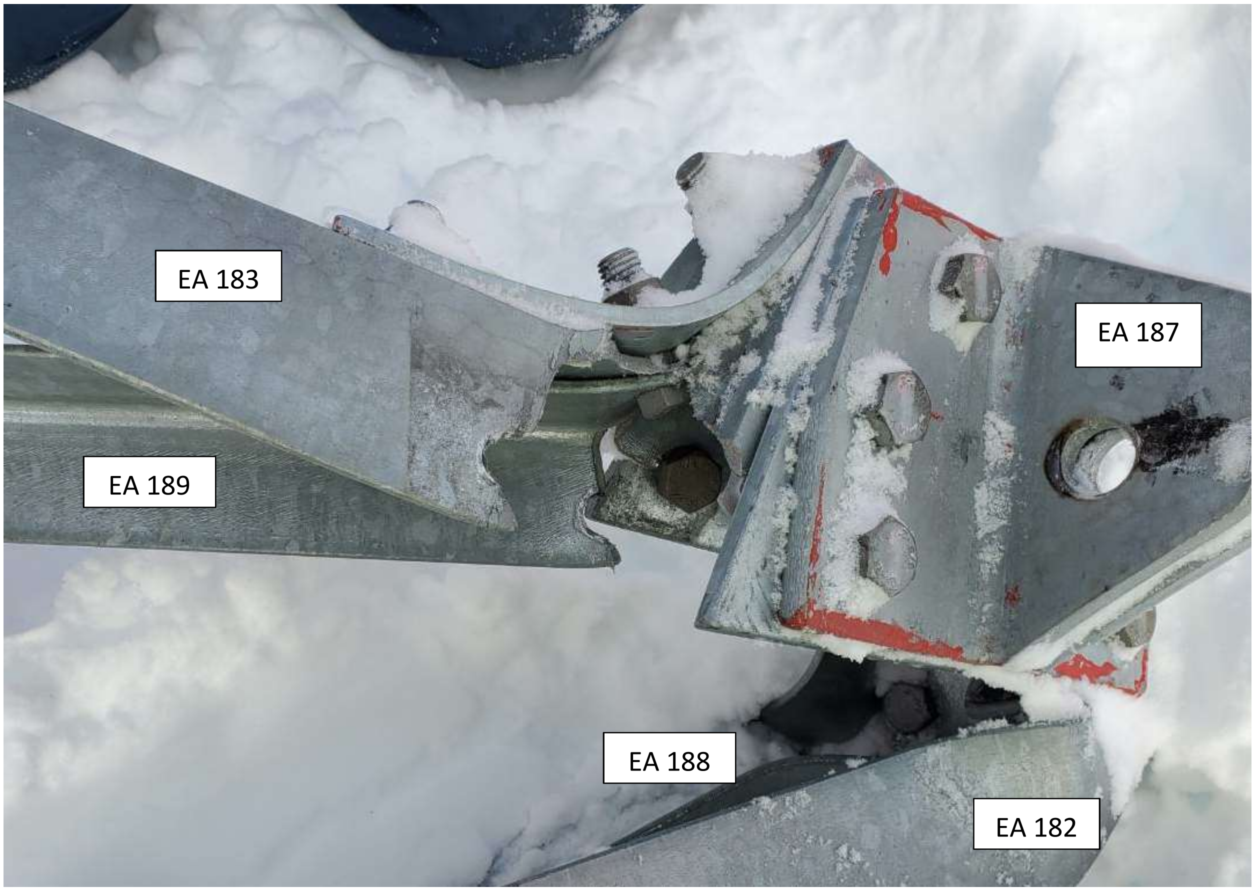

Figure 37 – Str. 343 Alternate View

9.1 Conductor Failure

The majority of conductor Failure has been longitudinal slippage through the suspension clamp as shown in Section 4, Photo 2. This is indicative of ice shedding/unbalanced loading of heavy ice loads.

The external consultant, EFLA, reviewed the photos pertaining to the conductor breakage at tangent structures and provided the following observations of the failure:

- Multiple broken strands close to the suspension clamps;
- Complete removal of sections of the aluminum close to the suspension clamps;
- Indentations on the top aluminum layer close to the suspension clamps;
- Complete failure of the conductor (all strands broken);
- Conductor strands have broken in two modes, i.e. tensile and fatigue or shock loading;
- Conductor strands show signs of excessive rubbing/fretting; and
- Second layer aluminum strands have fatigue or shock loading type failures.

Figure 38 – Damaged EL1 Conductor at Str. 343

Further indication of this theory was presented upon the analysis of the reduction in tensile capacity of the conductor. One broken conductor on EL2 at structure 526 showed only 10 visible broken strands prior to its breakage. With 10 broken strands the conductor tensile capacity would still be approximately 166 kN. See Figure 39.

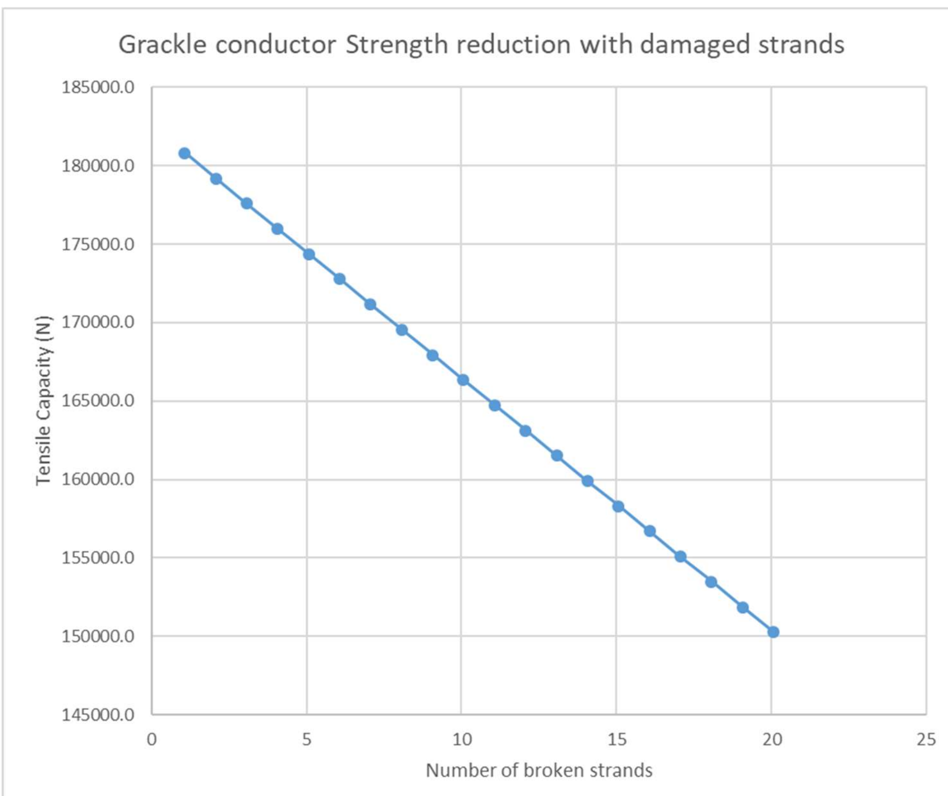

Figure 39 – Electrode Conductor Strength Reduction with Damaged Strands

The conductor would require approximately 16 kg/m of ice load to get to fail under a tensile force of 173kN. See Figure 40

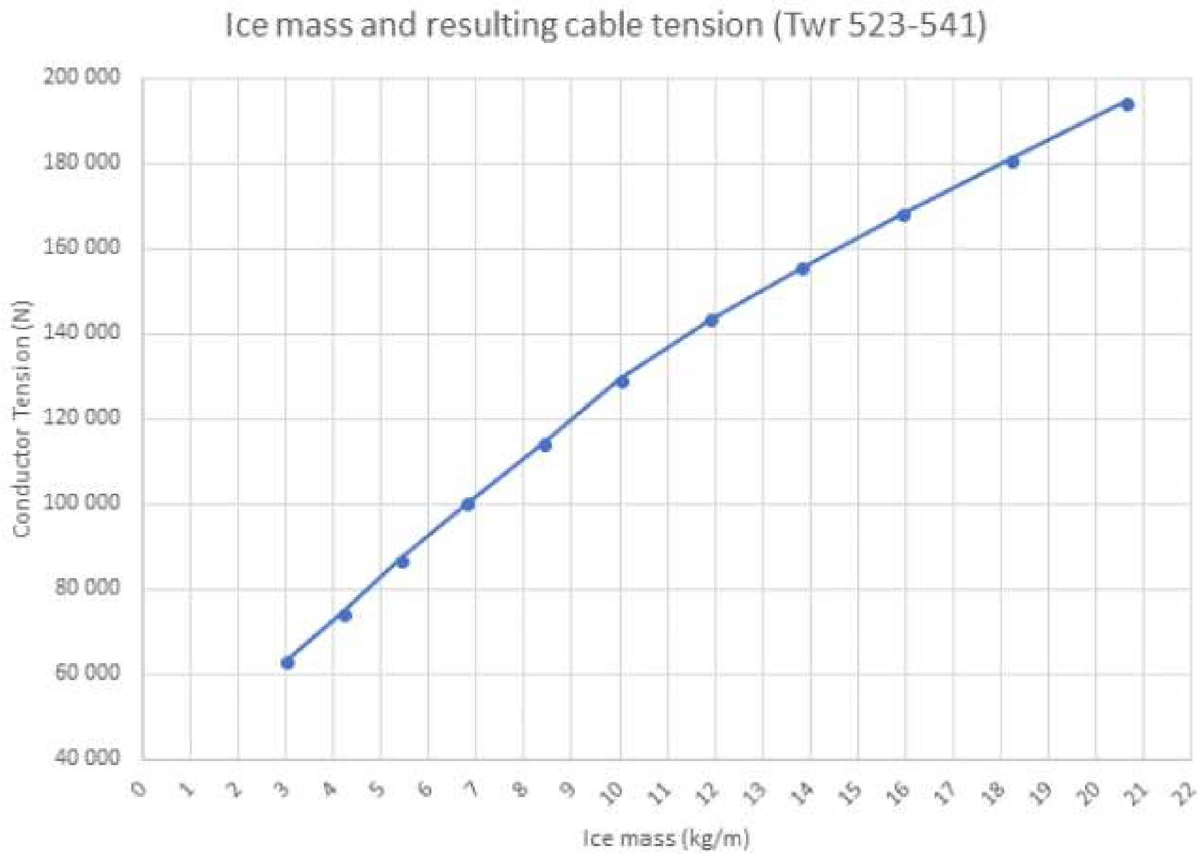

Figure 40 – Conductor Tension vs Ice Mass

Estimated ice loading is described in detail in Section 6.4 above Weather Modeling, however, it can be stated that the estimated ice load is not quite as high as 16 kg/m.

From the aforementioned section, a more accurate ice loading on the conductor is approximately 13.3 kg/m. This loading would induce a 150 kN load in the conductor. If this indeed was the load, then more than 25 strands would need to have been broken for the conductor to fail. These could have been fractures in the 1st and 2nd layers of aluminum which are not all visible from a visual surface inspection.

During vibration or galloping, the 1st and 2nd layer (inner layers) of aluminum tend to have the worst damage as the strands experience fretting from the strands above and below it. The outer layer of aluminum on the Electrode Line ACSR conductor has fretting only due to abrasion from the strands below, hence shows less damage. Figure 41 shows examples of damage on inner layers that are not visible under the outer strands. These are example only and not samples from L3501/2.

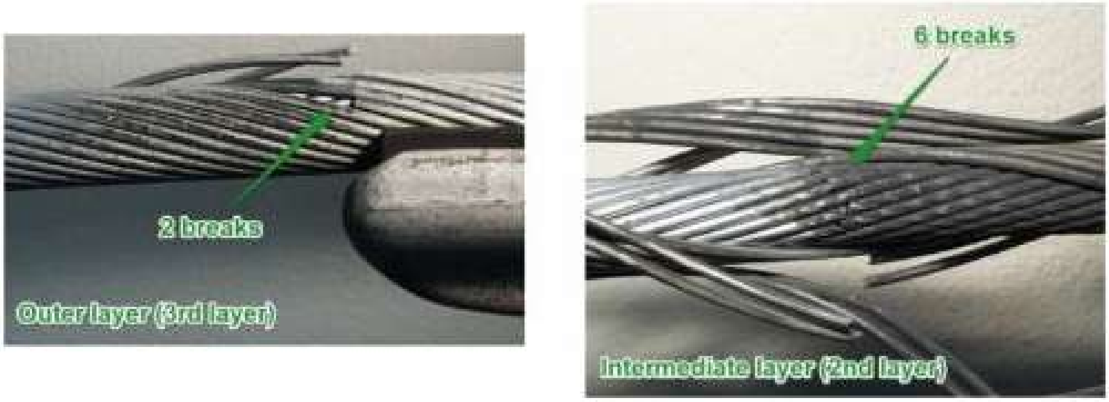

Figure 41 – Example Inner Aluminum Strand Damage (not L3501/2)

Figures 42 and 43 show the damage strands from the Broken EL2 conductor at Str. 526. There are indications from inspection of both fatigue and fracture failures to inner and outer strands.

It should be noted that this analysis is based on the details of the failure and the pictures reviewed. EFLA did not inspect a physical sample of the conductor or complete any testing. Conductor testing completed by Acuren shows no indications of fatigue failure. See the complete report "Conductor Failures – LITL" attached in Appendix C.

Figure 42 – Failed EL2 Conductor at Str. 526

Figure 43 – Failed EL2 Conductor at Str. 526 (2)

9.2 Line Modeling of Observed Conditions

It should be noted that in an as-built state even though the input maximum ice loading is 50 mm of radial ice, the line is able to withstand greater loading depending on the span length and specific tower conditions at site. For those reasons, the line was modelled to check the lines performance under the ice and wind loading experienced during the event.

For the purpose of attempting to recreate the conditions at site that caused the failures a range of conditions were modeled in PLS-CADD. As the exact amount of ice on the line in any given span can vary, the following radial thicknesses were modeled all with a density of 0.75 g/cm^3: 58, 65, 70, 75 mm. For each of these thicknesses the following load cases were modeled:

- Ice only;
- Ice with low wind of 22 km/h;
- Unbalanced ice of 70/100% ice thickness on EL1; and
- Unbalanced ice of 28/100% ice thickness on EL1.

As there is no way to know how much ice will shed for adjacent spans, the unbalanced ice percentage are based on the design loads (70/100) and CSA 60826 recommendations (28/70).

The total L3501/2 is broken into 37 separate PLS-CADD files due to the long length. The three clusters of failures are in three separate PLS-CADD files from structures:

- 243 to 341 (99 towers, 88 A1 towers);
- 341 to 388 (48 towers, 44 A1 towers); and
- 497 to 596 (100 towers, 90 A1 towers).

There were no failures of any A1 towers in any of the load cases 58 mm of ice thickness. With 60 mm of ice thickness there are failures in the unbalanced ice load cases. With 70 mm or more of ice thickness there are some failures in the ice and Ice + wind load case with many more failures in the unbalanced ice load cases.

Table 5 – Towers Exceeding Max Capacity Section from Str. 243 to 341

Ice Thickness (mm)	Number of Str. Above Maximum Capacity per Load Case			Str. Damaged in Field/Over Max Cap		
	Ice	Ice + Wind	UBI	Ice	Ice + Wind	UBI
58	0	0	1	None	None	None
65	1	1	40	None	None	335, 340
70	25	26	88	None	None	318, 335, 336, 340
75	60	61	88	340, 335, 336	340, 335, 336	318, 335, 336, 340

Table 6 – Towers Exceeding Max Capacity Section from Str. 341 to 388

Ice Thickness (mm)	Number of Str. Above Maximum Capacity per Load Case			Str. Damaged in Field/Over Max Cap		
	Ice	Ice + Wind	UBI	Ice	Ice + Wind	UBI
58	0	0	0	0	0	0
65	0	0	15	0	0	343, 364, 365, 367, 369
70	7	8	44	0	0	343, 344, 363, 364, 365.367, 369
75	22	25	44	364, 369, 367, 365, 343, 344, 363	364, 369, 367, 365, 343, 344, 363	343, 344, 363, 364, 365.367, 369

Table 7 – Towers Exceeding Max Capacity Section from Str. 497 to 596

Ice Thickness (mm)	Number of Str. Above Maximum Capacity per Load Case			Str. Damaged in Field/Over Max Cap		
	Ice	Ice + Wind	UBI	Ice	Ice + Wind	UBI
58	0	0	0	NA	NA	NA
65	0	0	40	NA	NA	526
70	28	29	83	None	None	526, 513, 518, 527
75	60	62	90	526, 527	526, 527	All

This suggests that the unbalanced load case is more critical. Also, assuming a uniform ice thickness from span to span there would be more towers failures if the failures were due to ice, or ice + wind. Ice shedding is a more random occurrence. The failures due to unbalanced ice would only occur in the location were the ice has shed.

These finding also suggest the ice load is equivalent to a radial thickness somewhere in the range of 65 to 70 mm. Under this range we are less likely to see failures, and over this range we are likely to see more failures due to ice only. The modelling indicates that considering the loading seen during the icing event structural failures would be expected.

9.2.1 **Affects of Wind**

The initial analysis was ran for a wind + ice combination with a low wind of 22 km/h. The WRF model and near by station suggest the wind could be higher. A wind + ice combination with a wind of 43 km/h was modeled in PLS-CADD for Cluster 3. The results show that the increase in wind would increase the utilization of the structures in this section on average by 3%.

A wind perpendicular to the line is generally consider the most critical for the strength analysis of tangent structures. It was noted the wind at the time of the incident was North-west, or generally parallel to the line. Changing the wind direction from perpendicular to parallel decreased the utilization of the structures in this section on average by 3%.

9.3 Analysis of Failure Condition

9.3.1 **Cross Arm Failure**

The PLS-TOWER model for each tower that experience cross arm failure in the field was reviewed to determine the load case that would produce this failure. Table 8 summarizes the load cases that would causes a failure under damage limit (using a 0.9 strength factor for the tower steel) and the ultimate limit. It should be noted that these load cases do not take in to account the dynamic force that would occur during an ice shedding event or conductor galloping. If dynamic loading is taken in to account the ice thickness at which unbalanced ice (UBI) load cases would cause failures would be lower. The table notes the thickness of ice in mm (from 58 to 75 mm), and the combination of unbalanced ice by % of the thickness (28/70% or 70/100%).

Table 8 – Load Cases which Cause Failure

Str. #	Damage Limit Load Case	Ultimate Limit Load Case
335	UBI 65 mm 28/70	UBI 70 mm 28/70
340	UBI 65 mm 28/70	UBI 75 mm 70/100
343	UBI 70 mm 70/100	UBI 75 mm 70/100
362	NA	NA
363	UBI 70 mm 70/100	UBI 75 mm 70/100
364	UBI 65 mm 28/70	UBI 70 mm 28/70
366	UBI 75 mm 70/100	UBI 75 mm 28/70
368	UBI 75 mm 70/100	NA
514	UBI 65 mm 70/100	UBI 70 mm 70/100
526	UBI 65 mm 28/70	UBI 70 mm 28/70
527	UBI 70 mm 70/100	UBI 75 mm 28/70

9.3.2 **Conductor Slippage**

The slip strength of the conductor is 65.2 kN. Under normal conditions the longitudinal loads on the tangent assemblies should be balanced between spans resulting in a 0 longitudinal on the clamps. Unbalanced ice loads, due to ice shedding, will cause longitudinal loads on the clamp. The table below summarizes the longitudinal loads at the attachment. Note that this is the static load caused by the unequal weight of ice between spans. There will also be a dynamic load during shedding of ice. Also, suspension clamp slip strength is dependent on correct install and proper torqueing of the bolts.

The below numbers indicate that the loading seen during the event could exceed the slip strength of the conductor.

Table 9 – Longitudinal Loads at the Attachment

Str. #	UBI 58 mm EL1 70/100	UBI 58 mm EL1 28/70	UBI 65 mm EL1 70/100	UBI 65 mm EL1 28/70	UBI 70 mm EL1 70/100	UBI 70 mm EL1 28/70	UBI 75 EL1 70/100	UBI 75 mm EL1 28/70
318	34.0	48.2	38.3	54.3	41.7	58.5	45.4	62.7
335	34.5	48.7	38.9	54.9	42.4	59.2	46.1	63.4
336	34.5	48.7	38.9	54.9	42.4	59.2	46.1	63.4
340	34.5	48.7	38.9	54.9	42.4	59.2	46.1	63.4
342	33.3	48.0	37.6	53.9	41.0	58.0	44.7	61.9
343	33.3	48.0	37.6	53.9	41.0	58.0	44.7	61.9
344	33.3	48.0	37.6	53.9	41.0	58.0	44.7	61.9
361	33.5	47.9	37.8	53.9	41.1	58.0	44.8	62.1
362	33.5	47.9	37.8	53.9	41.1	58.0	44.8	62.1
363	33.5	47.9	37.8	53.9	41.1	58.0	44.8	62.1
364	33.5	47.9	37.8	53.9	41.1	58.0	44.8	62.1
365	33.5	47.9	37.8	53.9	41.1	58.0	44.8	62.1
366	33.5	47.9	37.8	53.9	41.1	58.0	44.8	62.1
367	33.5	47.9	37.8	53.9	41.1	58.0	44.8	62.1
368	33.5	47.9	37.8	53.9	41.1	58.0	44.8	62.1
369	33.5	47.9	37.8	53.9	41.1	58.0	44.8	62.1
513	34.7	48.6	39.2	54.9	42.6	59.3	46.4	63.6
514	34.7	48.6	39.2	54.9	42.6	59.3	46.4	63.6
518	34.7	48.6	39.2	54.9	42.6	59.3	46.4	63.6
525	33.1	47.8	37.4	53.6	40.7	57.7	44.4	61.6
526	33.1	47.8	37.4	53.6	40.7	57.7	44.4	61.6
527	33.1	47.8	37.4	53.6	40.7	57.7	44.4	61.6

9.4 Block Failure (Rupture) Calculations

In each cross arm failure, member 188/189 suffered block shear tear out failure such as the one shown below on member 188 on Str. 340.

Figure 44 – Block Tear Out on Member 188 from Str. 340

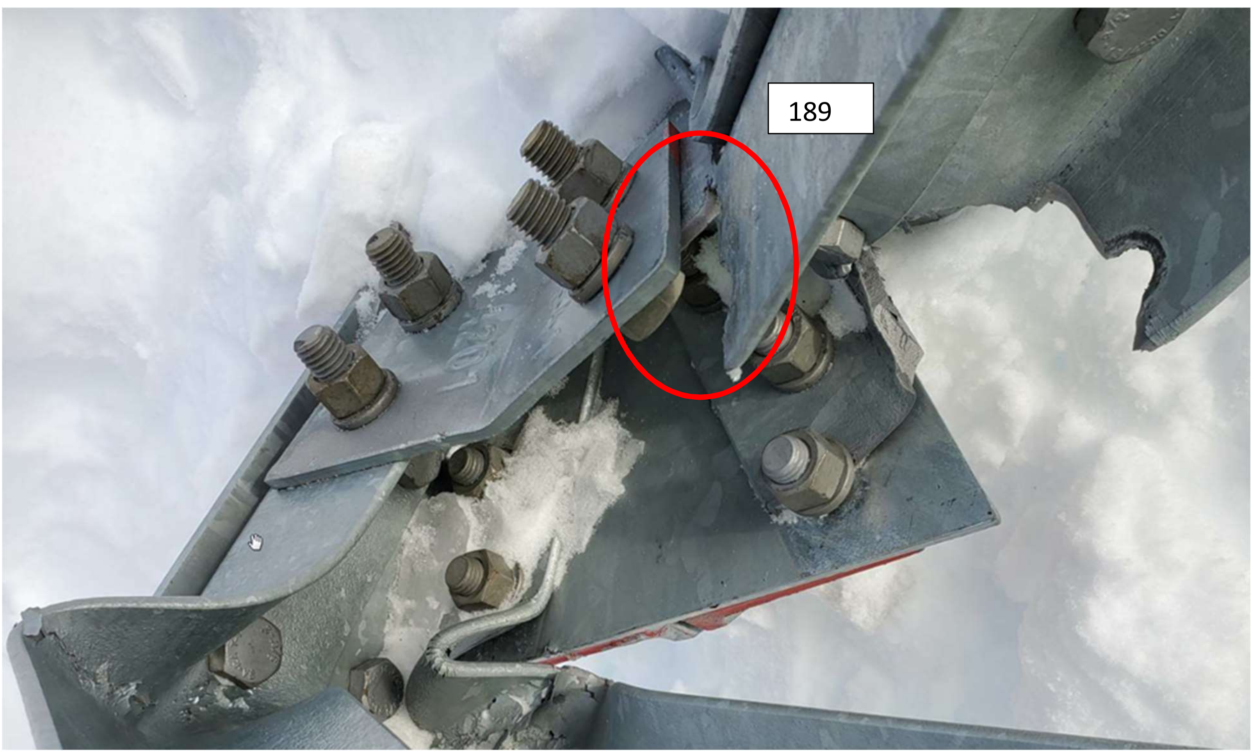

Figure 45 – Block Tear Out on Member 189 from Str. 343

The failure path which occurred above was calculated to happen at roughly 123 kN. This calculation is shown in Mathcad calculation shown below as the Rupture (R_n) value. The Design Max load taken from of ILK-JY-SD-6200-TL-H03-0001-01 (350 kV HVdc Line Tower Type A1 Design Calculations) is roughly 100 kN for that specific member. This proves that the applied load during the ice event must have exceeded the design load for the failure path shown above to occur.

Area Descriptions:

A_{gv}	Gross Area in Shear (don't subtract bolt diameters)
A_{nv}	Minimum Net Area in Shear (along line of force)
A_{nt}	Minimum Net Area in Tension (perpendicular to line of force)

Following calculations are for the failure in:

Member: **188/189**

Members size: **63.5 x 63.5 x 4.8 mm**

Member: 182/183

Member size: 76.2 x 76.2 x 6.4 mm

Bolt Hole Diameter: $d_{bh} := 17.5\ mm$

$A_{gv} := 58\ mm \cdot 4.8\ mm$

$A_{gv} = 278.4\ mm^2$

$A_{nv} := 4.8\ mm \cdot (58\ mm - (0.5 \cdot 17.5\ mm))$

$A_{nv} = 236.4\ mm^2$

$A_{nt} := 4.8\ mm \cdot (24\ mm + 24\ mm - 17.5\ mm)$

$A_{nt} = 146.4\ mm^2$

Constants:

$F_u := 448\ MPa$ $\quad F_y := 345\ MPa$ $\quad U_{bs} := 1$

Formulae:

$$R_{nnet} := 0.6\ F_u \cdot A_{nv} + F_u \cdot U_{bs} \cdot A_{nt} \qquad R_{ngross} := 0.6 \cdot F_y \cdot A_{gv} + F_u \cdot U_{bs} \cdot A_{nt}$$

$$R_n := min\left(R_{nnet}, R_{ngross}\right)$$

Outputs:

$R_n = 123.216\ kN$

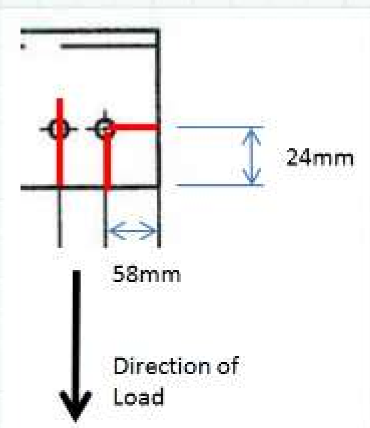

Figure 46 – Block Tear Out Calculations from Mathcad

9.5 FEM

EFLA has modeled the cross arm in a finite element model to better understand the failure. The model replicated the failure observed in the field with a rupture failure at the bolt holes at the end of the angles on the electrode cross arm.

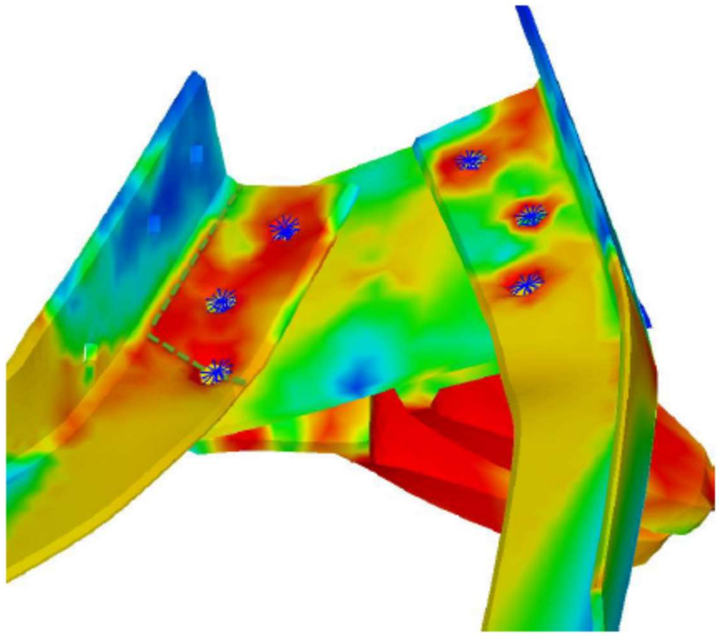

Figure 47 – Block Tear out Failure Path on FEM

The figure below shows the failure envelop for the vertical and longitudinal loads. The failure envelop for the FEM model is shown in red based on the local strain and local buckling. It should be noted that the PLS-TOWER model under estimates the vertical and over estimates the longitudinal capacity according to the FEM. Also note that the maximum vertical design load on the electrode cross arm is 64.9 kN (under maximum ice) and the maximum longitudinal design load is 52.7 kN (under broken conductor condition), both which are within the failure limits based on the FEM. The arm design is consistent with the requirements under the design loadings and loading seen during the icing event could exceed this capacity. The failure pattern seen in cross arms are consistent with the loading seen.

Note that a longitudinal load of 65 kN will cause failure in the cross arm according to the FEM. This is approximately the slip strength capacity of the suspension clamp were we are also seeing failures. A combination of the vertical and longitudinal load caused by unbalanced icing would fall outside the failure limits of the chart. For example, the unbalanced ice load case 75 mm of radial ice with 28/70% of ice thickness on the ahead/back span for str. 525 has a 62 kN longitudinal load and a 41 kN vertical load. The FEM plot suggests this will result in a failure of the cross arm. See Appendix F for complete report "Failure Analysis of Electrode Cross Arm in Labrador-Island Transmission Link (LITL)".

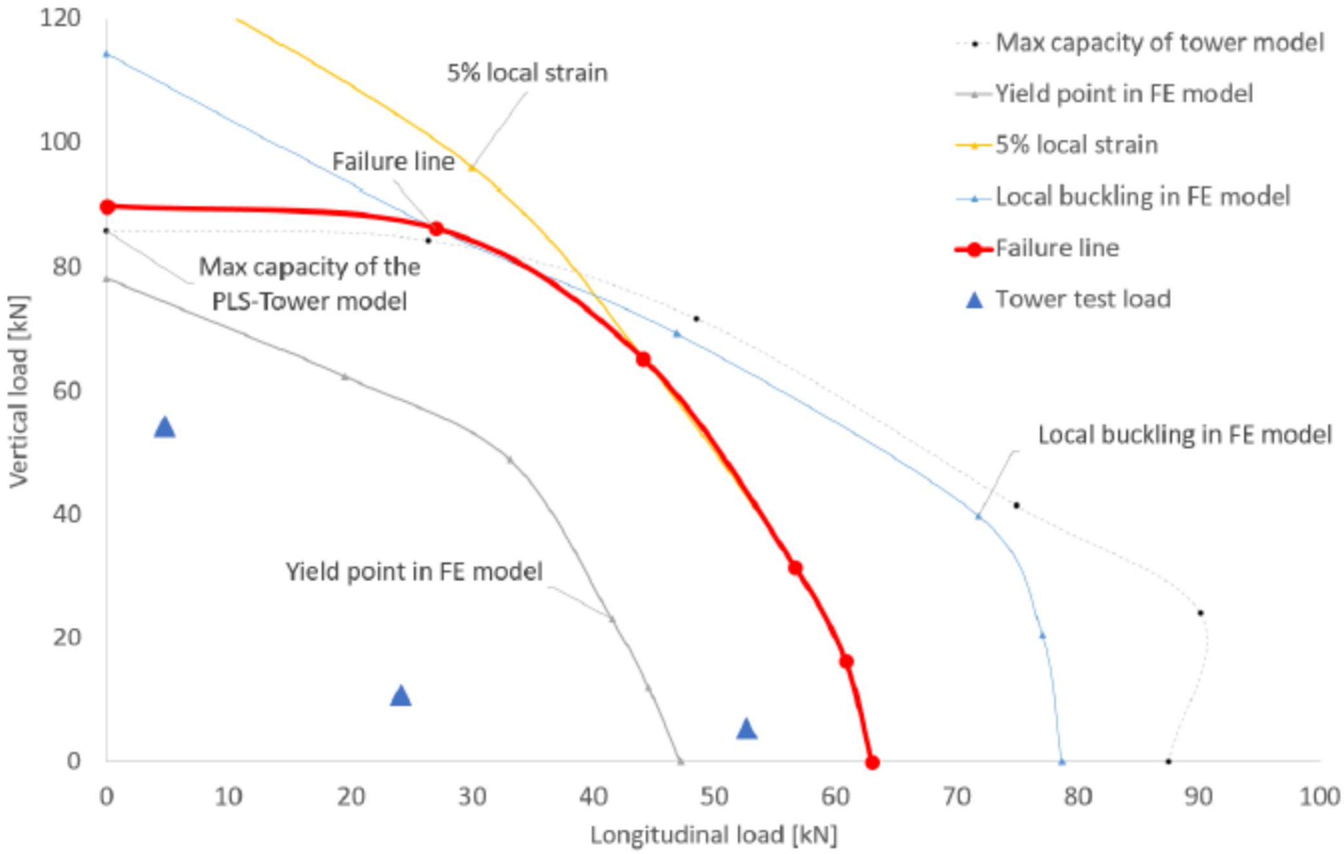

Figure 48 – Failure Envelope for the Cross Arm

9.6 Hardware Performance

Due to the short length of the electrode insulator assembly, and the large insulator swing due to unbalanced ice, it was observed that the insulator can contact the conductor. See Photo 22. It was calculated that this switch can be created by a difference of approximately a 4.5 kg/m ice load on adjacent spans. See Appendix C for more details.

Photo 22 – Insulators on Electrode Assembly Contacting the Conductor

There have been dents observed in the conductor near the insulator assembly. These dents are likely due the insulator contact. The hardness of the glass is greater than the hardness of the conductor. The denting could be a contributing factor to the conductor damage.

Photo 23 – Dent in the conductor near the tangent assembly

The slip strength of suspension clamps can be affected by the torqueing of the bolts. If the bolt were not torqued as specified on the drawing the slip strength of the clamp will be less than specified, and a lower longitudinal load caused by unbalanced icing will cause the clamp to slip. The lockwashers may not have adequately prevented the bolts from backing off if exposed to movement or vibration. The slipping of the clamp can contribute to conductor failures.

9.7 Galloping and Damper Failures

Galloping in these regions has been observed on the line since construction. Galloping is an extreme movement of the conductors in a sine wave motion. It can be caused by specific wind conditions, and is sometimes observed on lines with small amounts of icing. The towers on L3501/2 have been designed so the wires can gallop without flash over between wires. Galloping will cause fatigue on hardware and conductors over time.

In contrast to galloping, Aeolian vibration protection is designed into the line using Stockbridge vibration dampers. Damper failures have been occurring on the line since construction. An initial study in to the damper failures found that the messenger wire was failing due to fatigue. The initial batch of dampers tested also found a material defect that could lead to this failure.

Additional damper testing was completed in 2019, and it was again determined that failure was due to fatigue. The investigation in to damper failures is continuing with laboratory testing of the dampers in cold temperatures, and a field vibration monitoring program to determine if the line is adequately protected from Aeolian vibration.

There were also failures of corona rings noted on the pole conductor tangent assemblies. These corona rings have also been sent for testing.

The possible cause of the damper and corona ring failures could be vibration or galloping. Galloping and vibration issue, while a contributing factor have been ruled out as the root cause of the cross arm and conductor based on loading scenarios, material testing and failure pattern but a detailed damper study is ongoing.

10 Conclusion and Observations on Root Cause

There are numerous indications that lead to the conclusion that the ice loads experience at site were above the design ice load.

- Measurements from pictures vary from span to span and wire to wire from 56 to 105 mm, but all exceed the design radial ice thickness of 50 mm.
- Samples weights vary but a sample consider representative of what was observed on the line was calculated to have a 13.3 kg/m unit weight and 880 kg/m^3 density. This would be an equivalent to 54 mm of radial ice exceeding the design.
- The WRF model and ice accretion model suggest the ice load greater than the design in some locations.
- PLS-CADD modeling predicts the members in the electrode cross arm are critical under maximum ice and unbalanced ice loads for thickness greater than 65 mm.
- The FEM failure envelop suggest ice thickness greater than design are required to failure.
- Conductor meets specifications. Conductor failure determined to be a tensile failure due to overloading.
- Cross arm meets specification. Cross arm failure was a ductile failure due to overload.

Storm Observations and Design Loads:

- The original design for the region was selected in 2010 and bordered on a CSA standard 500-year ice loading.

- The modeling of the storm suggests the icing event exceeds the CSA standard 500-year ice load, and the design load.
- Recent Modelling using newer WRF modelling methods suggest this storm event would exceed a 50-year event.
- The storm itself had a very long duration (in excess of a month) due to drastic temperature swings which is not common for freezing rain events.

Line Component Performance:

- PLS-CADD tower modelling indicates that ice shedding causing an unbalanced loading situation would cause the type of failures experience.
- Finite Element Modelling and Design Calculations for the cross arm component indicate there are no significant design issues and the loads seen would cause the failure pattern seen along the line.
- Material testing suggest there were no issue with the material and they meet the specifications.
- Despite ice loads above the design, there were no complete tower failures, or failure of the pole conductor.
- There are some indications that bolts of the suspension clamps were not evenly torqued. This could be an error during construction, or a results of vibration or galloping. The bolts being under torqued will result in the slip strength of the clamps being lower than the design. Testing of suspension clamps is ongoing.

Galloping/Vibration issues on the line:

- Fatigue failure observed on conductor at tangent assembly clamps is indicative of galloping or vibration wear.
- Damper failures have been experience in the sections of the line where we are experience the current line failures.
- Galloping has been observed on the L3501/2 in Labrador in the past.
- These issues are being investigated separately, but are not believed to be the root cause of failure of the cross arms or electrode conductor.

11 Recommendations

Some possible recommendations at this stage are listed below. These recommendations will require further study.

- Monitoring of ice and removal as required. Both real time monitoring and line patrols.
- Additional bracing on electrode cross arm to increase longitudinal capacity.
- Alternate damper design – to improve damping, and reduce failures due to harsh conditions.
- Air spoiler to reduce the effects of galloping.
- Alternate electrode suspension clamp design with increased slip strength.
- Increase distance between insulator and conductor in the electrode conductor.

11.1 Ice Monitoring and Removal

Incorporating ice monitoring and removal in to the maintenance plan for L3501/2 could prevent the ice accumulating to a thickness that would over load the line. This would include line patrols and real time monitoring equipment. It is difficult to patrol the line by helicopter during an icing event. Alternatives could be to monitor the icing through a ground patrol or real time monitoring equipment.

11.2 Additional Bracing

Addition bracing in the electrode cross arm could strengthen the longitudinal capacity and protect against failures due to unbalanced ice. Any changes to the tower design would have to be reviewed by a structural Engineer to understand how the changes would affect the structure and loading path, as well as the failure method. The design shouldn't be strengthened such to create additional problems to the overall tower.

Changes to the line design capacity due to bracing, or physical line changes in this zone would have to be reviewed to determine what level of icing is required from a system perspective and would need to be consider in comparison to the overall line importance and other regions.

11.3 Alternate Damper Design

A possible alternate damper design is the Bretelle damper, which is used by Statnett and Landsnet in Norway and Iceland which experience similar icing as Newfoundland and Labrador. It is a simple design of a wire clamped to the conductor which is relatively inexpensive and easy to install.

Photo 24 – Bretelle Dampers

11.4 Air Spoilers

Air spoilers are a galloping prevention device that are designed to disrupt the flow of air over the conductor preventing the mechanism that creates galloping.

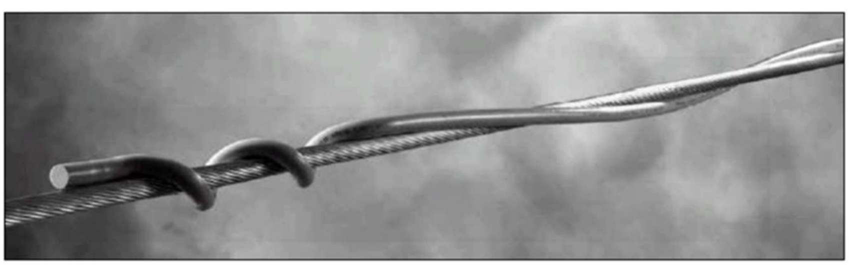

Photo 25 – Air Spoilers

11.5 Suspension Clamp Design

The current suspension clamp design does not use armor rods to protect the conductor at the attachment point. A larger clamp with armor rods could be considered. As mentioned in Section 7.2, the locking washer and general clamp design is not as robust as it could be. Loads seen during the storm were in excess of this slip strength but substitution to a different strong clamp could aid in the long term.

Appendix A - Icing Storm in Labrador in January 2021 – Assessment of Icing in LITL

ICING STORM IN LABRADOR IN JANUARY 2021
-ASSESSMENT OF ICING IN LITL-

14.04.2021

REPORT – INFORMATION SHEET

DOCUMENT SYSTEM CODE	REPORT TITLE
8321-004-MIN-003	Icing storm in Labrador in January 2021 – Assessment of icing in LITL
REPORT NUMBER / TOTAL PAGES	**PROJECT**
01 / 25	Labrador Island Transmission Link
PROJECT MANAGER – CLIENT REPRESENT.	**CLIENT**
Trevor Andrews	Newfoundland and Labrador Hydro
PROJECT MANAGER – EFLA	**AUTHOR**
Viven Naidoo	Egill Thorsteins

KEYWORDS

Glaze ice, WRF, icing model

REPORT STATUS

☐ Draft
☐ Copy editing
☒ Final

REPORT DISTRIBUTION

☐ Open
☒ With client permission
☐ Confidential

TABLE OF CONTENTS

1 INTRODUCTION AND MAIN CONCLUSION

1.1 Introduction

This study uses an icing model combined with WRF hindcast simulation to evaluate the January icing storm experienced on the Labrador Island Transmission Line (LITL) in Labrador. The storm is referred to as the January 2021 although the study considers the period that extended into February.

The main underlying questions in the study are:

- Can icing models using a WRF hindcast simulation predict the icing reasonably?
- How much icing does the icing model predict in the event in January 2021?
- What is the return period of the icing event when using the icing model on long-term data?
- How is the variability of the predicted ice load along the LITL?
- How frequent are icing storms similar to the January 2021 storm

EFLA Consulting Engineers performed this analysis with assistance by Kjeller Vindteknik (KvT). KvT provided the input data into the icing model by performing a hindcast simulation of the weather condition in January 2021 and a long-term simulation of the weather in 1979-2020. KvT has presented a comparison of the hindcast simulation to freezing rain conditions in [1].

Three icing models are used in the study: (i) Chainé model, (ii) Simple model by K. Jones at CRREL. (iii) M1 icing model made by EFLA.

1.2 Main conclusion

The main conclusion of the preliminary analysis are the following:

- The icing model using WRF simulation as input data does capture the icing accumulation in the January ice storm quite well.
- Detailed measurements of ice weight and icing extension in the January icing storm are unavailable. Damage to structures shows that towers from 318 to 344, 361 to 369 and 507 to 527 were most exposed to icing. The icing models show that the area between tower 318 to 550 had the highest predicted ice load. Thus, the icing model captures the icing area quite well.
- The M1_H icing model predicts the highest ice load at tower 531 as 13.3 kg/m (on 30 mm conductor at 20m), equal to 56 mm radial ice. The ice samples measured and weighed had unit weights ranging from 5.1 to 10.6 kg/m. Some of the ice samples did not represent the total ice cross-section. The whole ice cross-section weight of sample 10.6 kg/m is believed to be 13.3 kg/m at tower 340. It is not known if the sample is from the pole conductor, electrode, or the OPGW. Overall the ice weight of the M1_H model is found to be convincing compared to available icing data.
- The 50 years return period was estimated using 40 years of hindcast simulation. The ice load in the January ice storm exceeded the 50-years loading at most tower locations between 350 to 600.

- The icing type in the January ice storm was mostly glaze ice, but partly combined with rime icing. The glaze icing was due to supercooled rain in some areas, but the supercooled rain was mixed with snow and graupel in other areas.

2 ICING STORM IN JANUARY 2021

2.1 General

During the first week of January 2021, a freezing rain storm event occurred within central NL with significant precipitation. This storm caused damage to a section of the LITL in Labrador. Three specific sections of the line sustained damage; towers from structure 318 to 344, 361 to 369, and towers 507 to 527.

Kjeller Vindteknikk (KvT) made a WRF hindcast simulation of the January 2021 ice storm and assessed the weather condition. The main findings and conclusions are as follows:

- A low-pressure system caused the icing event with a stationary front located over Labrador, separating warm and moist maritime air to the southeast from the cold continental air on the north-western side, producing a belt of freezing precipitation across the Labrador region.
- The WRF model results correspond well with both surface observations and vertical soundings at Goose Bay weather stations.
- A persistent melting layer was aloft for both areas with affected towers (near 340 and 530) while the temperature near the ground is below 0°C. The predicted hourly precipitation rates indicate that the main freezing precipitation event duration is approximately 48 hours. The main event is followed by one additional day of light, scattered precipitation.
- At tower 340, the predominant predicted precipitation type is snow, but graupel (ice pellets/sleet) and freezing rain is also present most of the time. At tower 530, freezing rain is the predominant precipitation type but occasionally mixed with snow and graupel. Note that the ice accretion model used to calculate the conductor loading associated with freezing rain takes contributions from both snow and graupel into account when they occur simultaneously.
- Wind speeds of 10 - 12 m/s are predicted at both sites during the main icing period. The relatively high wind speed has probably contributed significantly to the ice accumulation rate on the power line.
- Even though there are apparent terrain effects on the horizontal precipitation distribution, it is difficult to evaluate the exact location of the maximum zones of freezing precipitation.

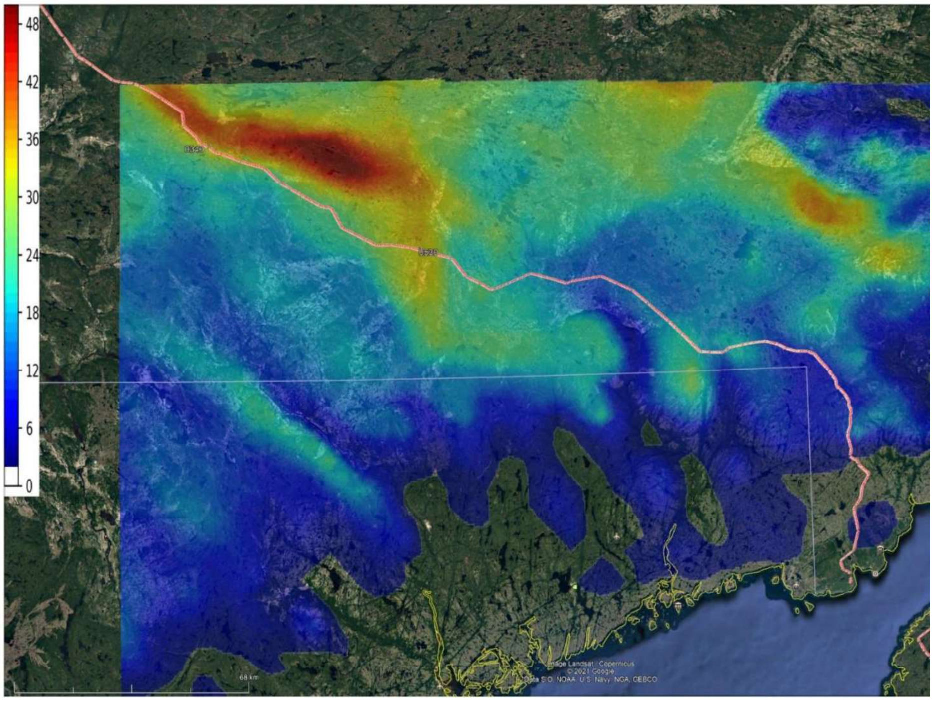

FIGURE 1 KvT result on the accumulated amount of Freezing rain + graupel [mm] at surface level in the WRF 4km domain for the simulated period 4-9 January 2021.

2.2 Areas exposed to icing and quantification of icing

Detailed quantification of icing within the icing area is not available, but it can be expected that failures represent the most exposed icing areas. Failures were experienced in four areas, in three of the areas, there were multiple failures; they are clustered together:

i. Tower 318
ii. Cluster 1. 335-344
iii. Cluster 2. 361-369
iv. Cluster 3. 513-527

Few icing samples were measured and weighted by Nalcor. The ice samples measured and weighed were calculated to have unit weights ranging from 5.1 to 10.6 kg/m. Note that the ice samples do not represent the total cross-section of ice that was present on the line. For example, the 10.6 kg/m sample was estimated to represent approximately 80% of the total cross-section. The total estimated unit weight of ice on the line based on this sample is 13.3 kg/m (at tower 340).

The densities calculated from the samples range from 600 to 880 kg/m^3. These densities suggest a mix of rime and glaze ice.

FIGURE 2 Ice falling from the conductor at tower 340, date 2021-01-18

2.3 Description of the icing

The icing appearance varied along the line. In some areas, it was with a white appearance quite dense, see Figure 3. It was mixed with rime in some areas, see Figure 5, and in others, it was a clear glaze with icicles; see Figure 4.

FIGURE 3 Icing at tower 340, date 2021-01-15

FIGURE 4 Glaze icing with icicles. Date 2021-01-15.

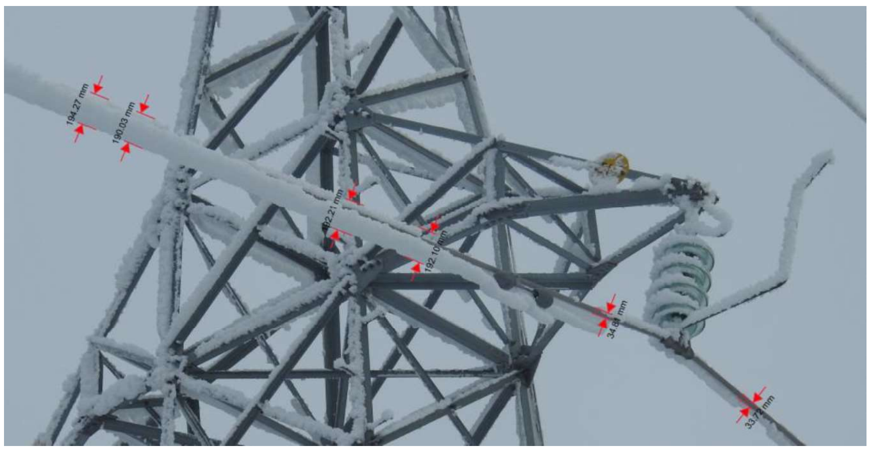

FIGURE 5 Rime icing on structure 527, date 15-01-2021.

FIGURE 6 Rime icing onto glaze icing

3 ICING MODELS

3.1 Icing models

An icing model needs to have the following processes (i) ice accumulation, (ii) ice persistence, and (iii) ice removal. The icing accumulation process consists of an accumulation of rime icing (in-cloud icing), wet-snow icing and glaze icing. The ice removal processes are sublimation, melting and ice shedding. Change in icing mass at each hour consists of the following processes:

$$\left({dM}/{dt}\right)_{Tot} = \left({dm}/{dt}\right)_{Rime} + \left({dm}/{dt}\right)_{Wet-snow} + \left({dm}/{dt}\right)_{Glaze} - \left({dm}/{dt}\right)_{Sublimation} - \left({dm}/{dt}\right)_{Melting} - \left({dm}/{dt}\right)_{Shedding}$$

Three icing models are used in this study:

- Chainé model.
- Simple model
- M1 model

The Chainé model, developed by Chaine and Skeates' (1974), has been widely studied and used in Canada. It models the accumulation from freezing rain and it is the underlying model used to make the glaze ice loading map in the CSA standard. It has mainly been used with input data from meteorological field measurements and observations. Thus, some additional assumptions are needed when using WRF data as an input[1]. In this study, The Chainé model is assumed to have the same ice removal as the M1 model.

The Simple model for freezing rain accumulation was developed by Kathleen Jones at CRREL. The model is often used with weather observations, like the Chainé model, but some papers show its use combined with WRF data. The Simple model is believed to overestimate the loading since it assumes that all water flux will freeze. Generally, it predicts lower icing than the Chainé model. In this study, The Simple model is assumed to have the same ice removal as the M1 model. !

The M1 model includes accumulation from glaze icing, rime icing and wet-snow and it models the ice persistence and ice removal. The model is based on the standard cylindrical icing model with some adjustments, especially to improve the freezing rain accumulation. The M1 icing model is made by EFLA. Detailed assumptions of the Chainé, Simple and M1 model will be given in the upcoming report on glaze icing prediction in the LITL.

Following is a short description of the M1 model.

- The model includes the following icing types: Rime ice, wet-snow and glaze ice.

[1] Hourly weather code e.g. Observations of freezing rain is used to classify freezing rain, thus temperature is not used. Temperature is used when using WRF data and therefore influences the icing prediction sensitivity around 0°C.

- Rime ice accumulation is primarily according to the Makkonen model with recent improvement using Langmuir droplet size distribution for freezing efficiency ($\alpha3$). This study uses Langmuir B distribution.
- The wet-snow model follows the proposal from B.E. Nygaard.
- The glaze ice model is a model with some modifications compared to other models. It uses information on the temperature inversion layer to shift the modeled temperature slightly to increase potential icing around 0°C. Glaze icing conditions are defined when the wet temperature (Tw) < 0°C. Water content is a mixture of rain+snow+graupel. Collision efficiency ($\alpha1$) = 1.0. Sticking efficiency ($\alpha2$) is introduced in the model, and it varies depending on the mass ratio of rain/(rain+snow+graupel) and Tw. Alpha3 is calculated according to energy balance but assumed > 0.7 due to icicle growth and diverse uncertainty. The accumulation area is assumed larger than circular, can be up to 30% larger. Density = 890 kg/m^3. It is expected that the M1 model tends to overestimate glaze icing around Tw=0°C since the minimum value of $\alpha3 \geq 0.7$.
- Ice removal is modeled with the following processes: ice melting, sublimation and ice shedding. Melting is modeled using energy balance. Sublimation is modeled with energy balance, surface temperature unknown and found by iteration. Ice shedding is modeled with simple assumptions using temperature and wind speed.
- The model considers the actual line direction when calculating the icing.

3.2 Assumptions in icing calculations

Following assumptions are made in the analysis:

- Conductor diameter = 30 mm.
- Height of conductor above ground = 20 m.
- Icing is evaluated considering line direction, i.e., transversal wind speed is used. Models are identified with "_H" (M1_H, Simple_H and Chaine_H). "H" indicates horizontal span model to distinguish from vertical cylinder models resulting in accumulation from all directions ("_V").
- The 40 years of input data use WRF hindcast simulation between 1979-2020.
- Calculations start in tower 300 since the WRF simulation domain has insufficient accuracy at the beginning of the line.
- Icing calculations are made in WRF model points closest to the line and not with significant height deviation.
- Criteria for glaze ice are wet-temperature (Tw) < 0°C in M1 and the Simple model. Chainé is analyzed with criteria of ambient temperature T < 0°C since the temperature goes into the model.
- Icing event is defined as follows:
  - Start when icing exceeds 0.1 kg/m
  - Need to have maximum icing ≥ 1 kg/m
  - Ends when icing becomes lower than 0.05 kg/m
- The 50 years return period of icing values is calculated using the Peak-over-threshold method (POT) using a higher expected value when using the Pareto distribution (estimated with

Probabilistic-Weighted-Moments) or the Exponential distribution. I.e., it is assuming that the tail of the distribution is at least according to Gumbel distribution.

3.3 WRF hindcast data used as input data into icing models

The input data into the icing models were obtained by performing a WRF hindcast simulation. An explanation of the WRF analysis, method and assumptions used in the study can be found in the supplemental report from KvT [2]. The study uses WRF model hindcast simulation made in a 4 km x 4 km grid resolution. Two datasets are used:

- Simulation for the years 1979 – 2020. The period 01.Oct. to 30. April was simulated for each year.
- Simulation for the period 1.1.2021- 21.2.2021

The grid setup gives unreliable results for the first part of the LITL. Thus results are only presented from tower 300.

FIGURE 7 Setup of the WRF model simulations. The WRF4km domain is shown as the white rectangle. The two green rectangles show the two WRF500m domains not used in this study.

4 RESULTS FROM ICING MODEL

4.1 General

The ice load calculated is presented as mass (kg/m). It can be converted into a radial glaze ice, with a density 890 kg/m3, using the following table.

TABLE 1 Conversion between ice weight (kg/m) into radial ice (mm) for 30mm conductor.

Ice weight	kg/m	0.0	1.0	2.0	3.0	4.0	5.0	6.0	7.0	8.0	9.0	10.0	11.0	12.0
Diameter	m	0.030	0.048	0.061	0.072	0.081	0.090	0.097	0.104	0.111	0.117	0.123	0.129	0.134
Radius	m	0.000	0.009	0.016	0.021	0.026	0.030	0.034	0.037	0.041	0.044	0.047	0.049	0.052

4.2 On icing in zone 1 and 2 in Labrador

Figure 8 shows the total ice accumulation for the different types of icing between towers 307 and 1007. Glaze ice has the highest overall mass and 56 % of the total ice mass accumulation. Rime icing has 35 % of the total ice mass; the amount varies within the zone and is highest at towers 518 and 443. Wet snow icing has 9 % of the total ice accumulation mass for all towers.

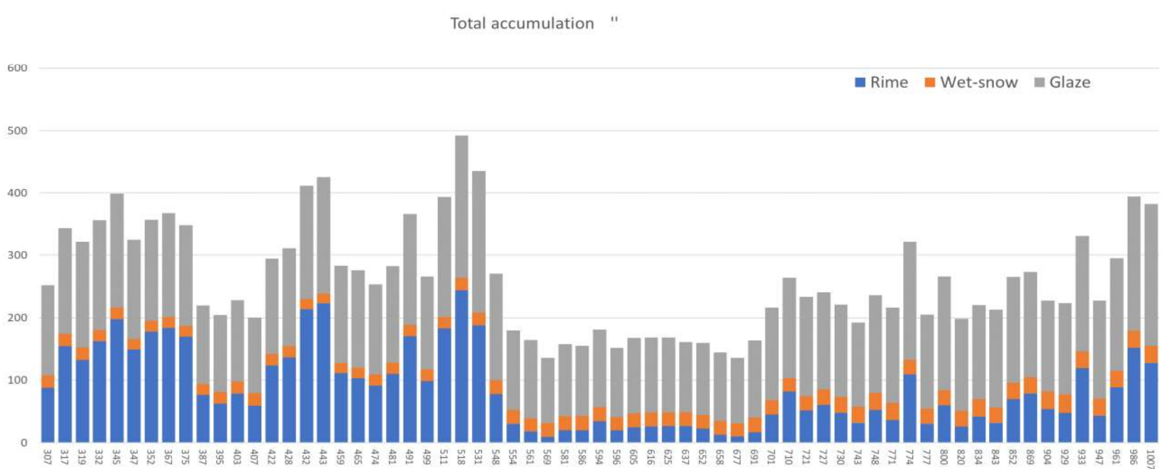

FIGURE 8 Total ice accumulation (kg/m/40years) in the M1_H model for the different types of icing, data from 1979-2019.

The length of the icing remaining on the line varies and is primarily influenced by the ambient temperature. Figure 9 shows the largest predicted ice load in tower 518 in the period 1987-2-11 to 1987-3-31. The total icing event is fairly long and lasts 48 days from first accumulation till total ice removal. Rime ice has larger accumulation than glaze ice in this event. Total accumulation ("Icing-Tot") is the total icing at each time considering ice removal, while lines for each icing type are without ice removal and show the total accumulated ice. Ice removal in this event is a mixture of sublimation melting and ice shedding in the end.

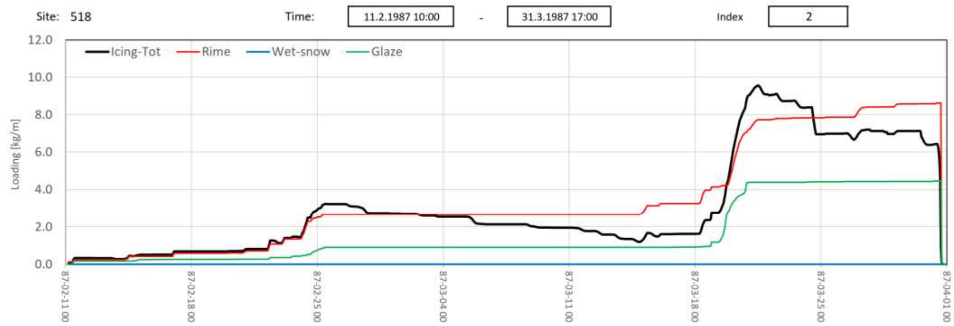

FIGURE 9 Icing event with highest ice load at site 518 in the M1_H model, data from 1979-2019.

Figure 10 shows the estimated 50 years icing value at different tower sites and a comparison to the design ice load and proposed glaze ice loading in the CSA standard. The solid black line represents design loading used in the LITL (converted to 30 mm conductor) and the orange lines show proposed loading in the CSA standard. The results show that there is a consistency in the icing prediction between tower sites. The Chainé model predicts the highest icing in most cases. The M1_H model predicts higher loading in few instances, e.g., towers 518 and 531, partly because rime icing and wet-snow icing are included. Generally, the predicted ice values are well within the design loading. Predicted icing is above the 50-years proposal in the CSA standard in some towers, and the M1_H model is above the 150-years proposal in two cases.

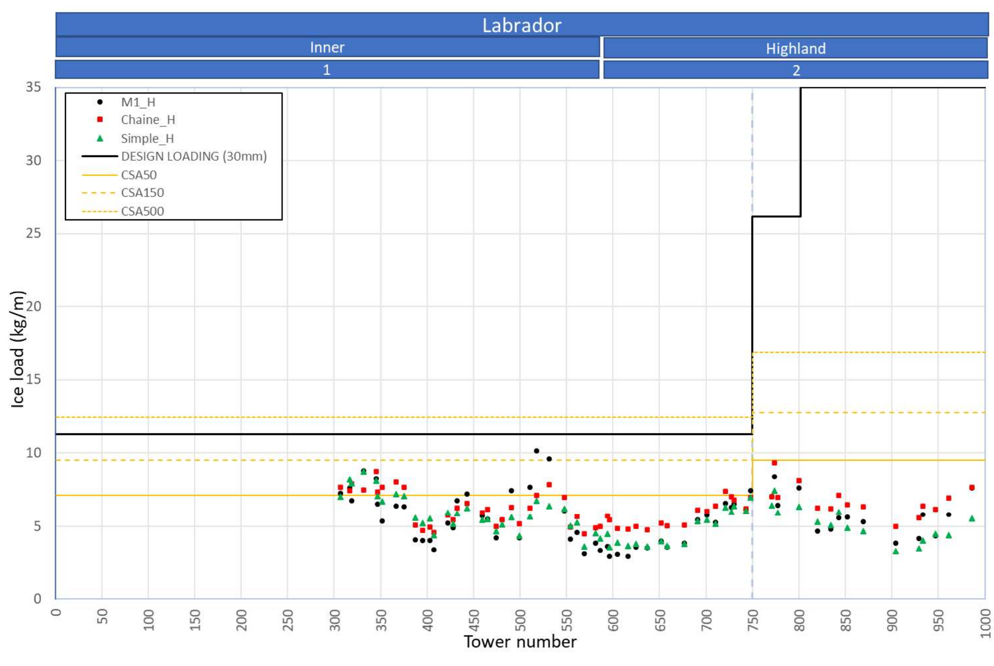

FIGURE 10 Prediction of 50 years icing of the three icing models (30mm conductor). The black line represents the design loading in the LITL.

Figures 11 to 13 show the evaluation of the 50-years icing value for each calculation point in the three models. In most cases, the reference calculation point in the WRF hindcast data is within 2 km from the tower site it is representing. Actual tower numbers in the LITL are identified with a white-balloon stepping at every 100 towers.

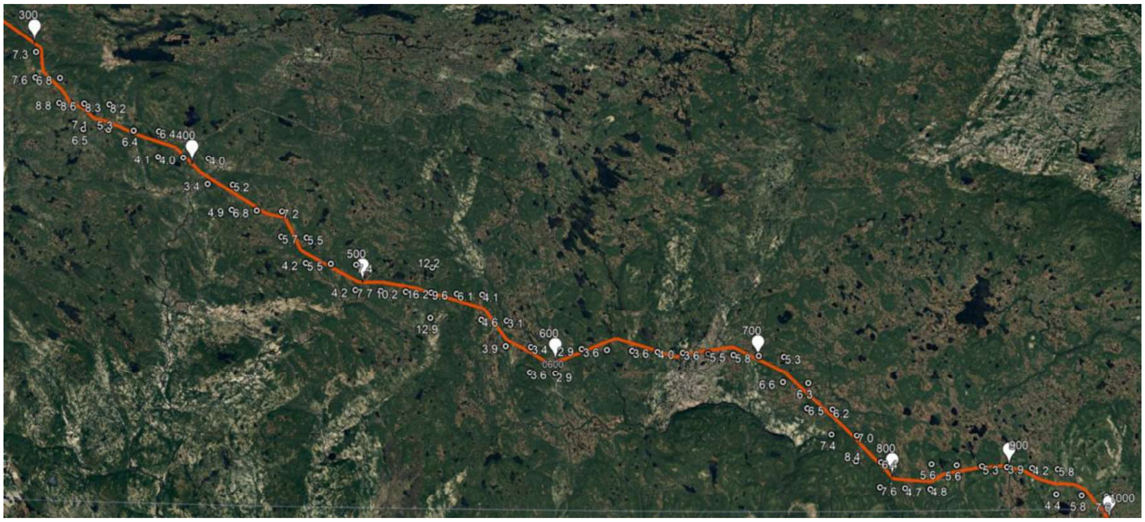

FIGURE 11 M1_H models evaluation of 50-years icing value (kg/m) on a 30 mm conductor at a height of 20m.

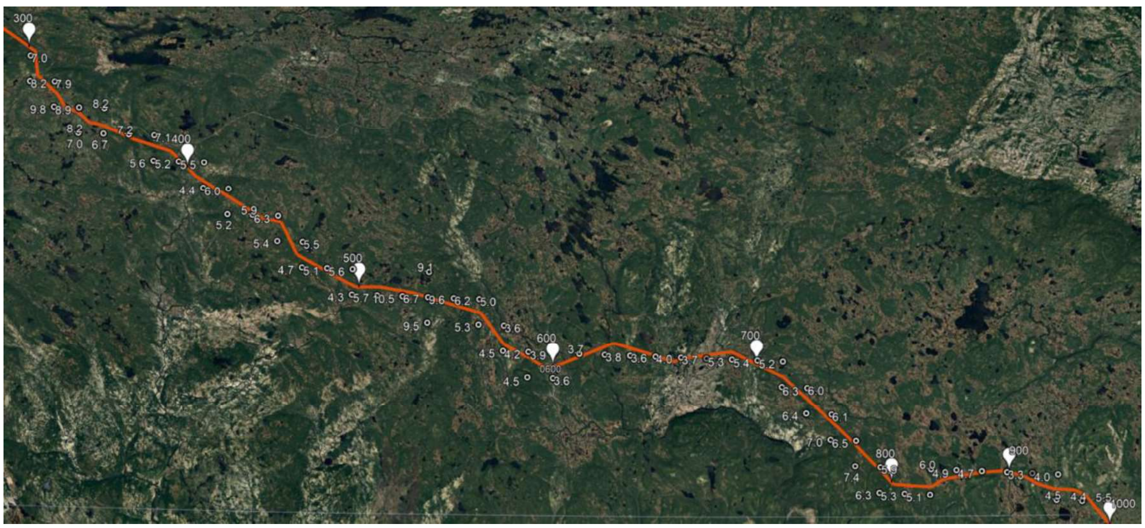

FIGURE 12 Simple models evaluation of 50-years icing value (kg/m) on a 30 mm conductor at a height of 20m.

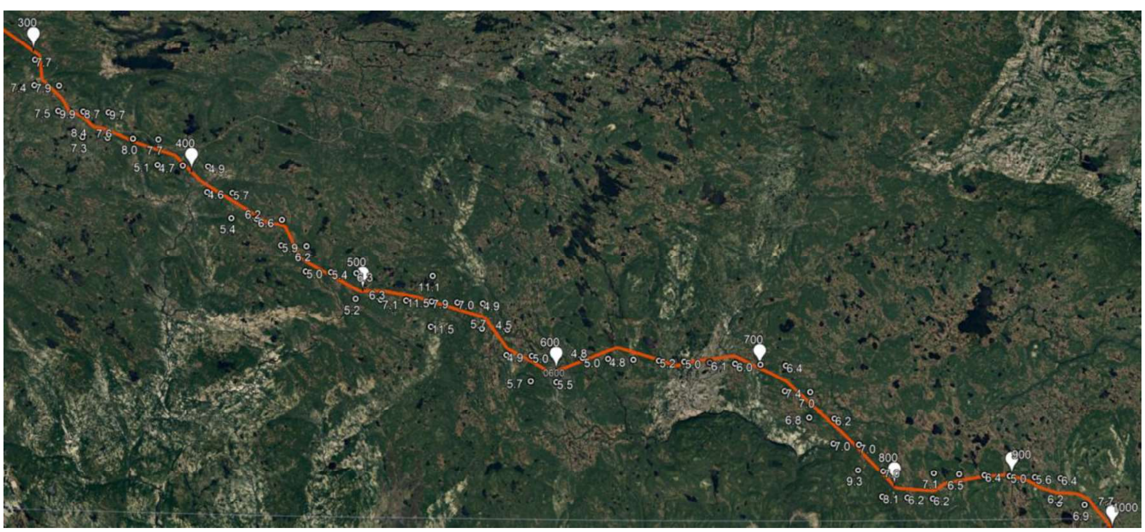

FIGURE 13 Chainé models evaluation of 50-years icing value (kg/m) on a 30 mm conductor at a height of 20m.

4.3 Icing storm in January 2021 in Labrador

The icing models predict that the icing starts early on the 06. January and has steep accumulation till around 12 on the 08. January. A strong temperature inversion layer is present in the WRF model during this period. The most significant part of icing accumulation is freezing rain, but the ice accumulation is in some areas mixed with rain, snow, and graupel. Rime icing is also part of accumulation in some areas. Temperature is below zero for an extended period and icing remained on the conductors. Additional accumulation occurs on 04. Feb. Full ice shedding has not happened in the icing model when the WRF data ends at 21. Feb.

Figures 14 to 17show examples of accumulation in WRF points close to tower sites 345, 367, 443 and 531. Glaze icing is dominant in all cases, although rime icing is also present. Peak icing is evaluated as 13.3 kg/m at site 531. Total accumulation (”Icing-Tot”) is the total icing at each time considering ice removal, while lines for each icing type are without ice removal and show the total accumulated ice. Ice removal in this event is a mixture of sublimation melting and ice shedding in the end.

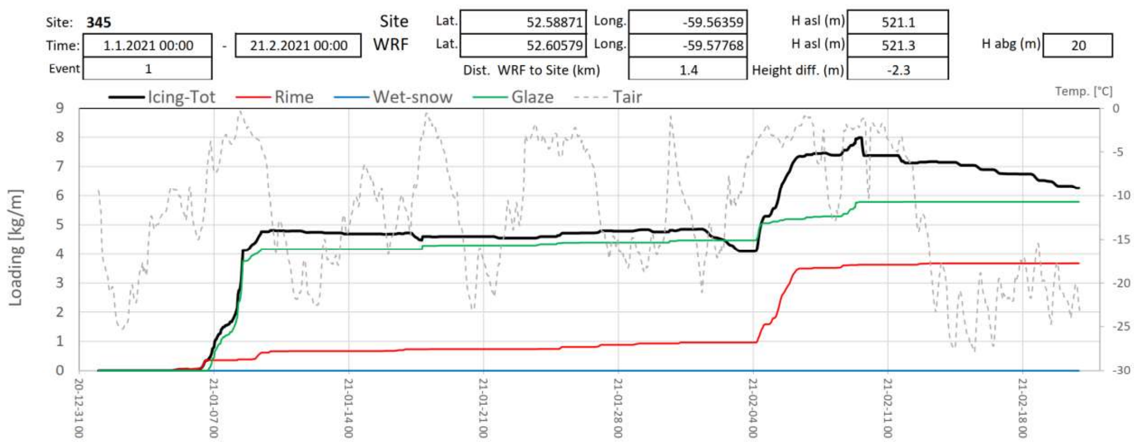

FIGURE 14 M1_H model, icing prediction at tower site 345 in the period of 01.Jan.-21.Feb. 2012. The larger part of accumulation is due to freezing rain, but rime icing is also present. Temperature varies but does not exceed 0°C in the period.

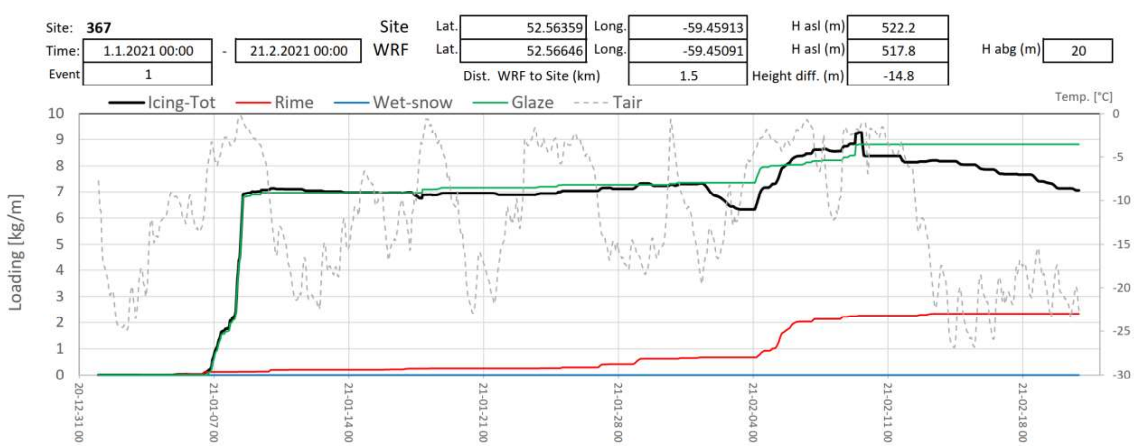

FIGURE 15 M1_H model, icing prediction at tower site 367 in the period of 01.Jan.-21.Feb. 2012. The larger part of the accumulation is due to freezing rain, but some rime icing is also present. Temperature varies but does not exceed 0°C in the period.

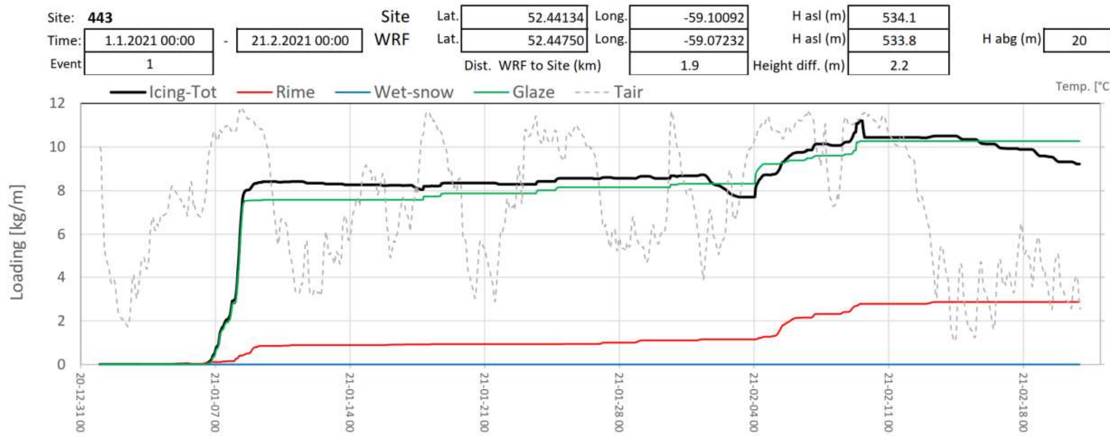

FIGURE 16 M1_H model, icing prediction at tower site 443 in the period of 01.Jan.-21.Feb. 2012. The larger part of accumulation is due to freezing rain, but rime icing is also present. Temperature varies but does not exceed 0°C in the period.

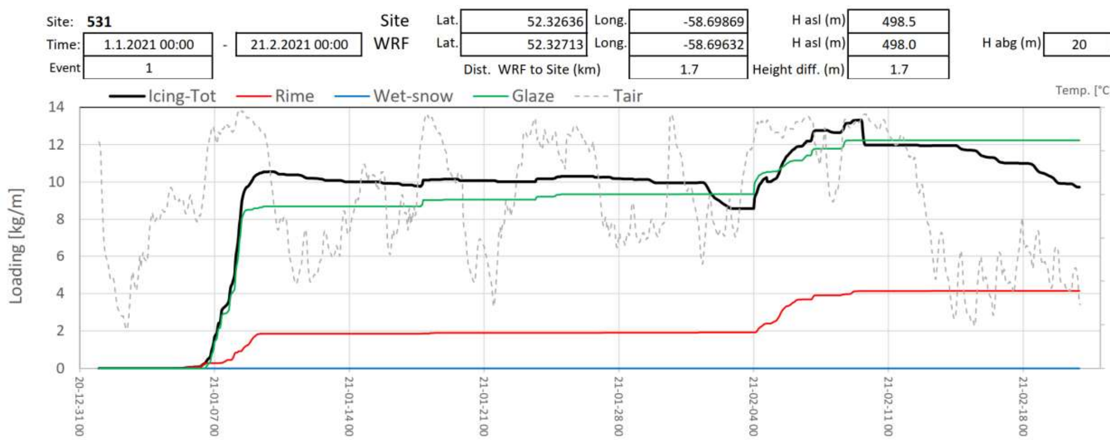

FIGURE 17 M1_H model, icing prediction at tower site 531 in the period of 01.Jan.-21.Feb. 2012. The larger part of accumulation is due to freezing rain, but rime icing is also present. Temperature varies but does not exceed 0°C in the period.

Figure 18 shows icing results from the three icing models (M1_H, Chainé and Simple). The results show that there is a consistency in the icing prediction between tower sites. The Chainé model predicts the highest icing in most cases. The M1_H model usually predicts the second-highest icing. In few cases, the M1_H model predicts the highest loading, e.g., towers 518 and 531, partly because it includes rime icing accumulation that is missing in the Chainé model.

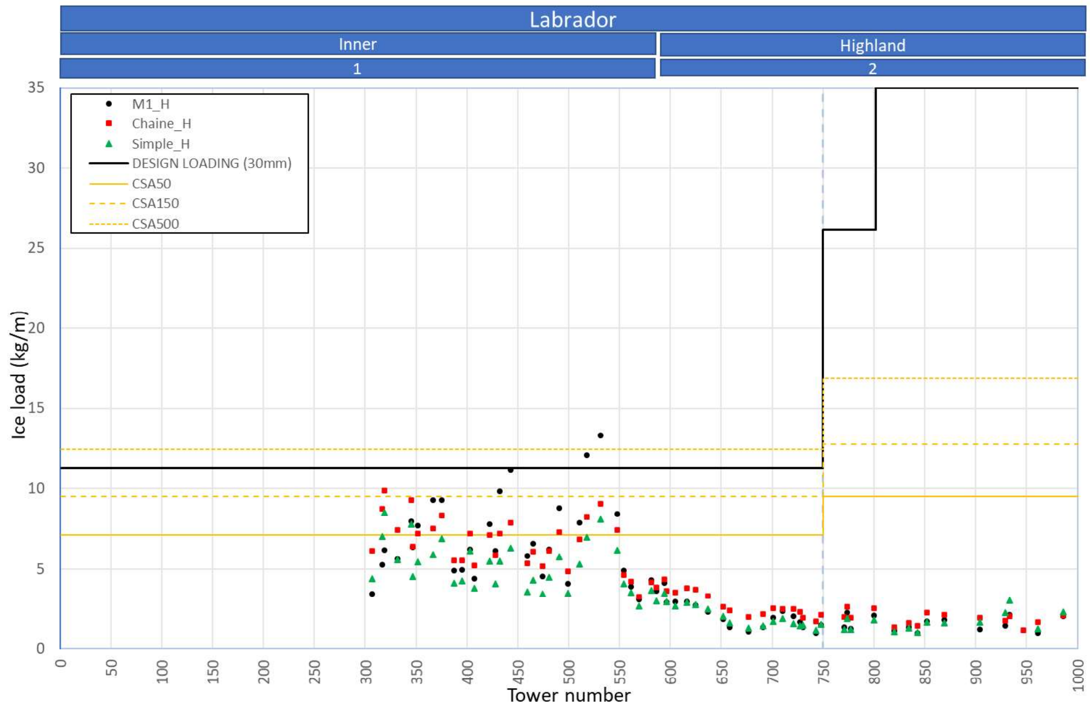

FIGURE 18 Comparison of maximum ice load in the January ice storm using three different icing models.

Figure 19 shows a comparison of icing in the January storm to the predicted 50 years icing. The January storm has values exceeding the 50 years value in several cases between tower sites 360 to 550.

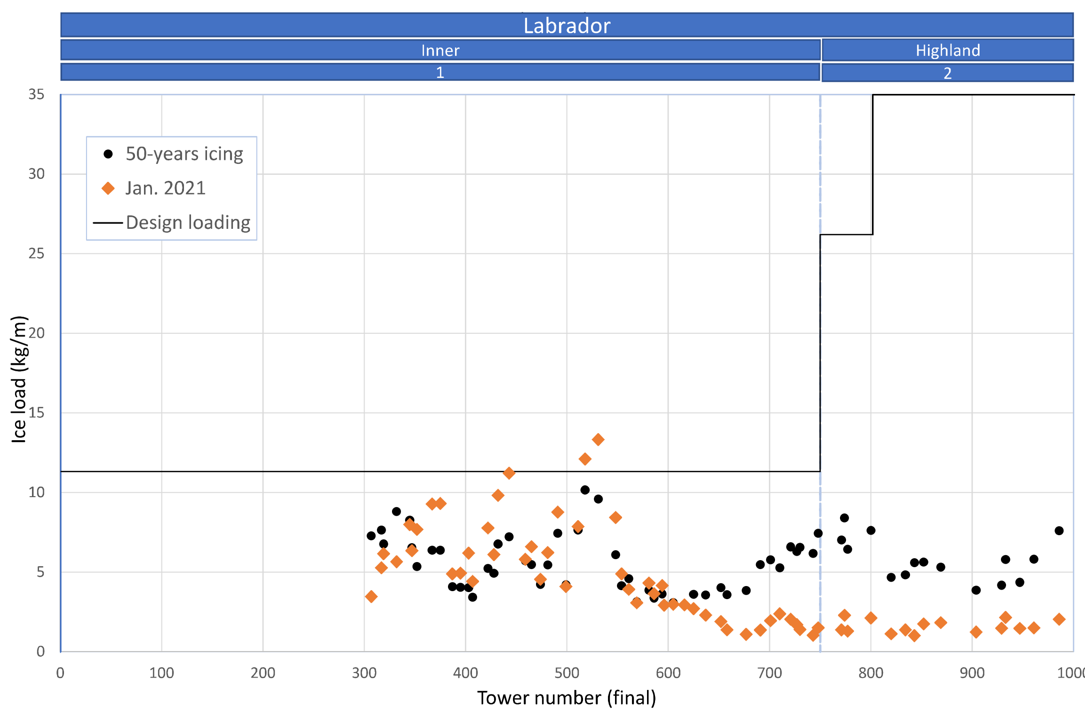

FIGURE 19 Comparison of January ice storm to predicted 50 years icing in the M1H model.

Figure 20 shows the three largest events at each site in 1979-2019 compared to the January icing event. The January event 2021 is exceeding the historical highest loading in areas between towers 360-531.

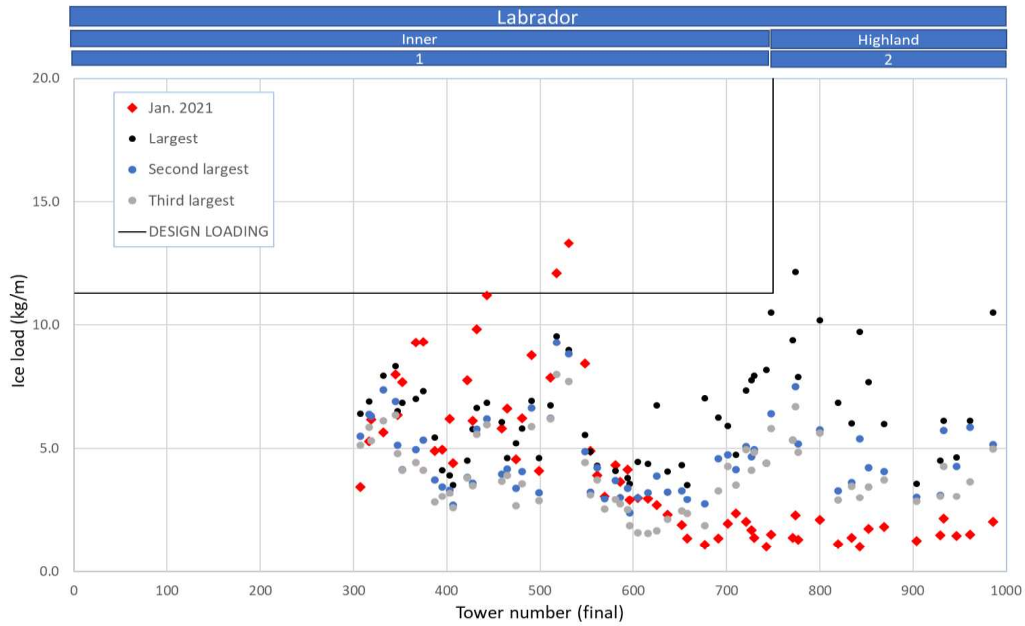

FIGURE 20 Comparison of January ice storm to the three largest icing events in 1979-2019 in the M1H model.

It may be expected that the highest icing has occurred where the damages in towers in LITL was experienced. Damages occurred at: (i) Tower 318, (ii) Cluster 1. 335-344, (iii) Cluster 2. 361-369 and (iv) Cluster 3. 513-527. The M1_H icing model predicts high icing in all of these areas. Limited direct measurements of ice weights are available in the weather. One weight sample of 13.3 kg/m is available from tower 340 but unknown from which conductor (Pole, electrode or OPGW). The nearest calculation point is tower 345, where the M1_H model predicts 8.0 kg/m, the Chainé model predicts 9.3 kg/m and the Simple_H model predicts 7.8 kg/m.

Figures 21, 22 and 23 show extreme icing evaluation (kg/m) in the period of 01.Jan.-21.Feb. 2021 at all WRF calculation points between towers 300 and 1000 for the three icing models. Tower numbers are shown in the figures as white-ballons stepping at 100 towers. Ice loading is calculated for a 30 mm conductor at the height of 20 m above ground.

FIGURE 21 M1H models evaluation of max. icing (kg/m) between 01.Jan.-21.Feb. 2021.

FIGURE 22 Simple models evaluation of max. icing (kg/m) between 01.Jan.-21.Feb. 20212.

FIGURE 23 Chainé models evaluation of max. icing (kg/m) between 01.Jan.-21.Feb. 2021.

REFERENCES

[1] K. Vindteknikk, "Simulation of the January 2021 ice storm in Labrador," KvT, Oslo, 2021.

[2] K. Vindteknikk, "Rime ice loads for the LITL HVDC overhead line," Oslo, 2020.

[3] Kathleen F. Jones, "Evaluate extreme ice loads from freezing rain for Newfoundland and Labrador Hydro," Cold Regions Research and Engineering Laboratory, Hanover, New Hampshire, 2010.

[4] Canadian Standards Association, "CAN/CSA-C22.3 No. 60826-10: Design criteria of overhead transmission lines," Canadian Standards association, 2010.

[5] P. M. E. L. a. P. P. J. Hosek, "Forecsting severe ice storms using numerical weather prediction: the March 2010 Newfoundland event," Natural Hazards and Earth System Sciences, 2011.

[6] D. B. A. H. M. A. J. E. &. J. T. W. Henson, "Forecasting of Icing Events and Icing Accumulation on a Test Transmission Line at Hawke Hill, Newfoundland and Labrador".

[7] K. F. Jones, "A simple model for freezing rain ice loads," *Atmospheric Reserach,* vol. 46, pp. 87-97, 1998.

[8] P. M. C. P. Asim Haldar, "Validation of Ice Accretion Models for Freezing Precipitation Using Field Data," Canadian Electricity Association, 1998.

[9] K. F. Jones, "Ice Accretion in Freezing Rain," CRREL 96-2, 1996.

[10] C. P. P. M. M. M. M. I. A. G. M. K. A. Haldar, "Validation of Ice Accretion Models for Freezing Precipitation Using Field Data," in *IWAIS 1996*, Chicoutimi, 1996.

[11] K. Y. R. M. P. Jarrett, "Update of the reference ice thickness amounts due to freezing rain for Candadian codes and standards," in *IWAIS 2019*, Reykjavik, 2019.

[12] L. Makkonon, "Modeling power line icing in freezing precipitation," in *IWAIS 1996*, Chicoutimi, 1996.

[13] K.-H.-Y. R. M. Philip Jarrett, "Update of the Reference Ice Thickness Amounts due to Freezing Rain for Canadian Codes and Standards," in *IWAIS 2019*, Reykjavik, 2019.

[14] K. F. Jones, "Ice Storms in the St. Lawrence Valley Region," ERDC/CRREL TR-03-1, 2003.

[15] J. S. H.F. Young, "Icing damage tor ransmission facilities in Newfoundland," Quebec, 1971.

[16] A. Haldar, "Twenty Years of Ice Monitoring Experience On Overhead Lines In Newfoundland and Labrador," in *12th International Workshop on Atmospheric Icing of Structure (IWAIS)*, Japan, 2007.

APPENDIX A LIST OF LARGEST ICING EVENTS AT SELECTED SITES

Following is a list of the largest icing events (kg/m) predicted by the model in 1979-2020.

Largest events at tower site 345 in 1979-2020

Time from	Time to	Max Value (kg/m)	Length (days)	Weighted. acc.time
2001-11-06	2001-11-20	8.3	13.8	2001-11-10
1987-02-17	1987-03-31	6.9	42.7	1987-03-14
1981-11-07	1981-11-08	6.3	1.3	1981-11-07
1990-11-09	1990-12-06	5.6	27.4	1990-11-20
2013-02-20	2013-03-13	5.6	21.3	2013-03-02
2016-10-22	2016-10-23	5.2	0.9	2016-10-23
1996-04-03	1996-04-15	3.7	11.7	1996-04-05
2009-11-16	2009-11-28	3.7	12.8	2009-11-26
2018-11-25	2018-12-22	3.6	26.7	2018-12-08
2006-01-15	2006-03-09	3.3	52.8	2006-01-23
1979-11-28	1980-01-14	3.2	46.9	1979-12-26
2015-04-27	2015-10-01	3.0	156.2	2015-04-28
2005-04-12	2005-04-16	3.0	4.5	2005-04-13

Largest events at tower site 531 in 1979-2020

Time from	Time to	Max Value (kg/m)	Length (days)	Weighted. acc.time
1987-02-11	1987-03-31	9.0	48.3	1987-03-13
2013-02-28	2013-03-13	8.8	13.5	2013-03-03
2005-04-12	2005-04-16	7.7	4.1	2005-04-13
2015-11-23	2015-12-12	5.6	18.8	2015-11-24
1986-04-10	1986-04-12	5.2	2.0	1986-04-11
1990-11-19	1990-11-24	4.1	4.4	1990-11-20
2009-11-27	2009-11-28	3.8	1.7	2009-11-28
1998-02-27	1998-03-10	3.6	10.9	1998-03-06
1981-11-07	1981-11-08	3.5	1.1	1981-11-07
1995-04-22	1995-04-24	3.0	1.8	1995-04-23

APPENDIX B GRAPHS SHOWING ICING EVENTS IN THE HINDCAST SIMULATION FROM 2021

Attached are plots showing the weather parameters from the WRF simulation and resulting icing values from the M1_H model for the following tower sites:

- 345
- 367
- 443
- 531
- 652
- 774

Site:	**345**		Site	Lat.	52.58871	Long.	-59.56359	H asl (m)	521.1	
Time:	1.1.2021 00:00	- 21.2.2021 00:00	WRF	Lat.	52.60579	Long.	-59.57768	H asl (m)	521.3	H abg (m) 20
Event	1			Dist. WRF to Site (km)			1.4	Height diff. (m)	-2.3	

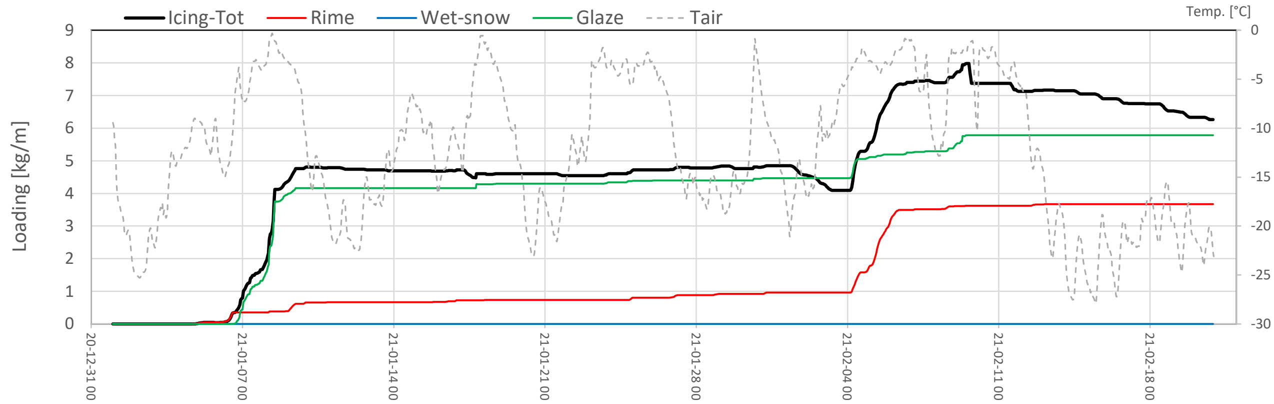

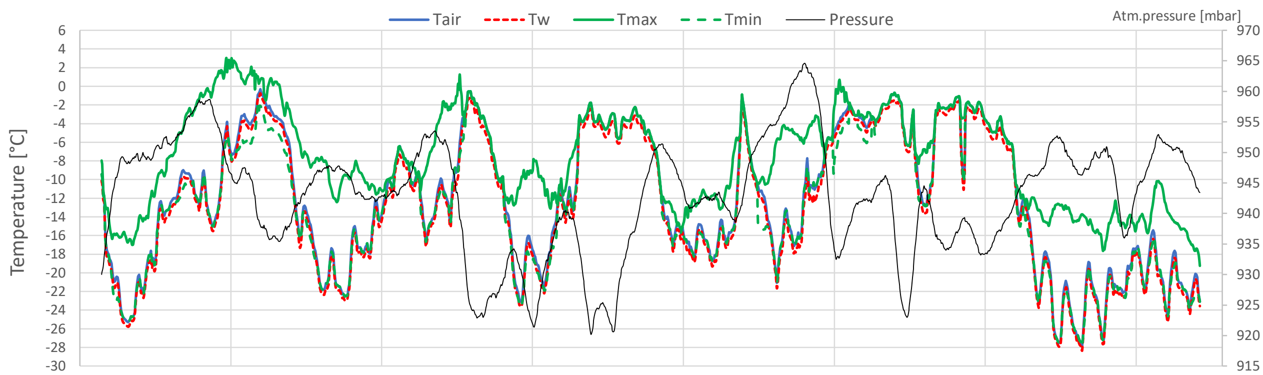

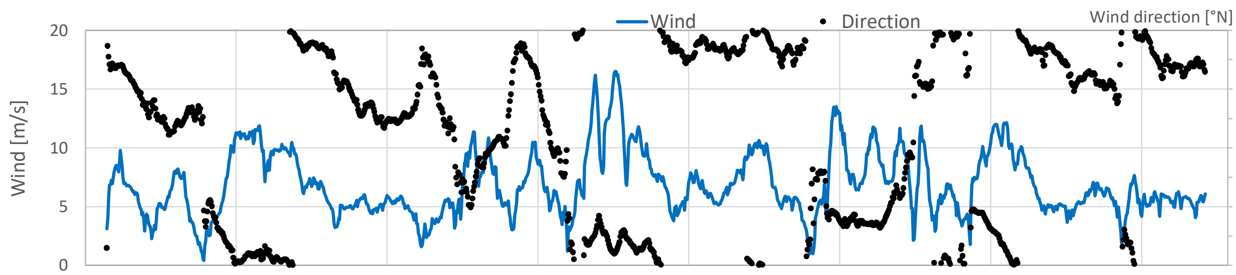

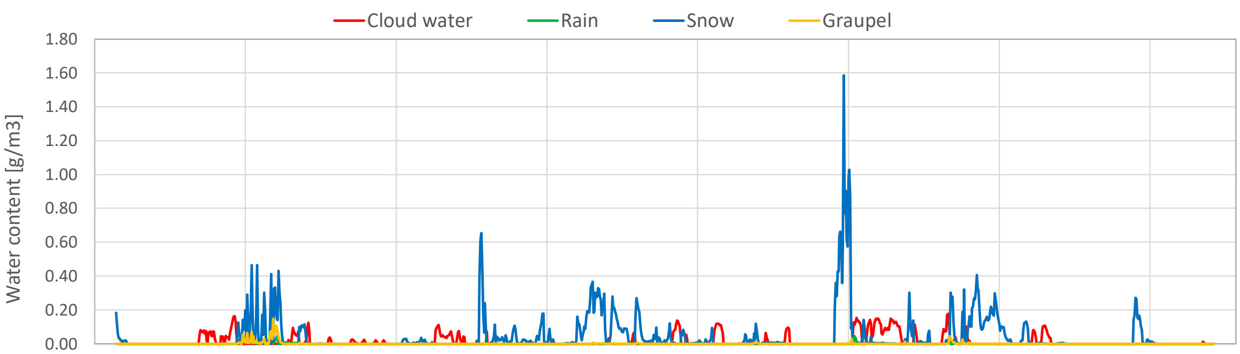

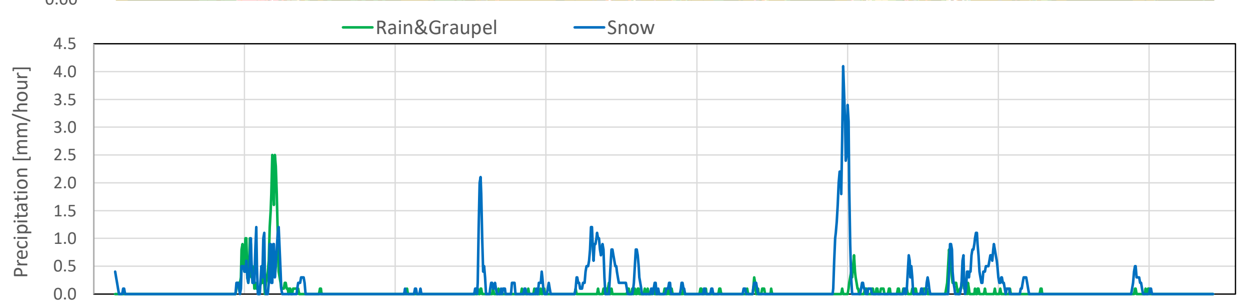

Site:	**367**		Site	Lat.	52.56359	Long.	-59.45913	H asl (m)	522.2	
Time:	1.1.2021 00:00	- 21.2.2021 00:00	WRF	Lat.	52.56646	Long.	-59.45091	H asl (m)	517.8	H abg (m) 20
Event	1			Dist. WRF to Site (km)			1.5	Height diff. (m)	-14.8	

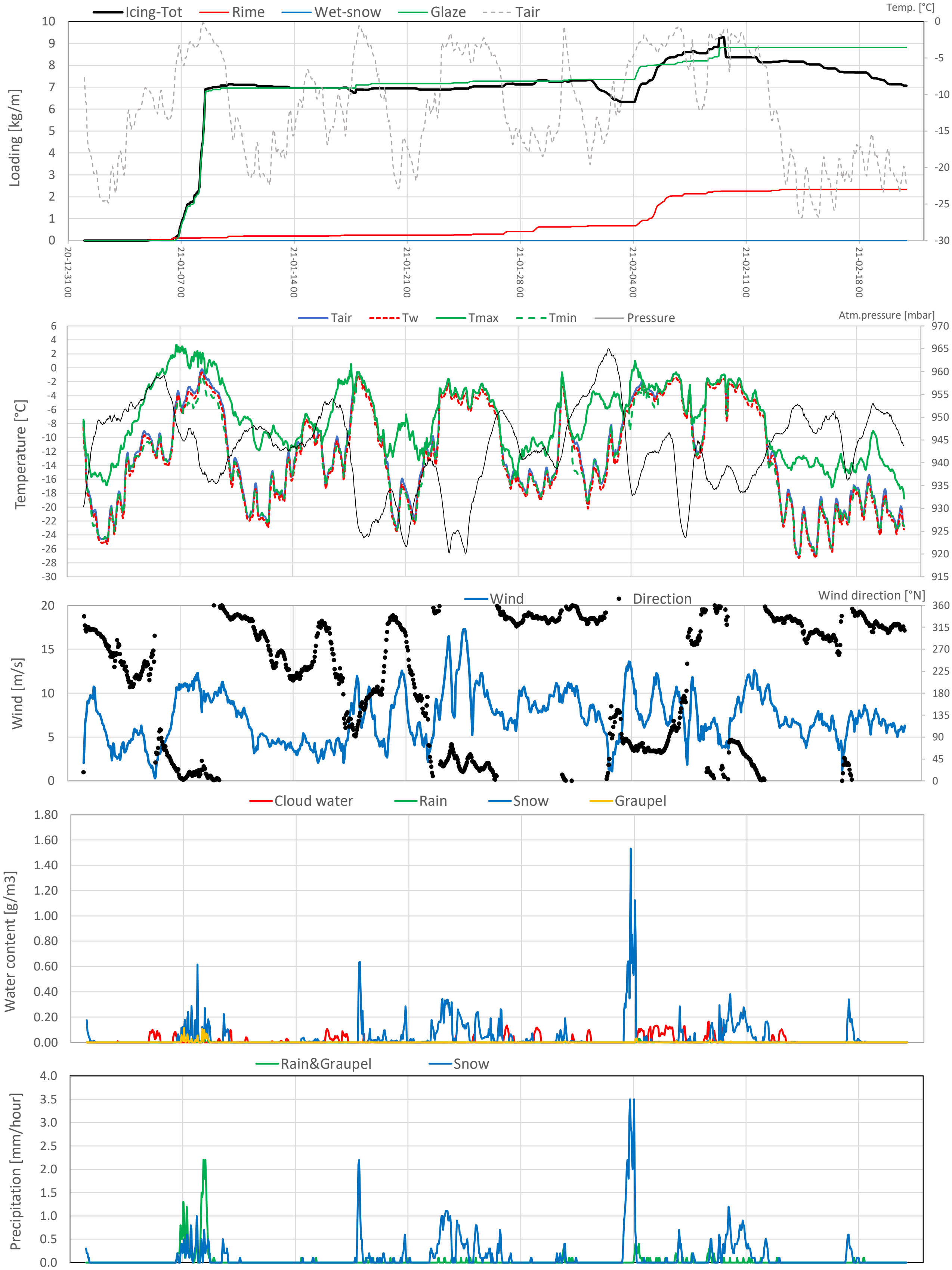

Site:	**443**		Site	Lat. 52.44134	Long. -59.10092	H asl (m) 534.1		
Time:	1.1.2021 00:00	- 21.2.2021 00:00	WRF	Lat. 52.44750	Long. -59.07232	H asl (m) 533.8	H abg (m)	20
Event	1			Dist. WRF to Site (km)	1.9	Height diff. (m) 2.2		

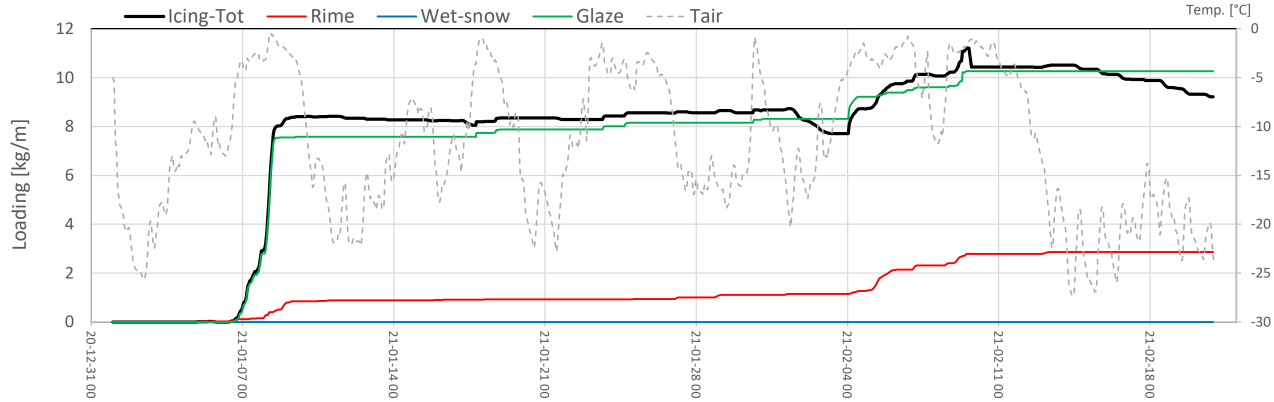

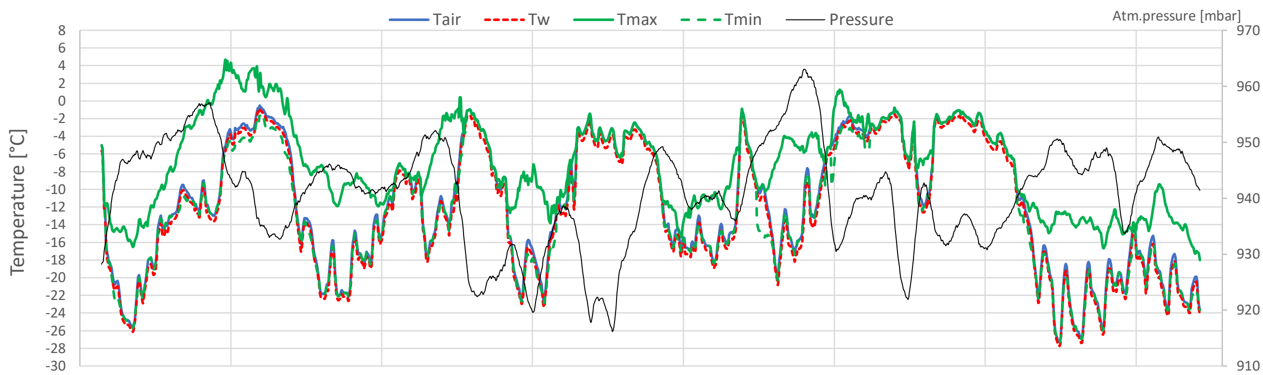

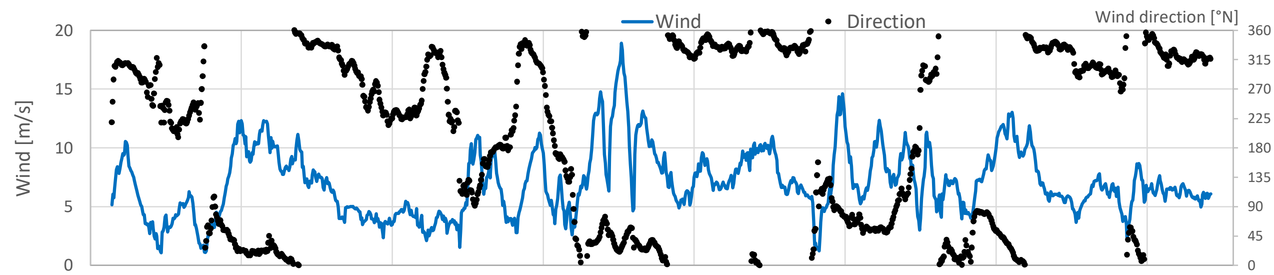

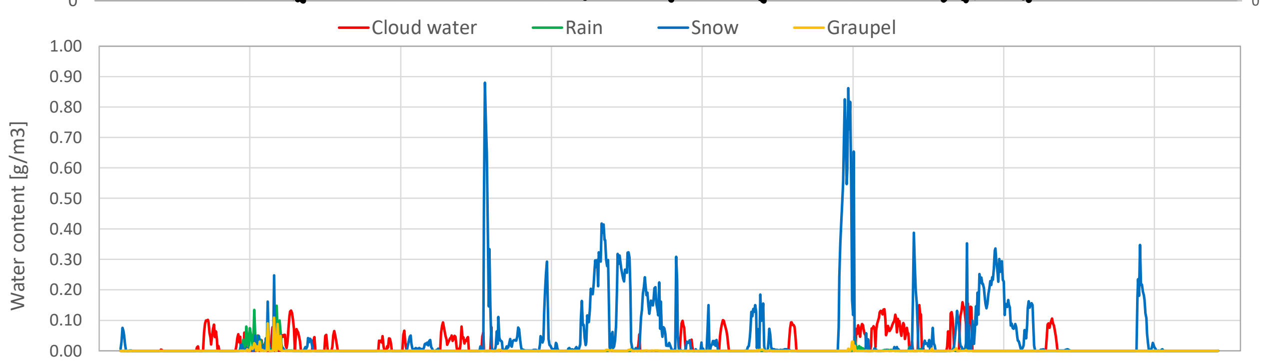

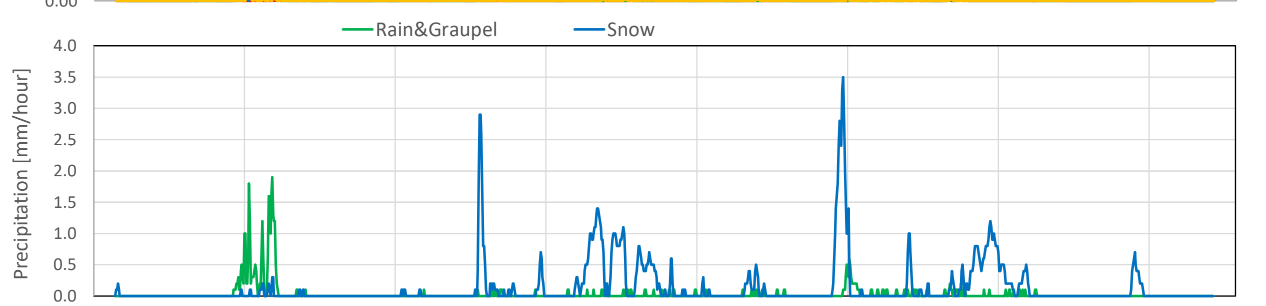

Site: **531** | Site Lat. 52.32636 | Long. -58.69869 | H asl (m) 498.5

Time: 1.1.2021 00:00 - 21.2.2021 00:00 | WRF Lat. 52.32713 | Long. -58.69632 | H asl (m) 498.0 | H abg (m) 20

Event 1 | Dist. WRF to Site (km) 1.7 | Height diff. (m) 1.7

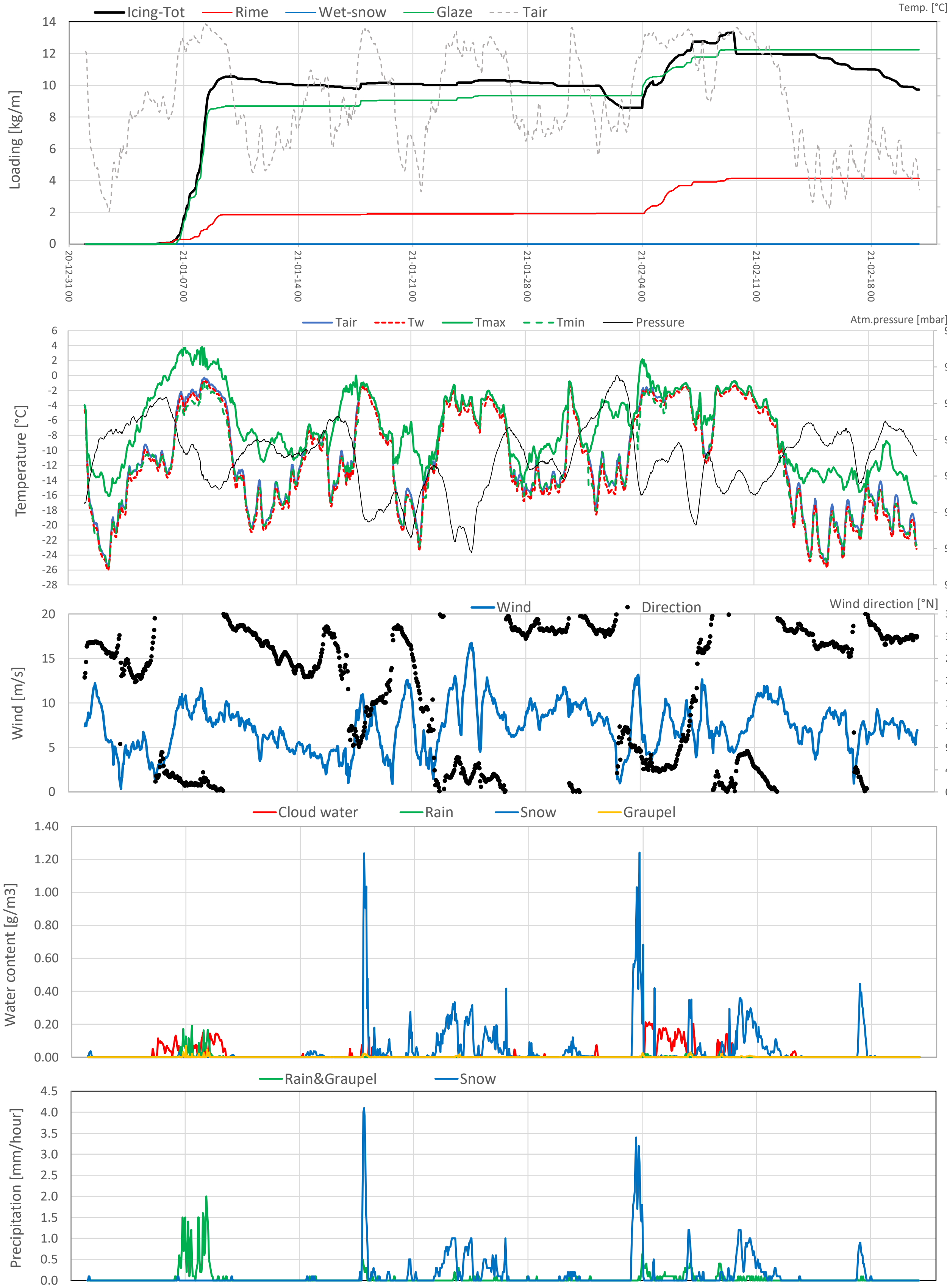

EFLA **Icing event plot** **Prepared:** **14.4.2021 15:04** **Version 1.11**

Site:	**652**		Site	Lat.	52.23905	Long.	-58.12488	H asl (m)	370.1
Time:	1.1.2021 00:00	- 21.2.2021 00:00	WRF	Lat.	52.24032	Long.	-58.13206	H asl (m)	366.7
Event	1			Dist. WRF to Site (km)			2.3	Height diff. (m)	-48.4

H abg (m) 20

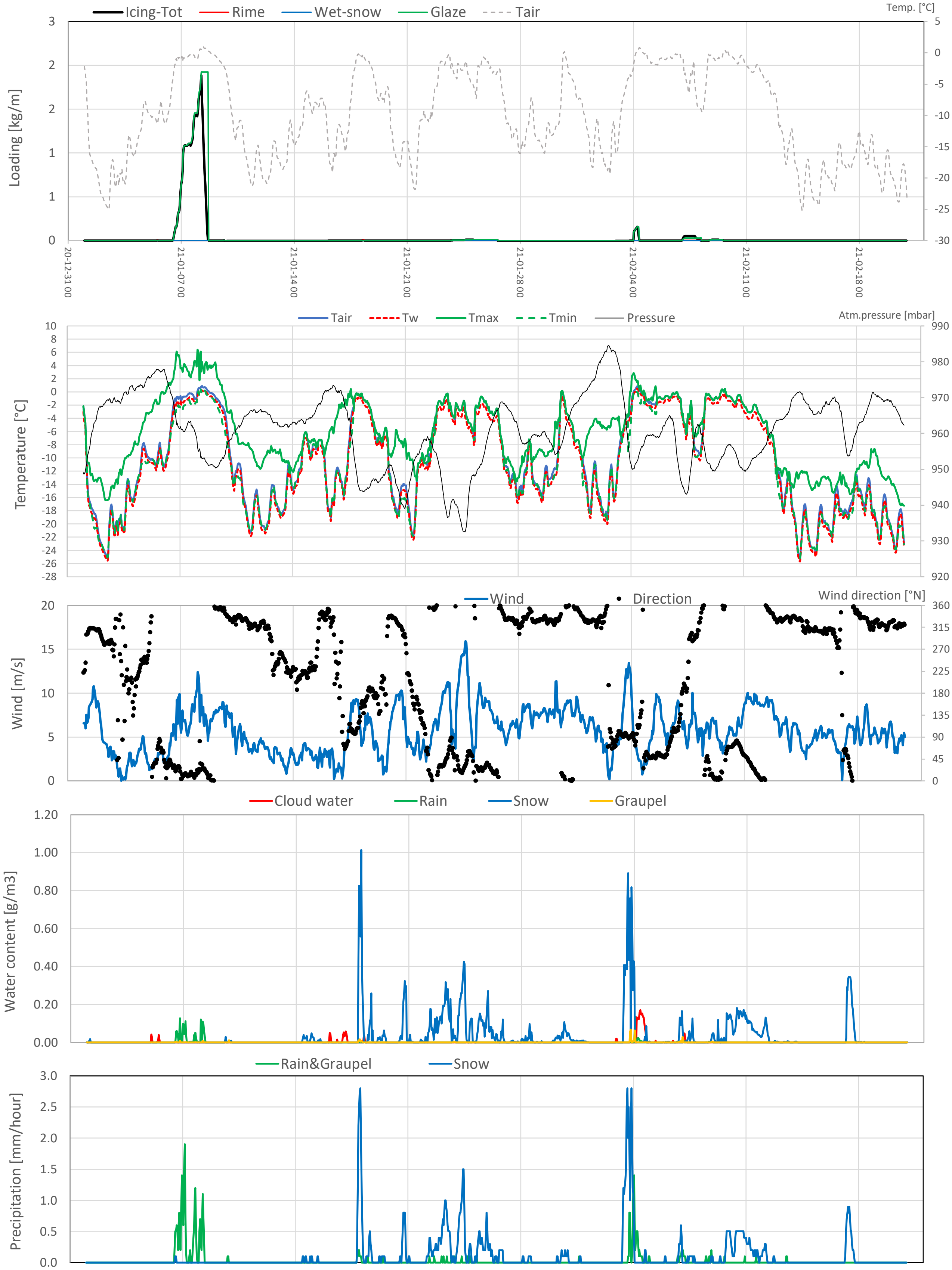

Site:	**774**		Site	Lat.	52.08908	Long.	-57.61169	H asl (m)	387.8
Time:	1.1.2021 00:00	- 21.2.2021 00:00	WRF	Lat.	52.07473	Long.	-57.63863	H asl (m)	409.1
Event	1			Dist. WRF to Site (km)			0.7	Height diff. (m)	75.6

H abg (m) 20

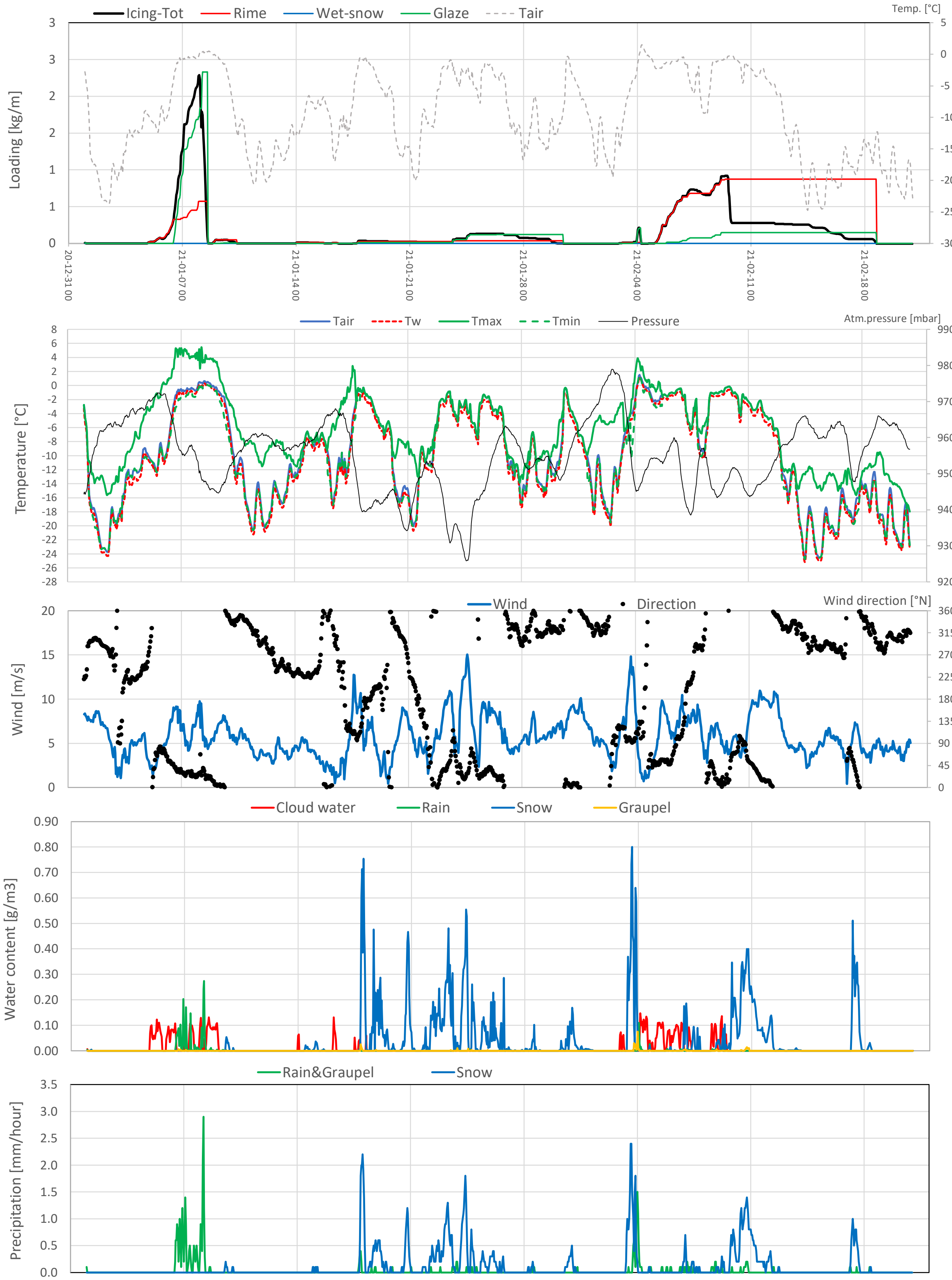

Appendix B – Quality Control Check Sheets

Valard	Document Description			Lattice Tower Inspection
	Created By: Eric Winter	Doc. Number **VC-F0112**		Revision **R007**
	Date: 01/Jan/2013	VC Number: VC7343	Contract no.: CT0327-001	
	Revised By: Michael Grieve	Client: Nalcor Energy	Project no.: 505573	
	Rev Date: 07/Feb/2016	Crew:	Supervisor:	
	Tower Number: 317	Line Number: 1	Date: **30/Mar/2016**	

Inspection Type (●) Climbing ( ) Visual ( ) Helicopter Patrol

Body Extension: 9 + ☐ | Leg Extension: ☐ ☐ ☐ ☐ | Tower Type: A1

Soldiers Pond
3 C | 4 D
2 B | 1 A
Muskrat Falls

	Check
1. Review the line data to verify structure type	☒
2. Ensure that erected tower on site is correct (str type & extensions)	☒
3. Inspect all steel for debris and damage	☒
4. Report any shortages or damage to the Material Coordinator	☒
5. Refer to structure layout drawing for steel placement and orientation	☒
6. Erected Steel as per Manufacturers drawings (no missing parts or damaged members)	☒
7. Climbing inspection of all crossarm connections-torque check all bolts	☒
8. Climbing inspection of all splice locations-torque check all splice bolts	☒
9. Climbing inspection of all body extension connections-torque check all bolts	☒
10. Torque check on all stub leg bolts	☒
11. Torque check on all floors not checked during assembly stage-torque check all bolts	☒
12. All step bolts installed on step bolt legs	☒
13. Tower Checked for any loose bolts, nuts & washers during climbing inspection	☒
14. All erection materials removed from tower (sling, tag lines, etc.)	☒
15. Danger & number signs installed as per design	☒
16. Aerial marker signs installed as per design (every tenth structure)	☐ Yes ☒ N/A
17. Visual inspection of tower using binoculars completed	☒

Notes:

Checked by:

Soldiers Pond
Jamie G — 3 C | 4 D — Jamie G
Terrel P — 2 B | 1 A — Terrel P
Muskrat Falls

	Name (Print)	DATE	Signature
Crew	Jaime Governo	30/Mar/2016	Jaime Governo
Valard QA Review	Jon Power	02/Apr/2016	[signature]
Nalcor QC Inspector	A. CORCORAN	15-APR-16	ACorcoran

M.M FOR REVIEW ONLY

MBOS Mobile Business Operations System

VC-F0113 : R003

Valard	Document Description		Lattice Tower Assembly Check	
	Created By: Eric Winter	Doc. Number VC-F0113	Revision R003	
	Date: 01/Jan/2013	VC Number: VC7343	Contract no.: CT0327-001	
	Revised By: Evan McKinnon	Client: Nalcor Energy	Project no.: 505573	
	Rev Date: 13/Mar/2015	Crew: T. Wright (QA)	Supervisor: Evan McKinnon	
	Tower Number: 317	Line Number: S1	Date: 09/04/15	

Area of Tower Checked:			
Crossarm/peaks	☑ Complete	*Capture all Defects on F0147 Deficiency Form and all Missing steel on F0140 Missing Steel Form*	**Tower Type & Body Extension**
Cage	☑ Complete		A1+9.0m
Body	☑ Complete		
Extensions	☑ Complete		

Check torque 30% for guy towers and 50% for self support towers unless otherwise directed

Item Description	Check
1. Review the line data to verify structure type	☑
2. Correct Tower and extension are assembled (see staking list)	☑
3. Inspect all steel for quantities and damage	☑
4. Report any shortages or damage to the Material Coordinator	☑
5. Refer to structure layout drawing for steel placement	☑
6. Install correct bolts as per Manufacturers drawings	☑
7. Install lock washers as per Manufacturers drawings	☑
8. All Installed bolts torqued to Manufacturers specifications	☑
9. All Torqued bolt heads to be identified with RED marker	☑
10. All verified torqued bolts indicated with BLACK marker	☑
11. OPGW support installed to inside of line angle	☑
12. All step bolts installed as per design (refer to tower drawing for each tower type)	☑
13. Tower checked for any loose bolts, nuts & washers or debris	☑
14. Danger & number signs installed as per design	☐

Notes:

	Name (Print)	DATE	Signature
QC Crew	Tom Wright	09/04/15	[signature]
Valard QA Review	Evan M	09/04/15	[signature]
Nalcor QA Inspector	DAVE PARROTT	12/APR/15	[signature]

Appendix C –Conductor Failures – LITL

MEMO

DOCUMENT SYSTEM CODE	PROJECT
8321-004-MIN-002	**LITL failure investigation**
DATE	**CLIENT**
13.04.2021	nalcor
SENDER	**RECEIVER**
Viven Naidoo	John Walsh (nalcor) Maria Vietch (nalcor)

SUBJECT

Conductor failures - LITL

Purpose

The purpose of this document is to highlight the types of electrode line conductor and damper failures that have occurred on the LITL resulting from the ice storm of January 2021. The memo is based on an assessment of the images and documents provided by nalcor as well as simulations conducted in PLS-Cadd of the affected areas to determine the loads and impact on the lines. No metallurgy reports for the conductor were available at the time of writing this memo.

Failures of electrode conductor

The electrode line uses Grackle ACSR. Failures have occurred at several locations in the Labrador area between tower 318 and 367 and tower 513 and 528. The conductor damage varies from a few broken strands to complete failure of the conductor.

The list of observed damages from the images provided by nalcor include:

- Multiple broken strands close to the suspension clamps
- Complete removal of sections of the aluminium close to the suspension clamps
- Indentations on the top aluminium layer close to the suspension clamps
- Complete failure of the conductor (all strands broken)
- Conductor strands have broken in two modes, i.e. tensile and fatigue or shock loading.
- Conductor strands show signs of excessive rubbing/fretting
- Second layer aluminium strands have fatigue or shock loading type failures

In addition to the conductor damage:

- Electrode line dampers show signs of fatigue
- Clamps look like they have not been bolted down correctly
- Hardware shows signs of wear associated with galloping

The most serious failure occurred at tower 526 were the EL2 conductor failed. At the time of failure, only 10 damaged strands could be seen by the workmen working on EL1. The load on the line was estimated at 11.25 kg/m which results in a conductor tension of around 95 kN in the affected span assuming a uniformly distributed ice load along the spans in the strain section. This tensile load is substantially lower than the conductor RTS (about half). **TABLE 1** shows a list of towers with conductor damage on both EL1 and EL2.

TABLE 1 List of towers with conductor damage.

TOWER NUMBER	CONDUCTOR	TOWER NUMBER	CONDUCTOR
318	EL1	368	EL1
335	EL1	369	EL1
336	EL1	513	EL1
340	EL1	514	EL1
342	EL2	518	EL1
343	EL2	524	EL1
344	EL1	525	EL1
361	EL1	526	EL2
362	EL1	526	EL1
363	EL1	527	EL1
365	EL1	527	EL1
367	EL1	528	EL1

Measured ice loads

Nalcor removed and weighed samples from the line. There is some difficulty in calculating the density due to the irregular shape of the samples. Density was estimated at 750 kg/m^3. The sample mass was calculated as 11.25 kg/m. The pictures below show the ice samples removed from the line. The samples show a mixture of icing types which corresponds well with the results of the climatic studies performed by KvT. The ice seems to be a combination of glaze ice and wet snow or rime ice at towers 330 and glaze at towers around 550.

FIGURE 1 Ice sample dimensions and mass, tower: 525

Nalcor scaled some of the images to obtain an estimate of the radial ice thickness. EFLA used these values and applied them to the PLS models to assess the loading on the conductors and to evaluate if these loads are likely, i.e. within the capacity of the line. The table below shows the results of the ice loads scaled from images. The figures in Red text indicate that this load is not possible as they exceed the capacity of the conductor and would have resulted in failure of the conductor if this load was evenly distributed along the spans in the strain section. If only two or three spans on the pole conductor were loaded with the 116 kg/m ice load, and the remaining spans at 23 kg/m, the tension would go down but would still exceed the rated tensile capacity of the conductor.

TABLE 2 Estimated ice loads scaled from images

Image	Tower #	Conductor	Conductor Diameter (mm)	Total Diameter (mm)	Radial Ice (mm)	Weight (kg/m)	Force (N/m)	Tension (% RTS)	Tension (kN)
DSCN6402	340	Electrode	33.9	146	56.3	12	113		
DSCN6380	?	Electrode	33.9	150	58.1	13	128	80	150
DSCN6494	527	Electrode	33.9	194	80.2	22	211	107	200
DSCN6501	528	OPGW	14.5	119	52.3	8	78		
DSCN6511	530	OPGW	14.5	126	55.8	9	89		
DSCN6515	531	OPGW	14.5	133	59.1	10	100		
525 OPGW	525	OPGW	14.5	142	63.8	11	108		
DSCN6506	529	OPGW	14.5	162	73.6	15	142	98	139
DSCN6515	531	OPGW	14.5	224	104.5	28	275	149	214
DSCN6489	526	Pole	57	186	64.7	19	183		
DSCN6402	340	Pole	57	207	75.1	23	229		
IMG_2608	?	Pole	57	237	90.0	31	306	87	331
IMG_2608	?	Pole	57	450	196.5	116	1 136	184	698

Conductor strength reduction with broken strands

The electrode conductor between towers 330 and 550 is ACSR Grackle 54/19. The technical specification for the conductor can be found in Annexure A. The conductor has 19 steel strands 2.26mm diameter and 54 aluminium strands 3.77mm diameter (1350-H19) creating a cable with a rated tensile strength of 194 kN and unit weight of 2.27 kg/m.

FIGURE 2 shows the reduction in the conductor strength with breaking of aluminium strands. The steel in the conductor accounts for 47% (91kN) of the conductor strength. The maximum tensile strength of aluminium strands (AL 1) is 160 MPa in EN 60889.

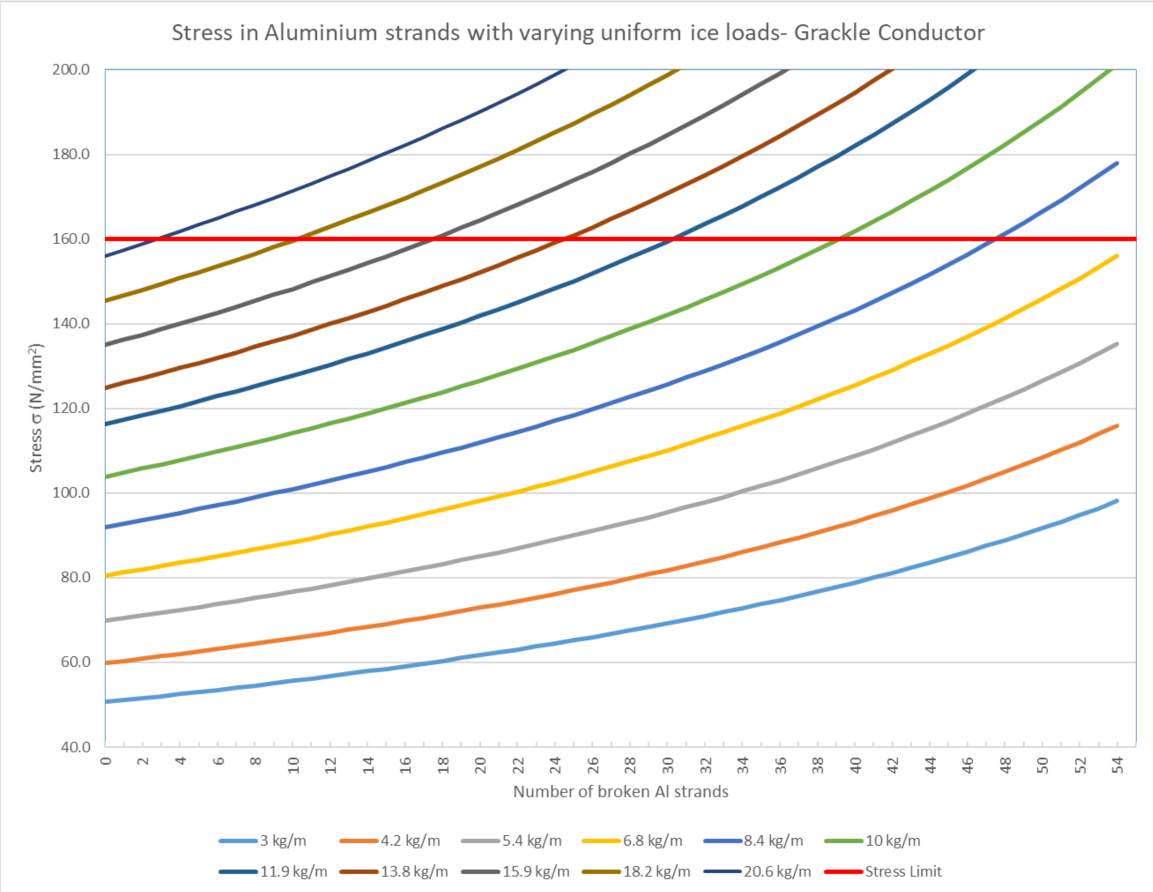

FIGURE 2 Stress in Aluminium strands of Grackle with varying ice loads

FIGURE 3 below shows how the electrode conductor strength is reduced by breaks to the aluminium strands.

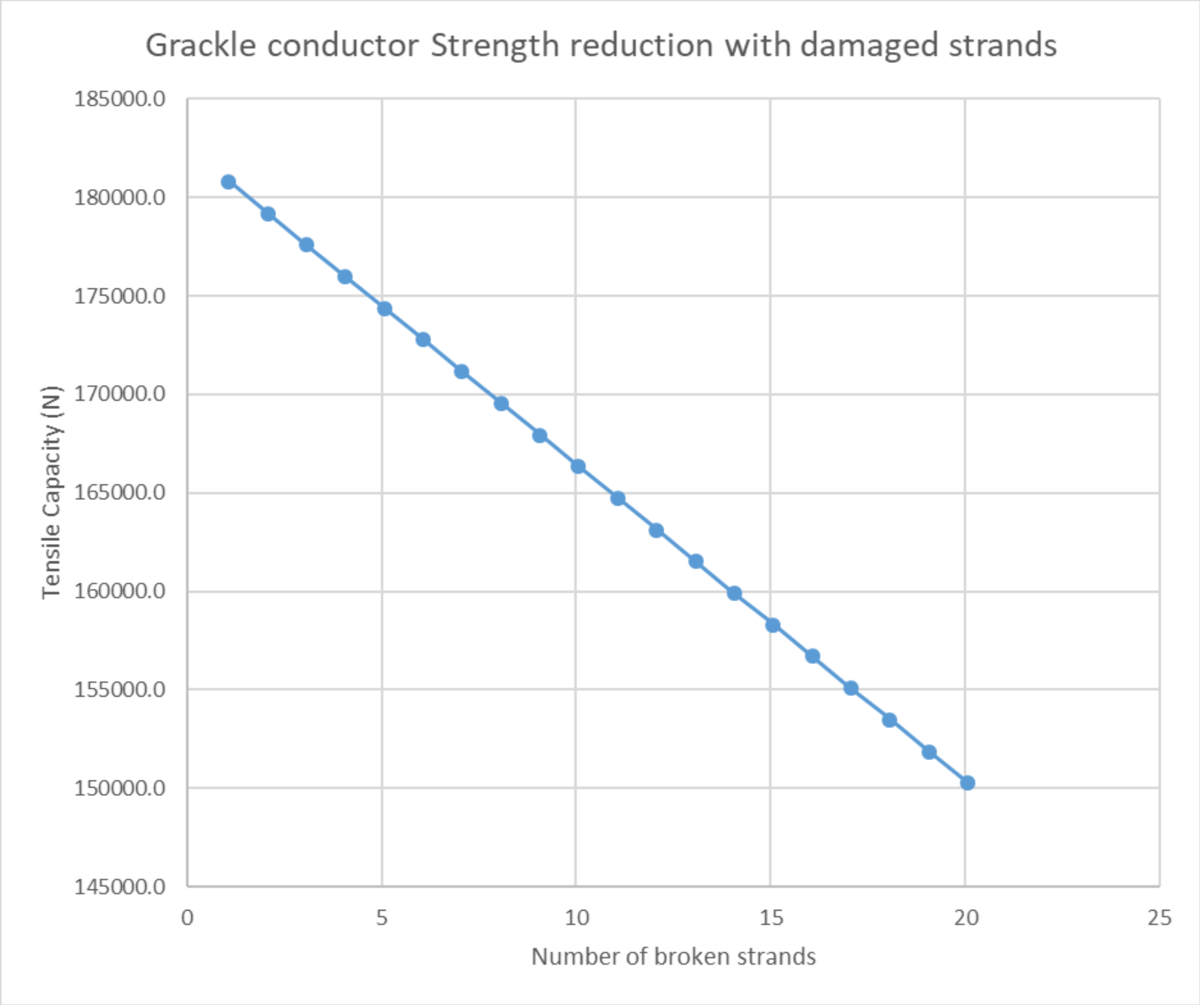

FIGURE 3 Electrode conductor strength reduction with damaged strands

FIGURE 4 below shows the increase in conductor tension with ice load for section between towers 523-541.

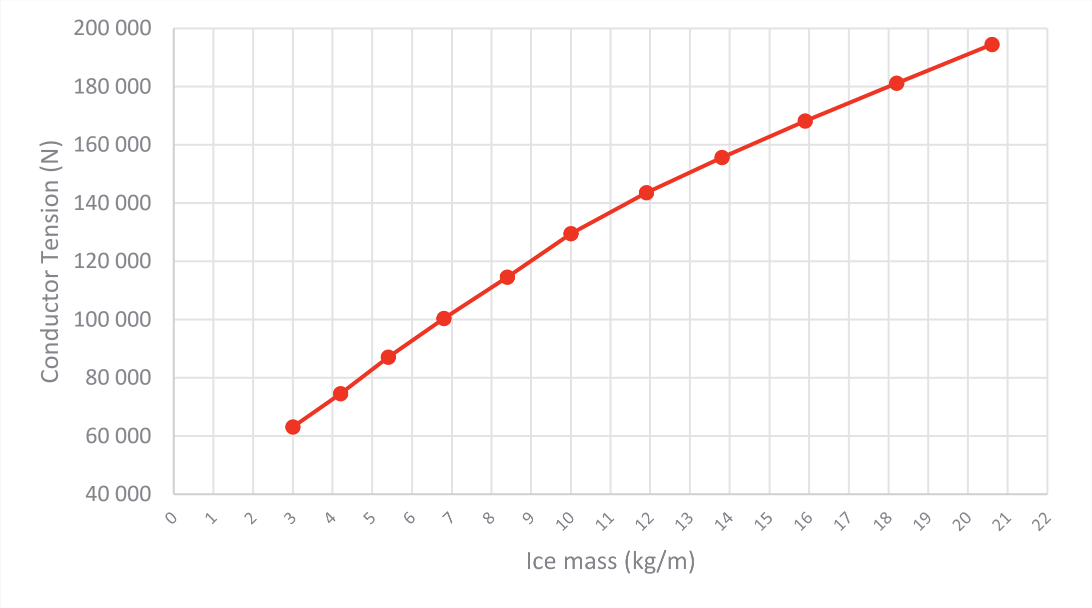

FIGURE 4 Increase in conductor tension with increasing ice mass

The force distribution within bimetallic conductors such as ACSR changes constantly with temperature. The thermal coefficient of aluminium is twice that of steel hence at high temperatures, the Aluminium may go into compression and all of the tensile load is transferred to the steel core. The converse is true for cold temperatures. The stress increases significantly within the aluminium strands. **FIGURE 5** below shows the increase in stress in the Al strands with decrease in temperature for Drake ACSR. The stress at 20% RTS is approximately the same as the stress at 60 degrees conductor temperature. The change in stress in the Al wires between 60 degrees and -20 degrees is 20 N/mm2 (67% increase). Unfortunately, no similar data is available for Grackle conductor, however it is reasonable to assume that the number of broken strands that can be tolerated for a given ice load will be marginally lower than that shown in **FIGURE 2** at reduced temperatures.

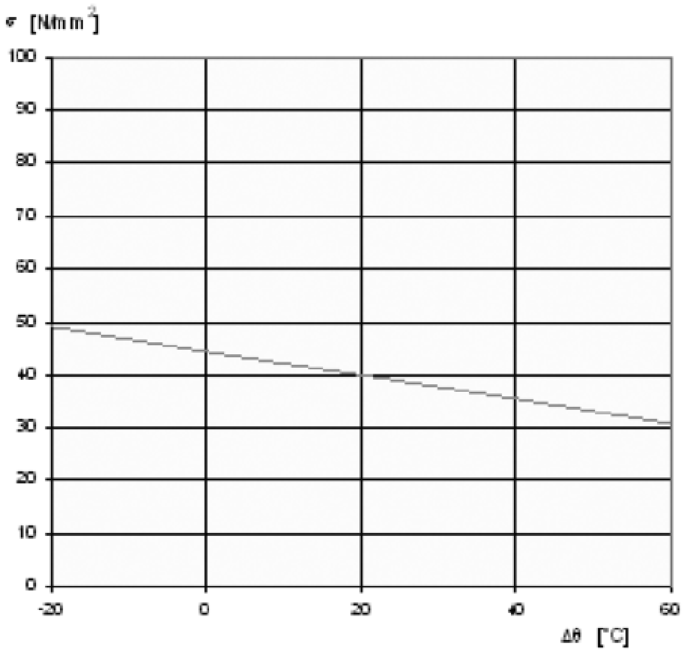

FIGURE 5 Change in stress of aluminium strands with temperature for Drake conductor (EPRI orange book)

Insulator swing and conductor contact

The photo in **FIGURE 6** below shows the electrode insulator at tower 527 in contact with the conductor. The insulator glass has a higher Mohrs hardness than that of the conductor and hence can damage the conductor strands.

FIGURE 6 Maximum Insulator longitudinal swing

The assembly was modelled to ascertain the capable longitudinal swing with unbalance ice loads. The longitudinal swing was estimated to 55 degrees creating a horizontal offset of 833mm before the insulator makes contact with the conductor, see **FIGURE 7** .

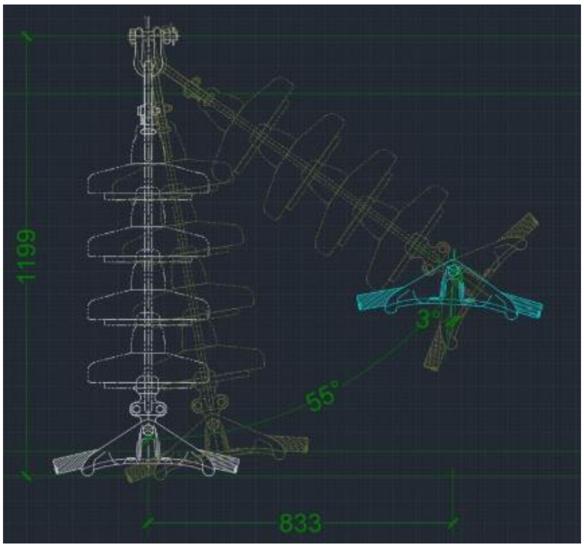

FIGURE 7 Maximum Insulator longitudinal swing

To obtain 55 degrees longitudinal movement of the insulator at tower 527 requires an unbalanced ice load of 4.5 kg/m. This was simulated by applying a load of 3 kg/m ice to spans 524-526 and 8 kg/m in spans 527 to 539 resulting in a longitudinal displacement of the insulator of 850 mm. This situation can arise when some spans are loaded with ice while others have shed theirs. Note that the 4.5 kg/m unbalanced load is not exact and cannot be applied to all tower locations as the longitudinal displacement of the insulator is dependent on the conductor temperature, weight span at the structure and the variation of ice loading on each span. Some spans may require a greater unbalanced load to cause the same insulator movement when applying the same ice loading assumptions.

Conductor damage and failure

Assessing a conductor's condition for fatigue breaks is not easy as often the inner layers are broken while the outer layers are intact. The 1st and 2nd layers of aluminium tend to experience greater amounts of fretting caused by the rubbing action of the strands from below and above. The fretting results in loss of material and microcracks. Outer layer damage therefore does not necessarily reflect the true extent of damage to the conductor as damage in the inner layers may not be visible. Fatigue damage is related to inadequate damping and often affects the whole section or sections of the line.

The images below show fatigue damage to conductors in multiple layers of aluminium. Images taken from CIGRE brochure 322.

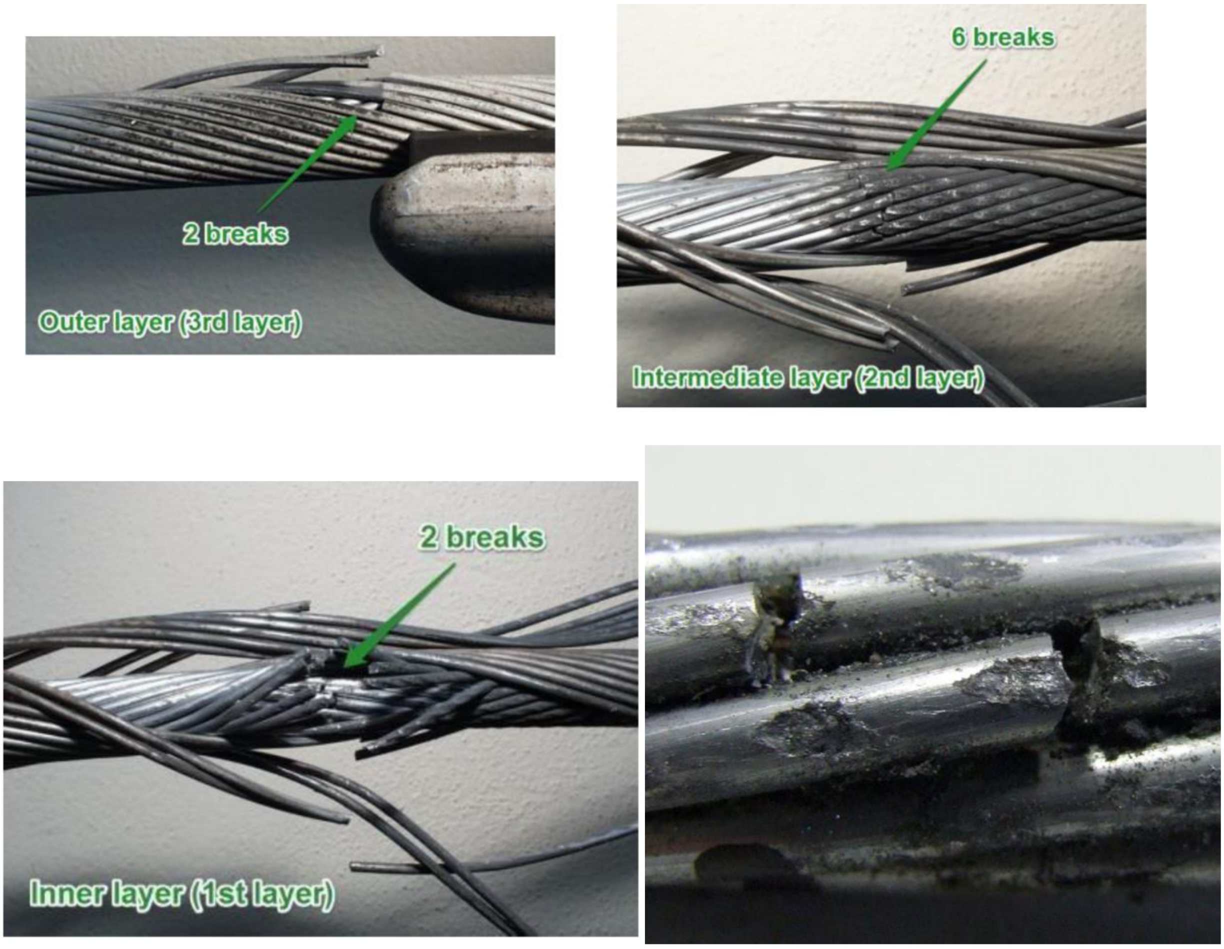

FIGURE 8 Conductor damage due to fatigue

LITL conductor damage

The aluminium strands shown in **FIGURE 9** failed in tensile mode as indicated by the cone shaped ends of the broken strands. This failure is possible if the insulator swing is great enough to result in the insulator rubbing against the aluminium conductor strands. The glass disk has a higher hardness than that of the aluminium strands and hence would cut into the aluminium with movement of the conductor or insulator. The cutting action would reduce the area of the aluminium thereby reducing its tensile capacity. The increase in ice load coupled with the decrease in temperature and subsequent increase in tension in the aluminium strands will then result in the tensile failure of the strands.

FIGURE 9 Conductor damage: Tensile failure of strands

Conductor failure at Tower 526

FIGURE 10 and **FIGURE 11** show the damaged electrode 2 conductor removed from Tower 526. The strands in the second layer of aluminium in **FIGURE 10** show fretting which is a sign of movement between the strands possibly created by conductor galloping, aeolian vibration or large amplitude oscillations.

When the conductor failed (broke), the load on the conductor was estimated at 11 kg/m based on the ice sample taken from site. A uniform load of 11 kg/m applied to all spans in the tension section between towers 523 and 541, gives an electrode conductor tension of 140 kN or 72% of the conductor RTS (rated tensile strength). The same ice load applied as an unbalanced load will give a lower conductor tension due to suspension insulator movement and lower overall ice loads being applied.

The workmen indicated that they saw 10 broken strands on the conductor. This would reduce the tensile capacity of the conductor from 194 to 170 kN, see **FIGURE 3**. This is still sufficient to carry the ice load calculated above with a 20% margin of safety. The stress in the aluminium strands would be approximately 125 N/mm^2 according to **FIGURE 2**, well below the maximum stress level. The shift of load from the steel core to the aluminium strands is difficult to calculate, however the increase according to **FIGURE 5** seems to be in the order of magnitude of 10% from 0 ^{0}C to minus 20 ^{0}C. This implies that the conductor should not have failed under these loads.

FIGURE 10 Conductor damage from tower 526: Fretting marks visible

FIGURE 11 shows 42 of the 54 Aluminium strands of which 19 show signs of fractures due to fatigue loading while the remaining strands have a tensile failure mode. The fractured strands are from the outer (1st), 2nd and 3rd layer of aluminium. Fracture breakages from the 2nd and 3rd layers are associated with fatigue failure and are likely caused by a combination of galloping, aeolian vibration or large amplitude low frequency movement of iced conductors.

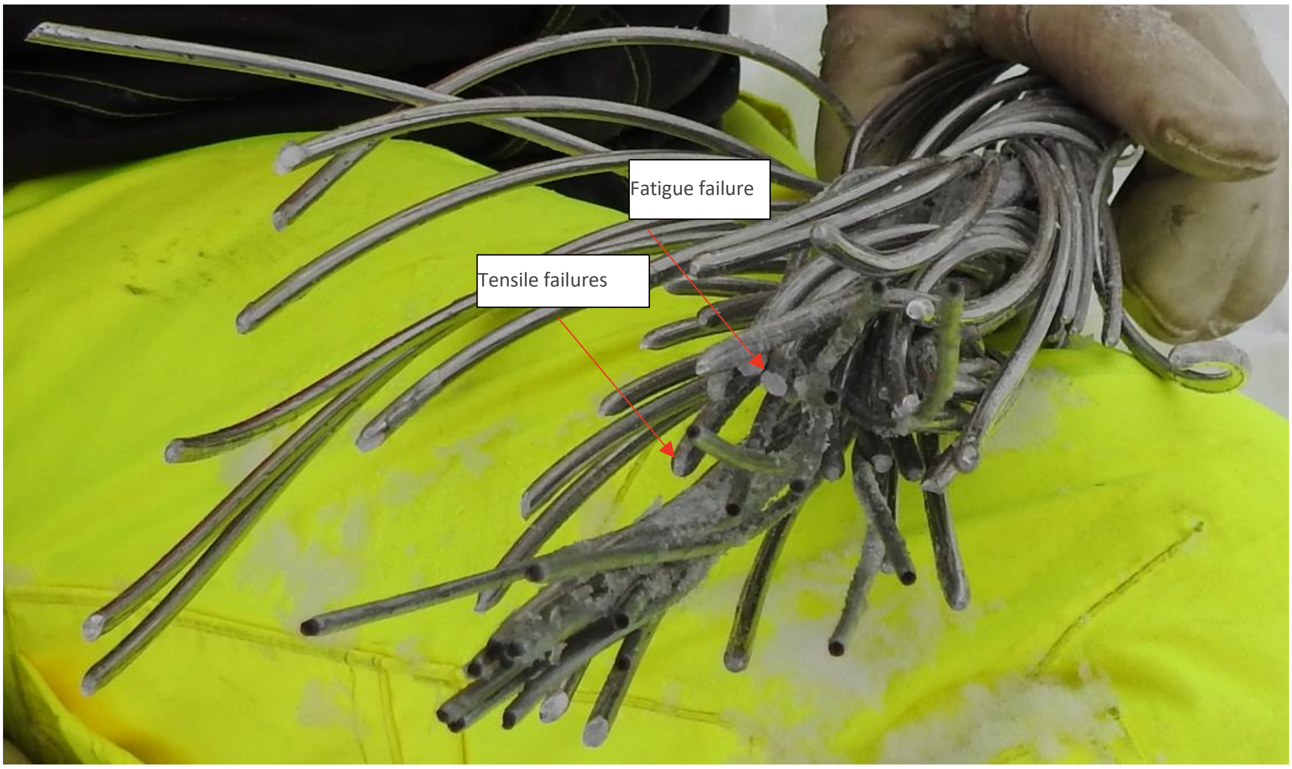

FIGURE 11 Conductor damage from tower 526: Tensile and fatigue failures visible

FIGURE 12 shows a conductor from Statnett damaged by galloping. The large outer strands are armour rods with a diameter of 10 mm. Note the similarities between the failed strands and the mixture of fractures and tensile breaks in the aluminium wires. Fretting between the strands is also evident.

FIGURE 12 Statnett conductor failure due to conductor galloping

The hardware from tower 1209 shows signs of wear possibly resulting from galloping of the conductors.

FIGURE 13 Hardware from tower 1209 showing signs of wear

While galloping may not have been occurring when the conductor failed, conductor galloping could have damaged strands in the first and second layer of aluminium which resulted in the premature failure of the conductor at tower 526. No detailed images of the hardware from tower 526 were available.

Stockbridge Dampers

Drooping stockbridge dampers or sagging weights as shown in **FIGURE 14** are a sign of overloading. The damage can be caused by excessive bending of the messenger wire, large dynamic loads such as ice shedding or galloping or high amplitude low frequency vibrations that normally occur on ice covered conductors. Fatigue failure of stockbridge dampers can also indicate excessive vibration levels or inferior materials used in manufacture.

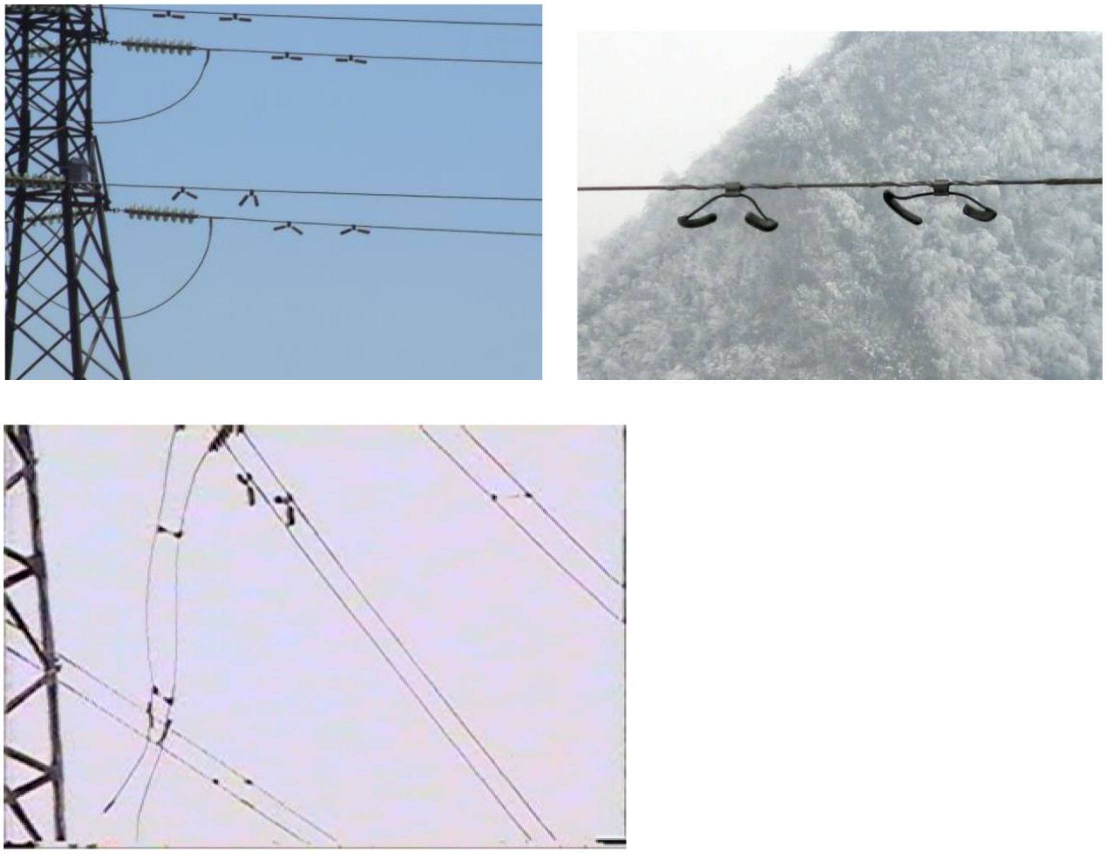

Damper failure (Wang, 2008).

FIGURE 14 Stockbridge dampers – fatigue failure

The dampers on EL 1 and EL 2 at towers 526 (see Figure 16) and 527 (see Figure 17 and Figure 18) show signs of fatigue similar to that shown in Figure 14. Some of the dampers however seem intact. Damaged dampers will significantly reduce the span damping and has the potential of resulting in fatigue failure of the conductor close to the attachment points at the hardware.

Nalcor indicated that there have been previous failures of dampers in this area and the failures are currently under investigation.

A brief assessment was conducted of the vibration damping on the Str 340 section of the line. The damper specification was assessed, the ability of the spans to be damped was assessed in line with the recommendations of CIGRE TB 273 and test certificates for the dampers was reviewed.

Figure 15 below shows that section Str 340 should be possible to damp with end span damping when the line is in open flat ground with no trees or obstructions.

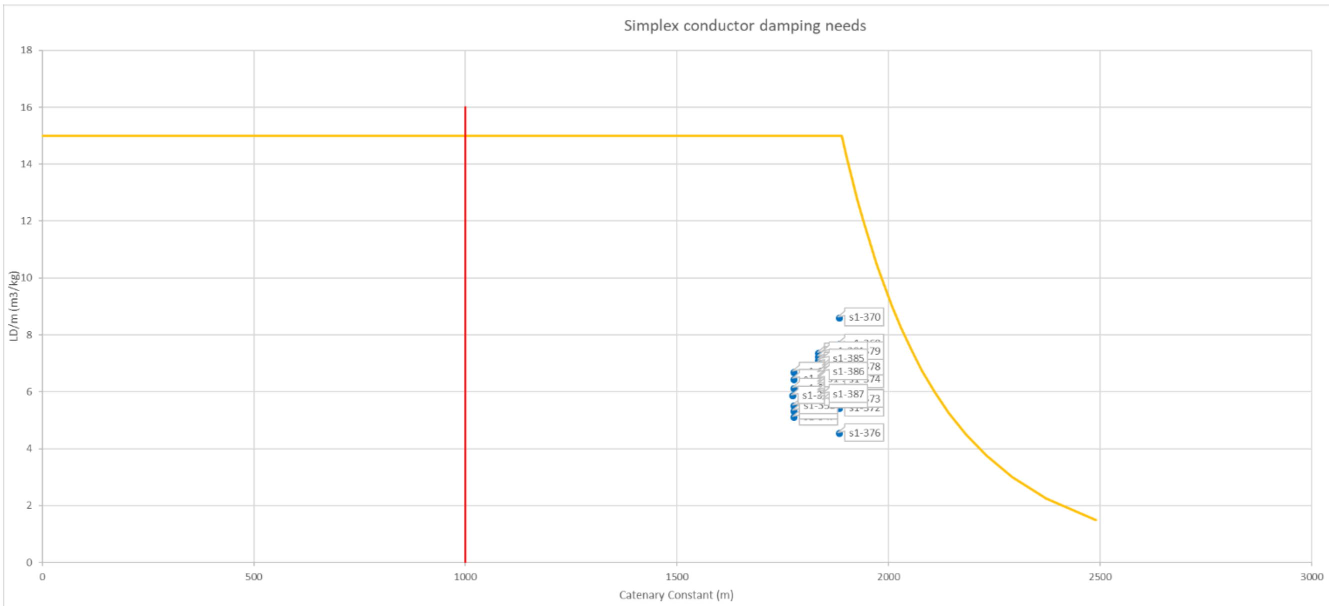

FIGURE 15 Damping requirements for simplex grackle conductor (section str 340)

The specification ILK-SN-CD-6200-TL-TS-0011 -01 states the following:

- The dampers shall effectively dampen conductor movement caused by aeolian vibration for an expected line life of 40 years.
- Supplier shall submit data to show that the design of dampers, when installed as specified by Supplier, will effectively limit aeolian vibration and effectively prevent any fatigue damage and abrasion to conductor for an expected conductor life of 40 years.
- Avoid damage to the conductor under specified service conditions;
- Withstand mechanical loads imposed during installation, maintenance and specified service
- conditions;
- The Stockbridge type dampers are expected to withstand the mechanical loads under the extremes of service conditions. The dampers shall effectively dampen conductor movement caused by aeolian vibration for an expected line life of 40 years.
- Refer to Appendix A for sag-tension tables for each conductor.

While many references are made to service conditions, no specific section in the specification is dedicated to defining the expected service conditions. The specification also references the sag and tension tables. The damper suppliers are not guided with respect to the design conditions that must be used for designing the damping system, e.g. should ice be considered when designing the damping system and if so, what radical thickness and density should be used? Omission of this information allows the different suppliers to chose what to use thereby making it difficult to compare offers from suppliers as the inclusion of ice in the damping study may result in the need for additional dampers. The specification provides no guidance regarding the level of conductor self-damping that should be considered when designing the damping system. Depending on the catenary constants used for the spans, the influence of conductor self-damping on the power balance can be up to 20%. It is unclear if the level of icing to be considered has been discussed elsewhere and considered in the damping design

The wind power input is affected by the diameter of the conductor. The following equation is generally used to estimate the wind power input a span. It is important to note that the input power is proportional to the fourth power of the conductor diameter however the overall impact is influenced by the fn(Y/d) as well.

$$P_w = S \times \ d^4 \times \ f^3 \times F_n\left(\frac{Y}{d}\right)$$

Where:

P_w: Wind power input (W)
S: Span Length (m)
d: conductor diameter (m)
f: vibration frequency (Hz)
$F_{n:}$ function derived from experimentation
Y: peak to peak vibration amplitude at the antinode

The following is therefore suggested:

- The following should be confirmed with the supplier of the damping system
    - What level of conductor self-damping was considered in the study?
    - Why was the excitation level chosen as 3/f p—p?
    - What radial ice value was considered when performing the damping study?
- If no ice was considered in the damping study, a new damping study should be conducted with a suitable ice value. The power curve for the dampers and wind power input with ice considered must be compared to ensure the dampers can damp the vibrations in the span. Consideration must be given to the level of turbulence and conductor self-damping that must be considered in the design.

FIGURE 16 Tower 526 – EL2, prior to failure

FIGURE 17 Tower 527 EL 1 – Prior to EL2 failure at Tower 526

FIGURE 18 Tower 527 –After EL2 failure at Tower 526

FIGURE 19 Tower 360 – Dampers showing signs of fatigue

Conductor damage due to slippage in clamp

FIGURE 20 shows conductor slippage in the electrode conductor clamp from tower 513. While the reasons for slippage are not easily explained at this stage there are concerns with the spring lock washers used in the bolting arrangement.

The spring lock washers are not considered an effective means for bolting this assembly and have been known to come loose during vibration. The NASA fastening manual states the following regarding spring lock washers, "*The lockwasher serves as a spring while the bolt is being tightened. However, the washer is normally flat by the time the bolt is fully torqued. At this time, it is equivalent to a solid flat washer, and its locking ability is non-existent. In summary, a lockwasher of this type is useless for locking.*"

Eskom, the utility in South Africa that operates around 30 000 km of Transmission lines from 220 kV to 765 kV stopped using spring lock washers around 2012 due to their unreliability. Landsnet the Icelandic utility has also moved away from spring lock washers on hardware and both the utilities opt for bevel type washers.

It is possible that vibration has been causing the nuts to loosen and hence allow for slippage of the conductor in the clamp. The clamp shown in Figure 20 has bolts torqued to different levels as evidenced by the varying number of threads protruding from the nuts. The loose nuts could have resulted from:

- Excessive vibration (aeolian or galloping)
- Poor installation practice
- They were loosened by the workmen when the clamps were removed from the line

Further investigation is required to ascertain the cause of the conductor slippage in the clamps.

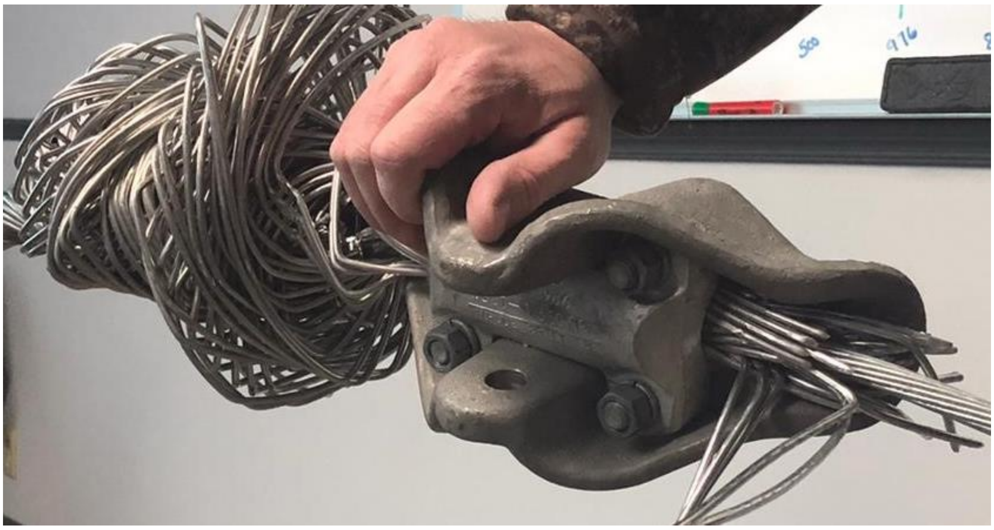

FIGURE 20 Conductor damage and slippage in clamp.

Conclusion and recommendations

1. The conductor failure at tower 526 is a concern as the conductor should not have broken with the 11kg/m ice load and 10 damaged strands. The visible damage to 10 strands does not weaken the conductor enough for a 11 kg/m ice load to break it. This suggests more damage in the inner layers. Approximately 28 broken conductor strands would be required for the conductor to failure (see **FIGURE 2**) with an 11kg ice load.

   The images of the conductor strands indicate the conductor had several strands which failed due to fatigue in the 1st and 2nd layers which was not visible by the workmen. The fatigue could have been caused by galloping or aeolian vibration. It is therefore possible that other areas of the conductor are damaged in the 1st and 2nd layers of aluminium which cannot be seen.

   It is important to conduct metallurgical tests on the conductor as soon as possible to establish the failure mechanism. It is also suggested to cut open and inspect the conductor sections that have been removed from the line. The sections close to the old suspension clamp positions should be inspected to check for fatigue failures in the conductor.

2. Nalcor should investigate alternatives for the damping system and seek a solution that is more robust against conductor galloping, such as the Bretelle dampers used in Norway and Iceland, shown in the images below. The Helix damper is also an option for lines experiencing conductor galloping.

3. A very low unbalanced load of 4 kg/m can cause the electrode insulator glass disk to rub against the electrode conductor and damage the strands. The loading required is well within the design loads of 10 kg/m. Nalcor must investigate the possibility of increasing the distance between the conductor clamp and the insulator closest to the conductor so that the string can accommodate greater longitudinal swing than 55 degrees and not damage the conductor.

4. The hardware used to support the electrode conductor is a normal bolted clamp without armor rods. The clamp uses spring lock washers to secure the bolt and nuts which are commonly considered as unreliable. More work must be done to investigate if the clamp arrangement was vibration tested and if the slip load tests were completed. The impact of correct torqueing procedure must be assessed in relation to the slip load capability of the clamps.

5. It is common practice in Norway and Iceland that armor rods are used together with similar bolted clamps with bevel washers. Based on the results of the tests mentioned above, nalcor may need to investigate the possibility of installing larger clamps with an improved clamping system design and armor rods over

the conductor. An alternative would be to utilise an AGSC (armor grip suspension clamp) which has long helical rods and an elastomer insert, similar to those used on the OPGW which has had minimal clamp slippage. The latter alternative is more costly.

6. The vibration damper failures could be attributed to ice shedding, galloping or fatigue due to aeolian vibration. Should the metallurgy tests indicate that fatigue is the cause of failure, then it is suggested that the damper study be redone. The level of conductor self-damping, turbulence and radial ice on the conductors must be considered in the design of the damping system. From the documentation provided, it seems that ice has not been considered in the design of the aeolian vibration damping system.

2 CONDUCTORS

2.1 1192.5 kcmil 54/19 Grackle ACSR Conductor (Galvanized Steel Core)

1192.5 kcmil 54/19 GRACKLE ACSR CONDUCTOR (GALVANIZED STEEL CORE)				
ITEM	**DESCRIPTION**	**UNIT**	**REQUIRED**	**GUARANTEED**
1.0	***Manufacturer Name***	-		Midal Cables
2.0	***Location of Manufacturing Plant***	-		Bahrain
3.0	***Technical characteristics***			
3.1	Type	-	ACSR	ACSR
3.2	Code name	-	GRACKLE	GRACKLE
3.3	Rated tensile strength	kN	187	194
3.4	Unit weight of complete conductor	kg/m	2.28	2.27
3.4.1	Unit weight of aluminum	kg/km		2,229
3.4.2	Unit weight of steel	kg/km		803
3.5	Coefficient of thermal expansion (aluminum portion)	Per °C	23.04×10^{-6}	23×10^{-6}
3.6	Modulus of elasticity (aluminum portion):	-		
3.6.1	*Final*	MPa	49,090	49,090
3.6.2	*Initial lower*	MPa		36,600
3.6.3	*Initial upper*	MPa		36,600
3.6.4	*Change of slope*	MPa		NQ
3.7	Coefficient of thermal expansion (steel portion)	Per °C	11.52×10^{-6}	11.52×10^{-6}
3.8	Modulus of elasticity (steel portion):	-		
3.8.1	*Final*	MPa	21,580	21,580
3.8.2	*Initial lower*	MPa		16,090
3.8.3	*Initial upper*	MPa		16,090
3.8.4	*Change of slope*	MPa		NQ
3.9	Maximum dc resistance at 20 ° C	Ohms/km	0.0472	0.0479
3.10	Maximum dc resistance at 25 ° C	Ohms/km		0.04887
3.11	Maximum dc resistance at 75° C	Ohms/km		0.05852
3.12	Minimum conductivity	%		61
3.13	Emissivity coefficient		0.5	0.5

Form Number F-0000-31AF-I-0019 Revision 01 SNC-Lavalin Inc.

1192.5 kcmil 54/19 GRACKLE ACSR CONDUCTOR (GALVANIZED STEEL CORE)				
ITEM	**DESCRIPTION**	**UNIT**	**REQUIRED**	**GUARANTEED**
3.14	Solar absorption coefficient		0.5	0.5
3.15	Aluminum portion heat capacity	Watt-s/m-°C		1,537.2
3.16	Steel portion heat capacity	Watt-s/m-°C		274.9
3.17	Nominal cross-sectional area (total)	mm^2	680.64	680.07
3.18	Overall diameter	mm	33.85	33.94
3.19	Number of conductors per pole	unit	1	1
3.20	Number of aluminum wires (stranding)	unit	54	54
3.21	Diameter of aluminum wires	mm	3.77	3.774
3.22	Type of weld for aluminum wire joint	-		
3.23	Number of steel wires (stranding)	unit	19	19
3.24	Diameter of steel wires	mm	2.26	2.26
3.25	Zinc Coating	-		
3.25.1	*Thickness*	g/m^2		230
3.25.2	*Class (as per CSAStandard)*	-	Class A	Class A
3.26	PLS-CADD conductor file (*.wir) provided	Yes/No	Yes	Yes
4.0	***Reel***			
4.1	Reel construction	Wood/Metal	Metal	Metal
4.2	Flange	m	2.13	2.22
4.3	Traverse	m	1.47	1.25
4.4	Drum	m	0.91	0.78
4.5	Arbor hole	m	0.127	0.127
4.6	Drive pin	-		
4.6.1	*Diameter*	mm		65
4.6.2	*Distance offset from center*	mm		300
4.7	Maximum gross reel weight	kg		6,700
4.8	Empty reel weight	kg		500
4.9	Nominal conductor length per reel	m	2,700	2,700

Appendix D - Metallurgical Failure Analysis of Suspension Tower Cross Arm

QT-5-1
REV 20-04

Metallurgical Failure Analysis of Suspension Tower Cross Arms

K-314022-RC-0001 R00

Prepared for

Labrador Island Link Ltd Partnership
Purchase Order # 4600 OS

Issue Date

2021-May-28

Prepared by	Reviewed by	Reviewed by	Approved by
Digitally signed by Dean Finlayson Date: 2021.05.28 17:22:17 -04'00'	Digitally signed by Dean Finlayson Date: 2021.05.28 17:22:39 -04'00'	Digitally signed by Andrew Rizzetto Date: 2021.05.28 17:30:40 -04'00'	Digitally signed by Zsolt Peter Date: 2021.05.31 06:32:14 -04'00'
Signature	*Signature*	*Signature*	*Signature*
Dean Finlayson	Guylaine Haché	Andrew Rizzetto	Zsolt Peter
Engineer	Principal Scientist	Senior Engineer	Business Area Director
Materials & Major Components	Materials & Major Components	Transmission & Distribution Technologies	Transmission & Distribution Technologies

Revision History

Rev	Description				
D00	**Draft issue for client review and comment.**				
	Issue Date 13May2021	Prepared by D. Finlayson	Reviewed by G. Haché	Verified by A. Rizzetto	Approved by Z. Peter
Rev 00	Description **Final report issued to client.**				
	Issue Date 28May2021	Prepared by D. Finlayson	Reviewed by G. Haché	Verified by A. Rizzetto	Approved by Z. Peter
Rev	Description				
	Issue Date		Issue Date		Issue Date

DISCLAIMER

Kinectrics prepared this report as a work of authorship sponsored by their customer. This report has been prepared solely for the benefit of the customer and may not be used or relied upon in whole or in part by any other person or entity without customer permission or without Kinectrics' permission if required by the contract between the customer and Kinectrics Inc. Neither Kinectrics, their customer nor any person acting on behalf of them: (a) makes any warranty or representation whatsoever, express or implied, or assumes any legal liability of responsibility for any third party's use, or the results of such use, with respect to (i) the use of any information, apparatus, method, process, or similar item disclosed in this report including the merchantability or fitness for any particular purpose of any information contained in this report or the respective works or services supplied or performed or (ii) that such use does not infringe on or interfere with privately owned rights, including any party's intellectual property; or (b) assumes responsibility for any damages or other liability whatsoever (including any consequential damages) resulting from a third party's selection or use of this report or any information, apparatus, method, process, or similar item disclosed.

Table of Contents

List of Figures

List of Tables

1 Introduction

This report summarizes the metallurgical failure analysis of two failed suspension tower cross arms from Nalcor. A third (new) cross arm was provided by Nalcor as an exemplar and was also examined in this investigation. The cross arms were fabricated from High-Strength, Low-Alloy (HSLA) Steel as per the CSA G40.21-13 GR 350WT Specification. The failure was identified during the winter period during which the suspension tower structures, and transmission lines were ladened with ice.

The investigation consisted of the following activities for all three cross arms:

Receipt of parts and incoming inspection,

1. Visual examination,
2. Chemical analysis,
3. Hardness testing, and
4. Low-temperature Charpy V-notch impact testing.

In addition to the above, the failed cross arms were also subjected to:

1. Disassembly of the two failed cross arms to obtain sections for detailed examination, and
2. Detailed examination including fractography (photographs, optical microscopy, scanning electron microscopy (SEM)).

All work was carried out under the Kinectrics' QA Program Manual, Revision 20, dated June 26, 2020, which meets the requirements of ISO 9001.

2 Incoming Inspection and Visual Examination

The three cross arms were received at Kinectrics' facility in Toronto, ON in individual crates and subsequently unpacked and transported indoors for initial examination followed by disassembly.

The failed cross arms were received labelled as "526-EL1" and "343-EL2", with the new cross arm labelled as "New". These labels were retained for the investigation and the cross arms referred to as such through-out this report. Figure 1 is an excerpt from the cross arm general arrangement drawing [1] which shows the failure locations on each cross arm component.

2.1 Cross Arm 526-EL1

Cross arm 526-EL1 was received with multiple failures (cracks and bent components) observed in areas highlighted in Figure 2. A closer view of these damaged areas is presented Figure 3 and Figure 4.

The cracked area of the cross arm at the top of the image in Figure 2 was selected for detailed examination and fractography for a more direct comparison to the failure on cross arm 343-EL2 since both cross arms failed in this location. Heavy deformation (bent and twisted components) were observed as well as a complete fracture through the bolt holes of one component. Detailed images are presented in Figure 5. Fracture face F1 shown in Figure 5 (F) was selected for fractography.

2.2 Cross Arm 343-EL2

Cross arm 343-EL2 was received with similar damage as observed on cross arm 526-EL1. The more severe damage was however limited to the area highlighted at the top of the image in Figure 6 and in Figure 7.

The identical region (at the top of Figure 6) was selected for detailed examination and fractography. Similar damage to what was observed in cross arm 526-EL1 was present. Heavy deformation (bent and twisted components) was observed with multiple fractures through the bolt holes of several components. Detailed images are presented in Figure 8. Fracture face D1 show in Figure 8 (D) was selected for fractography.

2.3 New Cross Arm

The new cross arm was received in good condition with no obvious damage present (Figure 9). The corresponding areas on the new cross arm where the failures occurred on cross arms 526-EL1 and 343-EL2 are shown in Figure 10. These areas appeared as-manufactured with no signs of damage.

3 Fractography

To facilitate fractography, the selected fracture faces (Figure 11 and Figure 12) were cleaned in a warm detergent solution to remove corrosion build-up that would mask observation of the features on the fractured metal surface. Due to their size, the fracture faces were then sectioned into four segments (labelled Segment A to Segment D) that would enable microscopic observation.

3.1 Cross Arm 526-EL1

The fracture face segments of cross arm 526-EL1 are shown in Figure 13 to Figure 16 as observed under the light microscope. Generally, the fracture face segments appear dull and fibrous, which is characteristic of a ductile failure mode in metals. Smeared metal can also be observed which was likely due to contact with other components during the failure event, or during post-failure transportation and handling.

Further examination of the fracture face segments was performed by Scanning Electron Microscopy (SEM) and representative images from each segment are presented in Figure 17 to Figure 20. The key observation from the SEM micrographs was the predominantly oval-shaped dimple morphology of the fracture face. Oval-shaped dimples are characteristic of a shear loading induced ductile fracture but is also characteristic of a tensile tear loading induced ductile fracture. Based on the visual examination of the cross arm, heavily deformed (bent and twisted components) tear loading is the more likely candidate.

3.2 Cross Arm 343-EL2

The fracture face segments of cross arm 343-EL2 are shown in Figure 21 to Figure 24 as observed under the light microscope. Generally, the fracture face segments appear dull and fibrous, which is characteristic of a ductile failure mode in metals. Fracture Segment B (Figure 22) had a mixed appearance with a combination of dull, fibrous areas, as well as “river patterns” that are characteristic of a moderately ductile failure mode. Smeared metal can also be observed which was likely due to contact with other components during the failure event, or during post-failure transportation and handling.

Representative SEM micrographs from each fracture face segment are presented in Figure 25 to Figure 28. Fracture Segments A, C, and D had a regular dimple morphology, which is characteristic of a tensile loading induced ductile fracture. Fracture Segment B (Figure 26) had regions of quasi-cleavage morphology (moderately ductile fracture) and dimple morphology. Based on these observations, tensile overload leading to ductile and quasi-cleavage fracture was the likely cause of the cross arm failure.

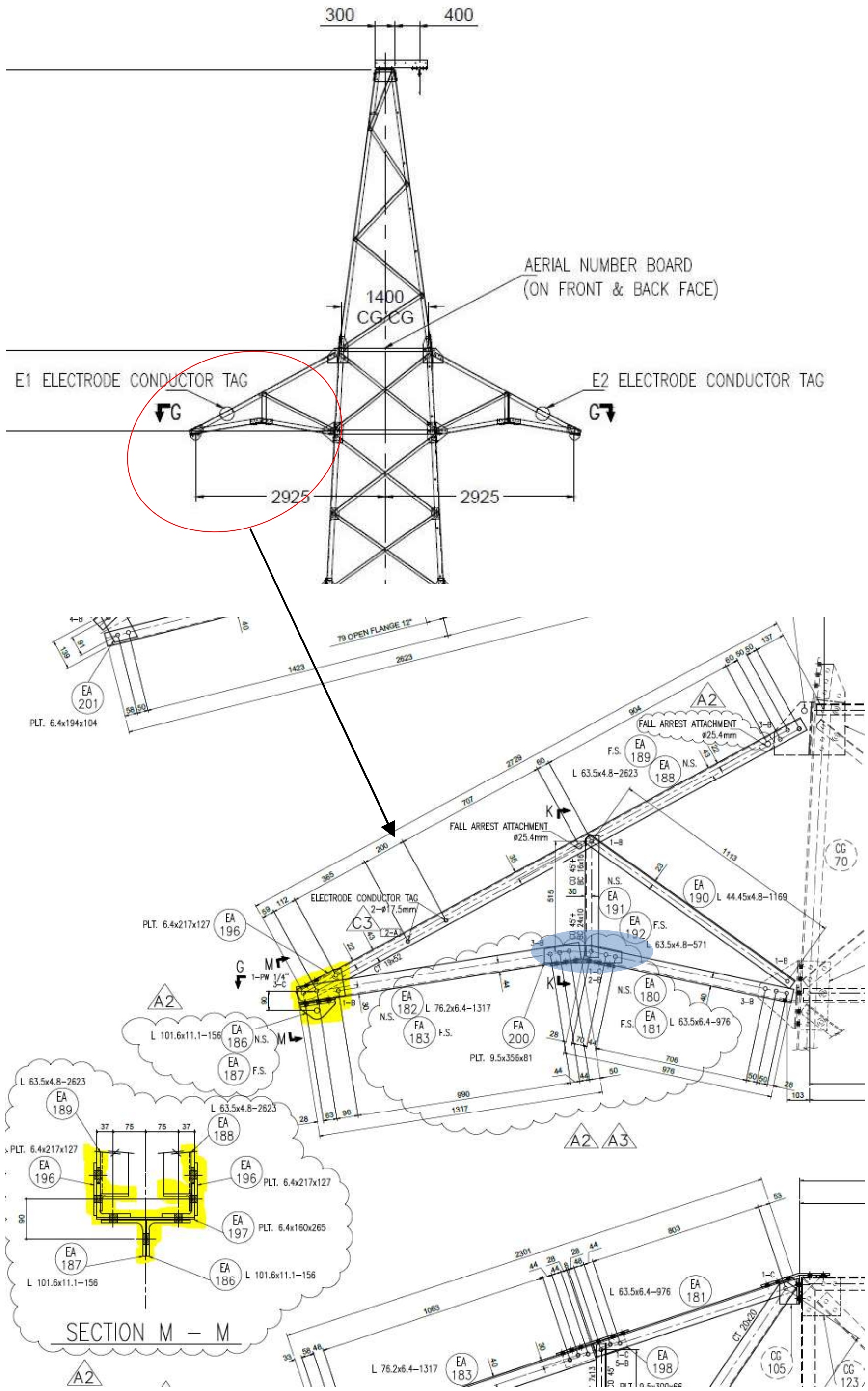

Figure 1: Excerpt from Drawing [1] showing Cross Arm Location on Tower and the Areas of Damage. Damage to Cross Arm 526-EL1 in Yellow and Blue. Damage to Cross Arm 343-EL2 in Yellow.

Figure 2: Cross Arm 526-EL1 As-Received

Figure 3: Damage to Cross Arm 526-EL1

Figure 4: Damage to Cross Arm 526-EL1

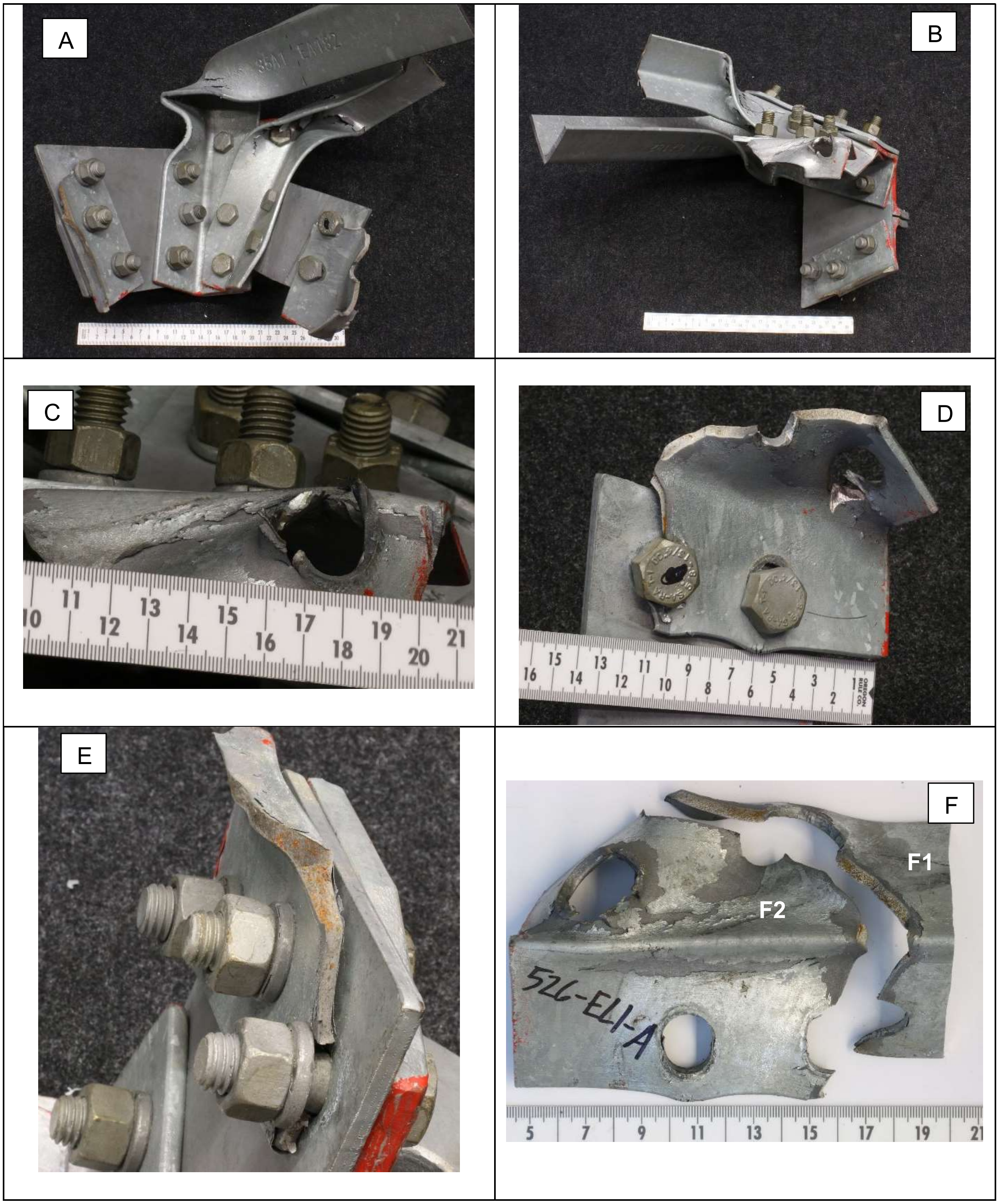

Figure 5: Damaged Section of Cross Arm 526-EL1. (F), Fracture Faces F1 and F2 Retained for Further Examination

Figure 6: Cross Arm 343-EL2 As-Received

Figure 7: Damage to Cross Arm 343-EL2

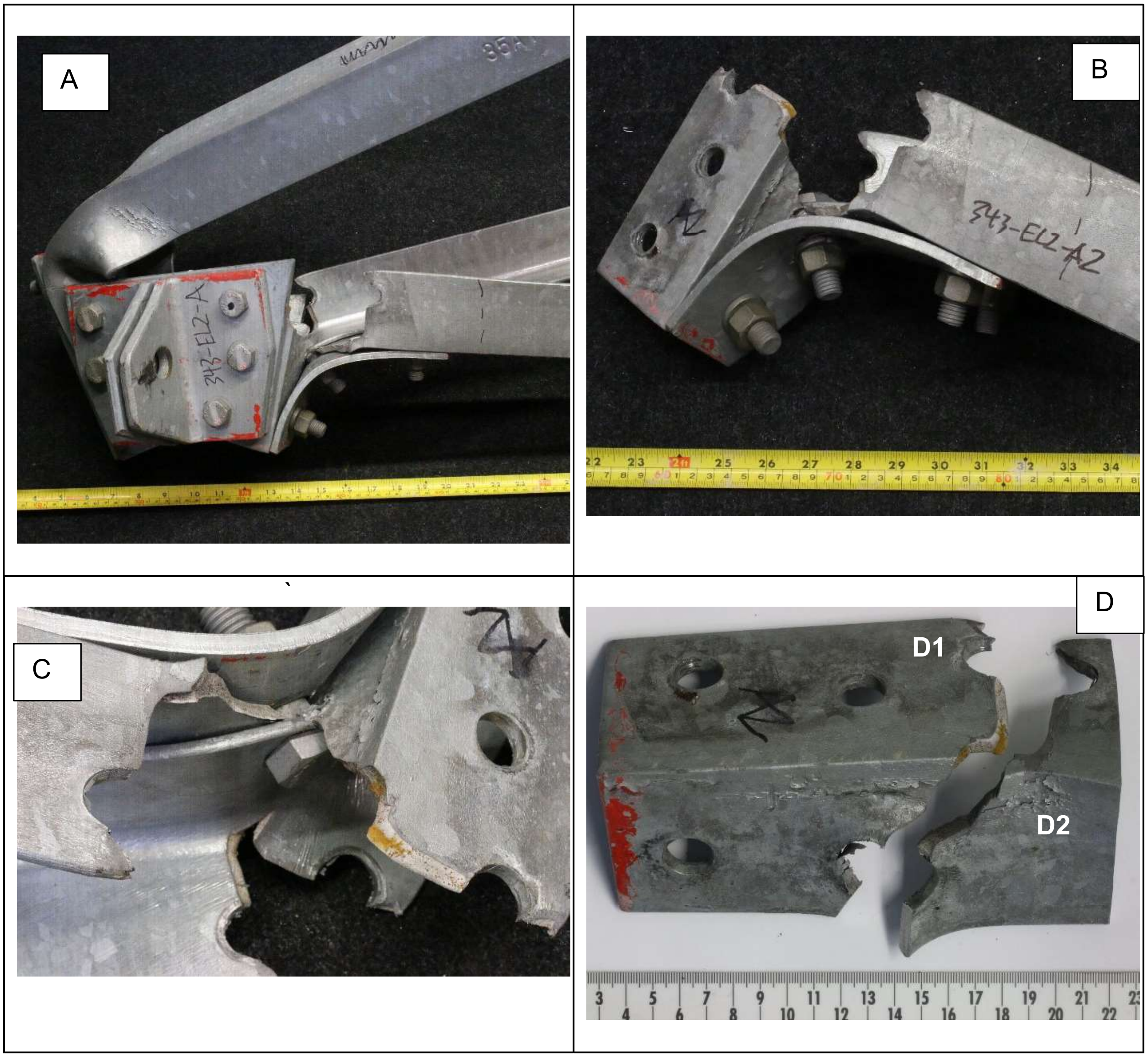

Figure 8: Damaged Section of Cross Arm 343-EL2. (D), Fracture Faces D1 and D2 Retained for Further Examination

Figure 9: New Cross Arm As-Received

Figure 10: New Cross Arm As-Received

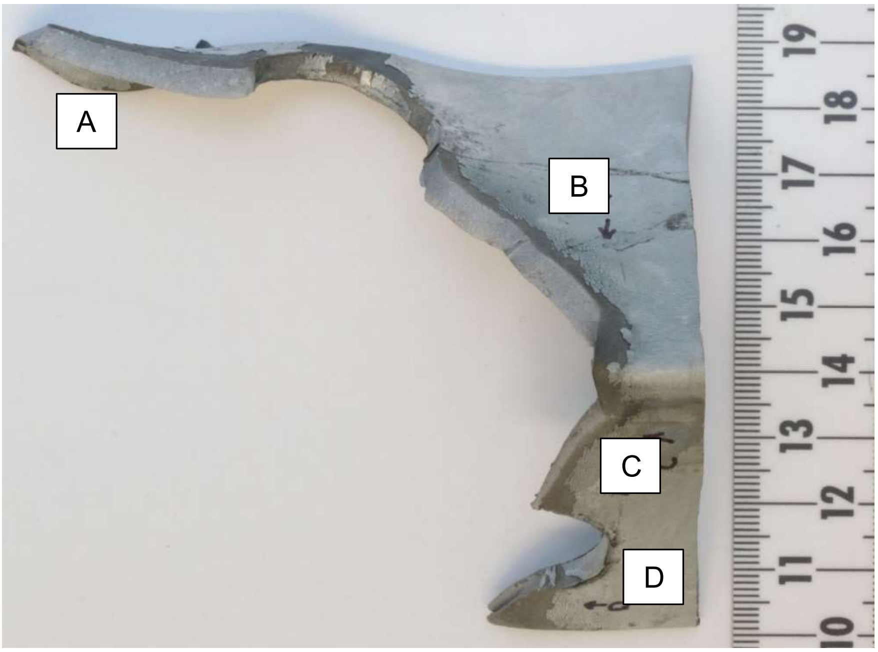

Figure 11: Cross Arm 526-El1 Fracture Face F1 Post-Cleaning

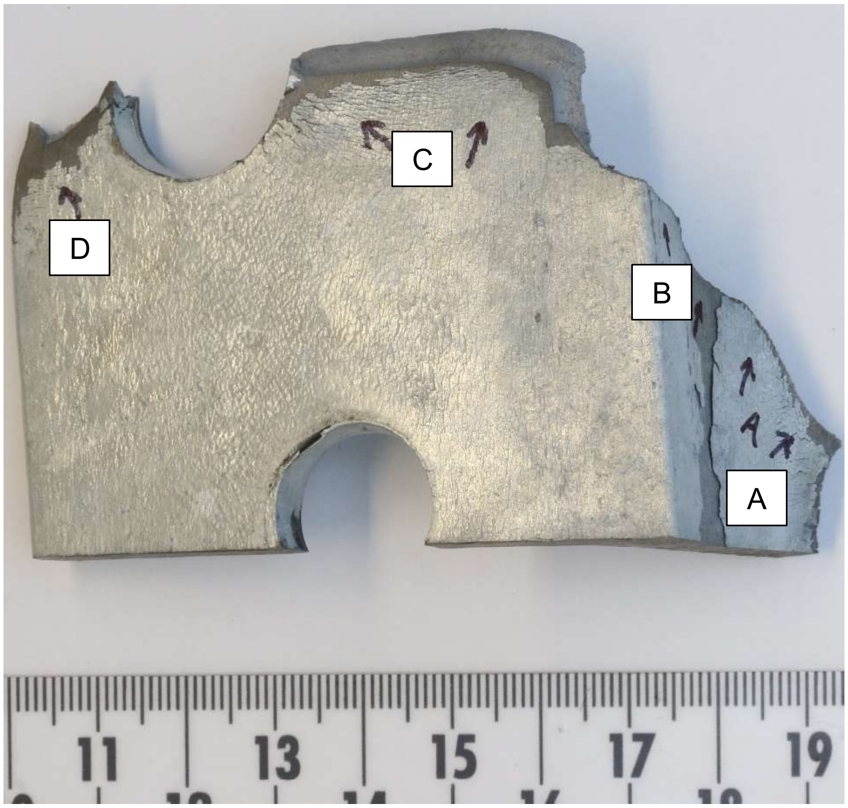

Figure 12: Cross Arm 343-EL2 Fracture Face D1 Post-Cleaning

Figure 13: Cross Arm 526-EL1 Fracture Face Segment A

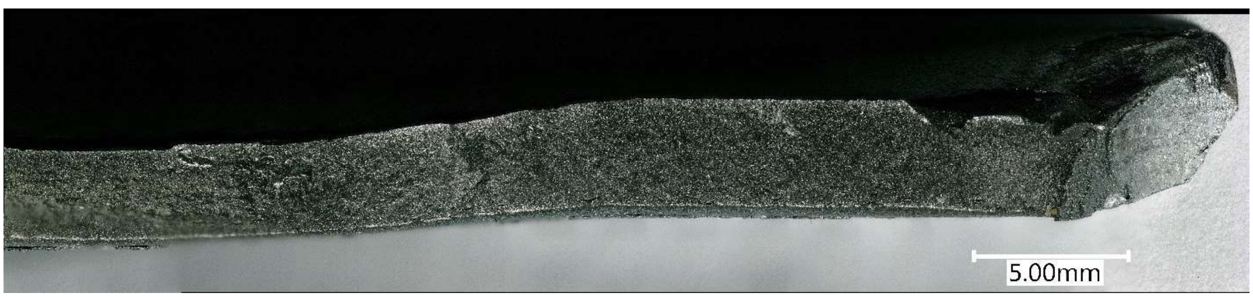

Figure 14: Cross Arm 526-EL1 Fracture Face Segment B

Figure 15: Cross Arm 526-EL1 Fracture Face Segment C

Figure 16: Cross Arm 526-EL1 Fracture Face Segment D

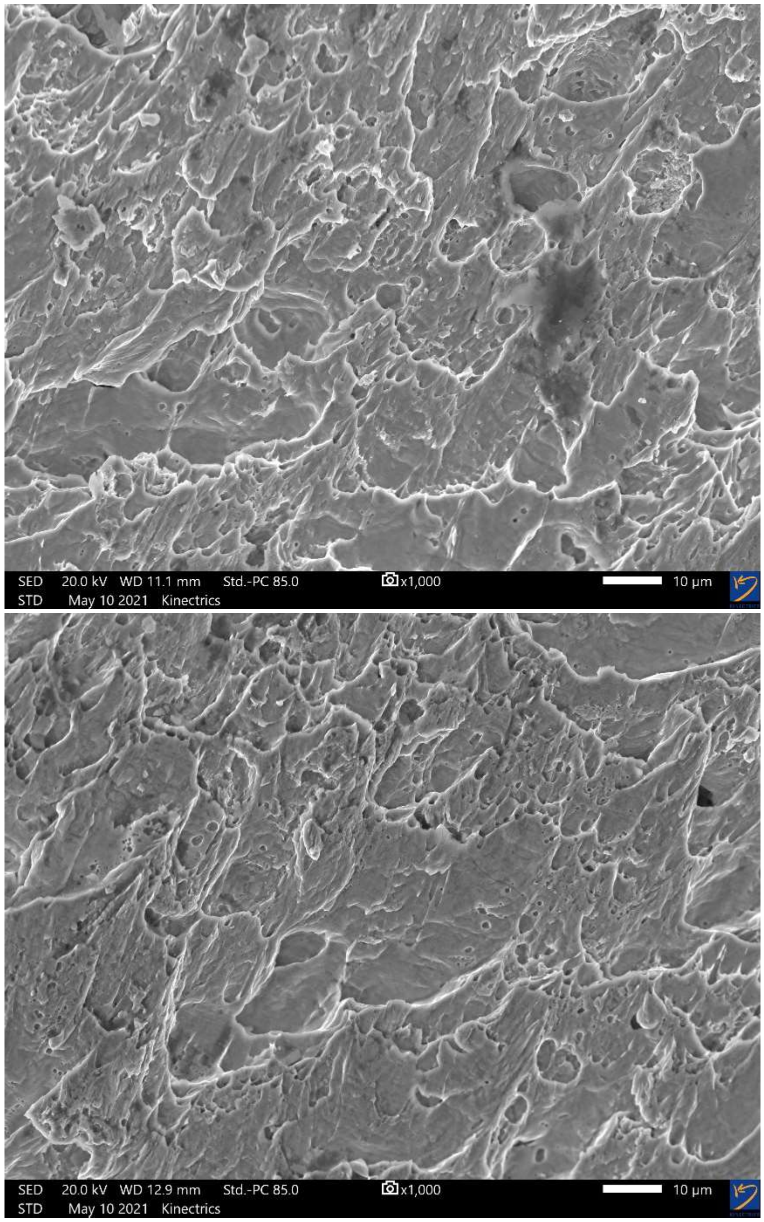

Figure 17: Cross Arm 526-EL1 Fracture Face Segment A SEM Micrograph showing smeared dimple morphology.

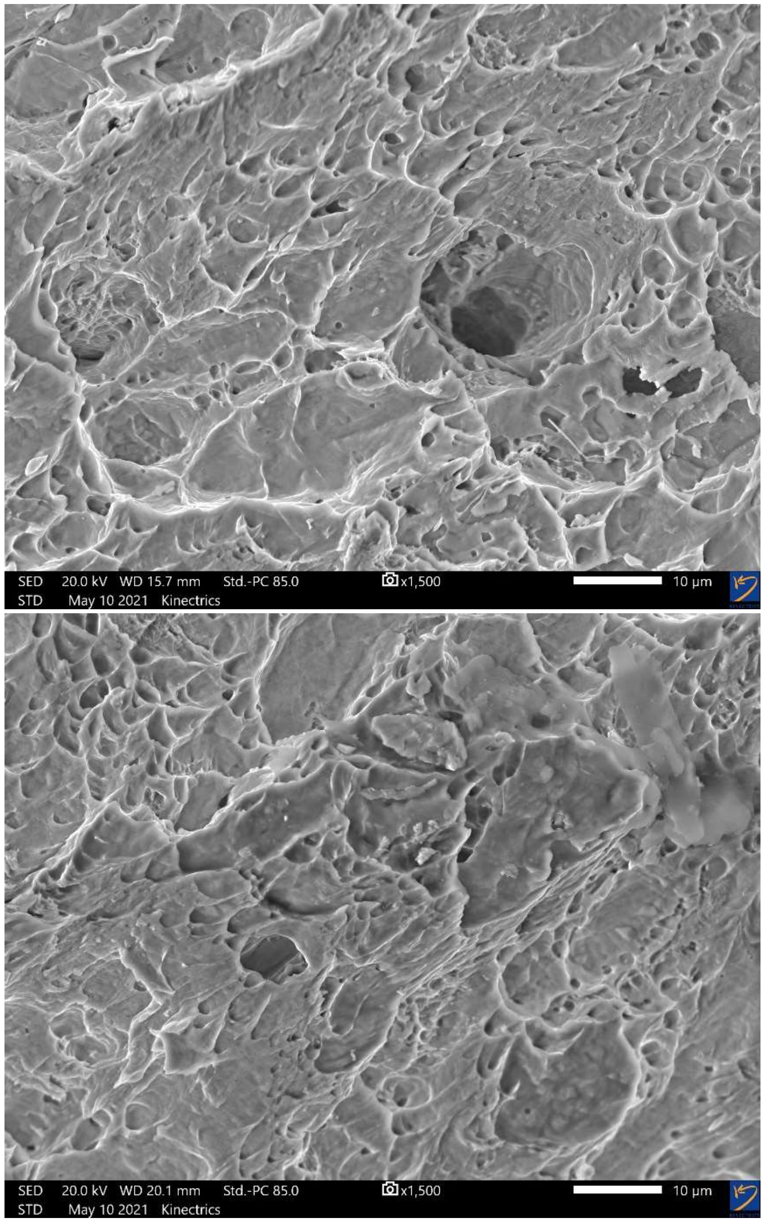

Figure 18: Cross Arm 526-EL1 Fracture Face Segment B SEM Micrograph showing smeared dimple morphology.

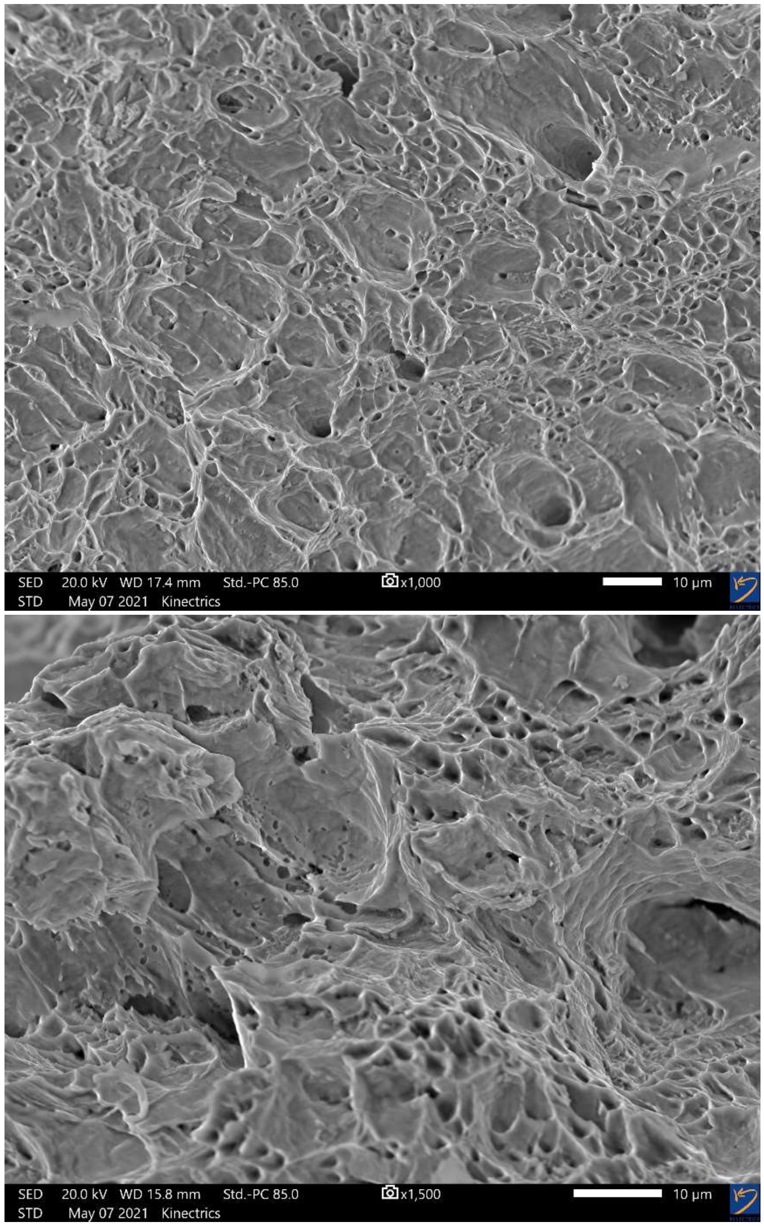

Figure 19: Cross Arm 526-EL1 Fracture Face Segment C SEM Micrograph showing smeared dimple morphology.

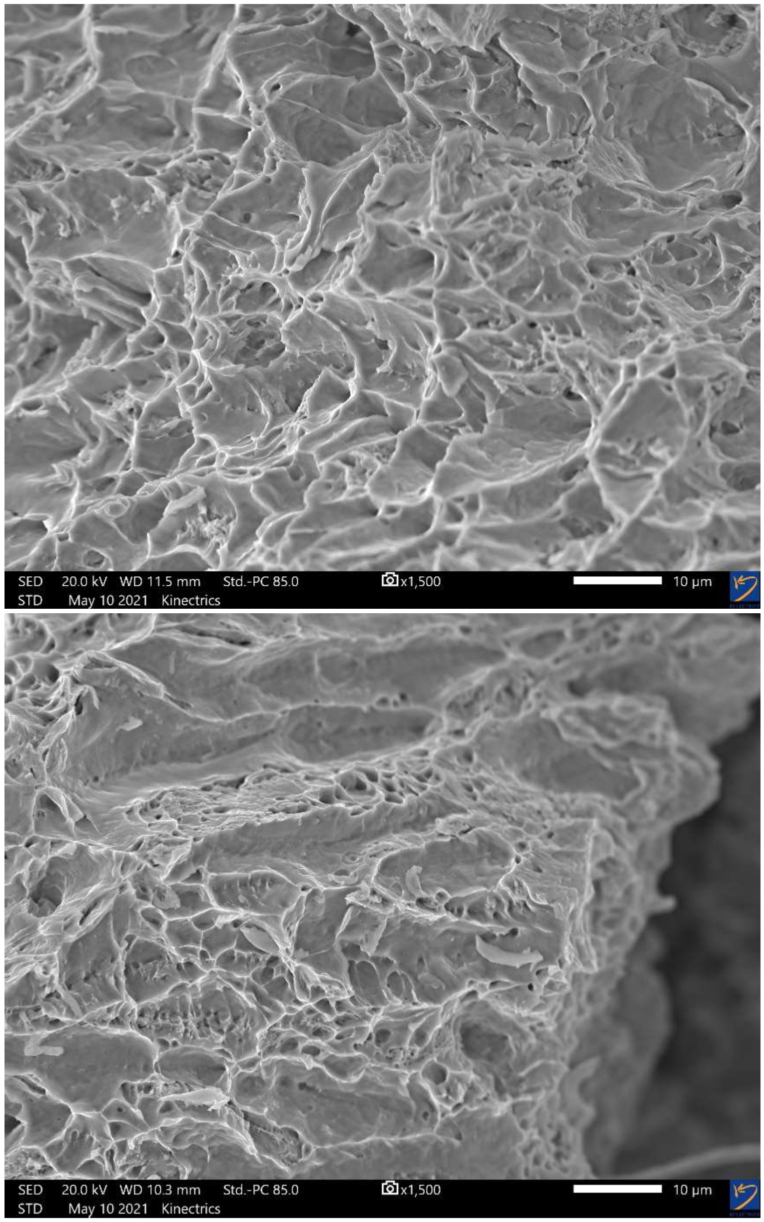

Figure 20: Cross Arm 526-EL1 Fracture Face Segment D SEM Micrograph showing dimple morphology

Figure 21: Cross Arm 343-EL2 Fracture Face Segment A

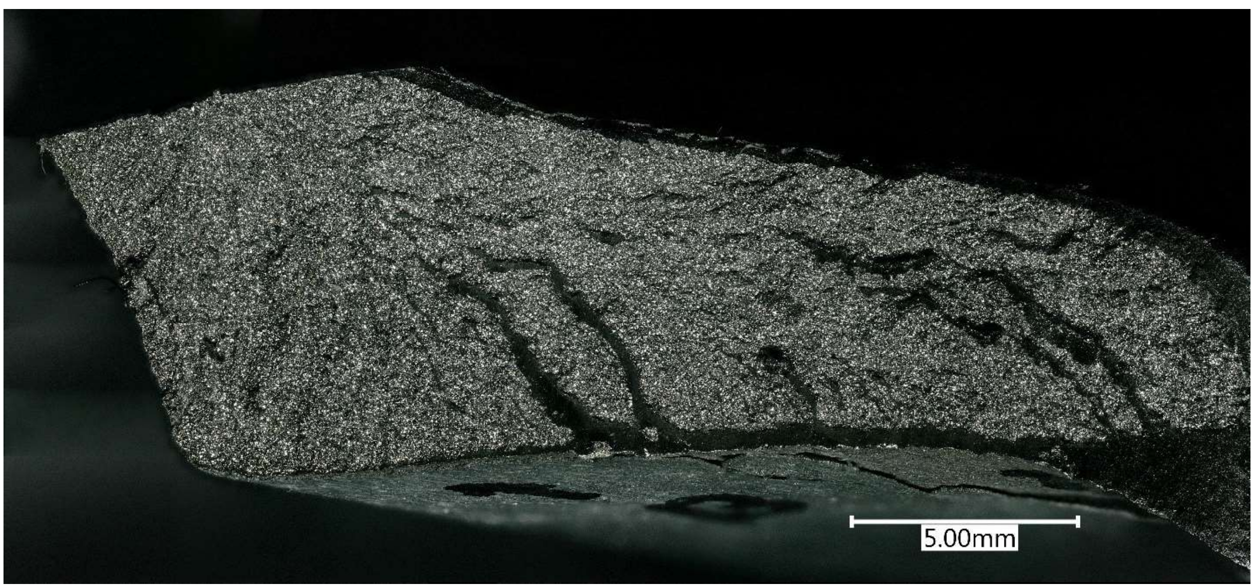

Figure 22: Cross Arm 343-EL2 Fracture Face Segment B

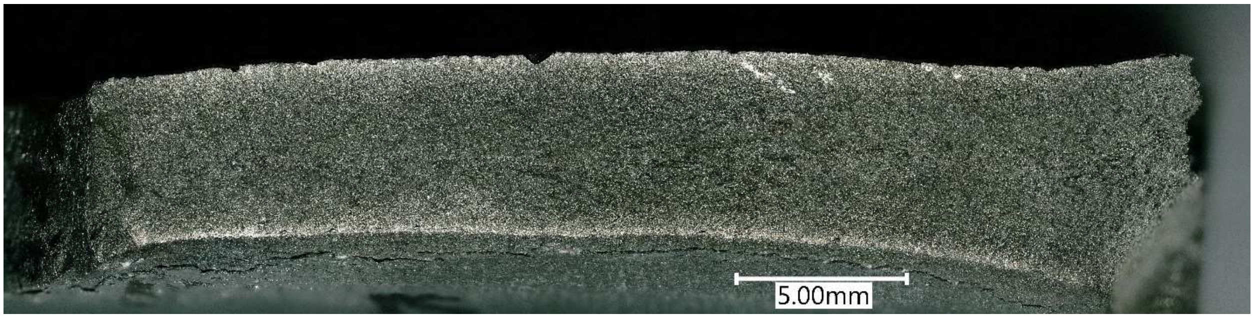

Figure 23: Cross Arm 343-EL2 Fracture Face Segment C

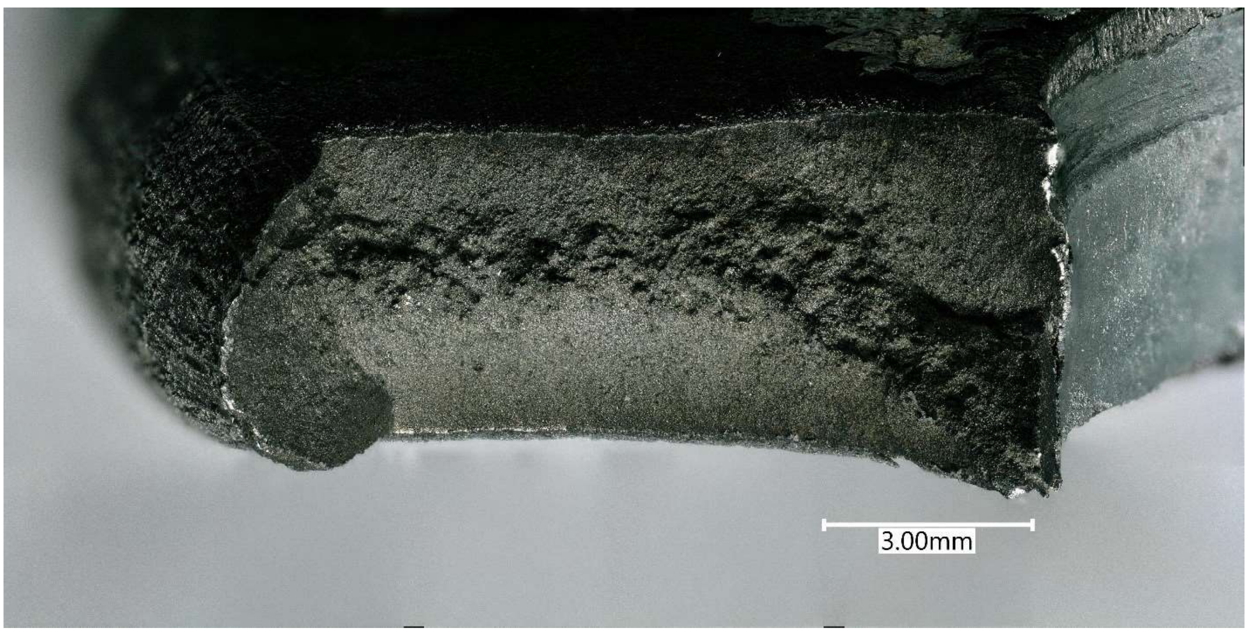

Figure 24: Cross Arm 343-EL2 Fracture Face Segment D

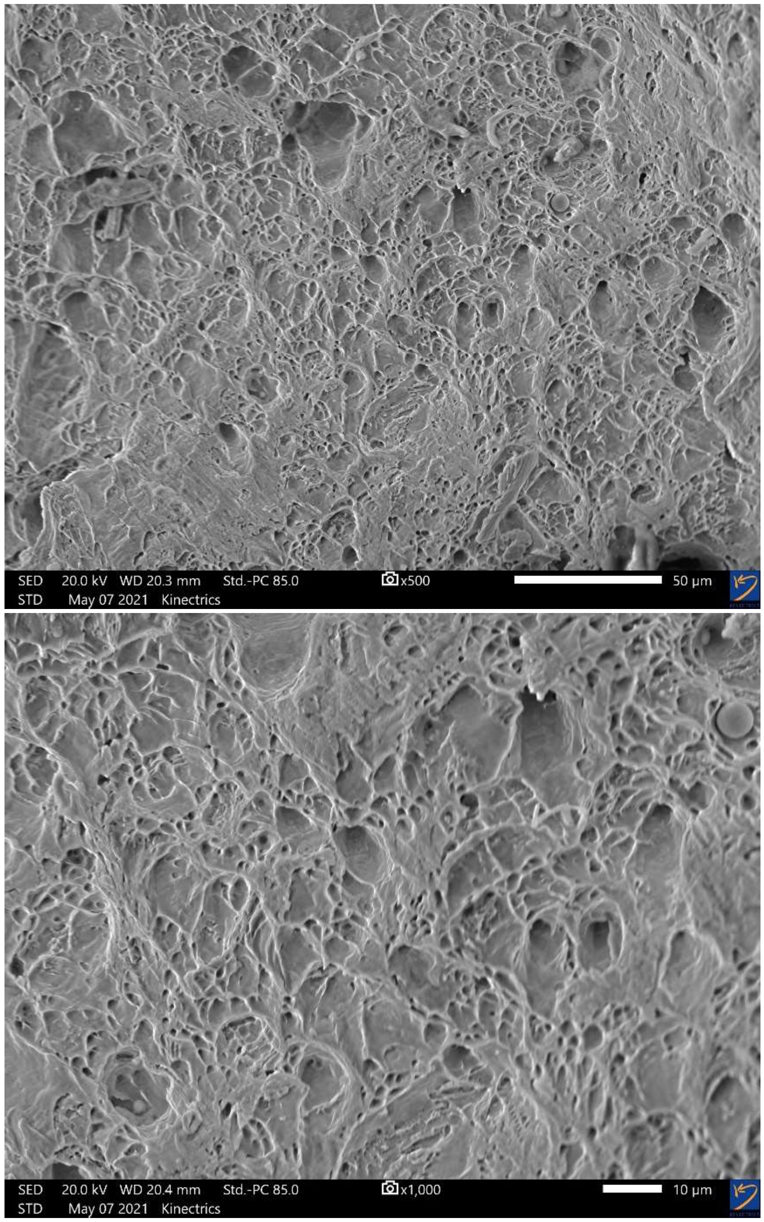

Figure 25: Cross Arm 343-EL2 Fracture Face Segment A SEM Micrograph showing dimple morphology

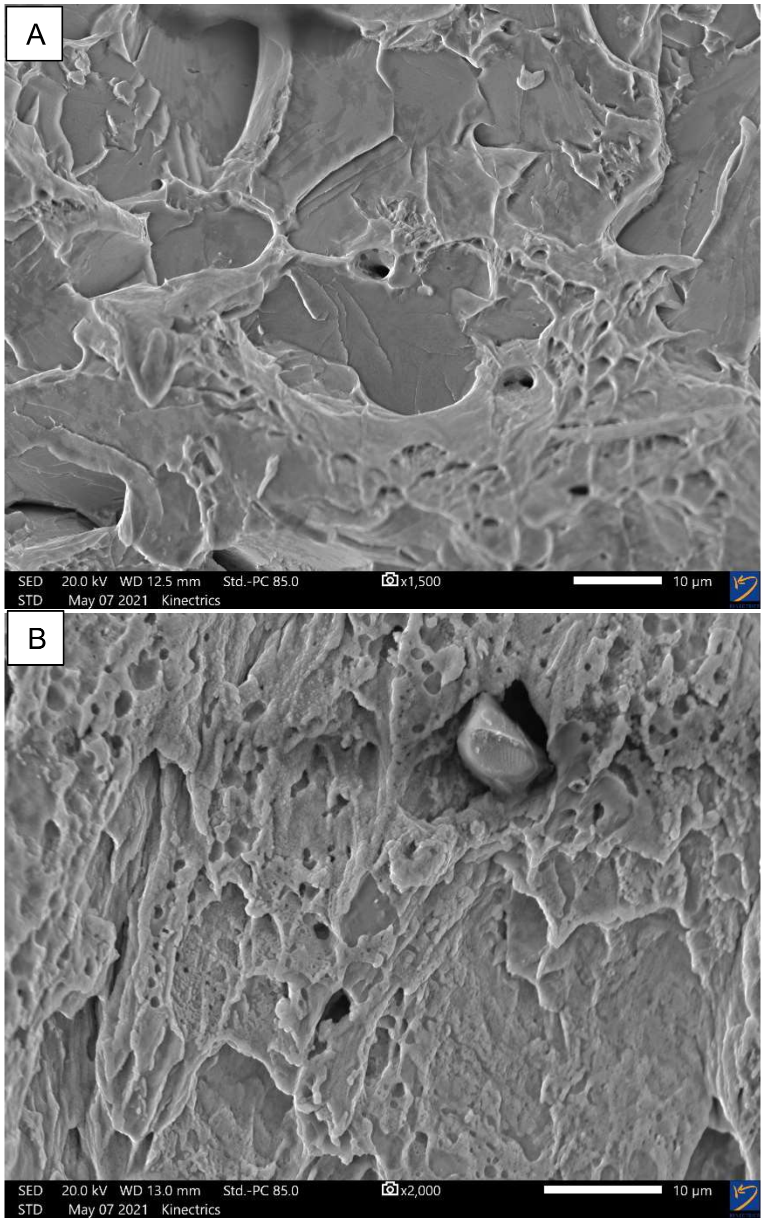

Figure 26: Cross Arm 343-EL2 Fracture Face Segment B SEM Micrograph showing, (A) Quasi-Cleavage and (B) Dimple Morphology

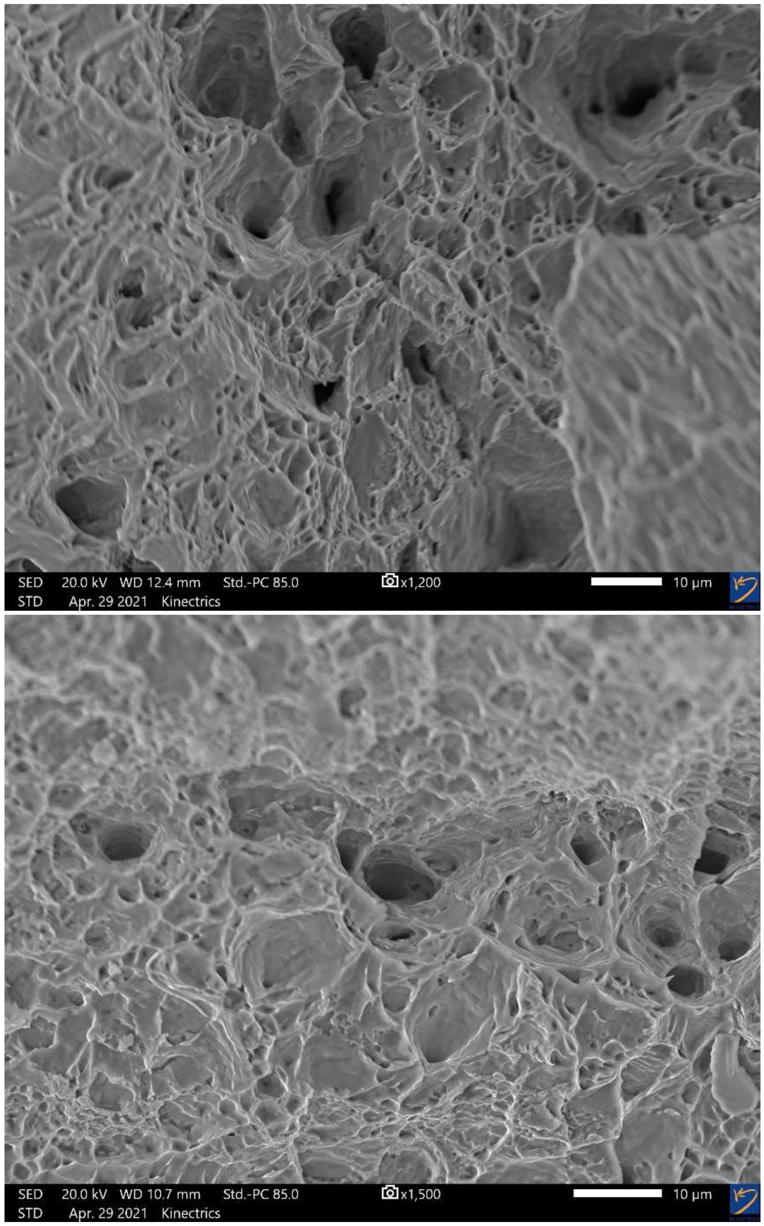

Figure 27: Cross Arm 343-EL2 Fracture Face Segment C SEM Micrograph showing dimple morphology

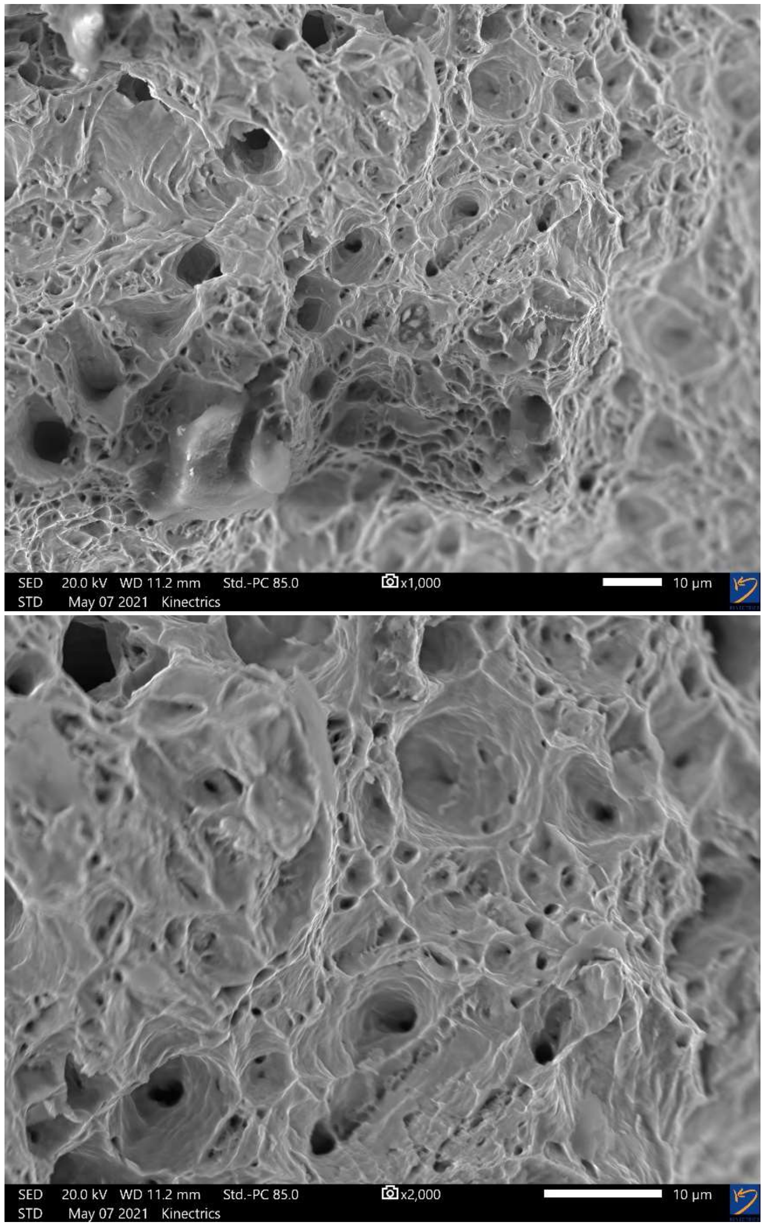

Figure 28: Cross Arm 343-EL2 Fracture Face Segment D SEM Micrograph showing dimple morphology

4 Metallurgical Characterization of Cross Arm Material

Material was selected from an undamaged region of each of the cross arms to perform the following metallurgical characterization tasks:

1. Charpy V-notch impact testing.
2. Hardness testing,
3. Chemical analysis, and
4. Metallography.

4.1 Charpy V-notch Impact Testing

Charpy v-notch impact testing was performed by a subcontractor, Acuren, on material submitted from the three cross arms. Three tests were performed at -20 °C on material from each cross arm and the results are presented in Table 1. The three cross arms met the minimum absorbed energy requirement of 20 Joules at -20 °C [1]. The complete report from Acuren is included as Appendix A.

4.2 Hardness Testing

Hardness testing was performed on a metallurgical cross-section of material from the three cross arms. Ten (10) hardness idents were performed on each cross-section and the average Rockwell B hardness (HRB) are presented in Table 2. The average hardness values ranged from approximately 81 HRB to 83 HRB, which corresponds well with the expected hardness value for this grade of High-Strength, Low-Alloy Steel (HSLA), approximately 75 HRB to 90 HRB [2].

4.3 Chemical Analysis

Chemical analysis was performed by the Inductively Coupled Plasma atomic emission spectroscopy (ICP-AES) for metals, and by LECO for Carbon and Sulphur[1]. The galvanized coating was removed prior to collecting the samples for chemical analysis. The results of the chemical analysis for each cross arm are tabulated and compared to the standard specification (CSA G40.21-13 GR 350WT) [3] in Table 3. The cross arms were found to be within the

[1]Carbon and Sulphur content analysis was subcontracted to Acuren.

specified chemical composition. The complete chemical analysis report is included as Appendix B.

4.4 Metallography

Optical metallography was performed on prepared (polished and micro-etched) metallurgical cross-sections from the three cross arms to examine the microstructure of the HSLA steel. Figure 29 to Figure 31 show the representative microstructure observed in the steel from each cross arm. The microstructures are similar in appearance, possessing a ferrite-pearlite structure characteristic of a HSLA in the normalized condition. There were no signs of deleterious features in the microstructures.

[The remainder of this page intentionally left blank.]

Table 1: Average Charpy V-Notch Impact Test Results

Absorbed Energy (Joules) at -20°C			
Cross Arm 343-EL2	**Cross Arm 526-EL1**	**New Cross Arm**	**Requirement as per Drawing** [1]
39	**41**	**27**	**20**

Table 2: Average Hardness Test Results

	Rockwell B Hardness (HRB)		
	Cross Arm 343-EL2	**Cross Arm 526-EL1**	**New Cross Arm**
Average	**80.7**	**81.8**	**82.8**

Table 3: Chemical Analysis Results

Chemical Composition	Cross Arm 343-EL2	Cross Arm 526-EL1	New Cross Arm	CSA G40.21-13 GR 350WT Specification [3]
Carbon (%)	0.08	0.07	0.19	0.22, max
Manganese (%)	1.04	1.05	1.04	0.80 – 1.50
Phosphorus (%)	0.021	0.0226	0.02	0.03, max
Sulphur (%)	0.009	0.015	<0.005	0.04, max
Silicon (%)	0.199	0.167	0.19	0.15 – 0.40
Niobium + Vanadium (%)	<0.04	<0.05	<0.02	0.15, max
Chromium (%)	0.195	0.156	0.149	Not Specified
Nickel (%)	0.154	0.184	0.123	Not Specified
Copper (%)	0.31	0.353	0.237	Not Specified
Molybdenum (%)	0.0486	0.0403	0.0132	Not Specified

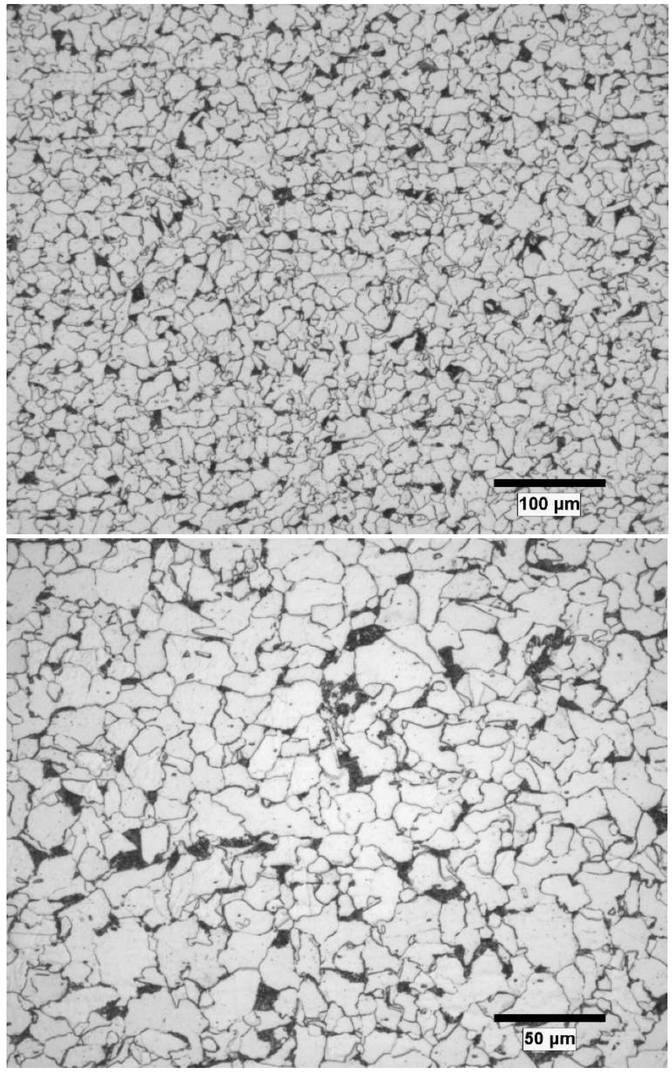

Figure 29: Representative Microstructure of Steel from Cross Arm 526-EL1

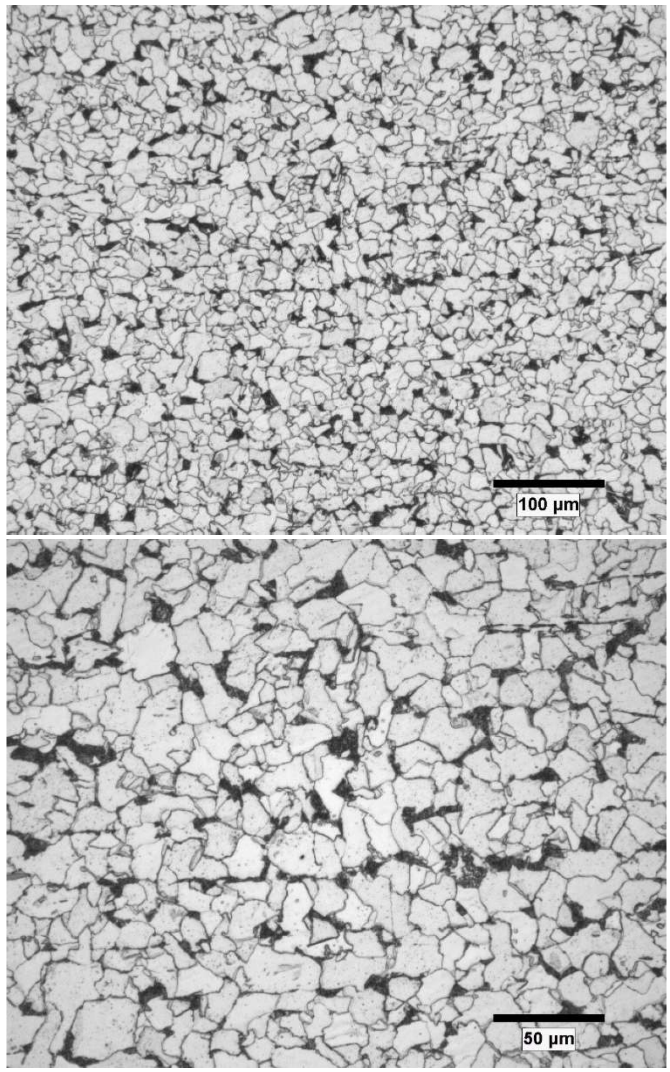

Figure 30: Representative Microstructure of Steel from Cross Arm 343-EL2

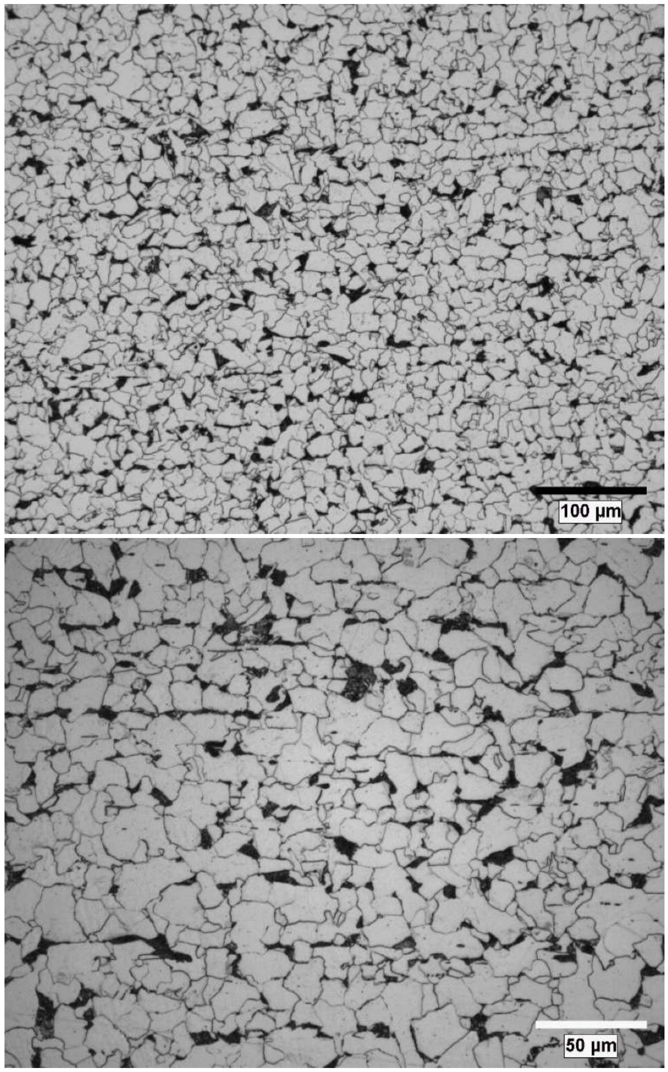

Figure 31: Representative Microstructure of Steel from the New Cross Arm

5 Discussion

The two failed cross arms examined (526-EL1 and 343-EL2) showed evidence of failure due to an overload event which caused the heavy deformation (bent and twisted components) of the HSLA steel structure. There were no signs of fatigue or other insidious failure mechanisms.

The examined fracture faces reveal that the cross arms fractured in a predominantly ductile manner, despite the ice-ladened conditions, due to a mix of pure tensile and tensile tear loading. The HSLA steel of the cross arms has demonstrated good low-temperature mechanical properties as evidenced by the Charpy V-notch impact test results. The fact that the fractures occurred through the bolt holes with damage elsewhere limited to deformed members is further evidence that the material was well suited for the application. The fractures occurring through the bolt holes due to an overload in an upset, out of design specification scenario, is not surprising since the cross-sectional area available to carry loads is reduced. Therefore, the highest stresses would likely be experienced at the bolt holes of the various cross arm components.

Metallurgical characterization of the failed cross arms and an exemplar revealed that all three cross arms were nominally identical. There were no harmful microstructural features observed in any of the samples studied. Hardness testing and chemical analysis did not reveal any out of specification items. All the cross arms in this investigation appeared to have met specifications.

6 Conclusion

The metallurgical failure analysis of the suspension tower cross arms revealed that the failure was likely due to an overload event during an up-set condition such as ice shedding off of the conductor on one side of the structure causing an unbalanced loading condition, which resulted in deformation and fracture of the components. There was no evidence implicating fatigue, or other failure mechanisms that could be attributed to poor design and/or application. The cross arms met the specifications for the properties tested and did not appear compromised from a materials property standpoint.

7 Recommendations

Based on the results of the metallurgical tests performed on the cross arms and based on the potential root cause of failure, the following recommendations are presented to Labrador Island Link Ltd. Partnership:

1) Perform a study to understand the stresses on the structure due to various atmospheric conditions (i.e. wind, icing, snow, etc.). This study can provide insight into the baseline conditions in the field and be used to evaluate mitigation techniques such de-icing/anti-icing and strengthening of the structure.
2) Perform laboratory testing to investigate and confirm the maximum load that a new/unused tower cross arm can withstand without damage. The maximum load can then be measured and compared to actual field (ice, wind, snow) combined loads. Based on the outcome a decision can be made to either reduce potential load (ice removal, prevention) or increase the strength of the tower at key locations.
3) Investigate potential means to mitigate ice buildup on the conductors and reduce uncontrolled ice removal events. This can be achieved using various techniques and methods. Some examples are provided below; however, a thorough review of alternative ice prevention or ice removal techniques should be performed. Additional techniques and methods can be found in resources such as "*Atmospheric Icing of Power Networks*" [4], and "*De-icing/Anti-icing Techniques for Power Lines: Current Methods and Future Direction*" [5].

    a. Load shifting method (reactive method): A higher load is forced through the circuit by transferring or shifting loads from another circuit that is linking the same two substations.
    b. Reduced-Voltage Short Circuit Method (reactive and preventative method): A three phase short circuit at a reduced voltage level (<100 kV) is applied to melt ice off the conductors either during a storm or during weather events that could lead to a buildup of ice on the conductors.
    c. High-Voltage Short Circuit Method (reactive method): A short circuit current at the rated voltage of the transmission line is applied to the circuit. The short circuit causes electromagnetic forces that allow the conductors to knock against each other which aids in the de-icing of the conductors.
    d. Manual de-icing via helicopter (reactive method): A helicopter is flown along the line and ice is manually removed from the conductor using an insulated hot stick.

8 References

[1] Nalcor Drawing, "350 kV HVdc Line 0° - 1° Suspension Tower Type 'A1' - General Layout".

[2] J. R. Davis, "High-Strength Low-Alloy Steels," in *ASM Speciality Handbook Carbon and Alloy Steels*, ASM International, 1996.

[3] CSA, "CSA G40.20/G40.21," 2018.

[4] Masoud Farzaneh et al, Atmospheric Icing of Power Networks, Springer, Dordrecht, 2008.

[5] C. Volat, M. Farzaneh and A. Leblond, "De-icing/Anti-icing Techniques for Power Lines: Current Methods and Future Direction.," 2005.

Appendix A Charpy V-notch Impact Testing Results

Acuren Group Inc.
2190 Speers Road
Oakville, ON, Canada L6L 2X8
www.acuren.com
Phone: 905.825.8595
Toll Free: 877.299.2857
Fax: 905.825.8598

A Higher Level of Reliability

ACCREDITED CERT #3977.01 & 3977.04

Client	
KINECTRICS INC. 800 Kipling Avenue Toronto, ON, Canada M8Z 5G5	**Laboratory Report**

Attention	*Client's Order Number*	*Date*	*Report Number*
Dean D. Finlayson	280071269	Apr. 23, 2021	128-21-10KIN005-0015 Rev. 00

Client's Material / Product Description	*Date Sample Received*	*Material / Product Specification*
Three components (similar to angles), each measuring 2.5" x 2.5" x 0.20" thick by 29"-39" long Sample #1: 343-EL2 (marked on the sample) Sample #2: K-314022, NEW, AISM EA02, NAUOR (marked on the sample) Sample #3: 526-E1, Leg B (marked on the sample)	Apr. 15, 2021	---

1. <u>Charpy V-Notch Impact Test</u>
   (ASTM E23-18, ASTM A673-17, ASTM A370-20)

- Specimen Location: 3 specimens obtained from each sample, one third the distance from outer edge to the heel of the leg.
- Specimen Orientation: Longitudinal
- Specimen Dimensions: 3.3 mm x 10 mm x 55 mm
- Test Temperature: -20˚C

Sample ID	Specimen Number	1	2	3	Average
#1	Absorbed Energy (ft·lbf)	29	31	27	29
	Absorbed Energy (Joule) (1)	39	42	37	39
	Lateral Expansion (mils)	66	69	64	66
	Shear (%)	100	100	100	100
#2	Absorbed Energy (ft·lbf)	21	20	19	20
	Absorbed Energy (Joule) (1)	28	27	26	27
	Lateral Expansion (mils)	50	48	48	49
	Shear (%)	90	90	90	90
#3	Absorbed Energy (ft·lbf)	29	29	32	30
	Absorbed Energy (Joule) (1)	39	39	43	41
	Lateral Expansion (mils)	67	68	69	68
	Shear (%)	100	100	100	100

Note 1: Absorbed energy in Joules converted from values measured in ft.lbf

ACUREN

Acuren Group Inc.
2190 Speers Road
Oakville, ON, Canada L6L 2X8
www.acuren.com

Phone: 905.825.8595
Toll Free: 877.299.2857
Fax: 905.825.8598

A Higher Level of Reliability

Figure 1. Typical test set up with the Hammer up

Figure 2. Machined specimens before testing

Acuren Group Inc.
2190 Speers Road
Oakville, ON, Canada L6L 2X8
www.acuren.com

Phone: 905.825.8595
Toll Free: 877.299.2857
Fax: 905.825.8598

A Higher Level of Reliability

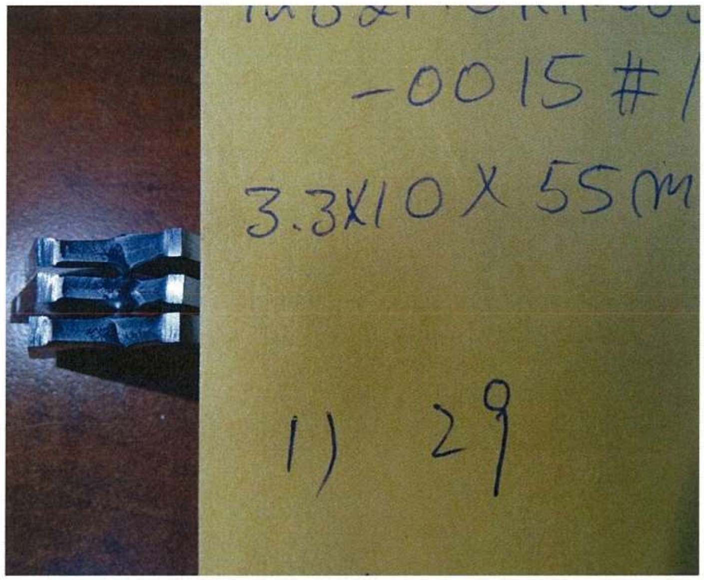

Figure 3. Specimens of #1 after testing

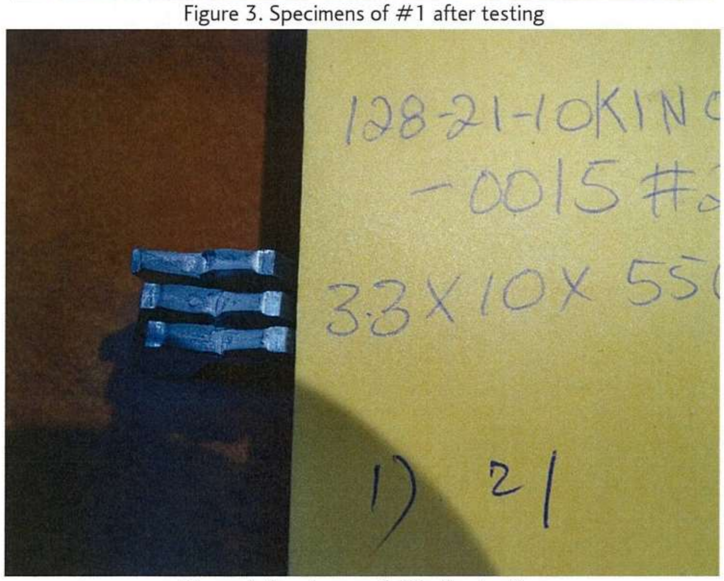

Figure 4. Specimens of #2 after testing

Acuren Group Inc.
2190 Speers Road
Oakville, ON, Canada L6L 2X8
www.acuren.com

Phone: 905.825.8595
Toll Free: 877.299.2857
Fax: 905.825.8598

A Higher Level of Reliability

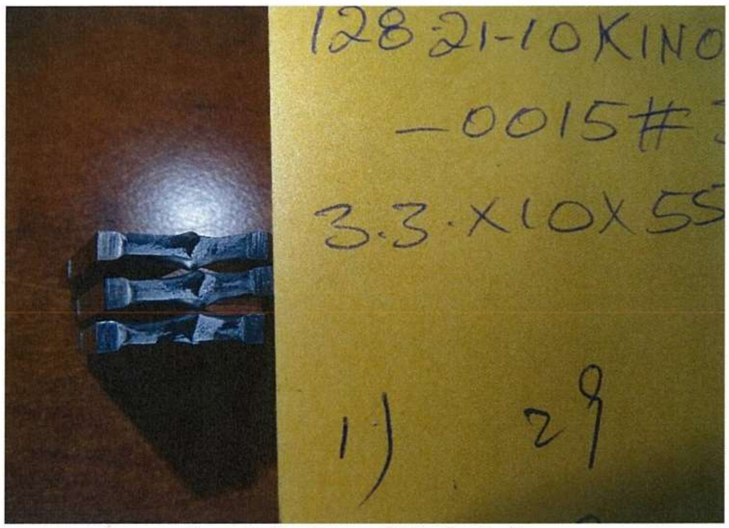

Figure 5. Specimens of #3 after testing

Feng Yan, Metallurgist,	**Donald Wang, B. Eng., Metallurgist,**
Test Specialist, Mechanical Testing	*Head: Mechanical Testing*

Client acknowledges receipt and custody of the report or other work ("Deliverable"). Client agrees that it is responsible for assuring that acceptance standards, specifications and criteria in the Deliverable and Statement of Work ("SOW") are correct. Client acknowledges that Acuren is providing the Deliverable according to the SOW, and not any other standards. Client acknowledges that it is responsible for the failure of any items inspected to meet standards, and for remediation. Client has 15 business days following the date Acuren provides the Deliverable to inspect it, identify deficiencies in writing, and provide written rejection, or else the Deliverable will be deemed accepted. The Deliverable and other services provided by Acuren are governed by a Master Services Agreement ("MSA"). If the parties have not entered into an MSA, then the Deliverable and services are governed by the SOW and the "Acuren Standard Service Terms" (www.acuren.com/serviceterms) in effect when the services were ordered

The Client Representative who receives this report is responsible for verifying that any acceptance standards listed in the report are correct, and promptly notifying Acuren of any issues with this report and/or the work summarized herein. The owner is responsible for notifying Acuren in writing if they would like their samples returned or placed into storage (at their cost) otherwise, all samples/specimens associated with this report will be disposed of 60 days after the report date.

NOTES:

A) Any tests subcontracted to an approved subcontractor are highlighted above (*)

B) Levels of Services :Regular Service: 3 to 5 business days; Next Day Service: 8 to 16 business hours; Same Day Service: within 8 business hours; Super Rush: Work will commence immediately regardless of the time and will continue until it is completed

C) The Client will be notified if completion of test will exceed the time specified as a result of the volume of work or the complexity of the test

D) The Client should specify the standards used for testing/comparison purpose. We have a comprehensive library and online subscription of commonly used standards, however, we may ask the client to supply the standards if not common or the Client requests to purchase standard(s) on his behalf.

E) Please provide all the necessary information/documents (MSDS) pertaining to any Toxic / Dangerous materials prior to their arrival in the Laboratory.

Appendix B Chemical Analysis Results

Analytical and Environmental Services Laboratory
Test Report

Report Number: 21-00569
Version: 1
Report Date: 12-Apr-2021

Attn: Dean Finlayson
Kinectrics Inc.
800 Kipling Ave., Unit 2
Toronto ON M8Z5G5
Canada
Purchase Order: N-314022-001.0130
Sample(s) received: 30-Mar-2021

Authorized by:

Andreas Rudolph
Laboratory Manager
andreas.rudolph@kinectrics.com

Description: Metal Samples

Sample ID	Sample Name	Matrix	Sample Point	Sample Date
21-00569-1	K-314022-343-EL2	Metal		29-Mar-2021
21-00569-2	K-314022-526-EL1	Metal		29-Mar-2021
21-00569-3	K-314022-NEW	Metal		29-Mar-2021

Special Instructions: Samples are Steel

Version comment: Initial report.

Analytical and Environmental Services Laboratory
Test Report

Report Number: 21-00569
Version: 1
Report Date: 12-Apr-2021

Sample ID	Sample Name	Matrix	Sample Point	Sample Date
21-00569-1	K-314022-343-EL2	Metal		29-Mar-2021

Parameter / Analyte	Result	Units	Uncert.	DL	Spec. Limt	Analyzed On dd-mmm-yy	Method
Carbon (by LECO)	0.08	%		0.01		06-Apr-21	LECO by Acuren*†
Sulfur (by LECO)	0.009	%		0.005		06-Apr-21	LECO by Acuren*†
Aluminum	0.00186	%		0.00025		08-Apr-21	TWI_ICPXX * / TWI_ICPMSXX*
Antimony	<0.00125	%		0.00125		08-Apr-21	TWI_ICPXX * / TWI_ICPMSXX*
Arsenic	<0.00100	%		0.001		08-Apr-21	TWI_ICPXX * / TWI_ICPMSXX*
Bismuth	<0.00250	%		0.0025		08-Apr-21	TWI_ICPXX * / TWI_ICPMSXX*
Boron	<0.00025	%		0.00025		08-Apr-21	TWI_ICPXX * / TWI_ICPMSXX*
Cerium	<0.00100	%		0.001		08-Apr-21	TWI_ICPXX * / TWI_ICPMSXX*
Chromium	0.195	%		0.00025		08-Apr-21	TWI_ICPXX * / TWI_ICPMSXX*
Cobalt	0.0087	%		0.00025		08-Apr-21	TWI_ICPXX * / TWI_ICPMSXX*
Copper	0.31	%		0.00025		08-Apr-21	TWI_ICPXX * / TWI_ICPMSXX*
Lead	<0.00050	%		0.0005		08-Apr-21	TWI_ICPXX * / TWI_ICPMSXX*
Manganese	1.04	%		0.0001		08-Apr-21	TWI_ICPXX * / TWI_ICPMSXX*
Molybdenum	0.0486	%		0.00025		08-Apr-21	TWI_ICPXX * / TWI_ICPMSXX*
Nickel	0.154	%		0.00025		08-Apr-21	TWI_ICPXX * / TWI_ICPMSXX*
Niobium	<0.00500	%		0.005		08-Apr-21	TWI_ICPXX * / TWI_ICPMSXX*
Phosphorus	0.021	%		0.001		08-Apr-21	TWI_ICPXX * / TWI_ICPMSXX*
Silicon	0.199	%		0.0005		08-Apr-21	TWI_ICPXX * / TWI_ICPMSXX*
Silver	<0.00025	%		0.00025		08-Apr-21	TWI_ICPXX * / TWI_ICPMSXX*
Sulfur	0.0282	%		0.001		08-Apr-21	TWI_ICPXX * / TWI_ICPMSXX*
Tantalum	0.0215	%		0.0025		08-Apr-21	TWI_ICPXX * / TWI_ICPMSXX*

Analytical and Environmental Services Laboratory

Test Report

Report Number: 21-00569
Version: 1
Report Date: 12-Apr-2021

Parameter / Analyte	Result	Units	Uncert.	DL	Spec. Limt	Analyzed On dd-mmm-yy	Method
Tin	0.0111	%		0.0005		08-Apr-21	TWI_ICPXX * / TWI_ICPMSXX*
Titanium	<0.00025	%		0.00025		08-Apr-21	TWI_ICPXX * / TWI_ICPMSXX*
Tungsten	0.0216	%		0.0025		08-Apr-21	TWI_ICPXX * / TWI_ICPMSXX*
Vanadium	0.0396	%		0.00025		08-Apr-21	TWI_ICPXX * / TWI_ICPMSXX*
Zinc	0.00887	%		0.0001		08-Apr-21	TWI_ICPXX * / TWI_ICPMSXX*
Zirconium	<0.00050	%		0.0005		08-Apr-21	TWI_ICPXX * / TWI_ICPMSXX*

Sample ID	Sample Name	Matrix	Sample Point	Sample Date
21-00569-2	K-314022-526-EL1	Metal		29-Mar-2021

Parameter / Analyte	Result	Units	Uncert.	DL	Spec. Limt	Analyzed On dd-mmm-yy	Method
Carbon (by LECO)	0.07	%		0.01		06-Apr-21	LECO by Acuren*†
Sulfur (by LECO)	0.015	%		0.005		06-Apr-21	LECO by Acuren*†
Aluminum	0.00167	%		0.00025		08-Apr-21	TWI_ICPXX * / TWI_ICPMSXX*
Antimony	<0.00125	%		0.00125		08-Apr-21	TWI_ICPXX * / TWI_ICPMSXX*
Arsenic	<0.00100	%		0.001		08-Apr-21	TWI_ICPXX * / TWI_ICPMSXX*
Bismuth	<0.00250	%		0.0025		08-Apr-21	TWI_ICPXX * / TWI_ICPMSXX*
Boron	<0.00025	%		0.00025		08-Apr-21	TWI_ICPXX * / TWI_ICPMSXX*
Cerium	<0.00100	%		0.001		08-Apr-21	TWI_ICPXX * / TWI_ICPMSXX*
Chromium	0.156	%		0.00025		08-Apr-21	TWI_ICPXX * / TWI_ICPMSXX*
Cobalt	0.00812	%		0.00025		08-Apr-21	TWI_ICPXX * / TWI_ICPMSXX*
Copper	0.353	%		0.00025		08-Apr-21	TWI_ICPXX * / TWI_ICPMSXX*
Lead	<0.00050	%		0.0005		08-Apr-21	TWI_ICPXX * / TWI_ICPMSXX*
Manganese	1.05	%		0.0001		08-Apr-21	TWI_ICPXX * / TWI_ICPMSXX*
Molybdenum	0.0403	%		0.00025		08-Apr-21	TWI_ICPXX * / TWI_ICPMSXX*

Analytical and Environmental Services Laboratory
Test Report

Report Number: 21-00569
Version: 1
Report Date: 12-Apr-2021

Parameter / Analyte	Result	Units	Uncert.	DL	Spec. Limt	Analyzed On dd-mmm-yy	Method
Nickel	0.184	%		0.00025		08-Apr-21	TWI_ICPXX * / TWI_ICPMSXX*
Niobium	<0.00500	%		0.005		08-Apr-21	TWI_ICPXX * / TWI_ICPMSXX*
Phosphorus	0.0226	%		0.001		08-Apr-21	TWI_ICPXX * / TWI_ICPMSXX*
Silicon	0.167	%		0.0005		08-Apr-21	TWI_ICPXX * / TWI_ICPMSXX*
Silver	<0.00025	%		0.00025		08-Apr-21	TWI_ICPXX * / TWI_ICPMSXX*
Sulfur	0.0295	%		0.001		08-Apr-21	TWI_ICPXX * / TWI_ICPMSXX*
Tantalum	0.0223	%		0.0025		08-Apr-21	TWI_ICPXX * / TWI_ICPMSXX*
Tin	0.0103	%		0.0005		08-Apr-21	TWI_ICPXX * / TWI_ICPMSXX*
Titanium	0.000305	%		0.00025		08-Apr-21	TWI_ICPXX * / TWI_ICPMSXX*
Tungsten	0.0202	%		0.0025		08-Apr-21	TWI_ICPXX * / TWI_ICPMSXX*
Vanadium	0.0457	%		0.00025		08-Apr-21	TWI_ICPXX * / TWI_ICPMSXX*
Zinc	0.00997	%		0.0001		08-Apr-21	TWI_ICPXX * / TWI_ICPMSXX*
Zirconium	<0.00050	%		0.0005		08-Apr-21	TWI_ICPXX * / TWI_ICPMSXX*

Sample ID	Sample Name	Matrix	Sample Point	Sample Date
21-00569-3	K-314022-NEW	Metal		29-Mar-2021

Parameter / Analyte	Result	Units	Uncert.	DL	Spec. Limt	Analyzed On dd-mmm-yy	Method
Carbon (by LECO)	0.19	%		0.01		06-Apr-21	LECO by Acuren*†
Sulfur (by LECO)	<0.005	%		0.005		06-Apr-21	LECO by Acuren*†
Aluminum	0.0204	%		0.00025		08-Apr-21	TWI_ICPXX * / TWI_ICPMSXX*
Antimony	<0.00125	%		0.00125		08-Apr-21	TWI_ICPXX * / TWI_ICPMSXX*
Arsenic	<0.00100	%		0.001		08-Apr-21	TWI_ICPXX * / TWI_ICPMSXX*
Bismuth	<0.00250	%		0.0025		08-Apr-21	TWI_ICPXX * / TWI_ICPMSXX*
Boron	<0.00025	%		0.00025		08-Apr-21	TWI_ICPXX * / TWI_ICPMSXX*

KINECTRICS

Analytical and Environmental Services Laboratory

Test Report

Report Number: 21-00569
Version: 1
Report Date: 12-Apr-2021

Parameter / Analyte	Result	Units	Uncert.	DL	Spec. Limt	Analyzed On dd-mmm-yy	Method
Cerium	<0.00100	%		0.001		08-Apr-21	TWI_ICPXX * / TWI_ICPMSXX*
Chromium	0.149	%		0.00025		08-Apr-21	TWI_ICPXX * / TWI_ICPMSXX*
Cobalt	0.0101	%		0.00025		08-Apr-21	TWI_ICPXX * / TWI_ICPMSXX*
Copper	0.237	%		0.00025		08-Apr-21	TWI_ICPXX * / TWI_ICPMSXX*
Lead	<0.00050	%		0.0005		08-Apr-21	TWI_ICPXX * / TWI_ICPMSXX*
Manganese	1.04	%		0.0001		08-Apr-21	TWI_ICPXX * / TWI_ICPMSXX*
Molybdenum	0.0132	%		0.00025		08-Apr-21	TWI_ICPXX * / TWI_ICPMSXX*
Nickel	0.123	%		0.00025		08-Apr-21	TWI_ICPXX * / TWI_ICPMSXX*
Niobium	<0.00500	%		0.005		08-Apr-21	TWI_ICPXX * / TWI_ICPMSXX*
Phosphorus	0.02	%		0.001		08-Apr-21	TWI_ICPXX * / TWI_ICPMSXX*
Silicon	0.19	%		0.0005		08-Apr-21	TWI_ICPXX * / TWI_ICPMSXX*
Silver	<0.00025	%		0.00025		08-Apr-21	TWI_ICPXX * / TWI_ICPMSXX*
Sulfur	0.0146	%		0.001		08-Apr-21	TWI_ICPXX * / TWI_ICPMSXX*
Tantalum	0.0223	%		0.0025		08-Apr-21	TWI_ICPXX * / TWI_ICPMSXX*
Tin	0.0141	%		0.0005		08-Apr-21	TWI_ICPXX * / TWI_ICPMSXX*
Titanium	0.000861	%		0.00025		08-Apr-21	TWI_ICPXX * / TWI_ICPMSXX*
Tungsten	0.0214	%		0.0025		08-Apr-21	TWI_ICPXX * / TWI_ICPMSXX*
Vanadium	0.0186	%		0.00025		08-Apr-21	TWI_ICPXX * / TWI_ICPMSXX*
Zinc	0.011	%		0.0001		08-Apr-21	TWI_ICPXX * / TWI_ICPMSXX*
Zirconium	<0.00050	%		0.0005		08-Apr-21	TWI_ICPXX * / TWI_ICPMSXX*

Instruments Used

Name	Serial Number	Last Calibration	Calibration Due
Spectro Ciros Vision ICPAES	Ciros Vision 4R0013	Calibrated Before Use	

Analytical and Environmental Services Laboratory

Test Report

Report Number: 21-00569
Version: 1
Report Date: 12-Apr-2021

The Analytical and Environmental Services Laboratory of Kinectrics is accredited by the Standards Council of Canada as conforming with ISO 17025.

The DL is the reported detection limit. All analytical data is subject to uncertainty, and is a function of the sample matrix, method and instrumental variations. As a general guideline, it can be expressed as +/-50% of the result at the detection limit (RDL) and approximately +/-10% of the result at greater than 10 times the RDL. Results in this report relate only to the items/samples tested and to all the items tested, as received. All tests are as defined by our understanding of customer requirements.

TECHNIQUE '*' = ISO 17025 accredited
TECHNIQUE '¤' = Indicates a modified test method
TECHNIQUE '†' = Indicates a sub-contracted analysis

Appendix E - Failure Analysis of a Conductor

Acuren Group Inc.
2190 Speers Road
Oakville, ON, Canada L6L 2X8
www.acuren.com

Phone: 905.825.8595
Toll Free: 877.299.2857
Fax: 905.825.8598

A Higher Level of Reliability

ACCREDITED
CERT #3977.01 & 3977.04

ISO 9001 : 2015 REGISTERED
An ISO 9001 certified company

April 12, 2021 **Our Project No.: 128-21-ACU020-0003**

Nalcor Energy
500 Columbus Drive
P.O.Box 12800
St. John's NL
A1B 0C9

Attention: Ms. Cheryl Sehn

Dear Ms. Sehn:

SUBJECT: FAILURE ANALYSIS OF A CONDUCTOR

Please find enclosed the above-named report. We trust you will find it satisfactory, and we appreciate the opportunity to be of service to Acuren Group Inc. Dartmouth, NS. At Acuren, we remain committed to providing you with world-class integrity management solutions.

Should you require any additional information, please do not hesitate to contact the undersigned at 905-673-9899 or by e-mail at Erhan.Ulvan@acuren.com

Please note that unless we are notified in writing, samples from this investigation will be disposed of after 60 days.

Sincerely,

Ethan (Erhan) Ulvan, PhD., P.Eng., FASM
Manager – Engineering, Laboratories, Nuclear and FES, Eastern Canada
Past President, Failure Analysis Society, American Society for Materials International

Acuren Group Inc.
2190 Speers Road
Oakville, ON, Canada L6L 2X8
www.acuren.com

Phone: 905.825.8595
Toll Free: 877.299.2857
Fax: 905.825.8598

A Higher Level of Reliability

ACCREDITED
CERT #3977.01 & 3977.04

ISO 9001 : 2015 REGISTERED

FAILURE ANALYSIS OF A CONDUCTOR

Prepared for

Ms. Cheryl Sehn

Nalcor Energy
500 Columbus Drive
St. John's NL, A1B 0C9

Prepared by

Ethan (Erhan) Ulvan, PhD., P.Eng., FASM
Manager – Engineering, Laboratories, Nuclear and FES, Eastern Canada
Past President, Failure Analysis Society, American Society for Materials International

Reviewed by

Yunlin Gao, MEng.
Head of Failure Analysis and Metallurgical Engineering Department

April 12, 2021
Acuren Project No.: 128-21-ACU020-0003

TABLE OF CONTENTS

LIST OF FIGURES

LIST OF TABLES

1.0 INTRODUCTION

We received two broken conductors, two conductor sections with multiple broken strands, and one new conductor section. We were informed that the broken conductor sections were found on the ground after a heavy weather condition creating excessive ice built up on the conductors. Figure 1, Figure 2, and Figure 3 show there of the broken wires received. Client requested us to examine the broken conductors and determine the root cause.

FIGURE 1. ONE OF THE BROKEN CONDUCTORS (PICTURE PROVIDED BY THE CLIENT)

FIGURE 2. ANOTHER BROKEN CONDUCTOR (PICTURE PROVIDED BY THE CLIENT)

1.1 SCOPE OF WORK

i) Visual examination
ii) Examination at low magnification
iii) Scanning Electron Microscopy

iv) Metallographic Examination
v) Tensile Testing
vi) Chemical Analysis
vii) Coating Weight
viii) Bending Test of Aluminum Wires
ix) Wrap Test of Steel Wires
x) Adherence of Coating Tests
xi) Discussion
xii) Conclusions

FIGURE 3. PARTIALLY BROKEN CONDUCTOR (PICTURE PROVIDED BY THE CLIENT)

2.0 VISUAL EXAMINATION

Figure 4 shows Sample #1. Sample #1 consisted of an aluminum conductor wire and a clamp. Figure 5 and Figure 6 show the front and back faces of the clamp, respectively. Figure 7 and Figure 8 show the markings on the front and back faces of the clamp, respectively.

i. The conductor was made of a steel core, made of 19 wire strands, each about 0.0880 inch to 0.0895 inch diameter, surrounded by 3 concentric layers of aluminum wires, Figure 9.
ii. First aluminum wire layer contained 24 wires, second layer contained 18 wires and the third layer contained 12 wires. All the wires in all the layers had the same diameter; 3.80 mm. Observations made indicate that this is an aluminum conductor steel-reinforced cable (ACSR). It is a high-capacity, high-strength stranded conductor, typically used in overhead power lines.
iii. Wires in the twisted portion were all entangled (recoiled) (see Figure 4) due to sudden release of the conductor internal forces, some of them bent but were not damaged (see Figure 10) and some of them were badly damaged, Figure 11. Portion of the cable secured by the clamp was still intact on the twisted side, Figure 12. The rest of the cable was intact on this side of the clamp, Figure 4. We observed a few wires broken on the twisted side, Figure 13.
iv. All the wires were apparently broken on the other side of the clamp, Figure 4 (we were informed by the client that, it was possible that this conductor was not fully broken and some wires could have been cut). All of the visible aluminum wires of the cable fractured at the end of the clamp, Figure 14. We removed the clamp to observe the wires behind the clamp cover, Figure 15. It was evident some of the wires broke in the clamped region, Figure 15 and Figure 16.
v. All of the broken aluminum wires showed plastic deformation in the vicinity of the fracture, Figure 14, Figure 15 and Figure 16.
vi. On the contrary, none of the steel wires showed discernible local plastic deformation possibly due to cutting of those wires. Figure 17, Figure 18 and Figure 19 show close view of all the steel wires. Steel wires were covered with a white substance (possibly aluminum based hydroxides) that could be removed by rubbing the wires.
vii. Steel wire fracture surface and aluminum wire fracture surfaces were 6” to 10” away from each other. Steel wires were longer than aluminum wires. However, this is possibly opposite on the mating side of the cable.

Sample #2

i. Figure 20 shows Sample #2. Sample #2 cable and clamp were identical to Sample #1. Client marked it as 5I3 EL1, Figure 21.
ii. Similar to Sample #1, this sample had all the wires appeared broken on one end of the clamp, Figure 22 (we were informed by the client that this sample comes from structure 513 and it did not fully break. Unbroken wires were cut to remove the damaged section and repair the conductor).

iii. All of the broken aluminum wires of the cable showed plastic deformation in the vicinity of the fracture, Figure 23. Some of the wires were damaged. Others did not show damage on the side surface.
iv. Fracture surface of the steel wires were mostly flat, crack propagated normal to the longitudinal direction of the wires. Some of the wires had wedges on one side of the fracture surface, Figure 25.
v. Side surfaces of the aluminum wires were generally shiny and clean. Some of them were damaged as a result of the incident.
vi. Steel wires were dull grey in colour with some apparent corrosion/oxidation products.
vii. Aluminum wires on the other end were twisted, Figure 26, and mostly free of scratches and rubbing.
viii. However, we observed a few of the aluminum wires badly damaged and a few of them broken as a result of damage, Figure 27.
ix. On the other hand, all of the steel wires showed no discernible plastic deformation. Steel wires were covered with a white substance that could be removed by rubbing the wires.

Sample #3

i. Figure 28 shows sample #3 section of conductor. The conductor cable was identical to the other two cables examined. This sample did not have a clamp (Client informed us that this sample might have been broken completely and fell to the ground. However, our observations suggest some of those may have also been cut).
ii. The broken aluminum wires fracture surfaces, were similar to those of the wires of cables Sample #1 and Sample #2. Local plastic deformation in the vicinity of the fracture surface of aluminum wires was evident, Figure 29. Figure 30 shows close view of the fractured aluminum wires. Some of the wires were damaged.
iii. Fracture surfaces of the steel core wires were mostly flat, crack propagated perpendicular to the longitudinal direction of the wires. Some of the wires showed wedges adjacent to the fracture surface. Those wires with wedges possibly the ones that were cut. Steel wires were dull gray in colour. Figure 31 shows the steel wires.
iv. Steel wires cracked significantly away from the aluminum wires. There was 25” to 30” distance between the fractured end of the steel wires and the fractured end of the aluminum wires.

Sample #4

i. Figure 28 shows Sample #4. Sample #4 showed some broken aluminum wires at the area marked in Figure 32, however, there was no complete separation. It was marked by the client with a red marker as “LTT str 339”, Figure 33 (client informed us that this sample was from structure 339).
ii. 12 of the 24 outer layer aluminum wires were broken. Figure 34 shows ten of these broken aluminum wires. These ten wires showed necking in the vicinity of the fracture surface.

iii. Ten of these wires were together in one area. We arbitrarily marked that as 4-8 o'clock region.
iv. The other two wires were also in the same region, however, several inches away from the others. These two were did not show visible necking while the other ten wires did. Two wires adjacent to those two broken wires showed necking yet no separation, Figure 35.
v. We observed two of the aluminum wires on the second layer with necking. None of the wires were broken on the second layer.

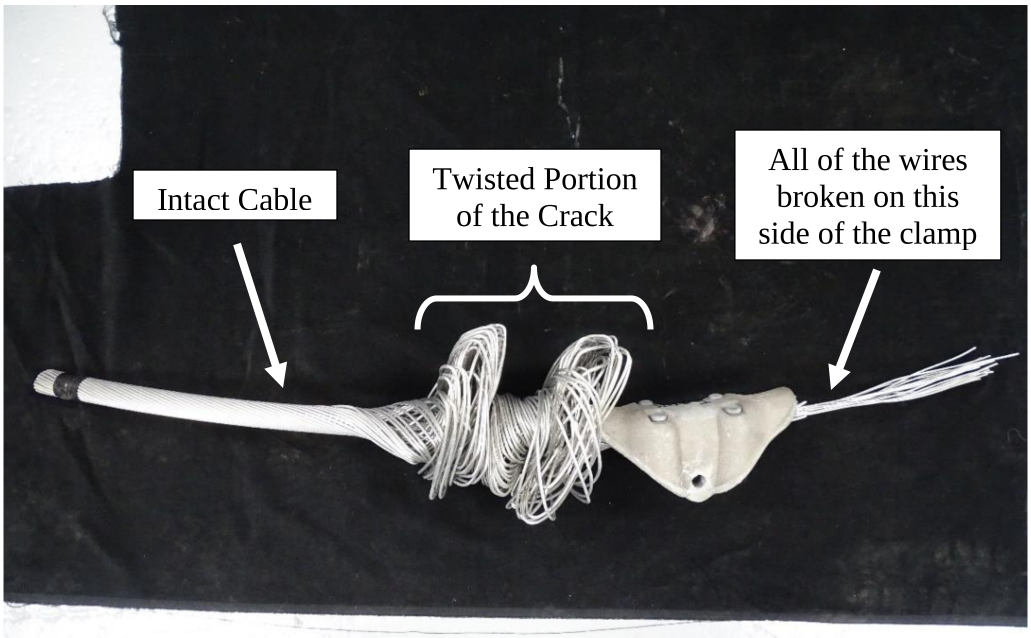

FIGURE 4: SAMPLE #1

FIGURE 5: CLAMP, FRONT FACE

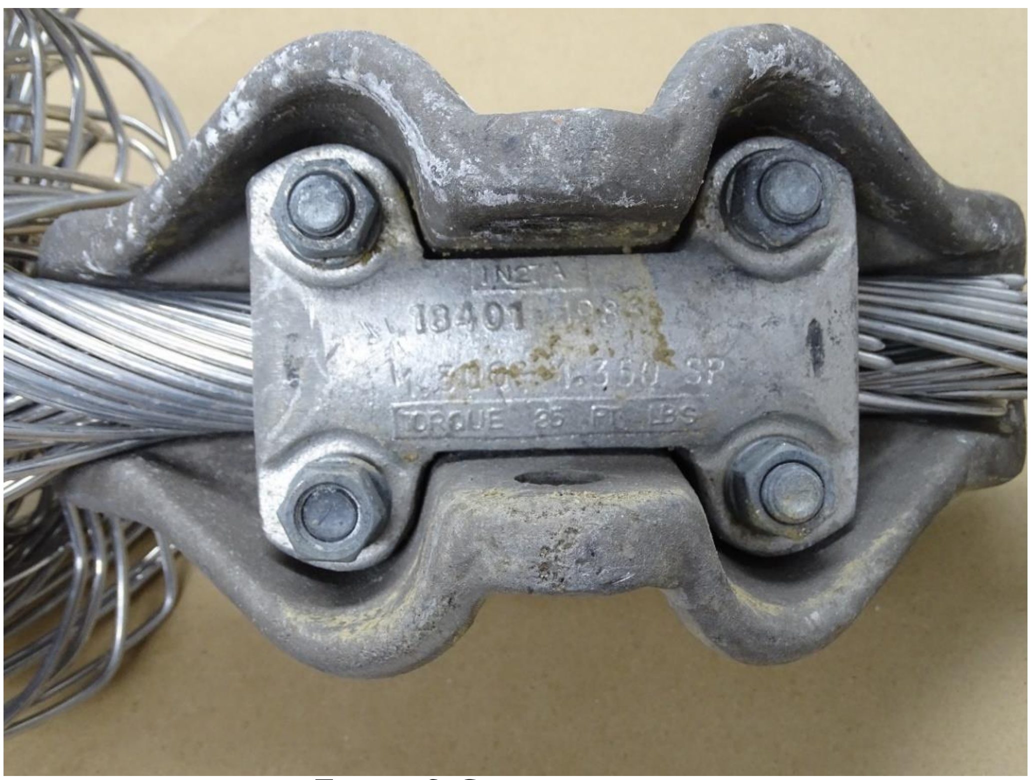

FIGURE 6: CLAMP, BACK FACE

FIGURE 7: MARKINGS ON THE FRONT FACE OF THE CLAMP, CUT END OF CONDUCTOR

FIGURE 8: MARKINGS ON THE FRONT FACE OF THE CLAMP, BROKEN END OF THE CONDUCTOR

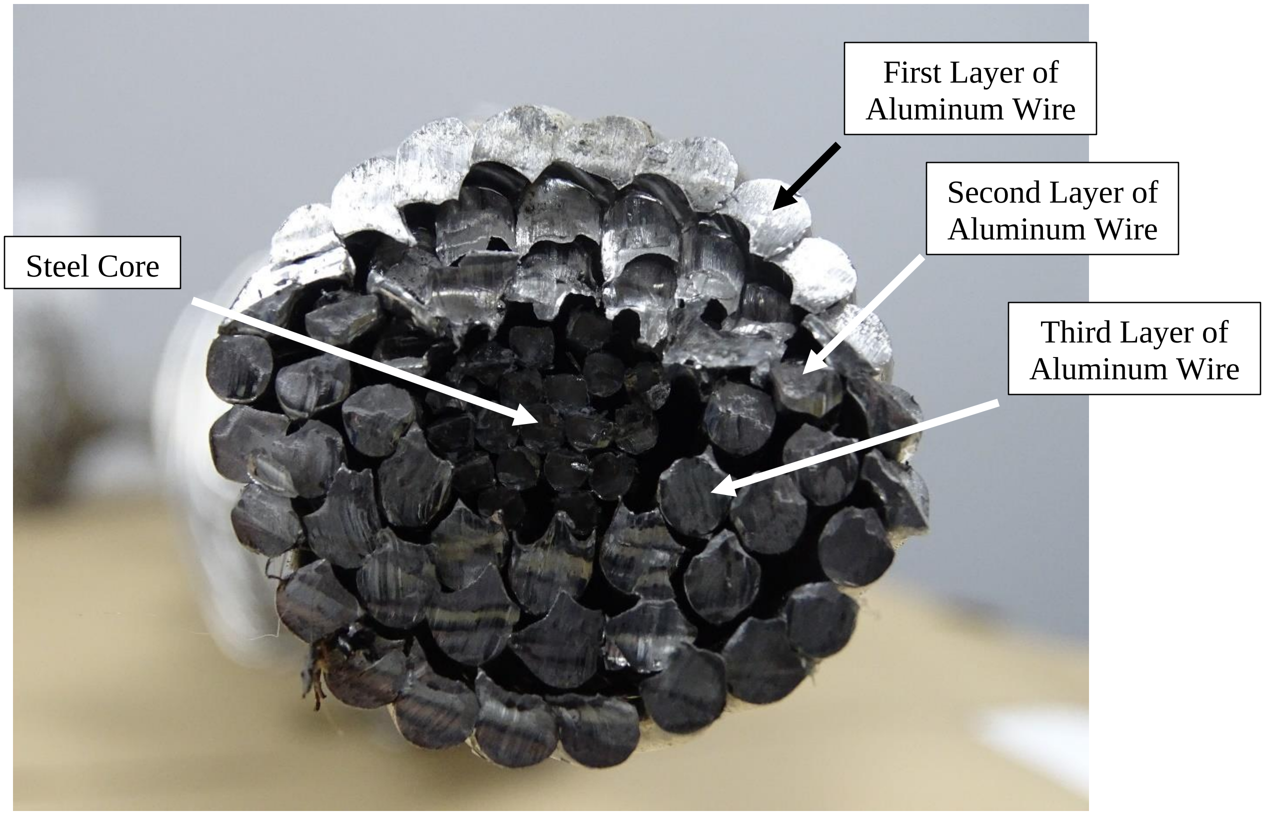

FIGURE 9: CROSS SECTION OF CONDUCTOR

FIGURE 10: WIRES BENT IN THE TWISTED PORTION OF THE CABLE

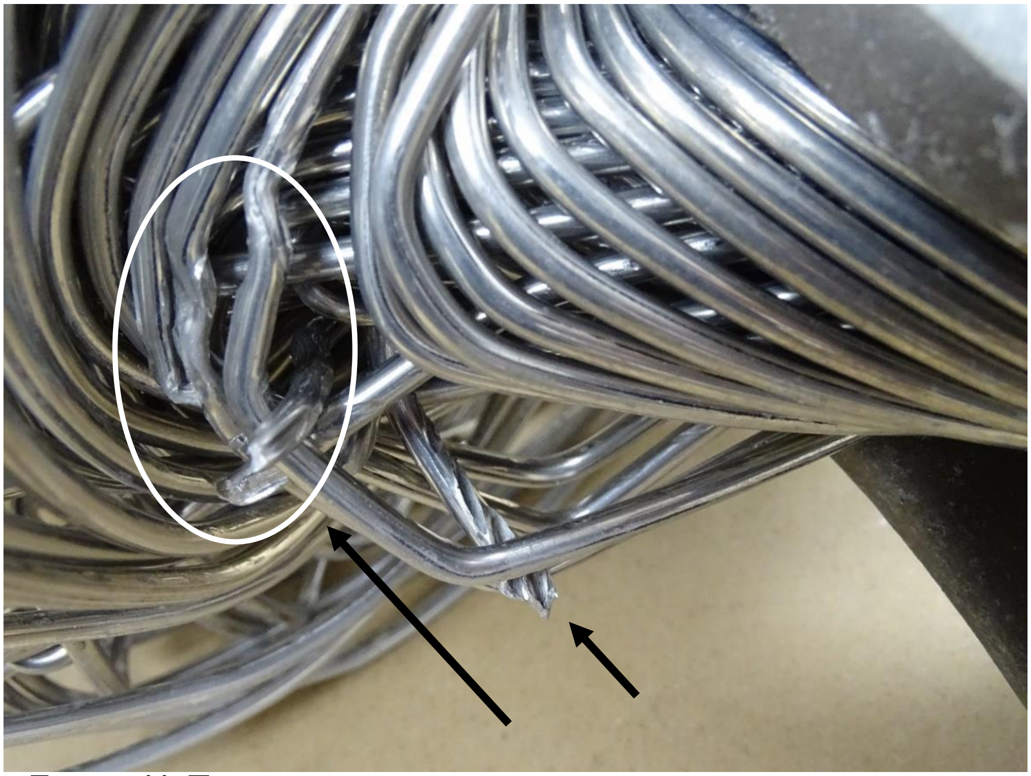

FIGURE 11: TWISTED PORTION OF THE CABLE, SOME OF THE WIRES WERE BADLY DAMAGED

FIGURE 12: INTACT CABLE JUST OUT OF THE CLAMP

FIGURE 13: SOME BROKEN ALUMINUM WIRES ON THE TWISTED SIDE, SAMPLE #1

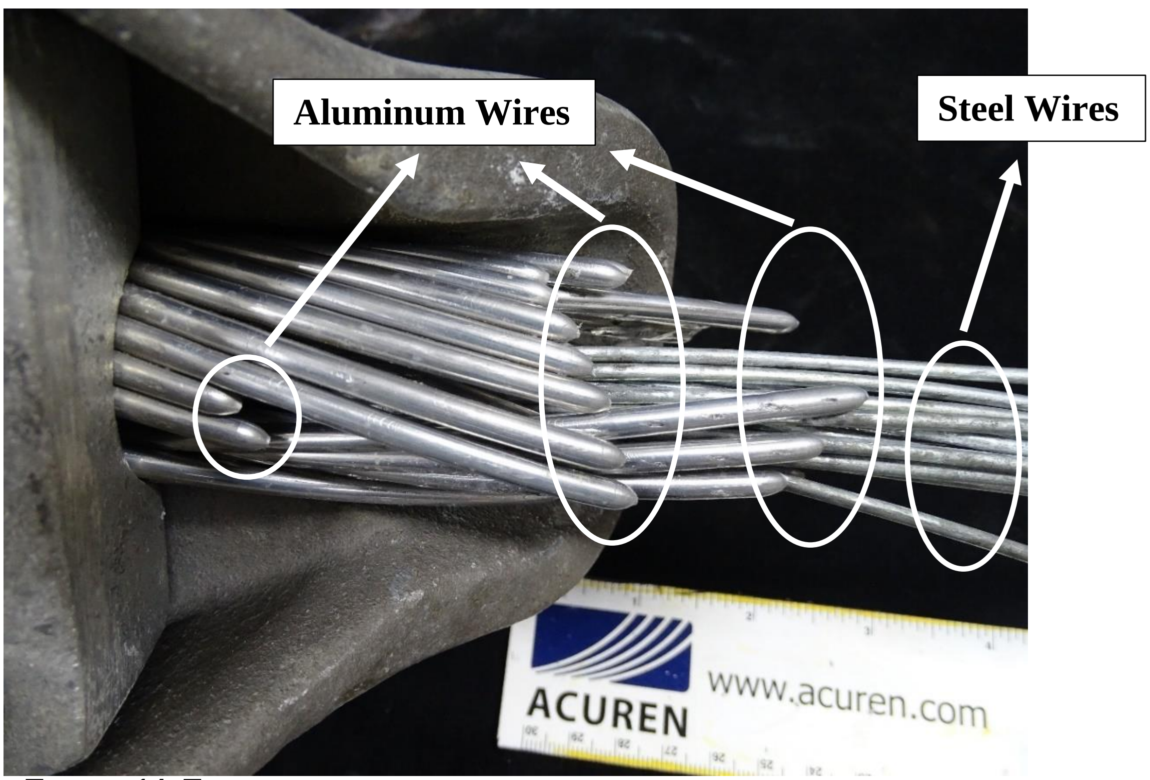

FIGURE 14: FRACTURED ALUMINUM WIRES IN THE VICINITY OF THE CLAMP

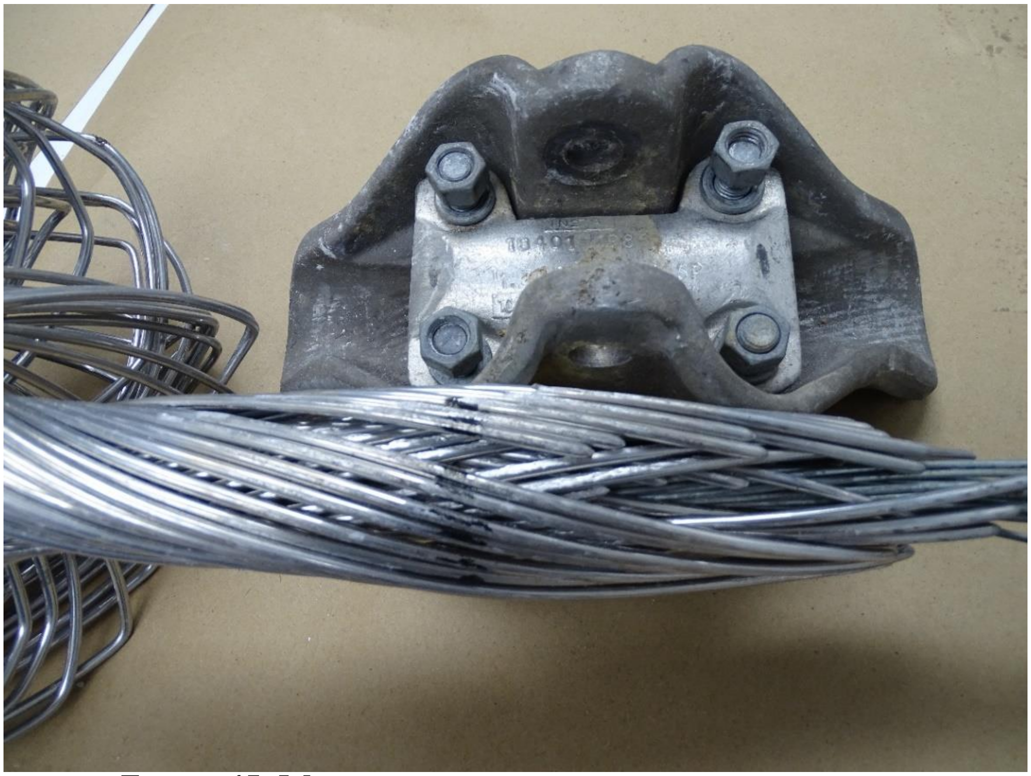

**FIGURE 15: WIRES OF THE CABLE IN THE CLAMPED REGION.
PHOTO TAKEN AFTER REMOVING THE CLAMP**

FIGURE 16: SOME OF THE BROKEN ALUMINUM WIRES IN THE CLAMPED REGION, PHOTO TAKEN AFTER REMOVING THE CLAMP

ACUREN

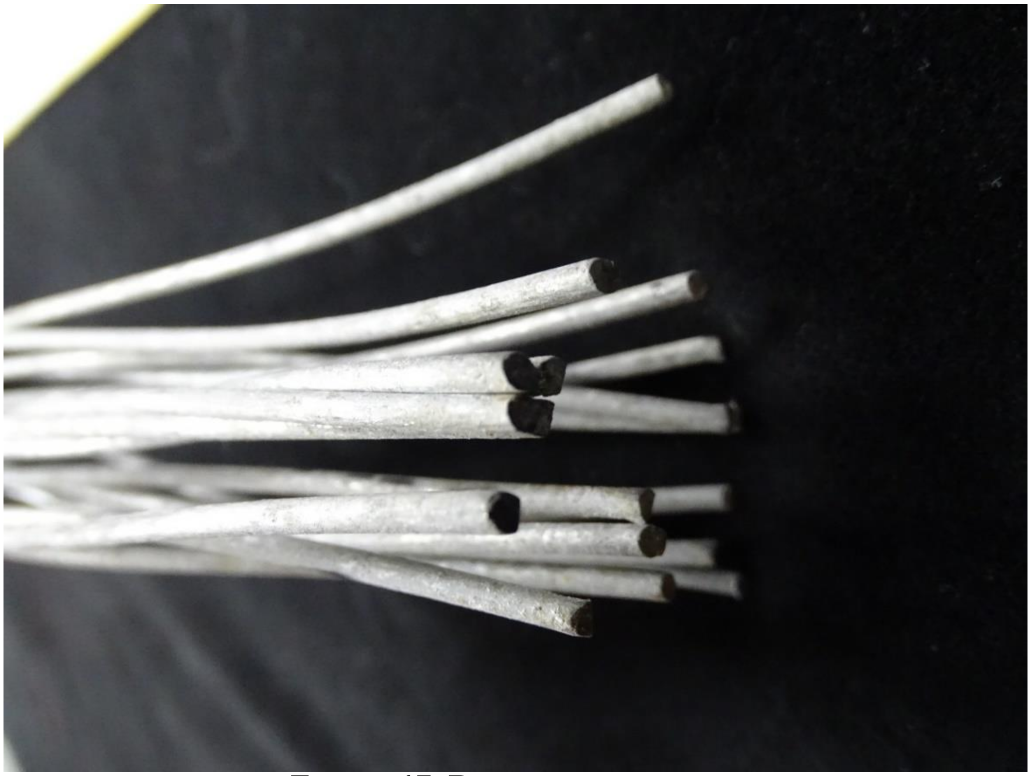

FIGURE 17: BROKEN STEEL WIRES

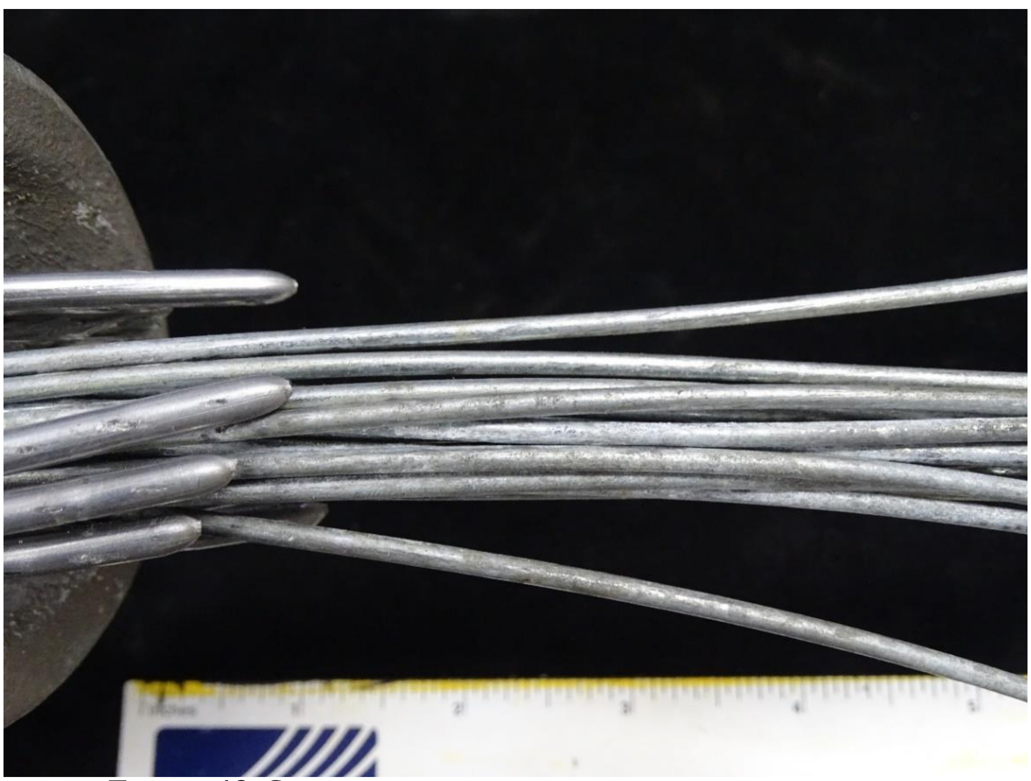

FIGURE 18: STEEL WIRES IN THE VICINITY OF THE CLAMP END

FIGURE 19: STEEL WIRES COVERED WITH A WHITE SUBSTANCE

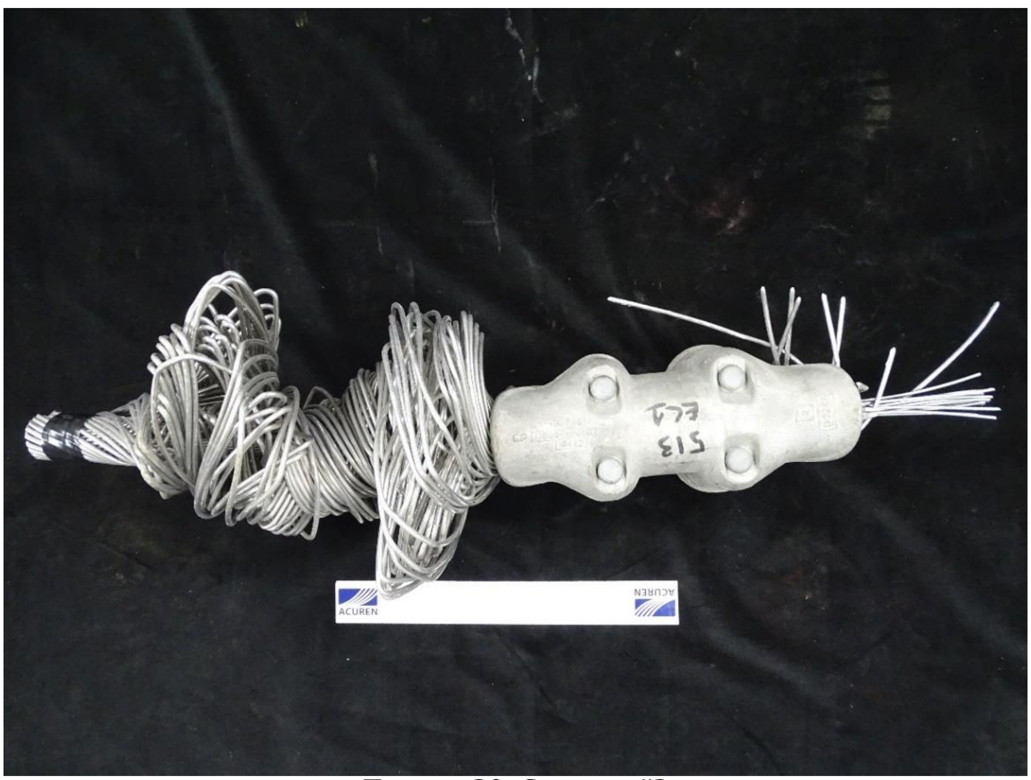

FIGURE 20: SAMPLE #2

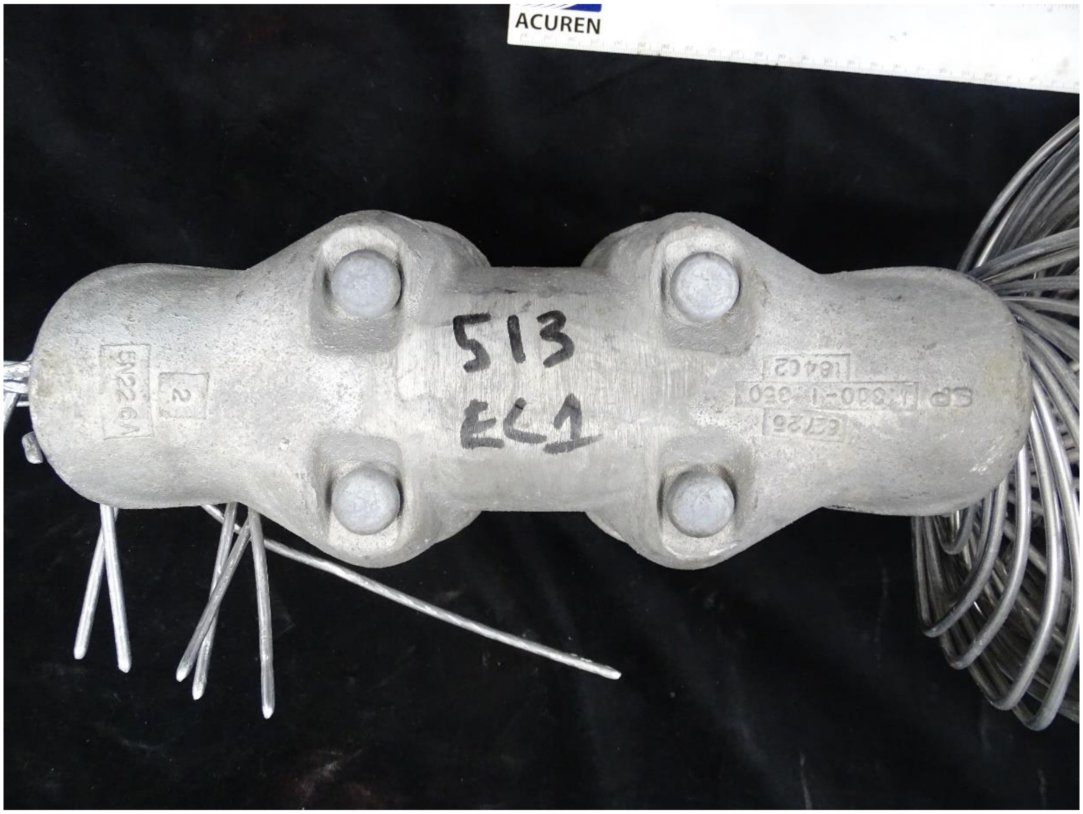

FIGURE 21: CLAMP AND MARKING ON SAMPLE #2

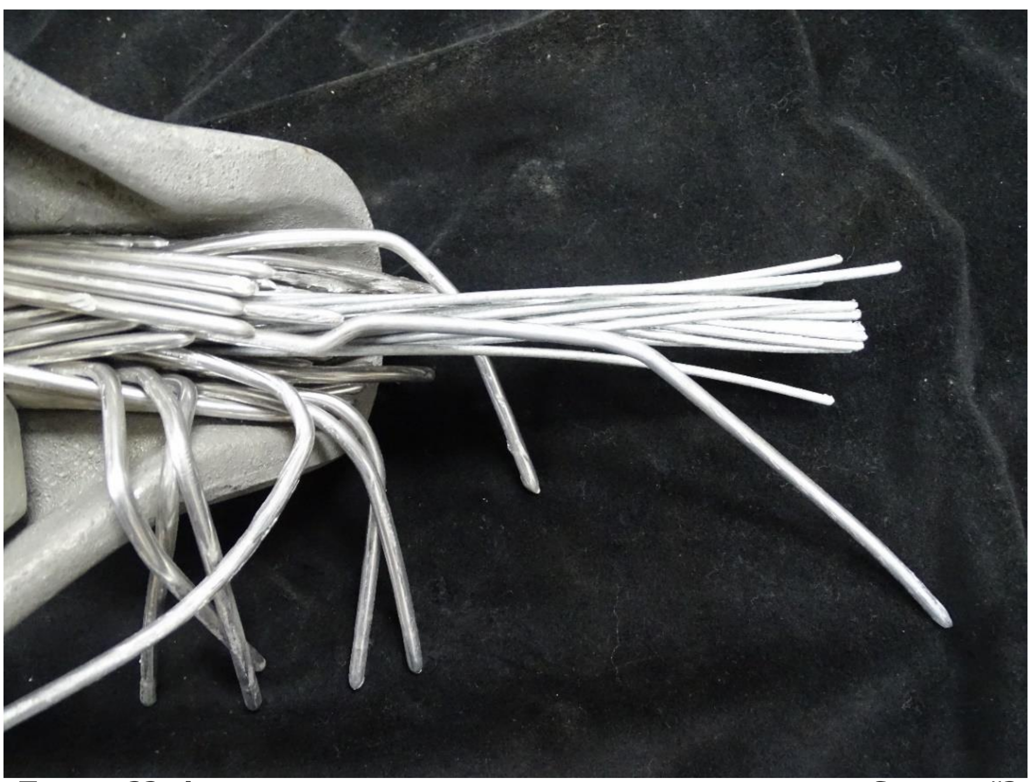

FIGURE 22: ALL THE WIRES BROKEN IN ONE END OF THE CLAMP, SAMPLE #2

FIGURE 23: BROKEN ALUMINUM WIRES, SAMPLE #2

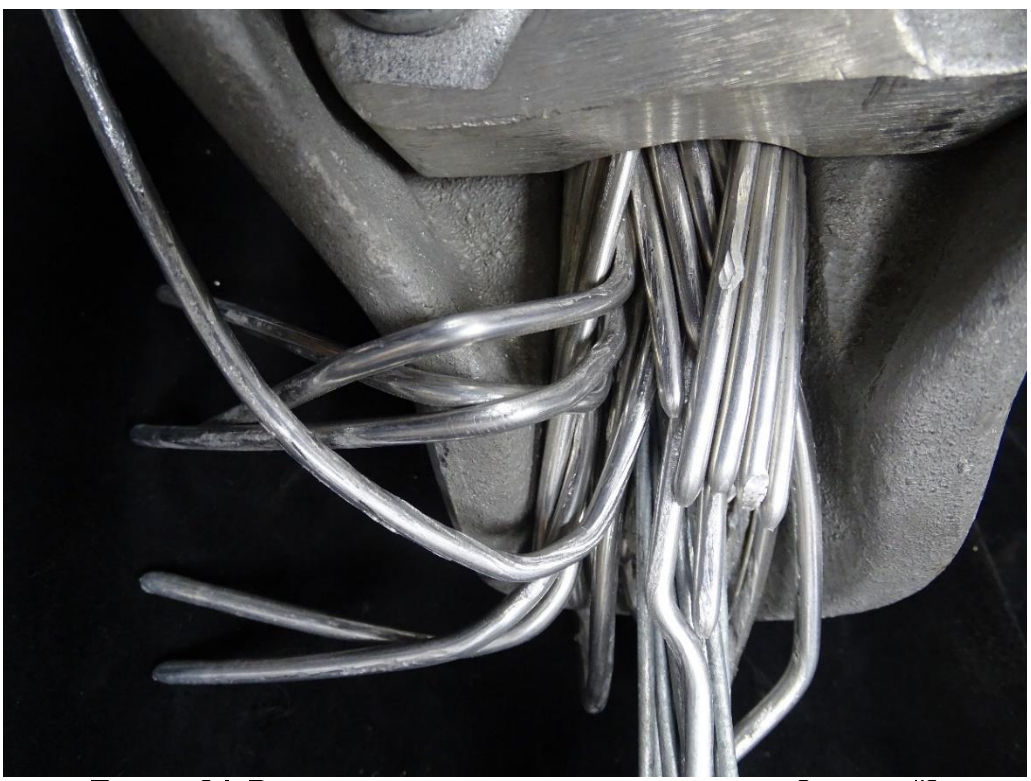

FIGURE 24: BROKEN ALUMINUM WIRES, OTHER SIDE, SAMPLE #2

FIGURE 25: FRACTURE SURFACE OF THE STEEL WIRES

FIGURE 26: TWISTED WIRES, SAMPLE #2

ACUREN

FIGURE 27: DAMAGED AND BROKEN FEW WIRES AWAY FROM THE TWISTED WIRES, SAMPLE #2

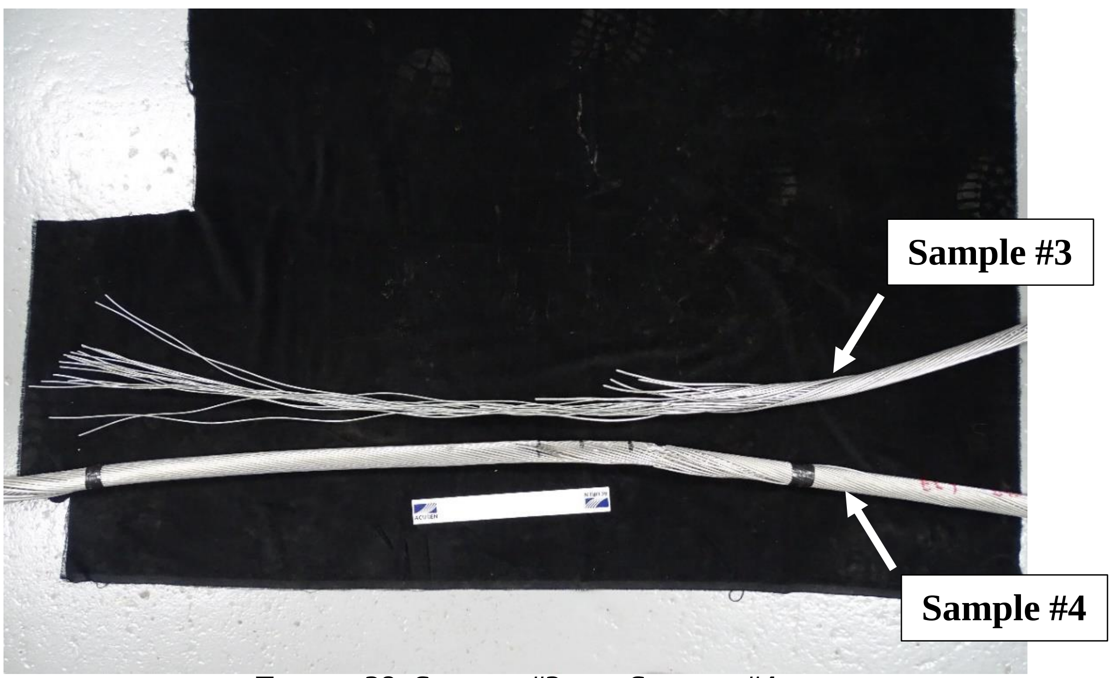

FIGURE 28: SAMPLE #3 AND SAMPLE #4

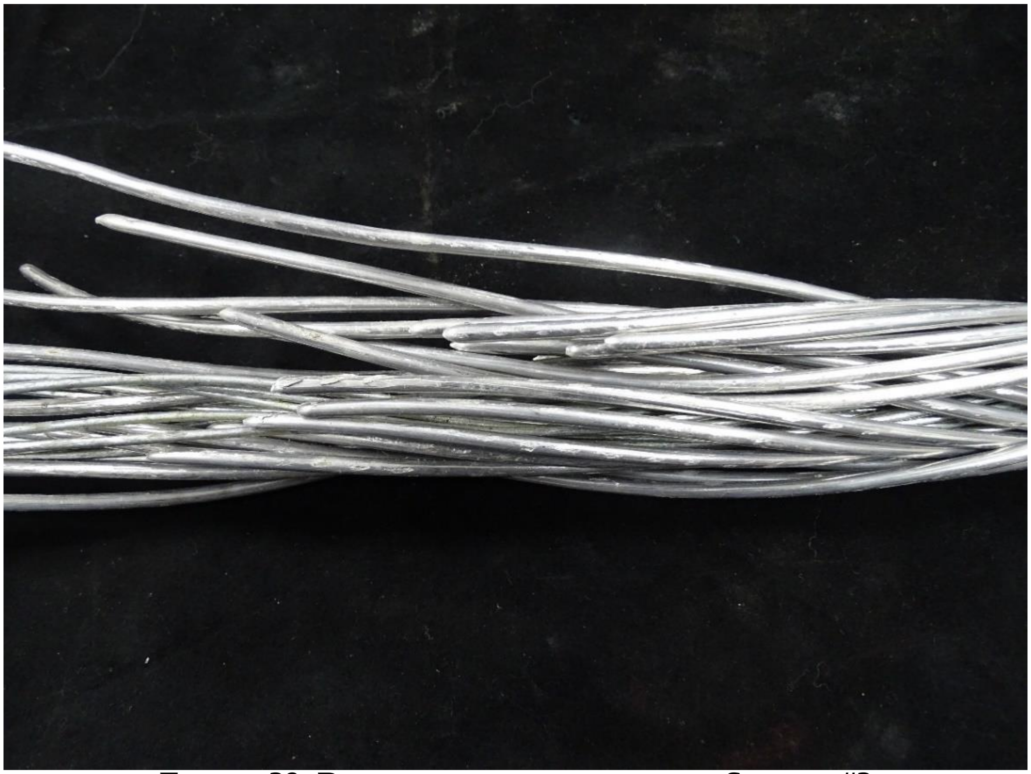

FIGURE 29: BROKEN ALUMINUM WIRES OF SAMPLE #3

FIGURE 30: FRACTURED ALUMINUM WIRES, SAMPLE #3

ACUREN

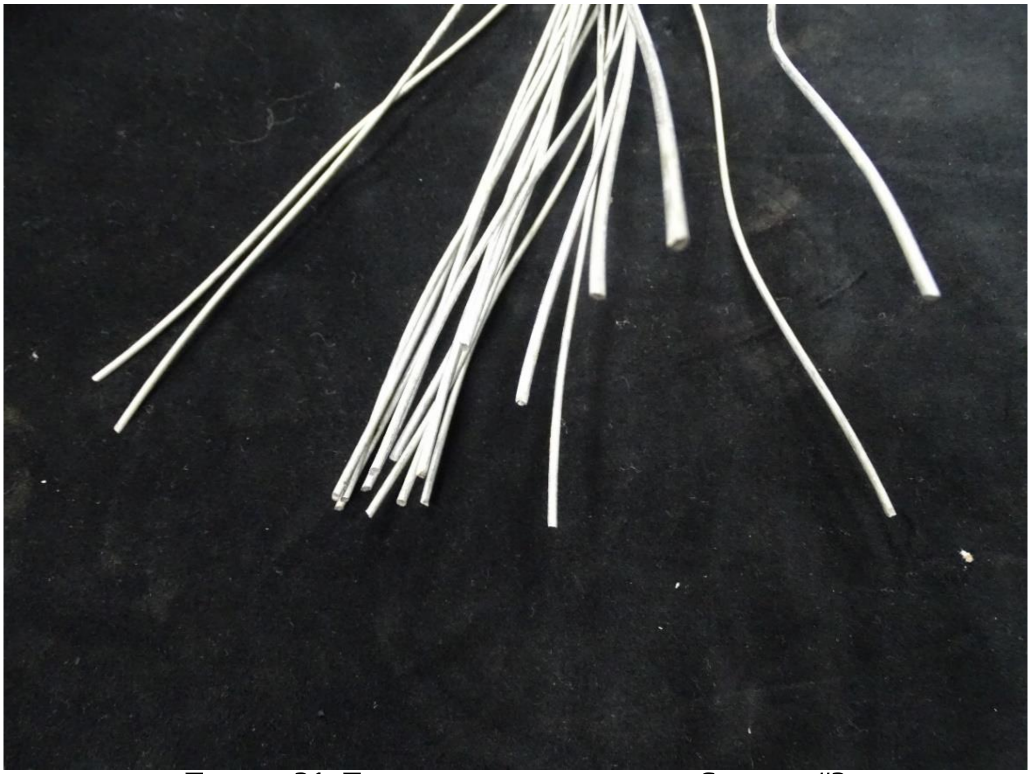

FIGURE 31: FRACTURED STEEL WIRES, SAMPLE #3

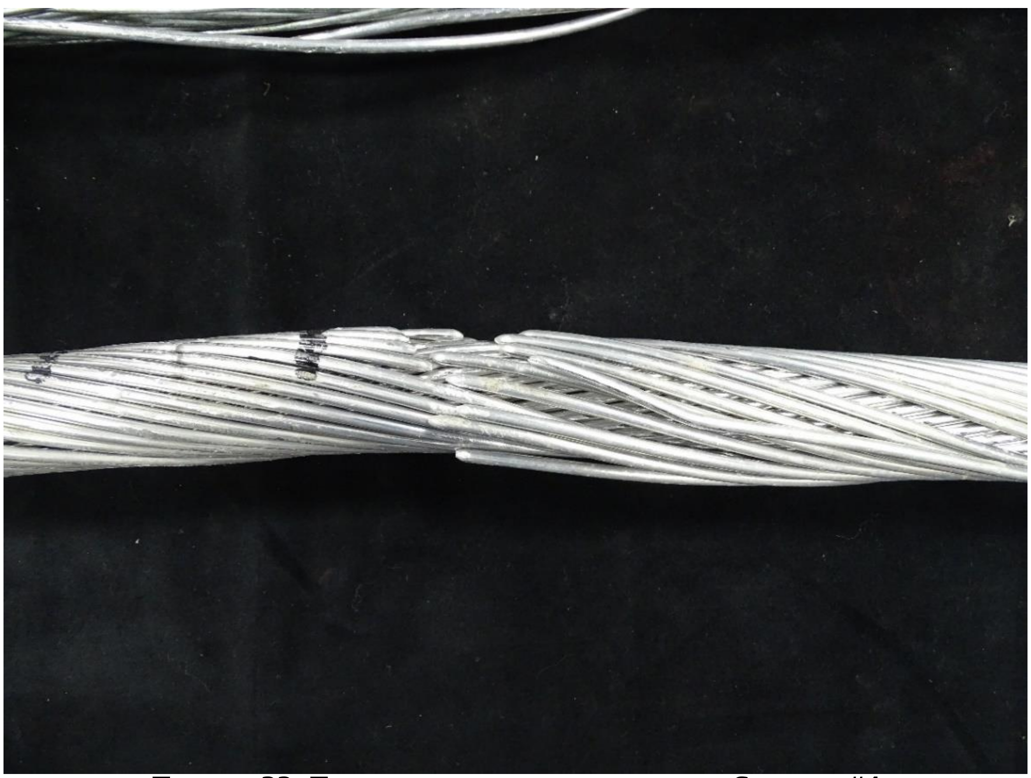

FIGURE 32: FRACTURED ALUMINUM WIRES, SAMPLE #4

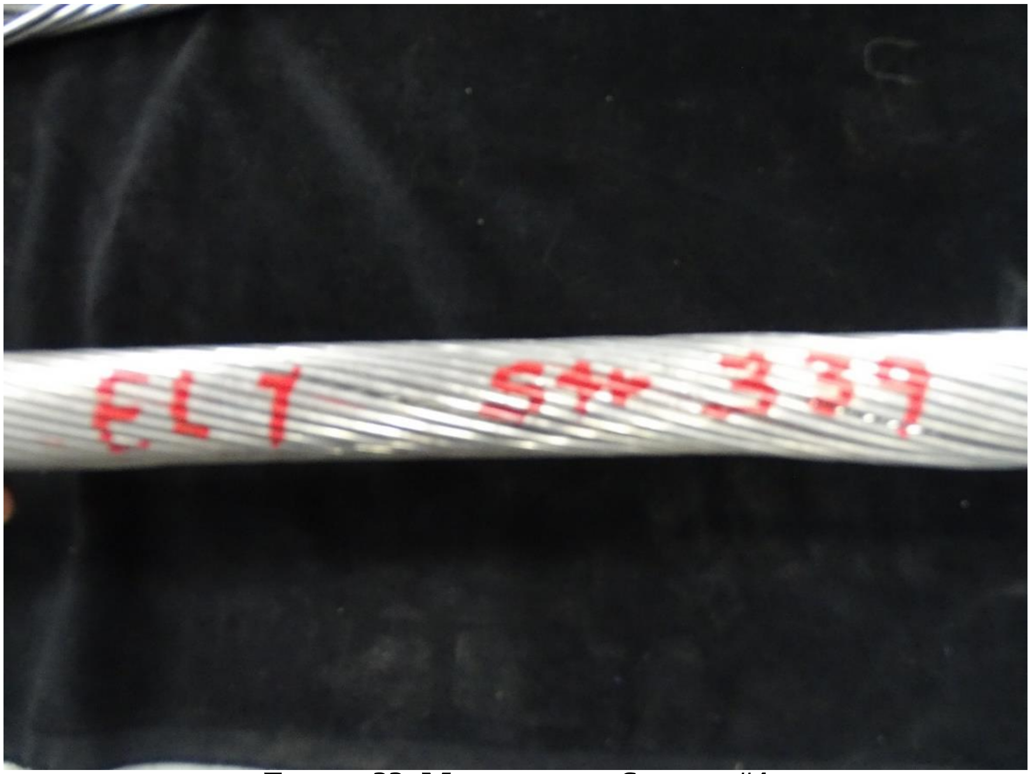

FIGURE 33: MARKINGS ON SAMPLE #4

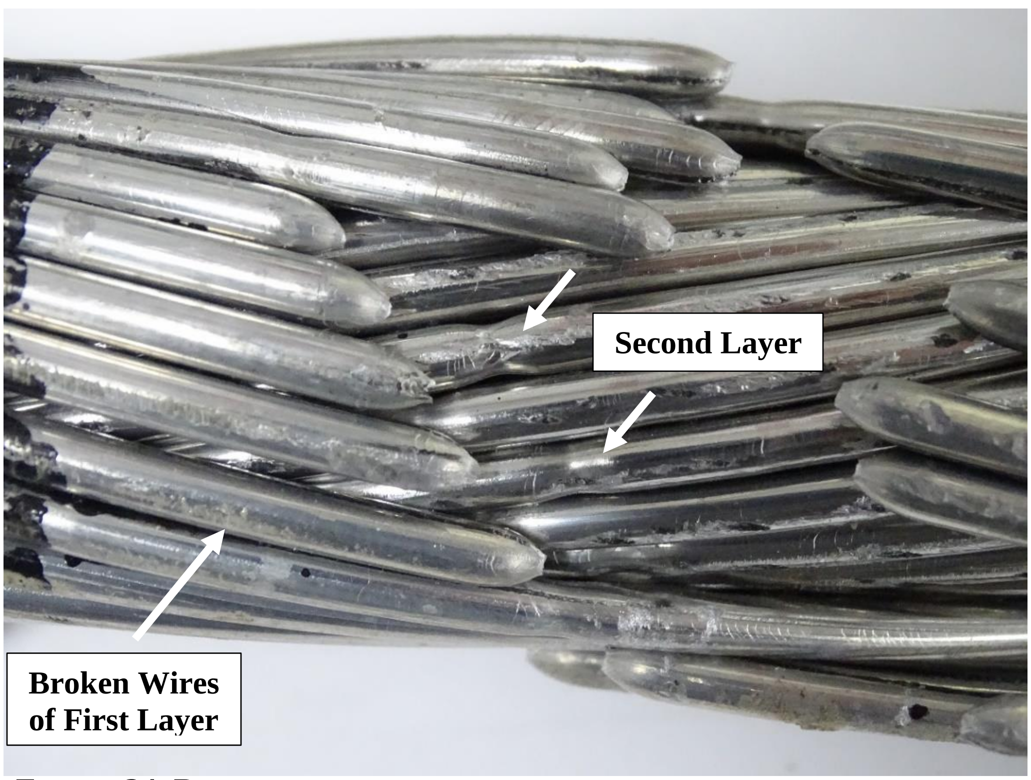

FIGURE 34: BROKEN WIRES OF THE FIRST LAYER AND NECKING OF WIRES ON THE SECOND LAYER, SAMPLE #4

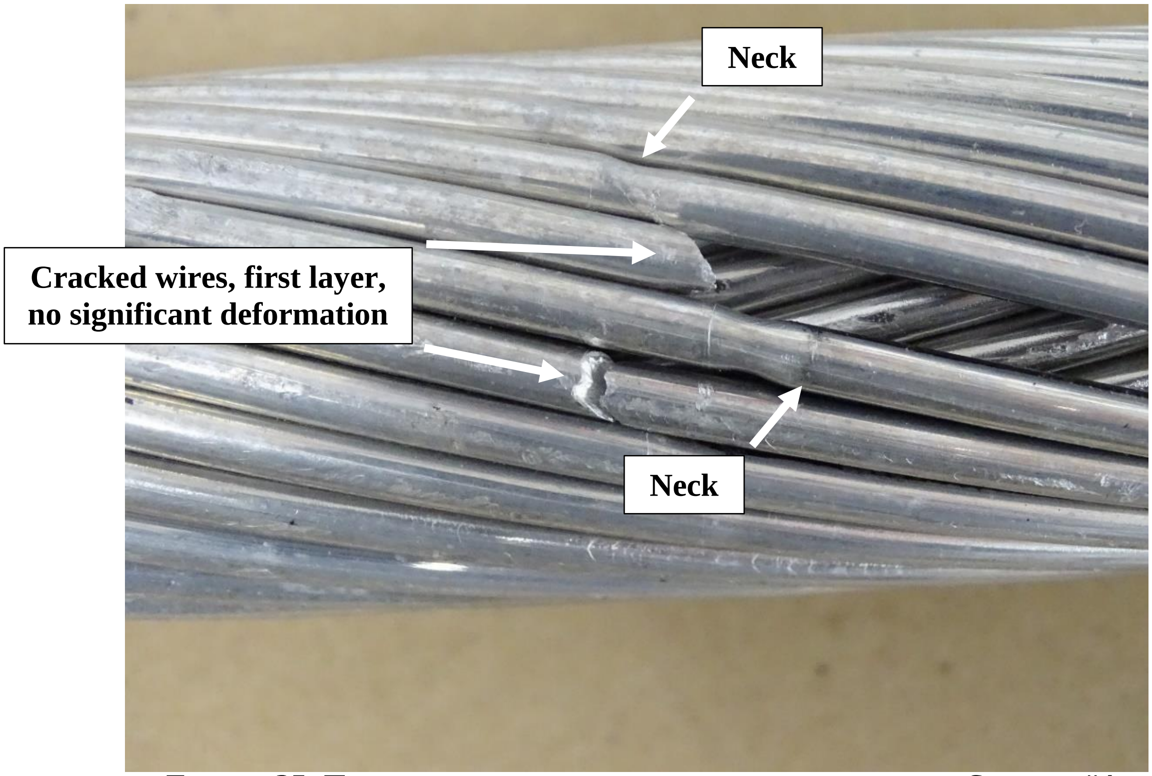

FIGURE 35: TWO BROKEN WIRES, NO SIGNIFICANT NECKING, SAMPLE #4

3.0 EXAMINATION AT LOW MAGNIFICATION

Some aluminium and steel sections with fracture surface were removed from the samples and examined at low magnification.

i. Figure 36 and Figure 37 shows the profile of two aluminium wires broken in the field.
ii. Aluminum wire surfaces were generally clean and free from corrosion/oxidation products.
iii. Aluminum wires showed some scratches that formed during the incident.
iv. Aluminum wires showed necking adjacent to the fracture surface.
v. Figure 38 shows profile of an aluminium wire with heavy deformation on the side surface. Observations made indicated that such deformation formed during the incident
vi. Heavy deformation on the side surface of the wires formed as a result of wires rubbing each other during the incident.
vii. Aluminum wires showed heavy localized deformation in the vicinity of the fracture, finally causing fracture in that area.
viii. Final fracture surface was very small, in other words, reduction in area of the aluminium wires was extremely high.
ix. Low reduction in area on the wire in Figure 38 is due to heavy deformation and surface damage formed during the incident.
x. Figure 39 shows profile of an aluminium wire from Sample #2. Similar observations were made on aluminium wires from Sample #2.
xi. Figure 40 shows profile of an aluminium wire from Sample #3. Similar observations were made on aluminium wires from Sample #3.
xii. Figure 41 shows profile of an aluminium wire from Sample #4. Similar observations were made on aluminium wires from Sample #4.
xiii. Figure 42 shows one of the aluminium wires which did not show any localized necking in the vicinity of the fracture. This is due to damage and stress state created on this aluminium wire during the incident.
xiv. Figure 43 and Figure 44 shows two of the wires necked but did not develop a fracture. Similar observations were made on some of the wires of the second layer.
xv. Figure 45Figure 44 shows the broken steel wires from Sample #1. Wire end surface was about 45° to the longitudinal direction of the wire.
xvi. Surface of the steel wires were zinc coated and some white powdery corrosion products and some brown patches of a substance (possibly foreign material or rust) were observed, Figure 45 and Figure 46.
xvii. Figure 47 shows another steel wire from Sample #1. This wire also showed some brown patches of rust or foreign material and white powdery corrosion products, Figure 48.
xviii. Second steel wire showed a wedged fracture surface. Wedging on both sides was evident, Figure 49 (this wire was possibly cut).
xix. Figure 50 shows a wire end surface from Sample #2. Figure 51 shows the fracture surface of a broken steel wire removed from Sam Sample #3.

xx. Wire end surface of steel wire from Sample #2 was normal to the longitudinal direction of the wire. Fracture surface of steel wire from Sample #3 was slightly at an angle.

xxi. No steel samples were removed from Sample #4 as there were no broken steel wires.

xxii. Figure 52 and Figure 53 show the fracture surface of aluminium wires from Sample #3 and Sample #4, respectively. High percentage of reduction of area for both wires was evident.

xxiii. Figure 54 shows wire end surface of a steel wire from Sample #3. Corrosion/oxidation products on the surface were evident. We also observed a wedge on one side.

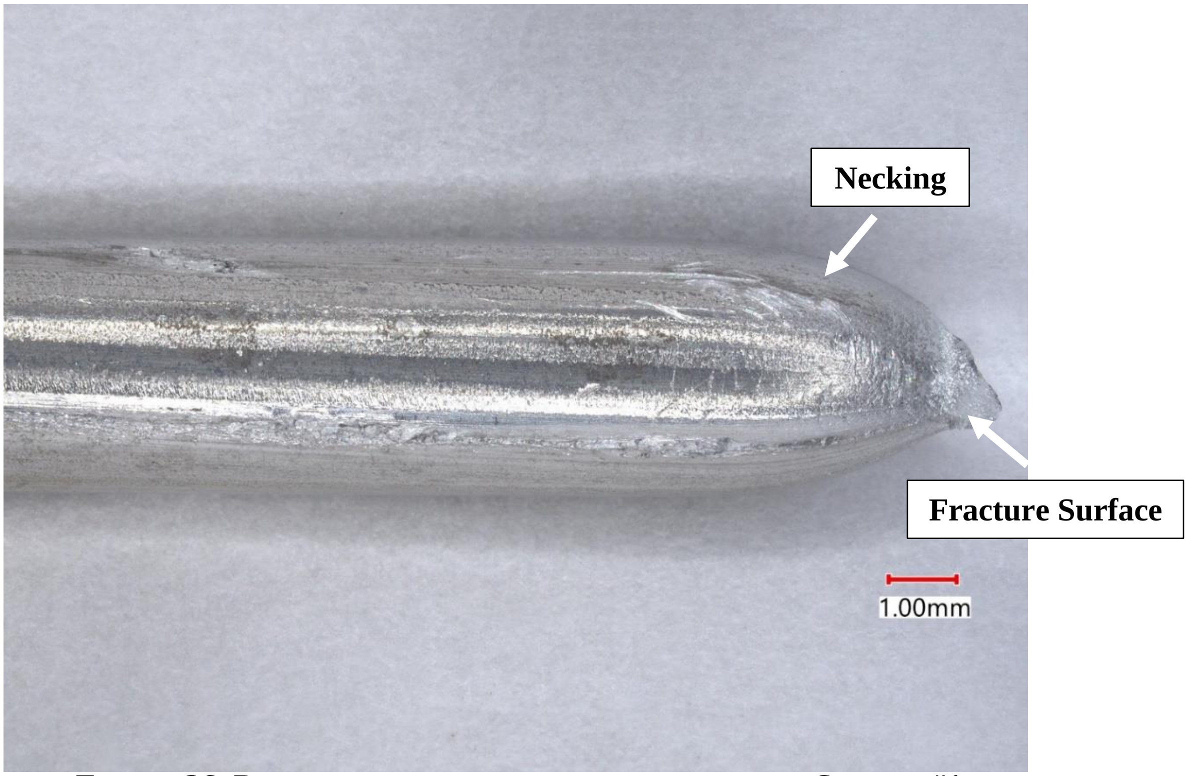

FIGURE 36: PROFILE OF ONE OF THE ALUMINUM WIRES, SAMPLE #1

FIGURE 37: PROFILE OF ANOTHER ALUMINUM WIRE, SAMPLE #1

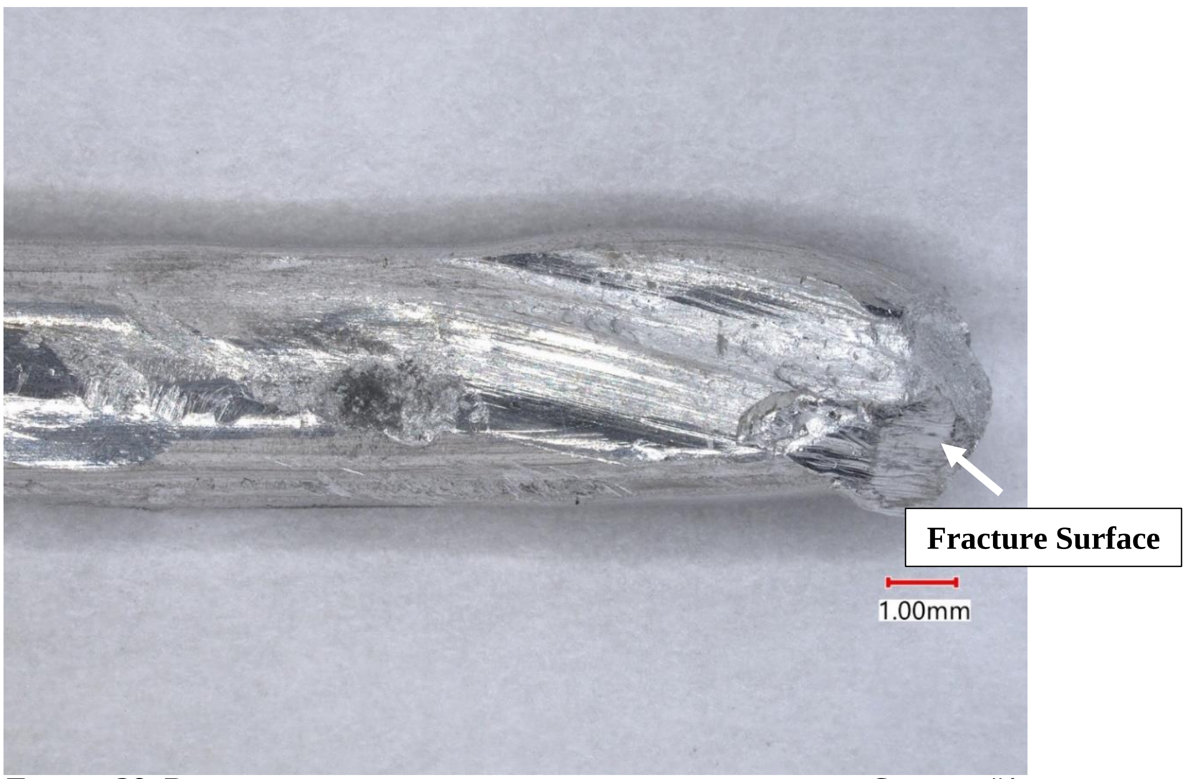

FIGURE 38: PROFILE OF A HEAVILY DEFORMED ALUMINUM WIRE, SAMPLE #1

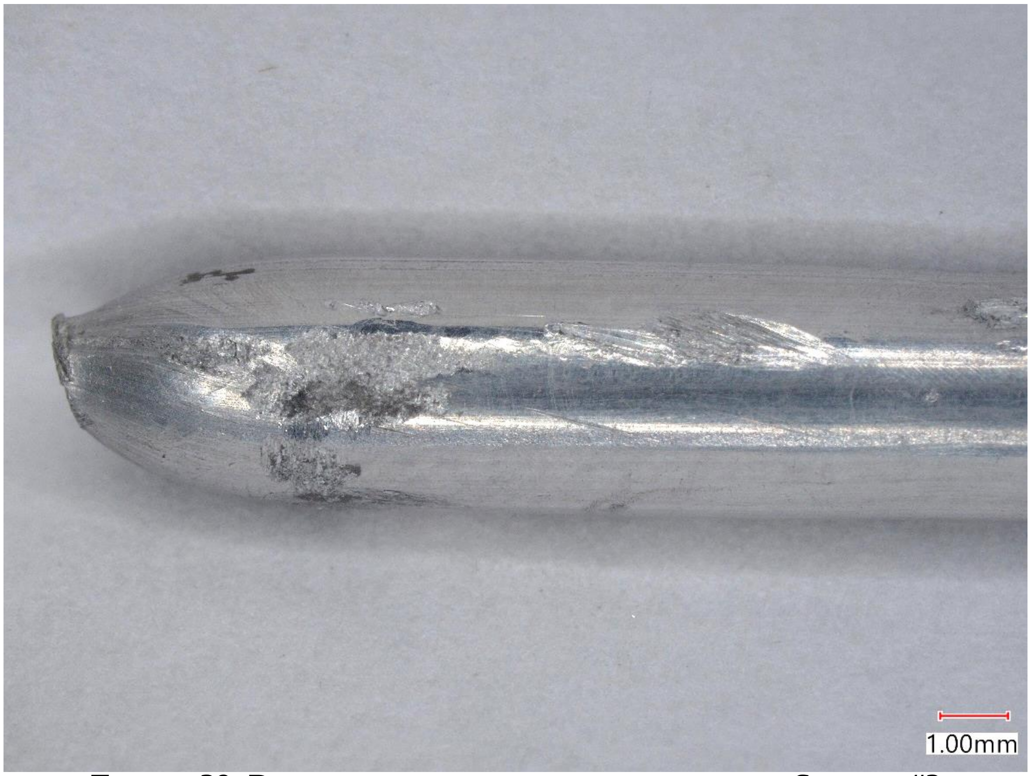

FIGURE 39: PROFILE OF A BROKEN ALUMINUM WIRE, SAMPLE #2

FIGURE 40: PROFILE OF A BROKEN ALUMINUM WIRE, SAMPLE #3

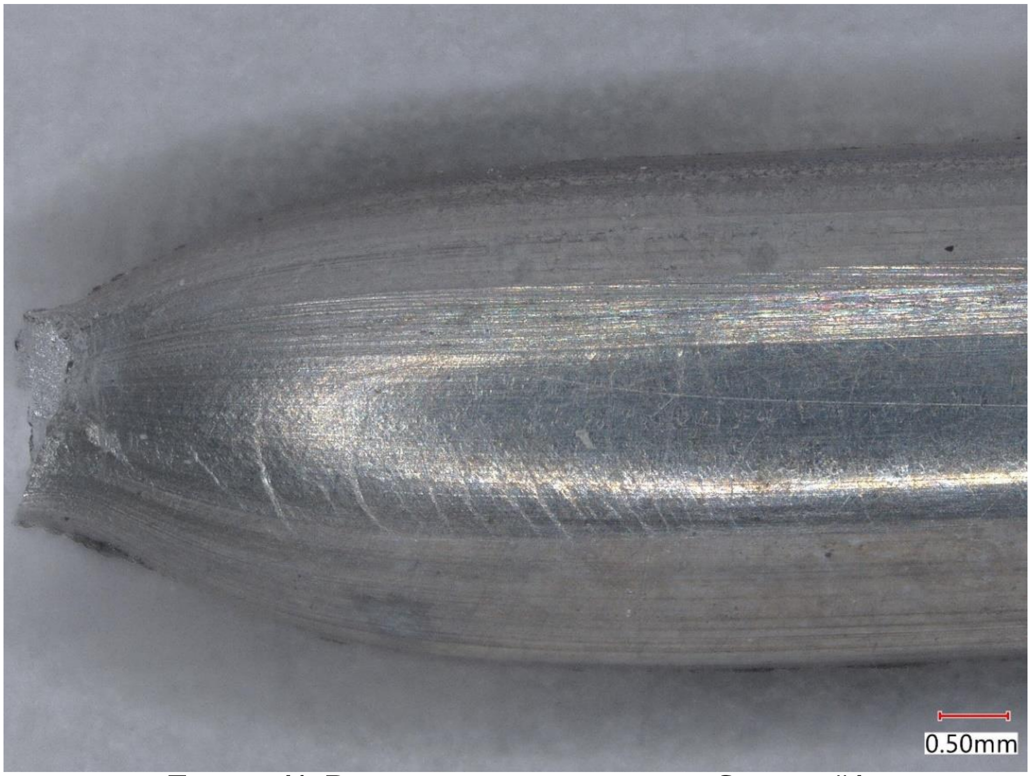

FIGURE 41: PROFILE OF A BROKEN WIRE, SAMPLE #4

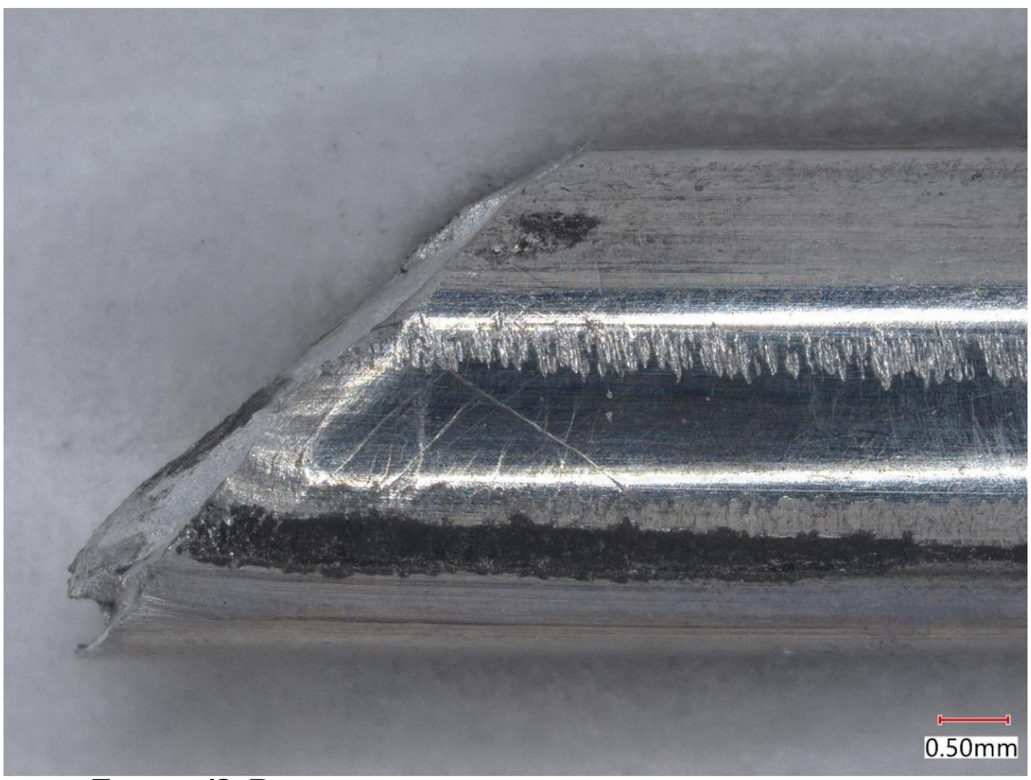

FIGURE 42: BROKEN ALUMINUM WIRE THAT SHOWED NO LOCAL DEFORMATION (NECKING) IN THE VICINITY OF THE FRACTURE SURFACE, SAMPLE #4

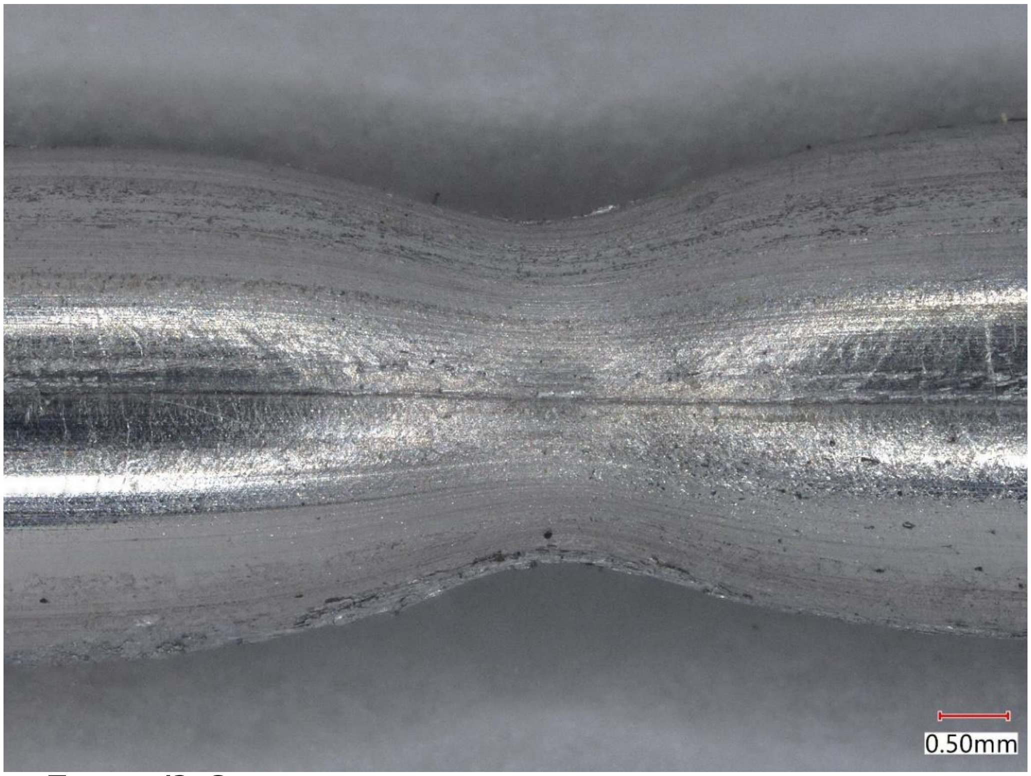

FIGURE 43: ONE OF THE ALUMINUM WIRES THAT NECKED BUT DID NOT CRACK, FIRST LAYER OF ALUMINUM WIRES ON THE CABLE, SAMPLE #4

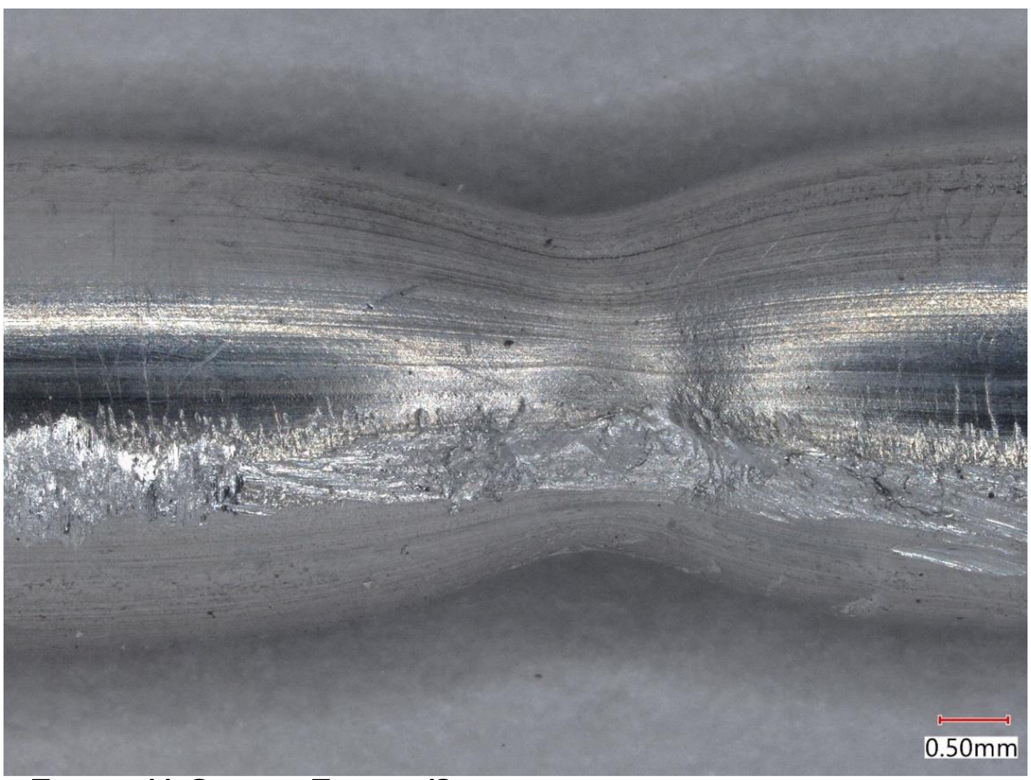

FIGURE 44: SAME AS FIGURE 43, THIS WIRE ALSO HAS SURFACE SCRATCH MARKS

FIGURE 45: ONE OF THE BROKEN STEEL WIRES, SAMPLE #1 (THIS WIRE WAS POSSIBLY CUT)

FIGURE 46: CLOSE VIEW OF STEEL WIRE SURFACE, SAMPLE #1

FIGURE 47: ANOTHER STEEL WIRE FROM SAMPLE #1 (THIS WIRE WAS POSSIBLY CUT)

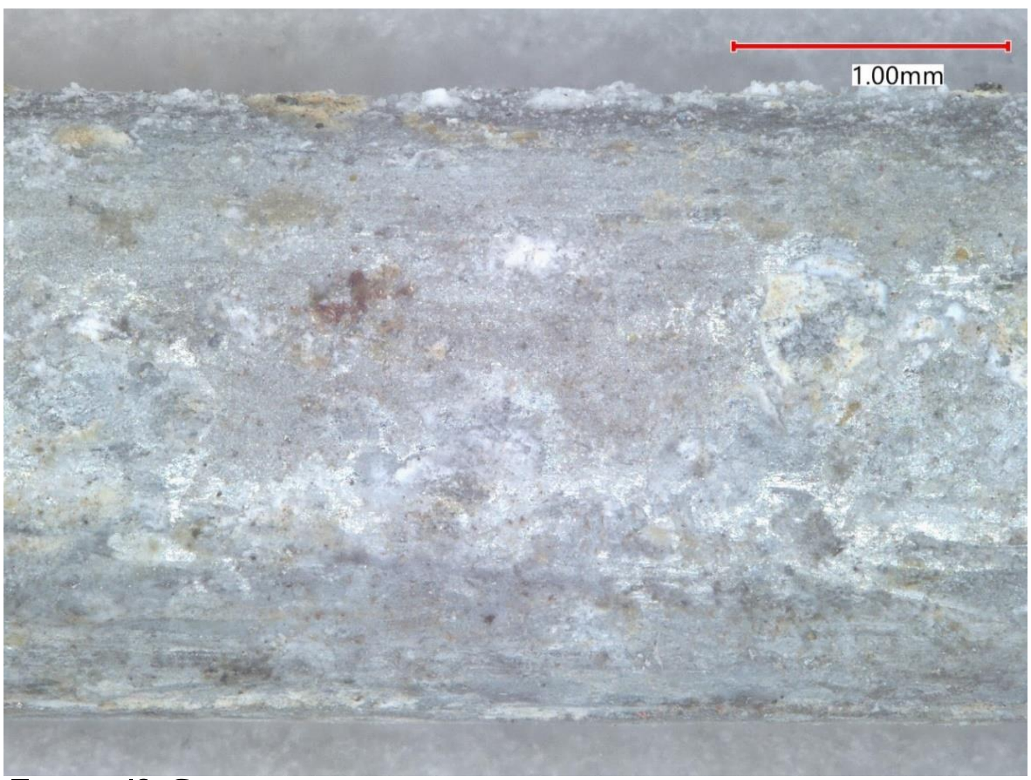

FIGURE 48: CLOSE VIEW OF THE SIDE SURFACE OF THE SECOND STEEL WIRE, SAMPLE #1

FIGURE 49: WEDGE FRACTURE SURFACE, STEEL WIRE #2, SAMPLE #1 (THIS WIRE WAS POSSIBLY CUT)

FIGURE 50: BROKEN STEEL WIRES FROM SAMPLE #2 (THIS WIRE WAS POSSIBLY CUT)

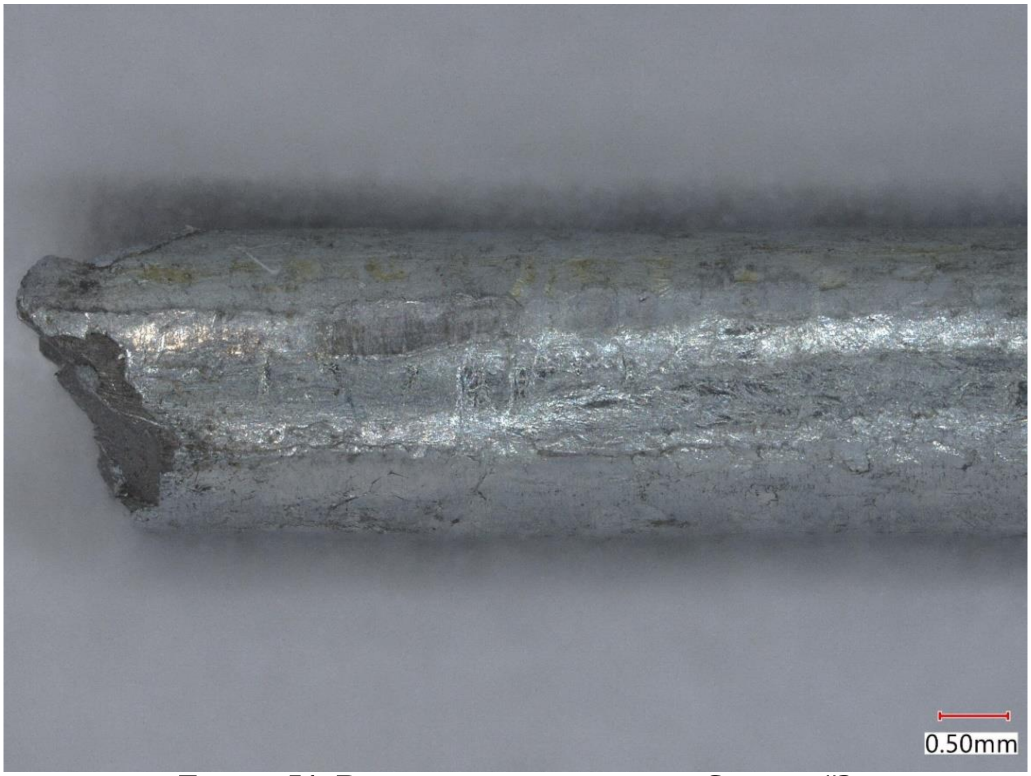

FIGURE 51: BROKEN STEEL WIRE FROM SAMPLE #3

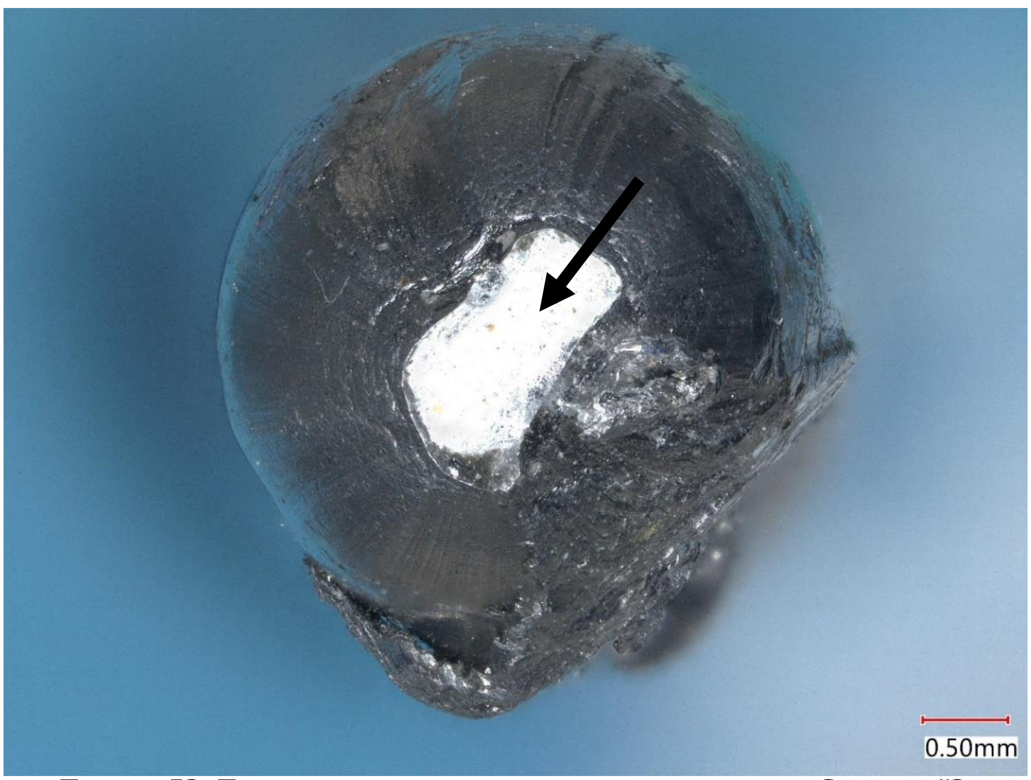

FIGURE 52: FRACTURE SURFACE OF AN ALUMINUM WIRE, SAMPLE #3

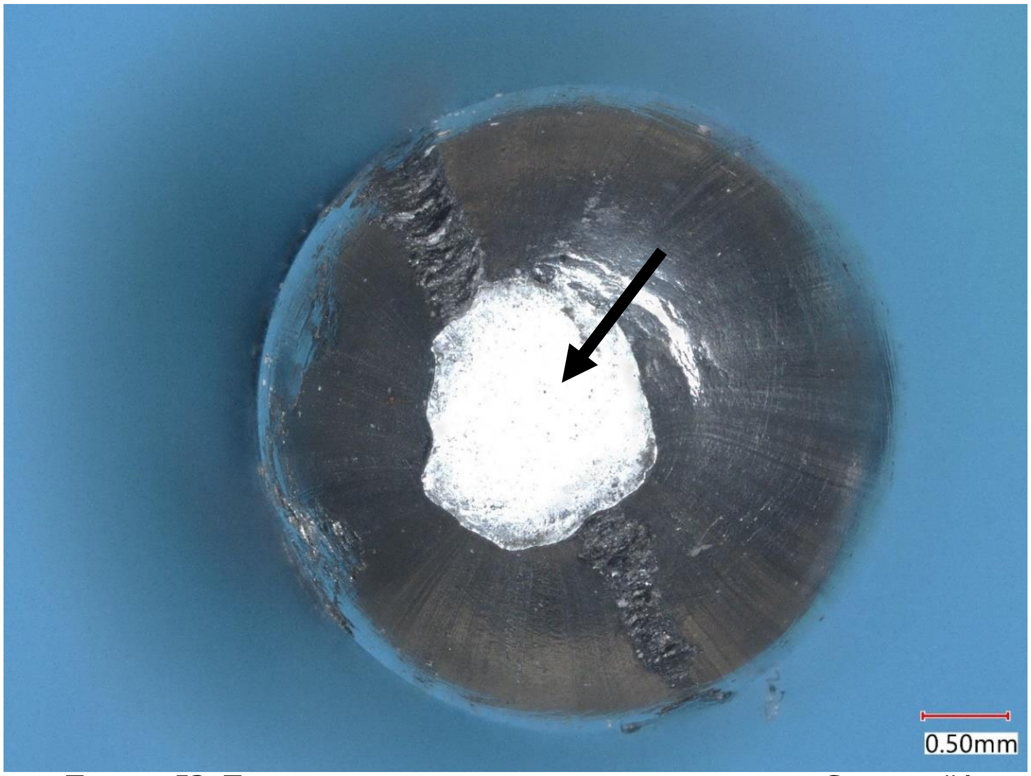

FIGURE 53: FRACTURE SURFACE OF AN ALUMINUM WIRE, SAMPLE #4

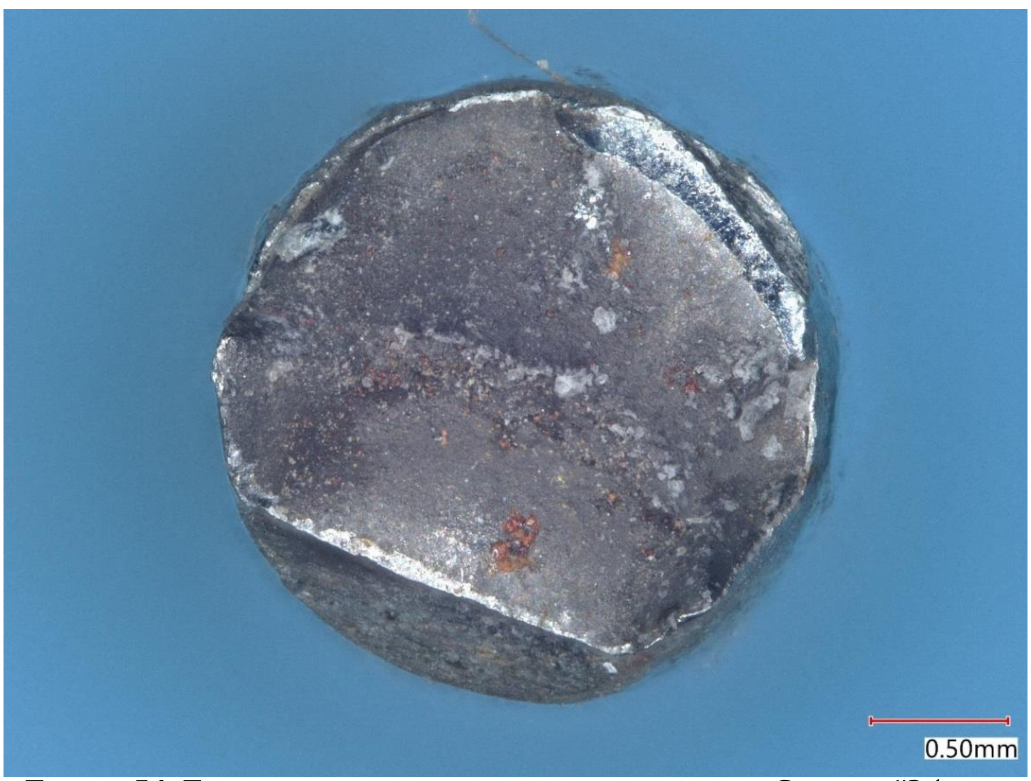

FIGURE 54: FRACTURE SURFACE OF A STEEL WIRE FROM SAMPLE #3 (THIS WIRE WAS POSSIBLY CUT)

4.0 SCANNING ELECTRON MICROSCOPY

We have examined the following wires by means of SEM:

a) Sample #1, steel wire #1 (wires numbers are for that section only)
b) Sample #1, steel wire #2
c) Sample #1, aluminum wire #1
d) Sample #1, aluminum wire #2
e) Sample #1, aluminum wire #3
f) Sample #2, steel wire
g) Sample #3, steel wire
h) Sample #3, aluminum wire
i) Sample #3, aluminum wire
j) Sample #4, aluminum wire

i. Figure 55 and Figure 56 shows a steel wire from Sample #1 in two different profiles. Steel wire #1 had a wedge. The second profile suggested the wire did not show local plastic deformation in the vicinity of the fracture surface. Wedges appeared in the vicinity and on the fracture surface of the steel wires. Appearance of the wedges suggested that the wedges formed as a result of rubbing of the wires against each other during the incident.

ii. As it was observed during the low magnification examination, the surface of the steel wires contained corrosion/oxidation products. Figure 57 shows the corrosion/oxidation products on the side surface of steel wire #1 (of Sample #1). Figure 58 and Figure 59 shows EDS analysis results of the compounds on the surface. Results show that they mostly contained zinc (possibly in the form of zinc oxides), oxygen (O), sodium (Na), chlorine (Cl), silicon (Si), aluminium (Al), sulphur (S) and iron (Fe). Results indicate mostly Zn, Na and Cl were involved. Some iron and aluminium compounds were also there.

iii. We cleaned Steel wire #1 and #2 from Sample #1 in 5% Alconox at 70°C for 30 minutes. Figure 60 and Figure 61 show the fracture surfaces after cleaning. Fracture surface of each wire showed very small dimples, resolvable at high magnifications. Some areas showed shear dimples, possibly due to cutting of those samples. Figure 62, Figure 63 and Figure 64 show dimples observed on Steel wire #1 of Sample #1 at various magnifications. Appearance of the dimples suggested steel wires were cold drawn prior to manufacturing conductors. Figure 65 shows the dimples observed on Steel wire #2, Sample #1.

iv. Figure 66 and Figure 67 show steel wire samples from Sample #2 and Sample #3. The steel wires were examined in the as-it-is condition. The wire from Sample #3 showed a wedge, Figure 68. Both fracture surfaces showed dimples, typical of overloading, Figure 69 and Figure 70. Similar to the observations made on the fracture surfaces of steel wires from Sample #1, dimples were small, resolvable at higher magnifications and suggested that the steel wires were cold worked.

v. No wire samples from Sample #4 were examined as there were no broken steel wires

vi. Figure 71 and Figure 72 show the profile and top of the fracture surface of aluminium wire #1, Sample #1. Significant necking was evident on the aluminium wire in the area adjacent to the fracture surface, Figure 71 and Figure 72. Reduction in area of the fracture surface was also very high, Figure 72. Dimples on the fracture surface could readily be observed at low magnifications. Dimples covering the entire fracture surface of the aluminium wires is the proof that the wire was overloaded during the incident, Figure 73.

vii. Figure 74 and Figure 75 show the profile of the fracture surface of aluminium wire #2 from Sample #1. Significant necking was evident on the aluminium wire in the area adjacent to the fracture surface, Figure 74 and Figure 75. Reduction in area of the fracture surface was also very high, Figure 76. Dimples on the fracture surface could readily be observed at low magnification. Dimples covering the entire fracture surface of the aluminium wires is the proof that the wire was overloaded during the incident.

viii. Figure 77 shows the side view of aluminium wire #2 of Sample #1. Rubbing and scratch marks as a result of relative motion of the wires of the cable were evident.

ix. We performed EDS analysis on the side surface of the aluminum wire (wire #2, Sample #1). Results are presented in Figure 78 and Figure 79. Results show presence of only aluminium oxide on the surface.

x. Figure 80 shows the fracture surface of aluminium wire #3 of Sample #1. Figure 81 shows shear dimples on the fracture surface of the wire.

xi. Figure 82 show aluminium wire #1 of Sample #4. This wire was one of those that broke with necking. Appearance of the fracture surface is very similar to those observed on Sample #1. Fracture surface was covered with readily observable dimples, Figure 83.

xii. Figure 84 shows one of the aluminium wires that cracked without readily observable neck and fracture surface at an angle (shear) to the longitudinal direction of the wire. This wire was from Sample #4. Figure 85 shows shear dimples on the fracture surface. This wire was damaged interacting with the neighbouring wires and showed extreme scratch and rubbing marks. It fractured by shear, and shear dimples were readily observable at low magnification was evident.

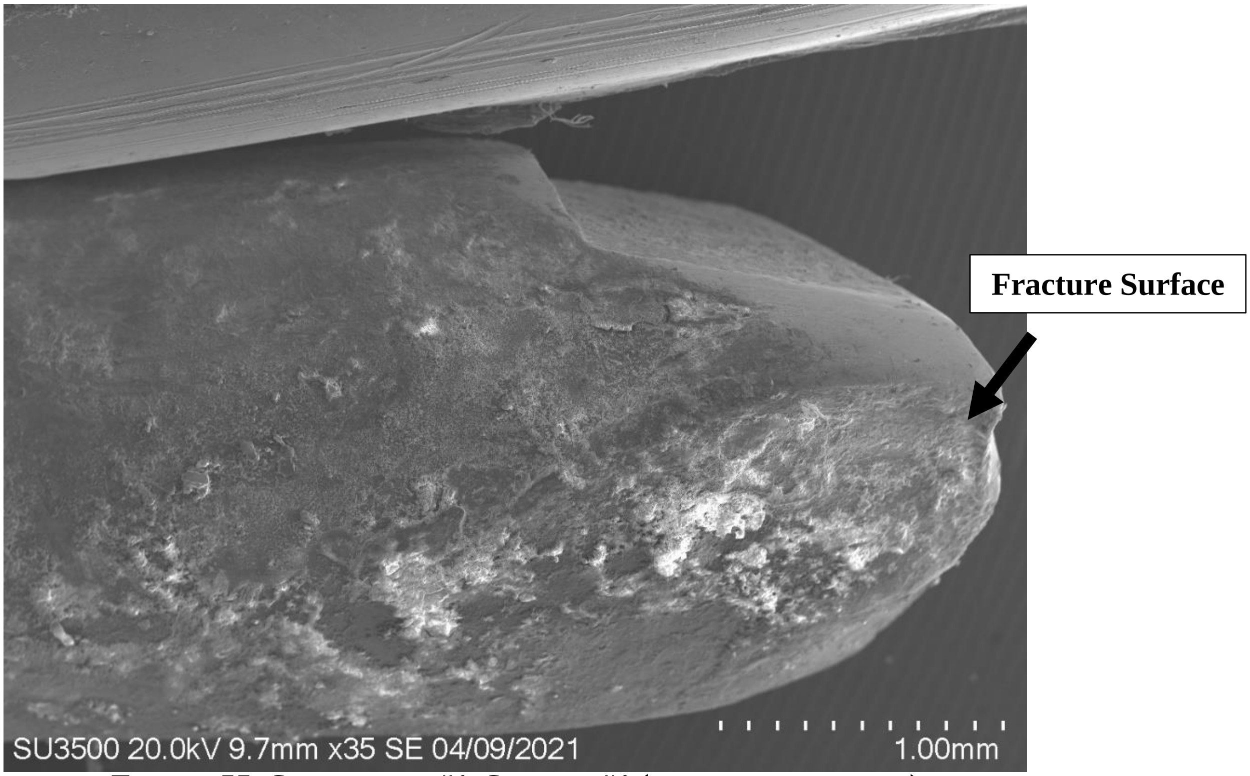

FIGURE 55: STEEL WIRE #1, SAMPLE #1 (THIS WIRE WAS CUT)

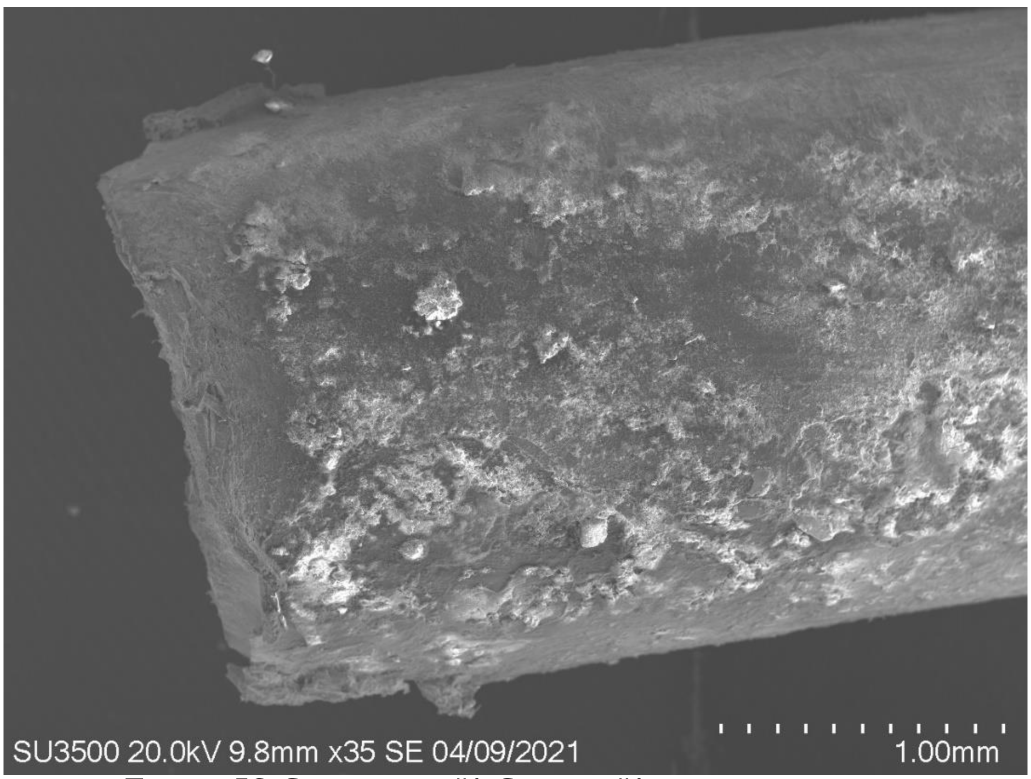

FIGURE 56: STEEL WIRE #1, SAMPLE #1, ANOTHER PROFILE

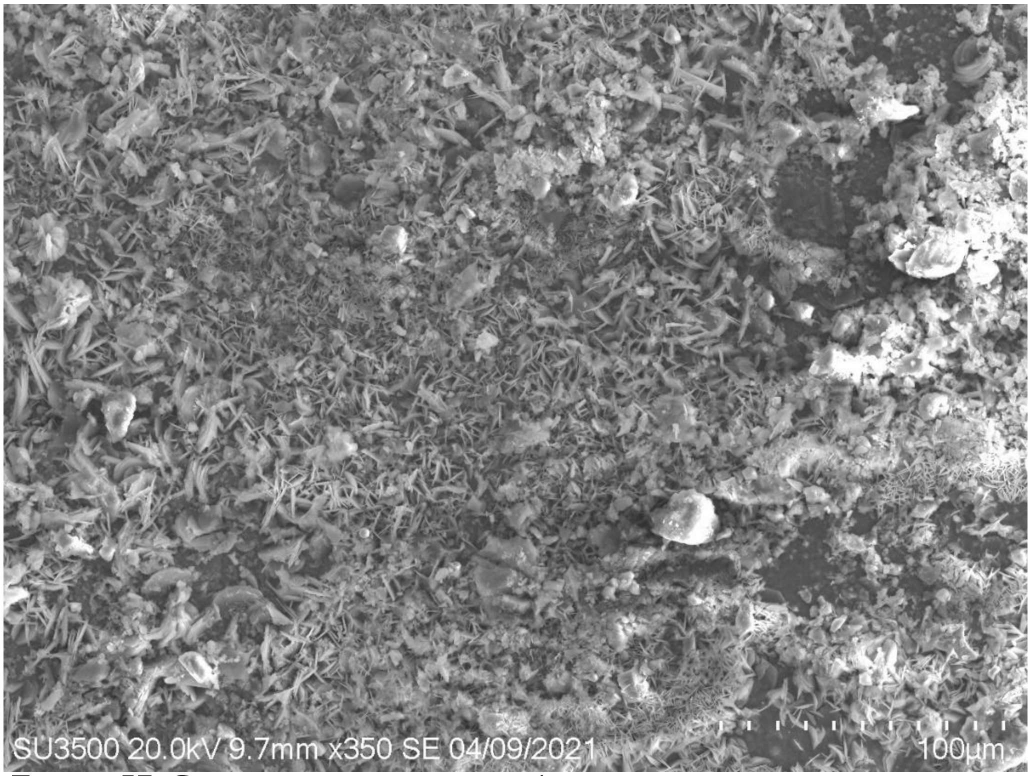

FIGURE 57: CLOSE VIEW OF OXIDATION/CORROSION PRODUCTS ON THE SIDE SURFACE OF STEEL WIRE #1, SAMPLE #1

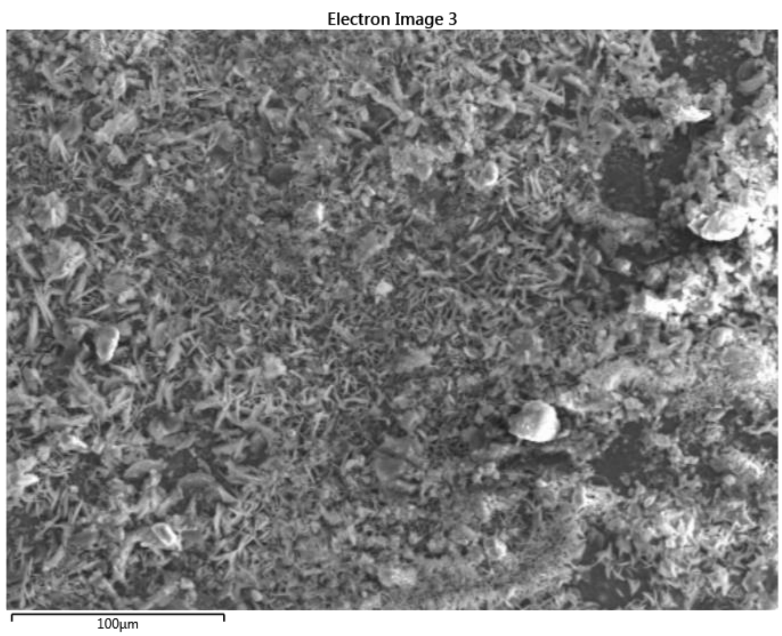

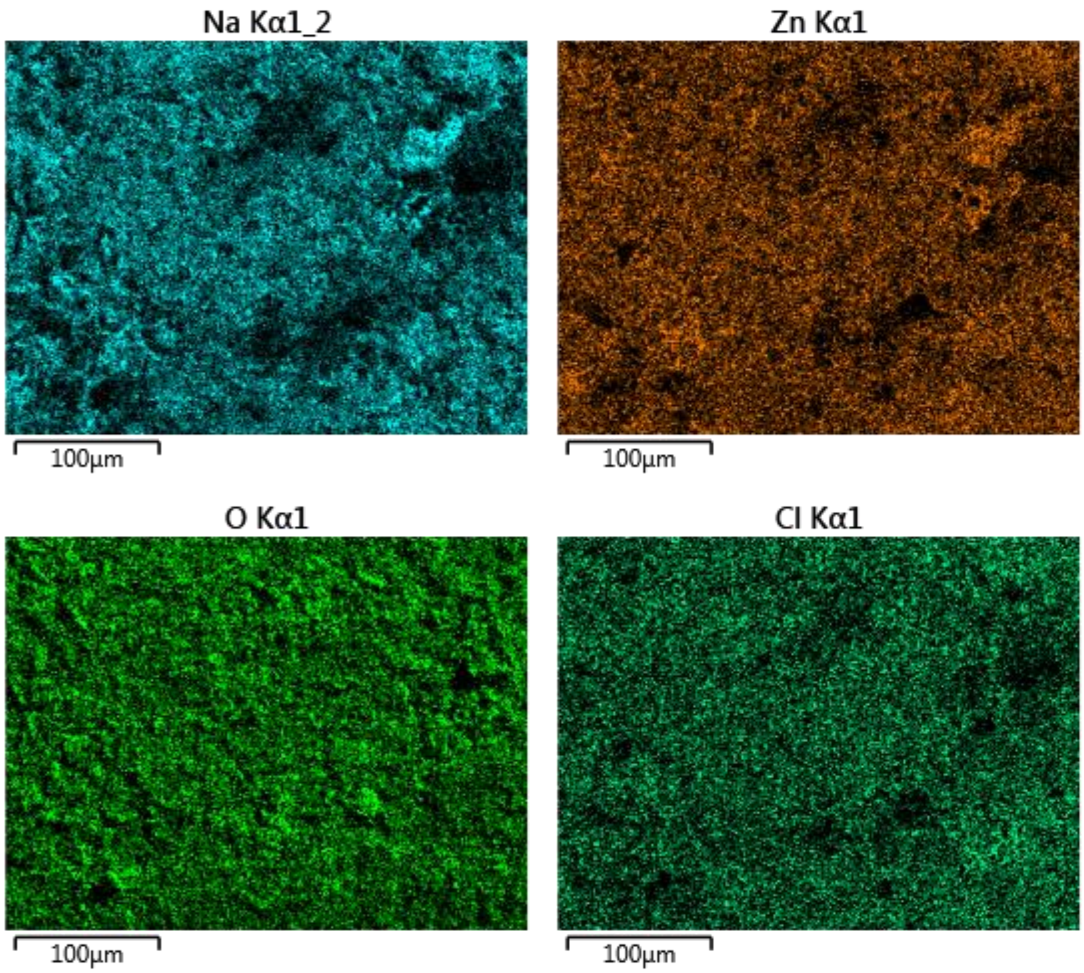
Na Kα1_2
100µm
Zn Kα1
100µm
O Kα1
100µm
Cl Kα1
100µm

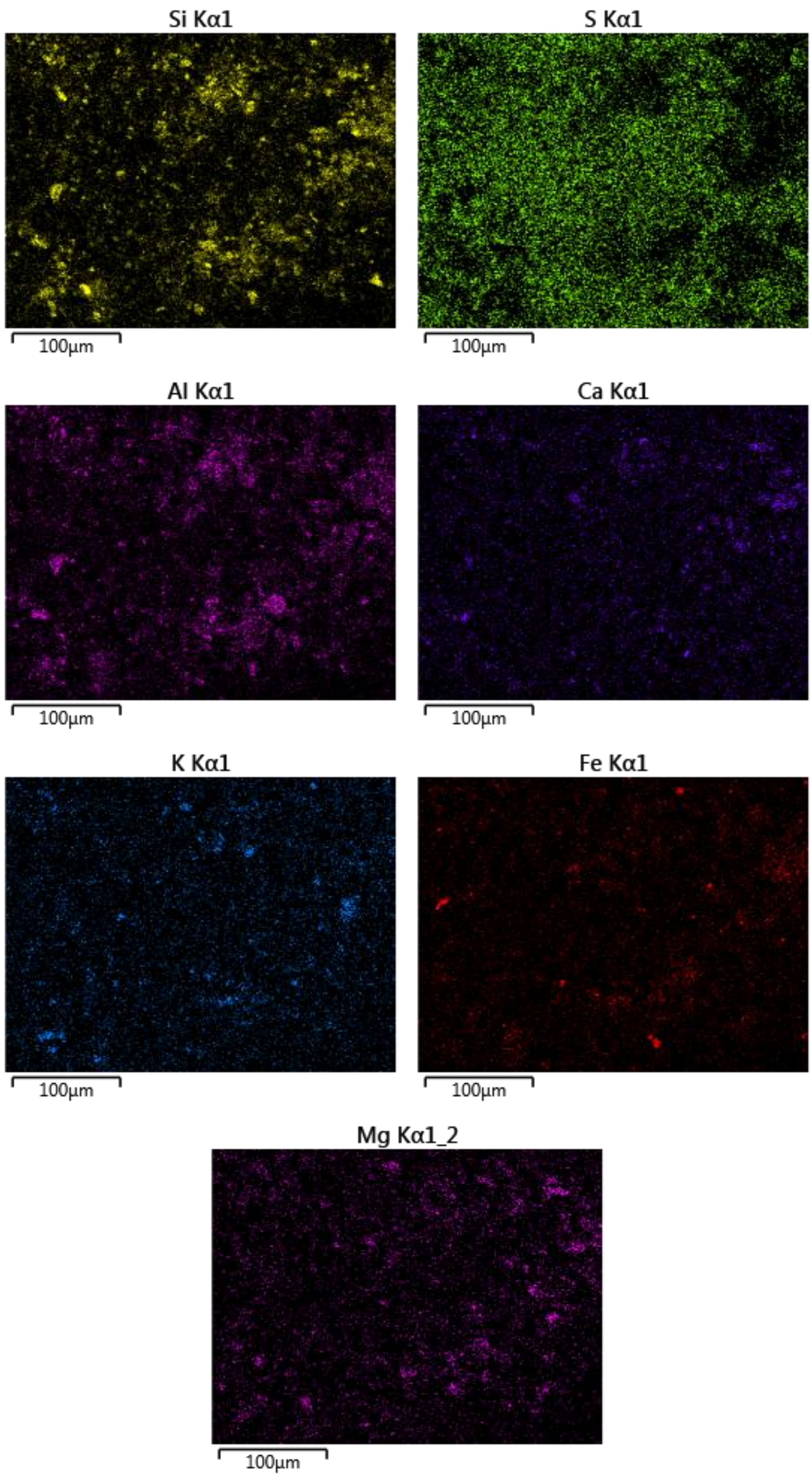

FIGURE 58: EDS MAP OF CORROSION PRODUCTS, STEEL WIRE #1, SAMPLE #1

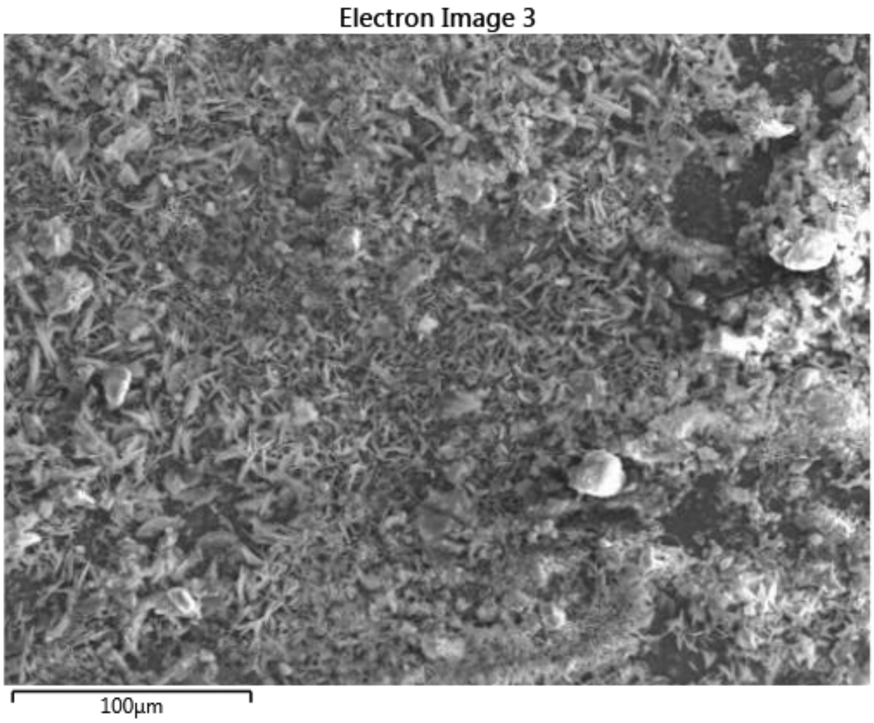

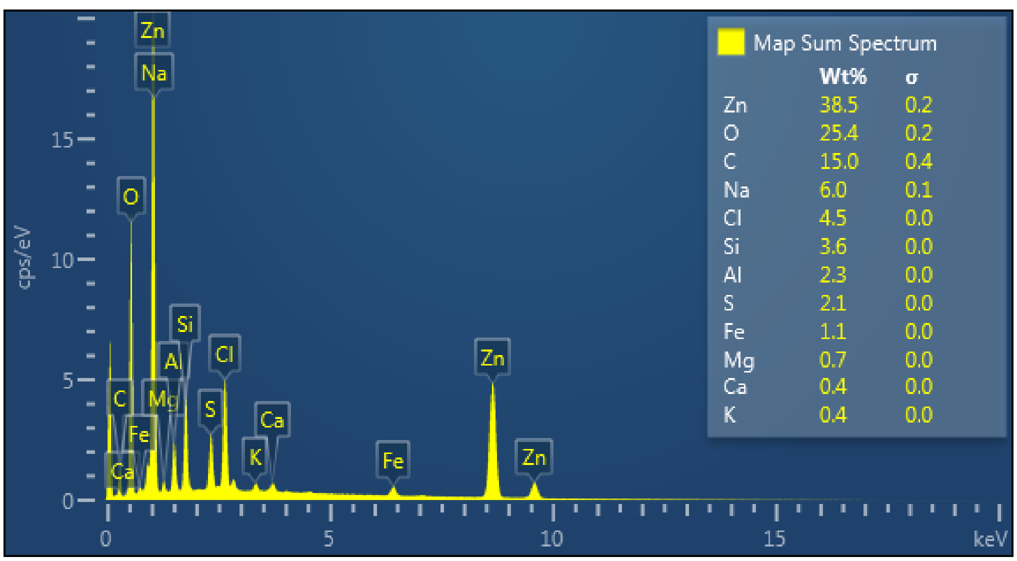

FIGURE 59: EDS (POINT) ANALYSIS RESULTS OF THE CORROSION PRODUCTS, STEEL WIRE #1, SAMPLE #1

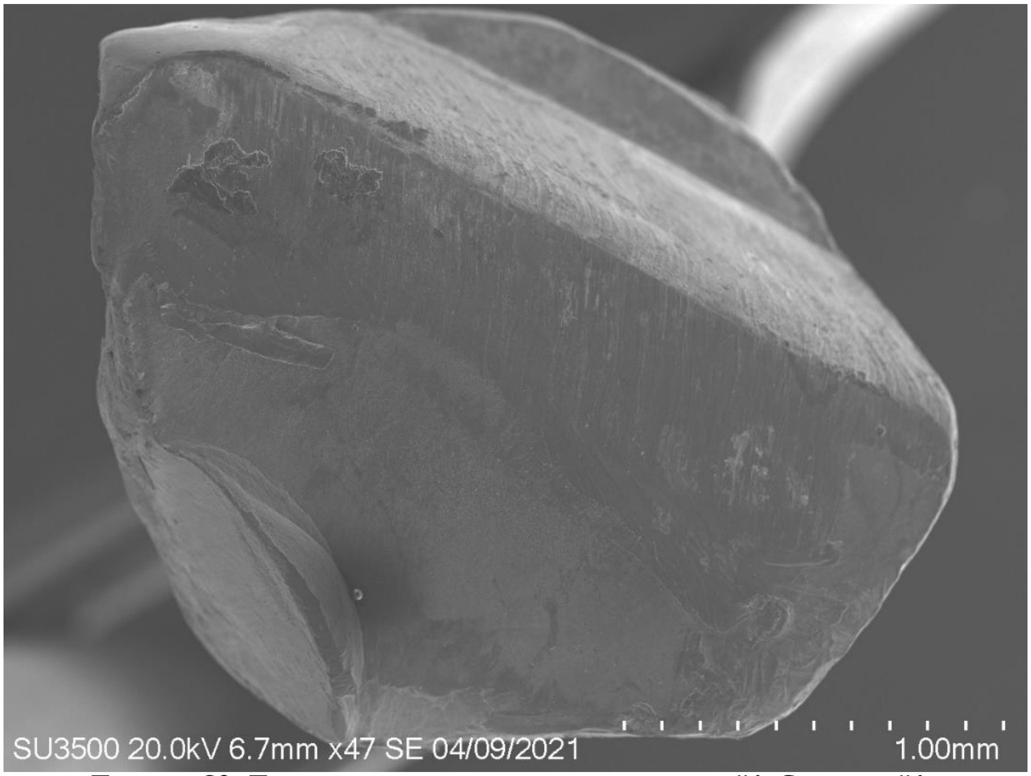

FIGURE 60: FRACTURE SURFACE OF STEEL WIRE #1, SAMPLE #1, AFTER CLEANING (THIS WIRE WAS POSSIBLY CUT)

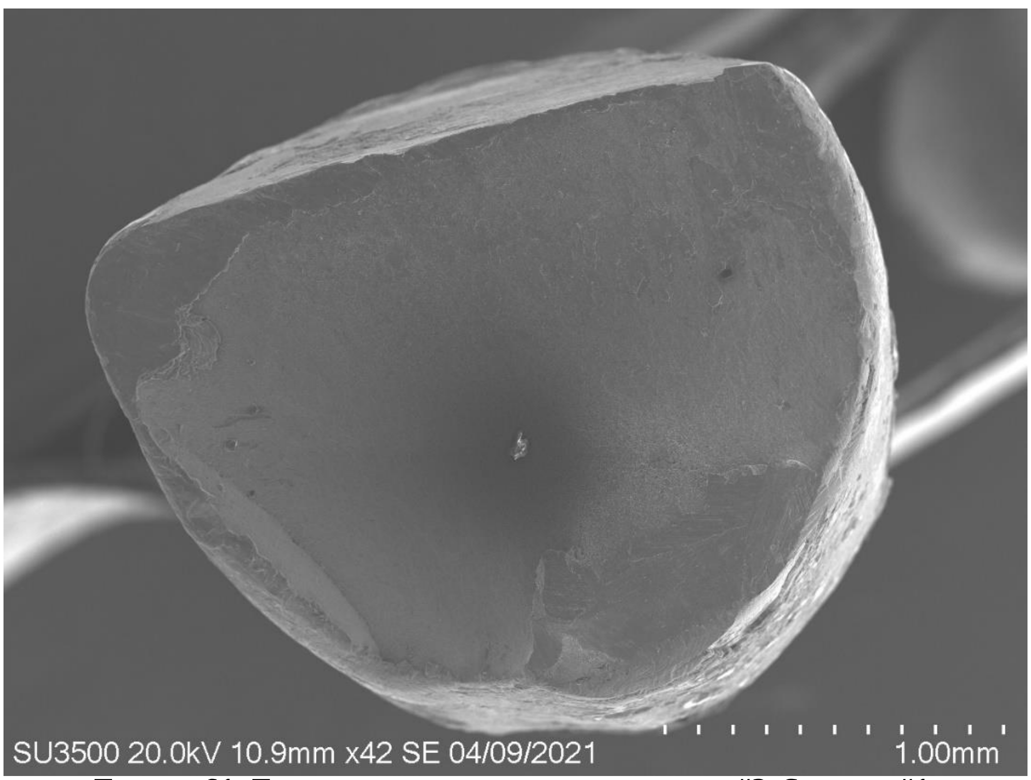

FIGURE 61: FRACTURE SURFACE OF STEEL WIRE #2, SAMPLE #1, AFTER CLEANING

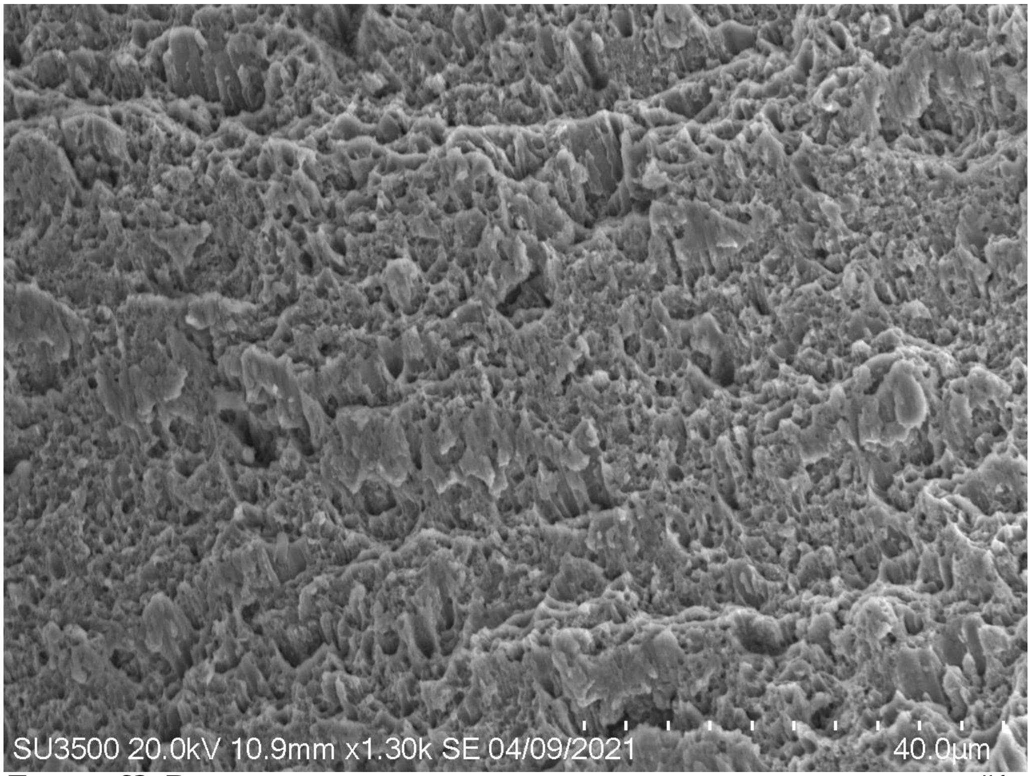

FIGURE 62: DIMPLES COVERING THE FRACTURE SURFACE OF STEEL WIRE #1, SAMPLE #1

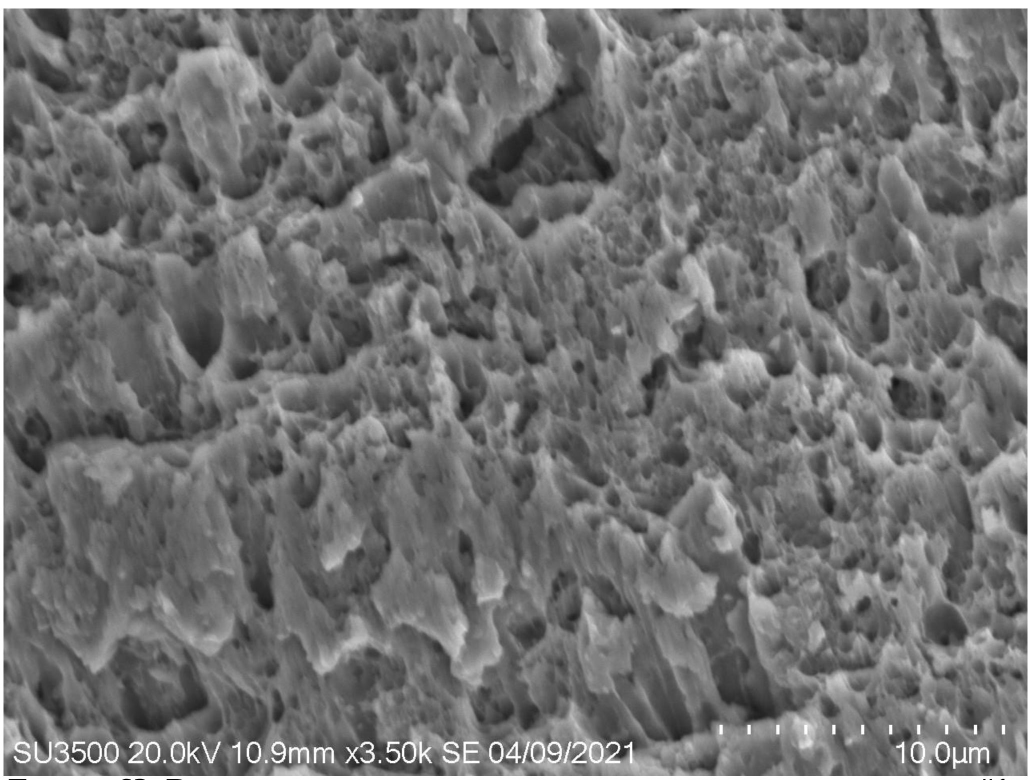

FIGURE 63: DIMPLES COVERING THE FRACTURE SURFACE OF STEEL WIRE #1, SAMPLE #1 AT HIGHER MAGNIFICATION

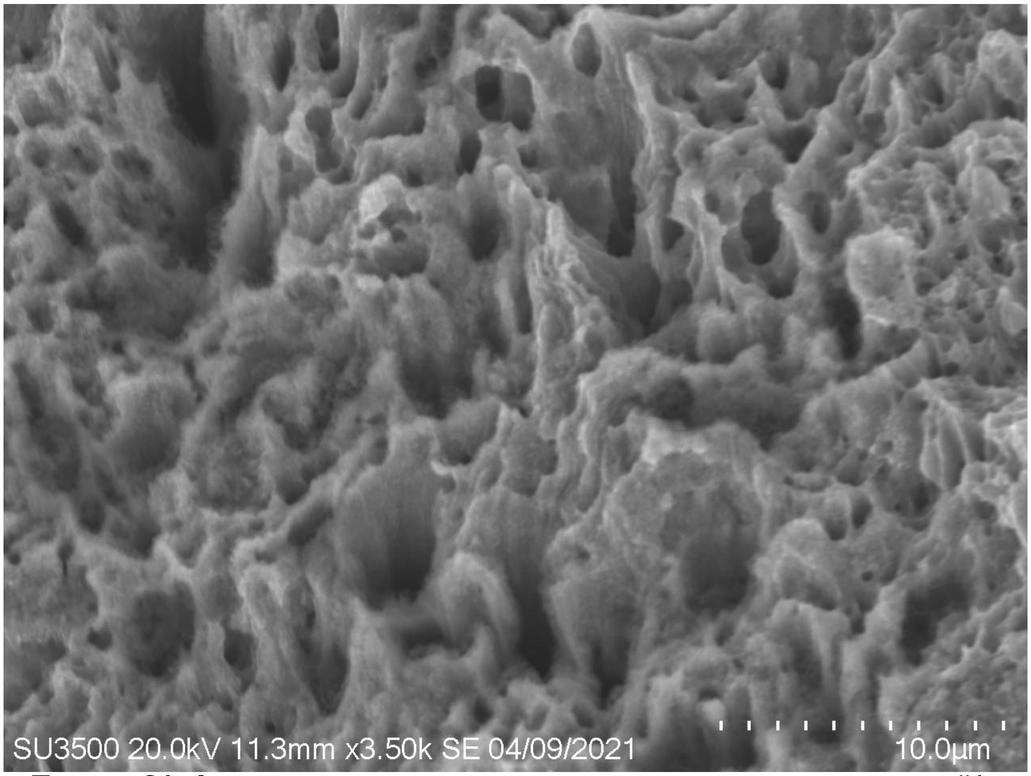

FIGURE 64: ANOTHER AREA OF THE FRACTURE SURFACE, STEEL WIRE #1, SAMPLE #1 AT HIGH MAGNIFICATION

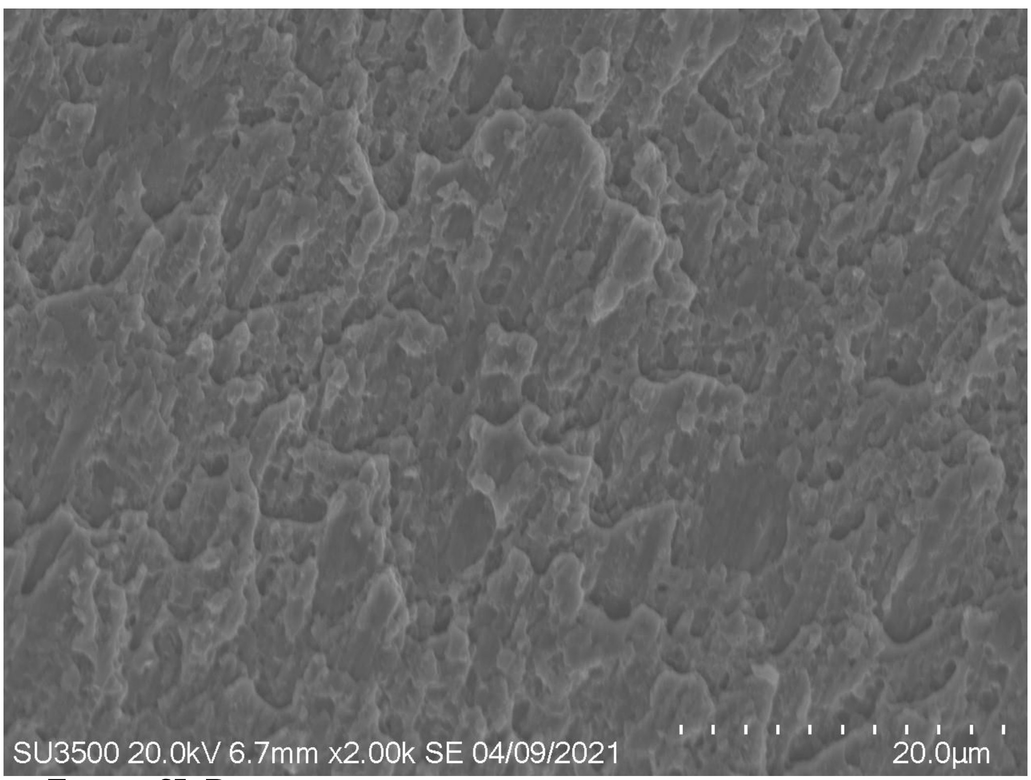

FIGURE 65: DIMPLES OBSERVED ON THE FRACTURE SURFACE OF STEEL WIRE #2 OF SAMPLE #1

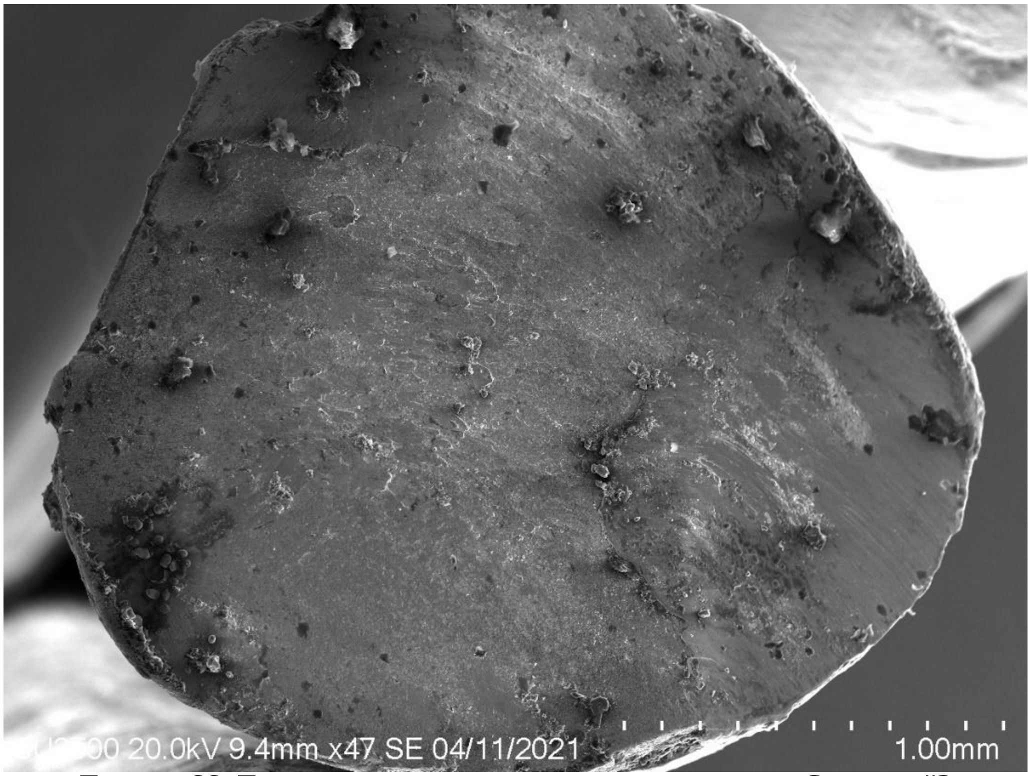

FIGURE 66: FRACTURE SURFACE OF STEEL WIRE FROM SAMPLE #2

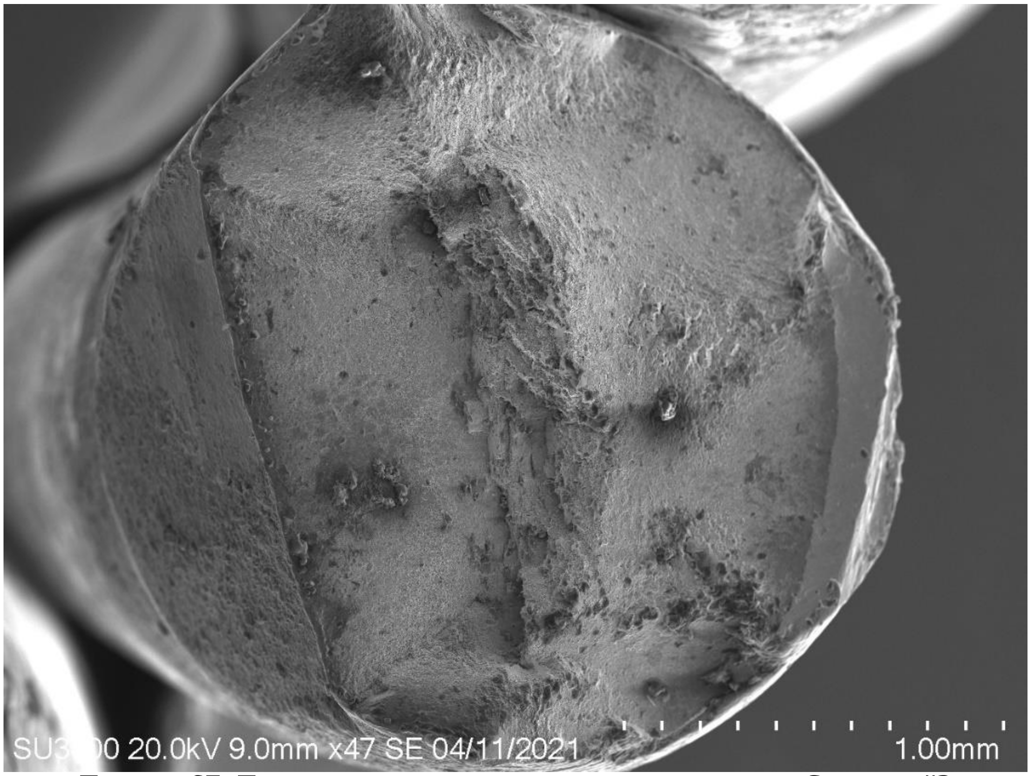

FIGURE 67: FRACTURE SURFACE OF STEEL WIRE FROM SAMPLE #3

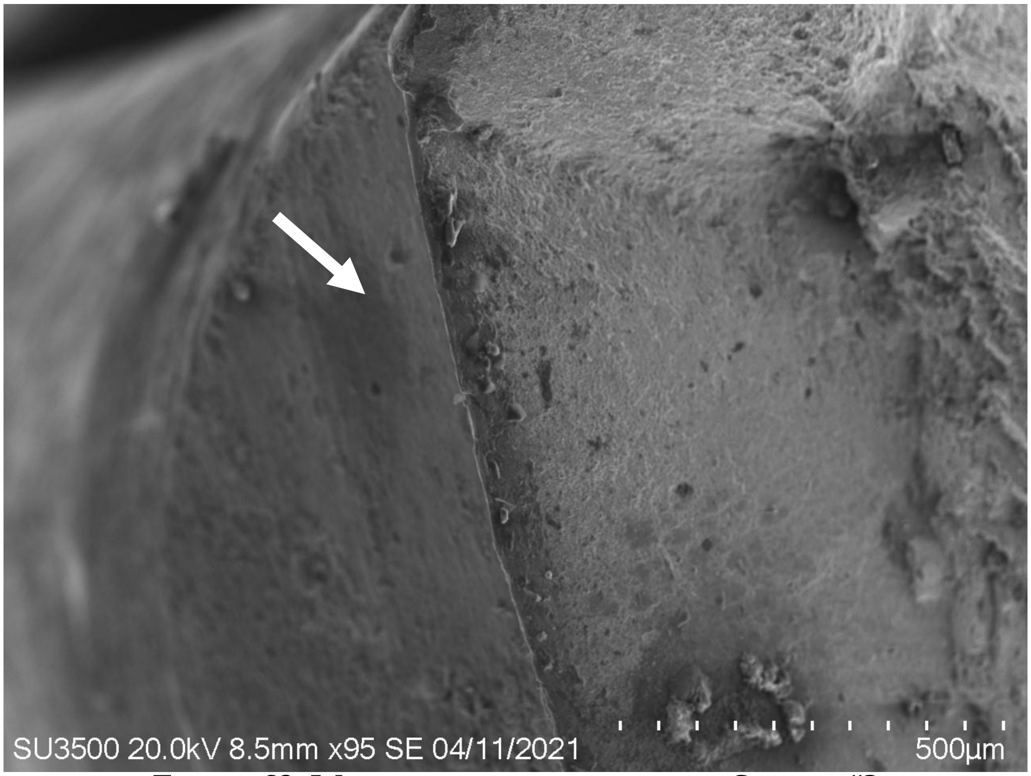

FIGURE 68: WEDGE ON THE STEEL WIRE OF SAMPLE #3

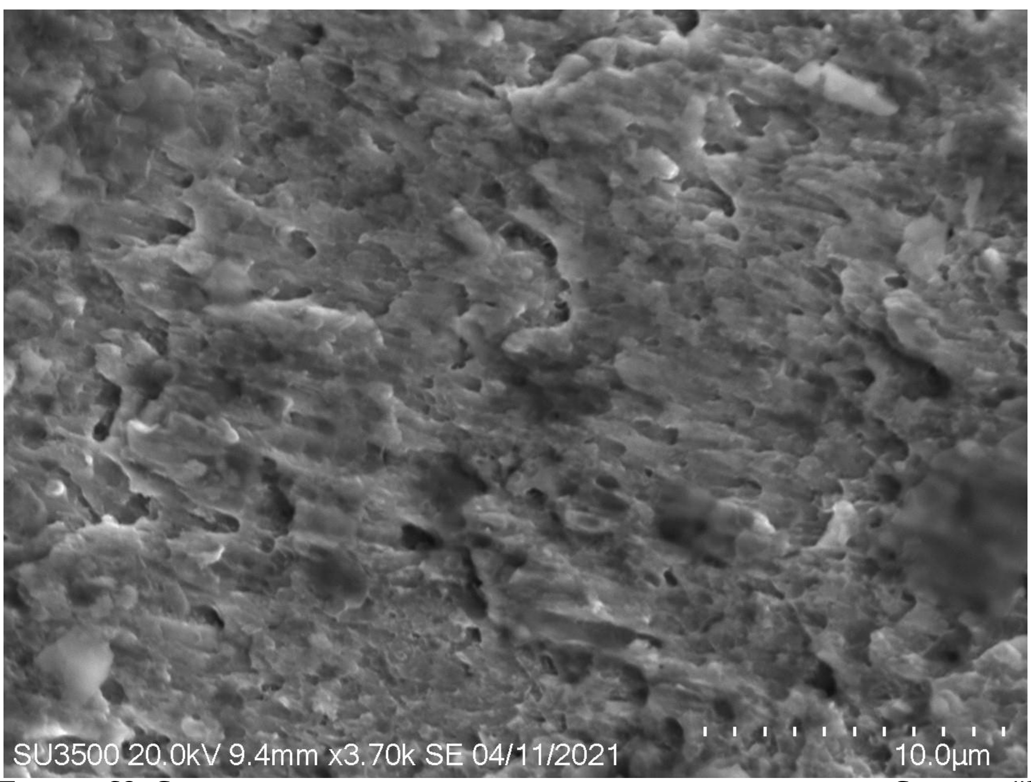

FIGURE 69: SHEAR DIMPLES ON FRACTURE SURFACE OF WIRE FROM SAMPLE #2

ACUREN

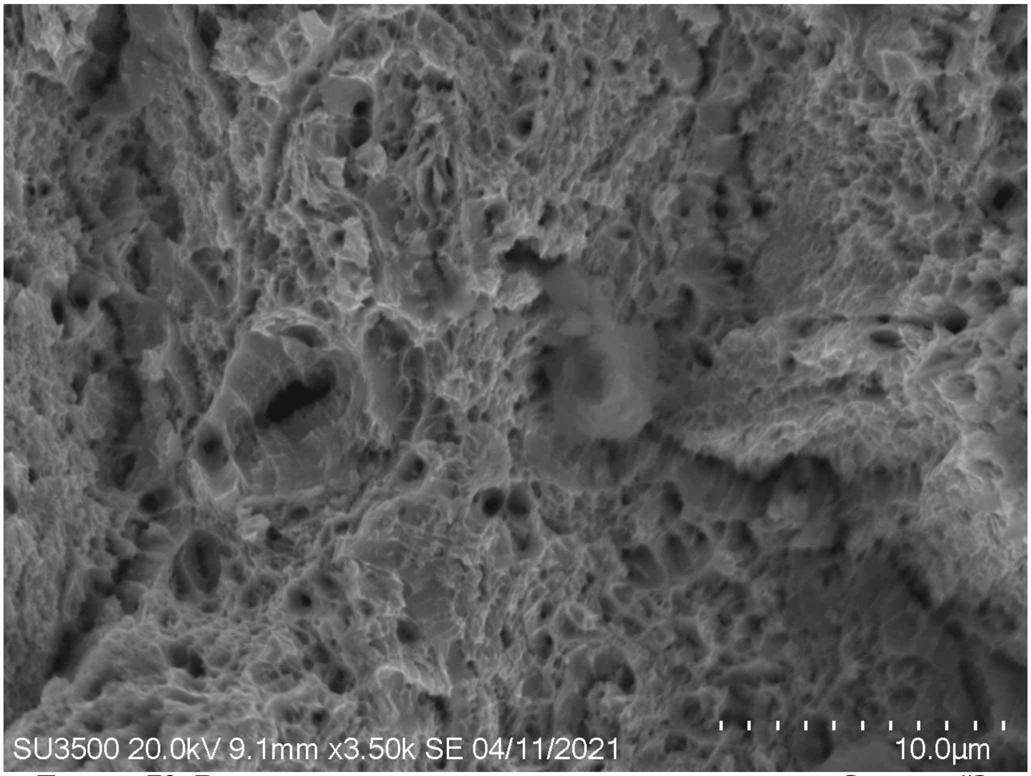

FIGURE 70: DIMPLES ON FRACTURE SURFACE OF WIRE FROM SAMPLE #2

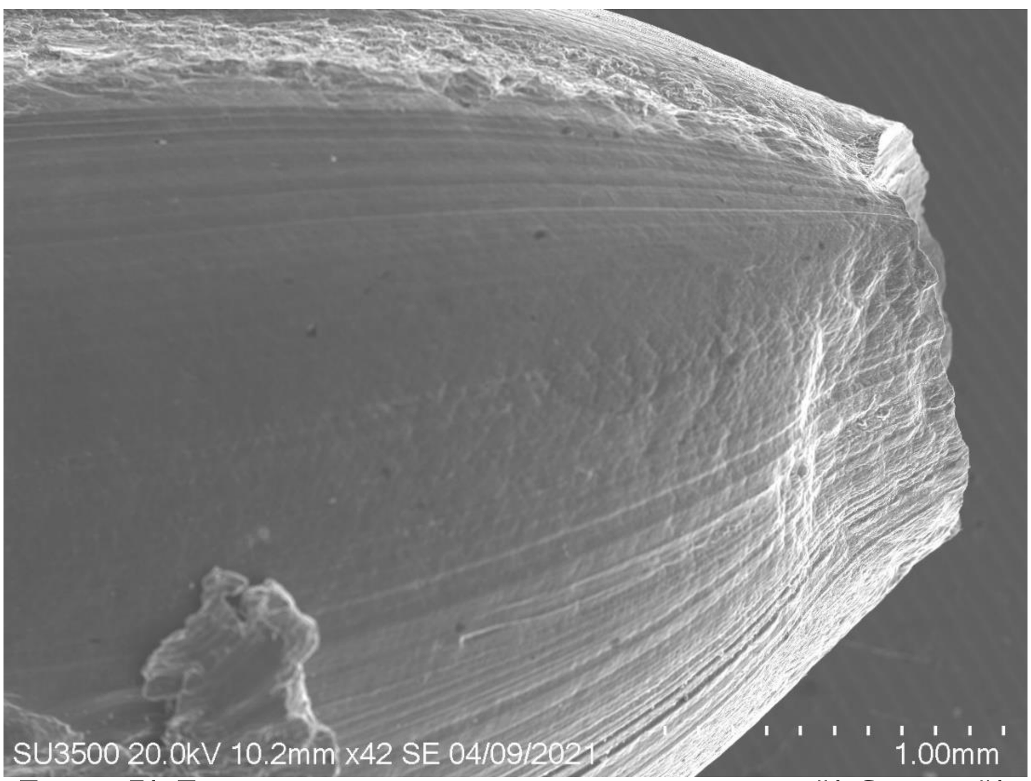

FIGURE 71: FRACTURE SURFACE PROFILE, ALUMINUM WIRE #1, SAMPLE #1

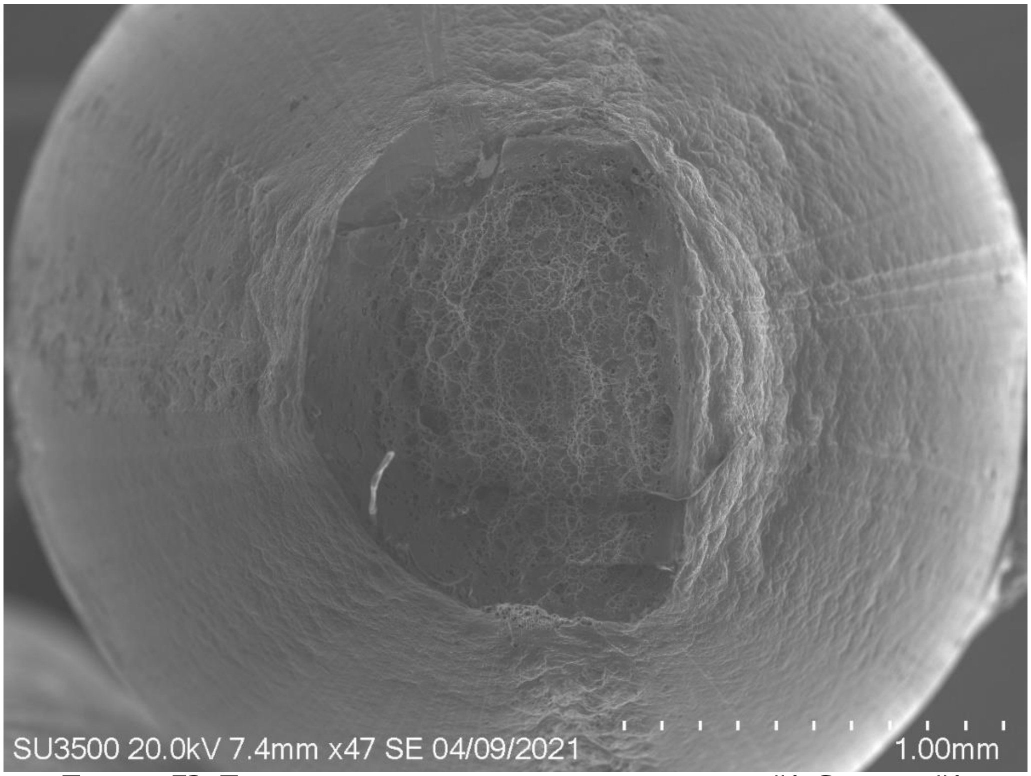

FIGURE 72: FRACTURE SURFACE OF ALUMINUM WIRE #1, SAMPLE #1

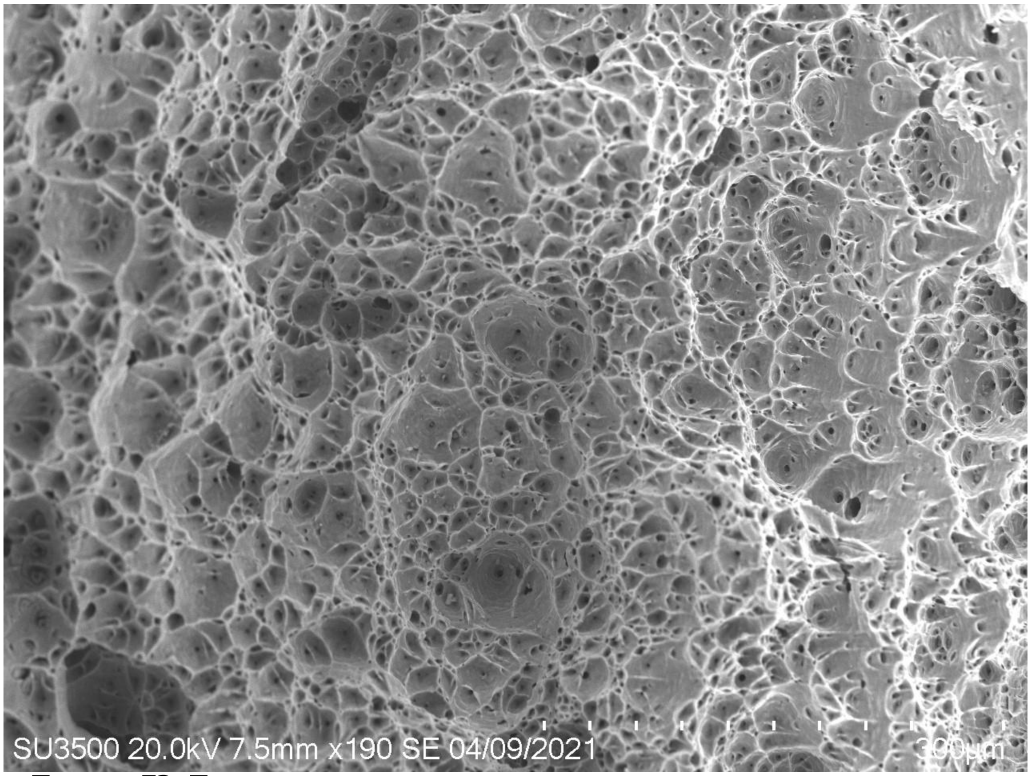

FIGURE 73: FINLEY DEVELOPED DIMPLES ON THE FRACTURE SURFACE OF ALUMINUM WIRE #1, SAMPLE #1

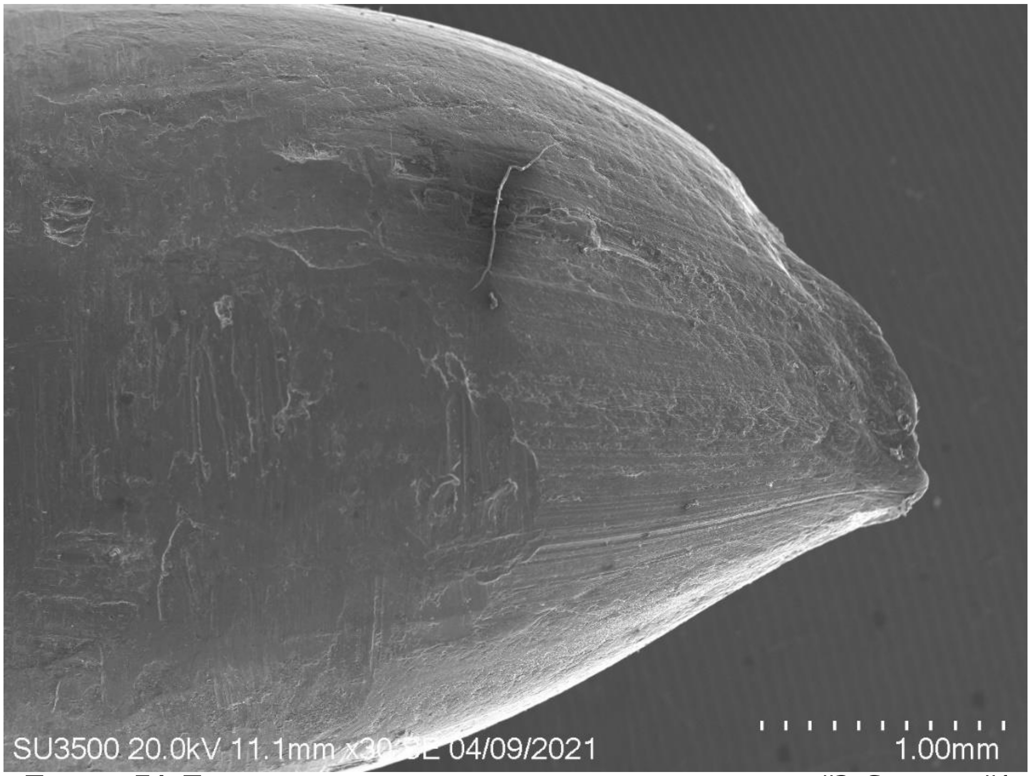

FIGURE 74: FRACTURE SURFACE PROFILE, ALUMINUM WIRE #2, SAMPLE #1

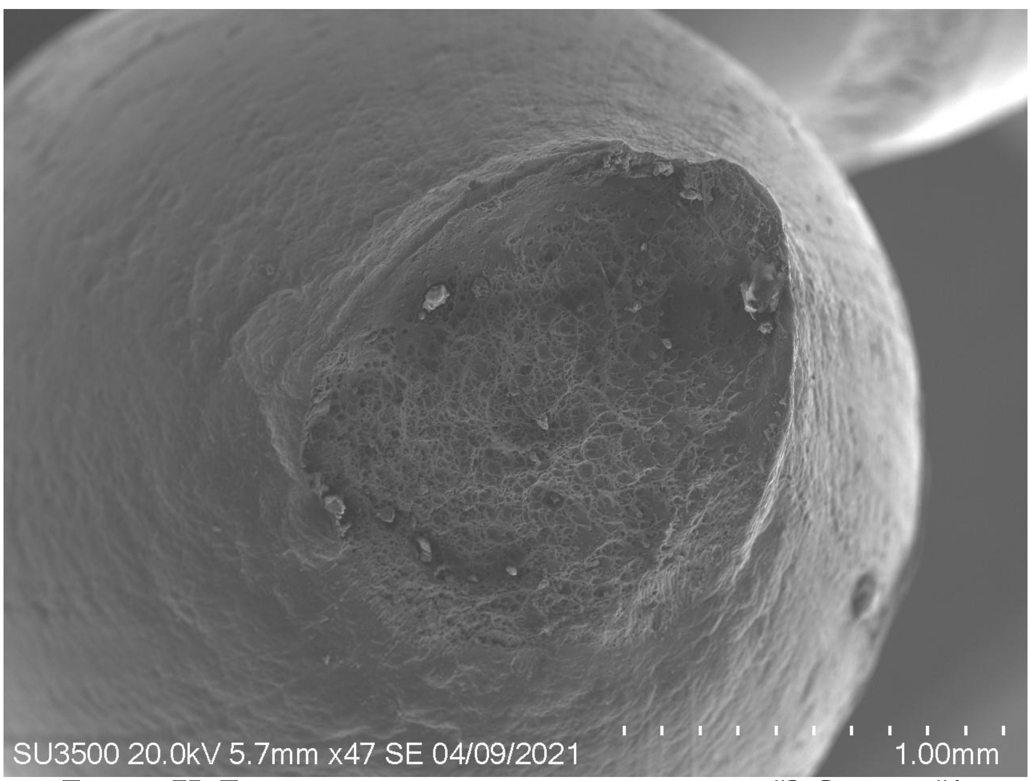

FIGURE 75: FRACTURE SURFACE OF ALUMINUM WIRE #2, SAMPLE #1

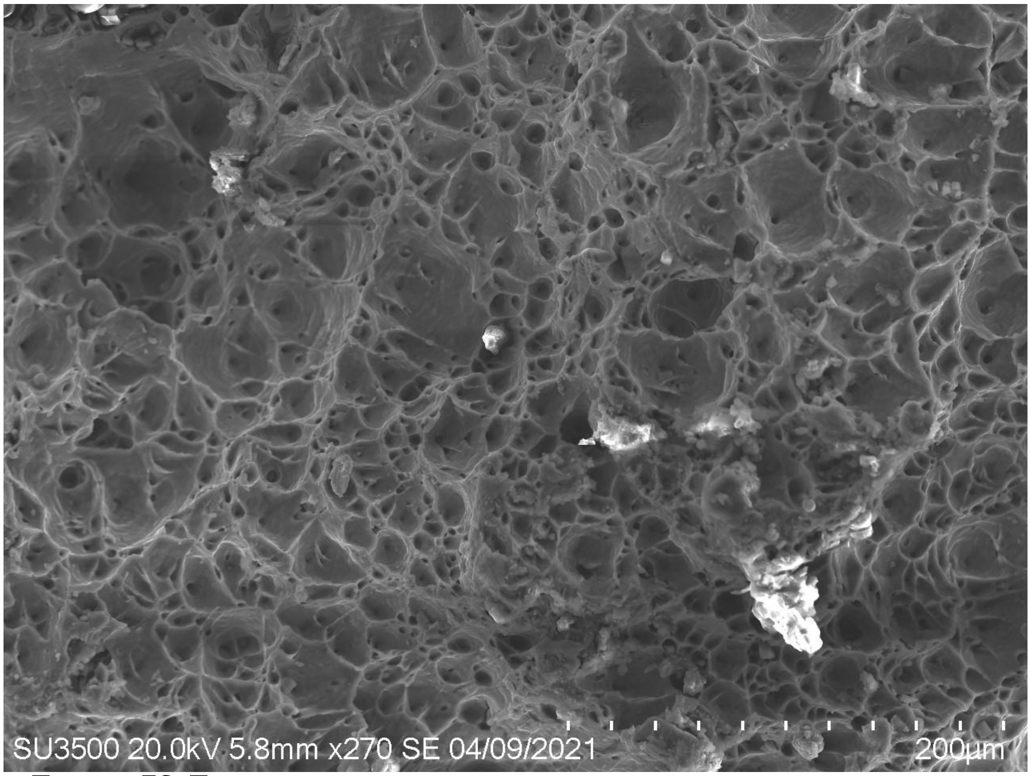

FIGURE 76: FINLEY DEVELOPED DIMPLES ON THE FRACTURE SURFACE OF ALUMINUM WIRE #2, SAMPLE #1

FIGURE 77: SIDE SURFACE OF ALUMINUM WIRE #2, SAMPLE #1

ACUREN

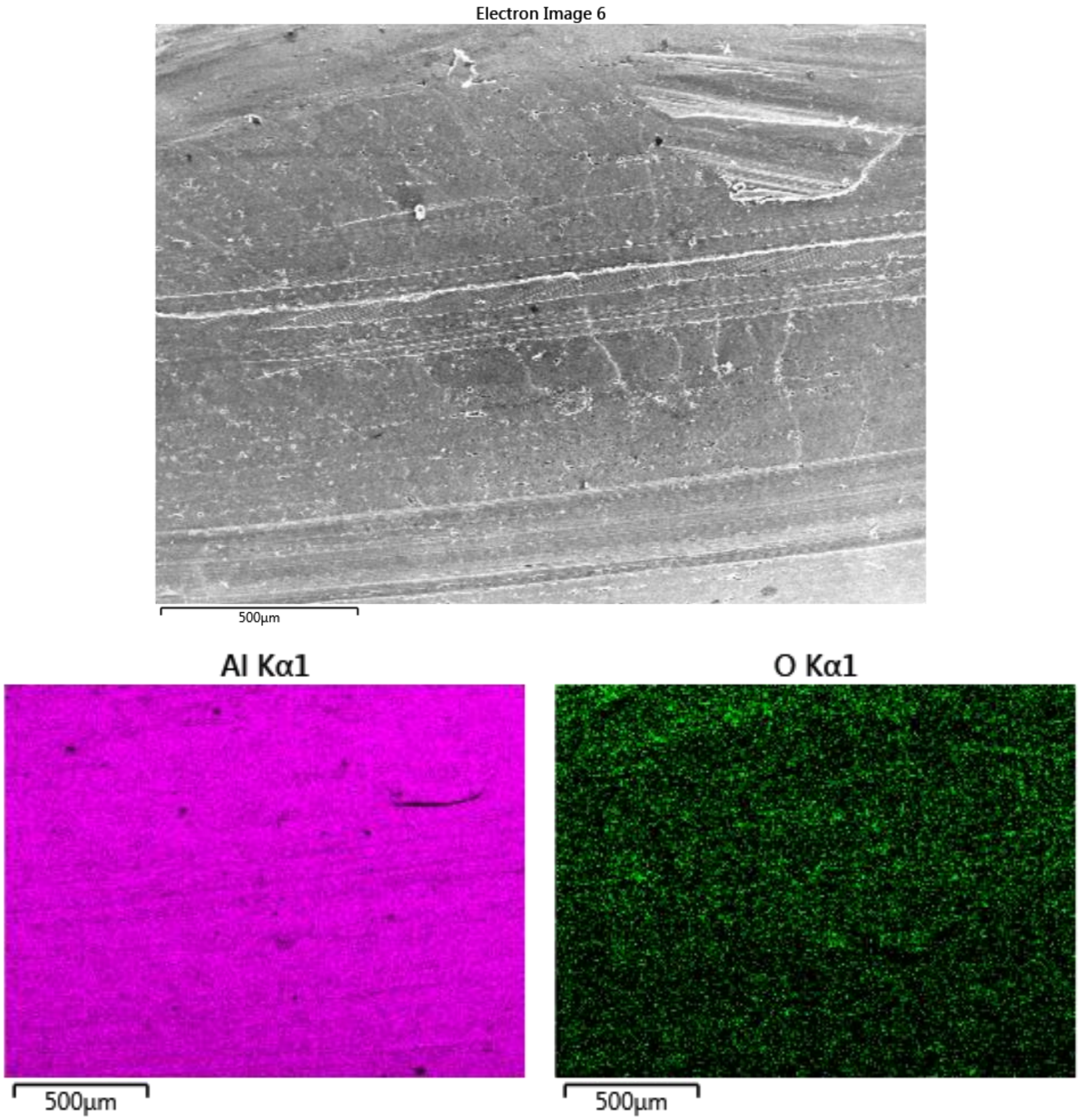

FIGURE 78: EDS MAP OF THE AREA IN FIGURE 76, WIRE #2, SAMPLE #1

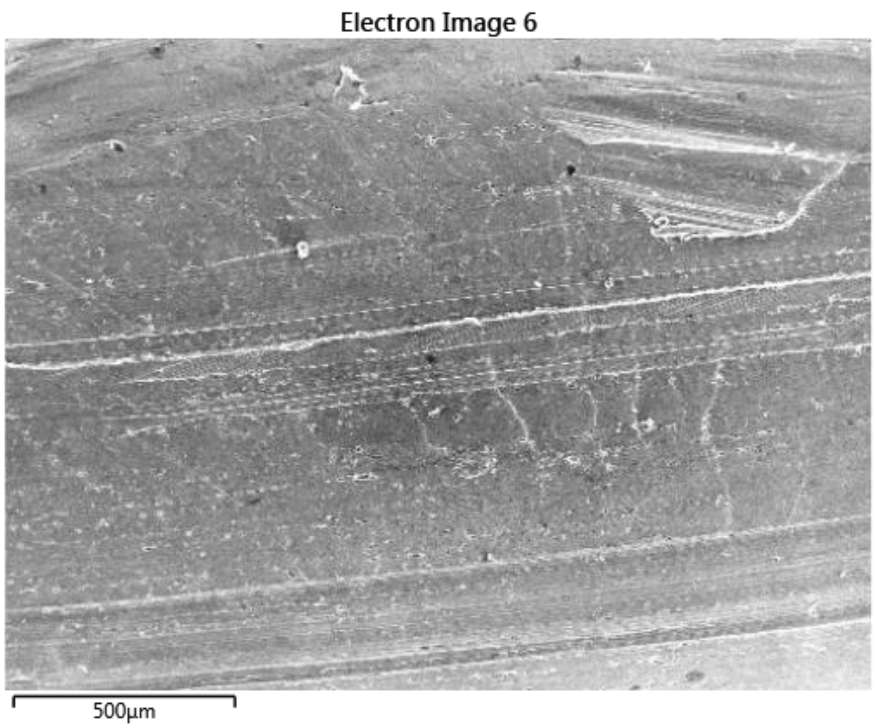

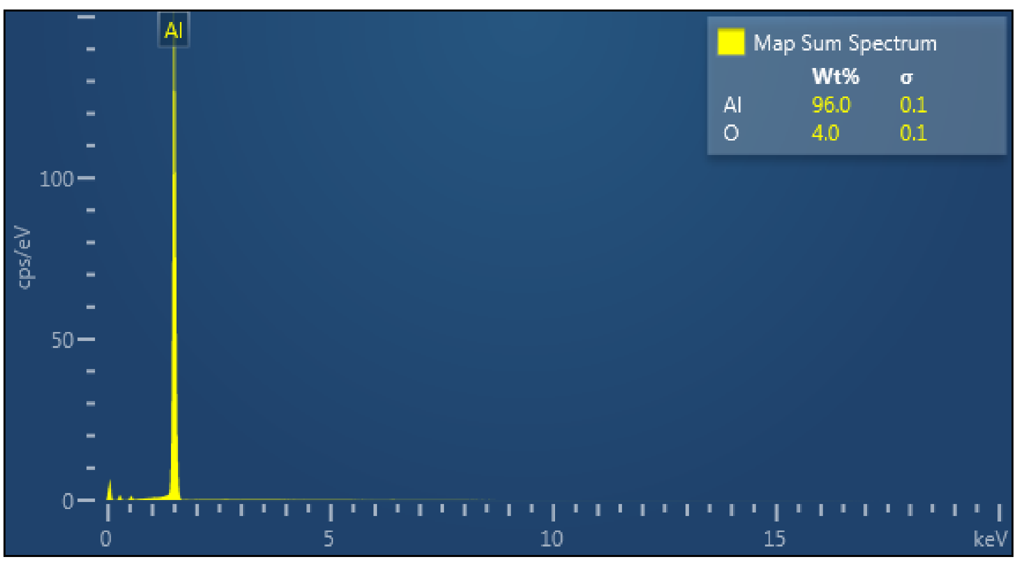

FIGURE 79: EDS ANALYSIS RESULTS OF WIRE #2, SAMPLE #1

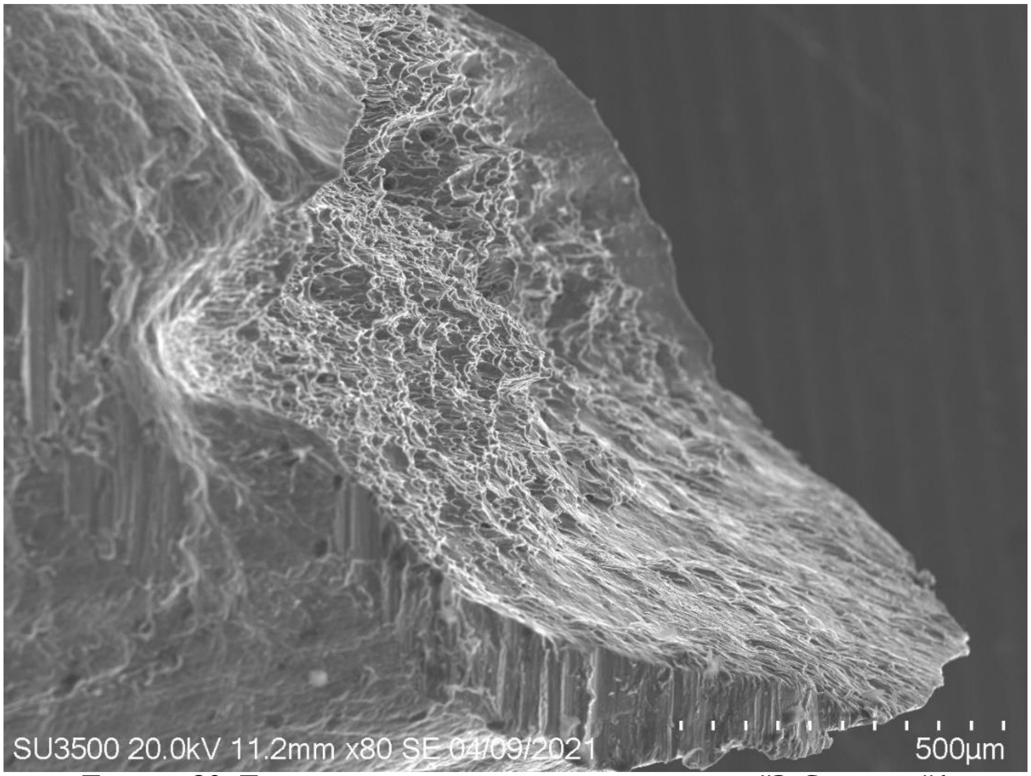

FIGURE 80: FRACTURE SURFACE, ALUMINUM WIRE #3, SAMPLE #1

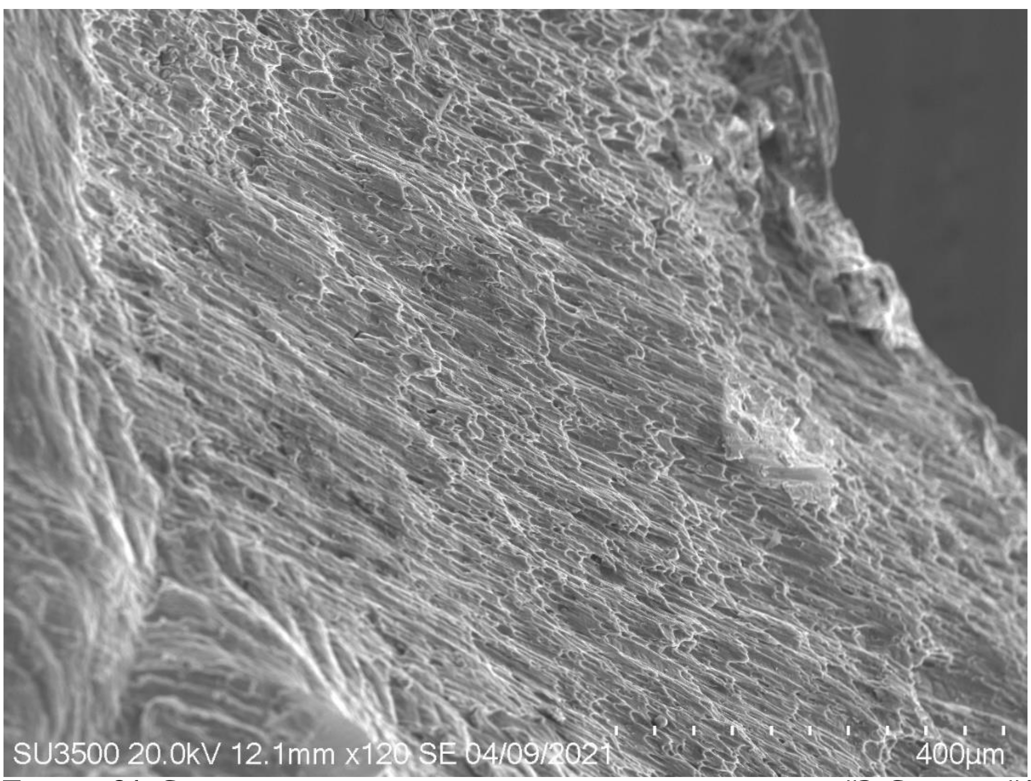

FIGURE 81: SHEAR DIMPLES ON THE FRACTURE SURFACE, WIRE #3, SAMPLE #1

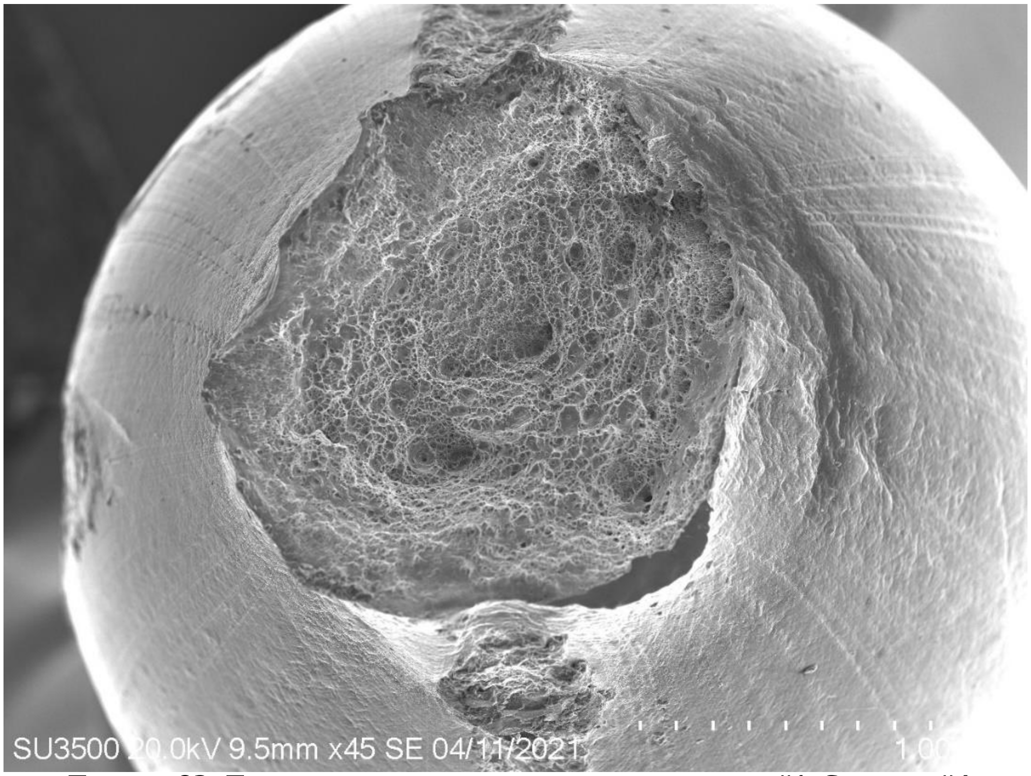

FIGURE 82: FRACTURE SURFACE OF ALUMINUM WIRE #1, SAMPLE #4

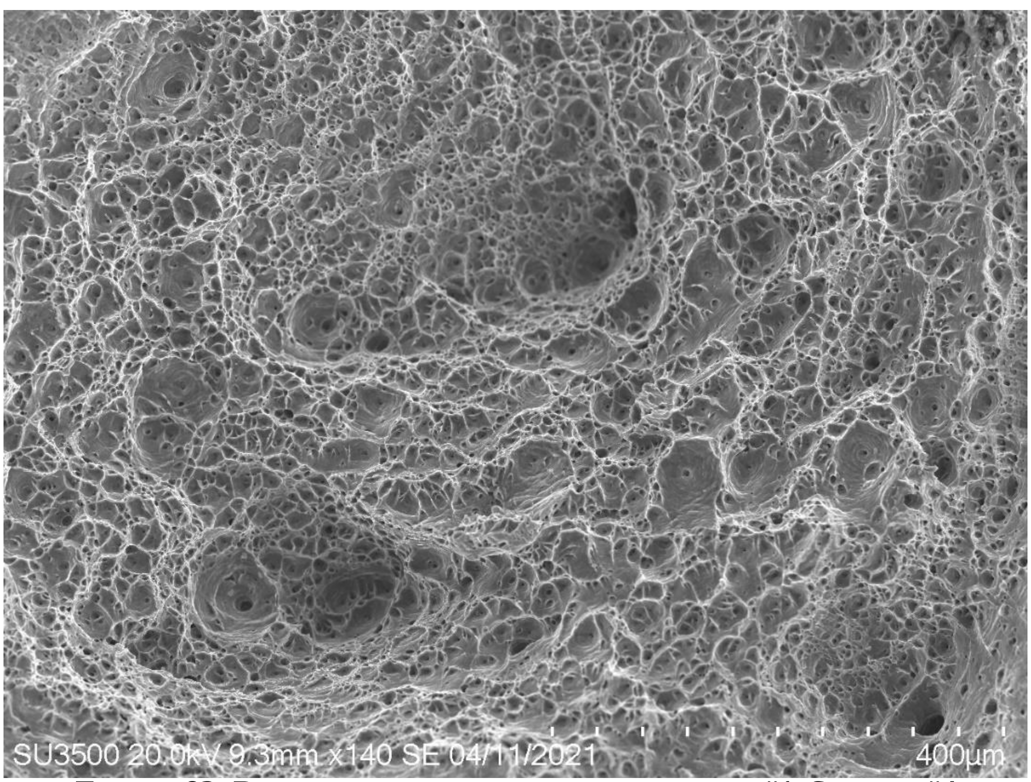

FIGURE 83: DIMPLES ON FRACTURE SURFACE, WIRE #1, SAMPLE #4

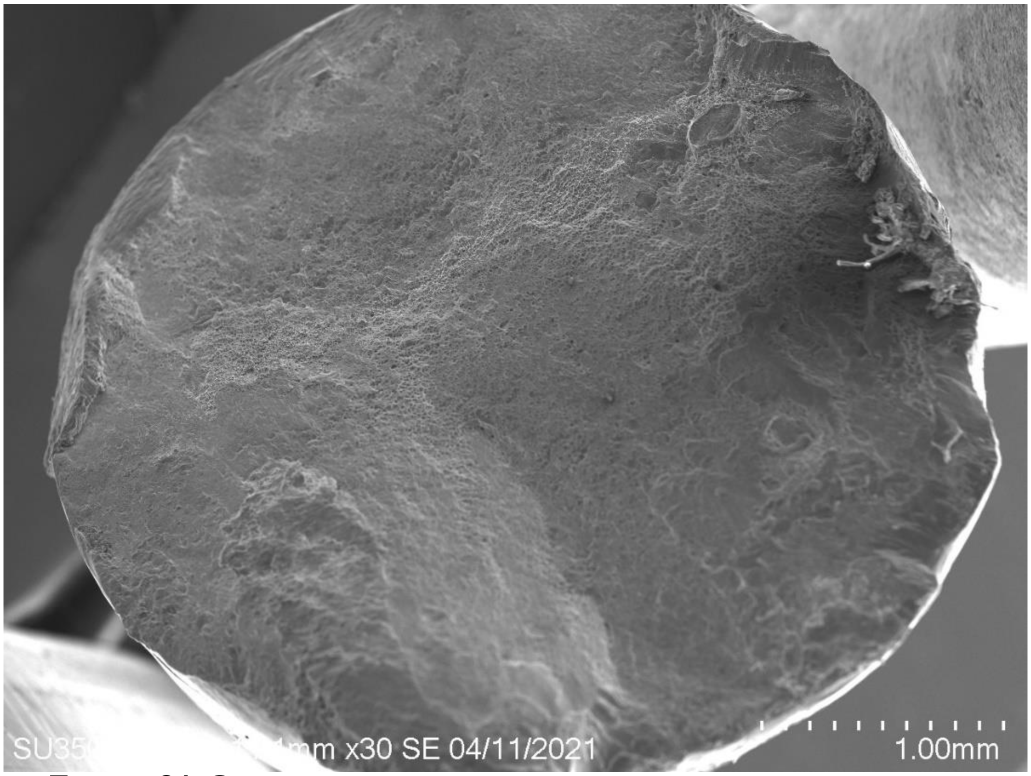

FIGURE 84: ONE OF THE ALUMINUM WIRES THAT SHEARED, FRACTURE SURFACE, SAMPLE #4

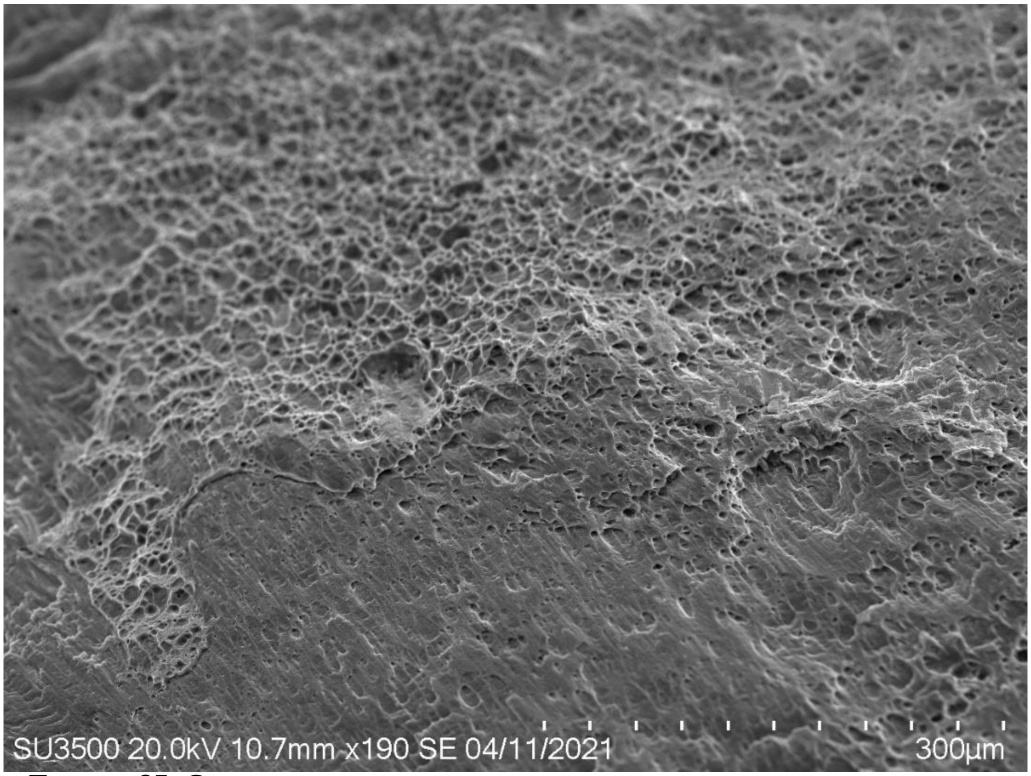

FIGURE 85: SHEAR DIMPLES ON FRACTURE SURFACE OF ALUMINUM WIRE, SAMPLE #4

5.0 METALLOGRAPHIC EXAMINATION

We have removed the steel wires with fracture surfaces from Sample #1,2 and 3. The steel wires were mounted in Bakelite, ground and polished in accordance with ASTM E3-11. Figure 86 and Figure 87 showed profiles of steel wires from sample #1. Wires were coated and coating appeared to have two layers, Figure 88. Coating appeared to be peeled off in some areas at low magnification, Figure 86 and Figure 87. However, examination at higher magnification revealed that these areas were stained during metallographic preparation, Figure 89 and Figure 90. It also showed some particles embedded in the coating, Figure87. We have performed EDS analysis on the coating, Figure 91. Mapping revealed zinc and sodium indicating that it was zinc coated (galvanized). Further tests on the galvanized layer revealed that the appearance on two layers were false (possibly small amount of concentration difference of sodium) and all the galvanized layer was homogeneous in zinc content, Figure 92. It is also indicated from the figure that the top layer contained some imperfections, while the bottom portion was pure galvanized layer. Figure 93 shows the elemental analysis of the galvanized layer.

Figure 94 through Figure 98 show the wire end (cut) or fracture profiles. Figure 97 shows a wire end that was deformed during cutting and covered by smeared zinc coating. Figure 99 shows close view of the corner of the fracture surface initiated in Figure 95.

Profiles of the undamaged fracture surface were generally flat and had no discernible necking. Close view of the profile revealed relatively rough, transgranular crack propagation, Figure 100. We observed numerous cracks in the galvanize layer in the vicinity of the fracture surface, Figure 95.

The steel samples were etched with 2% nital to reveal the microstructure. Figure 101 shows a typical cross section of a steel wire. The steel wires showed a completely deformed grain structure, heavily elongated in the longitudinal direction of the wire, Figure 102 and Figure 103. Figure 104 and Figure 105 show a couple of wire end (cut end) profiles after etching. Flow lines show the wires deformed during cutting. Figure 106 and Figure 107 show close view of the top corner of the wire end profile depicted in Figure 105. Flatness of the fracture profile at that corner and abrupt change of flow line direction is the evidence of cutting at that corner, Figure 107. It should be noted that the areas beneath galvanized layers did not etch. This is a common behaviour of materials due to presence of zinc in the vicinity.

We have examined the microstructure of the aluminium wires as well/ We have prepared metallographic samples of the following wires:

i. Sample #1 aluminium wire #1 (wires are numbered arbitrarily);
ii. Sample #1 aluminium wire #2;
iii. Sample #2 aluminium wire #1;
iv. Sample #2 aluminium wire #2;
v. Sample #2 aluminium wire #3 (this wire was cut);

vi. Sample #4 aluminium wire #2;
vii. Sample #4 aluminium wire #2;

Figure 108 and Figure 109 show fracture profiles of two aluminium wires. Local deformation in the vicinity of the fracture and high local reduction of area are evident.

Figure 110 shows a very flat and smooth profile. The sample were etched with Keller's reagent after the examination in the as-polished condition. Figure 111 and Figure 112 show the profiles of two wires. Flow lines in the longitudinal direction of the wires were evident. Figure 113 show profile of the wire with damage during cutting. Figure 114 shows the structure at a higher magnification. Flow lines were evident; however, grain boundaries could not be observed. Appearance of the structure suggested that the etchant also attacked the deformed material created during grinding of the samples showing dotted straight lies.

Figure 115, Figure 116 and Figure 117 show the close view of the fracture profiles. It was evident that the fracture was ductile transgranular.

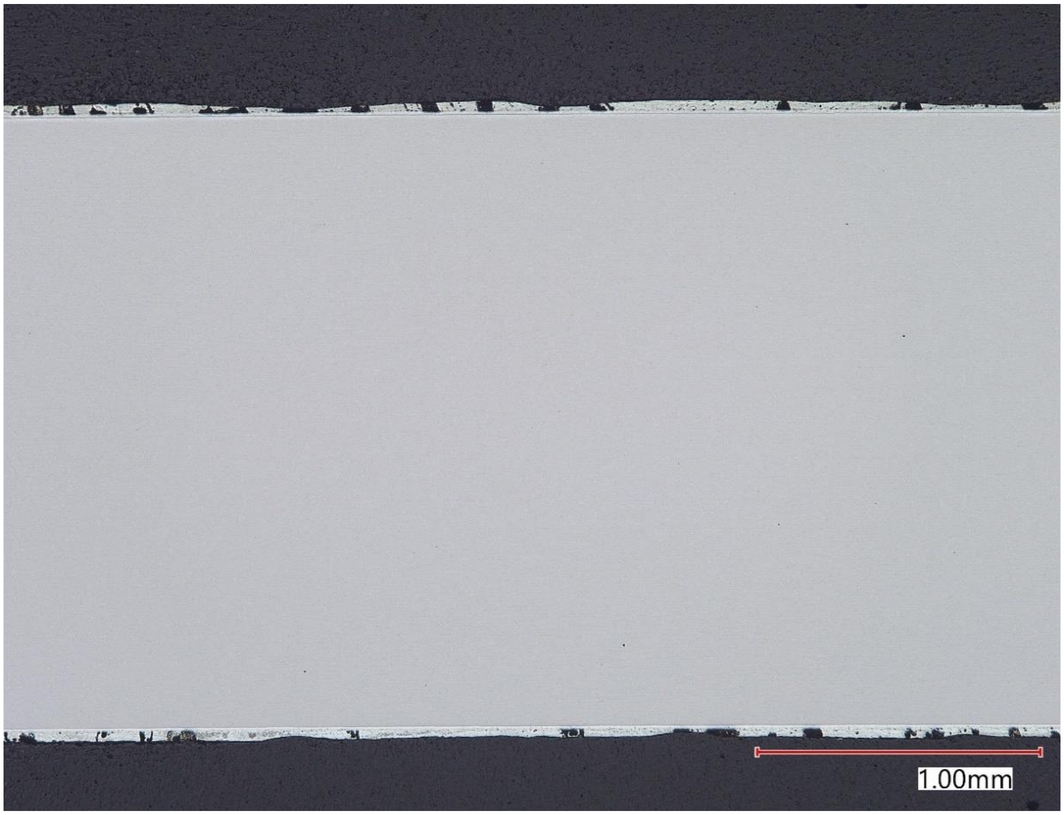

FIGURE 86. PROFILE OF STEEL WIRE #1, SAMPLE #1, AS-POLISHED

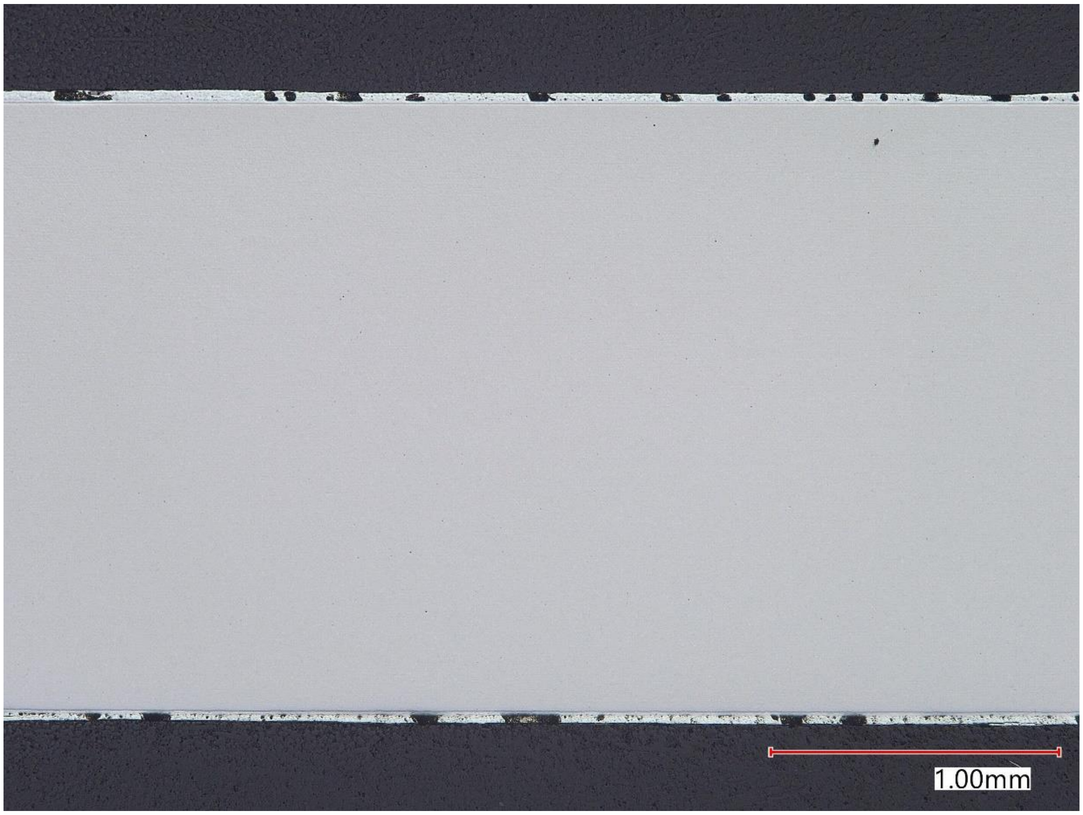

FIGURE 87. PROFILE OF STEEL WIRE #2, SAMPLE #1, AS-POLISHED

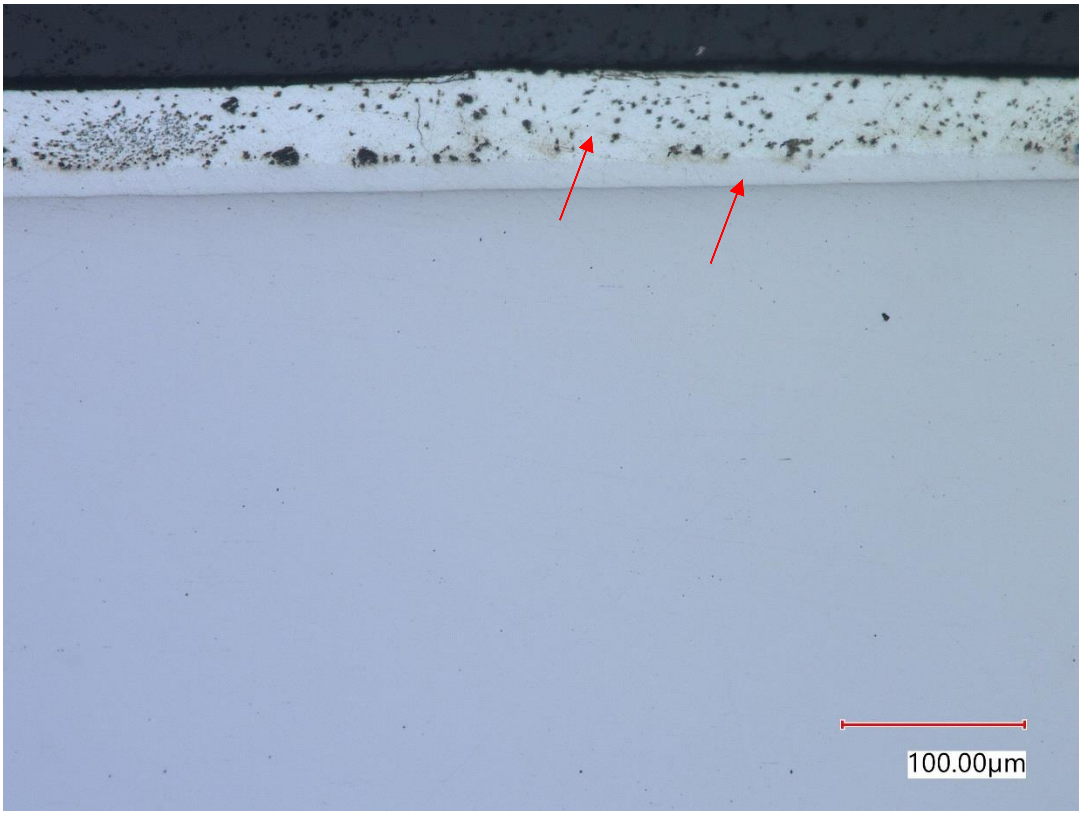

FIGURE 88. CLOSE VIEW OF COATING ON STEEL WIRE. STEEL WIRE #1 SAMPLE #3, AS-POLISHED

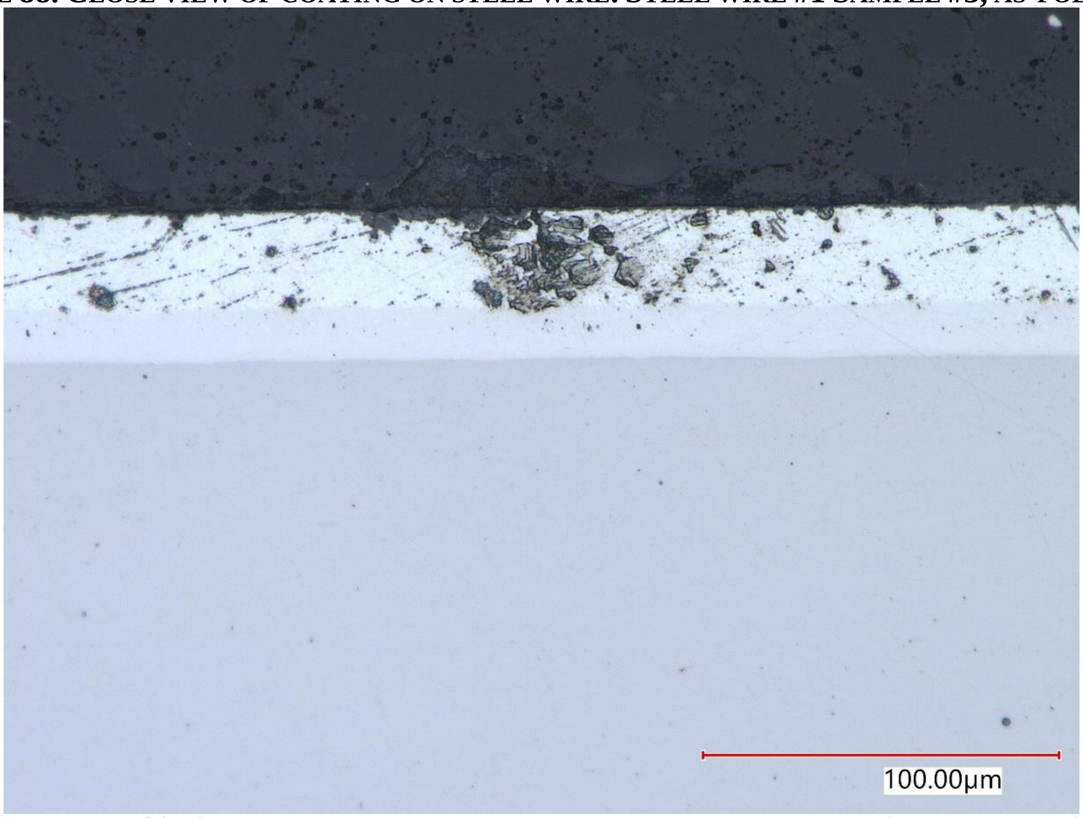

FIGURE 89. CLOSE VIEW OF THE DARK REGION IN THE COATING. STEEL WIRE #1 SAMPLE #1, AS-POLISHED

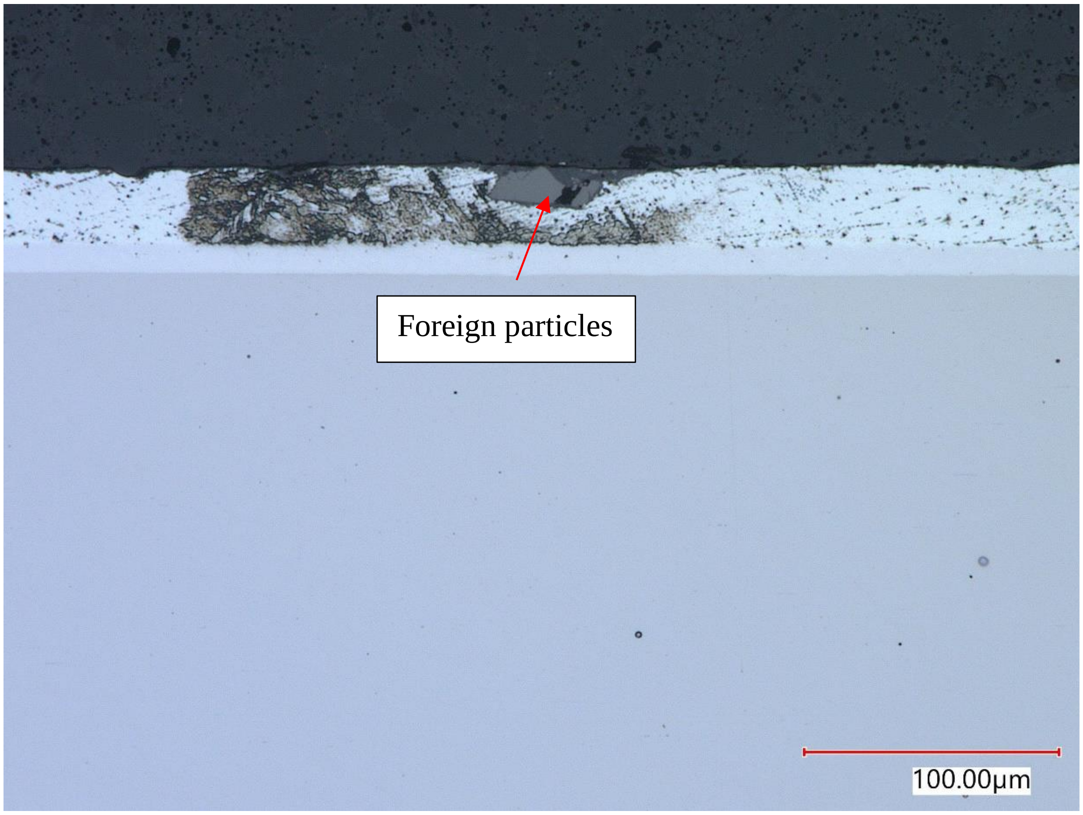

FIGURE 90. CLOSE VIEW OF THE DARK REGION IN THE COATING. STEEL WIRE #1 SAMPLE #2, AS-POLISHED

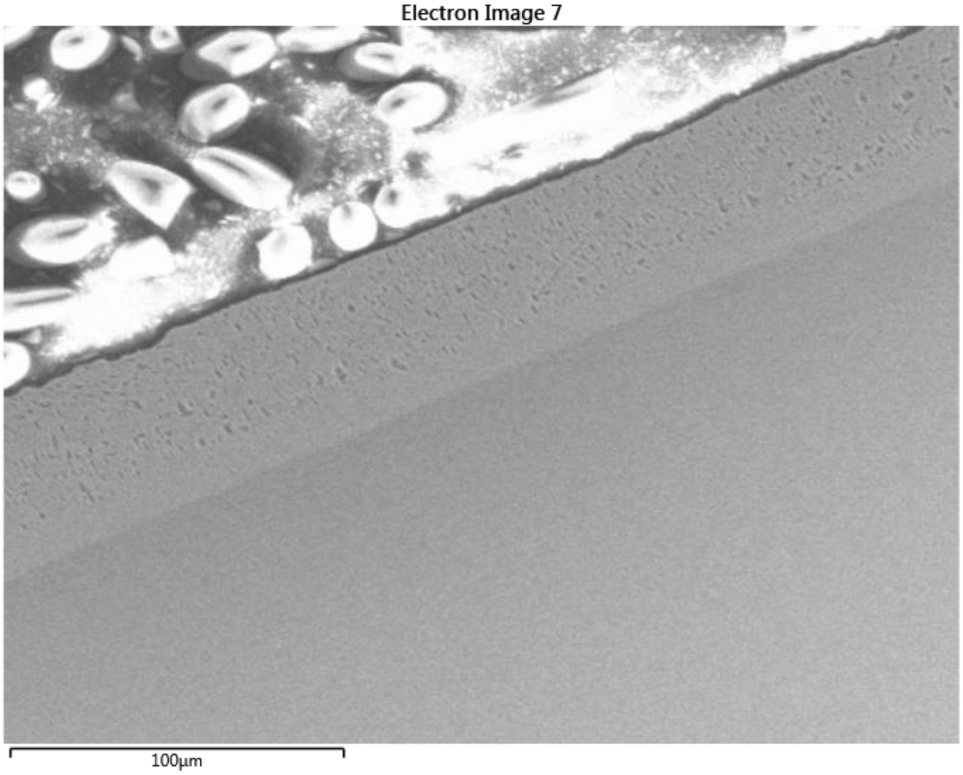

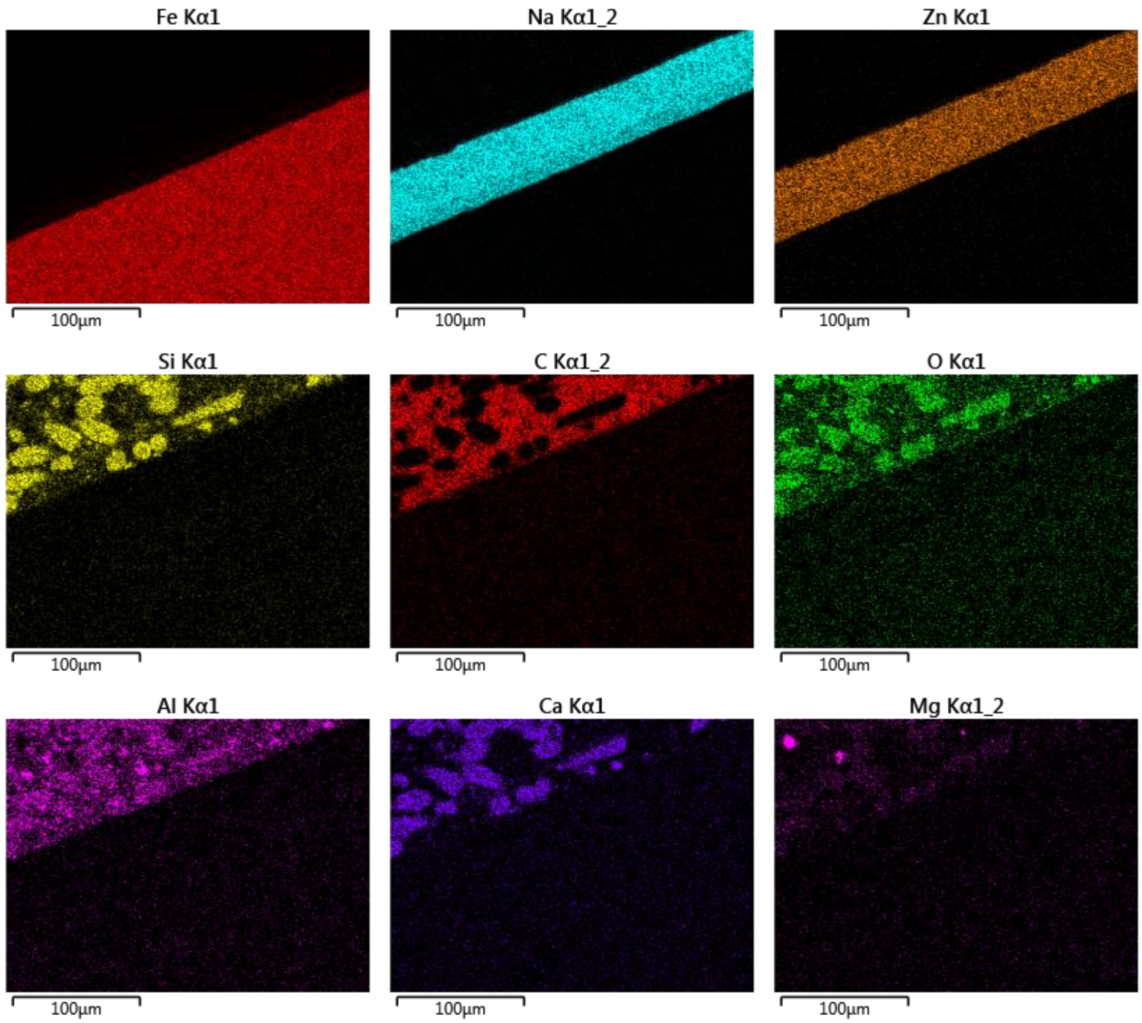

FIGURE 91. EDS MAPPING OF THE COATING

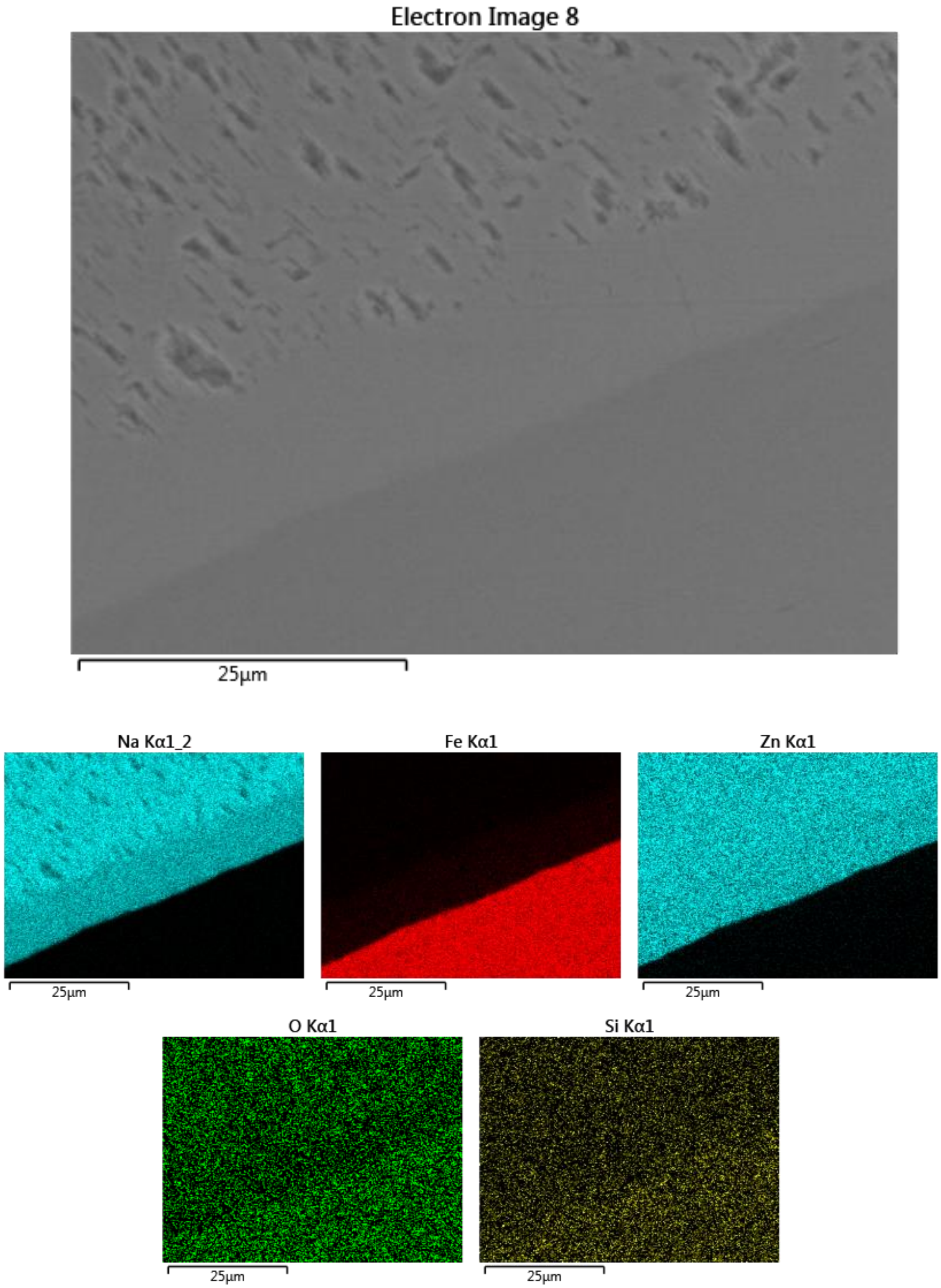

FIGURE 92. EDS MAPPING ON THE APPARENT BOTTOM LAYER OF THE COATING

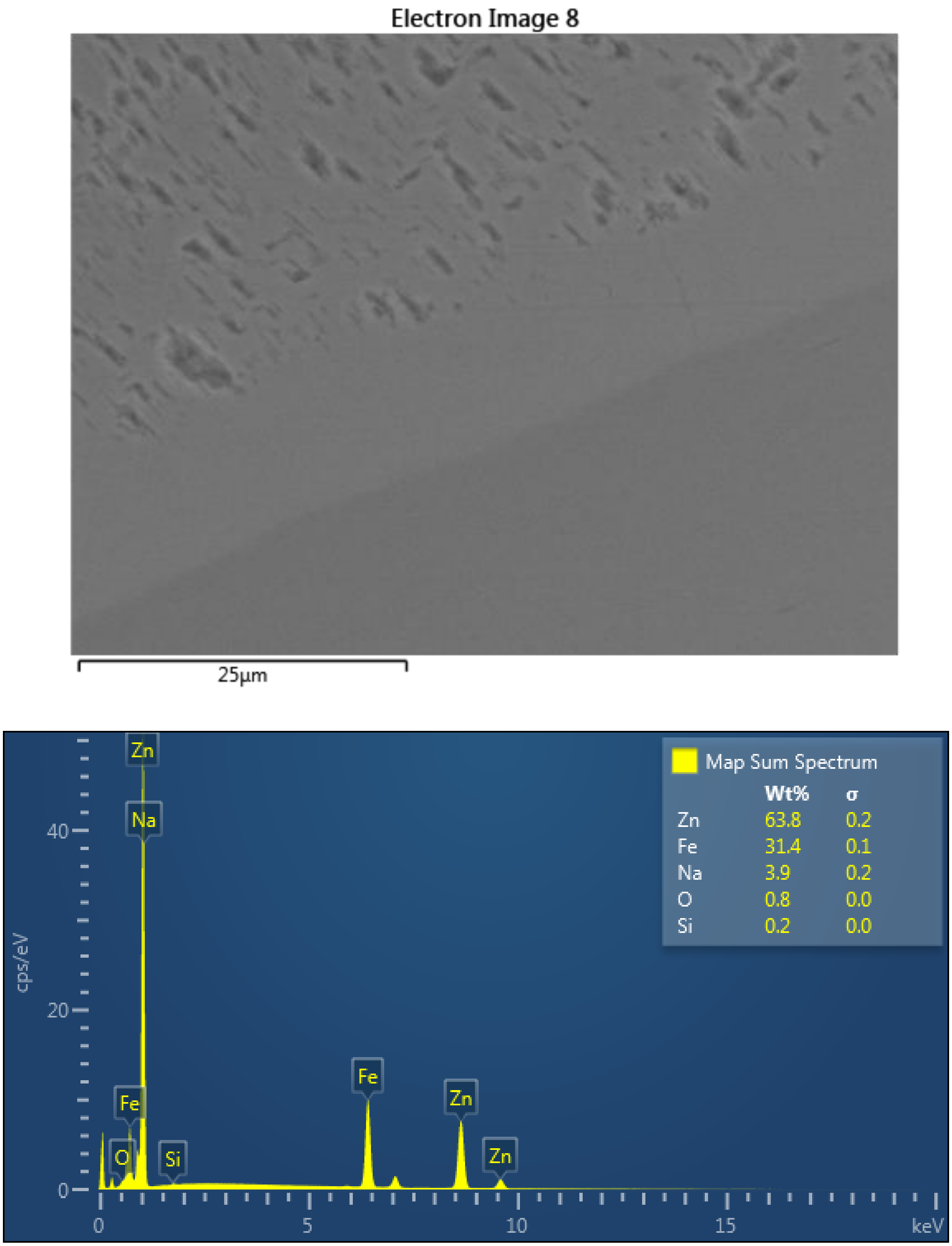

FIGURE 93. POINT EDS RESULTS OF THE GALVANIZED LAYER

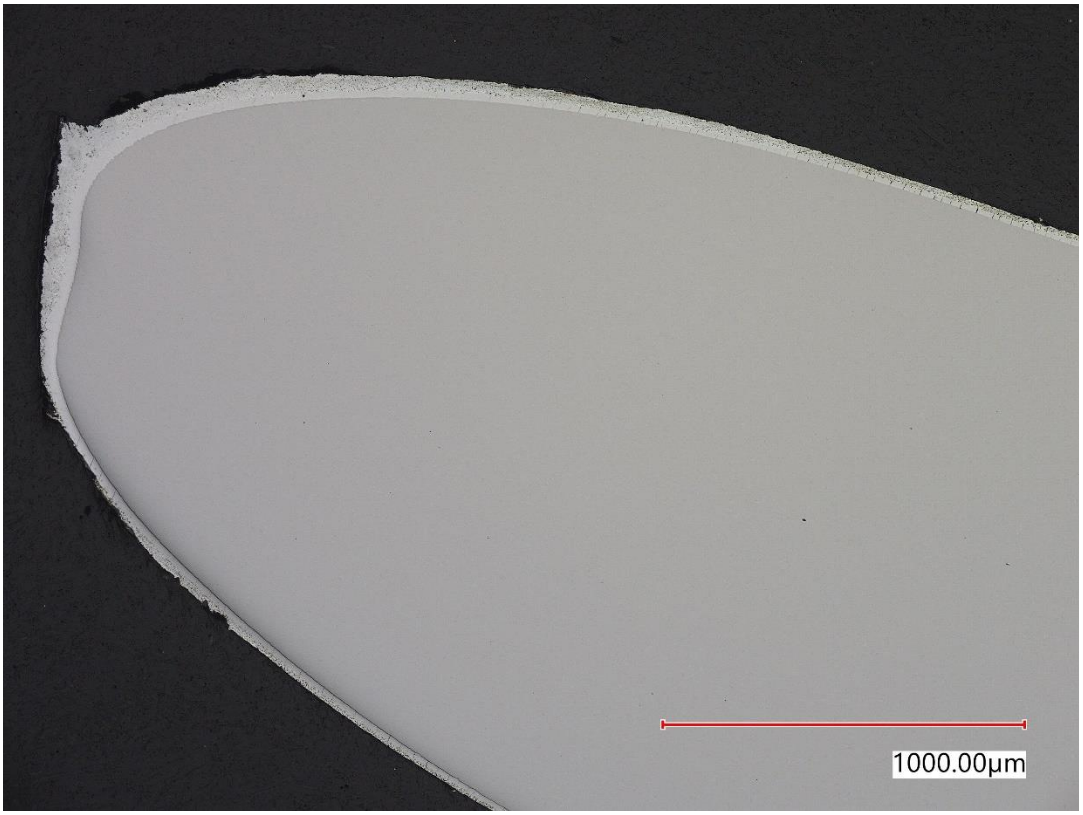

FIGURE 94. WIRE END PROFILE. STEEL WIRE #1 SAMPLE #1. AS-POLISHED

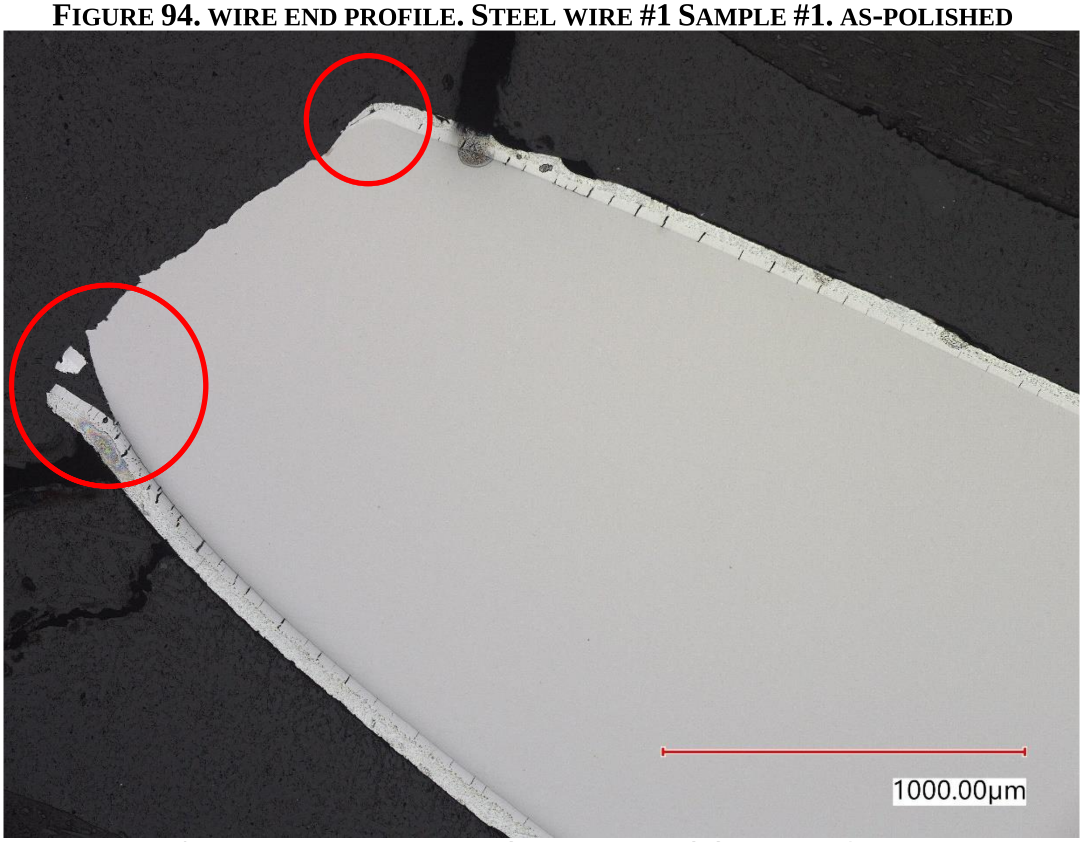

FIGURE 95. FRACTURE PROFILE. STEEL WIRE #2 SAMPLE #1. AS-POLISHED

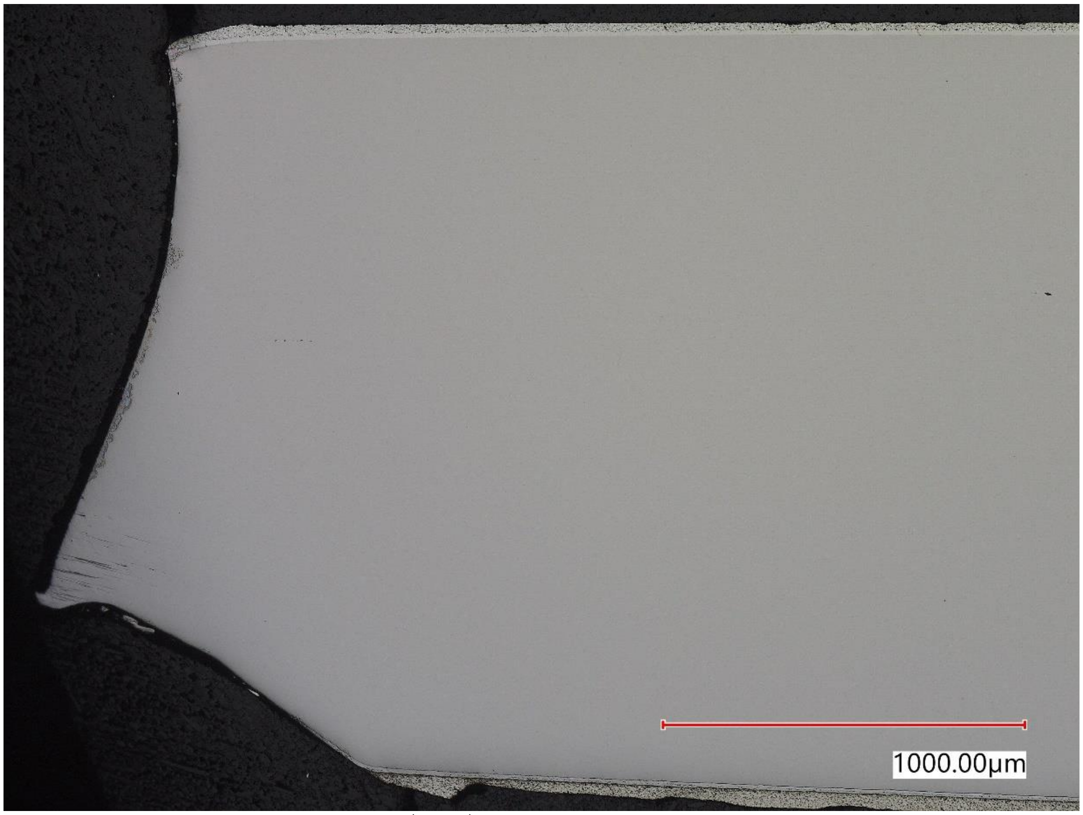

FIGURE 96. WIRE END (CUT) PROFILE. STEEL WIRE #2. AS-POLISHED

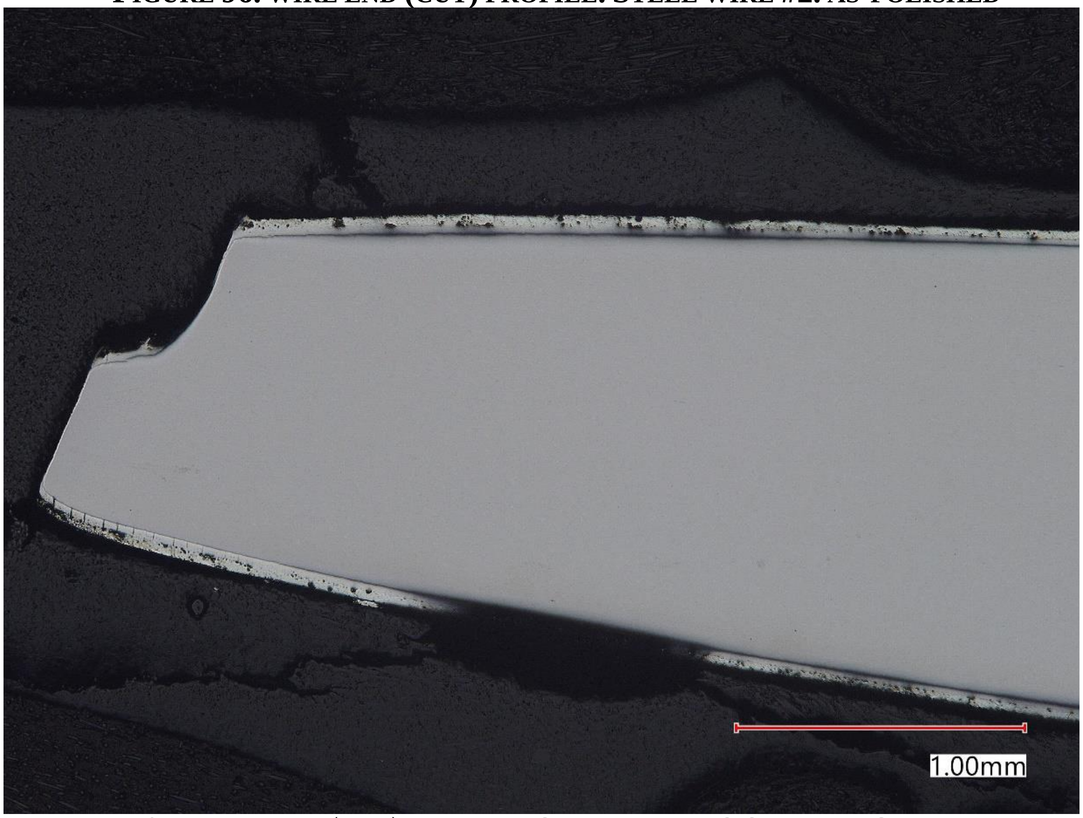

FIGURE 97. WIRE END (CUT) PROFILE. STEEL WIRE #2 SAMPLE #3. AS-POLISHED

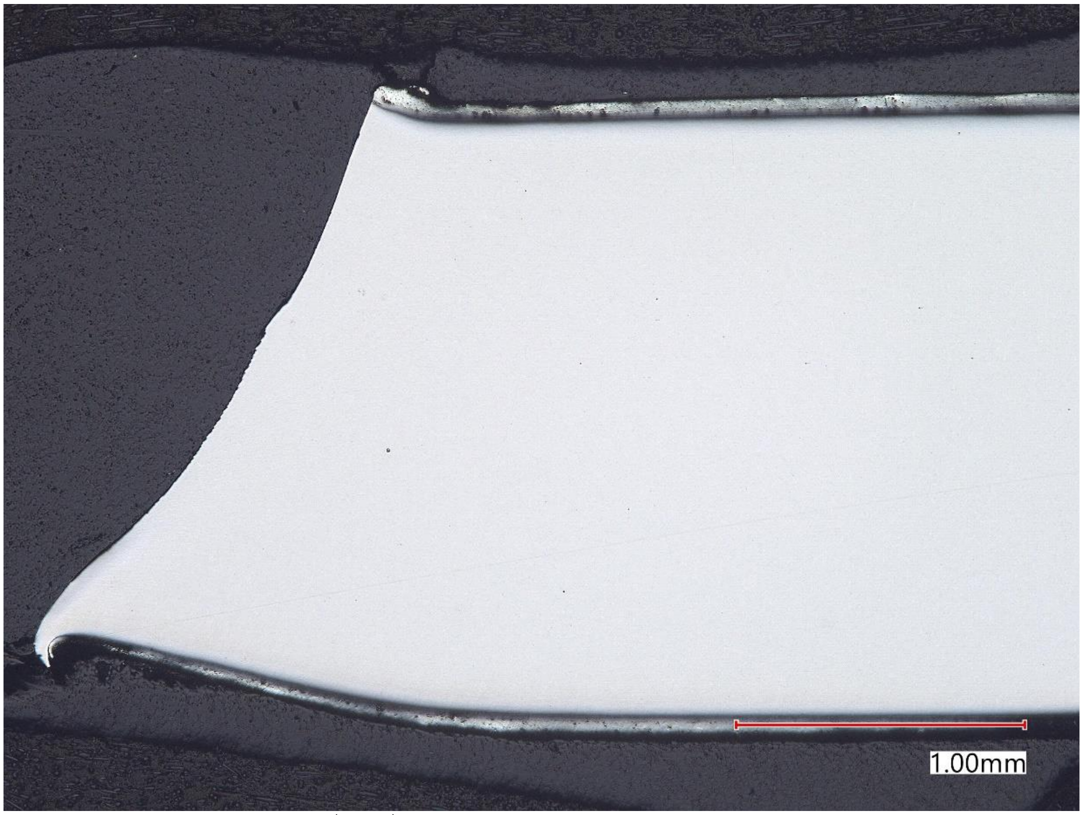

FIGURE 98. WIRE END (CUT) PROFILE. STEEL WIRE #1 SAMPLE #3. AS-POLISHED

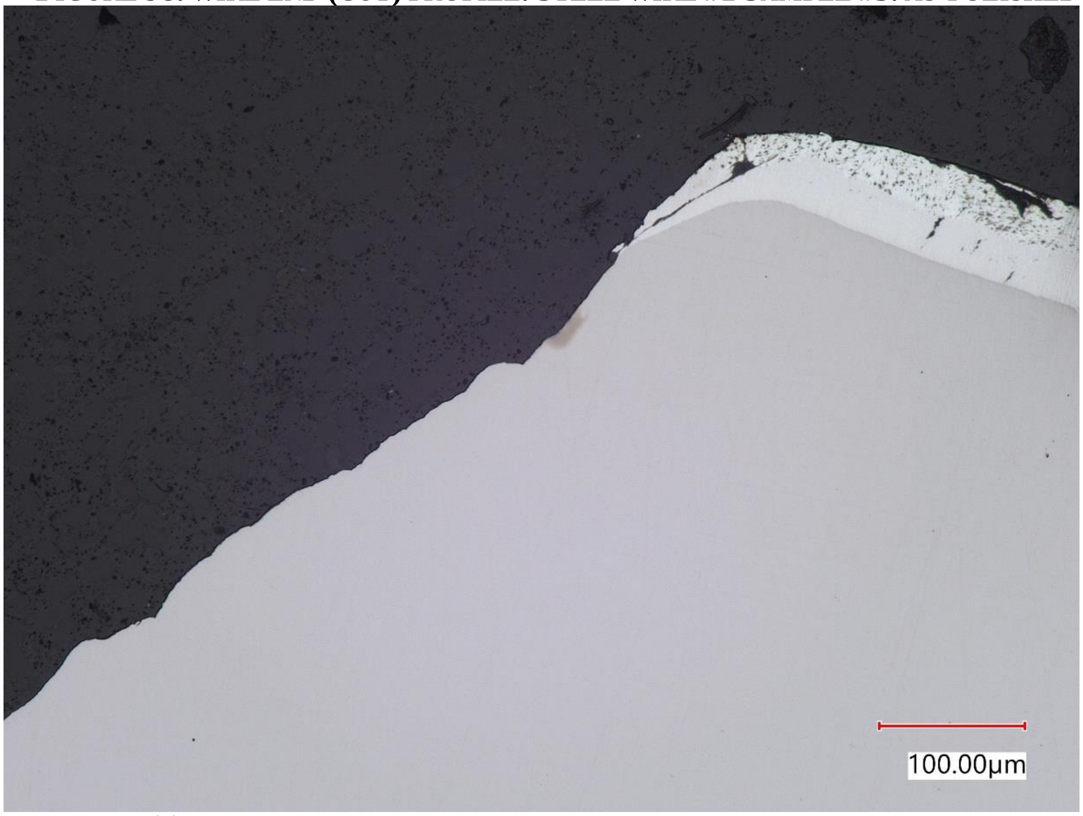

FIGURE 99. TOP CORNER OF THE FRACTURED WIRE END SURFACE DEPICTED IN FIGURE 95, STEEL WIRE #2 SAMPLE #1 AS-POLISHED

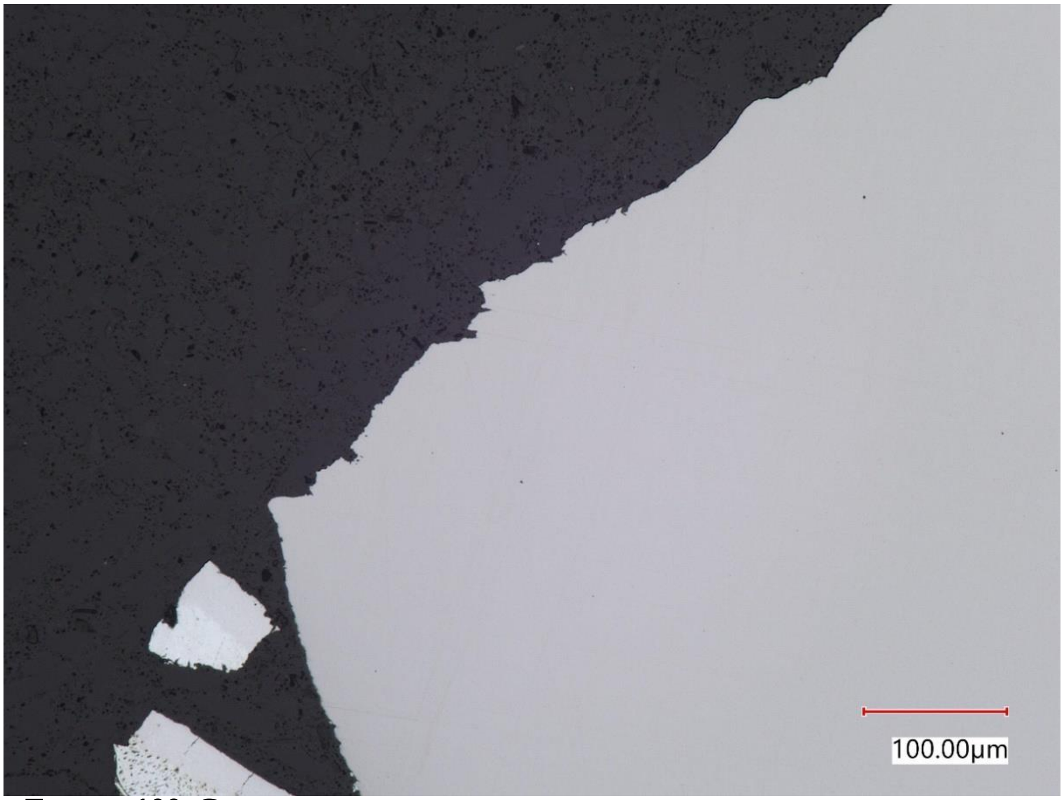

FIGURE 100. CLOSE VIEW OF THE BOTTOM CORNER OF THE FRACTURE PROFILE IN FIGURE 95, STEEL WIRE #2 SAMPLE #1 AS-POLISHED

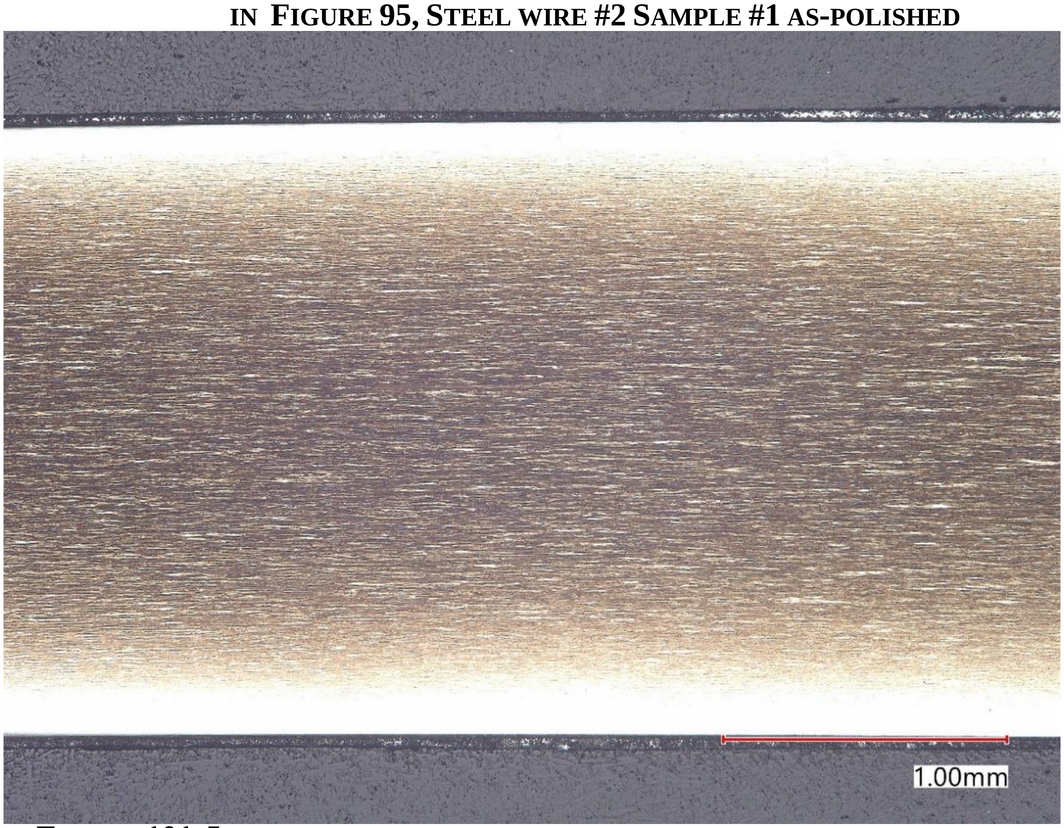

FIGURE 101. LONGITUDINAL CROSS SECTION OF STEEL WIRE AFTER ETCHING. STEEL WIRE #1 SAMPLE #3, AFTER ETCHING

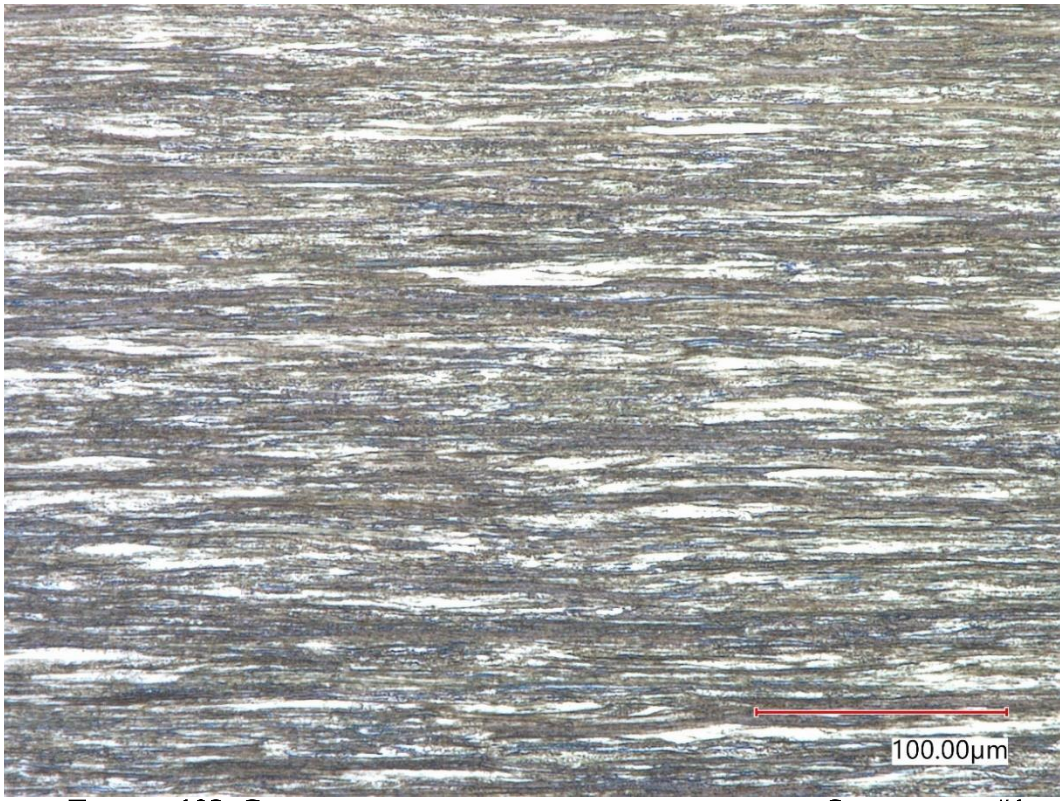

FIGURE 102. COLD WORKED STRUCTURE OF STEEL WIRE. STEEL WIRE #1 SAMPLE #3, AFTER ETCHING

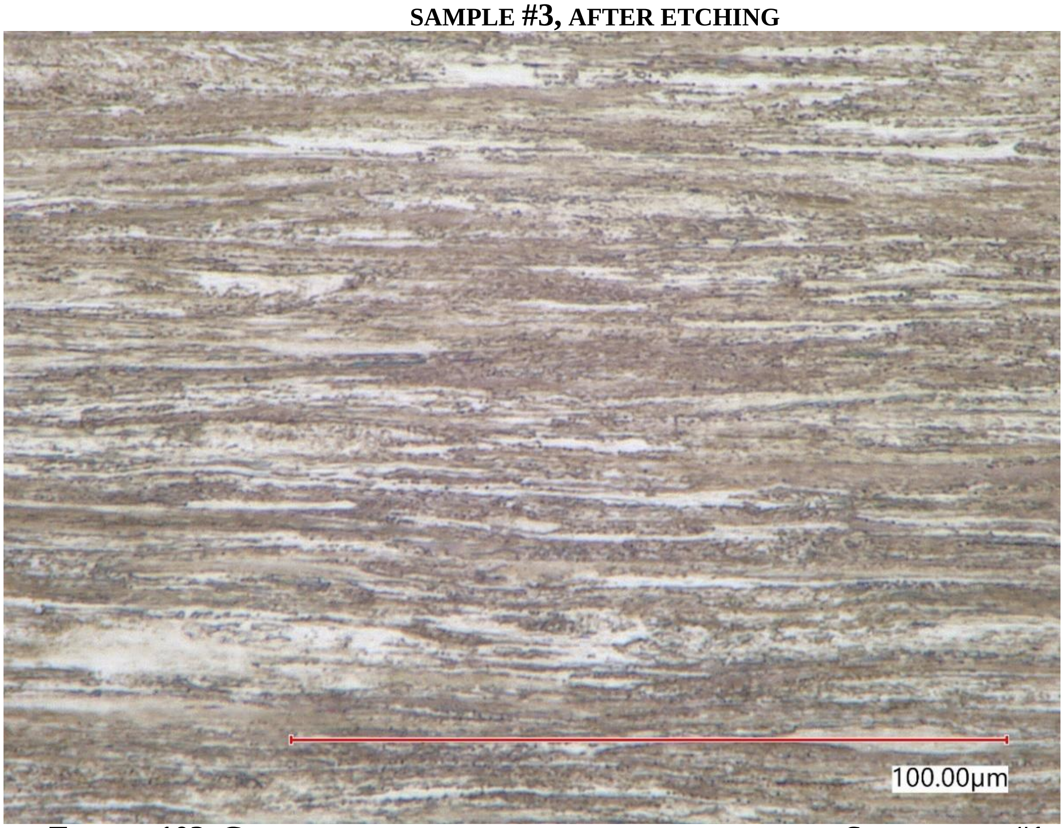

FIGURE 103. CLOSE VIEW OF THE STEEL MICROSTRUCTURE, STEEL WIRE #1 SAMPLE #3, AFTER ETCHING

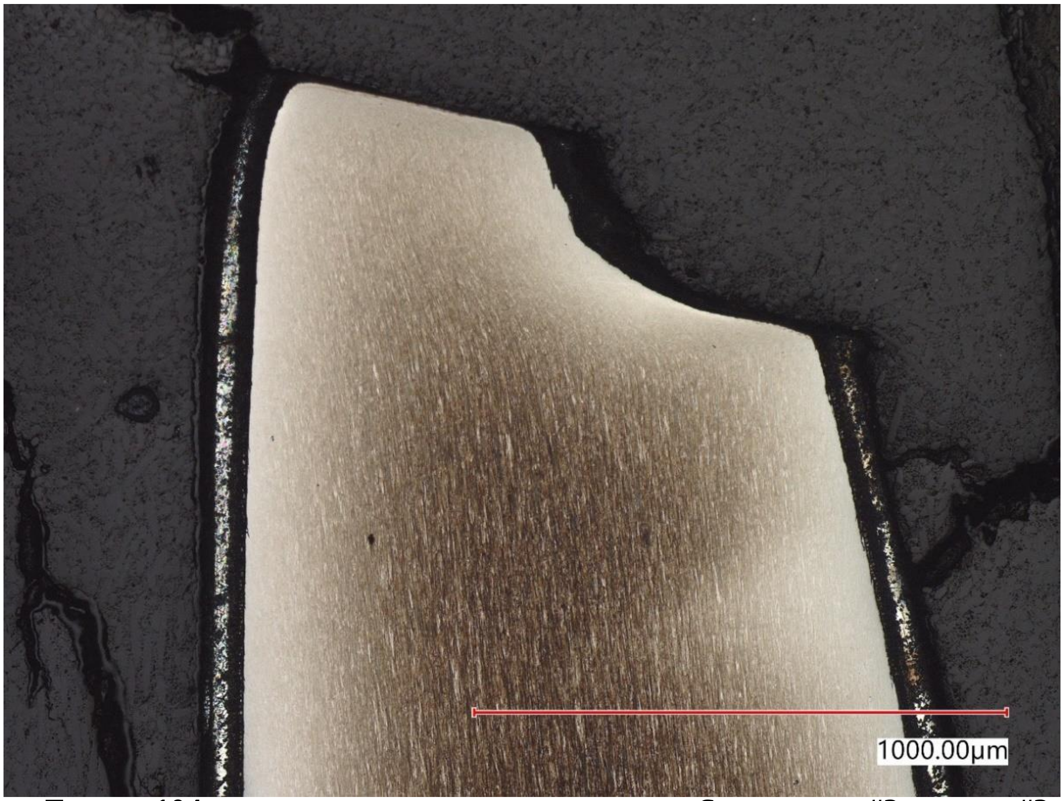

FIGURE 104. WIRE END PROFILE AFTER ETCHING, STEEL WIRE #2 SAMPLE #3

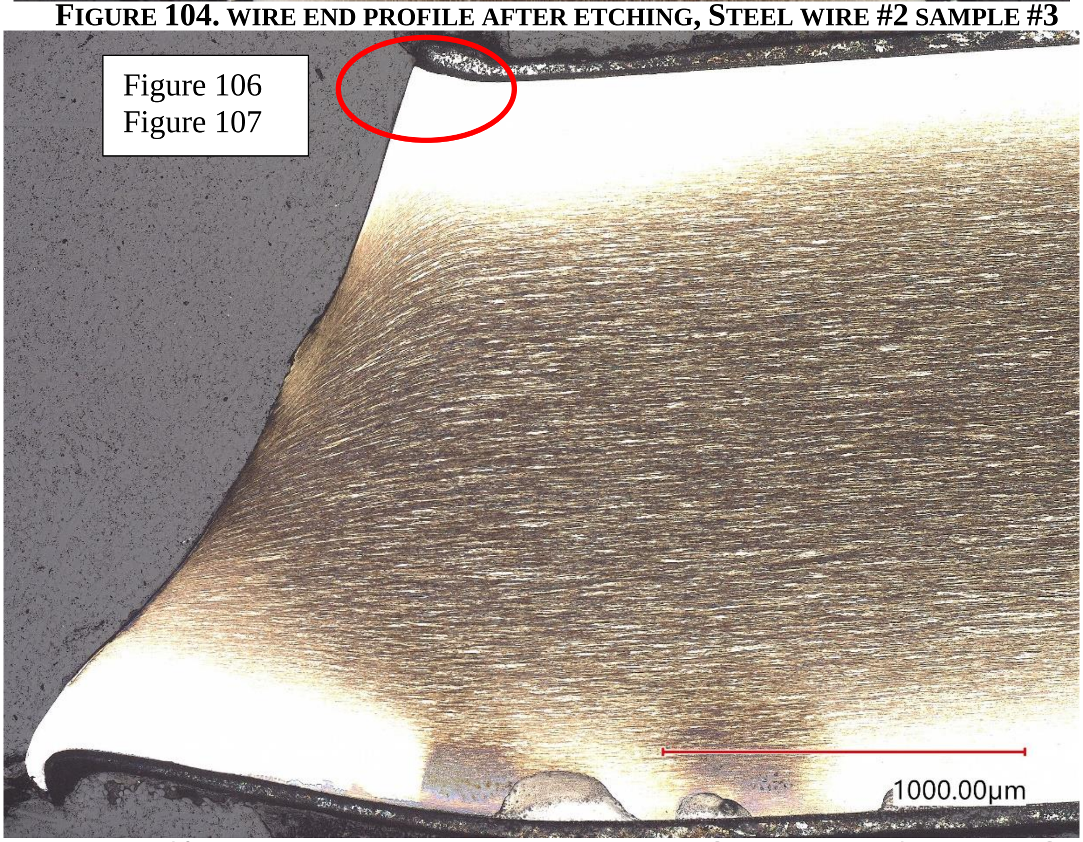

FIGURE 105. WIRE END PROFILE AFTER ETCHING, STEEL WIRE #1 SAMPLE #3

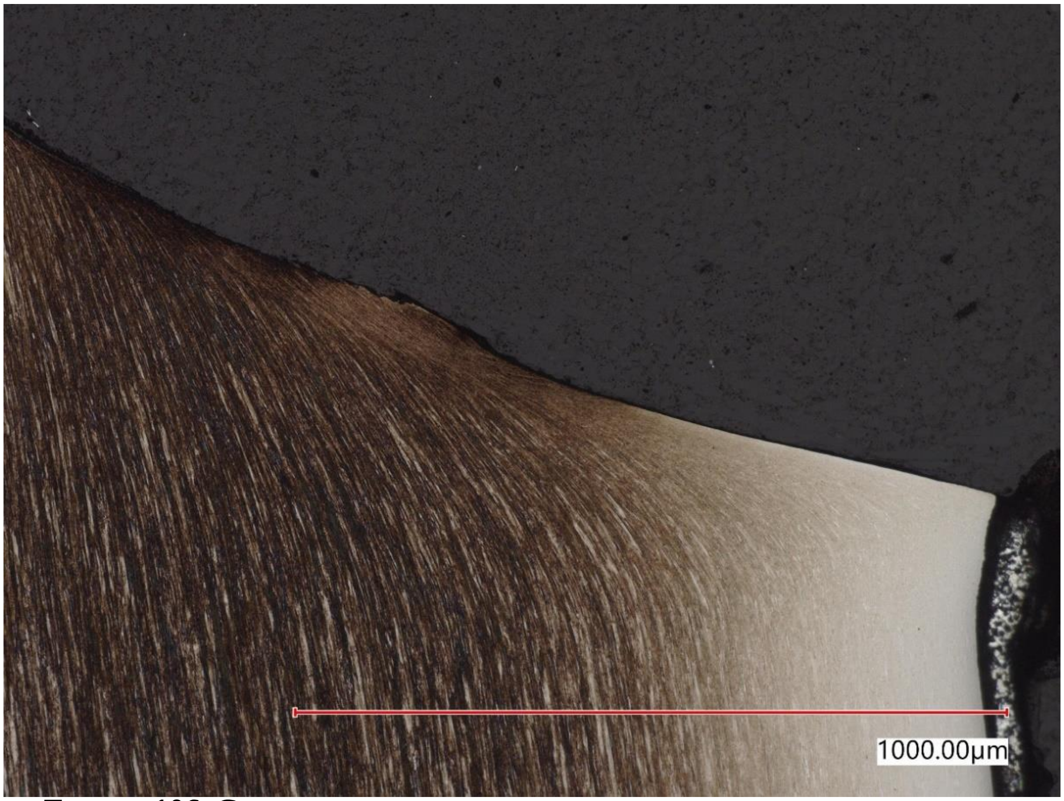

FIGURE 106. CLOSE VIEW OF THE TOP CORNER OF THE WIRE END PROFILE IN FIGURE 136 , STEEL WIRE #1 SAMPLE #3

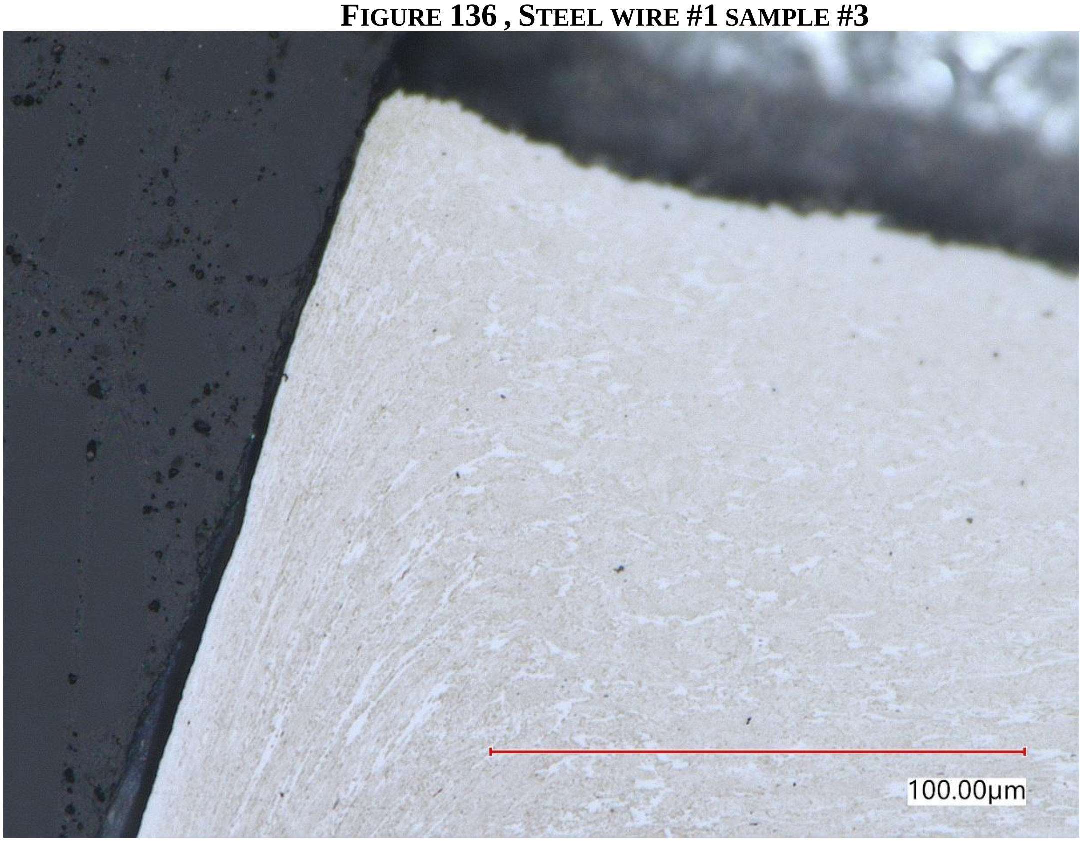

FIGURE 107. MICROSTRUCTURE AT THE AREAS OF THE CUT PROFILE IN FIGURE 106, STEEL WIRE #1 SAMPLE #3

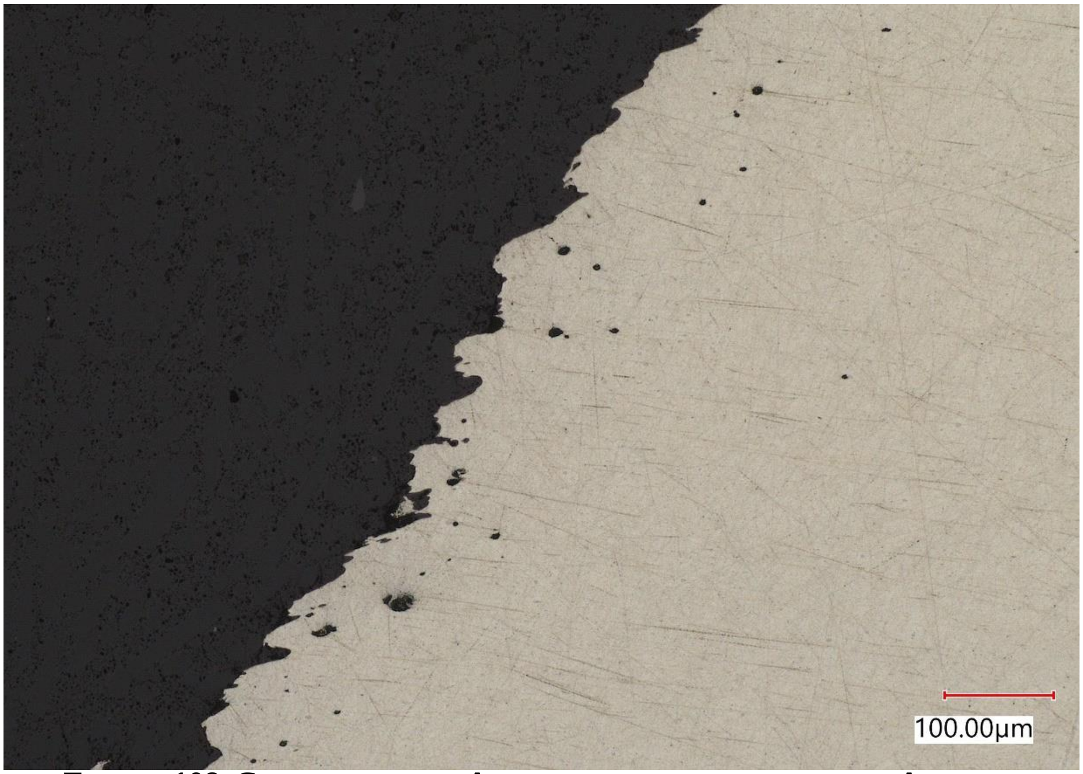

FIGURE 108. CRACK PROFILE, ALUMINUM WIRE, AS-POLISHED, ALUMINUM WIRE #1 SAMPLE #2

FIGURE 109. CRACK PROFILE, ALUMINUM WIRE, AS-POLISHED, ALUMINUM WIRE #1 SAMPLE #4

FIGURE 110. CRACK PROFILE, ALUMINUM WIRE, AS-POLISHED, ALUMINUM WIRE #4 SAMPLE #2

FIGURE 111. ALUMINUM WIRE #1 SAMPLE #1, AFTER ETCHING

FIGURE 112. ALUMINUM WIRE #2 SAMPLE #1, AFTER ETCHING

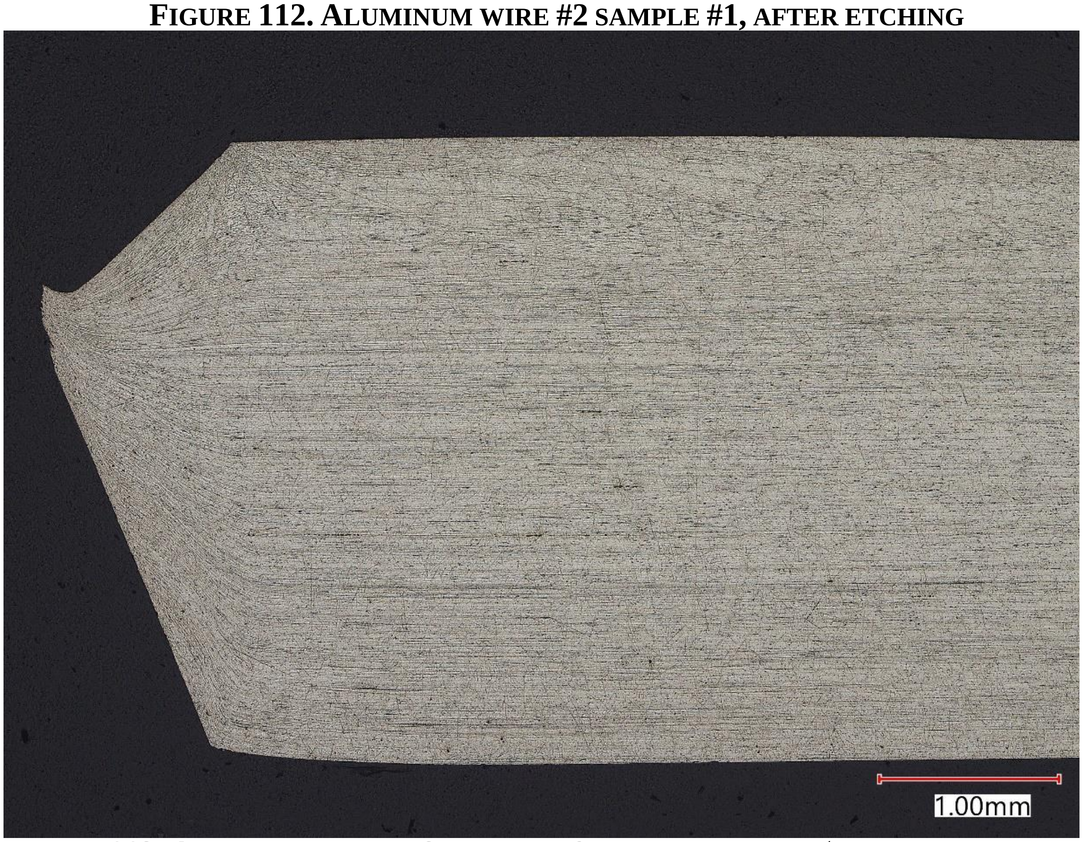

FIGURE 113. ALUMINUM WIRE #3 SAMPLE #2, AFTER ETCHING (THIS WIRE WAS CUT)

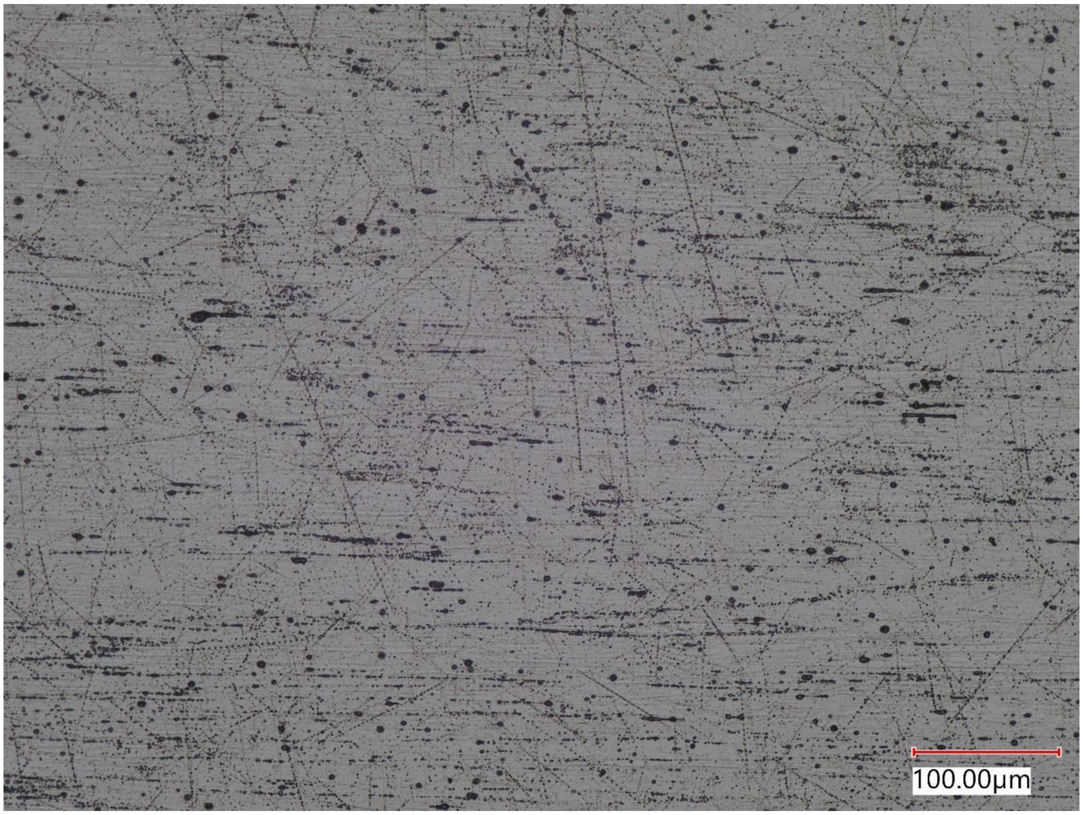

FIGURE 114. STRUCTURE AT A HIGHER MAGNIFICATION, ALUMINUM WIRE #3 SAMPLE #1, AFTER ETCHING

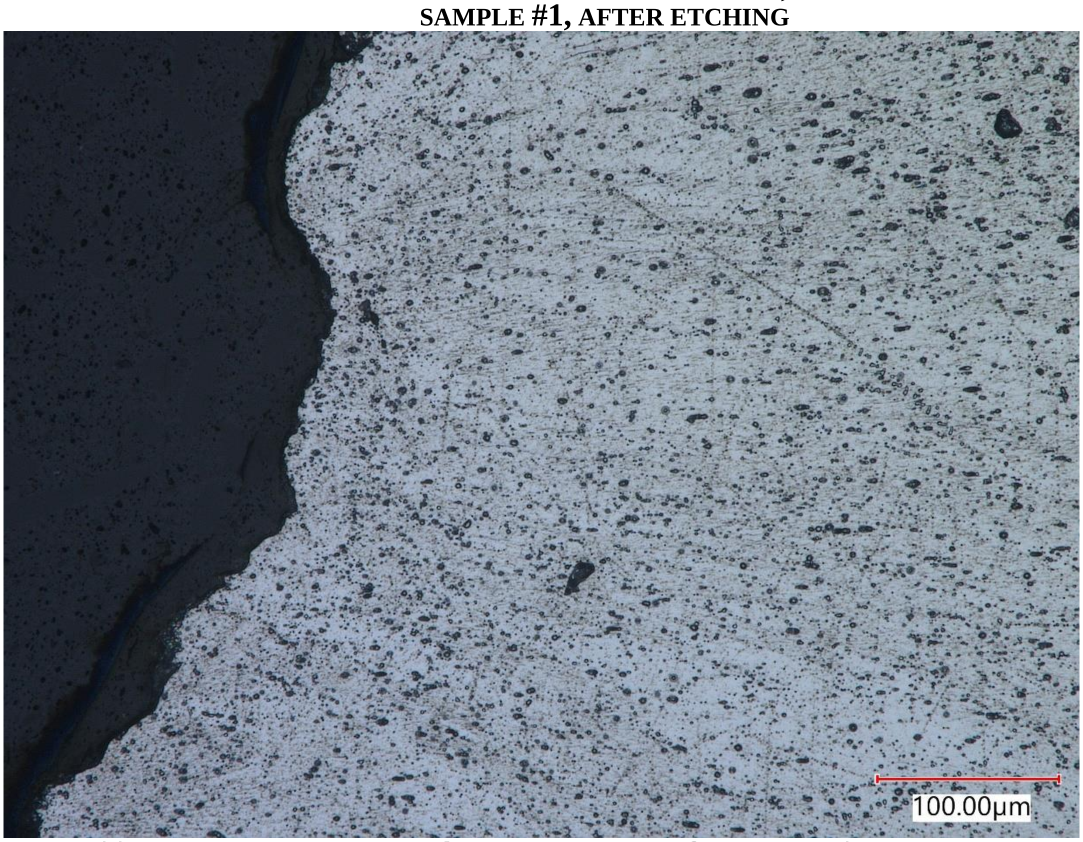

FIGURE 115. FRACTURE PROFILE, ALUMINUM WIRE #3 SAMPLE #1, AFTER ETCHING

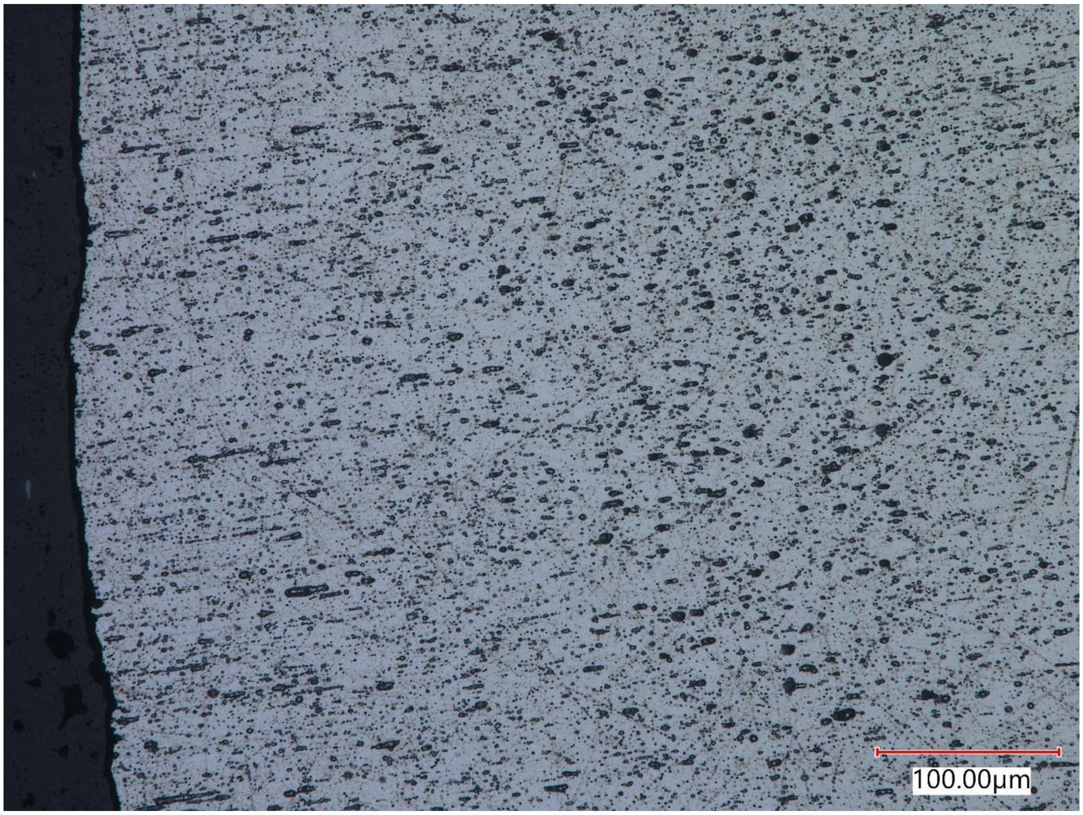

FIGURE 116. FRACTURE PROFILE, ALUMINUM WIRE #2 SAMPLE #2, AFTER ETCHING

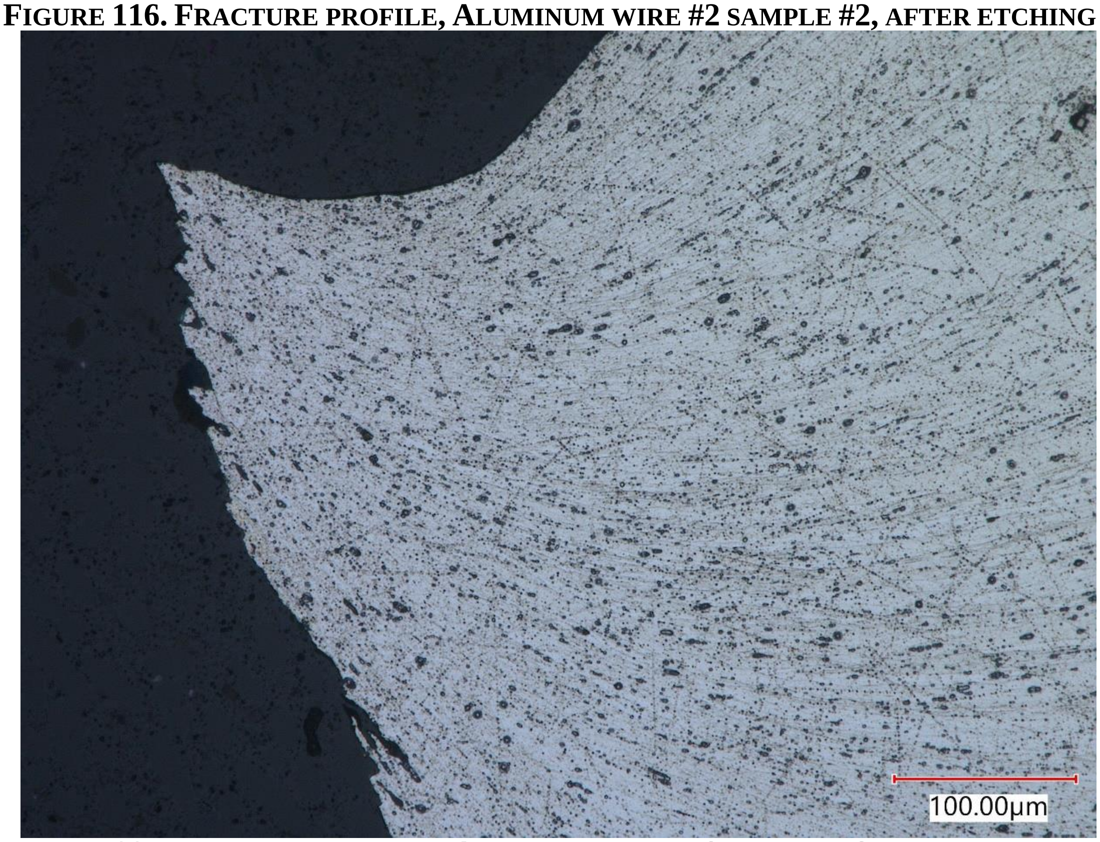

FIGURE 117. FRACTURE PROFILE, ALUMINUM WIRE #3 SAMPLE #3, AFTER ETCHING

6.0 TENSILE TESTING

We removed four 10 inches long aluminum wires from the new cable, Figure 118, and performed tensile tests in accordance with ASTMB557-15[1] and ASTM B606-19[2]. Results are presented in Table 1. Stress-strain curves of the wires are provided through Figure 119 to Figure 122. Ultimate tensile strength of all the aluminum wires tested exceeded the aluminum strength specified in ASTM B230-07(Reapproved 2016)[3]. However, elongation of all the aluminum wires tested was below the minimum elongation specified in the same standard and did not conform to the specified limits of the standard.

We removed four 10 inches long steel core wire samples from the new cable and performed tensile tests in accordance with ASTM A370-20[4]. Results are presented in Table 2. Stress-strain curves of the wires are provided through Figure 123 to Figure 126.

i) Ultimate tensile strength (UTS) of the steel wires were below the minimum UTS of ASTM B606/B606M-19[5] and did not conform to the standard.
ii) All the tensile properties of the steel wires tested conformed to the specified limits of ASTM B498/B498M-19[6] Class A and Class C.

We removed fracture surfaces of one steel and one aluminum wire tested for further examination.

i) Figure 127 shows the fracture profile of the steel wire tested. The wire tested showed some necking (see reduction in area in Table 1) which was not visible to the naked eye, nor at low magnification.
ii) Figure 128 shows one of the fracture surfaces. It was typical cup-and-cone fracture.
iii) We examined the fracture surface by means of SEM. Figure 129 shows the fracture surface.
iv) We observed zinc layer on the outer surface, Figure 130.
v) Area with the shear fractures showed shear dimples, Figure 131.
vi) Central, flat region of the fracture surface showed dimples, Figure 132 and Figure 133
vii) Observations made indicate that the tensile test sample fractured in a ductile manner. Dimples are a result of ductile transgranular cracking.

[1] ASTM B557 – 15: Standard Test Methods for Tension Testing Wrought and Cast Aluminum- and Magnesium-Alloy Products
[2] ASTM B606/B606M-19: Standard Specification for High-Strength Zinc-Coated (Galvanized) Steel Core Wire for Aluminum and Aluminum-Alloy Conductors, Steel Reinforced
[3] ASTM B230 / B230M - 07(2016): Standard Specification for Aluminum 1350–H19 Wire for Electrical Purposes
[4] ASTM A370 – 20: Standard Test Methods and Definitions for Mechanical Testing of Steel Products
[5] ASTM B606/B606M-19: Standard Specification for High-Strength Zinc-Coated (Galvanized) Steel Core Wire for Aluminum and Aluminum-Alloy Conductors, Steel Reinforced
[6] ASTM B498 / B498M – 19: Standard Specification for Zinc-Coated (Galvanized) Steel Core Wire for Use in Overhead Electrical Conductors

viii) Figure 134 shows the profile of the tensile tested aluminum wire. Some slip lines at 45° to the axis of the wire were evident in the vicinity of the necked region, Figure 134 and Figure 135. Figure 136 shows the fracture surface. Necking and high percentage of reduction in area were observed.

ix) Figure 137 shows the fracture surface of the aluminum wire under the SEM. Dimples are almost visible at low magnification.

x) Figure 138 shows the dimples covering the fracture surface of the tensile tested aluminum wire. Dimples are visible at very low magnification.

TABLE 1: TENSILE TESTING RESULTS ON FOUR ALUMINUM WIRES

Tensile Results	Aluminum #1	Aluminum #2	Aluminum #3	Aluminum #4	ASTM B230/B230M-07 (2016)
Diameter of the Wire (in)	Ø0.149	Ø0.149	Ø0.149	Ø0.149	0.4101-0.1500
Ultimate Tensile Strength (psi)	26,600	26,500	27,000	27,800	23,500
Yield Strength (offset = 0.2%) (psi)	24,100	24,400	25,000	24,700	N/A
Strength at 1% Extension (psi)	NA	NA	NA	NA	N/A
Elongation (in 10”-Manual Method) (%)	1.5	1.5	1.2	1.2	1.8

TABLE 2: TENSILE TESTING RESULTS ON FOUR STEEL WIRES

Tensile Results	Steel #1	Steel #2	Steel #3	Steel #4	ASTM B606/ B606M-19	ASTM B498/B498M-19	
						Class A	Class C
Diameter of the Wire (in)	Ø0.089	Ø0.089	Ø0.089	Ø0.089	0.0500-0.0899 inclusive		
Ultimate Tensile Strength (psi)	221,000	218,000	224,000	223,000	235	210	190
Yield Strength (offset = 0.2%) (psi)	184,000	182,000	193,000	192,000	N/A	N/A	N/A
Strength at 1% Extension (psi)	210,000	212,000	215,000	212,000	210	190	170
Elongation (in 10”-Manual Method) (%)	5.0	5.0	4.9	4.9	3.0	3	3

CSA C61232:03 (Reaffirmed 202), Aluminum Clad Steel Wires for Electrical Purposes:
20SA Type A, Diameter; 1.24mm-3.25mm, minimum UTS: 1,340MPa (194,351 PSI), Minimum stress at 1%extension: 1,200 MPa (174,045 PSI).
20SA Type B, Diameter; 1.24mm-5,50mm, minimum UTS: 1,320MPa (191,450 PSI), Minimum stress at 1%extension: 1,100 MPa (159,542 PSI)

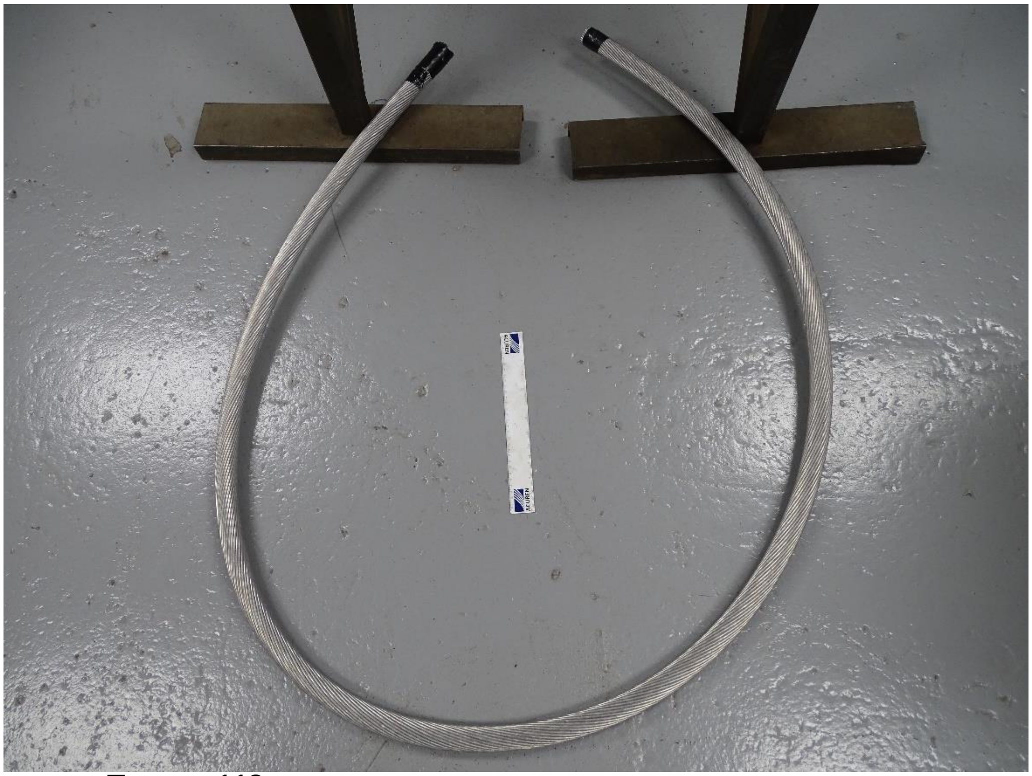

FIGURE 118: NEW CABLE SECTION FOR MECHANICAL TESTING

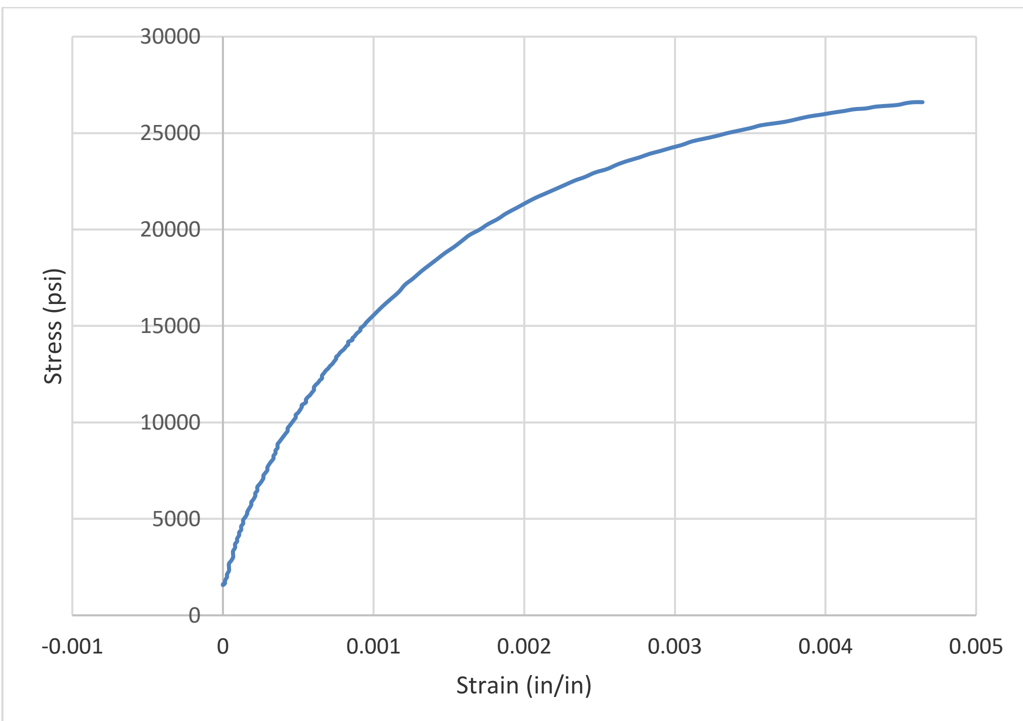

FIGURE 119: STRESS-STRAIN CURVE OF THE ALUMINUM WIRE #1

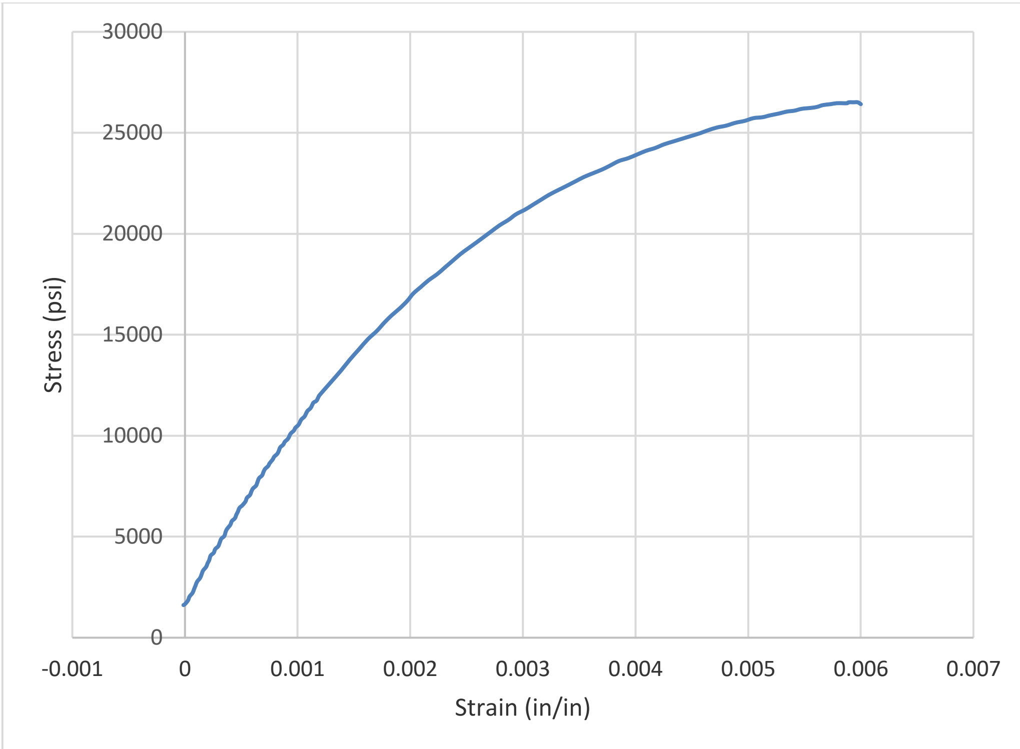

FIGURE 120: STRESS-STRAIN CURVE OF THE ALUMINUM WIRE #2

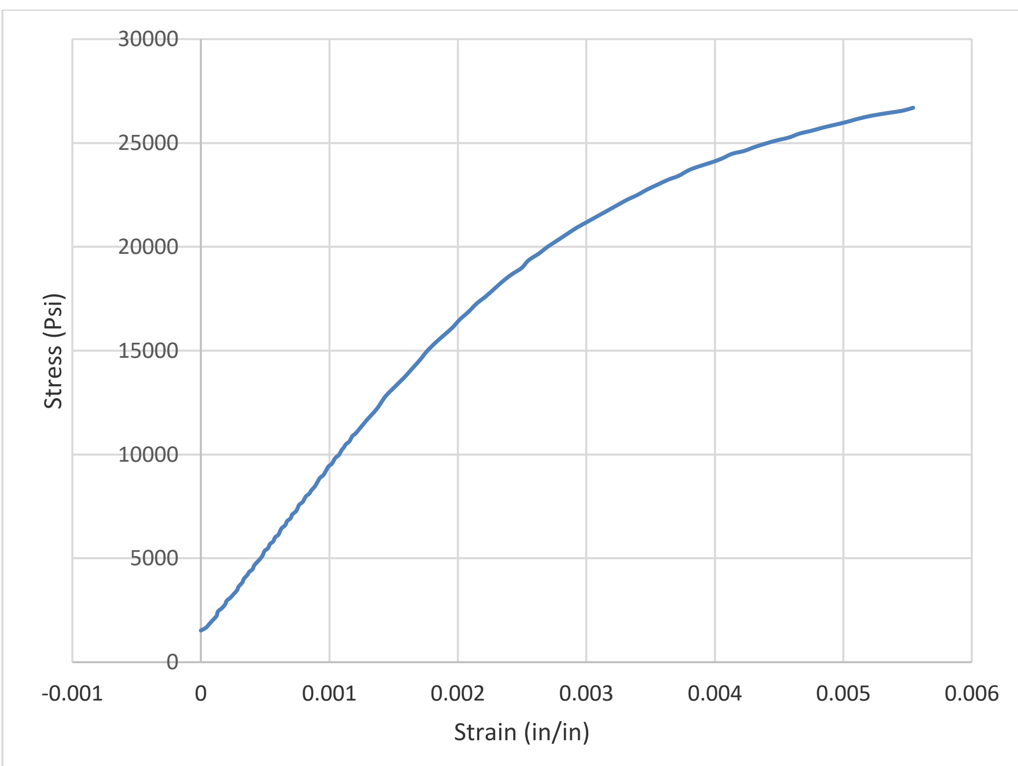

FIGURE 121: STRESS-STRAIN CURVE OF THE ALUMINUM WIRE #3

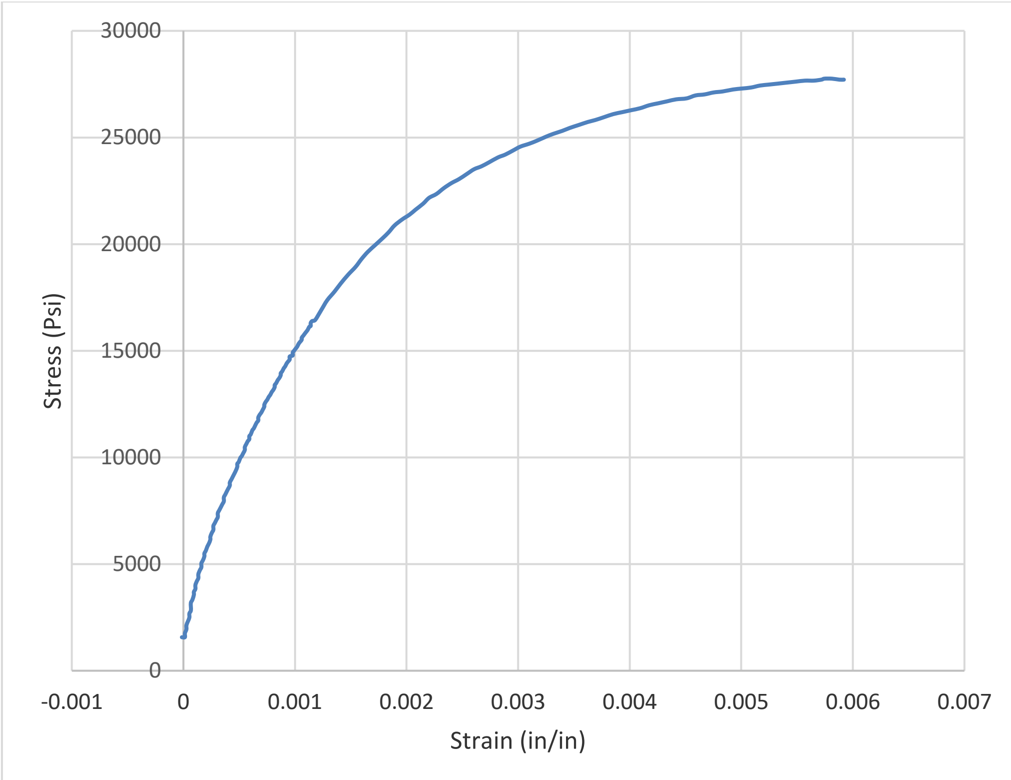

FIGURE 122: STRESS-STRAIN CURVE OF THE ALUMINUM WIRE #4

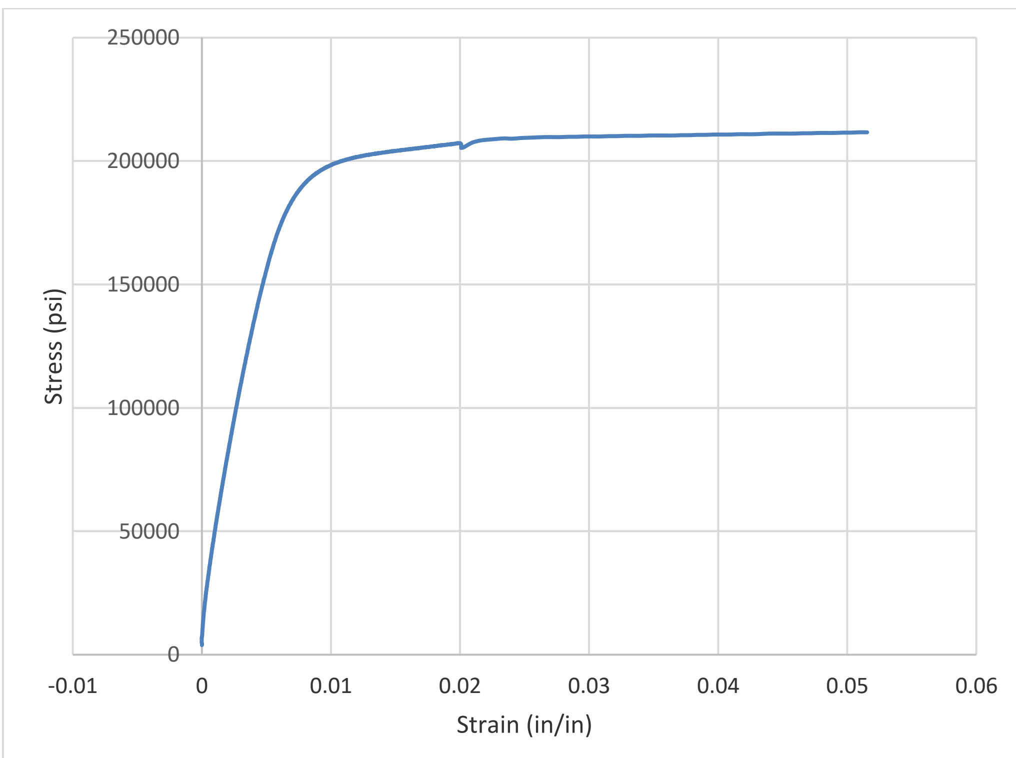

FIGURE 123: STRESS-STRAIN CURVE OF THE STEEL WIRE #1

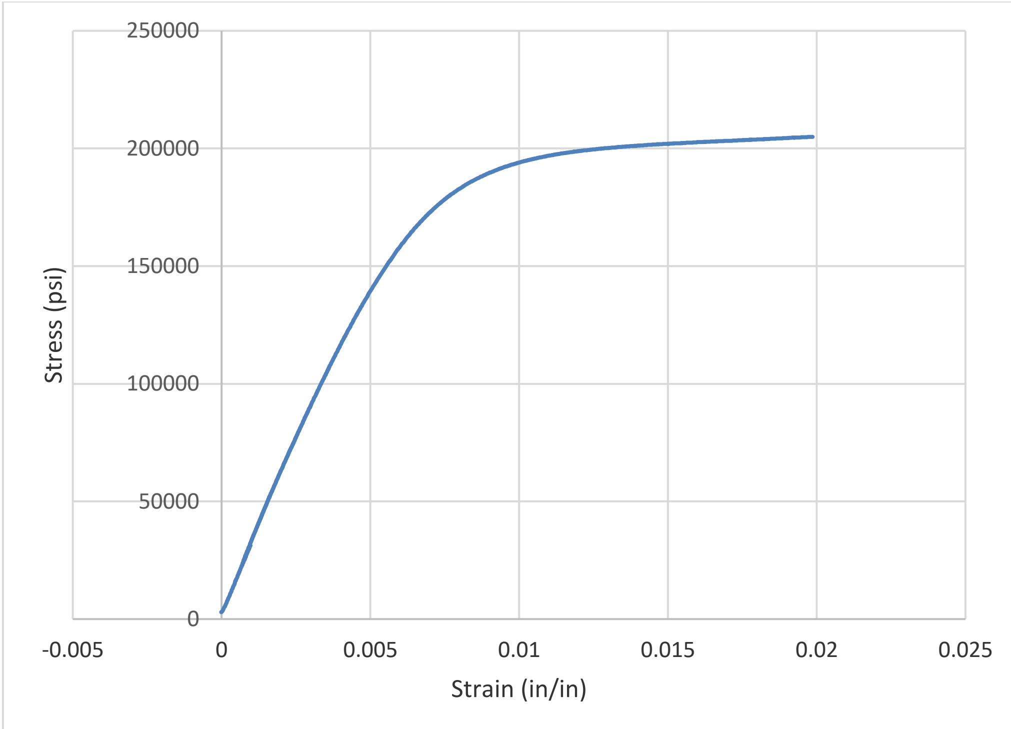

FIGURE 124: STRESS-STRAIN CURVE OF THE STEEL WIRE #2

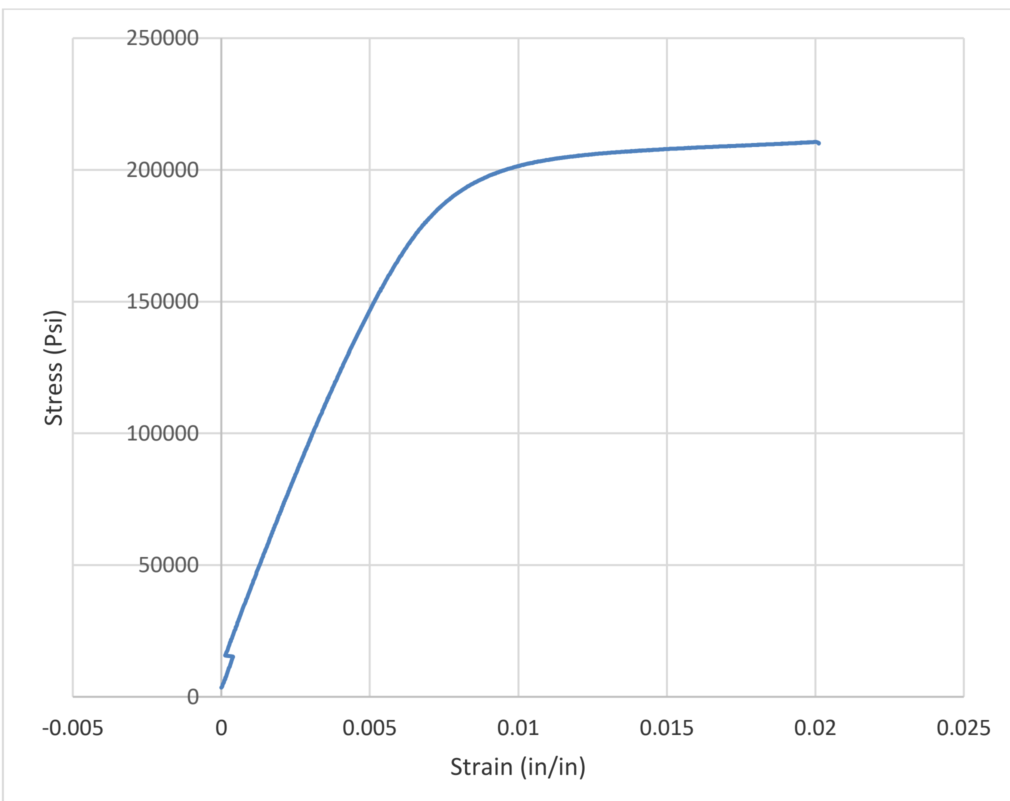

FIGURE 125: STRESS-STRAIN CURVE OF THE STEEL WIRE #3

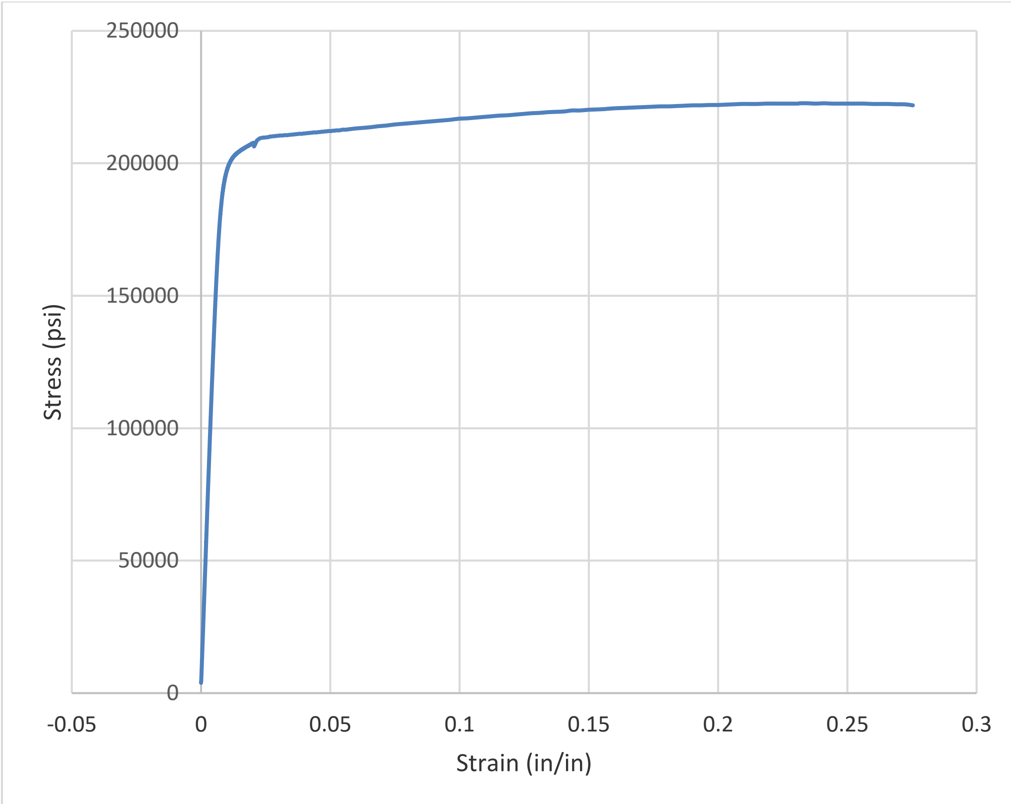

FIGURE 126: STRESS-STRAIN CURVE OF THE STEEL WIRE #4

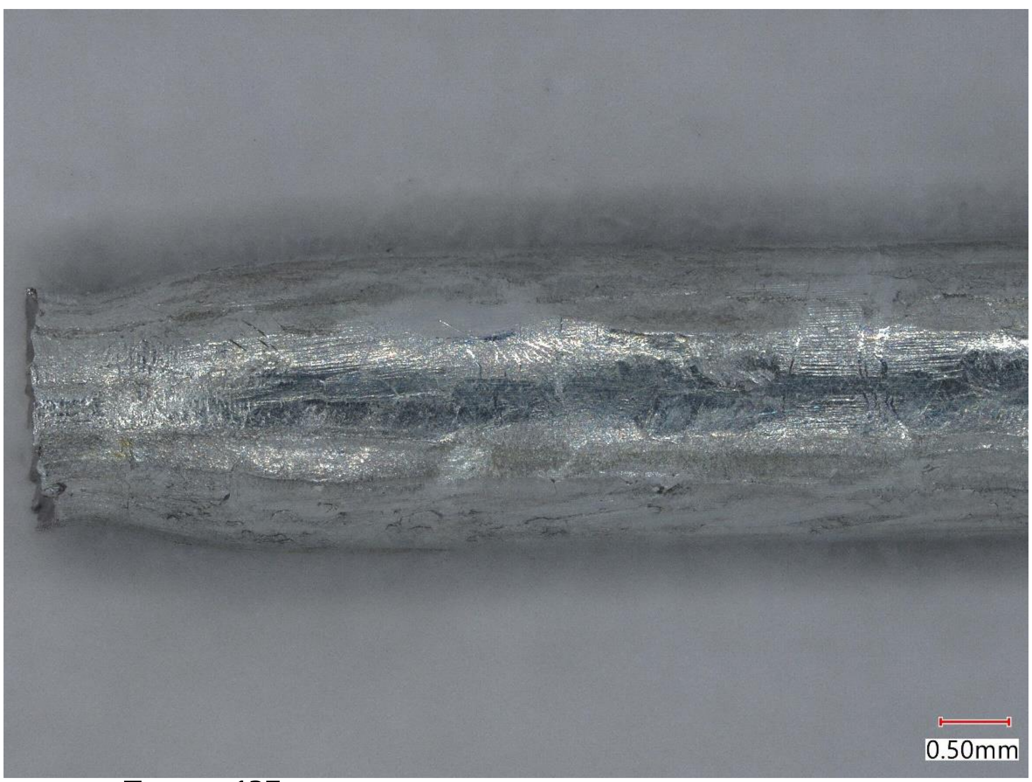

FIGURE 127: STEEL WIRE PROFILE AFTER TENSILE TESTING

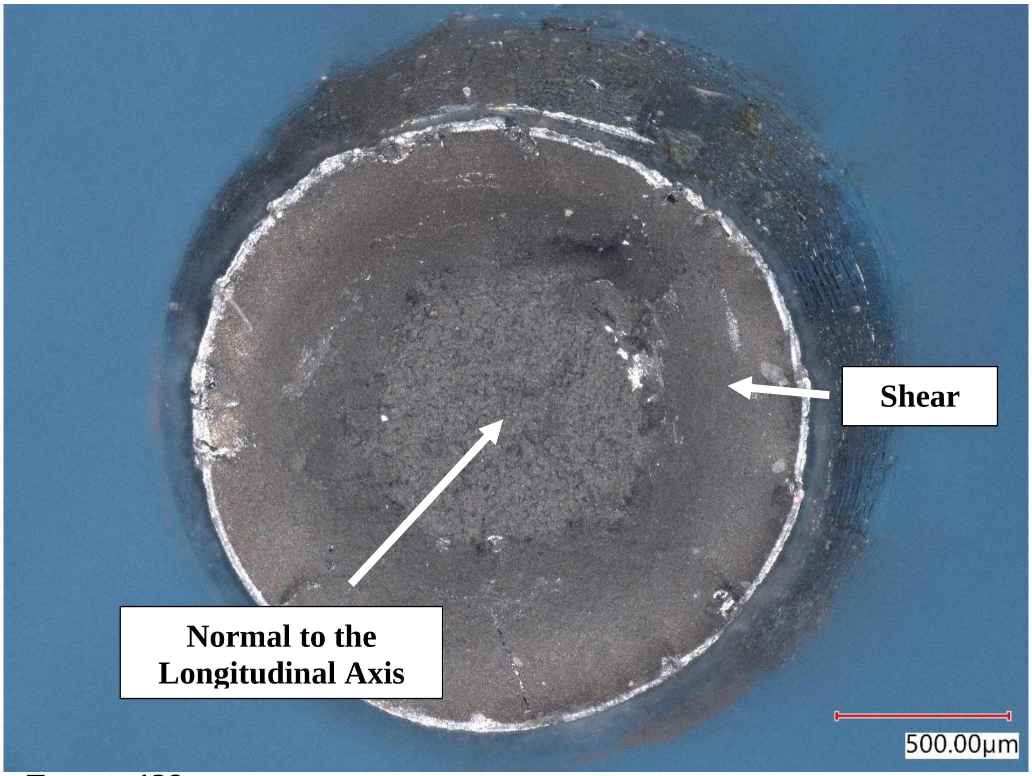

FIGURE 128: FRACTURE SURFACE OF THE TENSILE TESTED SAMPLE. STEEL WIRE

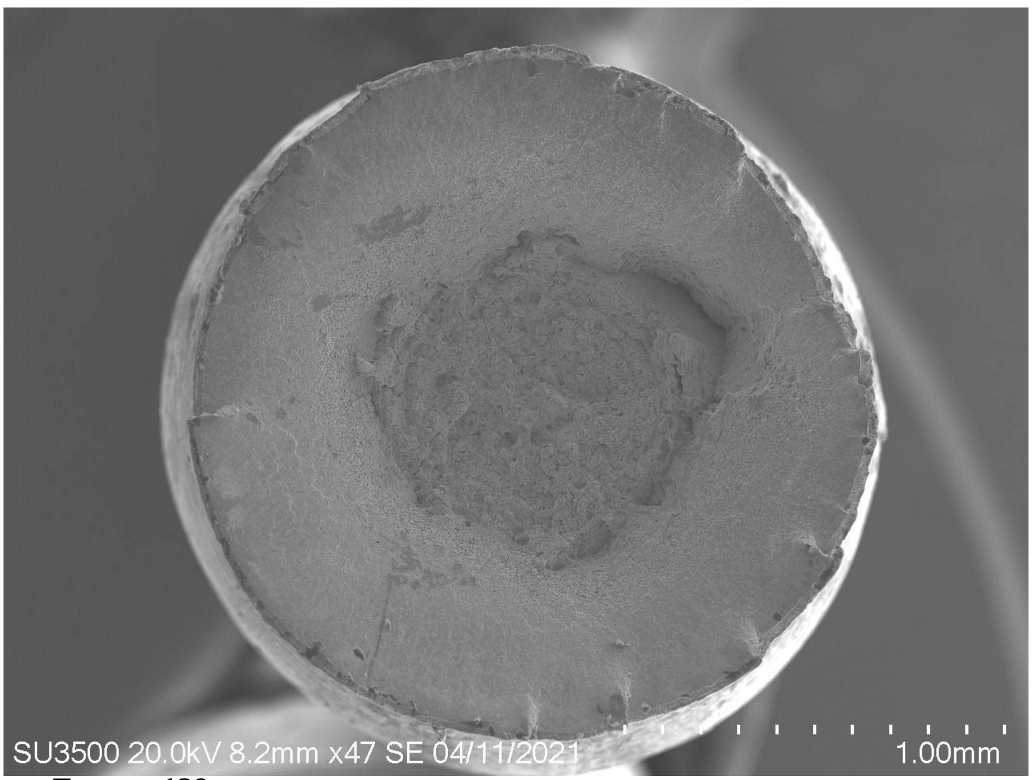

FIGURE 129: FRACTURE SURFACE. TENSILE TEST SAMPLE. STEEL WIRE

ACUREN

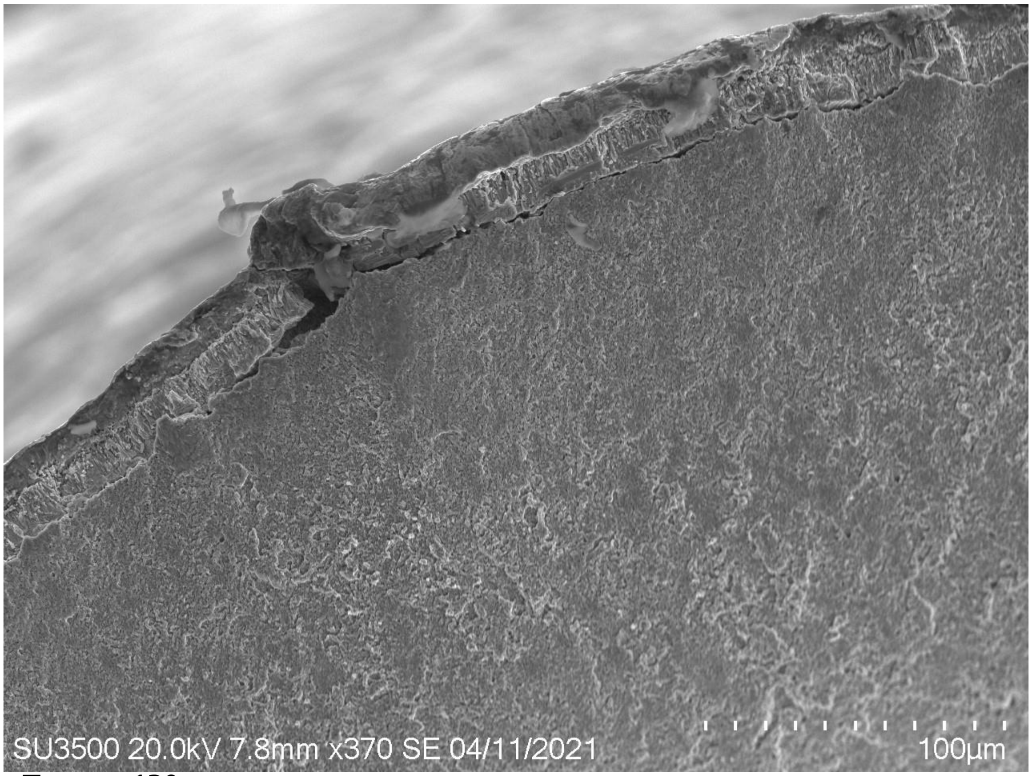

FIGURE 130: ZINC LAYER ON THE OUTER SURFACE. FRACTURE SURFACE OF STEEL WIRE. TENSILE TESTED

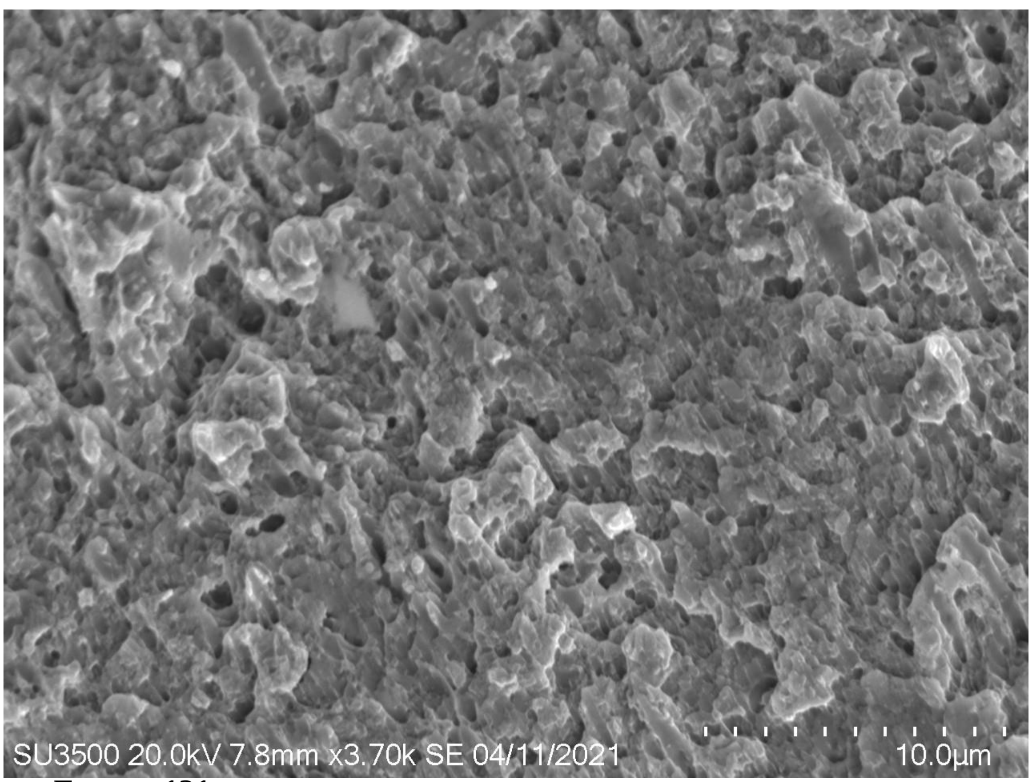

FIGURE 131: SHEAR DIMPLES ON THE SHEAR FRACTURE SIDE. TENSILE TESTED STEEL WIRE

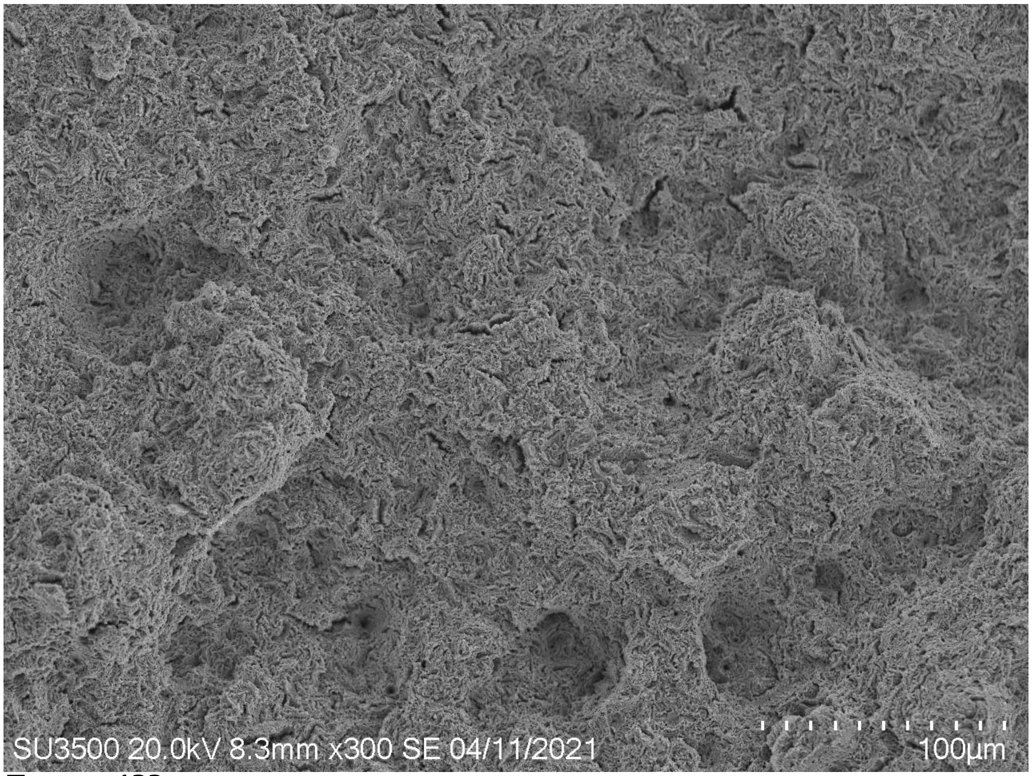

FIGURE 132: **CENTRAL REGION OF THE FRACTURE SURFACE. TENSILE TESTED STEEL WIRE**

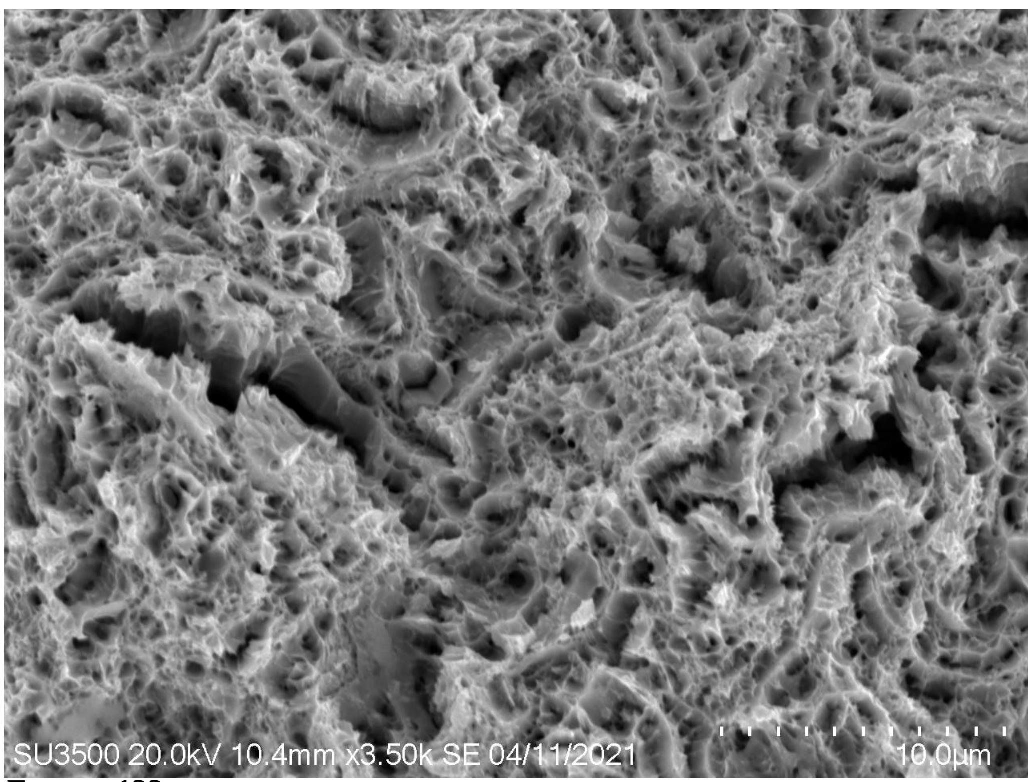

FIGURE 133: **CENTRAL REGION OF THE FRACTURE SURFACE. TENSILE TESTED STEEL WIRE. DIMPLES**

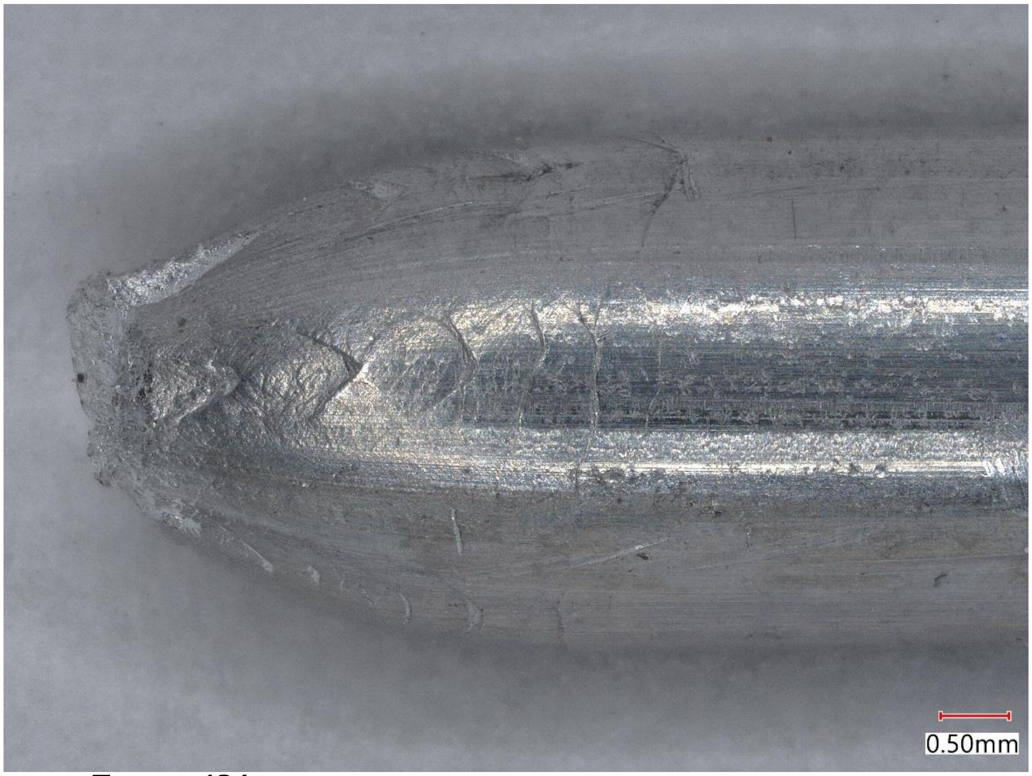

FIGURE 134: PROFILE OF THE TENSILE TESTED ALUMINUM WIRE

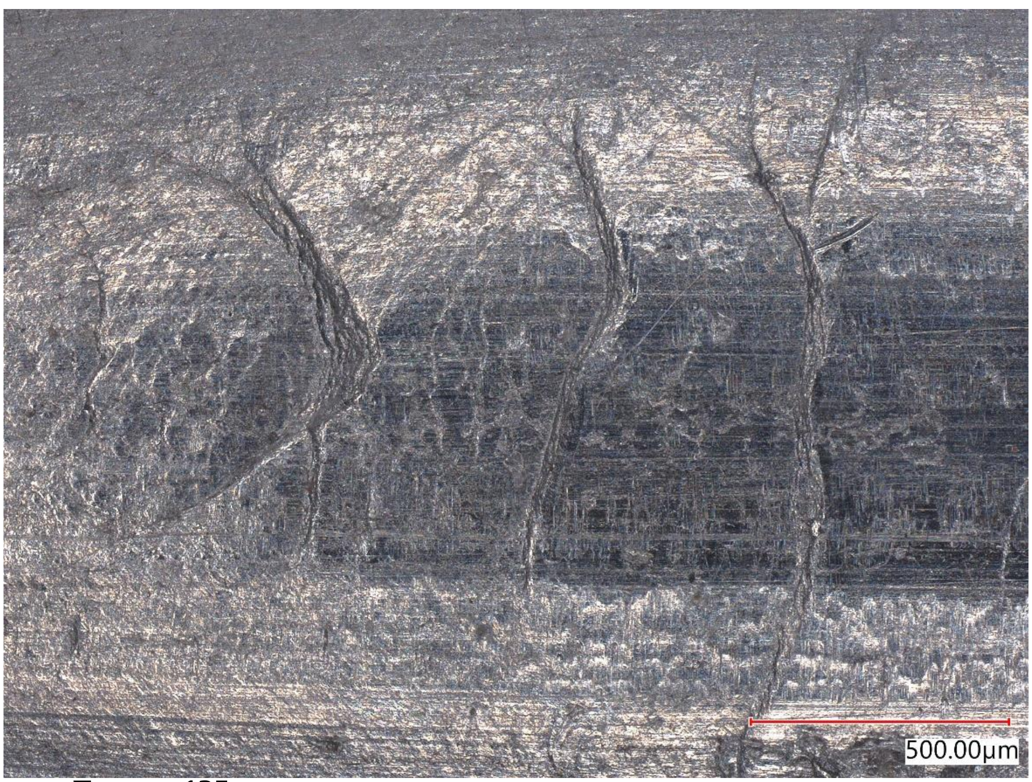

FIGURE 135: CENTER VIEW OF THE SIDE SURFACE. TENSILE TESTED ALUMINUM WIRE

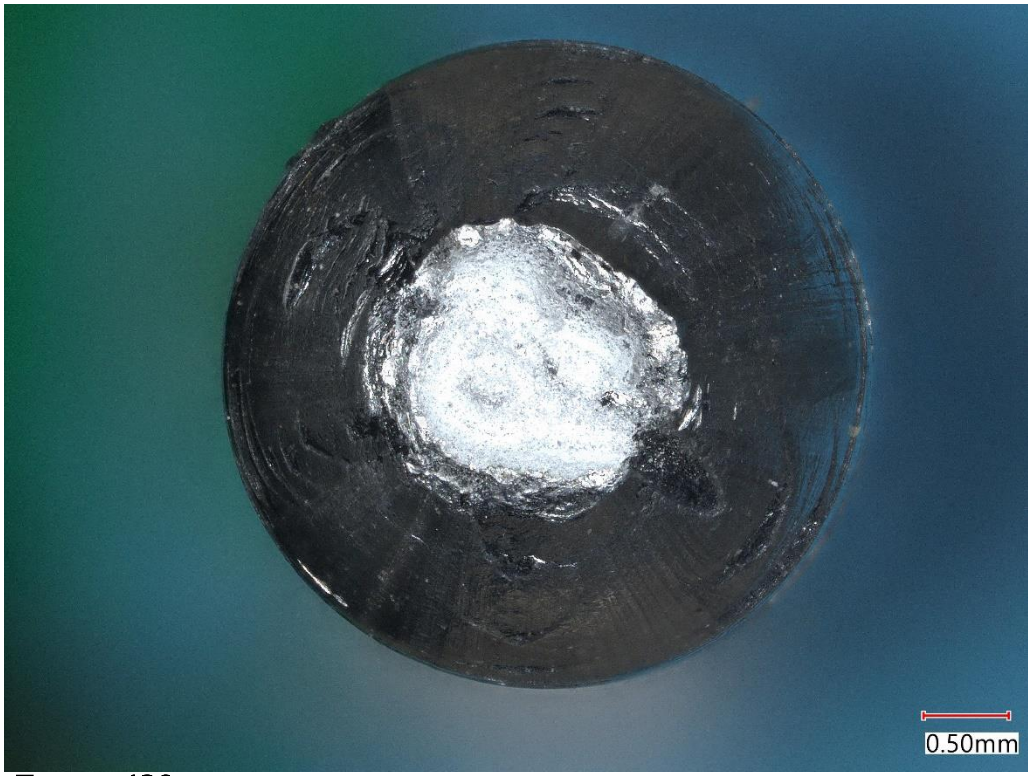

FIGURE 136: FRACTURE SURFACE OF THE TENSILE TESTED ALUMINUM WIRE

FIGURE 137: FRACTURE SURFACE OF THE TENSILE TESTED ALUMINUM WIRE UNDER THE SEM

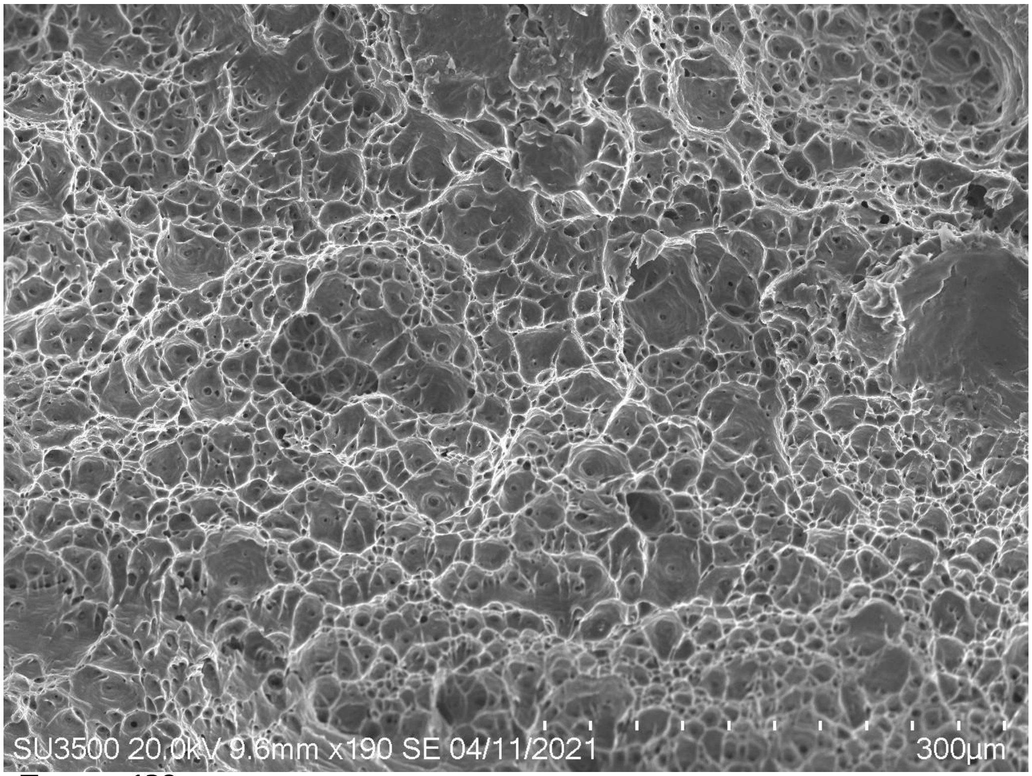

FIGURE 138: DIMPLES COVERING THE FRACTURE SURFACE OF THE TENSILE TESTED WIRE

7.0 CHEMICAL ANALYSIS

Chemical composition of the aluminium wire (removed from Sample #3) was analysed using optical emission spectroscopy (OES) in accordance with ASTM E1251-17a[7]. Results are presented in Table 3. Results show that the chemical composition of the aluminum wire conforms to the chemical composition limits of ASTM B230/B230M-01 (reapproved 2016) and ASTM B233-91[8] (reapproved 2016).

TABLE 3: CHEMICAL ANALYSIS OF THE ALUMINUM WIRE FROM SAMPLE #3

Elements	**#0003**	**ASTM B233-97 (2016)**
Al	99.7	99.5 MIin
Si	0.044	0.10 Max
Fe	0.11	0.40 Max
Cu	0.01	0.05 Max
Mn	< 0.005	0.01 Max
Mg	< 0.005	0.03 Max
Cr	< 0.00050	0.01 Max
Ni	0.01	0.03 Max
Zn	0.01	0.05 Max
Ti	< 0.005	-
Ag	< 0.00010	0.03 Max
B	0.002	0.05 Max
Be	< 0.0005	0.03 Max
Ga	0.01	0.03 Max
Pb	0.0145	0.03 Max
Sn	0.02	0.03 Max
V	< 0.0005	0.02 Max
Other Elements	0.0756	0.1 Max

[7] ASTM E1251 - 17a: Standard Test Method for Analysis of Aluminum and Aluminum Alloys by Spark Atomic Emission Spectrometry
[8] ASTM B233 - 97(2016): Standard Specification for Aluminum 1350 Drawing Stock for Electrical Purposes

Steel wire samples removed from sample #3 were subjected to a zinc coating removal process and then subjected to a chemical analysis in accordance with ASTM 415-17[9]. Results are presented in Table 4. Results show that the chemical composition of the steel wire conforms to the chemical composition limits of ASTM B498/B498M-19 and ASTM B606/B606M-19.

TABLE 4: CHEMICAL ANALYSIS OF THE STEEL WIRE FROM SAMPLE #3

Elements	**#0003**	**ASTM B606/B606M-19 and ASTM B498/B498M-19**
Fe	Rem.	Rem.
C	0.59	0.50-0.88
Si	0.21	0.10-0.35
Mn	0.60	0.50-1.30
P	0.020	0.035 Max
S	0.011	0.045 Max
Cr	0.02	-
Mo	0.01	-
Ni	0.02	-
Al	0.01	-
Co	< 0.0015	-
Cu	0.01	-
Nb	< 0.005	-
Ti	< 0.005	-
V	< 0.005	-

[9] ASTM E415 – 17: Standard Test Method for Analysis of Carbon and Low-Alloy Steel by Spark Atomic Emission Spectrometry

8.0 COATING WEIGHT

Steel wires removed from the cable were subjected to coating weight testing in accordance with ASTM A90-13(2018). Results were presented in Appendix A. Results show that the steel, for the diameter and the coating, conform to Class A for steel wire with a diameter of 0.0890 inch.

Coating Mass Test
(By ASTM A90/A90M-13(2018))

Specimen #	W1	W2	D (mm)	coating weight (g/m^2)	coating weight (g/m^2)	ASTM A498 B606
1	12.588	11.836	2.24	278.98	278.98	214 Min
2	12.597	11.876	2.25	267.61	267.61	
3	12.565	11.843	2.25	269.85	269.85	

8.2.2 *Results in Metric Units:*

8.2.2.1 Calculate the weight [mass] of zinc coating as follows:

$$C = [(W_1 - W_2)/W_2] \times D \times M \quad (6)$$

where:

C = weight [mass] of coating, g/m^2 of stripped wire surface,
W_1 = original weight [mass] of specimen, g,
W_2 = weight [mass] of stripped specimen, g,
D = diameter of stripped wire, in. or mm, and
M = a constant = 4.97×10^4 when D is in in., or = 1.96×10^3 when D is in mm.

9.0 WRAP TEST

9.1 BENDING TEST OF ALUMINIUM WIRES

Two aluminium wire section removed from the new coil and from sample #3 were subjected to bending test in accordance with ASTM B230/B230M-07 (reapproved 2016) Section 8. Figure 139, Figure 140 and Figure 141 show the wires looped around its own diameter. No fracture on the aluminium wires occurred.

FIGURE 139. ALUMINUM WIRES BEND TESTED

FIGURE 140. CLOSE VIEW OF ONE OF THE BEND SAMPLES. AL WIRE, DAMAGE OBSERVED ON THE WIRE WAS PRESENT PRIOR TO TESTING

FIGURE 141. CLOSE VIEW OF THE SECOND ALUMINUM WIRE

9.2 WRAP TEST OF STEEL WIRES

Two steel wires removed from the new cable were wrapped eight times around a cylindrical mandrel three times the diameter of the wires in accordance with ASTM B498/B498M-19 Section 9 and ASTM B606/B606M-19 Section 8. Figure 142 and Figure 143 show the wires wrapped. No cracks or fracture occurred on the loops of the wires.

FIGURE 142. STEEL WIRES WRAP TESTED

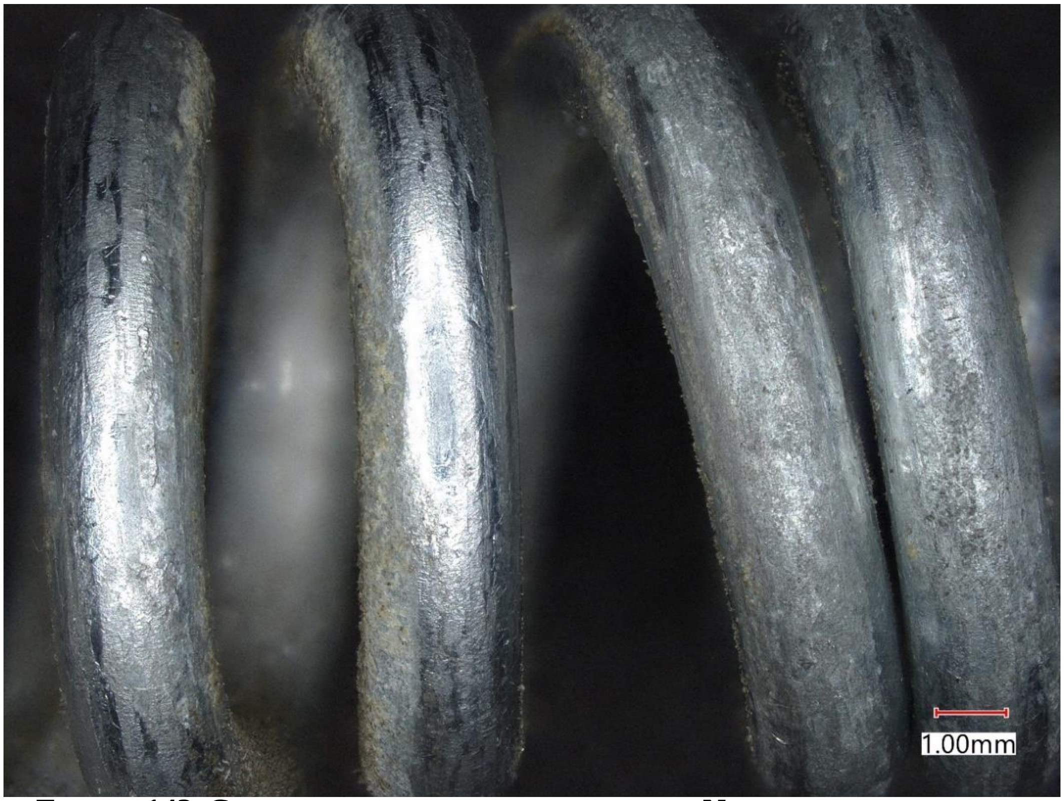

FIGURE 143. CLOSE VIEW OF FOUR OF THE LOOPS. NO CRACKS OR FRACTURE.

10.0 ADHERENCE OF COATING TEST

Two steel wires removed from the new cable were wrapped eight times around a cylindrical mandrel three times the diameter of the wires in accordance with ASTM B498/B498M-19 Section 9 and ASTM B606/B606M-19 Section 8. No zinc layer flaked off from the steel wire tested, Figure 144.

FIGURE 144. CLOSE VIEW OF FOUR OF THE LOOPS. NO FLAKING OF THE ZINC COATING

11.0 DISCUSSION

The conductor cables examined broke as a result of overloading,

All the aluminium wires examined showed dimples on their fracture surfaces (we observed one aluminum wire with cut surface). Similarly, fractured steel wires examined showed dimples on their fracture surfaces. Dimples formed on the fracture surfaces, typical of ductile overload fracture that propagates in a transgranular manner.

Dimples observed on the aluminium wires were large, readily observable at low magnifications. Steel wires showed extremely small dimples, not readily observable. Metallographic examination of the steel wires revealed that they were cold drawn to increase their yield strength. This is the reason that dimples observed on the steel wires fracture surfaces are resolvable at high magnification.

Three of the four samples were apparently completely separated. Visual, metallographic and SEM examinations suggested majority of the steel wires of those samples were badly damaged during and after the incident. We were informed later by the client that those samples did not separate completely and separation was completed by cutting the unfractured steel wires. One of the samples (sample #4) did not show complete separation, but some aluminium wires were broken. Broken and just necked aluminium wires had concentrated on one area. This suggested that area was at a higher stress when compared to the other areas on the circumference of the cable. We arbitrarily called that area as 6 o'clock. This observation suggests that the circumference of the cable was not exposed to equal loading. Unequal loading resulted in higher load levels on one side of the circumference (arbitrarily called 6 o'clock), aluminium wires started cracking there starting from the outer layers of the 3 layer aluminium wires and continued gradually towards the inner layers. Then breaking continued onto aluminium wires on the other side as the elongation on the aluminium wires is less than one third of that of steel wires. Even though aluminium wires are more on conducting the power than carrying the load, this decreased the load bearing capacity of the cable and the steel wires gave way.

Mechanical testing of the wires showed that the elongation of the aluminium wire is slightly below the minimum specified in ASTM B230/B230M-07(216). The standard specified 1.8% elongation minimum and test results varied from 1.2% to 1.5%. This implied that the aluminium wires do not conform to the specified limits. However, it should be borne in mind that the aluminium wires are tested prior to making cables. We removed sample from cables. The aluminium wires used for making conductors are highly pure not to sacrifice conductivity. Aluminium, especially in its unalloyed form, has a tendency for strain localization. As soon as dislocation starts moving in one plane (and in a few neighbouring planes) other dislocations continue moving in the same plane as the materials work hardening coefficient is low. This allows localization of the strain, and because material cannot distribute its plastic deformation over a wide region, it breaks where the strain is localized, creating local plastic deformation there and very low elongation percentage. This is the general reason for low elongation in aluminium wires. If we add twisting, deformation, scratching etc. while making cables, then the elongation will further decrease due to ease in crack initiation and localization of the strain in the affected areas. Therefore, it cannot be concluded that the aluminium wires had originally lower elongation percentages.

Steel wires showed that UTS of the wires were below the minimum required for ASTM 606/606M-19. Other values were within the specified limits. However, all the mechanical properties conformed to ASTM B498/B498M-19 for all classes.

Bending, wrapping and adherence of coating tests showed wires are within specified limits. Steel wires are zinc coated and the coating weight of the steel wires conform only to Class A of ASTM B498/B498M-19. We have observed some oxidation/corrosion products on steel wires. However, zinc coating of the examined steel wires was intact and examination did not reveal any relationship between the observed oxidation/corrosion products and the fracture. Table 5 shows a summary of the results and compares them to the minimum requirements of the standards. Table 6 shows the comparison the cable to ACSR cables in ASTM B232/B232M-12. Results suggest the conductor conforms to ASTM B232/B232M-12, Class AA, 54/9 for the properties tested.

TABLE 5. COMPARISON OF THE TEST RESULTS

	Aluminium		Cable	Steel	
	B233	**B230**	**B232**	**B498**	**B606**
Al wire chemistry	✓	✓	N/A	N/A	N/A
Steel wire chemistry	N/A	N/A	N/A	✓	✓
Al wire, UTS	✓	✓	N/A	N/A	N/A
Al wire, Elongation	✕ < 1.8	✕ < 1.8	N/A	N/A	N/A
Steel wire, UTS	N/A	N/A	N/A	N/A	✕
Steel wire, Strength at 1%	N/A	N/A	N/A	N/A	✓
Steel wire, elongation	N/A	N/A	N/A	N/A	✓
Al wire, Material 1350 H16 and H26	✓	✓	N/A	N/A	N/A
Steel wire – Material – Zinc coated – Cold Drawn	N/A	N/A	N/A	✓	✓
Steel wire – Zinc coating	N/A	N/A	N/A	Class A ✓ Class C ✕	Class A ✓
Al wire - Bending test	N/A	✓	N/A		
Steel wire – Wrap test	N/A	N/A	N/A	✓	✓
Adherence coating test	N/A	N/A	N/A	✓	✓

TABLE 6. COMPARISON TABLE

CONSTRUCTION REQUIREMENTS OF ALUMINUM CONDUCTORS, STEEL REINFORCED (ACSR), ASTM B232/B232M-17													
	Size		Code Words	Class	Stranding Design Aluminum/Steel	Stranding						Nominal OD of Conductor, In	Mass lb/1000ft
						Aluminum Wires			Steel Wires				
	cmil	AWG				Number	Diameter, In	Layers	Number	Diameter, In	Layers		
ASTM B232/B232M-17	1,192,500	N/A	GRACKLE	AA	54/19	54	0.1486	3	19	0.0892	2	1.338	1531
CABLE TESTED/ minimum values	Not Tested				54/19	54	0.1492*	3	19	0.0890*	2	1.3455#	Not Tested

*Wires from the broken samples

Average of 12 readings

ACUREN

12.0 CONCLUSIONS

It was concluded that:

1. The cables examined broke as a result of overloading;
2. Aluminium wires showed lower elongation when tensile tested. This could be due to natural effect of cable manufacturing;
3. Steel wires conform to the specified limits of ASTM B498/B498M-8 Class A wires;
4. Conductor conform to a 54/19 stranding, 3-layer aluminium, 2-layer steel wires, Class AA as per tests performed (we did not check cmil and mass).

We trust that this report provides the information that you require. Please contact me if you require any further information, or if we can be of assistance in any other way.

Yours Sincerely,

Prepared By,

Ethan (Erhan) Ulvan, PhD., P.Eng., FASM
Manager – Engineering, Laboratories, Nuclear and FES, Eastern Canada, Past President, Failure Analysis Society, American Society for Materials International

Reviewed By,

Yunlin Gao, MEng.
Head of Failure Analysis and Metallurgical Engineering Department

128-21-ACU020-0003 R0 Failure Analysis of A Conductor DRAFT.docx

Please note that unless we are notified in writing, samples from this investigation will be disposed of after 60 days.

Client acknowledges receipt and accepts custody of the report, work or other deliverable (the “Deliverable”). Client agrees that it is responsible for assuring that any standards or criteria identified in the Deliverable and Statement of Work (“SOW”) are clear and understood. Client acknowledges that Acuren is providing the Deliverable according to the SOW and not other standards. Client acknowledges that it is responsible for the failure of any items inspected to meet standards, and for remediation. Client has 15 business days following the date Acuren provides the Deliverable to inspect, identify deficiencies in writing, and provide written rejection, or else the Deliverable is deemed accepted. The Deliverable and services are governed by the Master Services Agreement (“MSA”) and SOW (including Job Sheet). If the parties have not entered into an MSA, then the Deliverable and services are governed by the Statement of Work and the “Acuren Standard Service Terms” (www.acuren.com/serviceterms) in effect when the services were ordered.

*The Client Representative who receives this report is responsible for verifying that any acceptance standard**s** listed in the report are correct, and promptly notifying Acuren of any issues with this report and/or the work summarized herein. The owner is responsible for notifying Acuren in writing if they would like their samples returned or placed into storage (at their cost) otherwise, all samples/specimens associated with this report will be disposed of 60 days after the report date.*

NOTES:

A) Any tests subcontracted to an approved subcontractor are highlighted above (*)
B) The Client will be notified if completion of test will exceed the time specified as a result of the volume of work or the complexity of the test
C) The Client should specify the standards used for testing/comparison purpose. We have a comprehensive library and online subscription of commonly used standards, however, we may ask the client to supply the standards if not common or the Client requests to purchase standard(s) on his behalf.
D) Please provide all the necessary information/documents (MSDS) pertaining to any Toxic / Dangerous materials prior to their arrival in the Laboratory.

Appendix F - Failure Analysis of Electrode Cross Arm in Labrador Island Transmission Link (LITL)

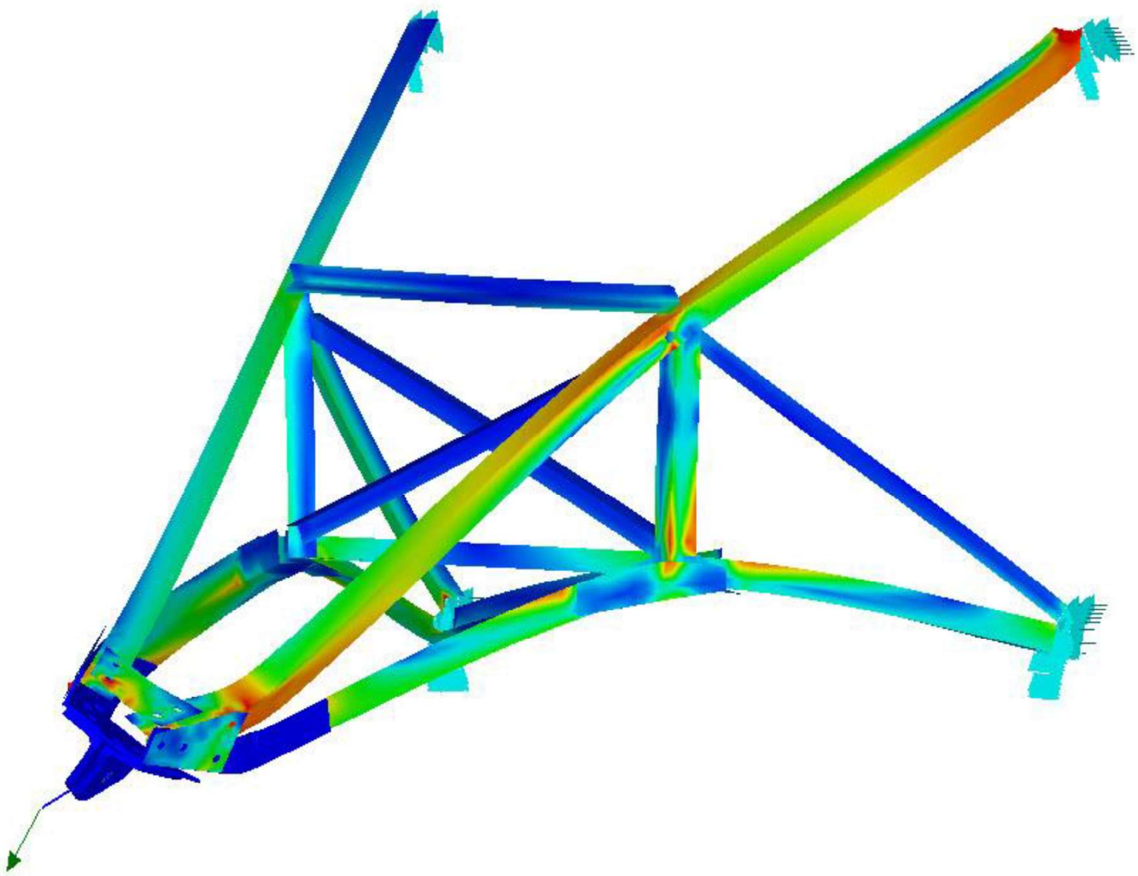

FAILURE ANALYSIS OF ELECTRODE CROSS ARM IN LABRADOR ISLAND TRANSMISSION LINK (LITL)

29.03.2021

REPORT – INFORMATION SHEET

DOCUMENT SYSTEM CODE	REPORT TITLE
8321-004-04-MIN-001	Failure analysis of electrode cross arm in Labrador Island Transmission Link (LITL)
REPORT NUMBER / TOTAL PAGES	**PROJECT**
01 /32	Labrador Island Transmission Link
PROJECT MANAGER – CLIENT REPRESENT.	**CLIENT**
Trevor Andrews	Newfoundland and Labrador Hydro
PROJECT MANAGER – EFLA	**AUTHOR**
Viven Naidoo	Guðni Páll Pálsson, Egill Thorsteins

KEYWORDS

Failure analysis, FE-analysis, Structural capacity

REPORT STATUS

☐ Draft
☐ Copy editing
☒ Final

REPORT DISTRIBUTION

☐ Open
☐ With client permission
☒ Confidential

VERSION HISTORY

NO.	AUTHOR	DATE	REVIEWED	DATE	APPROVED	DATE
	Guðni Páll Pálsson	2021-03-29	Egill Thorsteins	2021-03-29	Viven Naidoo	2021-03-29

TABLE OF CONTENTS

1 Introduction

This report covers the electrode cross-arm's failure analysis in the Labrador Island Transmission Link (LITL). In the ice storm in January 2021, failure occurred in some electrode cross-arms in the A1 tower. This report aims to understand the failure mechanism better and replicate the failure mechanism with a Finite element model (FEM). The goal is to predict the electrode cross-arm's capacity for different longitudinal and vertical loading combinations.

Drawings of the electrode cross arm can be seen in Appendix B.

The geometry of the cross arm is modeled in Inventor, as shown in the figure below. The attachment point was modelled such that it takes into account the shackle, which acts as a lever on the attachment plates creating additional moments and torsion in the cross arm.

FIGURE 1 Geometry of the electrode cross arm modeled in Inventor

For the failure analysis, the cross-arm was modelled in Inventor Nastran, an advanced Finite Element program integrated into Inventor. The model is described in detail in chapter 4.

In this report, the main focus is on modeling the behavior of the cross-arm tip. It is most likely that the failure initiates there, and there are local effects at the tip which cannot be accounted for using simple calculations.

2 Failure of tower type A1 in the January storm 2021

Several towers had damage in the electrode cross-arm in the January storm 2021. Below are a few examples of the failures that have occurred.

Figure 2 shows the failure of electrode cross-arm in tower 340. At least five failures can be identified. The first failure is believed to be a block-shear failure through one bolt hole and then along the L-profile radius, see Fig. 5. Failure "2" is partly a local failure of L-profile; see Fig.4.

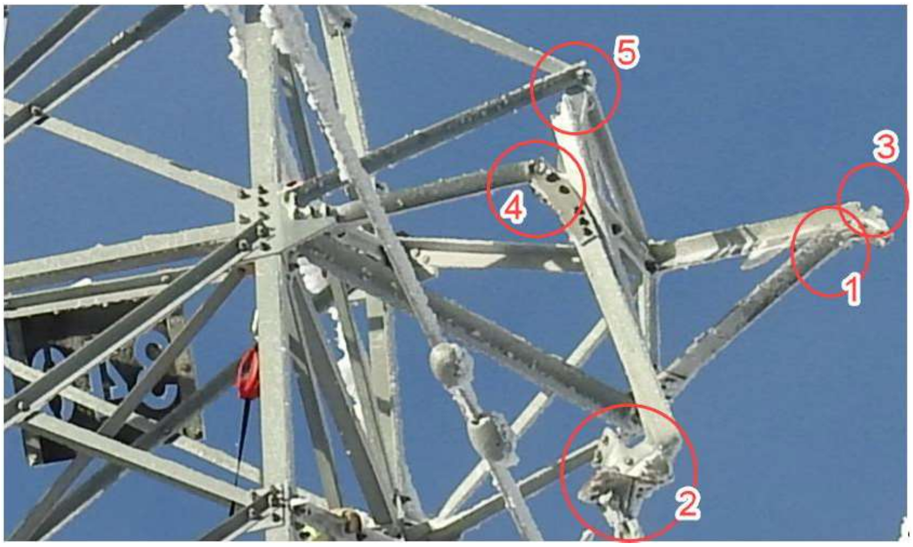

FIGURE 2 Failure in tower 340. At least 5 failures can be seen. It is believed that the first failure is where "1" is located. The next failure might be at "2" and the third at "3".

FIGURE 3 Failure location "1" and "3". Failure "1" is block shear failure through one bolt hole.

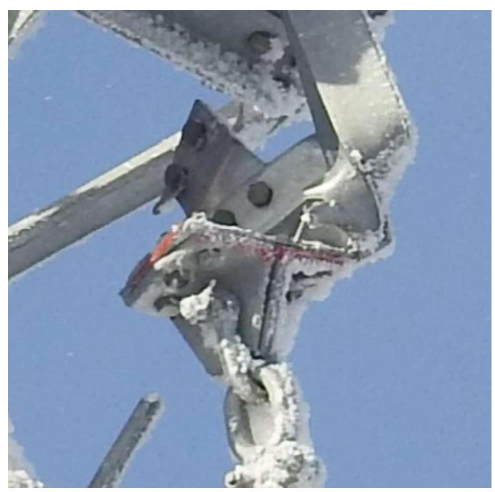

FIGURE 4 Failure location "2". Bolts are intact.

FIGURE 5 Examples of failure mechanisms. Block-shear failure of leg profile to the left and local buckling of the flange on the right

FIGURE 6 Examples of failure mechanisms, tower 330?

FIGURE 7 Tower 368. Cleats in electrode attachment bent in the longitudinal direction, indicating that the tower has experienced considerable longitudinal load.

3 PLS-Tower model

All tower design[1] in the LITL project was made using the PLS-Cadd and PLS-Tower programs. The design was based on a FEM program using a truss model with a few beam elements, i.e., members are only assumed to support axial force. The capacity of members and connections is calculated according to the project specification, mainly following the American standard ASCE 10-97. The model is shown in Figure 8.

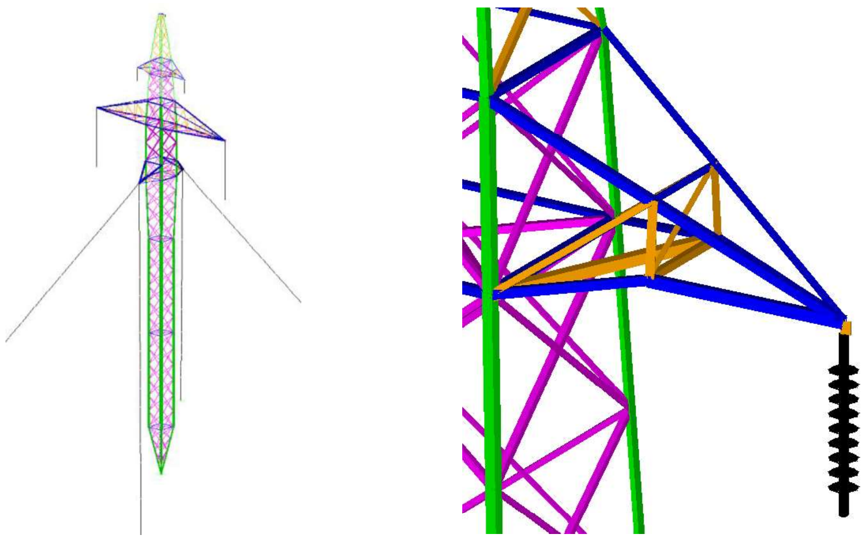

FIGURE 8 PLS-Tower model of the A1 tower and electrode cross arm

3.1 Limitations of the PLS-Tower model

The PLS-Tower models used in the design of the LITL are primarily truss models, meaning that members can only carry axial forces, bending moments and torsional moments are disregarded. This is the usual practice when designing lattice overhead transmission towers. Connections are not modeled in detail but are calculated based on user input on the number of bolts and spacing between them.

Lattice towers made from L-profiles have limited capacity for eccentricity in connections and where the load is applied. They require that detailing is made with small eccentricities in connecting members and that load is applied to a point with the intersection of three members. In other words, the connections need to be carefully designed such that the L-profiles do not experience bending and torsion.

A brief review of the PLS-Tower model used in the design of A1 towers revealed that two simplifications had been made in model assumptions that can be questioned:

1) All members at the tip of the cross-arm are assumed to be connected together into a single point

[1] Design was carried out by SNC-Lavalin.

2) The longitudinal eccentricity of loading, resulting from the shackle and cleats in the attachment point, is ignored.

At the tip of the cross arm, the main members are connected to a single point in the PLS-Tower model. In reality, there is a spacing of about 130 mm between the main members at the end. This can have a large influence on the force distribution in the members in the case of longitudinal force and may lead to some overestimation of the capacity.

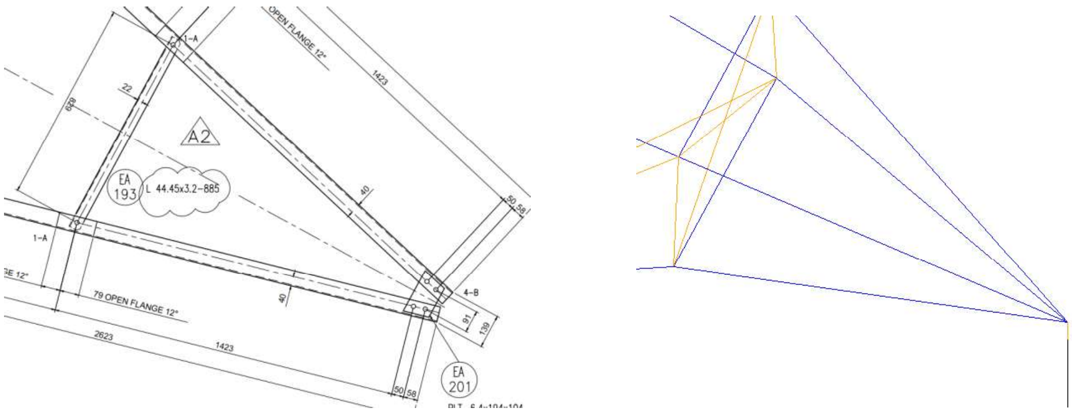

FIGURE 9 Geometry of the tip does not model the separation of members at the tip in the PLS-Tower model

The PLS-Tower model does not consider how the load is applied at the attachment point. There is a shackle where the insulator string is attached, which acts as a lever arm on the cross arm. A significant bending and torsional moment is acting on the cross arm in case of longitudinal force. This moment is ignored in the structural analysis due to the limitations of the PLS-Tower model.

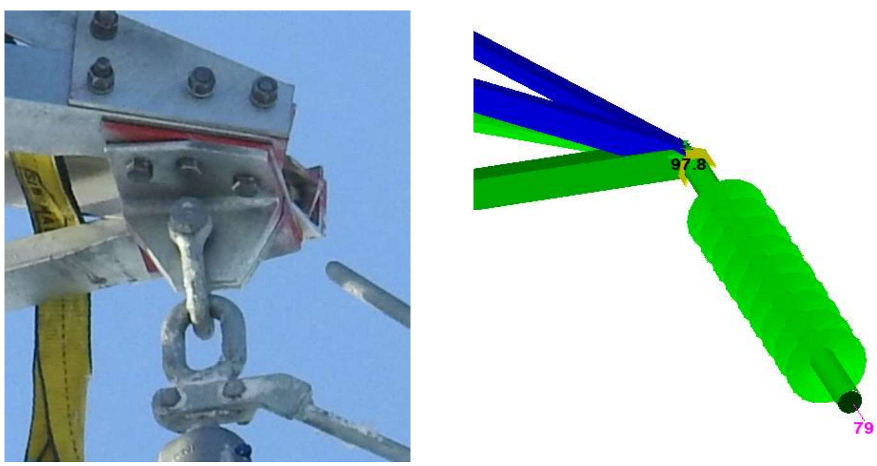

FIGURE 10 Shackle in the attachment point, not included in the PLS-Tower model

3.2 The capacity of the electrode cross-arm in the PLS-Tower model

The PLS-Tower model from the design of the A1 was used to make a loading failure envelope for the electrode cross-arm concerning combinations of longitudinal and transversal forces. Figure 10 shows the capacity of six different loading combinations of longitudinal and vertical loading. Table 3 shows utilization in critical members, and it reveals what is critical in each load case. Table 2 shows what is critical within each member. Rupture of connection is critical for all elements in tension, while buckling is critical in compression.

Design is made using a strength factor of 0.9 for normal loading and 1.0 for accidental loading. Here the strength factor has been removed for easier comparison with the FE-Analysis.

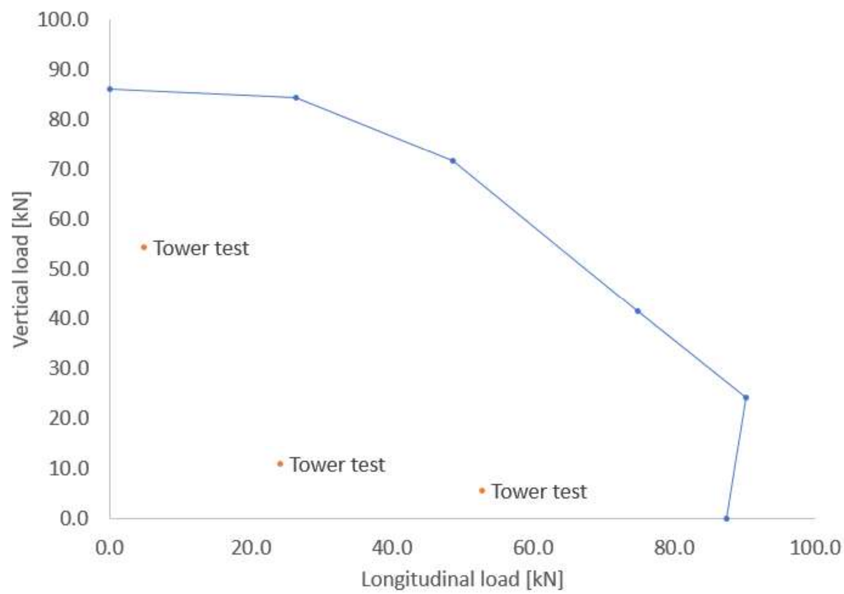

FIGURE 11 Failure envelope for the cross arm according to the PLS-Tower model. Three loading points from full scale tower test are included.

The A1 tower was full-scale tested. Figure 11 shows three of the load cases applied to the electrode cross-arm in the tower test, along with the capacity of the PLS-Tower model. There is some uncertainty if the longitudinal force was applied to the cross-arms tip with the correct eccentricity.

Note that the loading in Table 1 is scaled such that one or more members are at or around 100% utilization. It is done to understand what members are critical.

TABLE 1 Maximum load that the cross arm can carry according to PLS-Tower

LOAD NR	VERTICAL LOAD [KN]	LONGITUDINAL LOAD [KN]	RESULTANT LOAD [KN]	ANGLE OF OUTSWING
1	86.0	0.0	86.0	0.0
2	84.4	26.4	88.5	17.4
3	71.8	48.6	86.7	34.1
4	41.6	74.9	85.7	60.9
5	24.2	90.2	93.3	75.0
6	0.0	87.5	87.5	90.0

TABLE 2 Capacity [kN] of selected members in the PLS-Tower model

MEMBER NAME	TCA-02-2	TCA-02-1	TCA-01-1	TCA-03
Description	**Lower chord - tip**	**Lower chord - base**	**Upper chord - tip**	**Vertical bracing**
Block shear	**169***	**162***	**122***	**47**
Net section	252	203	153	98
Buckling	197	164	104	**39**
Bolt shear	304	304	304	101

*Capacity is a little conservative in PLS-Tower since standard end distances are used for connections.

TABLE 3 Utilization [%] of selected members in the tower model in different loading configurations

MEMBER NAME	TCA-02-2	TCA-02-1	TCA-01-1	TCA-01-2	TCA-03
Description	**Lower chord - tip**	**Lower chord - base**	**Upper chord - tip**	**Upper chord - base**	**Vertical bracing**
Load 1	55	65	**99**	75	68
Load 2	72	86	**101**	82	91
Load 3	79	95	91	86	**102**
Load 4	78	93	60	74	**101**
Load 5	76	92	42	66	**100**
Load 6	72	77	20	48	**102**

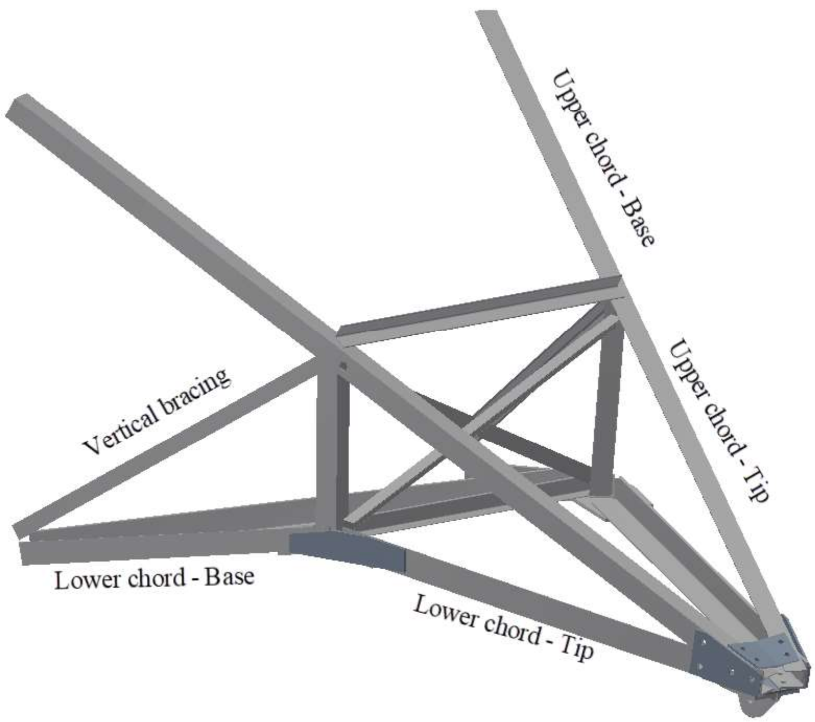

FIGURE 12 Member names for the cross arm

4 FE-model in Inventor Nastran

In this study, the FE-analysis was done using Inventor-Nastran, an advanced Finite Element software integrated into Inventor. The geometry of the cross arm was drawn in Inventor

4.1 Elements in the Nastran model

The model is created using a mix of solid and shell elements. Solid elements are used at the tip where the attachment point is to capture the local effects better. For the rest of the cross arm, shell elements were used, which are accurate enough for the structure's global behavior but are much less expensive when it comes to analysis time. In this manner, the boundary conditions of the cross-arm tip are accurately modeled. The solid elements are parabolic tetrahedron elements with ten nodes and three degrees of freedom in each node. The shell elements are linear quadrilateral elements with eight nodes and 5 degrees of freedom in each node. The six main bolts at the tip of the cross arm are modeled as bolt elements, which are essentially beam elements connected to the edge of the bolt hole. This is a fair approximation to the bolted connections but does not take into account slip in the bolt holes, for example. Another beam element was added to replicate the shackle where the load was applied. This beam has a length of 90 mm, which correlates with the fittings drawings of the shackle and cross arm tip.

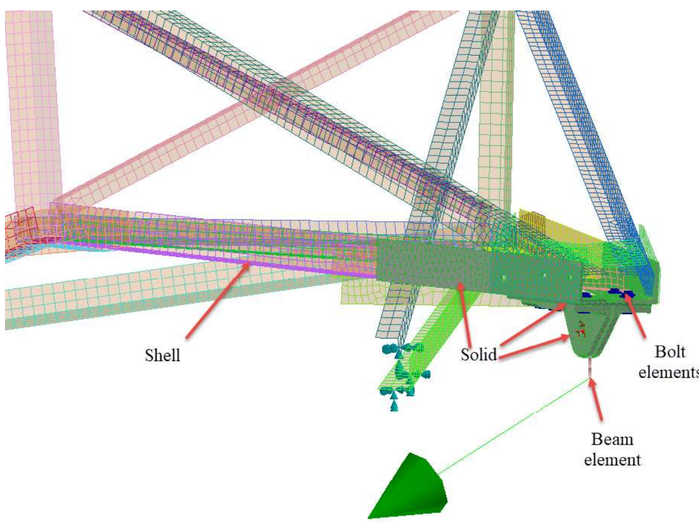

FIGURE 13 Different element types used in the model

4.2 Contacts

In the Inventor-Nastran program, there are several options to describe the contact between different elements. Most of the contacts in the model are "bonded," meaning they are practically glued or welded together. The exception is that the solid elements in the tip of the cross arm have "separation" contact. This means that they can separate, slide and move in relation to one another but are not allowed to pass through the boundary of the adjacent elements. This was vital to model the prying effects in the attachment point.

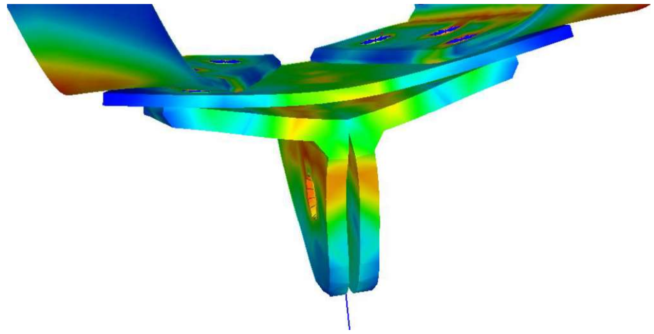

FIGURE 14 Example of "Separation" contact in the model under pure vertical load

4.3 Boundary conditions

The model is constrained where the cross arm should be connected to the tower.

Only the vertical flange is constrained in the upper chords, but in the lower chord, both flanges are constrained. The end face of the chord is restrained against translation and rotation in all directions.

4.4 Mesh

The mesh is defined such that the solid elements at the tip of the cross arm have a finer mesh than the shell elements that make up the rest of the structure. In addition, the mesh has local refinements around bolt holes and other geometric changes.

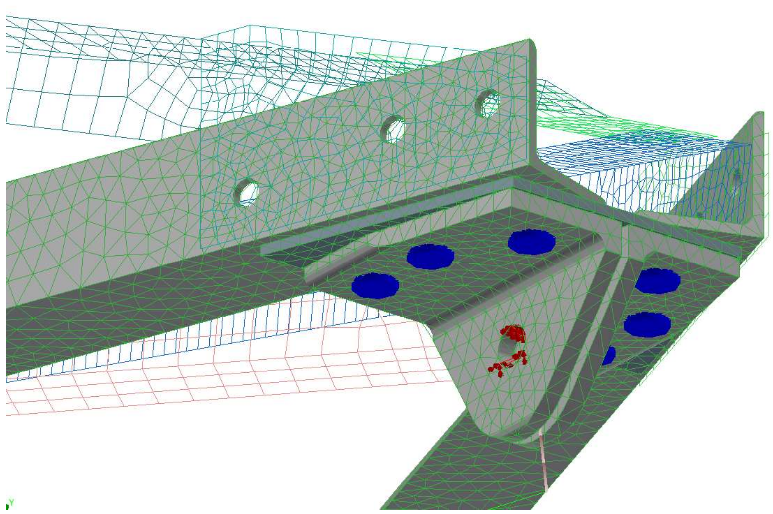

FIGURE 15 Example of the mesh used in the analysis

4.5 Non-linear analysis

In the beginning, linear analysis and normal modes analysis were performed to verify that the model behaves as expected. This gives a good first estimate but is nowhere near enough to capture the structure's highly non-linear behavior at or around failure load. Therefore, the model was run with non -linear analysis. The non-linear analysis in Inventor Nastran has both geometric and material non-linearity. The geometric non-linearity means that second-order effect are accounted for as the model solves the load in increments and updates the geometry after each step. The material non-linearity allows the steel material to yield and redistribute the stresses when the load exceeds the yield point.

The steel material used is CSA 350W with a yield stress of f_y=345 MPa and ultimate stress of f_u=450 MPa. The stress-strain curve was defined as an Elasto-Plastic material meaning that the curve has two different elastic moduli, one before yield and one after yield. The first modulus before yield is defined as E_1=210 GPa, but after yield, the modulus is defined as E_2=1.1 GPa, which is about a 200 fold drop in stiffness.

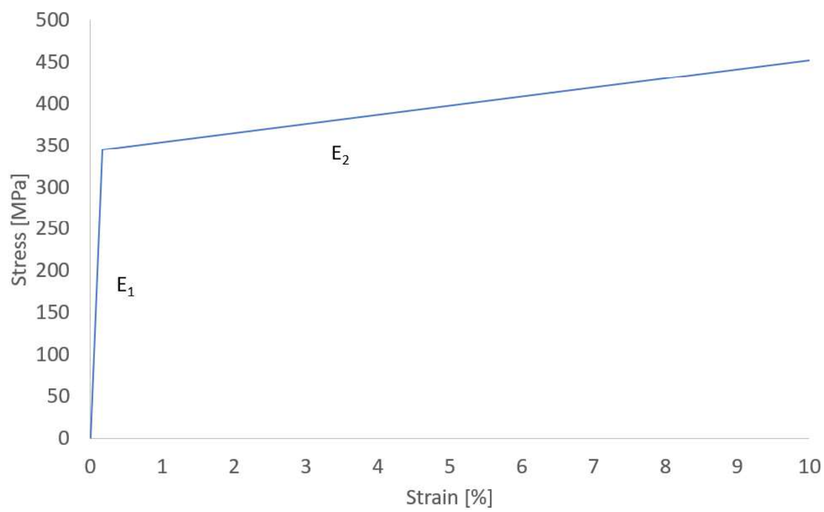

FIGURE 16 Elasto-plastic (By-linear) stress-strain curve used for the analysis

For this analysis, the load was divided into 20 increments for all load cases results saved after each increment. The results were analyzed afterward by stepping back the increments to find the failure point.

4.6 Loading

Loading is applied to a beam element attached to the attachment hole with a ridged body connection. This beam replicates the shackle that attaches to the attachment hole in the cleats and creates a torsional moment on the cross arm.

4.7 Stresses

The stresses shown in the report are based on the Von Mises yield criterion, which is the most commonly used method for displaying stress results. When displaying the stresses, corner stresses of each element are used. Averaging of the stresses is also applied to create smooth contours.

4.8 Limitations of the model

A model of a structure is always a simplification of reality to some degree. This model is no exception. The limitations of this model are based on the following points:

- Initial imperfections are not included in the model. It leads to that the second-order effects are under-estimated in the model, leading to a higher buckling capacity of the model than reality.
- Bolt slip is not included in the model. In reality, the bolts' diameter is 1-2 mm smaller than the holes. It leads to a slip in the bolt holes, which causes more deformations.
- The bearing of bolts is not accurately modelled. In reality, the bolt transfers load by a bearing surface in the bolt hole. The bolt elements used in the analysis transfer the load around the whole edge of the hole. It can have a significant effect locally around the hole and means that the capacity is over-estimated there.
- Dynamic loading is not considered in this analysis, although it is quite likely that some dynamic loading was involved in the failure, for example, due to ice shedding.

4.9 Failure criteria

One of the biggest challenges in this analysis is defining a failure criterion. That is, at what point will the cross arm fail. Analyzing structures with FEM models with this level of detail is relatively new in this field. Therefore, there are limited guidelines in standards on how these models should be interpreted. Engineering judgment is often needed to determine whether the structure will withstand a load or not. To get a better feel for what is happening in the model, the failure criterion is split into three different states: Yielding, high local strain, and local buckling. Each of these states will be described in more detail below

4.9.1 Yielding of the model

The yield point is when deformations are no longer elastic, meaning that the structure will be deformed after unloading. The yield point is estimated using two different methods. Firstly, the load-displacement graph is analyzed to find the point where the relationship becomes non-linear.

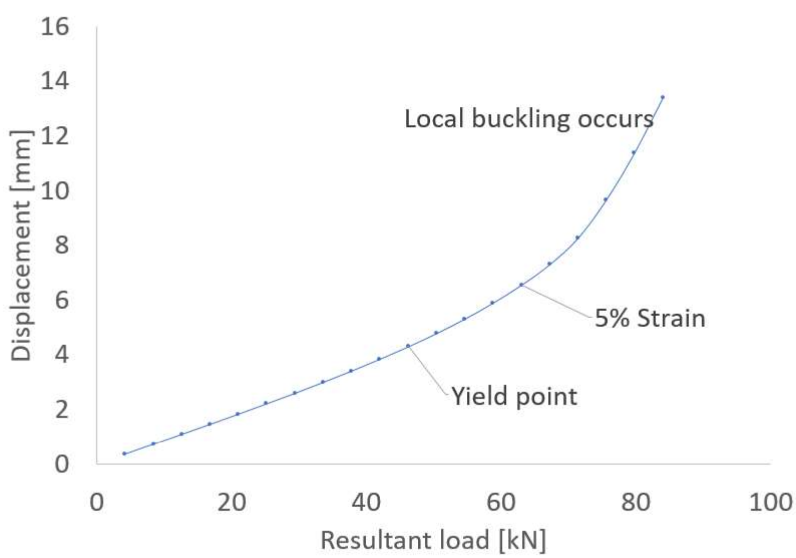

FIGURE 17 Example of a load-displacement graph from the analysis

Secondly the stresses at that increment in the analysis are considered to see if the model has stresses at or above the yield limit in large areas.

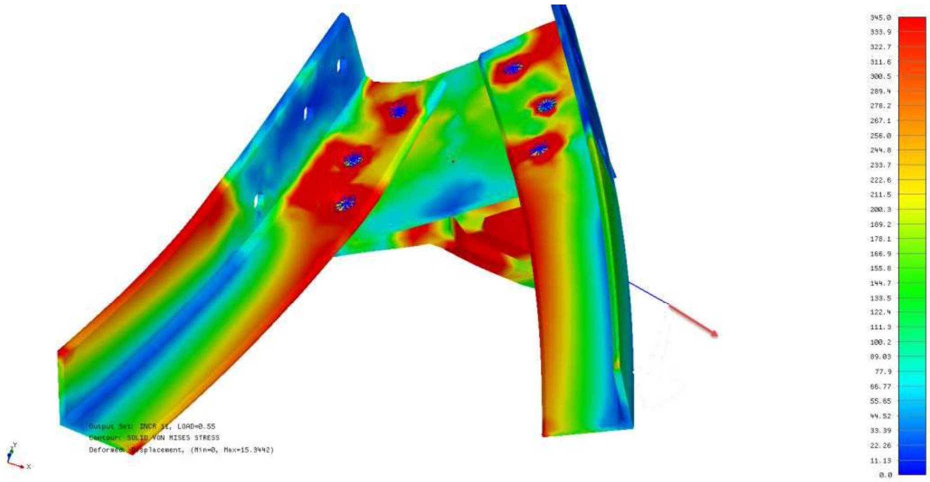

FIGURE 18 Example of stress distribution at yield point – Red is at or above the yield limit of 345 MPa

Generally, the structures' design is limited to yield stress, except for certain connections and local detailing.

4.9.2 High local strain

The second criterion that is considered is when local strain goes over 5%. The limit of 5% is recommended by the Eurocode standard, EN-1993-1-5 Annex C. It is likely that when the local strains reach this limit at and around bolt holes that the deformations are considerable and that rupture or block tear is imminent.

To find this point in the analysis, the strain distribution in the model is analyzed for the increments above the yield point until the limit of 5% strain is considered to be reached.

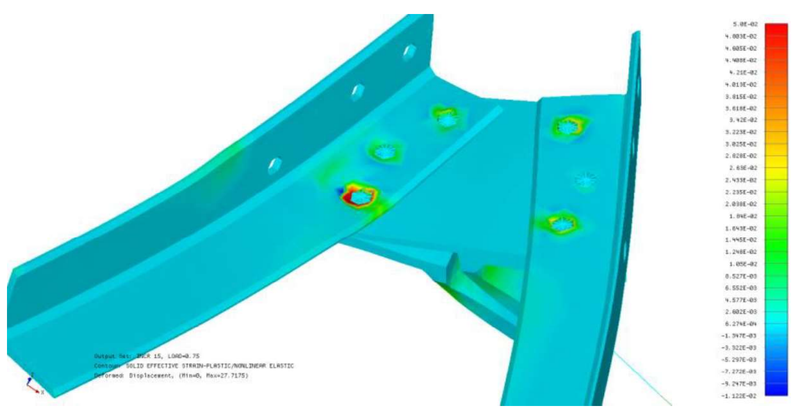

FIGURE 19 Example of strain distribution at 5% local strain – Red is at or above 5% strain

4.9.3 Local buckling

The final criterion is local buckling, which usually leads to excessive loss of stiffness and a progressive failure of the whole structure. Here the geometry of the deformed state is analyzed to look for signs of local buckling. To help with this, a strain limit of 2% was also considered as an indication that local buckling was imminent.

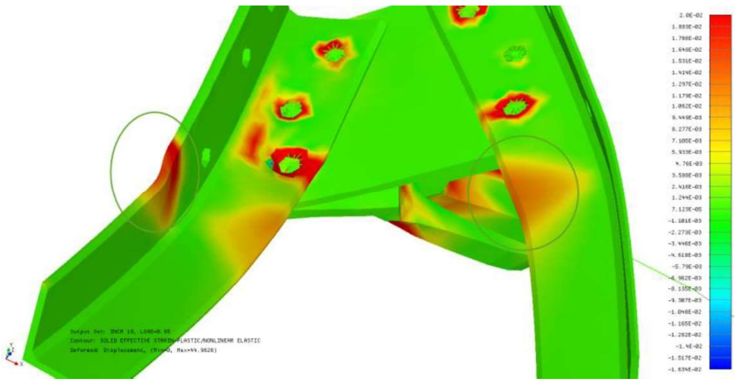

FIGURE 20 Example of local buckling – Red is at or above 2% strain

The analysis time increases drastically as the model approaches and, in some cases, exceeds the local buckling point. It is because that the model is more unstable, and solving for load and displacement becomes more challenging.

4.10 Replicating the failure mechanism

It was clear early in the process that the model accurately captures the local effect of the torsion on the tip of the cross arm. Both the stress distribution and deformed shape show similarities with the failure mechanisms documented on site. Figures 21 and 22 show the deformed shape of the tower and how the attachment cleat deforms. Figure 23 shows how well the program can replicate the local buckling of the flange. Figure 24 shows a high-stress level where the block-shear rupture has taken place in the failed cross-arms.

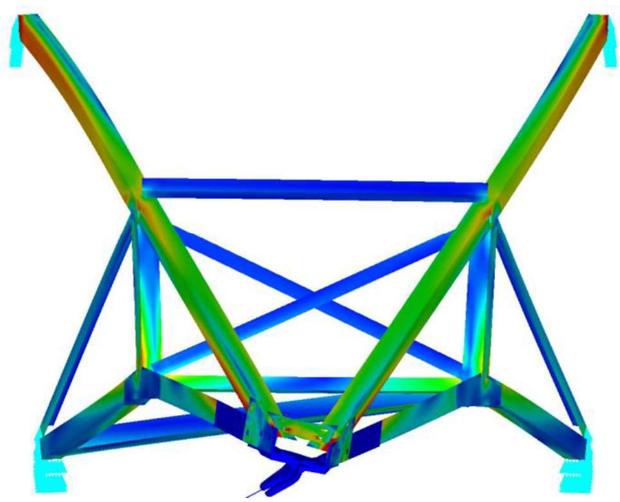

FIGURE 21 Deformed shape of the tower model scaled 5 times at 67 kN longitudinal load

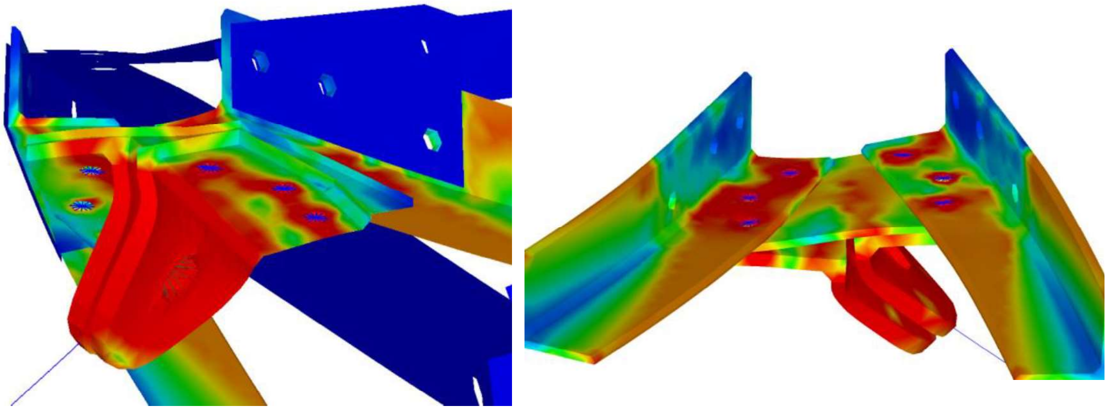

FIGURE 22 Deformed shape (scaled 5 times) and stress distribution at failure in longitudinal load 67 kN – scale set to 450 MPa

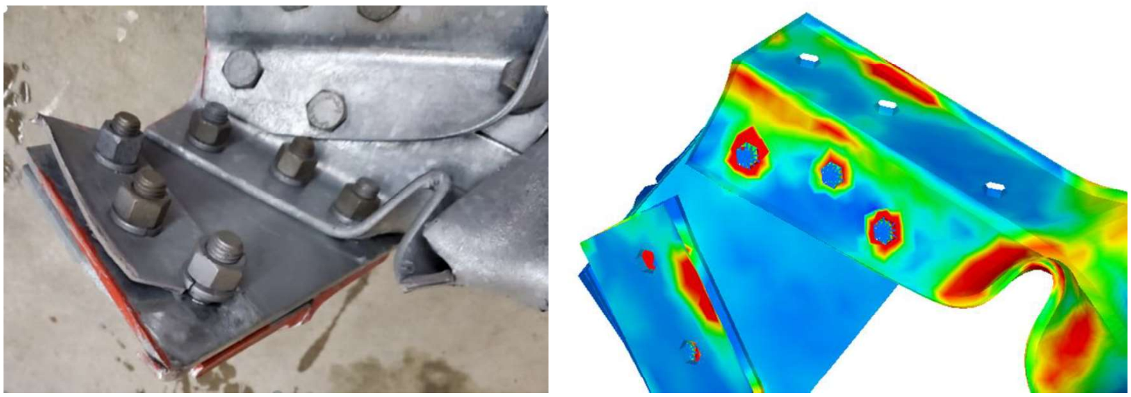

FIGURE 23 Comparison of failure mechanisms, local buckling of the flange, longitudinal load ~80 kN, Deformations NOT scaled.

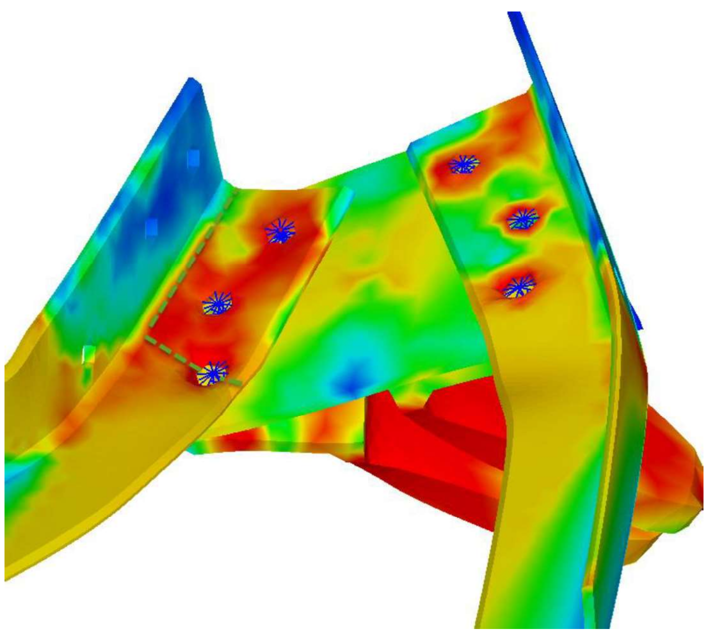

FIGURE 24 Signs of block tear in the model. Longitudinal load 67 kN

5 RESULTS

5.1 Estimating the failure load

In this chapter, the results are summarized, and a failure envelope for the cross-arm is presented. The results of this analysis involve a lot of data. Here the results are presented in a simple graph showing at what load combination of vertical and transversal load the cross-arm is expected to fail. The results of individual load cases can be seen in Appendix A

The failure line is composed using the FE-analysis results when failure is near the end of the cross-arm. The FE-analysis was not intended to model failure of elements in buckling or connection failure of members close to the tower body. Thus, those members' capacity is based on requirements in the design standard, which is represented in the PLS-Tower model. With reasonable longitudinal force, the envelope is determined from the FE-analysis, but for high vertical force and low transversal force, the PLS-Tower analysis is critical. Some engineering judgment in the transition zone.

Failure of the cross arm in FE-analysis is taken as the lower value of (i) the load at which local buckling occurs or (ii) the load at which 5% strain occurs. The analysis suggests that block-shear rupture (see example in Figure 24) will be the dominating failure mode when the load is predominantly longitudinal. But when the load is primarily vertical, the failure will be due to buckling or connection rupture.

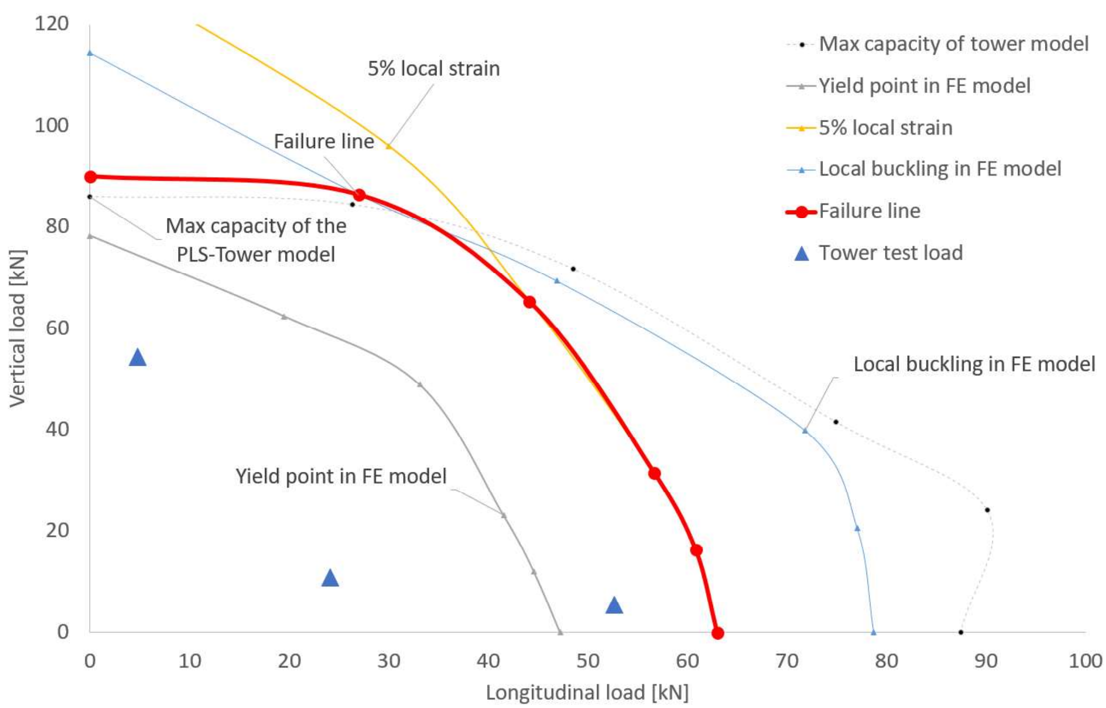

FIGURE 25 Failure envelope for the cross-arm

The following can be noted from Figure 25:

- The failure line has a lower capacity than presented in the PLS-Tower model. The largest difference is with high longitudinal force.
- The 5% rupture criteria are in most cases more critical than the local buckling in the FE-analysis
- The yield point in the FE-analysis is well below the failure line. Thus some permanent yielding will occur before failure.
- The loading applied used in the tower test is within the failure line.

The failure envelope presented in Figure 25 is without a strength factor.

APPENDIX A

Figure 26 shows the load-displacement within each analysis and Figures 27 to 32 show load-displacement for each load case. The reference point for the displacement is in the bottom plate of the cross-arm tip.

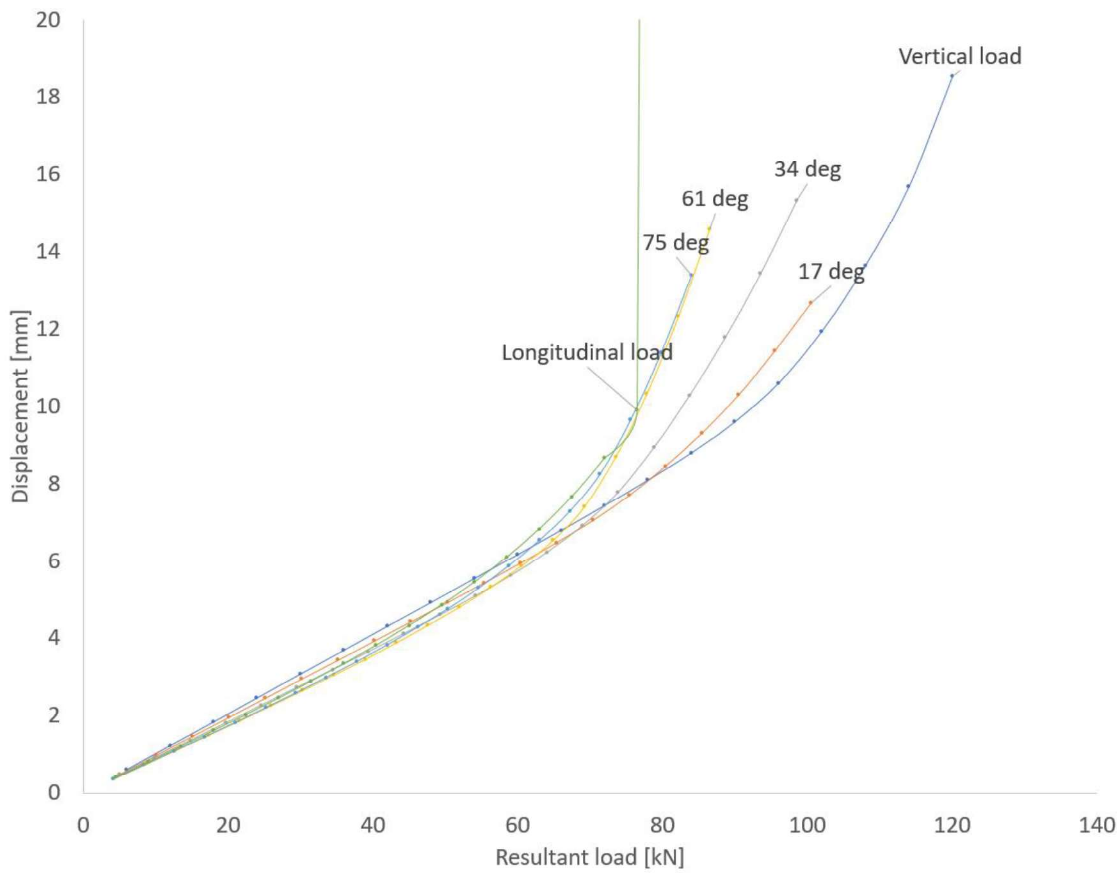

FIGURE 26 Load-displacement graph for the six different load cases.

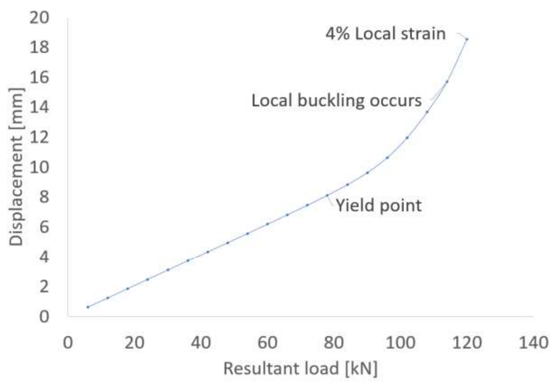

FIGURE 27 Load-displacement graph for load 1. Vertical load.

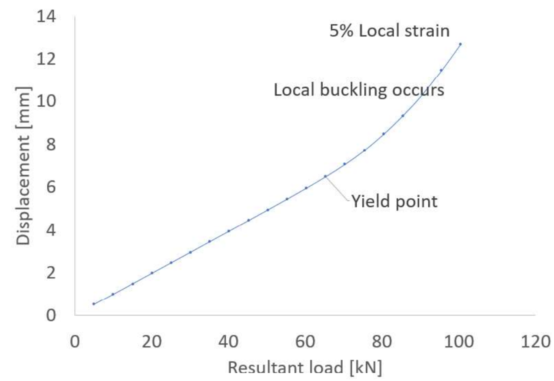

FIGURE 28 Load-displacement graph for load 2. 17 deg longitudinal swing.

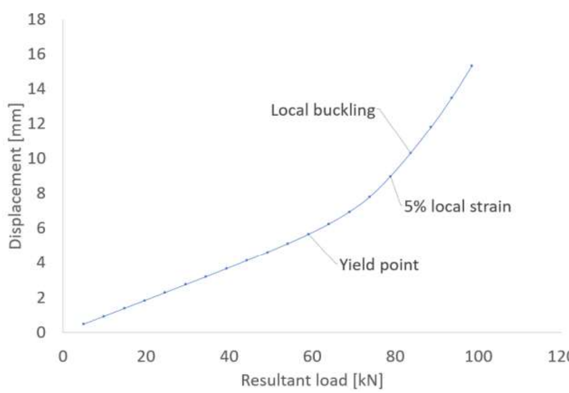

FIGURE 29 Load-displacement graph for load case 3. 34 deg longitudinal swing.

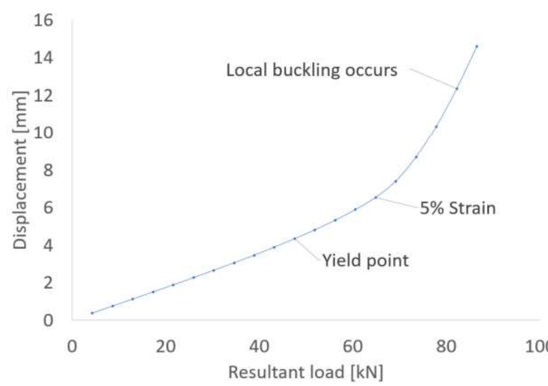

FIGURE 30 Load-displacement graph for load case 4. 61 deg longitudinal swing.

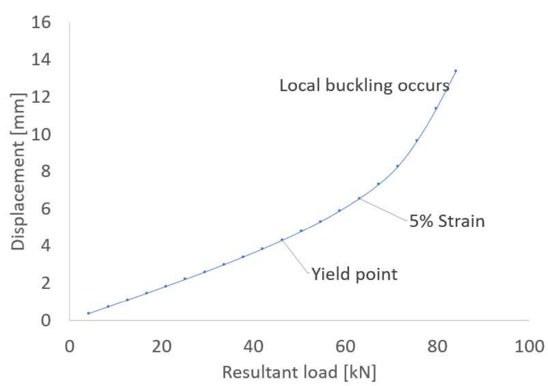

FIGURE 31 Load-displacement graph for load case 5. 75 deg longitudinal swing.

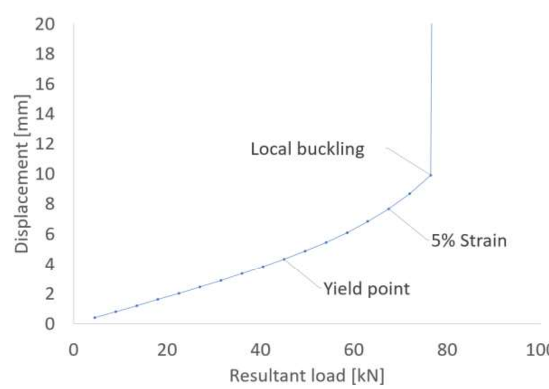

FIGURE 32 Load-displacement graph for load case 6. 90 deg longitudinal swing.

Load 1 – Vertical load

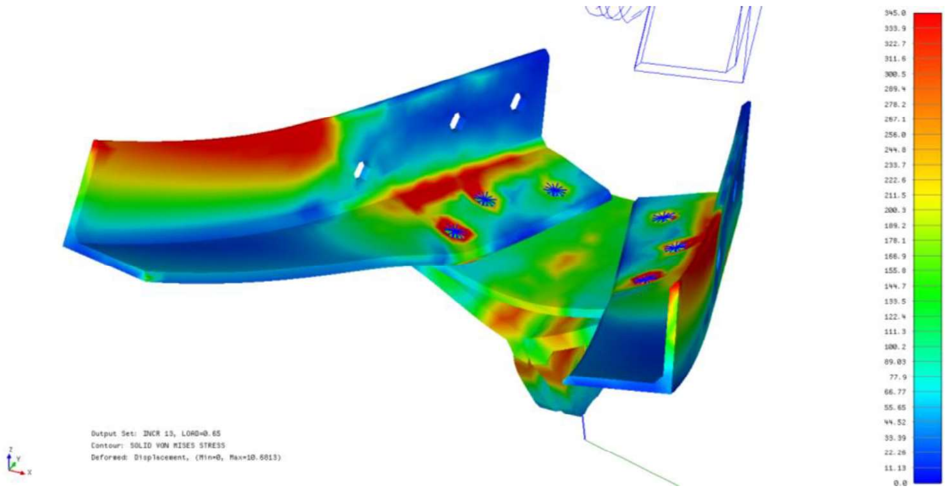

FIGURE 33 Load 1. Yield point estimated at resultant load 78 kN

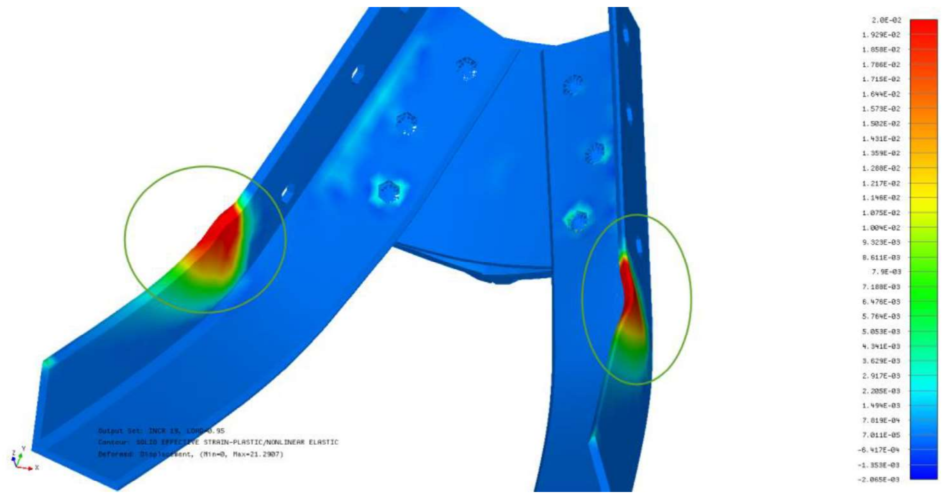

FIGURE 34 Load 1. Local buckling – Resultant load 114 kN

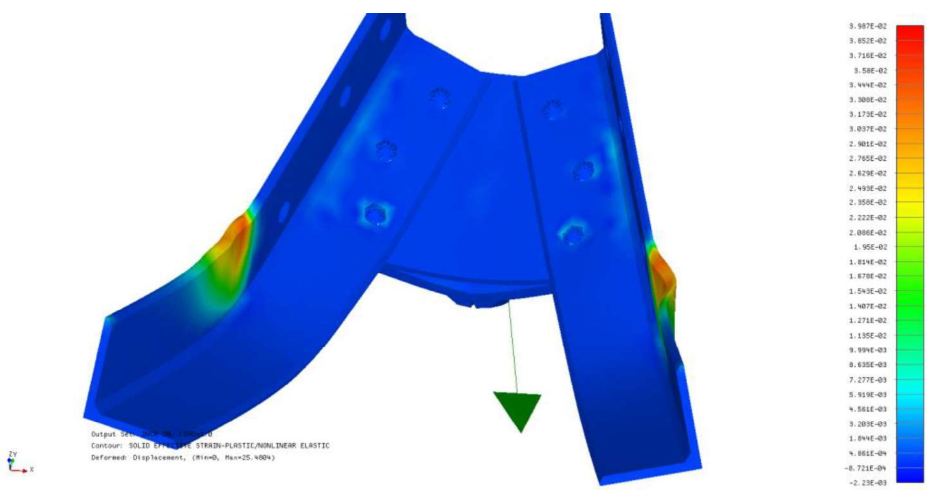

FIGURE 35 Load 1. Maximum local strain -4% - Resultant load 120 kN.

Load 2 – 17 deg longitudinal swing

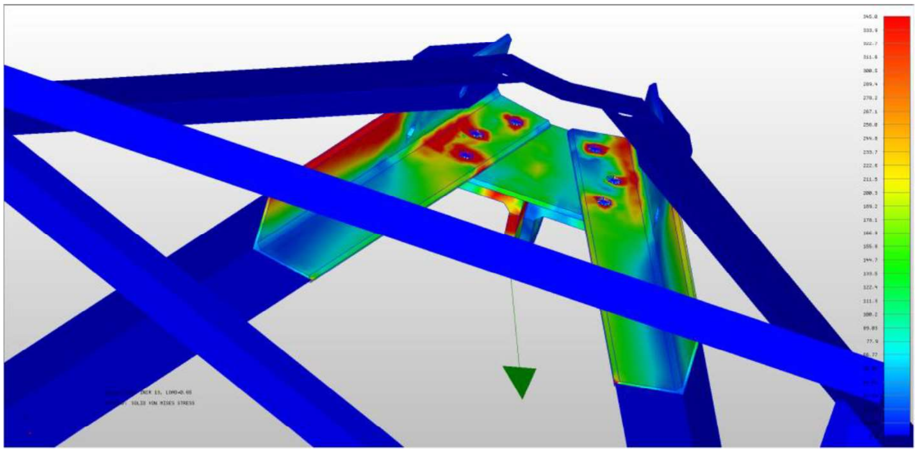

FIGURE 36 Load case 2. Yield point – Resultant load 65 kN

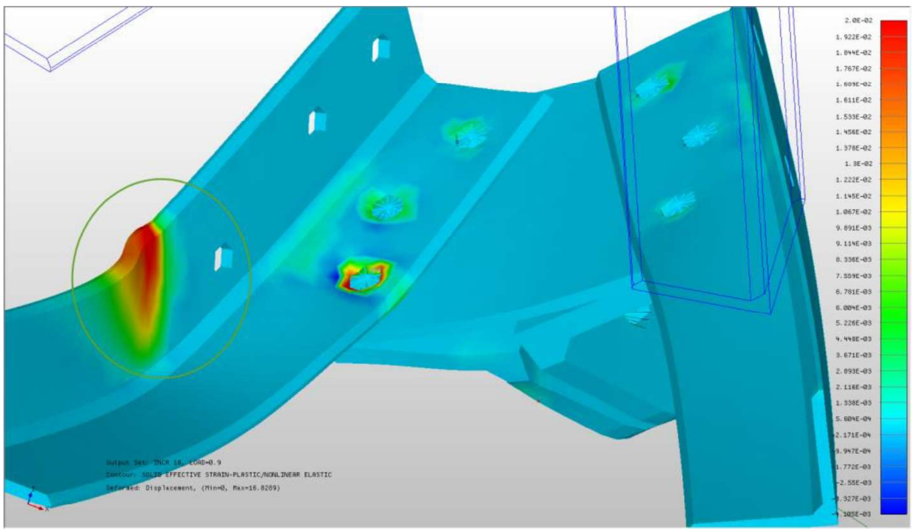

FIGURE 37 Load case 2. Local buckling - Resultant load 90 kN (2% strain).

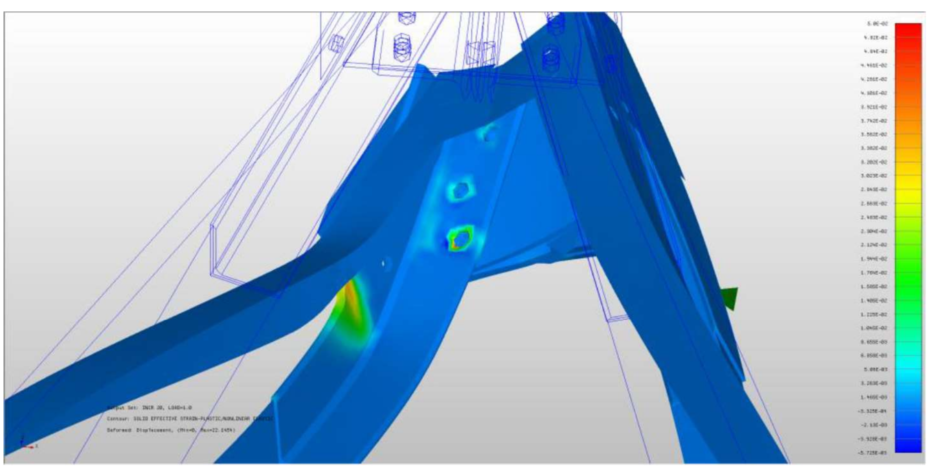

FIGURE 38 Load case 2. Maximum local strain – 4.5% - Resultant load 100 kN.

Load 3 – 34 deg longitudinal swing

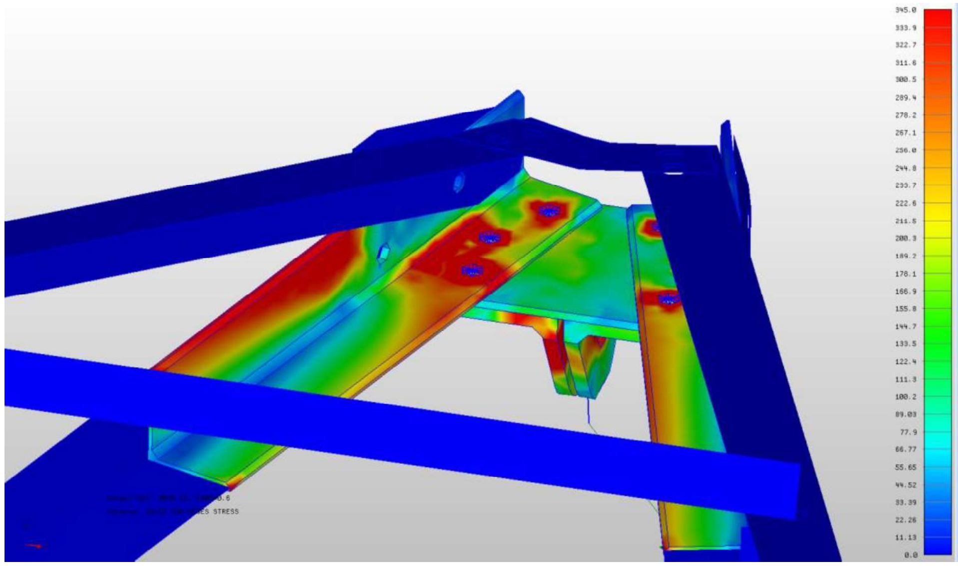

FIGURE 39 Load case 3. Yield point – Resultant load 60 kN

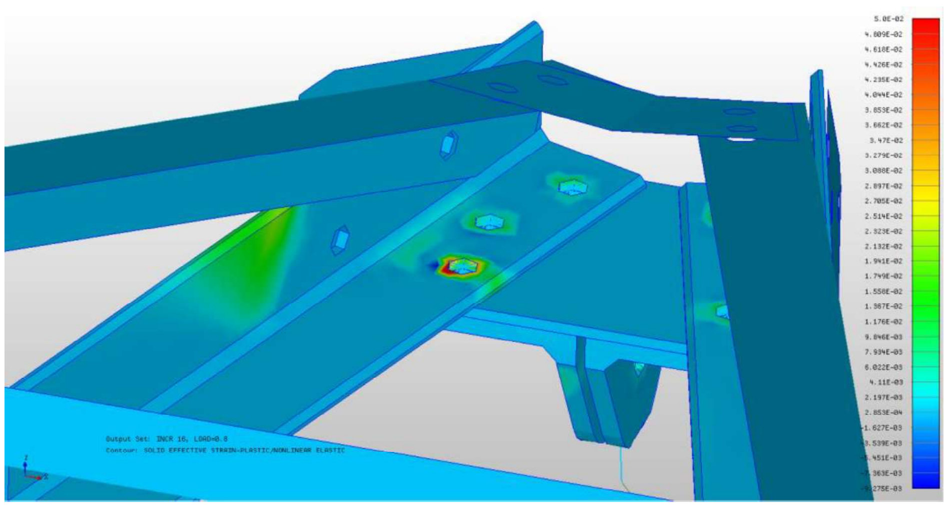

FIGURE 40 Load case 3. Local strain 5% - Resultant load 80 kN.

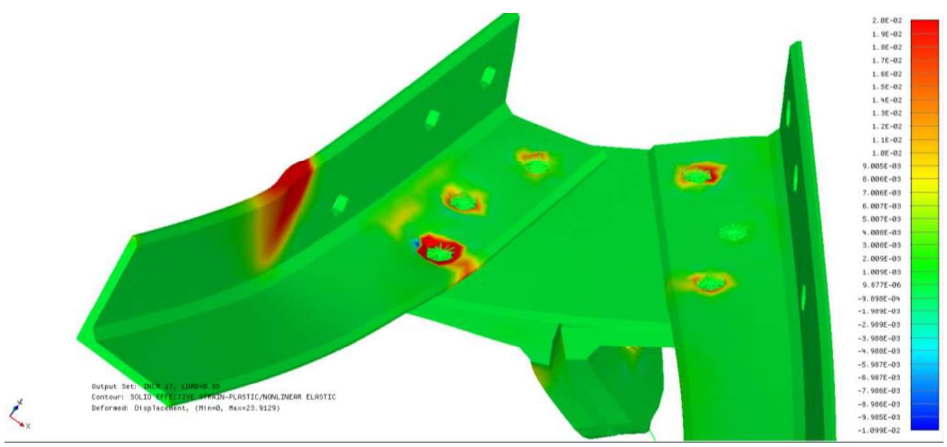

FIGURE 41 Load case 3. Local buckling – Resultant load 85 kN (2% strain)

Load 4 – 61 deg longitudinal swing

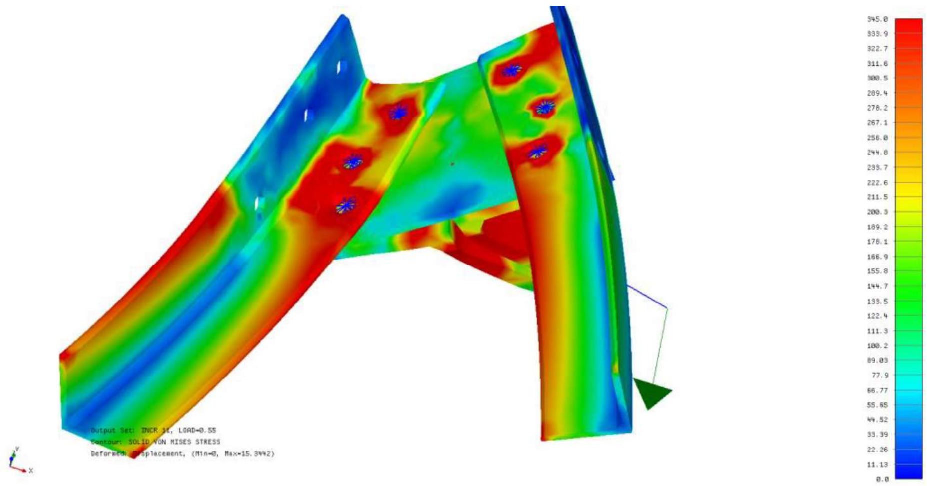

FIGURE 42 Load case 4. Yield point – Resultant load 48 kN.

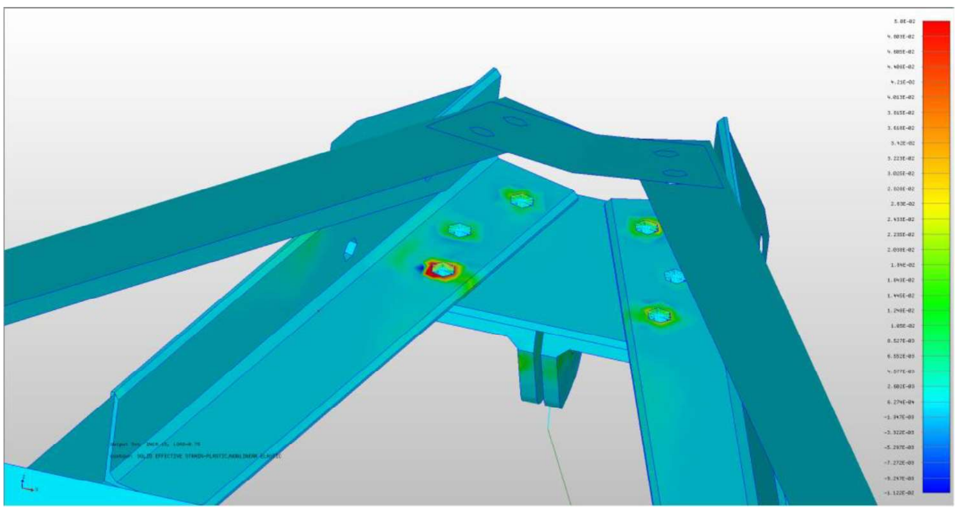

FIGURE 43 Load case 4. Local strain 5% - Resultant load 65 kN.

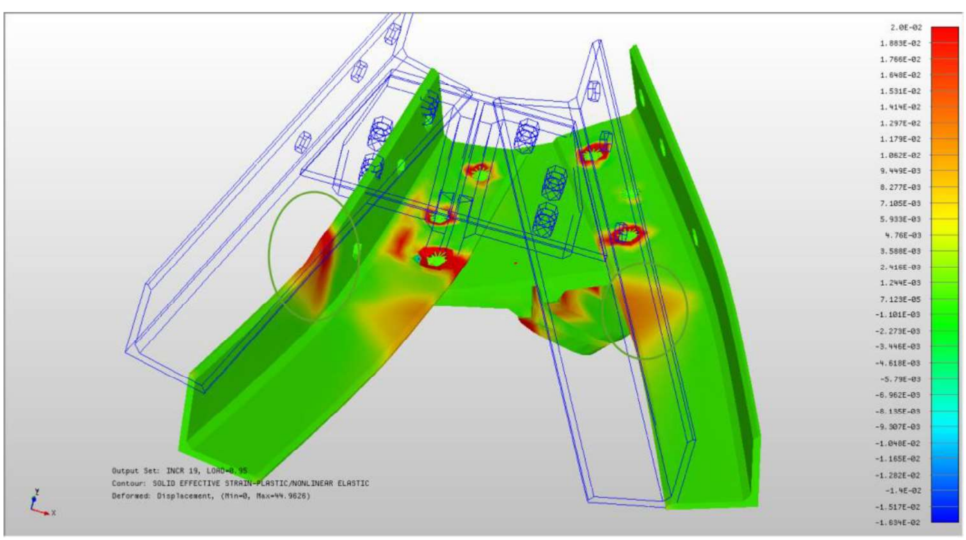

FIGURE 44 Load case 4. Local buckling – Resultant load 82 kN.

Load 5 – 75 deg longitudinal swing

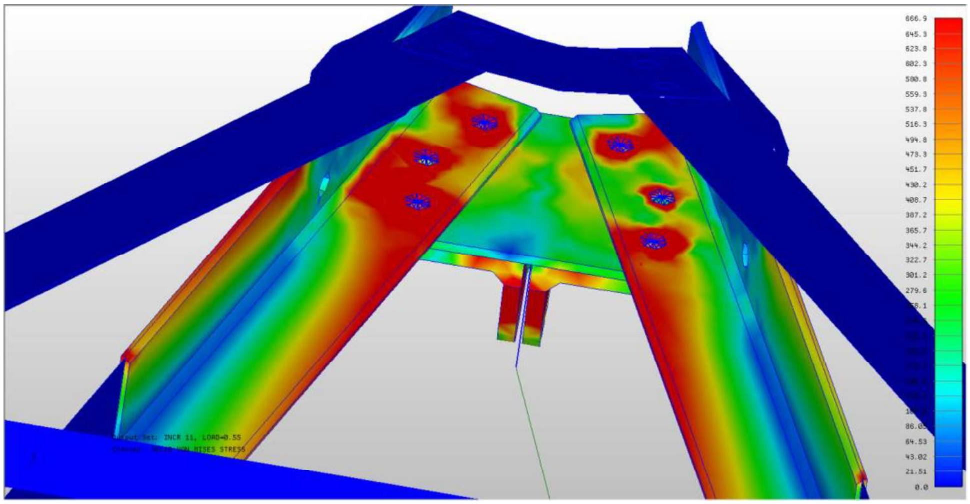

FIGURE 45 Load case 5. Yield point – Resultant load 46 kN

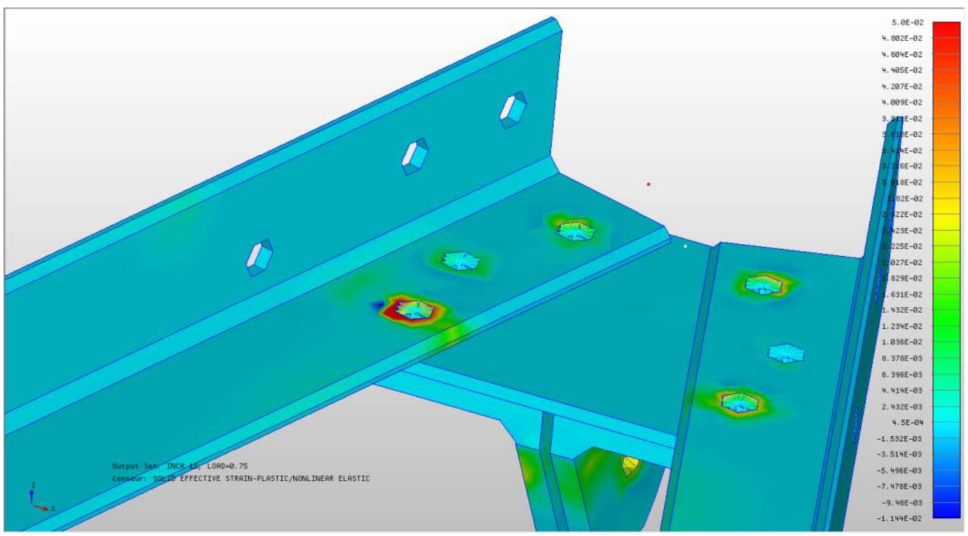

FIGURE 46 Load case 5. 5% local strain – Resultant load 63 kN.

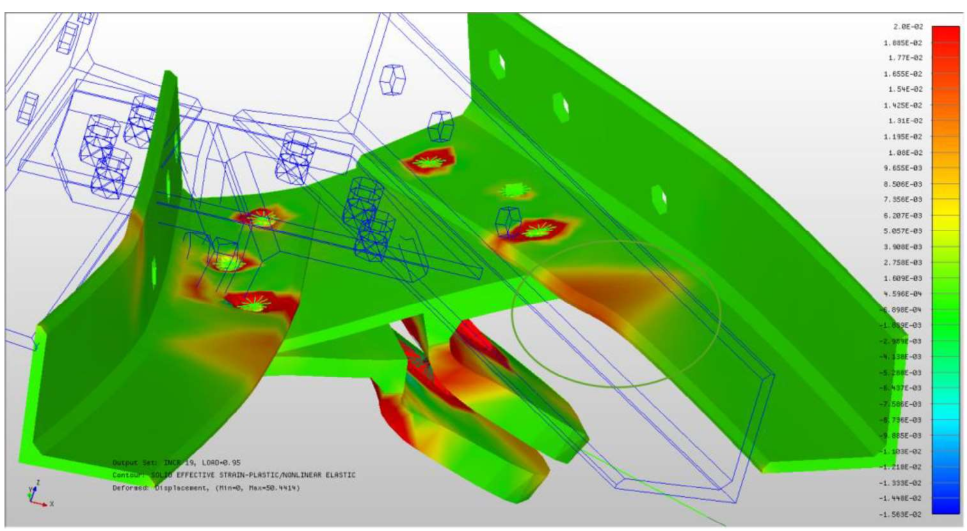

FIGURE 47 Load case 5. Local buckling – Resultant load 80 kN.

Load 6 – Pure longitudinal load

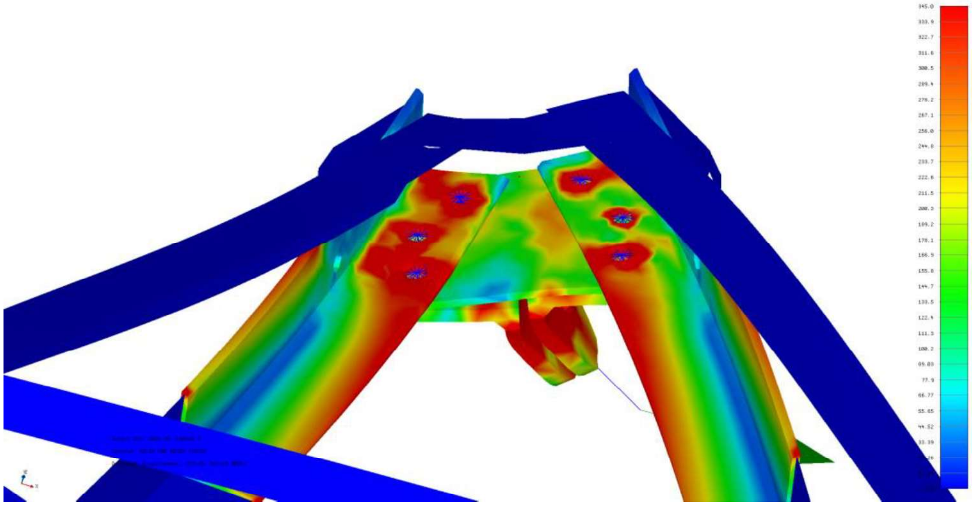

FIGURE 48 Load case 6. Yield point – Resultant load 50 kN.

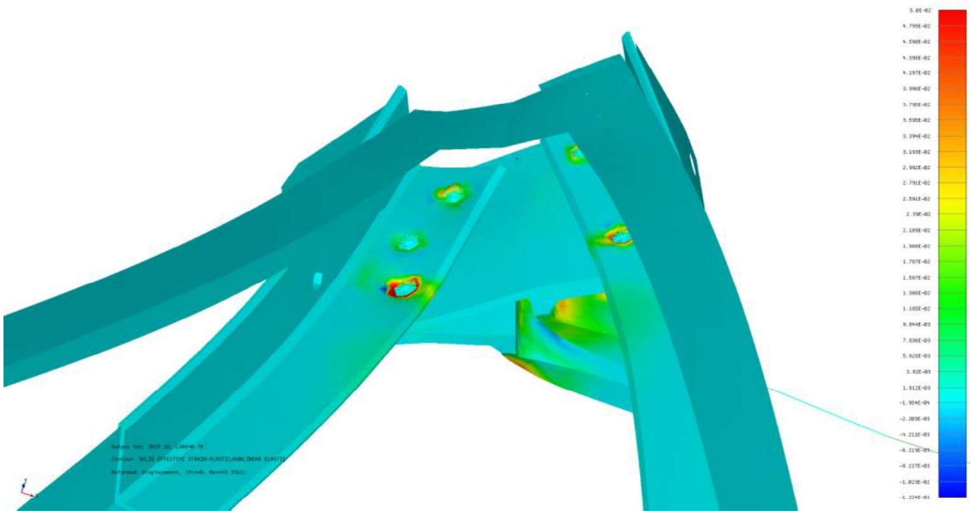

FIGURE 49 Load case 6. 5% strain – Resultant load 67 kN.

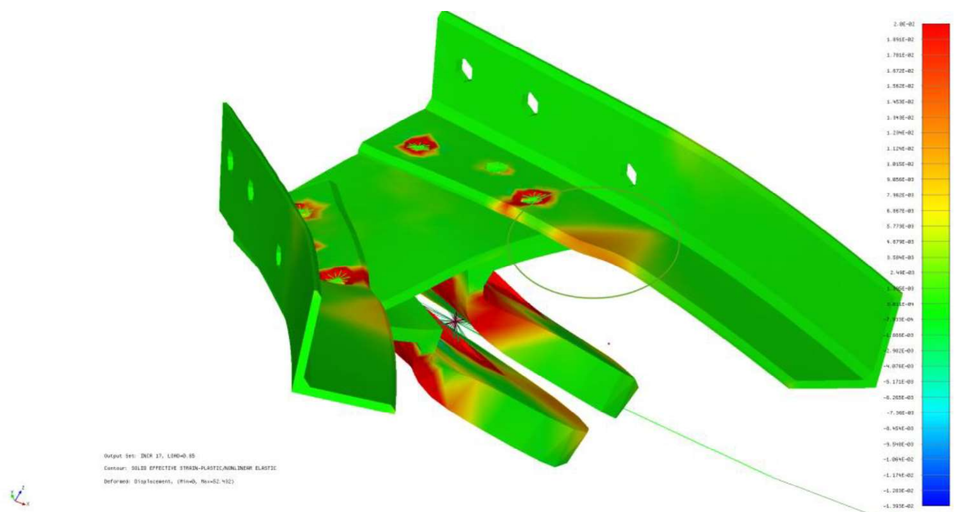

FIGURE 50 Load case 6. Local buckling starts (2% strain) – Resultant load 80 kN.

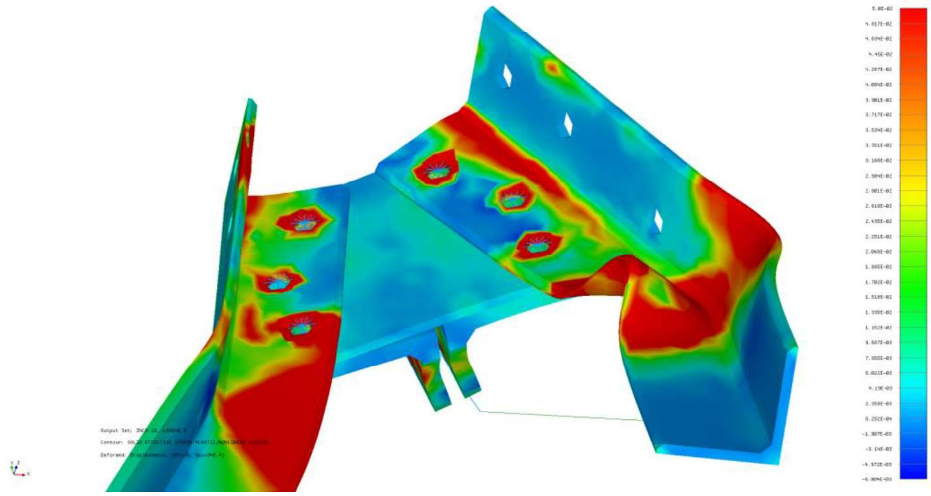

FIGURE 51 Load case 6. After local buckling.

APPENDIX B DRAWINGS OF THE CROSS ARM

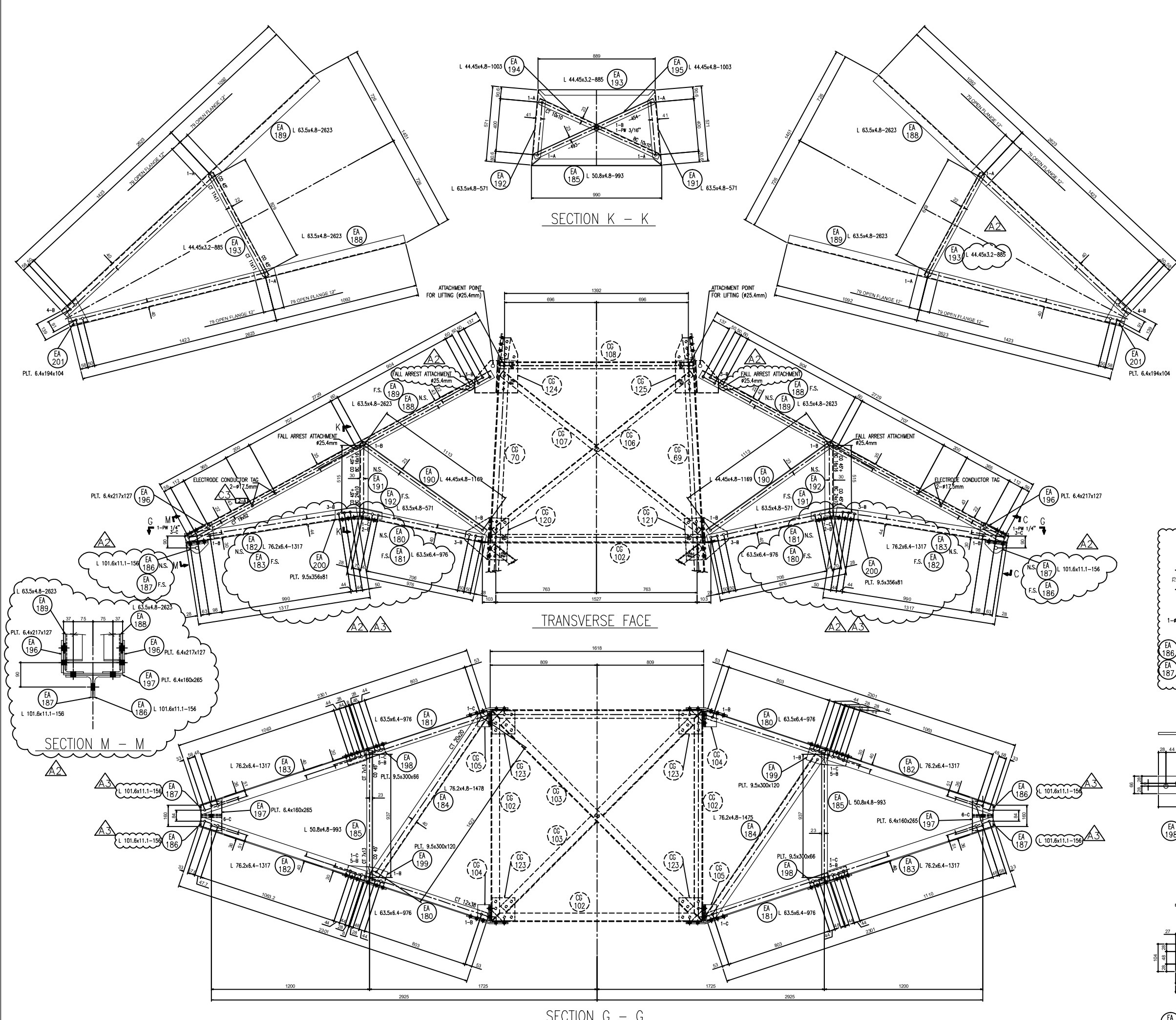

BILL OF MATERIAL (PER TOWER)
0° - 1° SUSPENSION TOWER TYPE 'A1' MKD '35A1'
ELECTRODE CROSS ARM — Rev C

Mark No.	Profile (mm)	Material Grade	Length(mm)	Width(mm)	Quantity	Unit Wt.(Kg/m)	Total Weight (Kg)
EA180	L 63.5x63.5x6.4	CSA G40.21 350WT	976		2	6.10	11.91
EA181	L 63.5x63.5x6.4	CSA G40.21 350WT	976		2	6.10	11.91
EA182	L 76.2x76.2x6.4	CSA G40.21 350WT	1317		2	7.29	19.21
EA183	L 76.2x76.2x6.4	CSA G40.21 350WT	1317		2	7.29	19.21
EA184	L 76.2x76.2x4.8	CSA G40.21 350WT	1478		2	5.52	16.32
EA185	L 50.8x50.8x4.8	CSA G40.21 350WT	993		2	3.63	7.21
EA186	L 101.6x101.6x11.1	CSA G40.21 350WT	156		2	16.82	5.25
EA187	L 101.6x101.6x11.1	CSA G40.21 350WT	156		2	16.82	5.25
EA188	L 63.5x63.5x4.8	CSA G40.21 350WT	2623		2	4.57	23.97
EA189	L 63.5x63.5x4.8	CSA G40.21 350WT	2623		2	4.57	23.97
EA190	L 44.45x44.45x4.8	CSA G40.21 350WT	1169		4	3.16	14.75
EA191	L 63.5x63.5x4.8	CSA G40.21 350WT	571		2	4.57	5.22
EA192	L 63.5x63.5x4.8	CSA G40.21 350WT	571		2	4.57	5.22
EA193	L 44.45x44.45x3.2	CSA G40.21 350WT	885		2	2.14	3.79
EA194	L 44.45x44.45x4.8	CSA G40.21 350WT	1003		2	3.16	6.33
EA195	L 44.45x44.45x4.8	CSA G40.21 350WT	1003		2	3.16	6.33
EA196	PL 6.4	CSA G40.21 350WT	217	127	4	49.85	5.50
EA197	PL 6.4	CSA G40.21 350WT	160	265	2	49.85	4.23
EA198	PL 9.5	CSA G40.21 350WT	299	66	2	74.75	2.95
EA199	PL 9.5	CSA G40.21 350WT	300	120	2	74.75	5.38
EA200	PL 9.5	CSA G40.21 350WT	356	81	4	74.75	8.62
EA201	PL 6.4	CSA G40.21 350WT	191	104	2	49.85	1.98
			Black Weight (Kg)				214.49
			+3.5 % Galv. (Kg)				7.51
			Total Weight (Kg)				222.00

Bolts/Nuts,Washer Summary	BOLT TYPE	Description	Grade	Quantity	Unit Wt. (Kg./Piece)	Total Weight (Kg)
	A	5/8 x 1-1/2"	ASTM 394 - T1	20	0.136	2.72
	B	5/8 x 1-3/4"	ASTM 394 - T1	88	0.145	12.76
	C	5/8 x 2"	ASTM 394 - T1	36	0.155	5.58
	SPRING WASHER	SPRING WASHER	B18.21.1	144	0.010	1.44
	PW 3/16"	PW 5/8 x 3/16"	B18.22.1	2	0.026	0.05
	PW 1/4"	PW 5/8 x 1/4"	B18.22.1	4	0.035	0.14
3% EXTRA BOLTS, NUTS & WASHERS SHALL BE DELIVERED WITH TOWER SUPPLY.				Total Weight (Kg)		22.69

Total Weight (Kg) of ELECTRODE CROSS ARM — 244.69

GENERAL NOTES:-

1. ALL DIMENSIONS ARE IN MILLIMETERS.
2. ALL STEEL SHALL BE CONFORMING TO CAN/CSA G40.21 350WT OR ASTM A572 GR. 65, (EXCEPT THE FILLER PLATE WHICH ARE CONFORMING TO ASTM 1011/1011M-14 CS TYPE B) AS PER THE BILL OF MATERIALS, WITH ABSORBED ENERGY OF 20 JOULES AT -20 DEGREE CELSIUS.
3. STRUCTURAL STEEL FABRICATION AND WORKMANSHIP SHALL BE IN ACCORDANCE WITH CAN/CSA-S16. ALL WELDING SHALL CONFORM TO CSA W59.1 OR AWS STANDARD D1.1. MINIMUM GUSSET PLATE THICKNESS IS 6.4mm.
4. BOLTS SHALL BE 5/8"ø HEX HEAD HOT DIP GALVANIZED ASTM A394 TYPE 1 C/W TYPE DH ASTM A563 HEX NUTS AND HEAVY HELICAL SPRING WASHERS ASME/ANSI B18.21.1. PLACE ONE SPRING LOCKWASHER UNDER EACH NUT. SHEAR PLANES SHALL BE OUTSIDE THE THREADED PORTION OF THE BOLTS AND THE BOLT LENGTH SHALL EXCEED ABOUT 3 FULL THREADS BUT NOT MORE THAN 6/10" (15mm). ADDITIONAL SPRING WASHERS SHALL BE USED WHEN REQUIRED BY THE THREADED LENGTH AND THE REQUIRED GRIP.
5. ALL STEEL ITEMS TO BE HOT DIP GALVANIZED AS PER ASTM A123 AND BOLTS AND WASHERS AS ASTM A 153 AND MINIMUM ZINC COATING REQUIRED 610 gm/m2 AND NOT LESS THAN 0.086 mm IN THICKNESS AS PER TECHNICAL SPECIFICATION NO. ILK-SN-CD-6200-TL-TS-0021-01 WHICHEVER IS STRINGENT.
6. 3/4" DIA STEP BOLT SHALL CONFORM TO ASTM A394 TYPE "1" STEP BOLTS SHALL HAVE TWO LOCK WASHERS AND TWO NUTS.
7. ⌖ INDICATES HOLES OF 11/16" DIA. FOR 5/8" DIA. BOLT. (END DISTANCE 1 3/32" OTHERWISE STATED.)
   ⌖ INDICATES HOLES OF 13/16" DIA. FOR 3/4" DIA. STEP BOLTS.
   ● THIS INDICATES MEMBERS BEING USED AS STEP BOLT.
   ⌖ INDICATES FILLERS FOR 5/8" DIA. BOLTS.
8. MEMBER MARK LABELING WILL BE MARKED AS SHOWN BELOW
   35A13M01
   35 – VOLTAGE RATING (350kV)
   A1 – TOWER TYPE
   3M – +3.0 MAST EXTENSION
   01 – MEMBER MARK NUMBER

SPACING OF 5/8" DIA BOLTS AND EDGE DISTANCE ON FINISHED MATERIAL

BOLT DIA	BOLT SPACING MINIMUM	ROLLED EDGE MINIMUM	SHEAR EDGE MINIMUM
5/8"	42	22	28

LEGENDS–
N.S.–NEAR SIDE
F.S.–FAR SIDE
P.PLT.–PACK PLATE
C.PLT.–COVER PLATE
CLT.–CLEAT
B/B–BACK TO BACK
EXTN.–EXTENSION

MARK NO. 180 TO 201

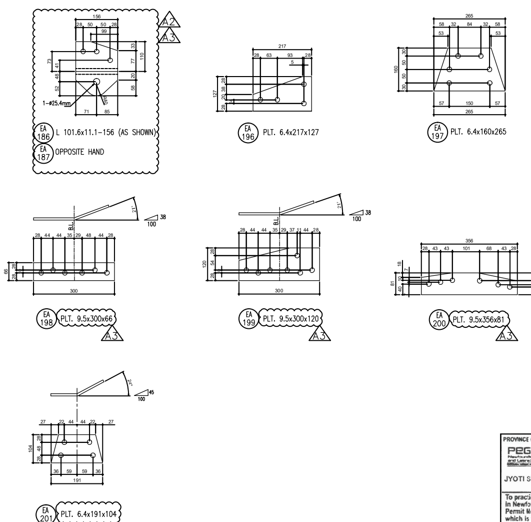

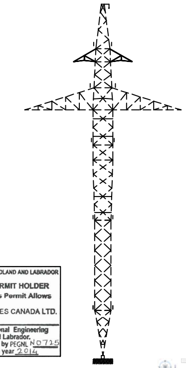

PROVINCE OF NEWFOUNDLAND AND LABRADOR
PEGL PERMIT HOLDER
This Permit Allows
JYOTI STRUCTURES CANADA LTD.
To practice Professional Engineering in Newfoundland and Labrador.
Permit No. as issued by PEGNL N0725 which is valid for the year 2014

***** DATUM REFERENCE: ALL ELEVATIONS ARE IN METRES REFERENCED TO GEODETIC. COORDINATE REFERENCE: UTM 6° (UNIVERSAL TRANSVERSE MERCATOR) PROJECTION, NAD83, ZONE __ CENTRAL MERIDIAN 63° 00' W LONGITUDE. *****

ISSUE	REV.	DATE	DISTRIBUTION & STATUS	No.	REFERENCE DRAWING	No.	DATE	REVISION	MOD.	VER.	APP.
						C3	23/OCT/2014	REVISED AS PER CLIENT COMMENTS	AMSO	NM	PK
						C2	20/AUG/2014	AS PER CLIENT COMMENTS DATED 09/JUL/2014	AMSO	NM	PK
						C1	30/MAY/2014	RELEASE FOR CONSTRUCTION	AMSO	NM	PK

ISSUE REGISTER — REFERENCE DRAWING — REVISION REGISTER

********** FOR INTERNAL USE ONLY **********
REVIEW CLASS: EQUIPMENT TAG NUMBER:
REVIEW DOES NOT CONSTITUTE APPROVAL OF DESIGN DETAILS, CALCULATIONS, TEST METHODS OR MATERIAL DEVELOPED AND/OR SELECTED BY THE CONTRACTOR, NOR DOES IT RELIEVE THE CONTRACTOR FROM FULL COMPLIANCE WITH CONTRACTUAL OR OTHER OBLIGATIONS.
- [x] 1. REVIEWED AND ACCEPTED NO COMMENTS
- [ ] 2. REVIEWED - INCORPORATE COMMENTS, REVISE & RESUBMIT
- [ ] 3. REVIEWED - NOT ACCEPTED
- [ ] 4. INFORMATION ONLY
- [ ] 5. NOT REVIEWED

This document has been reviewed & coded electronically via Aconex.
LEAD REVIEWER: D. Chakrabarti — Date (dd-mmm-yyyy): 18-Nov-2014
NE-LCP MANAGEMENT: Date (dd-mmm-yyyy):
PROJECT MANAGER: Date (dd-mmm-yyyy):

PROFESSIONAL STAMP
REGISTERED PROFESSIONAL ENGINEER — PEG Newfoundland and Labrador — Mrugesh J.Patel — SIGNATURE — 28/10/14 — DATE — NEWFOUNDLAND & LABRADOR

JYOTI AMERICAS, LLC.
CONROE (TEXAS)

DESIGNED	P.DESHMUKH	APPROVED (Discipline Lead Engineer)	-----
DRAWN	A.M.S.O.	APPROVED (Engineering Manager)	P.KUMAR
VERIFIED	B.KATE/N.M.		
DATE	12/JAN/2014	SCALE	1:10

CLIENT: nalcor energy
ENGINEER: SNC·LAVALIN
PROJECT: LOWER CHURCHILL PROJECT
TITLE: 350 kV HVdc LINE
0° - 1° SUSPENSION TOWER TYPE 'A1'
FABRICATION AND INSTALLATION
DRAWING FOR ELECTRODE CROSS ARM

SUPPLIER DOC No. JA-11-FID-A1-09 — NE DOC No. ILK-JY-SD-6200-TL-D04-0001-09 — Rev. C3

FORMAT ANSI D (22x34)

W:\SNC-NALCOR\Submittals\Tower A1\Detail Drawings\2014_1126 Submittal rev C3\ILK-JY-SD-6200-TL-D04-0001-09.dwg
2014.11.26/5:18pm

nalcor energy

Failure Investigation Report – L3501/2 Pole Assembly Turnbuckle Failure

Failure Event February 2021 in Labrador

May 28, 2021

REGISTERED PROFESSIONAL ENGINEER
PEG
MARIA VEITCH
SIGNATURE
28-May-2021
DATE
NEWFOUNDLAND & LABRADOR

Nalcor Reference No.: ILK-EG-ED-6200-TL-RP-0002-01 Rev.00

Prepared by:

Maria Veitch

Verified by:

Cheryl Sehn

Approved by:

John Walsh

REVISION LIST

Revision						Remarks
No	By	Rev.	Appr.	Appr.	Date	
1						
2						
3						

Table of Contents

Appendices

Table of Figures

1 Abbreviations and Acronyms

HVdc – High voltage direct current
TL – Transmission Line
L3501/2 – Line number assigned to the 350 kV HVdc line
LITL – Labrador-Island Transmission Link
Str. – Structure/Tower (used interchangeably)

2 Background

The Labrador-Island Transmission Link (LITL) is an important transmission line for the provincial energy grid due to its power carrying capacity and it will be used to deliver a large portion of the winter peak energy and demand to the Island Interconnected System. Line L3501/02 is an overland transmission line that is a specific component of the LITL. It is an HVdc line between Muskrat Falls and Soldiers Pond that is to be operated at +/- 350 kV DC bipole, capable of transferring 900 MW. The overhead transmission line is a bipole line, with a single conductor per pole, and galvanized lattice steel towers. This line is constructed in harsh terrain subjected to heavy wind and ice loads, has been built since 2017, and has experienced multiple winter seasons and weather events.

On February 4, 2021 a line patrol found pole 2 conductor on the ground near structure 1229 near the south coast of Labrador. A week later on February 12, 2021, pole 2 conductor was found on the ground near structure 1209. It was determined both line failures were due to a failed turnbuckle in the pole dead end assembly.

3 Purpose

Considering the importance of L3501/02 to the provincial energy grid, a detailed failure investigation was completed in order to take necessary precautions and address any issues to prevent further damage to the line.

The investigation will be described in detail within this report and include the following components:

1. Location of the Damaged Towers;
2. Weather Loadings;
3. Field Observations;
4. Construction Quality Review; and
5. Material Testing.

Upon completion of these investigations, the root cause of the failures and recommendations for prevention of further of damage will be presented.

4 Location of Failures

4.1 Tower Types

There are 11 different tower types on L3501/2, consisting of both guyed and self-support structures. See

Table 1 – Tower Types for more details.

Table 1 – Tower Types

Tower Type	Structure Type	Insulator Assembly Type	Deflection Angle Limit (degree)
A1, A2, A3, A4	Guyed	Suspension	0-1
B1	Guyed	Suspension	0-3
B2	Self-Support	Suspension	0-3
C1, C2	Self-Support	Dead End	0-30
D1, D2	Self-Support	Dead End	0-45
E1	Self-Support	Dead End	45-90

Ninety percent of all towers on the L3501/2 are suspension towers, types A1, A2, A3, A4, B1, and B2 respectfully. Figure 1 – Distribution of Tower Type on L3501/2 breaks down the tower distribution on the L3501/2.

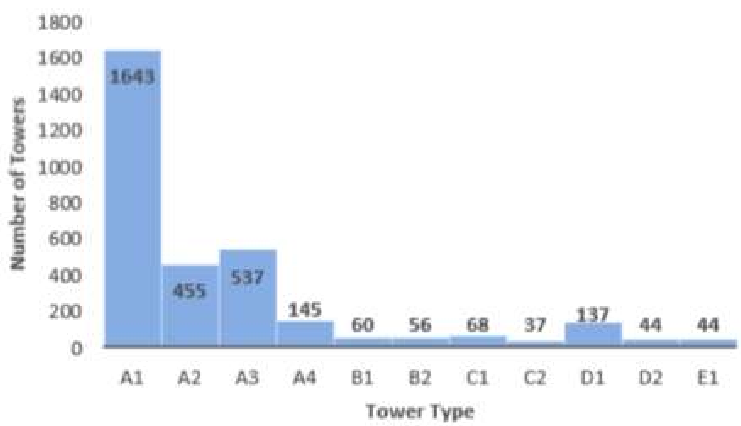

Figure 1 – Distribution of Tower Type on L3501/2

Structures 1209 is a type E self-support dead end structure. Structure 1229 is a type D self-support dead end structure.

4.2 Damaged Structure Locations

The whole HVdc line is broken into 5 segments, Segments 1 and 2 located in Labrador and Segments 3–5 located on the island.

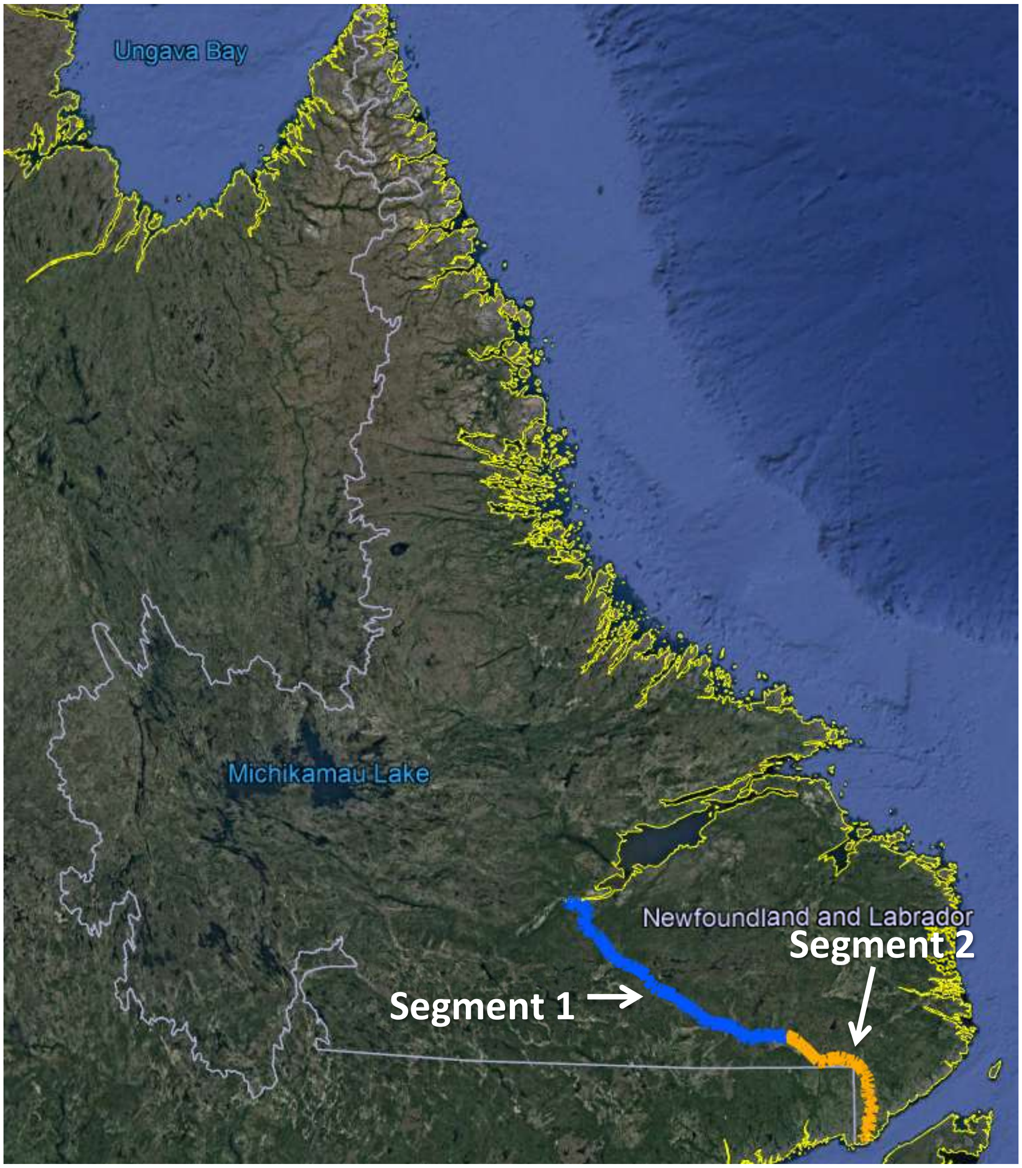

Figure 2 – Segments 1 and 2 of the L3501/2

The failures described within this report both occurred within Segment 2 of the L3501/2. Segment 2 is from structure 750 to 1282 near the south coast of Labrador. See Figure 2.

Structures 1209 and 1229 are in the same dead end to dead end section of line. Both failures were on the pole 2 side of the structures. Structure 1209 failure was on the ahead span and structures 1229 failure was on the back span.

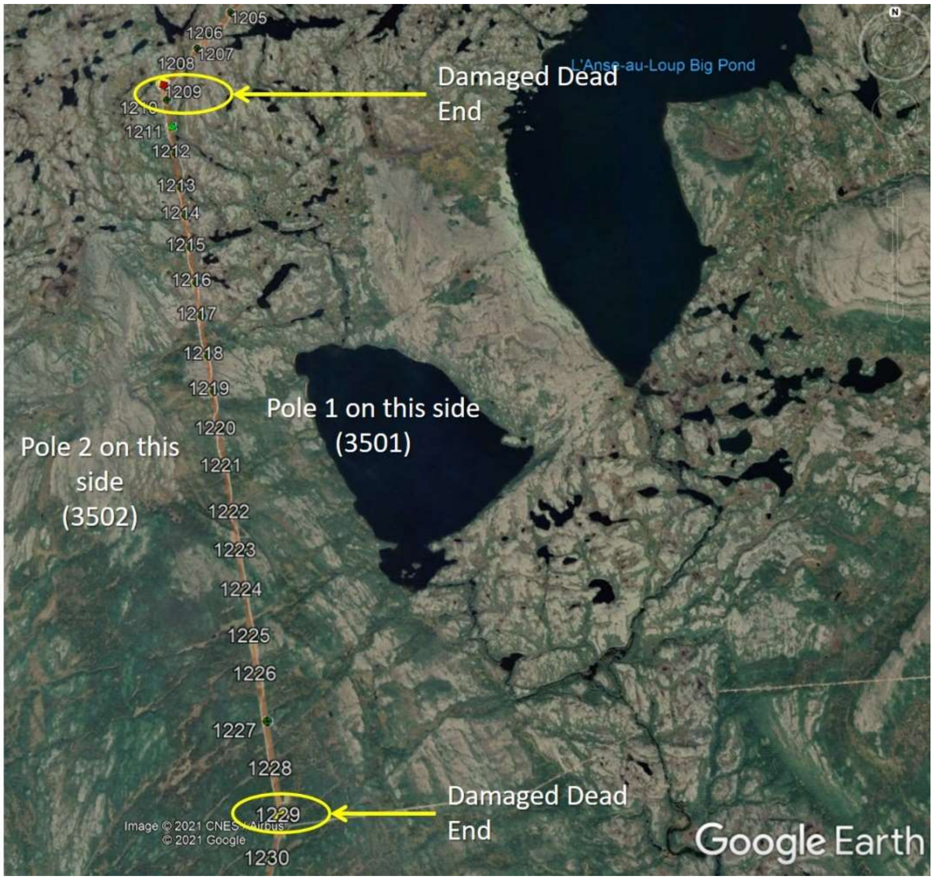

Figure 3 – Relative Location of Str. 1209 and 1229

5 Description of Line in Damaged Section

5.1 Zone 3a Description

L3501/2 is divided in to 11 different zones for climatic loading. The multiple loading zones are necessary due to the long line length and the variability in terrain including alpine, inland, and coastal regions. All damage that occurred during this event is in zone 3a of the line.

Zone 3a is the section of line from Str. 1209 to 1246. This zone is design for a max of 50 mm of radial glaze ice, 120 km/h of wind, and a 60 km/h, 25 mm wind and ice combination. See Table 2 for more details on the weather cases used for design. Although it is a small section of the line it fits in to the “Average Loading Zone” category as discussed in Section 5.2 and has loads similar to the majority of the line.

Table 2 – Weather Cases Used for Design

Weather cases	Wire / Conductor Temp (°C)	Ambient Temp (°C)	Radial Ice (mm)	Ice Density (kg/m3)	10 min. Average Wind Speed at 10 m Height Above Ground (km/h)	Cable Wind Pressure (Pa)
Heavy – CSA C22.3 No. 1-10	-20	-20	12.5	900	-	400
EDT	0	0	0	0	-	0
Max wind	-20	-20	0	0	120	1290[4]
Wind and Ice	-5	-5	25	900	60	305[4]
Max ice	-5	-5	50	900	-	0
Hot (Pole)	85[3]	30	0	0	-	0
Hot (Grackle)	72[3]	30	0	0	-	0
45 Pa	-30	-30	0	0	30[5]	45
Cold	-38	-38	0	0	-	0
Reduced Swing Wind (30%)	-20	-20	0	0	-	385[4]
Max Swing Wind (80%)	-20	-20	0	0	-	1030[4]
Galloping Swing	0	0	12.7	900	45[5]	95.8
Galloping Sag	0	0	12.7	900	0	0
Catenary Limit 1900 m	-20	-20	0	0	0	0
10% Winter Design Temperature	-30	-30	0	0	0	0

Zone 3a is designed utilizing A1, B1, B2, C1, D1, and E1 towers.

5.2 Design Loading Selection

L3501/02 has three general categorized loading zones throughout its length from Muskrat Falls to Soldier's Pond:

- Average Loading Zone;
- Eastern Loading Zone; and
- Alpine Loading Zone.

Zone 3a of TL3501/02, the subject of this investigation, would be classified as an Average Loading Zone with a "50 year Reliability Level Return Period of Loads, with respect to Nalcor Energy operating experience and LCP specific modelling and test programs" as specified in "Basis of Design – LCP-PT-ED-0000-EN-RP-0001-01" and "Overhead Transmission – Meteorological Loading for the Labrador-Island Link ILK-PT-ED-6200-TL-DC-0001-01".

Zone 3, 4, 6 and 8a (see Attachment B.1)

The following load case is to be applied in the location shown in attachment B.1. Please note that this loading is valid for the northern corridor alternative only.

Maximum Ice	50 mm radial glaze, 0.9 g/cm^3 density
Maximum Wind	120 km/h (10 minute average wind speed at 10 m height above ground)
Combined Ice and Wind	25 mm radial glaze, 0.9 g/cm^3 density 60 km/h (10 minute average wind speed at 10 m height above ground)

Maximum wind and combined wind values assume Terrain Type C as per CSA C22.3 NO 60826-10. Any deviation for this terrain type for select locations along the corridor must be included in the HVdc tower design criteria.

Figure 4 – Zone 3a Description

6 Field information

On the February 4, 2021 a failure was discovered at dead end structure 1229 during a line patrol with the back span pole 2 conductor on the ground. Further investigation showed that the failure occurred on the turnbuckle of the dead end assembly.

On the February 12, 2021 an additional failure was discovered at dead end structure 1209 with the ahead span of pole 2 conductor on the ground. Upon inspection it was noted that the failure was similar to the 1229 failure and occurred on the turnbuckle of the dead end assembly.

The turnbuckle is on the tower side of the assembly connected to the tower by a shackle, shown in Figure 5 as item 2.

There was little to no ice reported on the lines at the location of the failure.

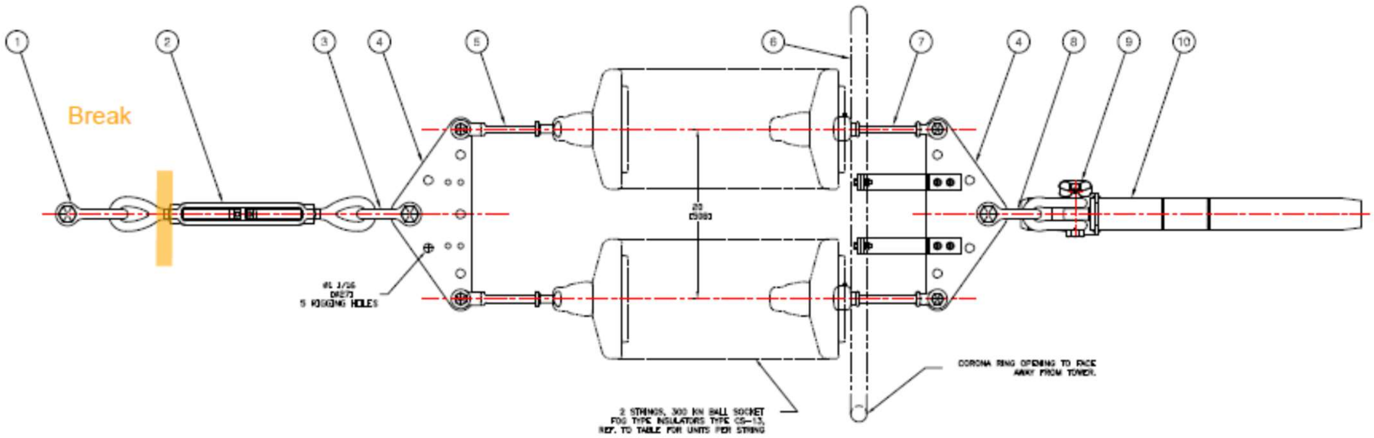

Figure 5 – Pole Conductor Dead End Assembly

Figure 6 – Structure 1229 Pole Conductor Assembly Failure

Figure 7 – Structure 1209 Pole Conductor Assembly Failures

The turnbuckles at both structures failed at the threaded section just under the eye closest to the tower. Both failures were similar and were noted to be a clean break with no necking or bending, see Figures 8 and 9.

Figure 8 – Fracture Surface of Str. 1229 Turnbuckle

Figure 9 – Fractured Surface of Str. 1209 Turnbuckle

All other components of the failed dead end assemblies were inspected for damage. There was noticeable wear on the shackle that connects to the turnbuckle and on the turnbuckle eye, see Figure 10 and 11. There was no other damage observed on other hardware or insulators.

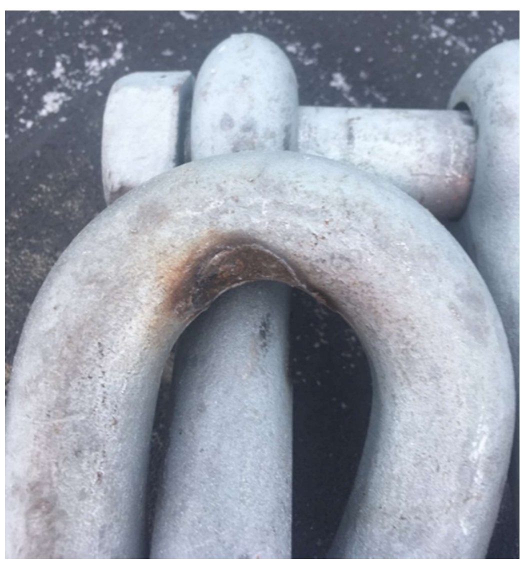

Figure 10 – Wear on Turnbuckle Str. 1229

Figure 11 – Wear on Shackle Str. 1229

6.1 Weather Data from Nearby Weather Stations

Wind Speed at Blanc-Sablon near the end of the Labrador section of the line ranged from 5 to 90 km/h on February 3, 2021 and February 4, 2021. This is the time when the failure at structure 1229 was expected to occurred. The wind direction was primarily North-East. The failure at 1209 could have occurred any time between 7th and the 12th when it was discover. The wind speeds during this time ranged from 5 to 55 km/h. Wind direction was varied from South-West to North, to North-East during this time.

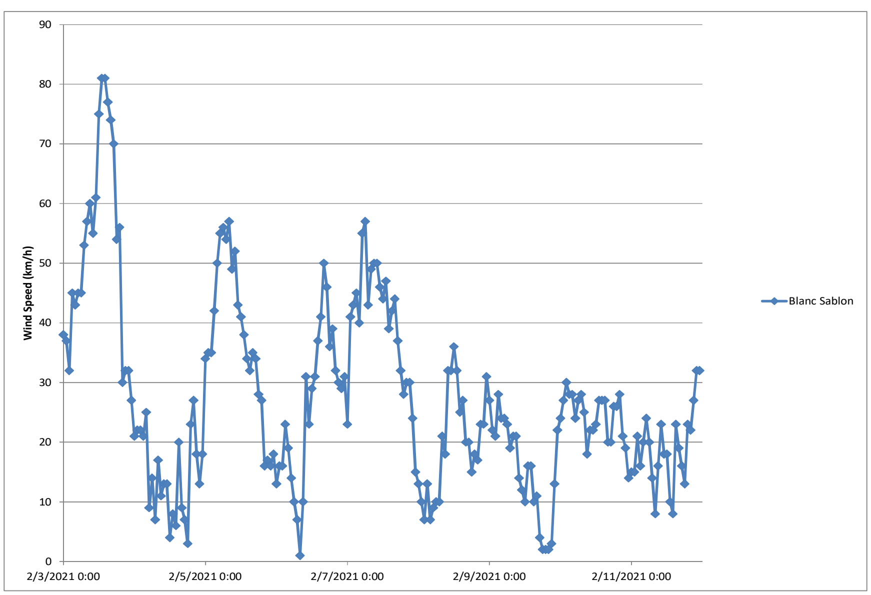

Figure 12 – Wind Speed at Blanc-Sablon

Temperatures at the time of the incidents ranged from 4°C to -8°C. There was little to no ice on the line at the time of the incidents.

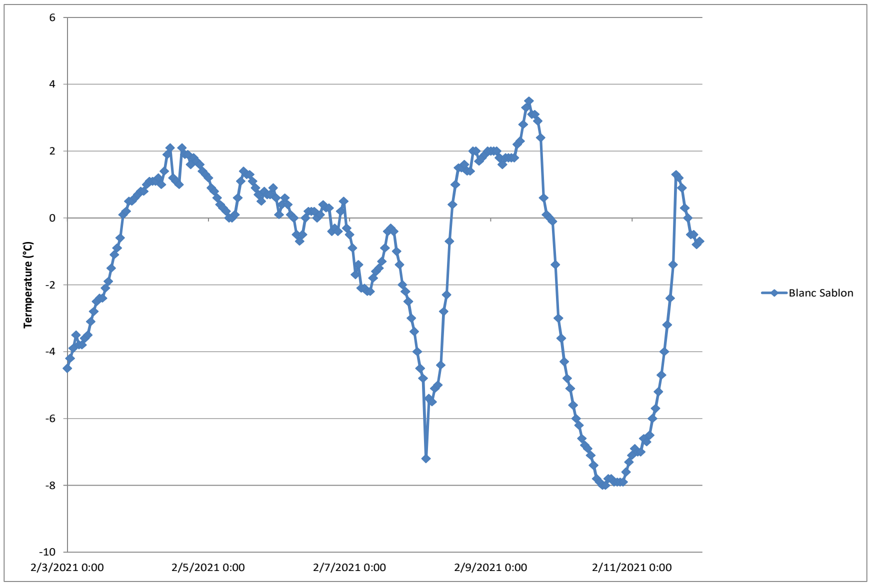

Figure 13 – Temperature at Blanc-Sablon

7 Construction Quality Review

It was noted that the failed turnbuckle at 1209 was installed so the two eyes were not in the same plan. This is not in accordance with the installation manual that states, "The eyes of the end fitting should be in the same orientation relative to each other."

It was also noted that the failed turnbuckle at 1209 had two locking bolts on each side. Both the drawing and installation manual from the supplier indicate there should only be one locking bolt on each side of the turnbuckle. See Figure 14 showing the orientation of the eyes and the four locking bolts.

Figure 14 – Turnbuckle 1209 Failed State

7.1 Documentation Review

The Quality Control Forms for the Conductor Tie In/Jumper indicated “turnbuckle installed in assembly as per design” for both structures 1209 and 1229. See Appendix A.

The drawing and the installation manual do not reference and maximum torque force for the turnbuckle. The turnbuckle can be used to adjust the sag of the pole conductor after stringing. With tensions on the pole conductor at approximately 17 kN, the amount of torque required to adjust the turnbuckle could be significant.

8 Material Testing

A failed turnbuckle was sent for testing. The turnbuckle from structure 1209 was sent to Acuren. They were tasked with completing the following testing to determine the failure mechanism of the turnbuckle:

- Visual examination;
- Examination at low magnification;
- Metallographic examination;
- Scanning electron microscope examination;
- Chemical analysis; and
- Hardness testing.

8.1 Material Test Results

8.1.1 Acuren Results

Acuren test results showed there were no issues with the material of the turnbuckles. The chemical composition and hardness meet the specifications.

Analysis of the failure surface determined that the turnbuckle fractured due to fatigue crack initiation, which propagated under combination of cyclic reverse bending and cyclic tension-tension loads that were induced by motion of the assembly. The most likely cause of significate movement of a dead end assembly on a transmission line is galloping.

There is evidence the fatigue cracking was initiated by over torqueing of the turnbuckle. This over torqueing could have occurred during installation, or movement of the turnbuckle while in service. Deviations from the installation procedure were evident on the turnbuckle which may have contributed to the failure. The first deviation was that the eyes of the end-pull were not in the same orientation relative to each other. The second deviation was that two locking bolts were used on each of the end-pull, which restrain any rotation motions of the end-pulls relative to the turnbuckle body. These two deviations did not directly stress the turnbuckle. However, orientation misalignment promoted wear damage on the end-pull and the additional lock bolt prevented the turnbuckle self-balance. This could intensify the cyclic loads on the turnbuckle. See Appendix B for complete report “Failure Analysis of a Turnbuckle”.

9 Galloping and Damper Failures

Galloping on the section of line near the south coast of Labrador has been observed on the line since construction. Galloping is an extreme movement of the conductors in a sine wave motion. It can be caused by specific wind conditions, and is sometimes observed on lines with small amounts of icing. The towers on L3501/02 have been designed so the wires can gallop without flash over between wires. Galloping will cause fatigue on hardware and conductors over time.

In contrast to galloping, Aeolian vibration protection is designed into the line using Stockbridge vibration dampers. Damper failures have been occurring on the line since construction. Locations of damper failures include area near the turnbuckle failure. An initial study into the damper failures found that the messenger wire was failing due to fatigue. The initial batch of dampers tested also found a material defect that could lead to this failure.

Additional damper testing was completed in 2019, and it was again determined that failure was due to fatigue. The investigation in to damper failures is continuing with laboratory testing of the dampers in cold temperatures, and a field vibration monitoring program to determine if the line is adequately protected from Aeolian vibration.

There were also failures of corona rings noted on the pole conductor tangent assemblies. These corona rings have also been tested and it was determine the main cause of failure was pool weld penetration, but vibration many have accelerated the occurrence of failure.

The possible cause of the damper failures could be vibration or galloping. Both could cause wear on the hardware and conductor that could contribute to the failures we are seeing in Labrador. The results of the damper investigation will give us possible causes to look at or rule out.

10 Conclusion and Observations on Root Cause

Galloping/Vibration issues on the line:

- Material testing determined the turnbuckle fractured due to a fatigue crack that propagated through a reverse bending cycle. There was noticeable wear on the turnbuckle eye and the connected shackle. Both of these are caused due to the movement of the assembly, most likely during galloping.
- Damper failures have been experience in the sections of the line where we are experience the current line failures.
- Galloping has been observed on the L3501/2 on the south coast of Labrador in the past.

Construction Issues:

- Turnbuckles were not installed with the eyes in the same orientation as per the installation requirement.
- The turnbuckle at 1209 was installed with two locking bolts per side when the drawing and installation requirements only indicate one per side.
- Wear on the shackle indicates the shackle was sitting tilted in the eye of the turnbuckle out of alignment.
- There were indications that the turnbuckle was over torqued. This could have occurred during installation or while in service.

11 Recommendations

Some possible recommendations are listed below.

- Air spoiler to prevent galloping;
- Galloping study;
- Check turnbuckle installation; and
- Alternate dead end assembly design.

Air spoilers are a galloping prevention device that are designed to disrupt the flow of air over the conductor reducing or preventing the mechanism that creates galloping. Air spoilers are the recommended solution based on utility experience in the past to address galloping.

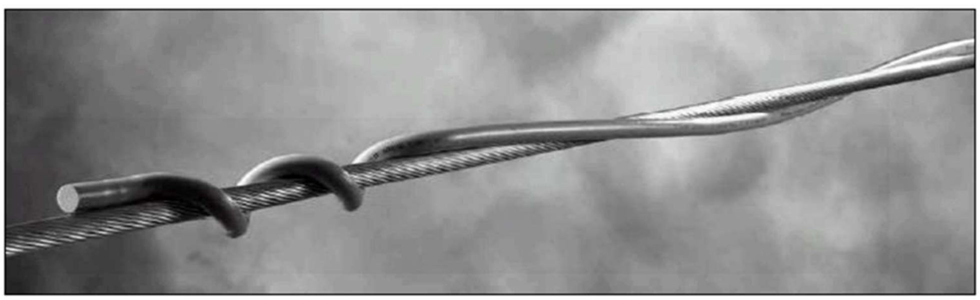

Figure 15 - Air Flow Spoiler

A galloping study would look at the weather modeling in Labrador and identify areas that are prone to the conditions that cause galloping. This study would identify locations to install air spoilers and areas to inspect hardware signs of fatigue.

The turnbuckles should be checked to ensure they are installed with the eyes in alignment and only one lock bolt per side in place. This may be able to be checked through drone inspections. Signs of wear from galloping would include wear on the turnbuckle eye and shackle. This can only be checked through climbing inspections, and taking the tension off the assembly. Cracks in the threads of the turnbuckle are the first sign of failure. This could likely only be checked through x-raying the turnbuckle.

A review of the dead end design should be complete to determine if there is an alternative to turnbuckles that would be better suited for galloping loads. Sag adjuster plates are one alternative to turnbuckles but more research would be required to determine if they would perform any better under galloping conditions.

Appendix A – Sample QC check sheets

Valard

Quality Control Form
Conductor Tie In / Jumper

nalcor

VC-F0100

Doc. Number	VC-F0100	Created By:	Eric Winter	Date: 1/1/2014	Client:	Nalcor Energy	Location:	DC Line Construction Corridor	
Revision R004		Revised By:	Michael Grieve	Date: 09/05/2016	VC Number:	VC7343	Supervisor: John Mitchell		
Project Name:	Muskrat Falls DC Line	Project no.:	505573		Contract no.:	CT0327-001	Voltage:	350 KV	
Tower #:	529	Line #:	2	Structure Type: E1+3.0	Date:	28/May/2016	Crew:	Stringing	

Complete all applicable sections Mark Not applicable "N/A"	Completed
Phases Completed	☒ Pole ☒ Electrode
1. Pole Conductor	
Insulators correct size, orientation and quantity (verify QTY on staking list)	☒
Insulators clean and free of defects/damage/contaminants	☒
All cotter keys fully seated	☒
Corona rings installed as per design	☒
Suspension insulator plumb	☒
All pins orientated to tower and source	☒
All keys (with exception of those with corona nut) bent 45-60°	☒
Dampers installed to specification	☒
2. Electrode	
Insulators correct size, orientation and quantity (verify QTY on staking list)	☒
Insulators clean and free of defects/damage/contaminants	☒
All cotter keys fully seated	☒
Suspension insulator plumb	☒
All pins orientated to tower and source	☒
Arcing horn installed as per design	☒
Dampers installed to specification	☒
3. Dead End — **Source Side Complete** ☒ **Load Side Complete** ☒	
Area cleared of all wildlife within 500m, 1 hour prior to use of implosive sleeves:	☒
Correct size and orientation	☒
Dead end cleaned and checked with "no go" gauge (If compression)	☒
Jumpers formed uniformly	☒
Correct assembly used	☒
Turnbuckle installed in assembly as per design	☒

Comments:

QA Review	Signature	Date
Crew	Stringing	28/05/2016
Valard QA	Drew Williams	06/08/2016
Nalcor QC Inspector		14 Nov 2016

Valard

Quality Control Form
Conductor Tie In / Jumper

nalcor

VC-F0100

Doc. Number VC-F0100	Created By: Eric Winter	Date: 1/1/2014	Client: Nalcor Energy	Location: DC Line Construction Corridor
Revision R004	Revised By: Michael Grieve	Date: 09/05/2016	VC Number: VC7343	Supervisor:
Project Name: Muskrat Falls DC Line	Project no.: 505573	Contract no.: CT0327-001	Voltage: 350 KV	
Tower #: 547	Line #: 2	Structure Type: D1+6.0	Date: 28/May/2016	Crew: Stringing

Complete all applicable sections Mark Not applicable "N/A"	**Completed**
Phases Completed	☒ Pole ☒ Electrode
1. Pole Conductor	
Insulators correct size, orientation and quantity (verify QTY on staking list)	☒
Insulators clean and free of defects/damage/contaminants	☒
All cotter keys fully seated	☒
Corona rings installed as per design	☒
Suspension insulator plumb	☒
All pins orientated to tower and source	☒
All keys (with exception of those with corona nut) bent 45-60°	☒
Dampers installed to specification	☒
2. Electrode	
Insulators correct size, orientation and quantity (verify QTY on staking list)	☒
Insulators clean and free of defects/damage/contaminants	☒
All cotter keys fully seated	☒
Suspension insulator plumb	☒
All pins orientated to tower and source	☒
Arcing horn installed as per design	☒
Dampers installed to specification	☒
3. Dead End — **Source Side Complete** ☒ **Load Side Complete** ☒	
Area cleared of all wildlife within 500m, 1 hour prior to use of implosive sleeves:	☒
Correct size and orientation	☒
Dead end cleaned and checked with "no go" gauge (If compression)	☒
Jumpers formed uniformly	☒
Correct assembly used	☒
Turnbuckle installed in assembly as per design	☒

Comments:

QA Review	Signature	Date
Crew	Jeff Ingraham	28/05/2016
Valard QA	Drew Williams	06/08/2016
Nalcor QC Inspector	ZA	14 Nov 2016

Appendix B – Acuren Group Inc.
Failure Analysis of a Turnbuckle

Acuren Group Inc.
2190 Speers Road
Oakville, ON, Canada L6L 2X8
www.acuren.com

Phone: 905.825.8595
Toll Free: 877.299.2857
Fax: 905.825.8598

A Higher Level of Reliability

April 23, 2021 **Our Project No.: 128-21-10ACU020-0002**

Nalcor Energy
500 Columbus Drive
P.O.Box 12800
St. John's NL
A1B 0C9

Attention: Mrs. Cheryl Sehn

Dear Mr. Cheryl Sehn:

SUBJECT: FAILURE ANALYSIS OF A TURNBUCKLE

Please find enclosed the above-named report. We trust you will find it satisfactory, and we appreciate the opportunity to be of service to Nalcor Energy. At Acuren, we remain committed to providing you with world-class integrity management solutions.

Should you require any additional information, please do not hesitate to contact the undersigned at 905-673-9899 or by e-mail at yunlin.gao@acuren.com

Please note that unless we are notified in writing, samples from this investigation will be disposed of after 60 days.

Sincerely,

Yunlin Gao
Head of Failure Analysis and Metallurgical Engineering

Acuren Group Inc.
2190 Speers Road
Oakville, ON, Canada L6L 2X8
www.acuren.com

Phone: 905.825.8595
Toll Free: 877.299.2857
Fax: 905.825.8598

A Higher Level of Reliability

FAILURE ANALYSIS OF A TURNBUCKLE

Prepared for

Mrs. Cheryl Sehn, P. Eng.
Transmission & Civil Engineering
Engr Services Power Supply
Nalcor Energy

Prepared by

Yunlin Gao, M.Eng
Head of Failure Analysis and Metallurgical Engineering

Reviewed by

Ethan (Erhan) Ulvan, PhD., P.Eng., FASM
Manager – Engineering, Laboratories, Nuclear and FES, Eastern Canada
Past President, Failure Analysis Society, American Society for Materials International

April 23, 2021
Acuren Project No.: 128-21-10ACU020-0002

TABLE OF CONTENTS

LIST OF FIGURES

LIST OF TABLES

1.0 INTRODUCTION

We (Acuren Group Inc. Oakville Lab) received two turnbuckles (one fractured and one intact) from the client (Nalcor Energy). The client requests us to perform a failure analysis to determine the cause of the fracture. The following information is provided by the client:

1. Turnbuckle is in tension on a transmission tower;
2. Two turnbuckles failed within two weeks of each other from two separate towers in the same area;
3. Turnbuckle failures happed Feb 4th and Around Feb 12th 2021. They have been installed since 2017. Service life is expected to be more than 50 years however similar low temperature material in Nalcor's system has lasted longer.
4. The weather condition when the failure occurred was:
    a. Str 1229 - High winds gusting 90 kmh+ (small amount of freezing rain on the line);
    b. Str 1209 - Assumed to be a couple days later (Snow and moderate winds). Temperatures were around -2 to 0 degrees;
5. The turnbuckle highlighted in Figure 1 is the turnbuckle that did not fail on the right side. A set of insulators is missing from the left side because the sister turnbuckle on the left side failed.

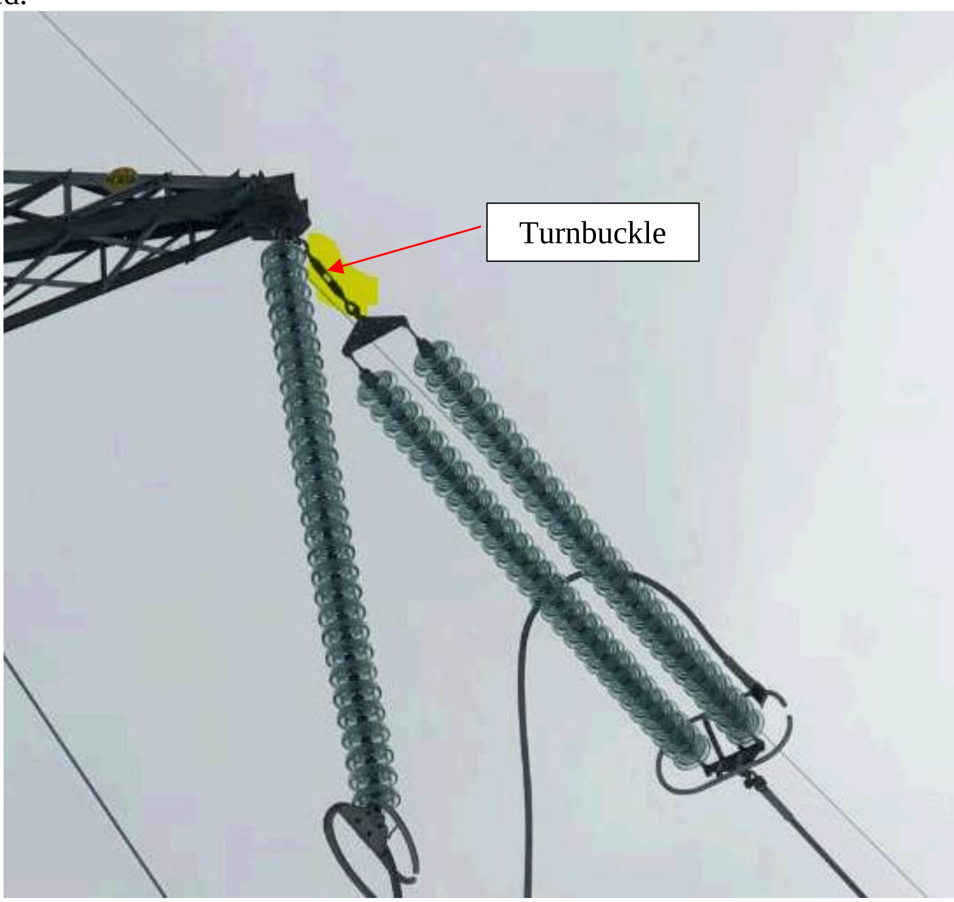

FIGURE 1. TURNBUCKLE ON A TRANSMISSION TOWER, PICTURE PROVIDED BY THE CLIENT

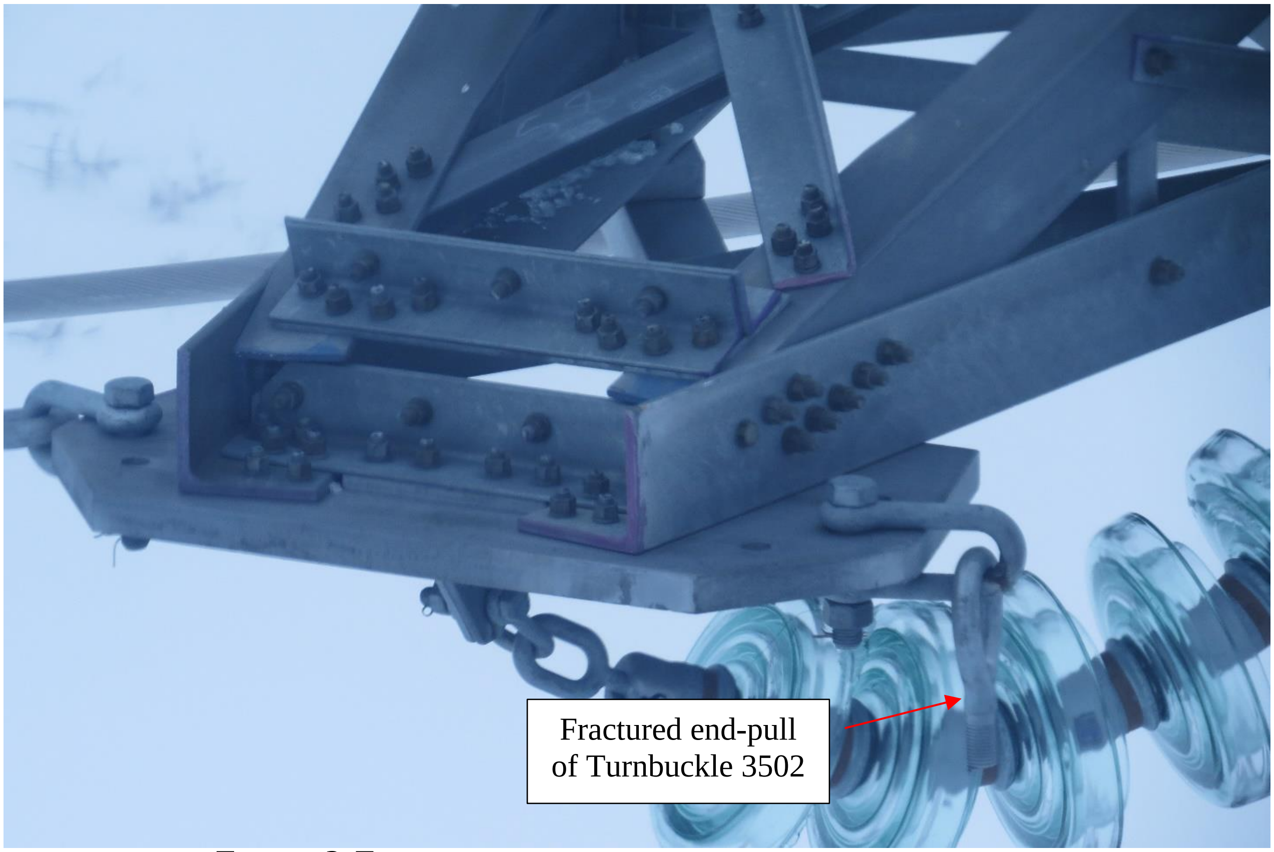

FIGURE 2. FRACTURED TURNBUCKLE, PROVIDED BY THE CLIENT

2.0 VISUAL AND LOW MAGNIFICATION EXAMINATION

The turnbuckles in as-received condition are shown in Figure 3. Both turnbuckles are eye and eye type open-body turnbuckle. Both turnbuckles show the appearance of galvanized steel, which is confirmed by examination and tests discussed in later sections. The dimensions of the eye end-pulls were measured and shown in Table 1. Client's markings were observed on the turnbuckles (Figure 4 and Figure 5). We will refer to the turnbuckles as Turnbuckle 3501 and Turnbuckle 3502 in this report in accordance with client's marking. The left-handed end-pull of Turnbuckle 3502 fractured at the thread root of the first unengaged thread outside turnbuckle body (Figure 3).

The dimensions of the turnbuckles were measured and the results are shown in Table 1.The dimensions of the turnbuckles were slightly over the specified limits in client's drawing (NE DOC #ILK-SI-SD-6200-TL-D04-0063-01 Rev.C1). The dimensions of the fractured end-pull and those of the intact end-pulls were close. No bending or necking was observed on the fractured eye end-pull.

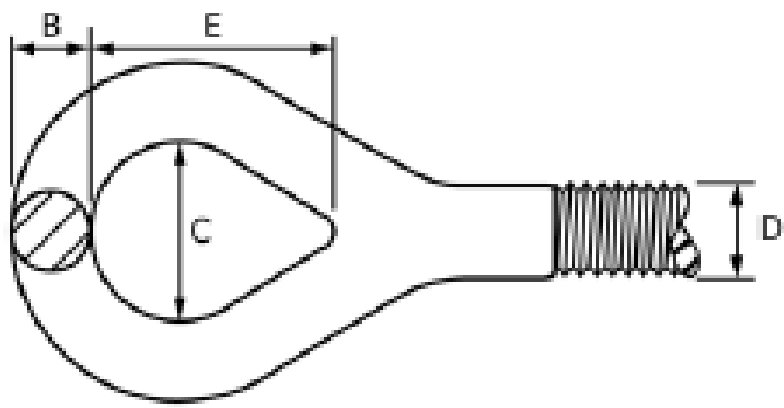

TABLE 1. DIMENSIONS OF TURNBUCKLES

Sample		Measurement results [mm]						
		D	**C**	**B**	**E**	**L_1 note 1**	**L_2 note 2**	**L_3 note 3**
3502	L	30.77	45.00	29.30	92.00	215	45	355
	R	31.09	45.50	29.60	91.30	216	52	
3501	L	31.35	45.50	29.60	91.28	214	47	355
	R	30.23	45.30	29.45	92.80	214	51	
Specified Dimensions		28.7±0.8	46.0±0.8	28.7±0.8	90.4±0.8	N.S.	N.S.	356±1.5

Note.1 – L_1: Total threaded portion length;
Note.2 – L_2: Threaded portion length outside of turnbuckle body;
Note.3 – L_3: Take up length;
Note.4 – Eye end-pull with severer wear damage was highlighted in Red.

The fracture surface of the fractured turnbuckle is shown in Figure 7 and Figure 8. The fracture surface was examined under stereomicroscope in as-received condition (Figure 9) and after cleaning by 5% Alconox solution ultrasonically for 30 minutes to remove oxides (Figure 10). The majority of the fracture surface is flat and smooth. Beach marks[1] were evident on the fracture surface, indicating fatigue fracture mode. Ratchet marks[2] were observed on one side of the fracture surface, indicating the crack initiation site. A dull color area with fibrous morphology[3] was observed on the other end of the fracture surface, indicating final fast fracture zone[4]. The crack propagation path marked by red arrow in Figure 10. A thin layer of fracture surface showing similar morphology as fatigue zone was observed on the final fracture end (Figure 11), which suggests that cracks were also initiated from this side of the fracture surface. Observation on the fracture surface suggests that the end-pull was under cyclic reverse bending[5] load with low nominal stress and medium stress concentration.

Threaded portion of the fractured end-pull on the eye end side were examined under stereomicroscope (Figure 12 and Figure 13). Opened cracks were observed at the thread roots adjacent to the fracture surface on the final fracture side of the end-pull (Figure 12). Small cracks were also observed at the thread roots on the fracture initiation side (Figure 14). However, the cracks appear to be only on the galvanized layer (further examinations will be shown in Metallographic Examination Section). Pitch length of the threads adjacent to the fracture surface is similar, indicating no elongation of the end-pull (Figure 15).

By mating the fracture surfaces of the eye end-pull, it was observed that the two end-pulls of Turnbuckle 3502 were not in the sample plane during operation (Figure 16). The planes, where the flat face of eye end-pull s sits, were perpendicular to each other.

Wearing and rubbing marks were observed on the intrados of eye end for all eye end-pulls. The wearing damage was severer on the left-handed end-pull for Turnbuckle 3502 and the right-handed end-pull for Turnbuckle 3501. Material on the end-pull surface was removed, smeared and folded, which indicates relative motions with high contact stresses. The wearing mark on the right-handed end-pull of Turnbuckle 3501 (Figure 21) was smaller and more circular comparing to that on the left-handed end-pull of Turnbuckle 3502 (Figure 18). The wear mark on left-handed end-pull of Turnbuckle 3502 appeared in an oval shape and its long axis aligned with the crack path on the fracture surface (Figure 18). It was also observed that there were two lock bolts on each end-pull for Turnbuckle 3502 (Figure 19 and Figure 20), which restrain the rotation of the eye end-pulls. On the other hand, there was only one lock bolt on each of eye end-pull for Turnbuckle 3501 (Figure 21 and Figure 22), which allows some degree of rotation for the end-pulls.

[1] Beach marks: Typical features seen on fatigue fracture surfaces. Beach marks indicate the successive positions of advancing crack front.
[2] Ratchet marks: Typical features seen on fatigue fracture surfaces. They formed after merging of two cracks on different planes. Fatigue crack origin typically located at the middle of two ratchet marks.
[3] Fibrous morphology: Coarse and rough fracture surface features, typically seen in overloading fracture surface of ductile material.
[4] Final fracture zone: In contrast to the fatigue crack propagation zone where cracks propagated in a slow and progressive manner, the material in this zone had a fast (in seconds) fracture due to the very high stress in the small intact cross-sectional areas exceeding the ultimate tensile strength of the material.
[5] Cyclic reverse bending load: A loading condition that repeatedly bending the part towards one direction and then the opposite direction.

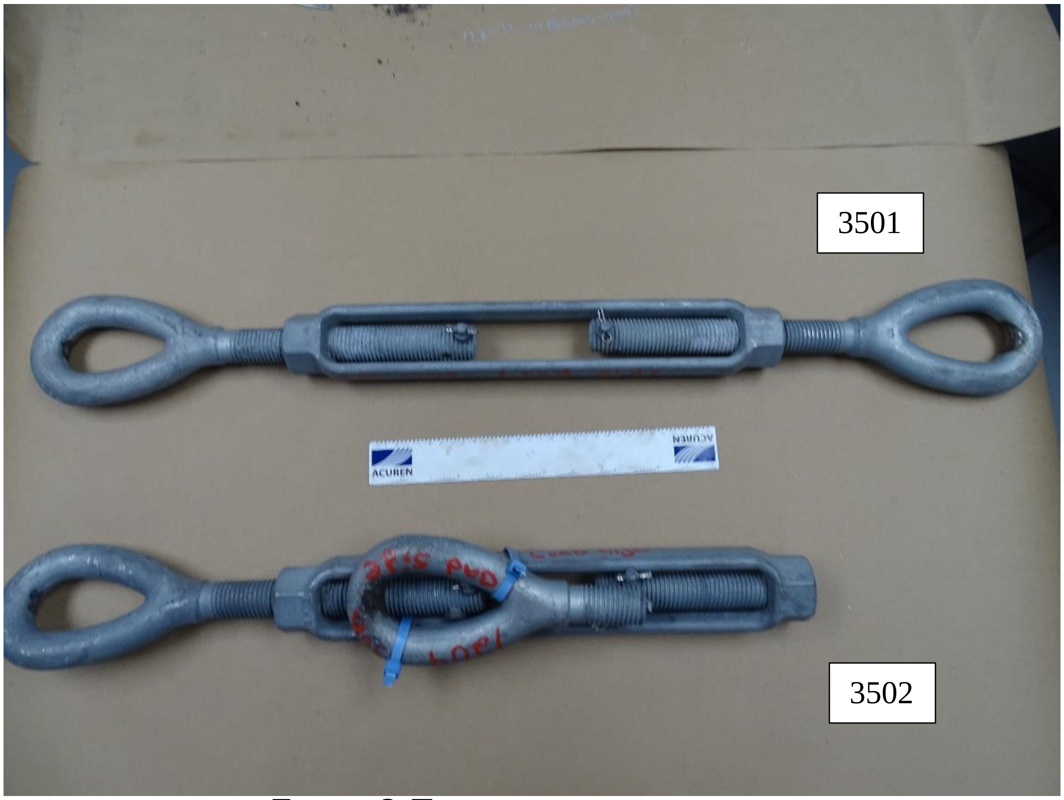

FIGURE 3. TURNBUCKLES AS-RECEIVED

FIGURE 4. CLIENT'S MARKING, TURNBUCKLE 3502

FIGURE 5. CLIENT'S MARKING, TURNBUCKLE 3501

FIGURE 6. TURNBUCKLE 3502 LOCATION OF FRACTUR

FIGURE 7. TURNBUCKLE 3502 FRACTURE SURFACE, HEAD SIDE

FIGURE 8. TURNBUCKLE 3502 FRACTURE SURFACE, BODY SIDE

FIGURE 9. TURNBUCKLE 3502 EYE END SIDE FRACTURE SURFACE, BEFORE CLEANING

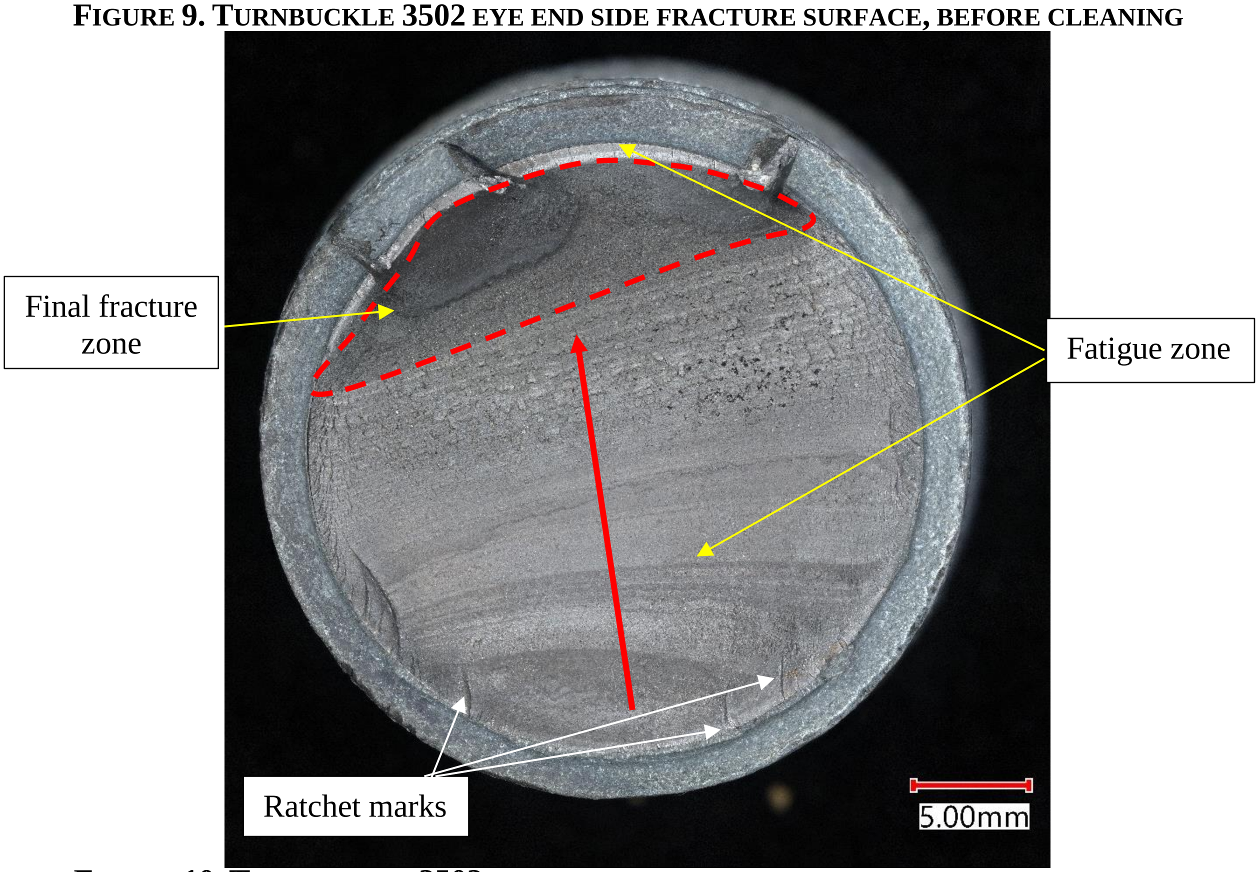

FIGURE 10. TURNBUCKLE 3502 EYE END SIDE FRACTURE SURFACE, AFTER CLEANING

FIGURE 11. BEACH MARK NEAR FINAL FRACTURE END, BEFORE CLEANING

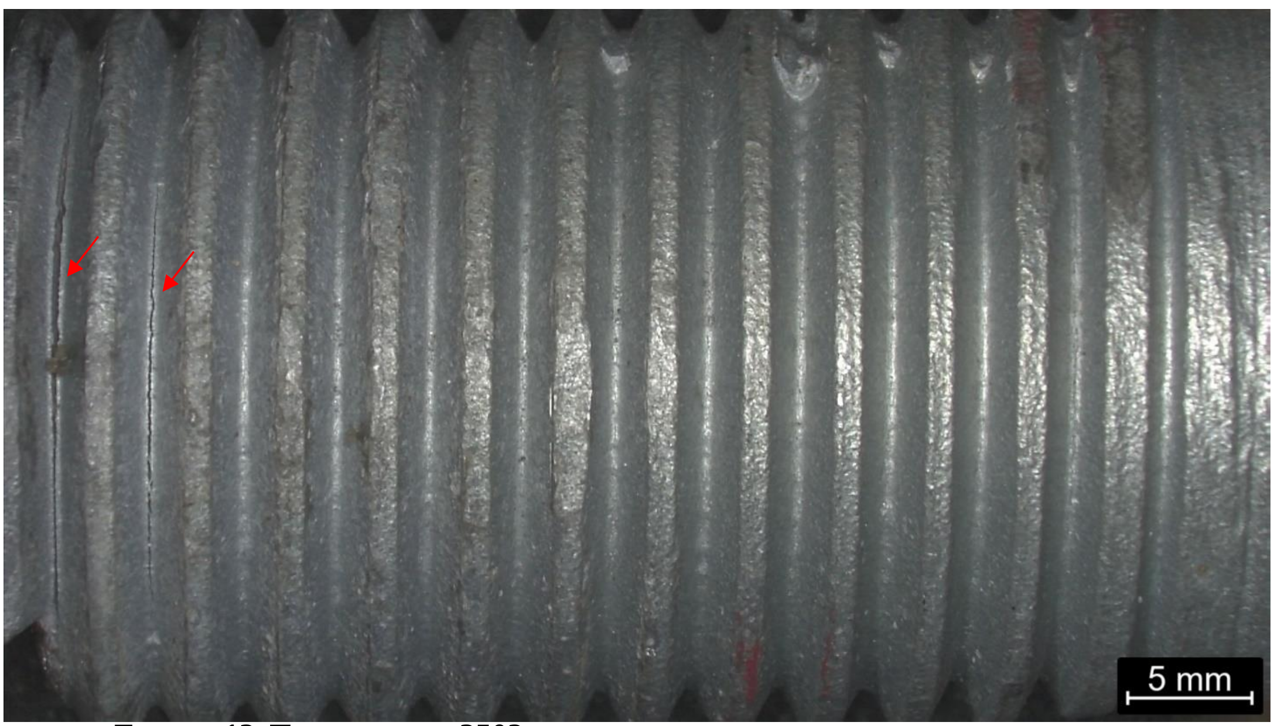

FIGURE 12. TURNBUCKLE 3502 EYE END SIDE THREADS, FINAL FRACTURE SIDE

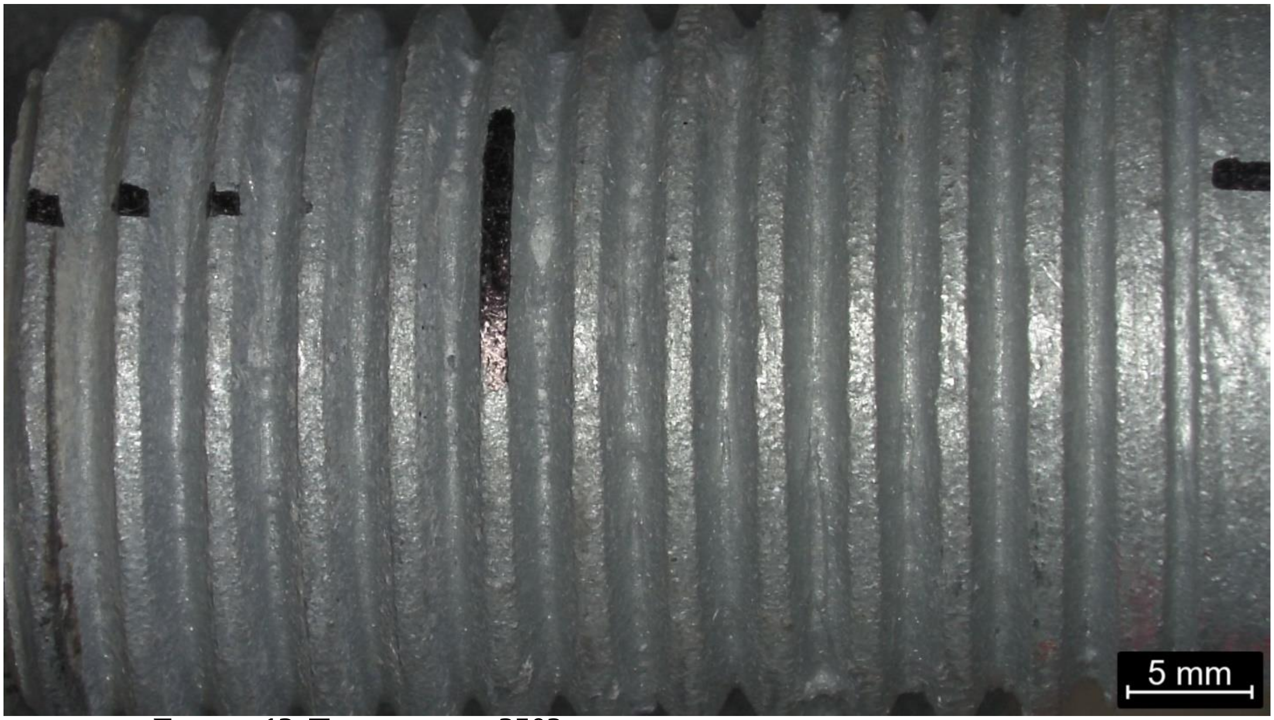

FIGURE 13. TURNBUCKLE 3502 EYE END SIDE THREADS, INITIATION SIDE

FIGURE 14. CRACKS ON GALVANIZED LAYER AT THREAD ROOT

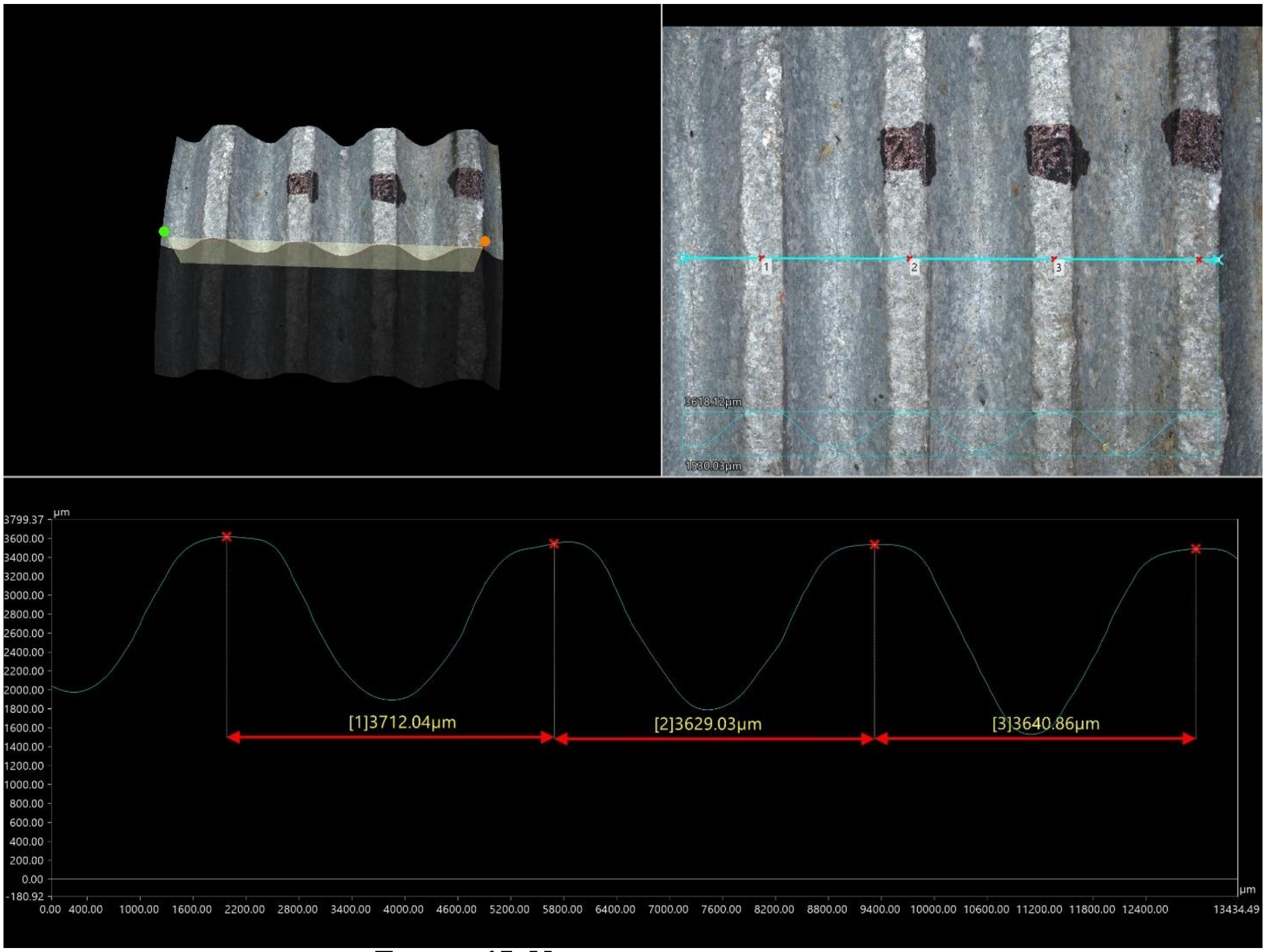

FIGURE 15. NO OBVIOUS ELONGATION

FIGURE 16. THE PLANES OF END-PULLS OF TURNBUCKLE 3502 WERE PERPENDICULAR

FIGURE 17. TURNBUCKLE 3502 HEAD SIDE

FIGURE 18. DIRECTION OF WEARING MARKS APPEARS TO ALIGN WITH CRACK PROPAGATION DIRECTION

FIGURE 19. TURNBUCKLE 3502 FRACTURED AT LEFT HANDED SIDE

FIGURE 20. TURNBUCKLE 3502, RIGHT HANDED SIDE

FIGURE 21. TURNBUCKLE 3501, RIGHT HANDED SIDE

FIGURE 22. TURNBUCKLE 3501, LEFT HANDED SIDE

3.0 SCANNING ELECTRON MICROSCOPY

The fractured surface of the fractured end-pull was examined by means of scanning electron microscopy. The entire fracture surface was examined and the locations where the SEM micrographs were taken are shown in Figure 23.

Fracture initiation site of the end-pull is shown in Figure 24. The galvanized layer was evident and no disruption was observed at the bonding between the galvanized layer and the base metal. Fine features adjacent to the surface and on the ratchet marks were flattened/removed most probably due to rubbing with mating fracture surface post fracture.

The general fracture surface morphology appeared identical near the crack initiation site (Figure 24) and in the majority of the fracture surface (Figure 25 and Figure 27). At higher magnifications, striations[6] were observed (Figure 26 and Figure 28), which indicates fatigue crack propagation.

The fracture surface morphology became rougher when moving closer towards the final fracture zone (Figure 29). Fissures were evident at low magnifications and striations with larger spacing were observed at higher magnifications (Figure 30). It indicates stresses on the end-pull increased as the intact cross section area decreased due to fatigue crack propagation.

The final fracture zone of the end-pull showed dimples[7] (Figure 31), indicating ductile final fracture of the end-pull. A thin layer of fatigue zone was observed on the final fracture side beneath surface (Figure 32). Ratchet marks were observed in this fatigue zone, indicating crack initiation from this side of the end-pull.

[6] Striation: Microscopic fatigue feature that shows the incremental growth of a fatigue crack. Typically, one striation formed at each cycle of load.

[7] Dimples: Microscopic feature on ductile fracture surface. When ductile material matrix plastically deformed, voids are nucleated at hard inclusions to accommodate the incompatibility. Dimples formed as micro-voids coalesces.

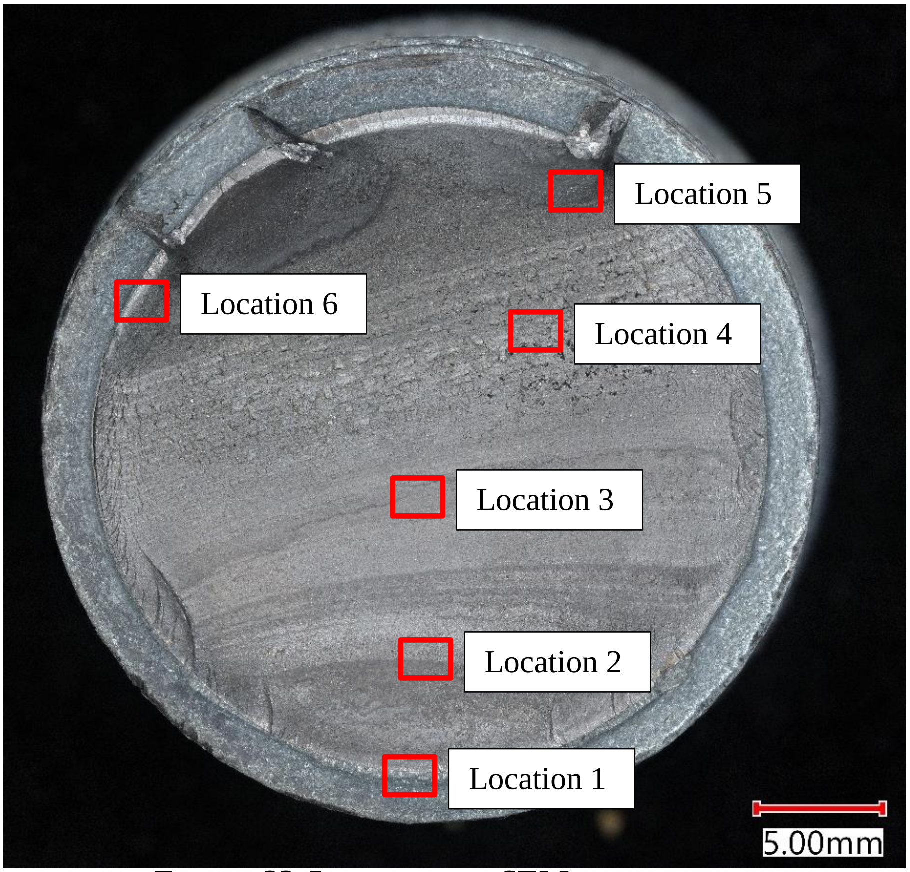

FIGURE 23. LOCATION OF SEM MICROGRAPH

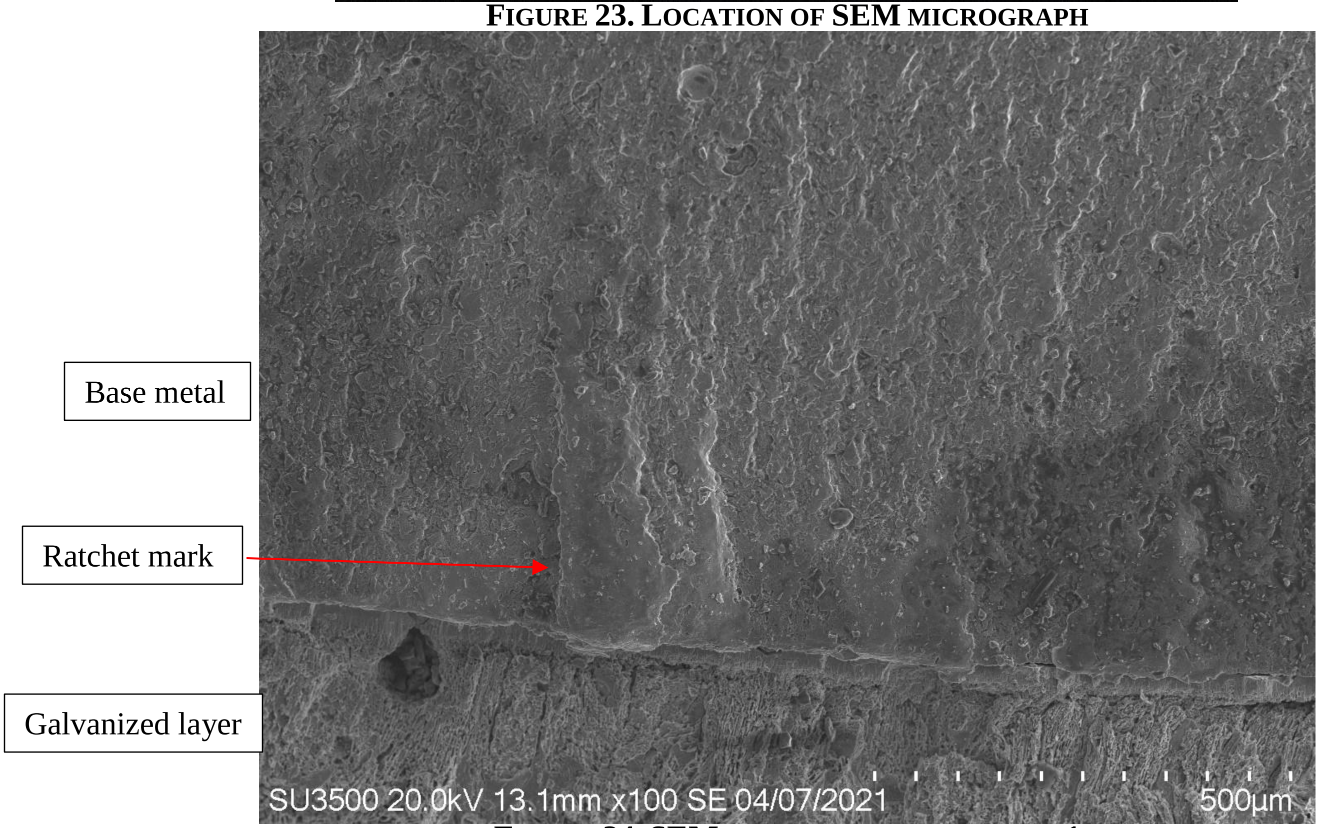

FIGURE 24. SEM MICROGRAPH, LOCATION 1

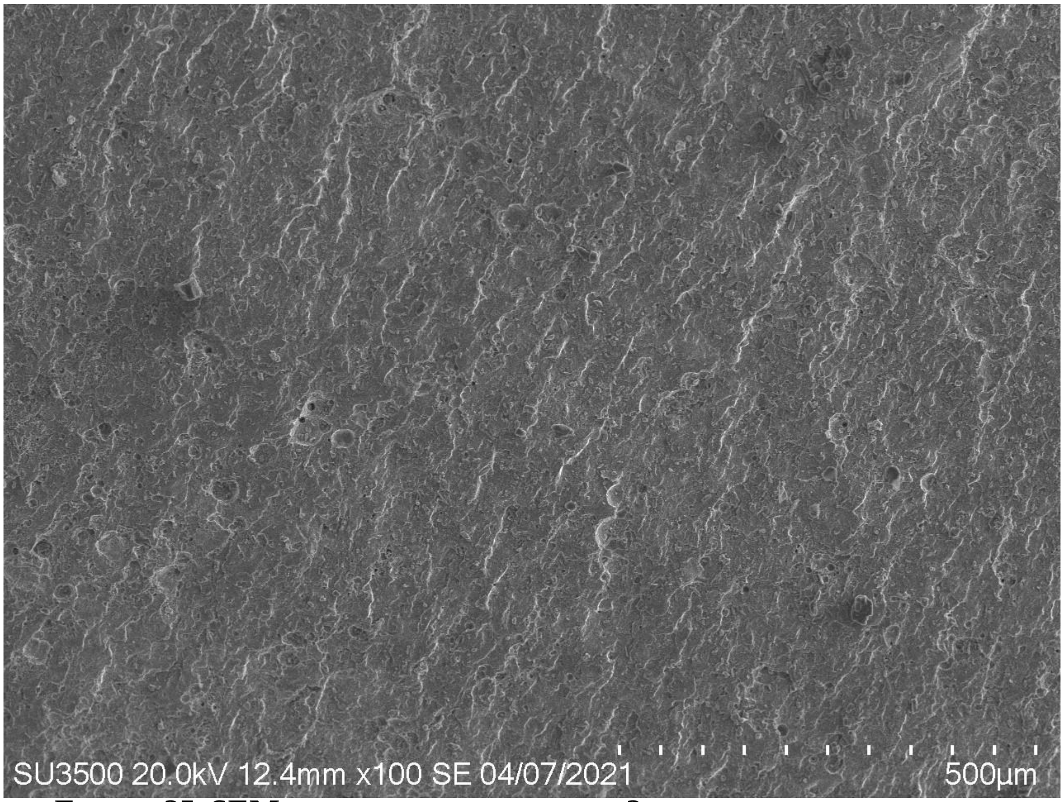

FIGURE 25. SEM MICROGRAPH, LOCATION 2, GENERAL MORPHOLOGY

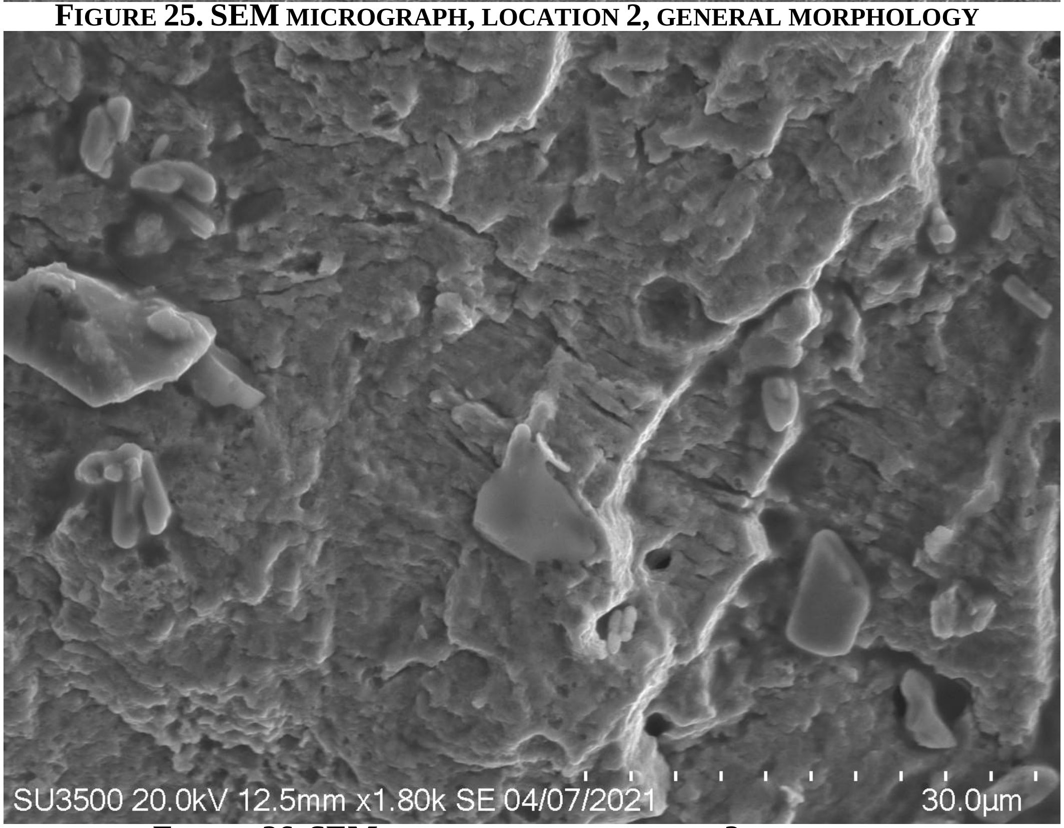

FIGURE 26. SEM MICROGRAPH, LOCATION 2, STRIATIONS

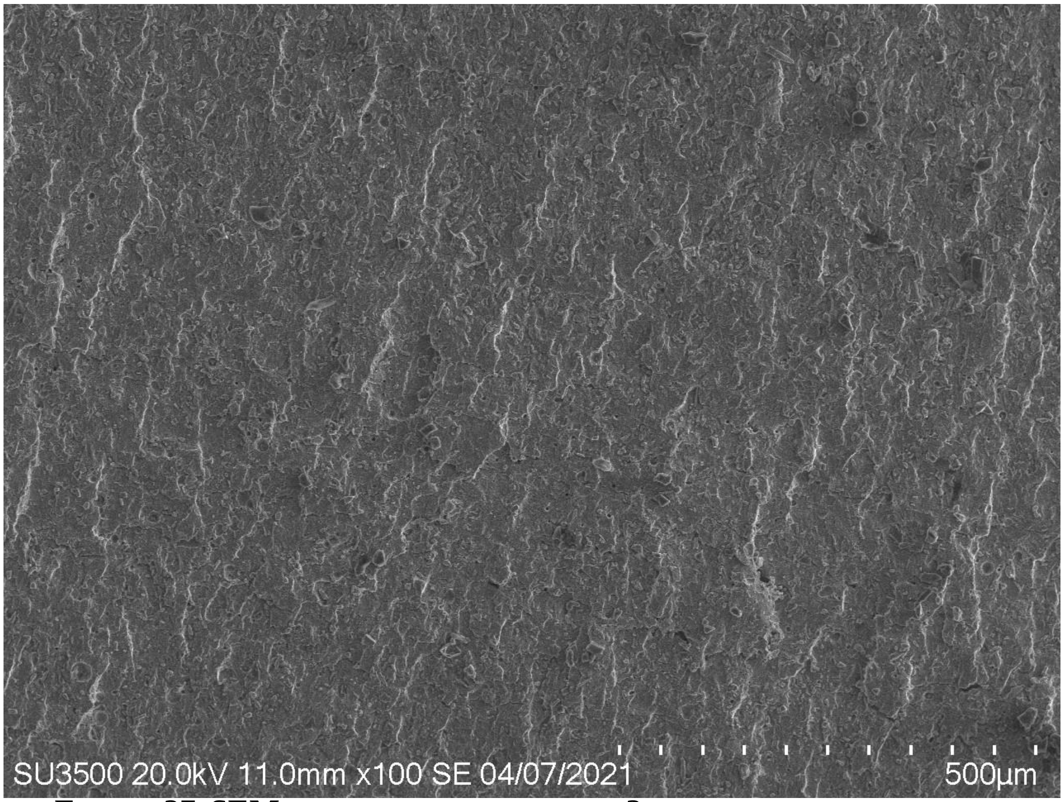

FIGURE 27. SEM MICROGRAPH, LOCATION 3, GENERAL MORPHOLOGY

FIGURE 28. SEM MICROGRAPH, LOCATION 3, STRIATIONS

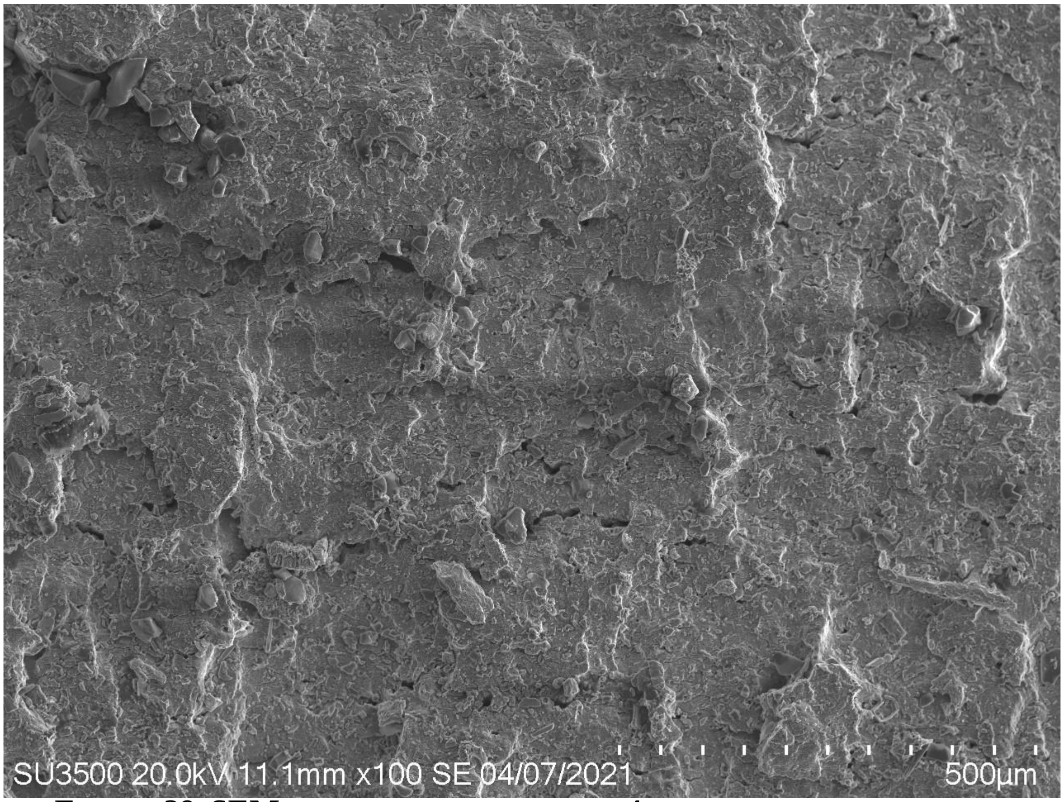

FIGURE 29. SEM MICROGRAPH, LOCATION 4, GENERAL MORPHOLOGY

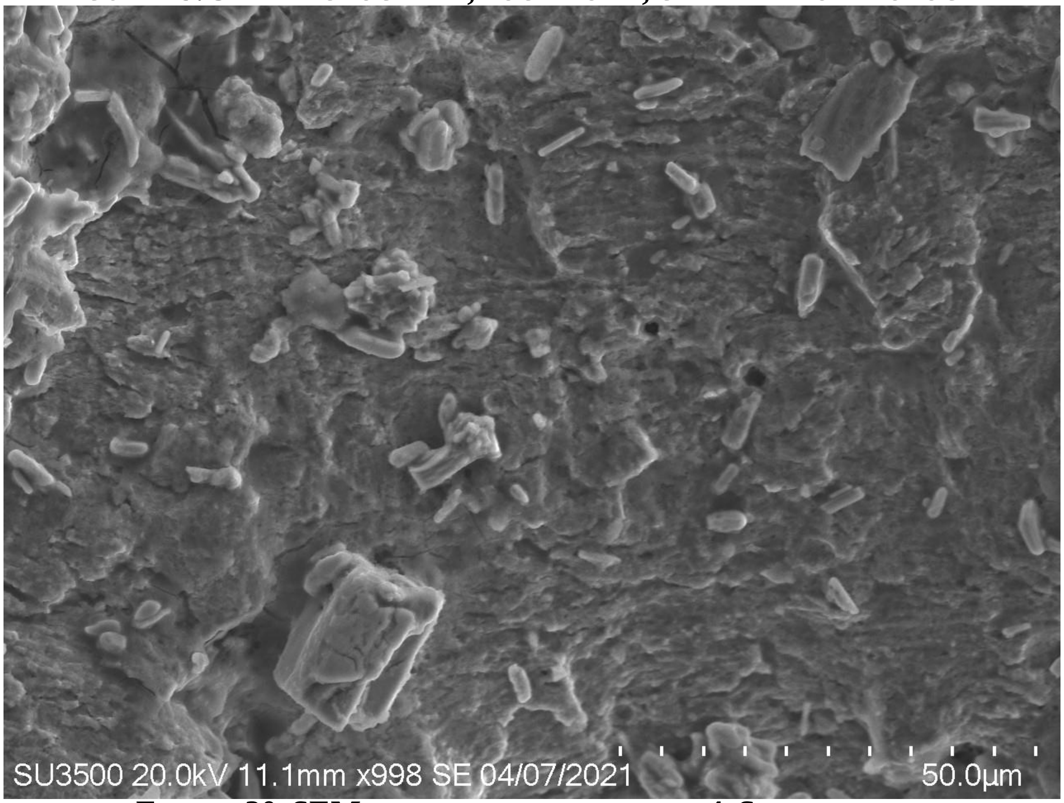

FIGURE 30. SEM MICROGRAPH, LOCATION 4, STRIATIONS

FIGURE 31. SEM MICROGRAPH, LOCATION 5, DIMPLES

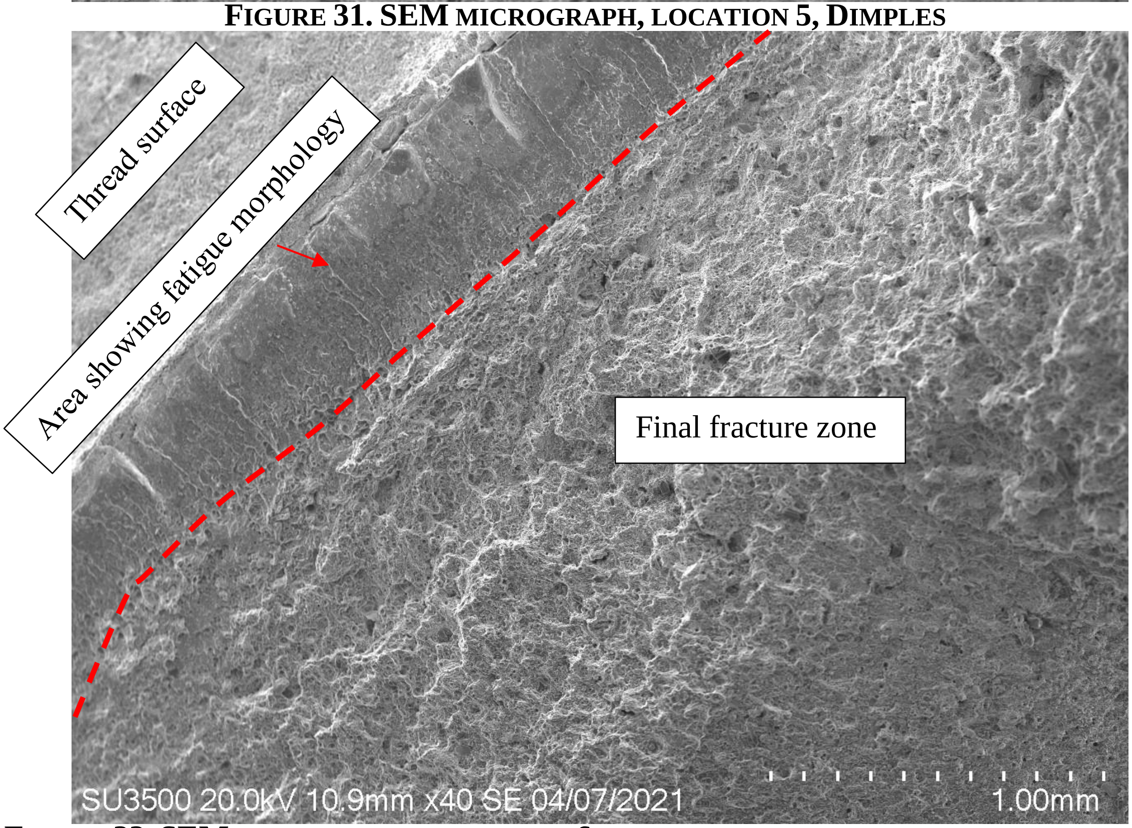

FIGURE 32. SEM MICROGRAPH, LOCATION 6, FATIGUE ZONE ON FINAL FRACTURE SIDE

4.0 METALLOGRAPHIC EXAMINATION

A sample was removed from the fractured eye end-pull for metallographic examination of the longitudinal cross section (Figure 33). The samples were mounted in Bakelite, ground and polished in accordance with ASTM E3-11. After examination in the as-polished condition, we etched the sample using 2% nital in accordance with ASTM E407-07(2015)E1 to reveal their microstructure (Figure 34). The end-pull showed tempered martensitic microstructure in the entire cross section examined (Figure 35), which indicates the end-pull was through hardened. A layer of the base metal near thread surface appeared in white colour in etched condition because the zinc coating was preferentially etched by the etchant, leaving the adjacent base metal only lightly etched.

The metallographic was subjected to inclusion rating as per ASTM E45-18, Method A (Worth Field). For this purpose, the sample was examined in as-polished condition under light microscope at 100X magnification. The sample's surface was checked to find the worth fields. The image displayed (Figure 36) was compared with the Plate 1A to determine inclusions' severity level. Results of evaluation are presented in Table 2.

TABLE 2. INCLUSION CONTENT ANALYSIS (AS PER ASTM E45-18)

Type A Sulfide		Type B Alumina		Type C Silicate		Type D Globular Oxide	
Thin	Heavy	Thin	Heavy	Thin	Heavy	Thin	Heavy
1	1.5	0	0	0.5	0	1.5	1.5

Figure 37 shows the cross section at fracture initiation site. Galvanized layer was evident and some excessive zinc deposit were observed at the thread root. The fracture surface cut through grains at initiation site, indicating transgranular crack propagation mode[8]. An unopened crack was observed parallel to the fracture surface at the same thread root (Figure 38). This crack also showed transgranular crack propagation without branching.

Same type of cracks were observed at all the thread root in the sample examined on the initiation side (Figure 39, Figure 40, Figure 41 and Figure 42), indicating fatigue crack initiation on these thread roots. Similarly, cracks were observed at all the thread root in on the final fracture side (Figure 43 to Figure 46). The cracks were more open at the first and second thread root adjacent to the fracture surface (Figure 43 and Figure 44), which was a result of the jerk during final fracture. Cracks away from the fracture surface show identical features as the cracks on the fracture initiation side, indicating they are fatigue cracks.

The head side of the fractured end-pull was sectioned longitudinally, polished and etched with 10% ammonium persulfate to reveal the material flow line (Figure 47). The flow lines follow the curvature of the end-pull, indicating that the end-pull was forged. The flow lines also follows the curvature of the threads(Figure 40, Figure 42, Figure 44 and Figure 46), indicating the threads were rolled.

[8] Transgranular crack propagation: In contrast to intergranular crack propagation where crack path follows the grain boundaries of the material, the crack path in transgranular crack propagation mode cut through grain boundaries.

ACUREN

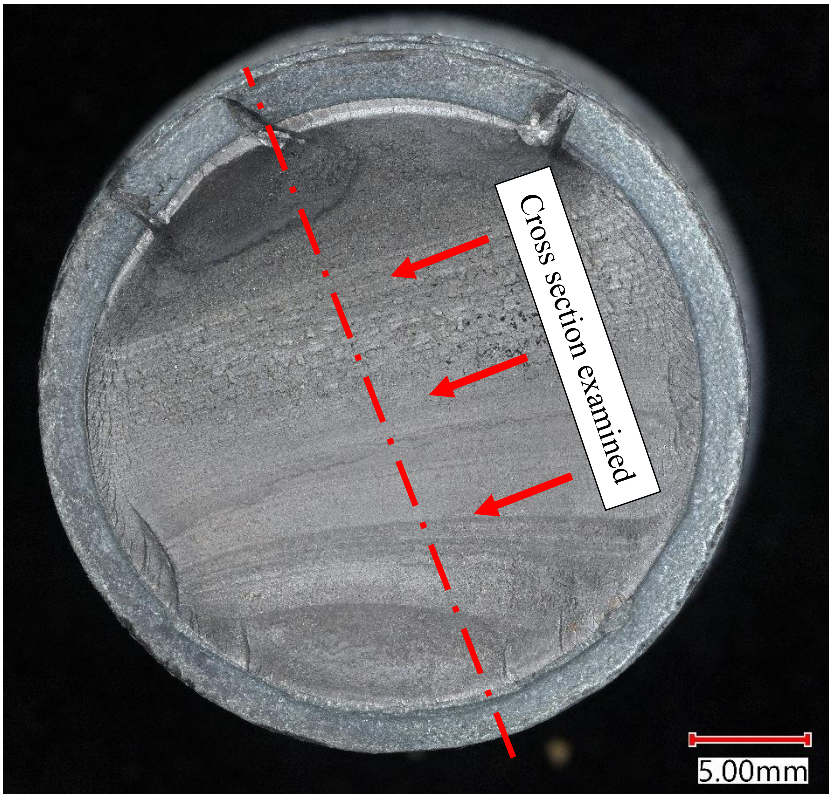

FIGURE 33. LOCATION OF CROSS SECTION EXAMINED

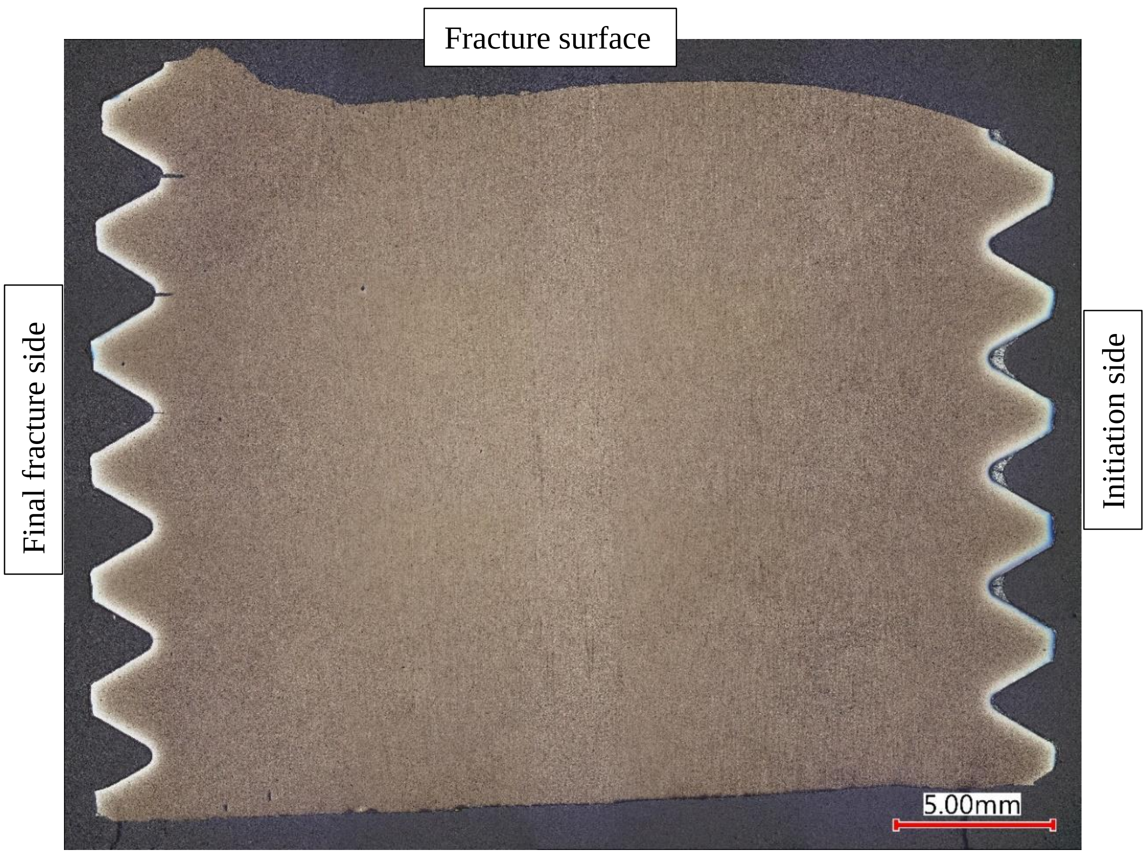

FIGURE 34. METALLOGRAPHIC SAMPLE, ETCHED CONDITION

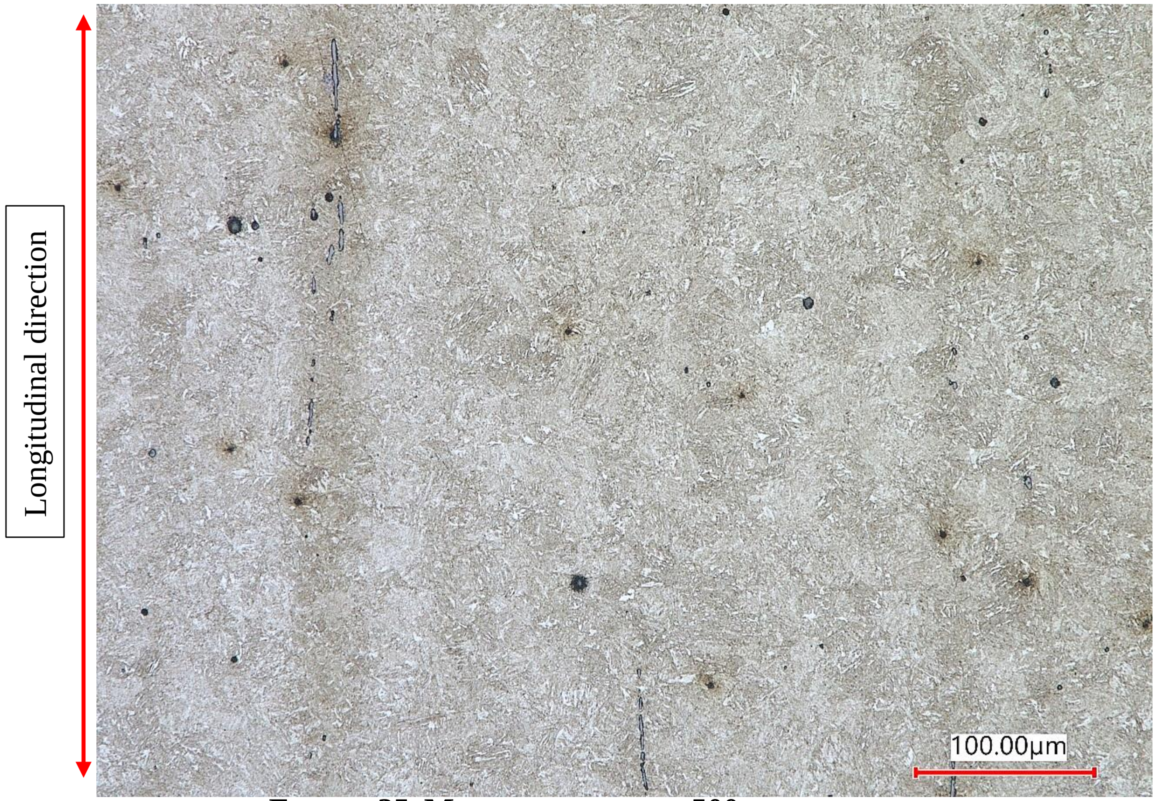

FIGURE 35. MICROSTRUCTURE, 500X MAGNIFICATION

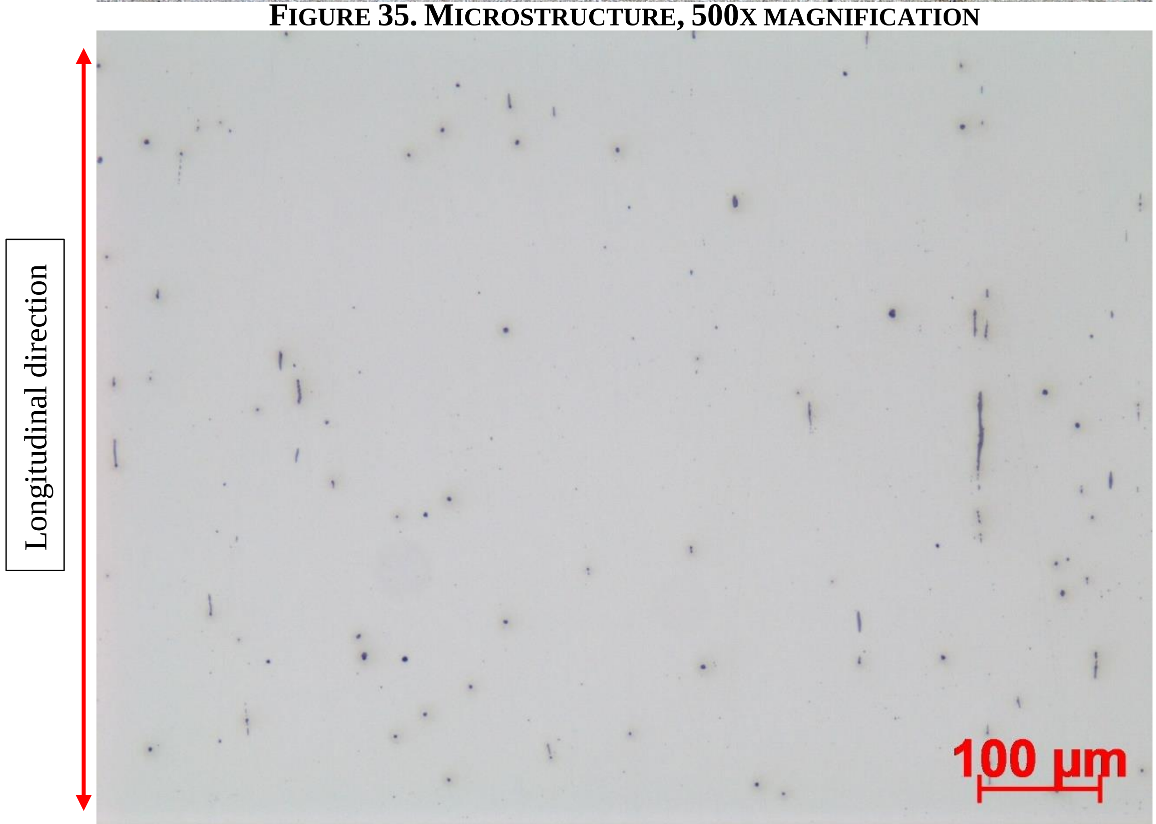

FIGURE 36. INCLUSIONS

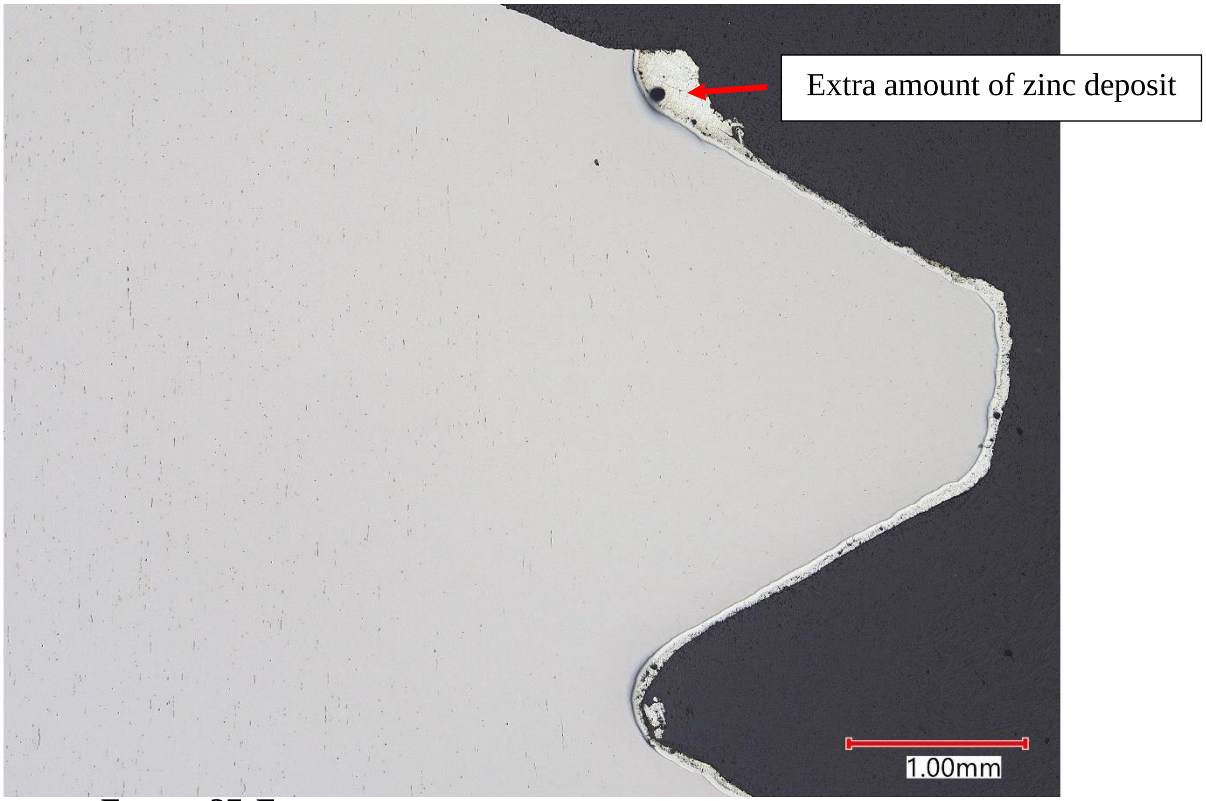

FIGURE 37. FRACTURE INITIATION SITE, AS-POLISHED CONDITION

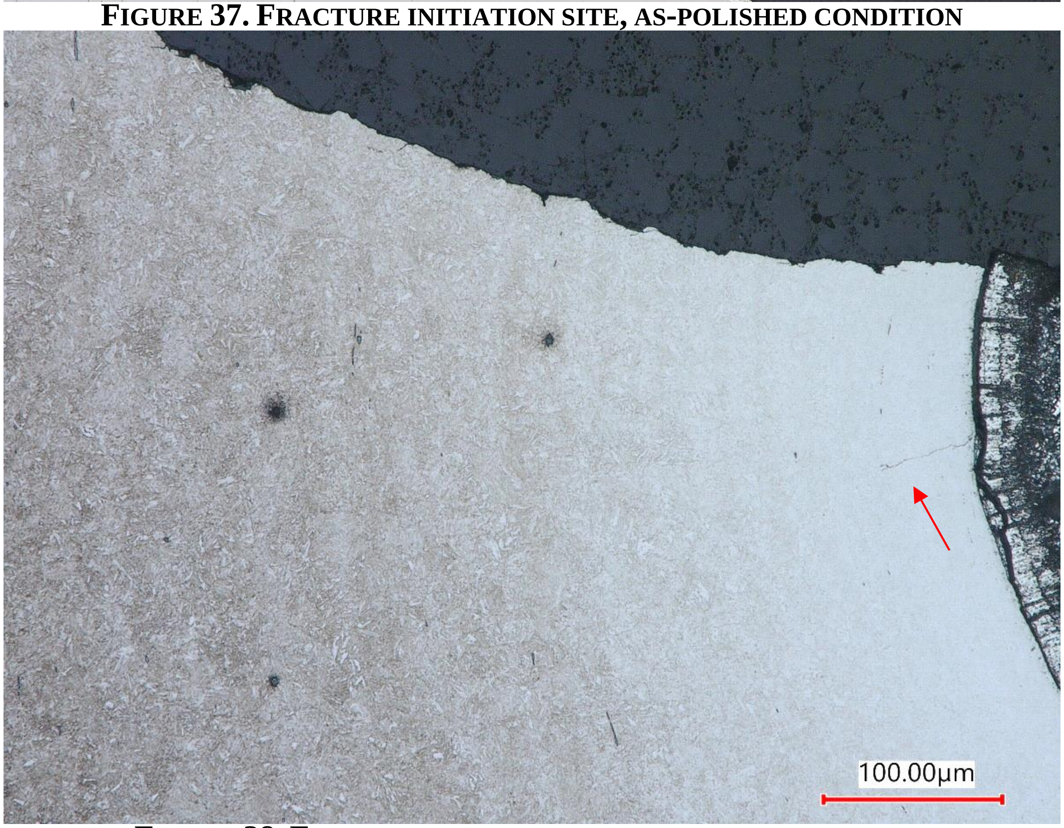

FIGURE 38. FRACTURE INITIATION SITE, ETCHED CONDITION

FIGURE 39. SECOND THREAD ROOT AT FRACTURE INITIATION SITE, AS-POLISHED CONDITION

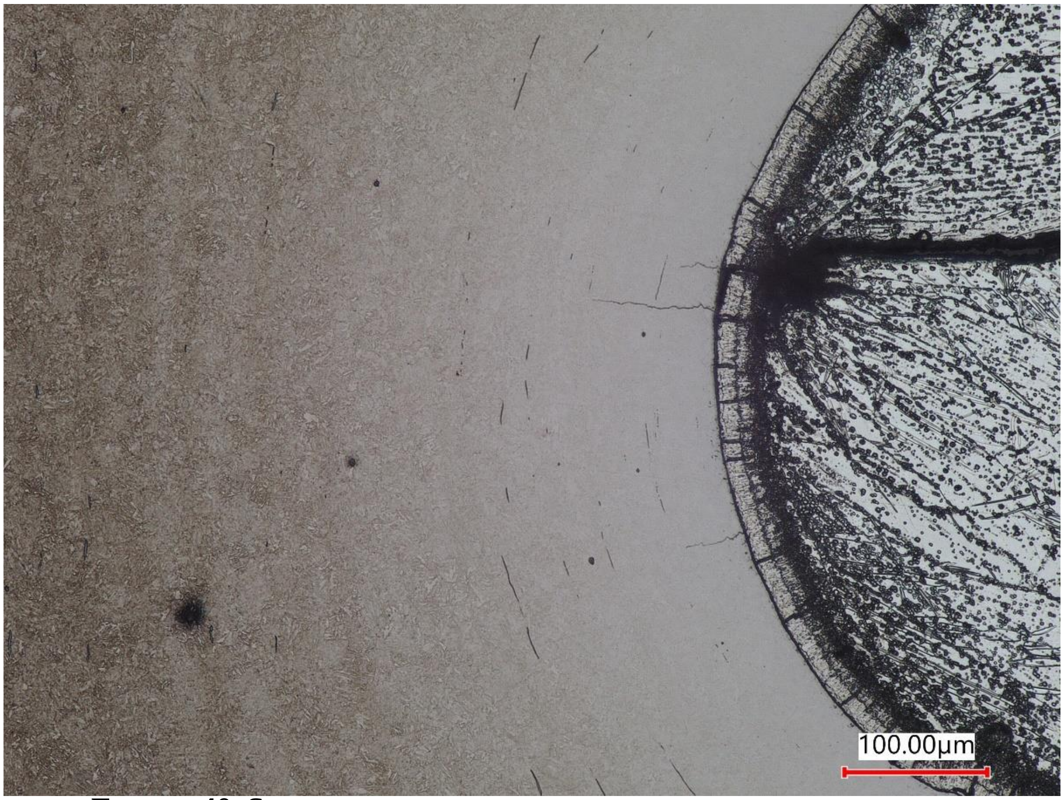

FIGURE 40. SECOND THREAD ROOT AT FRACTURE INITIATION SITE, ETCHED CONDITION

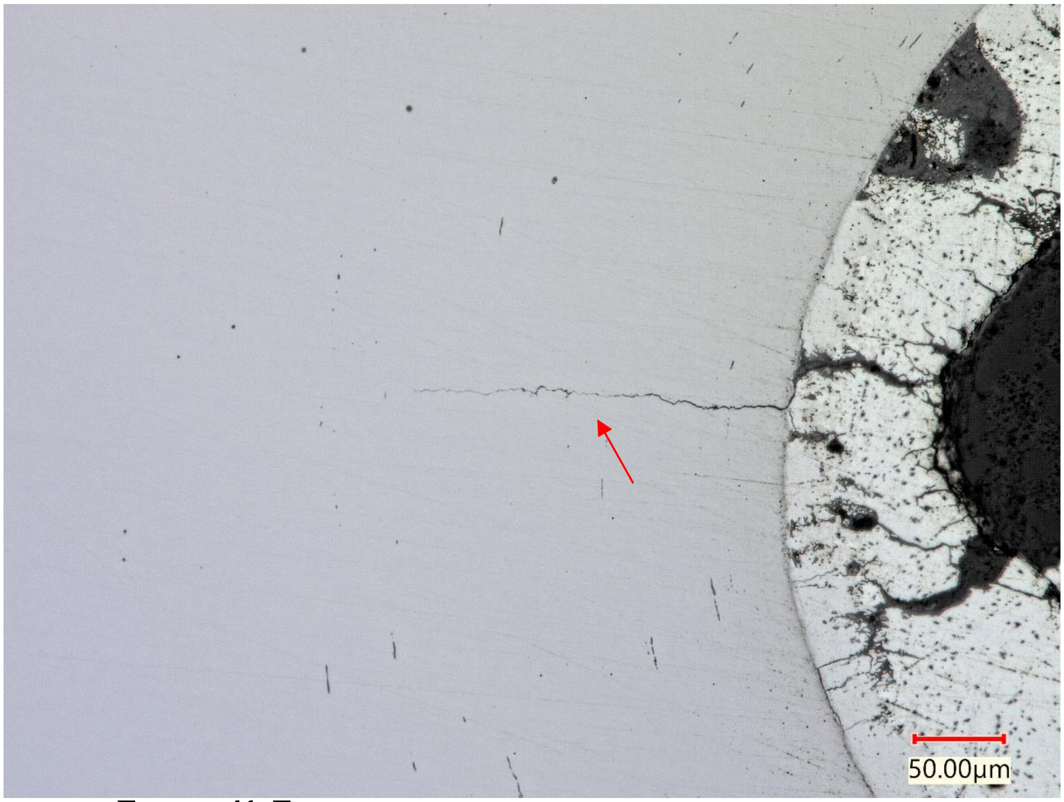

FIGURE 41. FIFTH THREAD ROOT AT FRACTURE INITIATION SITE, AS-POLISHED CONDITION

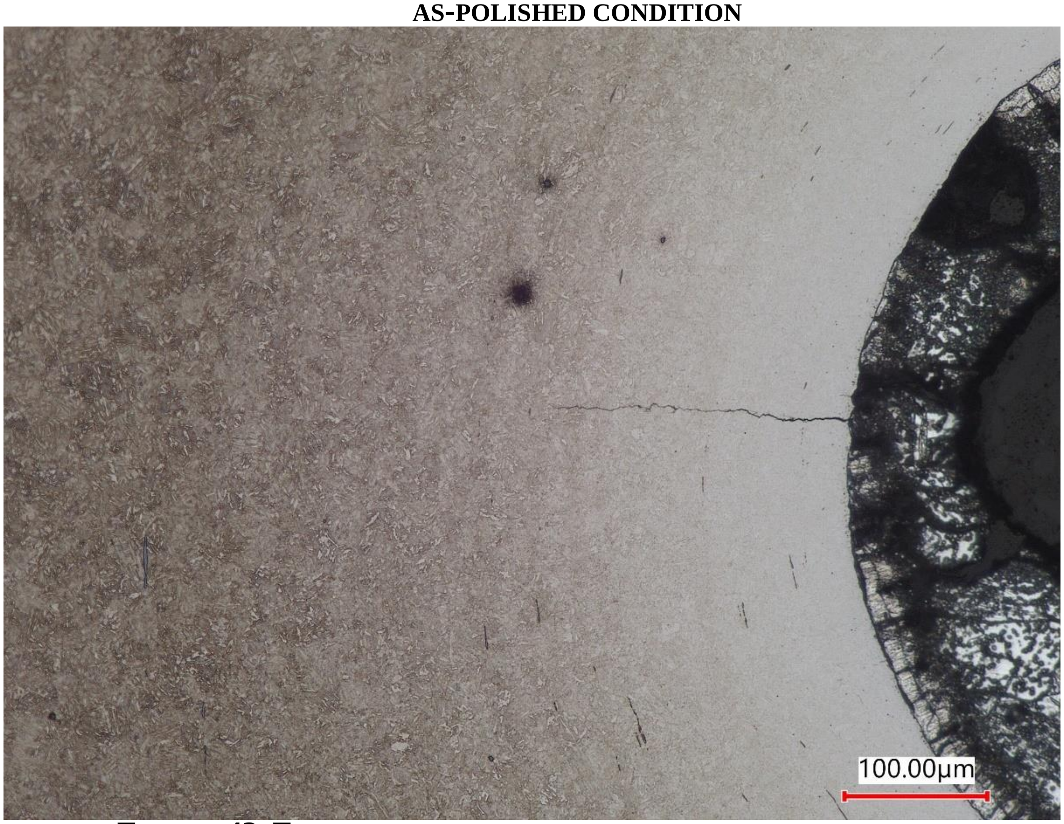

FIGURE 42. FIFTH THREAD ROOT AT FRACTURE INITIATION SITE, ETCHED CONDITION

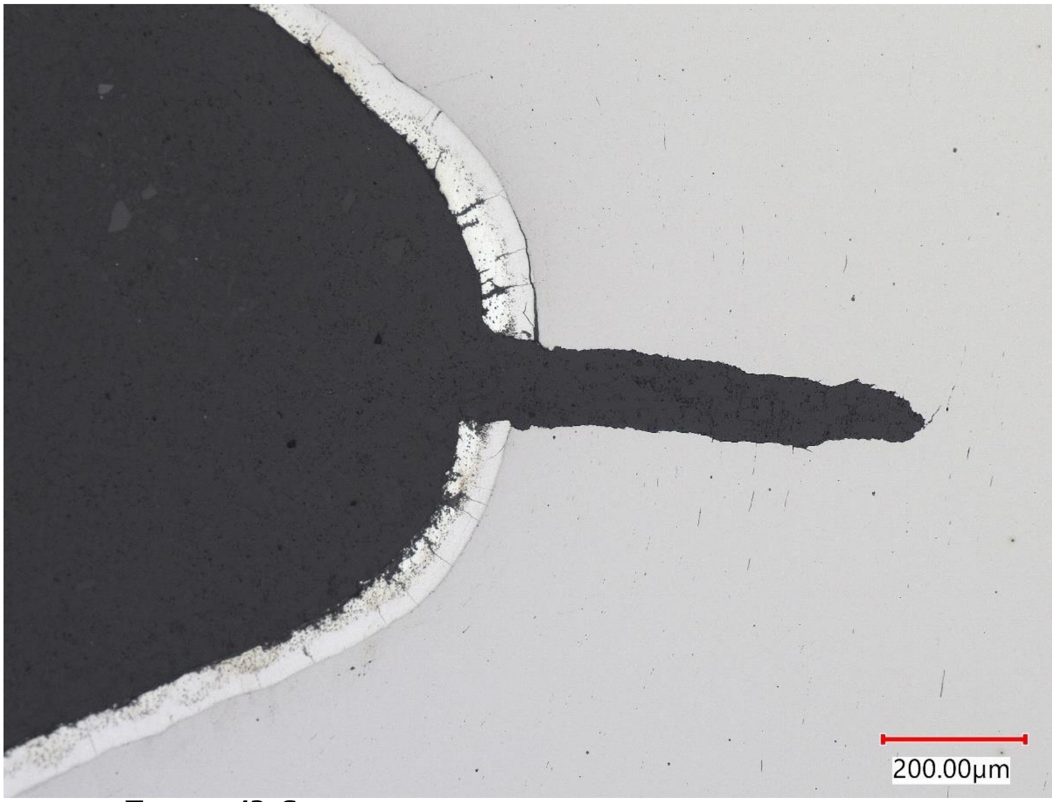

FIGURE 43. SECOND THREAD ROOT AT FINAL FRACTURE SIDE, AS-POLISHED CONDITION

FIGURE 44. SECOND THREAD ROOT AT FINAL FRACTURE SIDE, ETCHED CONDITION

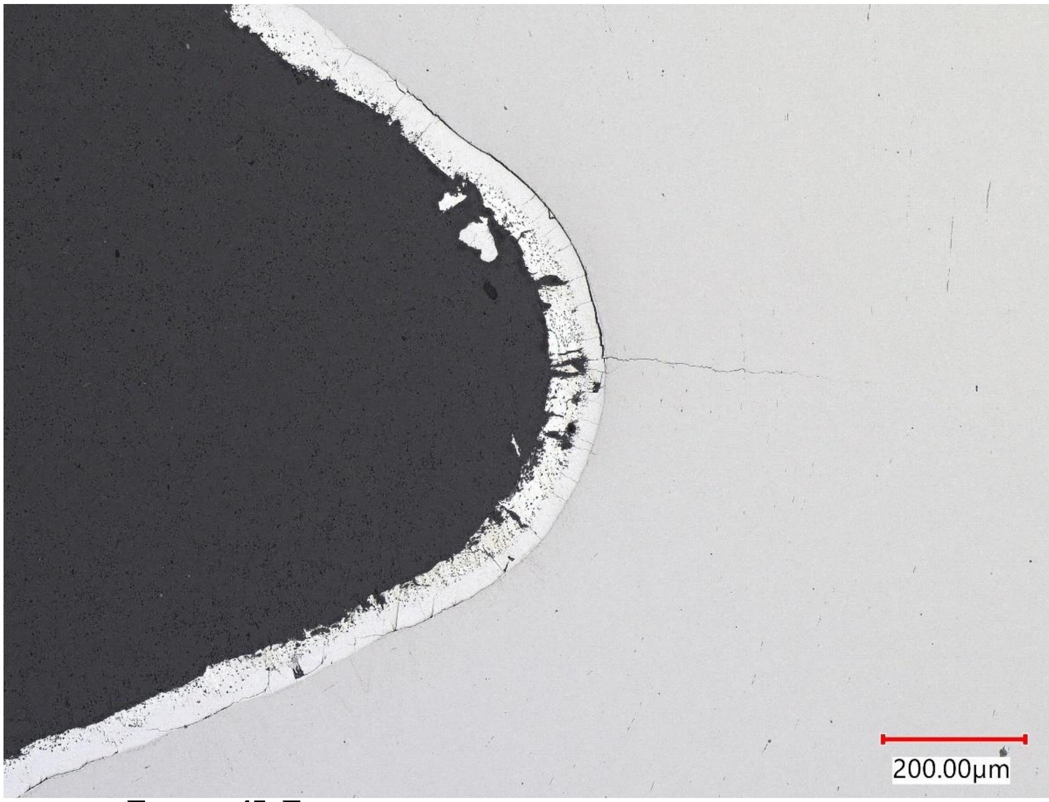

FIGURE 45. FIFTH THREAD ROOT AT FINAL FRACTURE SIDE, AS-POLISHED CONDITION

FIGURE 46. FIFTH THREAD ROOT AT FINAL FRACTURE SIDE, ETCHED CONDITION

FIGURE 47. MACRO ETCHED OF THE FRACTURED END-PULL

5.0 HARDNESS

Vickers micro hardness tests using 500gf were performed in accordance to ASTM E384-17 on the same samples used for metallography examination. The average Vickers hardness HV0.5 values were converted to Rockwell hardness numbers as per ASTM E140-12.

TABLE 3. HARDNESS RESULTS

Location	Measurement (HV0.5)					Average (HV 0.5)	Rockwell C (HRC)
	1	2	3	4	5		
Core	299.9	295.1	292.5	291.4	297.7	295.3	29
Threads	312.7	304.7	302.1	285.8	297.2	300.5	30

The hardness results agree with the microstructure observed.

6.0 CHEMICAL ANALYSIS

The chemical composition of the eye end-pull was analysed using optical emission spectroscopy (OES) test method, in accordance with ASTM E415-17. The test results were shown in **TABLE 4**.

TABLE 4. CHEMICAL ANALYSIS RESULTS, % BY WEIGHT

Elements	Fractured End-pull	ASTM A29 – 20[9] Grade 4140
Fe	Rem.	**Rem.**
C	0.41	0.38–0.43
Si	0.24	0.15-0.35
Mn	0.94	0.75–1.00
P	0.007	0.035 Max
S	0.019	0.040 Max
Cr	0.88	0.80-1.10
Mo	0.17	0.15-0.25
Ni	0.16	N/S[10]
Al	0.03	N/S
Co	0.01	N/S
Cu	0.22	N/S
Nb	< 0.0010	N/S
Ti	< 0.005	N/S
V	0.01	N/S

The chemical composition of the end-pull conforms to the specified limits as in ASTM A29 for Grade 4140 alloy steel.

[9] ASTM A29-20: Standard Specification for General Requirements for Steel Bars, Carbon and Alloy, Hot-Wrought
[10] N/S: Not Specified in the standard

7.0 DISCUSSION AND CONCLUSIONS

The left-handed end-pull of Turnbuckle 3502 fractured due to fatigue crack initiation and propagation. Since the turnbuckle was over-torqued (over tightened), fatigue cracks initiated and propagated under combination of cyclic reverse bending and cyclic tension-tension loads that were induced by vibration and motion from other components (most likely the insulator) in the assembly.

Fatigue fracture mode is evident for the fractured end-pull of Turnbuckle 3502. Macroscopically, the fracture surface is flat and smooth with obvious beach marks. Microscopically, fatigue striations were observed in the beach marks region on the fracture surface. Fatigue cracks were mostly initiated on one side of the cross section and propagated to the other side until ductile final fracture occur. However, a thin lip of fatigue zone was also observed on the final fracture side, indicating fatigue crack also initiating from this side. The contour and size of the fatigue zone indicates that the end-pull was under cyclic reverse bending and tension-tension loads with low nominal stress and medium stress concentration.

Evidence shows that the cyclic loads on the end-pull were related to the rubbing with the shackle. Wearing marks were evident on the intrados of the eye end of the end-pull, indicating relative motion and rubbing between the end-pull and the shackle. The oval shape wear mark indicates that the shackle was always sitting tilted on the eye, which tended to rotate the end-pull in counter-clockwise direction. Since this end-pull was left-handed, such wearing motion will tend to fasten the end-pull further. As a result, it induced a varying torque on the end-pull, which translated to tensile stresses with varying magnitude on the end-pull. The direction of oval wear mark’s long axis also aligned with the crack propagation direction on the fracture surface, which indicates that the rubbing along this axis also induced the reverse bending load on the end-pull. When the cyclic stresses in the end-pull exceeded the (fatigue) endurance limit of the material, fatigue cracks started to initiate and propagate in the end-pull.

The wearing and rubbing on the end-pull was a result of the vibration and motion from the part that the shackle was connected to. It is common in this application due to many possible environmental loads (i.e. wind load, unevenly deposit and removal of precipitations and etc.) during operating. However, fatigue cracks were observed initiating at thread roots of all adjacent threads to the fracture surface, which indicates that relatively high stress level in the strain potion of the end-pull. This showed that the turnbuckle was most likely over-torqued (over tightened) during installation by further tightening the turnbuckle beyond the desirable/required tension in the line.

Deviations from the client’s installation procedure were evident on Turnbuckle 3502, which may have contributed to the failure. The first deviation was that the eyes of the end-pull were not in the same orientation relative to each other. The second deviation was that two locking bolts were used on each of the end-pull, which restrain any rotation motions of the end-pulls relative to the turnbuckle body. These two deviations did not directly stress the turnbuckle. However, orientation misalignment promoted wear damage on the end pull and the additional lock bolt prevented the turnbuckle to self-balance. Subsequently, it could intensify the cyclic loads on the turnbuckle.

The chemical composition of the fractured end-pull of Turnbuckle 3502 conforms to the specified limit for ASTM A29-20 Grade 4140 alloy steel. The material flow lines show that the end-pull was forged and the threads were rolled. The end-pull shows tempered martensitic microstructure in the entire cross section examined, showing that is was full hardened. Hardness test results agree with the microstructure observed. This material can be further hardened to reduce the level of wear damage on the end-pull. It should be noted that the hardness of the shackle material should be adjusted accordingly to avoid excessive wear damage on the shackle. No corrosion damage was observed on the galvanized layer and it has decent adhesion to the base metal. However, extra amount of zinc deposits was observed at the threaded portion of the end-pulls, which can increase the risk of seizing and affect the localization of stresses.

Hydrogen embrittlement did not play a role in the failure as intergranular features were not observed on the fracture surface nor on the cross section samples.

ACUREN

8.0 CONCLUSIONS AND RECOMMENDATIONS

It is concluded that:

1. The end-pull of turnbuckle 3502 fractured due to fatigue crack initiation and propagation.
2. The turnbuckle was over-torqued (over-tightened), resulting in fatigue crack initiation under cyclic loads.
3. Two deviations from the client's installation procedure were evident on Turnbuckle 3502.
4. The chemical composition of the fractured end-pull of Turnbuckle 3502 conforms to the specified limit for ASTM A29-20 Grade 4140 alloy steel. The end-pull is forged and the through hardened. The material is adequate for the application.
5. Hydrogen embrittlement did not play a role in the failure.

We recommend that:

1. The installation procedure should be strictly followed.
2. The turnbuckles should be tightened/adjusted only to achieve desired tension (A cable tension meter or dynamometer can be used for this purpose). Over-tightening should be avoided.
3. Turnbuckles with larger end-pull major diameter can be used to decrease stresses in the end-pulls.
4. The material of the turnbuckle can be further hardened to reduce wear damage on the end-pull. It should be noted that the hardness of the shackle material should be adjusted accordingly to avoid excessive wear damage on the shackle.

We trust that this report provides the information that you require. Please contact me if you require any further information, or if we can be of assistance in any other way.

Yours Sincerely,

Prepared By,

Yunlin Gao, M.Eng
Head of Failure Analysis and Metallurgical Engineering

Reviewed By,

Ethan (Erhan) Ulvan, PhD., P.Eng., FASM
Manager – Engineering, Laboratories, Nuclear and FES, Eastern Canada
Past President, Failure Analysis Society, American Society for Materials International

Revision 01: Conclusions and recommendations added; Explaination of technical terms added.

128-21-10ACU020-0002 R1 Failure analysis of a turnbuckle

Please note that unless we are notified in writing, samples from this investigation will be disposed of after 60 days.

Client acknowledges receipt and accepts custody of the report, work or other deliverable (the "Deliverable"). Client agrees that it is responsible for assuring that any standards or criteria identified in the Deliverable and Statement of Work ("SOW") are clear and understood. Client acknowledges that Acuren is providing the Deliverable according to the SOW and not other standards. Client acknowledges that it is responsible for the failure of any items inspected to meet standards, and for remediation. Client has 15 business days following the date Acuren provides the Deliverable to inspect, identify deficiencies in writing, and provide written rejection, or else the Deliverable is deemed accepted. The Deliverable and services are governed by the Master Services Agreement ("MSA") and SOW (including Job Sheet). If the parties have not entered into an MSA, then the Deliverable and services are governed by the Statement of Work and the "Acuren Standard Service Terms" (www.acuren.com/serviceterms) in effect when the services were ordered.

*The Client Representative who receives this report is responsible for verifying that any acceptance standard**s** listed in the report are correct, and promptly notifying Acuren of any issues with this report and/or the work summarized herein. The owner is responsible for notifying Acuren in writing if they would like their samples returned or placed into storage (at their cost) otherwise, all samples/specimens associated with this report will be disposed of 60 days after the report date.*

NOTES:

A) Any tests subcontracted to an approved subcontractor are highlighted above (*)
B) The Client will be notified if completion of test will exceed the time specified as a result of the volume of work or the complexity of the test
C) The Client should specify the standards used for testing/comparison purpose. We have a comprehensive library and online subscription of commonly used standards, however, we may ask the client to supply the standards if not common or the Client requests to purchase standard(s) on his behalf.
D) Please provide all the necessary information/documents (MSDS) pertaining to any Toxic / Dangerous materials prior to their arrival in the Laboratory.

MASKWA HIGH VOLTAGE LTD.

Maskwa High Voltage Ltd
1817- 10 Ave SW
Calgary, Alberta T3C0K2
www.maskwahv.com

nalcor energy

Cold Eyes Review

Failure Investigation Report; L3501/2 Tower and Conductor Damage

PERMIT TO PRACTICE
MASKWA HIGH VOLTAGE LTD.
RM SIGNATURE: [signature]
RM APEGA ID #: 28281
DATE: 2021/05/26
PERMIT NUMBER: P014883
The Association of Professional Engineers and Geoscientists of Alberta (APEGA)

PROFESSIONAL ENGINEER
OWEN C. PERRY
28281
ALBERTA
2021/05/26

Revision Author(s): Owen Perry, P. Eng.
Revision: A : 2021-May-26
Status: External Release
Approver: Owen Perry

Revision History

Rev.	Date	Author(s)	Review By	Approved	Comments
A	2021-05-22	OP	SC	OP	Issued for Client Review
1	2021-05-26	OP	SC	OP	Issued - Final
	Click here to enter a date.				

Table of Contents

1. Introduction and Scope

During the first week of January 2021, a freezing rain and precipitation event occurred in southeastern Labrador resulting in damage to three segments of L3501/02 between Muskrat Falls and Forteau. Both tower and conductor damage resulted. Due to the importance of this transmission facility, Nalcor undertook an investigation of the event to determine the root cause of the tower and conductor failures.

Maskwa High Voltage Ltd. (MHV) was requested by Nalcor Energy to review their preliminary report titled "Failure Investigation Report – L3501/2 Tower and Conductor Damage", (hereafter referred to as the Nalcor Report). This report summarized the results of the investigation into tower and conductor failures resulting from the heavy icing event.

Following an initial review of the draft report a meeting was arranged to discuss preliminary findings and questions on the original draft report on April 22, 2021. Following this meeting, and the receipt of other investigative reports, some revisions were made to the Nalcor Report and a second draft was issued for review along with newly received reports on material testing and failure investigation.

This brief report summarizes our findings and recommendations to date. Initial comments which have been addressed in the revised report are not reiterated herein.

2. Review of Reports

2.1 General Comments

The failure investigation report is very comprehensive and detailed in many areas. Other reports by external parties were also reviewed by MHV as part of this study:

- Failure Analysis of Electrode Cross Arm in Labrador Island Transmission Link (LITL) by EFLA, 2021/03/29;
- Icing Storm in Labrador in January 2021-Assessment of Icing in LITL by EFLA, 2021/04/14;
- Conductor Failures – LITL by EFLA, 2021/04/13;
- Metallurgical Failure Analysis of Suspension Tower Cross Arms by Kinectrics, 2021/05/13;
- Failure Analysis of a Conductor by ACUREN, 2021/04/12.

The technical investigation and data collection for this icing event has been extensive.

There were three primary areas of focus in the failure investigation reports:

- Conductor Failure
- Suspension Clamp Failure
- Tower Arm Failure.

Our summary of these report findings are noted in the following discussion.

2.2 Conductor Failure

The conductor failure analysis by Acuren was clear in its findings: "the conductor failed as a result of overloading". This is reasonable based upon the observations in the Nalcor report. We note the following:

- We understand that complete conductor failures occurred only in cluster 3, between structures 525 and 527. The transmission line in this area is on a rather steep downhill segment with structure 525 at the peak. Weight spans in this location would be unusually long under the icing conditions observed and would result in stress concentrations in the ahead spans of structure 525 (where the failures occurred).
- Although the Conductor Failures report by EFLA indicated that there may have been some fatigue failures in the conductor strands prior to ice loading, the ACUREN report refuted that conclusion after examination of the failed conductor. Regardless, there was evidence of failed strands at other locations which were attributed to either shock or fatigue failure.
- Component tests of the conductor by ACUREN did not indicate any defects or manufacturing issues which would significantly contribute to the observed conductor failures.

Initial findings in the Nalcor Report noted that an ice loading of about 16kg/m would be required to exceed the rated strength of the electrode conductor, yet only 11kg/m was estimated based upon the observations following the event. However, in comparing the approximate 80mm of radial ice measured on the electrode conductor at structure 527 along with an estimated density of 0.75 g/cc and a maximum wind speed of 40 km/hr (which was observed at some meteorological stations nearby either during or following the icing events) MHV computed applied loads higher than 16 kg/m.

If a SAPS (conductor finite element) analysis of the downhill section past structure 525 was performed, we believe it would further increase the conductor loads from those computed assuming level terrain.

2.3 Suspension Clamp Failure

The Nalcor report also focused on the suspension clamps on the electrode conductor observing that bolt torque in some suspensions which were checked were inconsistent (although they may have been altered during repairs conducted following the conductor and tower arm failures). We note the following:

- Slip tests (at least type tests) were probably performed on this hardware at the time of original line construction. Unfortunately, this information was not available at the time of this report to confirm the clamp's design sufficiency.
- The slip strength of any suspension clamp will not exceed the tensile strength of the ACSR conductor which it supports.
- Under severe longitudinal loads the suspension will pull from its vertical state and can bend or lock the conductor due to articulation limits of the assembly, increasing its local stresses. This does not appear to be an issue with the suspension used on the electrode conductor based upon photographs in the report. However, the pull can also initiate contact with insulators or suspension hardware. Evidence of this was observed at some locations where mechanical deformation of the outer conductor strands was recorded.

There was some discussion in the EFLA and Nalcor reports about the "split washer" use on the bolts for the suspension clamp retainers. Such configurations are widely used in North America with few reports of problems.

Slip strength is normally specified to avoid situations where moderate longitudinal load imbalances do not result in clamp slip which could damage the conductor. In this case longitudinal load imbalances were extreme resulting in the failure of the electrode support arms. In such a situation, slip failure is unsurprising and should be expected.

2.4 Tower Arm Failure

Tower arm designs were extensively examined in Nalcor's investigation, including use of a finite element model (FEM) to validate the electrode arm capacity under heavy longitudinal loads. This analysis closely replicated the failure modes observed in the field. The following was noted following review of the Nalcor report and the accompanying investigations:

- Failure of the electrode arms resulted from heavy longitudinal loads believed to exceed their design capability.
- Tests of the steel materials within sample failed arms did not indicate any deviations from the specified steel properties.
- Markings on the failed arms remained indicating construction torque testing of bolts.

There was nothing in this investigation which indicated deficiencies in the tower design or construction.

From the Nalcor report, we presumed that the longitudinal design conditions for the tower basically used a 70/30% or 70/100% distribution of ice load on the back/ahead spans to generate a longitudinal load situation for the design of the transmission structures. This appropriately models a situation with uneven ice accretion which is known to occur in hilly or mountainous terrain.

This approach is not uncommon, but it may not reflect a typical situation in Labrador. The layer of ice next to the conductor will often melt first due to conductor heating. When the accreted ice drops from the line, it usually clears the entire span, and the net result is a 0/100% ice distribution at the adjacent tangent structures. Such a model may more accurately reflect what was experienced here and it is likely that such loadings would exceed the design strength of the towers for the levels of ice accretion seen in this event.

3. Conclusions and Recommendations

3.1 Conclusions

1. Following our review of the Nalcor report and the previously listed investigation reports, we agree with its primary conclusion that failures were a direct consequence of ice and wind loads beyond the design capacity of the transmission line facility.
2. Slip strength of the suspension assemblies is being questioned, but under the loads known to occur we feel it is unlikely that their performance presented a problem. With the tower arm failures, high dynamic loads could have been experienced by these clamps, resulting in conductor slip or damage under conditions for which they were never designed.
3. No issues were evident with the towers or the tower design. They performed as expected under extreme loads.
4. The transmission line was appropriately designed for the known meteorological conditions at the time. The revised icing study suggests that the extreme ice loading experienced in this event may be more frequent than originally considered.

3.2 Recommendations

We support the recommendations contained in the Nalcor Report. In addition, we suggest the following for consideration:

1. The Nalcor Report discussed evidence of damper fatigue issues on this line. Due to the evidence of damper fatigue and failure – probably unrelated to this icing event – Nalcor should place a high priority on a vibration study of this line to reduce the likelihood of premature conductor replacement.
2. Heavy ice loading as experienced here often results in damage to stockbridge-style dampers. A priority should be placed on a patrol to assess their condition in the areas which experienced icing and replacing any which are "drooping". This should not be delayed pending completion of a vibration report.
3. If the icing conditions experienced during this event are more common than originally expected, enhanced patrols or remote monitoring stations could be considered to provide early warning of such an event so that activities can be undertaken to reduce the impact on the line.